Studying Turbulence Using Numerical Simulation Databases - IX

Proceedings of the 2002 Summer Program

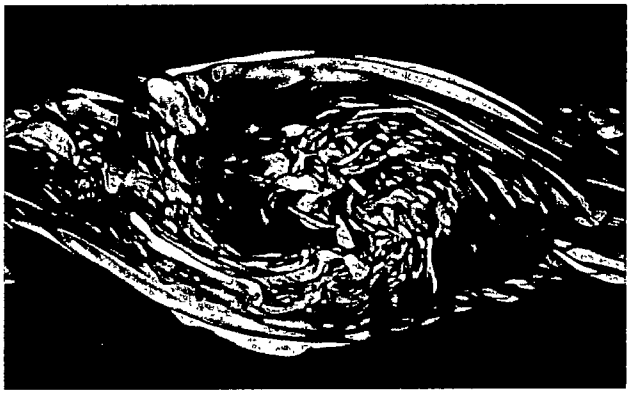

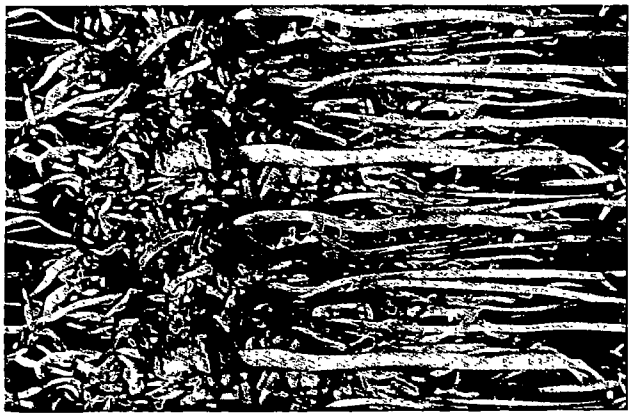

Center for Turbulence Research

December 2002

CONTENTS

Preface 1

I. Turbulent jet acoustics

Overview 3

An evaluation of LES for jet noise prediction. B. REMBOLD, J.B. FREUND and M. WANG 5

Turbulence interactions leading to far-field jet noise. J. B. FREUND, D.J. BODONY and S.K. LELE 15

Perturbation and adjoint analyses of flow-acoustic interactions in an unsteady 2D jet. L.I. CERVINO, T.R. BEWLEY, J.B. FREUND and S.K. LELE 27

II. RANS modeling

Overview 41

RANS calculations of secondary flow structures in ribbed ducts. A. OOI, B.A. PETTERSON REIF, G. IACCARINO and P.A. DURBIN 43

Modeling convection heat transfer and turbulence with fire applications: a high temperature vertical plate and methane fire. D. ROUSON, S.R. TIEZEN and G. EVANS 53

III. Large-eddy simulation

Overview 71

Evaluation of subgrid-scale models in terms of time correlations. G. HE, M. WANG and S.K. LELE 73

Large-eddy simulations with explicit equations for subgrid-scale quantities. D. CARATI and A. WRAY 79

Investigation of numerical error, subfilter-scale models, and subgrid-scale models in turbulent channel flow simulations. J. GULLBRAND and F. KATAPODES CHOW 87

Comparison of recent dynamic subgrid-scale models in the case of turbulent channel flow. H. JEANMART and G.W. WINCKELMANS 105

Tools for large-eddy simulation. D. CAUGHEY and G. JOTHIPRASAD 117

Toward optimal LES on unstructured meshes. A. HASELBACKER, R.D. MOSER, G. CONSTANTINESCU and K. MAHESH 129

IV. Large-eddy simulation numerics

Overview 141

Colocated finite-volume schemes for large-eddy simulation on unstructured meshes. S. BENHAMADOUCHE, K. MAHESH and G. CONSTANTINESCU 143

Discontinuous Galerkin methods for turbulence simulation. S. COLLIS 155

Toward the LES of flow past a submerged hydrofoil. A. PASCARELLI, G. IACCARINO and M. FATICA 169

V. Fundamentals

Overview 177

Characterization of near-wall turbulence in terms of equilibrium and periodic solutions. G. KAWAHARA, J. JIMENEZ, M. SHIBA AND M. SIEMENS 179

MHD turbulence in the presence of a strong magnetic field. S.C. KASSINOS, B. KNAEPEN and D. CARATI 191

Characteristics of scalar dispersion in turbulent-channel flow. J. DEL ALAMO and J. JIMENEZ 203

The turbulent flow over a permeable wall. W.P. BREUGEM and B.J. BOERSMA 215

Contrail formation in aircraft wakes using large eddy simulations. R. PAOLI, J. HELIE, T.J. POINSOT, and S. GHOSAL 229

VI. Stratified flows

Overview 243

Entrainment-zone restratification and flow structures in stratified shear turbulence. B. REIF, J. WERNE, O. ANDREASSEN, C. MEYER and M. DAVIS-MANSOUR 245

Waves in turbulent stably-stratified shear flow. F.G. JACOBITZ, M.M. ROGERS and J.H. FERZIGER 257

Adriatic simulations by DieCast. D. DIETRICH, G.F. CARNEVALE and P. ORLANDI 269

VII. Optimization

Overview 283

Optimization of aerodynamic and acoustic performance of supersonic civil transports. B. MOHAMMADI 285

Optimization of cylinder flow control via actuators with zero-net mass flux. P. CATALANO, M. WANG, G. IACCARINO, I. SBALZARINI, and P. KOUMOUTSAKOS 297

Machine learning for biological trajectory classification applications. I. SBALZARINI, J. THERIOT and P. KOUMOUTSAKOS 305

On the boundary condition for water at a hydrophobic dense surface. J.H. WALTHER, R.L. JAFFE, T. WERDER, T. HALCIOGLU and P. KOUMOUTSAKOS 317

VIII. Combustion

Overview 331

Large eddy simulation of turbulent combustion for gas turbines, with reduced chemistry. L. SELLE, G. LARTIGUE, T. POINSOT, P. KAUFMANN, W. KREBS and D. VEYNANTE 333

Non-reflecting boundary conditions for acoustic transfer matrix estimation with LES. W. POLIFKE and C. WALL 345

Large eddy simulation of pool fires with detailed chemistry using an unsteady flamelet model. R. RAWAT, H. PITSCH and J.F. RIPOLL 357

Lagrangian PDF mixing models for reacting flows. R. FOX, C. CHA and P. TROUILLET 369

Dynamics and dispersion in Eulerian-Eulerian DNS of two-phase flows. A. KAUFMANN, O. SIMONIN and J. HELIE 381

Analysis and modeling of the dispersion of vaporizing polydispersed sprays in turbulent flows. J. REVEILLON, M. MASSOT and C. PERA 393

Participants countries/institutions 405

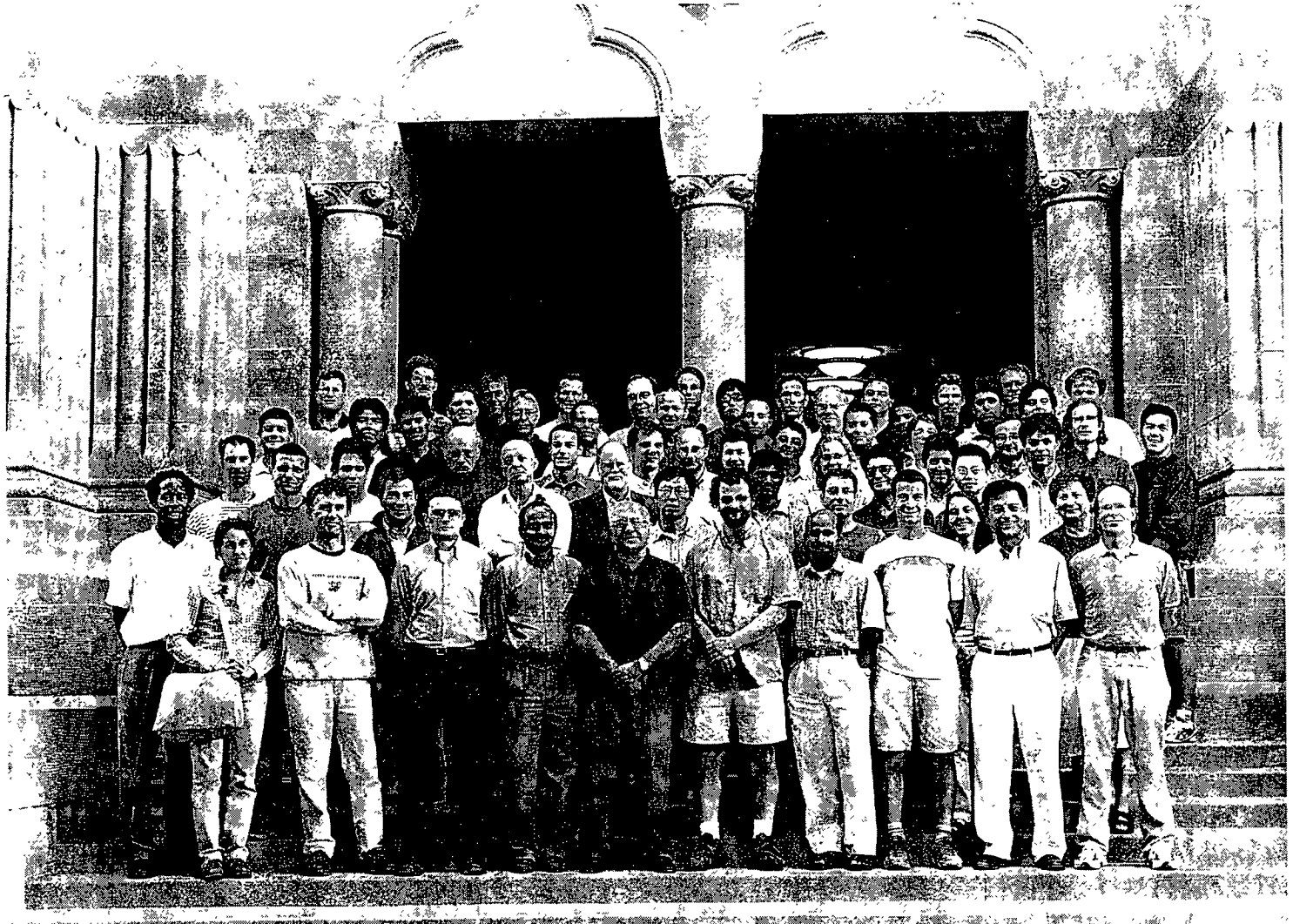

Preface

The ninth Summer Program of the Center for Turbulence Research was held during the period July 29th – August 23rd, 2002. The increase in number of participants, noted in the Preface to the Proceedings of the 2000 Program, continues: this year there were 50 participants from ten countries, and 30 hosts from Stanford and NASA-Ames.

This Proceedings volume contains 32 papers that span a wide range of topics and an enormous range of physical scales. The papers have been divided into seven groups: Acoustics, RANS modeling, Combustion, Large-eddy simulation (LES), LES Numerics, Stratified Flows, and Fundamentals, In several cases, a paper could have fitted in more than one group so the classification is somewhat arbitrary.

Combustion has been a topic of interest at CTR for many years. New advances are noted, with chemistry models increasing in realism as available computing power has increased. A related topic, essential to combustion of liquid fuels or pulverized solids, is the behavior of sprays. A newly appearing sub-grid stress model for mono-disperse particles is shown to be important. The paper by Selle *et al.* merits special attention because it demonstrates how the basic research work done at CTR over the years is now being applied to real-life problems, in this case, the burner of an existing gas-turbine combustor. Calculations were done using large-eddy simulation and a combustion model, on an unstructured grid fitted to this extremely complicated geometry. CTR's work on LES for combustors has attracted a great deal of attention from the leading companies in the gas turbine industry, because simpler methods of predicting turbulence, mixing and combustion are unable to deal satisfactorily with this very important problem, while direct numerical simulation of the exact Navier-Stokes equations (DNS) is impossibly expensive at full-scale Reynolds number.

In **aero-acoustics**, Large-eddy simulation is emerging as a cost-effective prediction technique, while DNS continues to be a powerful method for answering basic questions about noise production by turbulence that could not possibly be answered by experiments. Reynolds-averaged turbulence models in Navier-Stokes codes (**RANS**) provide the standard technique for turbulence prediction in industry. One of the papers in this group relates to traditional RANS-model calculations, and the other is a comparison of RANS, DNS and Detached-Eddy Simulation (DES, which treats regions near a solid surface by RANS and regions further from the surface, in particular separated regions, by LES).

Work on large-eddy simulation comprised a large part of the Summer Program activities, and in these Proceedings the papers on LES are divided into two sections. The first is on **Large-eddy Simulation** proper, with an emphasis on subgrid-scale modeling. Accurate subgrid-scale modeling near solid surfaces – or the development of alternative near-wall treatments –is a prerequisite for the application of LES to flows with separation. The papers in this group deal both with new concepts and with detailed analysis of existing ones. The **LES Numerics** group addressed worked on numerical issues for LES in complex geometries. New numerical schemes such as the discontinuous Galerkin method, and new computational paradigms are being introduced to build LES codes. This is another trend indicating that LES is moving out of the proof-of-concept stage, to become part of the application tools for engineering analysis.

The **Fundamentals** group is composed of papers that address specific issues. The wall modeling effort in this group is of particular importance for LES modeling as a practical engineering tool. NASA's increased interest in Earth Science is motivating CTR's renewed

attention to **Stratified Flows** and geophysical flows. Two of the papers in this section are on idealized flows; while the third presents a simulation of the flow in the Adriatic Sea. This last paper demonstrates one of the advantages of simulations; that one can, for heuristic purposes, add spurious terms to the equations or use artificial boundary conditions to test and improve understanding. In this case, the bathymetry of the Mid-Adriatic Pit is modified to demonstrate the cause of the current along its northern flank.

Optimization and the closely-related topic of airflow control are two important objectives in aerospace research. An outstanding demonstration of what can be achieved by applying optimization theory is the paper by Mohammadi on sonic boom minimization.

More detailed summaries of the accomplishments of each group can be found in the overviews that precede the grouped papers. This year four review tutorials were given: *Concepts for Analyzing the Structure of Complex Flows* (Julian Hunt), *LES on Unstructured meshes* (Krishnan Mahesh), *Computational Acoustics* (Sanjiva Lele), and *Turbulent Combustion* (Norbert Peters/Heinz Pitsch). The final presentation of research accomplishments on August 23rd was attended by a number of colleagues from universities, government agencies and industry. Early reports on some of the projects were presented at the Fifty-first Meeting of the Division of Fluid Dynamics of the American Physical Society in Dallas, TX, November 24th-26th, 2002.

We are grateful to Dr. Stavros Kassinos for his help with the final preparation of these Proceedings. Special thanks are due to Millie Chethik and Marlene Lomuljo-Bautista for their work on organizing the Program. Their help in the planning, operation and effective interface with the administrative requirements of Stanford University and NASA Ames Research Center are highly appreciated.

Parviz Moin
Nagi N. Mansour
Peter Bradshaw (editor)

This volume is available as a .pdf file on the Web at `http://ctr.stanford.edu`

Acoustics

Substantial reductions in jet noise have been made since the dawn of the jet age over 50 years ago, following for the most part the same simple approach: higher and higher bypass ratios. This reduces noise by reducing jet exit velocity, taking advantage of Lighthill's result that jet noise scales as a high power ("near the eighth") of the flow velocity. This was the first aeroacoustic theory and remains after 50 years the most effective theory for jet noise reduction. However, the gains it affords have been exploited to the utmost, and is unclear how to make further reductions. Trial-and-error experiments have shown that nozzle modifications can further reduce noise, but there is currently no predictive tool or modeling framework that can provide an engineer even the basic noise trends to expect for specific nozzle modifications. In light of this, our projects focused on key issues in jet noise physics, modeling, and prediction.

Large-eddy simulation is an attractive candidate for making jet noise predictions because it is the energetic scales, those that are resolved in a large-eddy simulation, that make most of the noise in a jet. However, early attempts suggest that the noise may be significantly more sensitive to the approximations made in large-eddy simulation than the standard flow quantities for which the large-eddy simulation was initially designed. Even in cases where the mean flow and basic turbulence statistics are well predicted, the predicted noise can be erroneous because it depends on subtle (quadrupole-like) cancellations. In this case, small errors made in the energetic flow field overwhelm the low energy sound field. Rembold, Freund, and Wang explored this directly by evaluating the far-field sound from a large-eddy simulation of a 5:1 aspect ratio rectangular jet, making a direct comparison to a corresponding direct numerical simulation. Results showed substantial errors especially in sideline and upstream directions, which has motivated an ongoing effort to identify their precise cause.

In the second project, Freund, Bodony, and Lele developed and implemented tools to quantify the turbulence interaction leading to jet noise. In a subsonic jet, most of the turbulence does not have a frequency-wavenumber makeup that allows it to radiate to the far acoustic field. In order to radiate, turbulence components must have supersonic phase velocity, which result from the growth, decay, and interactions of substantially convecting eddies. To quantify these dynamics, this group developed linearized equations for the very large turbulence scales, which are defined by a filter with a width greater than the integral scale of the turbulence but smaller than the wavelength of the dominant acoustic radiation. Using this formulation and tools they developed for analyzing the jet directly in wavenumber-frequency coordinates, they have initiated a study into the dynamics of these very large, radiation capable scales.

The third project examined flow-acoustic interactions in jets, which are important for statistical models of jet noise as well as for experimental identification of noise source location and spectral characterization. While it is widely accepted that the mean flow of a jet refracts some of the noise, the specific effect of the turbulence in scattering the noise, both in direction and frequency, is not understood. Cerviños, Bewley, Freund and Lele used a numerical solution of the adjoint flow equations to quantify the scattering of sound by the turbulence. The scattering of plane waves in the adjoint solution provides an adjoint Green's function for the unsteady jet flow. That is, this procedure gives the forward Green's function for the selected far field direction for all source points in the jet. A substantial broadening of the frequency spectrum was observed. Directivity will

be compared with a corresponding Green's function that accounts only for mean-flow refraction, to develop corrections for scattering by the turbulence.

John Freund

An evaluation of LES for jet noise prediction

By B. Rembold†, J. B. Freund‡ AND M. Wang

Large-eddy simulation (LES) is an attractive candidate for prediction of jet noise, since it resolves unsteady flow structures over a range of length scales, but it remains unclear how the subgrid-scale modeling affects its noise-prediction capability. The present study makes a direct evaluation of LES using the approximate deconvolution model against a corresponding direct numerical simulation (DNS) of a 5:1 aspect ratio rectangular jet at Mach 0.5. The DNS spectra and directivity are as anticipated for a low-Reynolds-number jet, and we compare these to LES predictions. We find that the LES spectra match the DNS ones at low frequencies, but the higher frequency portions are highly contaminated by spurious waves particularly at upstream angles. A correction for the subgrid-scale contribution to the Lighthill source terms based on approximate deconvolution of the velocities does not change the LES prediction.

1. Introduction

The success of efficient RANS models in fluids engineering has not extended to the prediction of noise, even when the only objective is to predict general trends, and it is not obvious how to improve their fidelity given the complexity of statistical noise sources. Since the inherent flow unsteadiness is the source of jet noise, LES is attractive for its prediction. The computation of flow induced noise has its unique difficulties, and several important issues arise when extending an established DNS capability, which of course is only applicable in the low-Reynolds-number limit (*e.g.* Freund 2001), to noise. With LES additional questions, such as the effects of subgrid-scale modeling and numerical errors, must be addressed.

LES can be most easily applied if the bulk of the noise, at least at frequencies of interest, comes from scales that are retained in the simulation, and do not have to be modeled. This is believed to be the case based on statistical analysis, and it seems that high-frequency noise does indeed come from the vicinity of the jet nozzle (Narayanan, Barber & Polak 2000). One objective of this study is to confirm that LES can predict the louder, lower-frequency noise. Another objective is to see if the subgrid-scale turbulence models directly affect the noise prediction. The subgrid-scale stress terms in the spatially filtered Navier-Stokes equations are closed by a model, which also appears as a noise source but is not necessarily accurate. Their effects on the resolved scales thus need to be evaluated. Discretization errors can also play a larger role in LES than in DNS since the spectra are typically truncated by the mesh at a much higher energy level, which is another potential problem for LES of jet noise. Thus, we also investigate a spurious generation of noise by numerical errors. A long-term objective is to correct this spurious effect.

To investigate these issues we use DNS results for a rectangular jet with Mach number

† Institute of Fluid Dynamics, ETH Zürich
‡ Department of Theoretical and Applied Mechanics, University of Illinois at Urbana-Champaign

0.5 and Reynolds number 2000 (based on theshorter dimension of the nozzle) rectangular jet (Rembold, Adams & Kleiser 2002). Rectangular jets are of current interest because in some cases they are quieter than their axisymmetric counterparts. They also have enhanced mixing properties (Grinstein 2001), which is important in some military applications. A previous LES study by Rembold, Adams & Kleiser (2001) using the approximate deconvolution subgrid-scale model (Stolz & Adams 1999, Stolz, Adams & Kleiser 2001) showed turbulence statistics in agreement with the DNS in the transition region, but the jet's noise was not computed. In this study we use Lighthill's theory to compute the far-field noise, and compare the noise predicted using the DNS and LES source terms. Our formulation of Lighthill's theory is outlined in section 2. Section 3 covers the results from the DNS database, and comparisons between LES and DNS are made in section 4.

2. Far-field sound computation

Lighthill's equation reads

$$\frac{\partial^2 \rho}{\partial t^2} - c_0^2 \frac{\partial^2 \rho}{\partial x_i \partial x_i} = \frac{\partial^2 T_{ij}}{\partial x_i \partial x_j} \quad , \tag{2.1}$$

with

$$T_{ij}(\mathbf{x}, t) = \rho u_i u_j + \delta_{ij}\{p - p_0 - c_0^2(\rho - \rho_0)\} - \tau_{ij}. \tag{2.2}$$

Here $\tau_{ij} = \mu\left(\frac{\partial u_i}{\partial x_j} + \frac{\partial u_j}{\partial x_i} - \frac{2}{3}\delta_{ij}\frac{\partial u_k}{\partial x_k}\right)$ is the viscous stress tensor. Taking $\frac{\partial^2 T_{ij}}{\partial x_i \partial x_j}$ as the equivalent noise source, the far-field sound at point $\mathbf{x}$ is evaluated using the free space Green's function and the divergence theorem as

$$\rho(\mathbf{x}, t) = \frac{1}{4\pi c_0^4} \int_V \frac{R_i R_j}{R^3} \frac{\partial^2}{\partial t^2} T_{ij}(\mathbf{y}, t - \frac{R}{c_0})\, \mathrm{d}\mathbf{y}, \tag{2.3}$$

where $R = |\mathbf{x} - \mathbf{y}|$ and $R_i = x_i - y_i$. Evaluation is simplified by reformulating (2.3) in frequency space in dimensionless form, as

$$\rho(\mathbf{x}, \omega) = \frac{M^4}{4\pi} \int_V \frac{R_i R_j}{R^3} \omega^2 T_{ij}(\mathbf{y}, \omega) e^{-iMR\omega} \mathrm{d}\mathbf{y}, \tag{2.4}$$

since this avoids the interpolation needed to compute retarded times in (2.3). Both formulations correctly represent the quadrupole nature of the source, and have been shown to facilitate an accurate numerical evaluation (Bastin, Lafon & Candel 1997). The variables are non-dimensionalized using jet exit quantities and $L_1/2$ defined in figure 1. In evaluating (2.4) we neglect τ_{ij} which is typically small (Goldstein 1976). The second term in the tensor is also small in nearly-isentropic flow, and so is also expected to be small here. Thus for the present analysis we retain only $\rho u_i u_j$ in the source tensor.

3. DNS results

3.1. *Database description*

The coordinate system and a visualization of the jet simulation are shown in figures 1 and 2, respectively. Relevant physical and computational parameters are listed in table 1. A high-order compact finite-difference algorithm was used to solve the compressible Navier-Stokes equations in Cartesian coordinates; it iss fully discussed by Rembold *et al.* (2002).

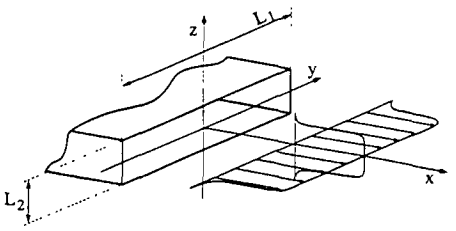

FIGURE 1. Inflow profile and coordinate system

FIGURE 2. Flow topology visualized by density isosurface

L_1/L_2	5
$Re_{L_{1/2,j}}$	5000
M_j	0.5
T_∞/T_j	0.936143
Strouhal Number ($= L_1\pi f/u_j$)	2.7066
grid (x, y, z)	$337 \times 229 \times 229$
box	$(15 \times 14 \times 14)\, L_1/2$
computational time	78.8
time samples used	552
average sampling interval	0.1435

TABLE 1. Parameters of the jet DNS database. The subscript j denotes jet-center quantities. Unless noted, quantities are non-dimensionalized by ρ_j, u_j, and $L_1/2$.

A smoothed laminar top-hat velocity profile, as suggested by Yu & Monkewitz (1990),

$$u(\eta,\zeta) = \frac{1}{(1+\sinh[|\eta|\sinh^{-1}(1)]^{2n_1})\,(1+\sinh[|\zeta|\sinh^{-1}(1)]^{2n_2})} \tag{3.1}$$

defined the inflow, where η and ζ are the cross-stream coordinates normalized by the corresponding velocity half-width $L_i/2$, $i = 1, 2$. The parameters $n_1 = 9$ and $n_2 = n_1 L_2/L_1$ gave a common vorticity thicknesses $\delta = \delta_i = L_i/[\sqrt{2}\, n_i \sinh^{-1}(1)]$ in both directions. A linearly-unstable eigenmode was superimposed on this inflow at $St = 2.7066$ in order to trigger transition.

A total of 552 samples in time (dimensionless time interval 78.8) of the full DNS fields were used to compute the sound sources. This set was subdivided into sub-intervals of five overlapping sets of 192 samples each. The Lighthill stress tensor was computed in each interval, and time transformed using a discrete Fourier transform. The samples were windowed in time using a function constructed from a half-period of a cosine function, which ramped the signal smoothly to zero over 50 samples at the beginning and end of each window to reduce spurious high frequencies introduced by the finite sample length. Figure 3 shows a windowed fluctuation pressure signal at $y = z = 0$, $x = 6.2$. The data was unfortunately stored at non-equidistant intervals, but the change of the interval length was less than one percent, and the associated error in the evaluation of Fourier sums was shown to have negligible consequence for the frequencies of interest.

The far-field sound spectra were obtained by numerical evaluation of (2.4) using trapezoidal rule quadrature. The source term T_{ij} goes to zero at large y and z and at the inflow boundary, which allows integrating all the way to the domain boundaries. At the outflow

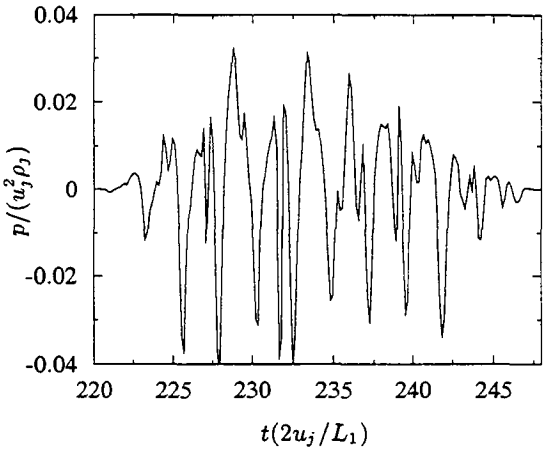

FIGURE 3. Pressure fluctuation signal at sensor point on the jet-center-axis in the transition region of the DNS field.

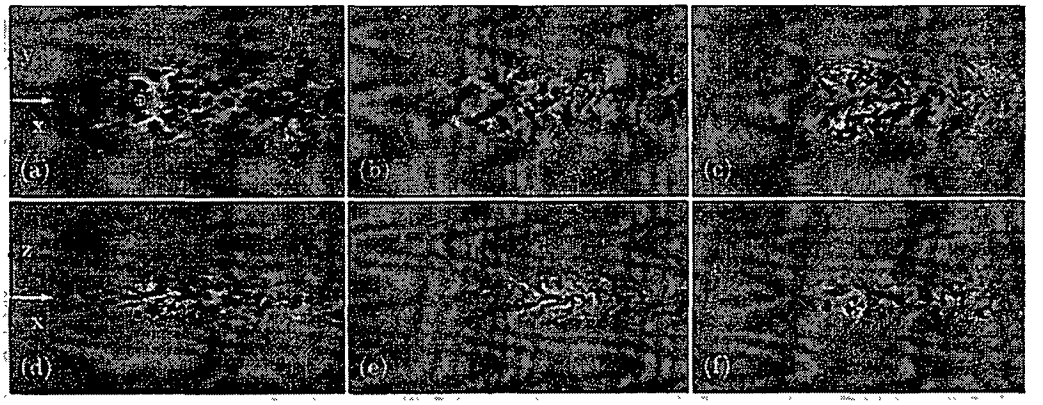

FIGURE 4. Instantaneous contours of T_{11} (a,d), T_{12} (b,e) and T_{13} (c,f) in the major (a-c) and minor (d-f) jet-plane, $\oplus$ origin of the far-field arcs.

boundary it is also small compared to its size in the transition area, though not zero since turbulent structures leave the domain. We therefore smoothly ramped down the source terms close to the outflow boundary in order to avoid affecting the volume integral by leaving sources. It was found that the influence on the particular form of the smoothing function is weak and therefore the same window function as in time was applied.

3.2. *Acoustic analysis*

In order to visualize the location and structure of the sound sources we plot in figure 4 contours of the dominant source tensor components T_{11}, T_{12}, T_{13} in the two jet-center planes. Here the flow is from left to right and in streamwise direction the entire physical domain is shown. In the lateral directions only the part with significant source terms is shown. From this visualization we see that the maximum source terms are obtained at

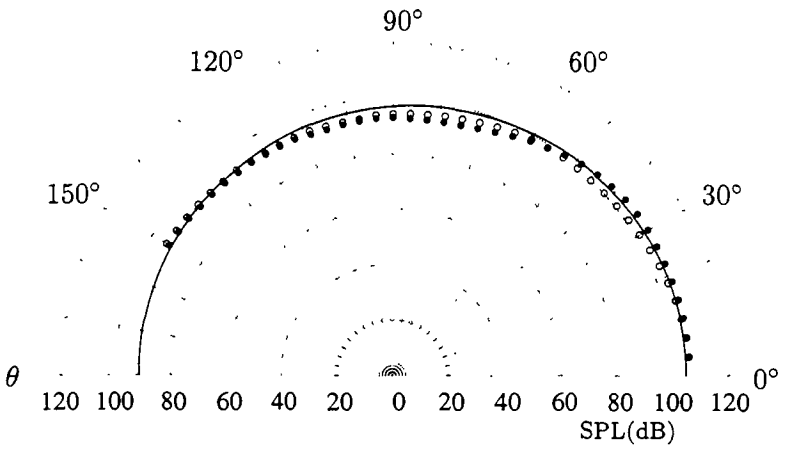

FIGURE 5. Sound pressure level along an arc of radius $60L_1/2$ around the transition area in the major ○ and minor • jet-planes; expected Doppler-scaling ——— .

the edges of the jet around the location where the potential core closes. The location of the peak of the source does not necessarily coincide with the virtual origin of the radiated sound, since most of the components do not radiate to the far-field. This was shown by Freund (2001), who actually filtered the source terms in order to only obtain the radiating components. However, it does give the indication that the dominant noise producing structures are located in the transitioning shear layers. Far-field spectra and intensities were computed on two arcs in the $y = 0$ and $z = 0$ planes at a radius of $60L_1/2$ and with angle θ measured from the downstream axis. The center of the arcs $x = 5, y = 0, z = 0$ is labeled in figure 4 (a). In figure 5 the radiated sound-pressure-level, $SPL = 10\log_{10}(p'^2/p_{ref}^2)$, is plotted for the two arcs, taking the standard dimensional reference condition $p_{ref} = 2 \times 10^{-5} Pa$. The anticipated directivity based on a Doppler scaling

$$SPL \sim \frac{1}{(1 - M_c cos(\theta))^5} \tag{3.2}$$

with assumed convective Mach number $M_c = 0.6M$ is also plotted.

We observe a directivity of the jet peaking near $\theta = 35°$. At this angle, the SPL in the major jet-plane is 5dB lower than that in the minor jet-plane. This effect is reversed at $\theta = 75°$. This trend is consistent with experiments of non-axisymmetric jets which typically show that noise is more directive in the minor plane (Kinzie & McLaughlin 1999), although we note that these observations are for supersonic jets. The overall directivity matches well with the expected directivity for uniformly moving sound sources.

Figure 6 shows noise spectra, $(pp^*)^{\frac{1}{2}}/\rho_j u_j^2$, at six angles for each of the two arcs. The spectra are highly peaked, as expected for a forced low-Reynolds-number jet. At $\theta = 5°$, the two spectra nearly coincide, which is not surprising since the observation points are very close at low angles to the jet. For $\theta = 30°$, the spectrum in the minor plane is slightly higher at most frequencies. By $\theta = 150°$, the spectra are flatter and now not dominated by the forced instability frequency. We observe a slight increase of the far-field spectrum at the high frequency end in this case, which is unphysical. This

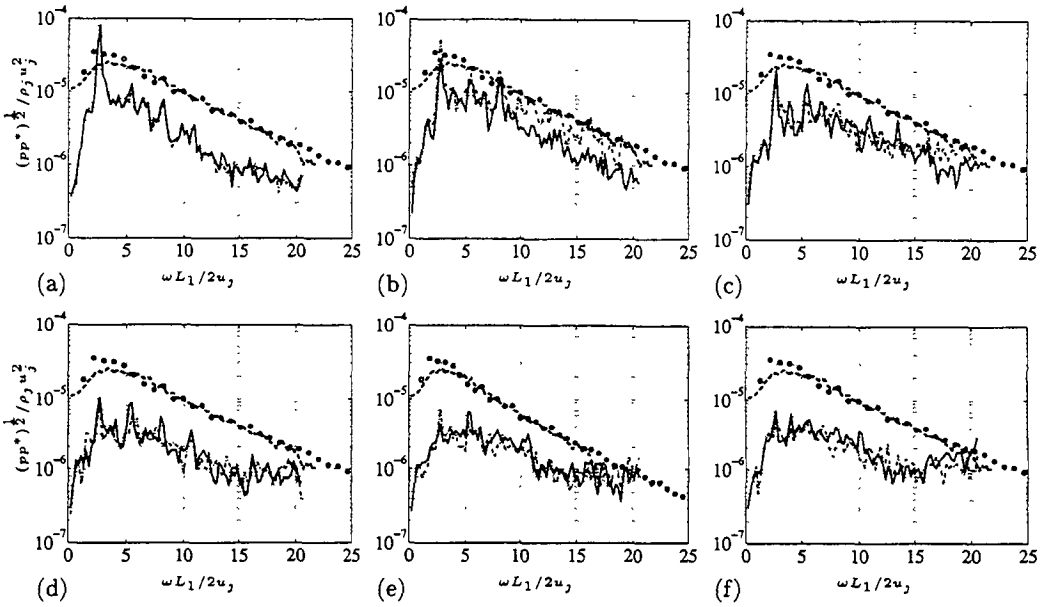

FIGURE 6. Far-field spectra for different θ ($\langle\langle\rangle\cdot\rangle^*$ denoted complex conjugate quantities). θ = (a) 5°, (b) 30°, (c) 60°, (d) 90°, (e) 120°, (f) 150°, on the arc at radius $60L_1/2$ in the major ——— and minor —·— jet-planes. Also plotted are the spectra from a round jet DNS (Freund 2001) ○ and experiments of Stromberg *et al.* (1980) - - - - at $\theta = 30$ degrees.

might be caused by the non-equidistant time steps which was neglected in the sound analysis and is being investigated further. For comparison we also plot for all angles the far-field spectrum (arbitrary units) of the DNS data of Freund (2001) and experiments of Stromberg, McLaughlin & Troutt (1980) at an angle of 30 degrees. If the Strouhal number is scaled such that L_2 corresponds to the jet diameter, the drop-off in the spectra matches the present data.

4. LES results

4.1. *LES database*

The physical parameters of the LES match the DNS. The flow was computed using the approximate deconvolution model, as described in Stolz *et al.* (2001) and Rembold *et al.* (2001) on a $141 \times 77 \times 77$ mesh, which corresponds to one-third the DNS mesh in each direction. We found, however, it necessary to increase the size of the downstream absorbing "sponge" layer over that used in the DNS to suppress reflections from the outflow plane (streamwise thickness of the sponge in DNS is $1.6L_1/2$, compared with $4.8L_1/2$ in LES). The simulation parameters are listed in table 2. Note that for the LES we used constant time steps, and the temporal sampling rate was approximately 1.5 times that of the DNS. Temporal windowing of the same form as for the DNS was applied to the entire data set. In figure 7 we show the analogous pressure-fluctuation signal at a sensor point in the transition region of the jet with the temporal window function

grid (x, y, z)	$141 \times 77 \times 77$
box	$(18 \times 14 \times 14)\, L_1/2$
computational time	90
samples used	1000
sampling interval	0.09

TABLE 2. Parameters of the jet LES database.

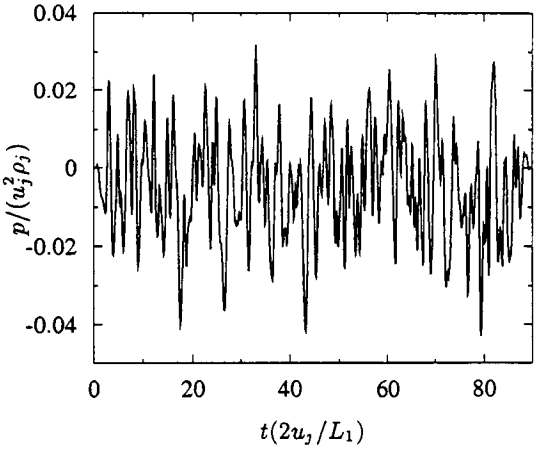

FIGURE 7. Pressure fluctuation signal at sensor point on the jet-center-axis in the transition region of the LES field.

applied. Instead of ensemble-averaging over several sub-samples, spectral binning, which like windowing is a rigorous means of reducing variance, was applied to smooth the spectra. A bin width of $\Delta\omega = 0.35$ was used. The spectra and far-field sound were computed in exactly the same way as for the DNS.

4.2. *Acoustic analysis*

Naturally, in LES only filtered quantities are directly available for computation of the Lighthill source, although deconvolution potentially offers a means of correcting this. In the approximate deconvolution model, an approximate inverse of the filter is used to partially recover unfiltered data, which is then used to model subgrid-scale effects on the filtered flow field, $\overline{\mathbf{u}}^{\mathbf{G}}$. The overbar denotes filtered quantities and the superscript G is used for represented quantities on the LES grid. We define $\mathbf{u}^\star$ as our best approximation for the unfiltered field. Stolz *et al.* (2001) and Rembold *et al.* (2001) discussed this in detail and showed that this approach is effective for flow simulations. Thus, it is tempting to ask whether parts of the sound spectrum can also be recovered in an LES.

The source tensor T_{ij} can be decomposed into a part that can be represented on the LES grid (T_{ij}^G) and a part that cannot (T_{ij}^{SG}), just as the velocity field $\mathbf{u}$ is decomposed into a filtered field represented on the grid $\overline{\mathbf{u}}^G$ plus two error terms:

$$T_{ij} = T_{ij}^G(\mathbf{u}) + \underbrace{T_{ij}^{SG}(\mathbf{u})}_{\text{modeled}}, \quad \mathbf{u} = \underbrace{\overline{\mathbf{u}}^G + (\mathbf{u}^G - \overline{\mathbf{u}}^G)}_{\approx \mathbf{u}^\star} + (\mathbf{u} - \mathbf{u}^{\mathbf{G}})$$

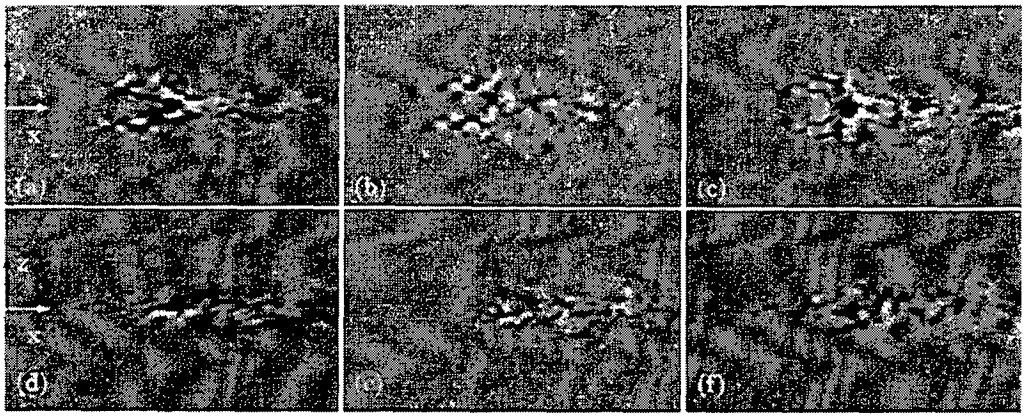

FIGURE 8. Instantaneous contours of T_{11} (a,d), T_{12} (b,e) and T_{13} (c,f) in the major (a-c) and minor (d-f) jet-planes from the LES database, $\oplus$ origin of the far-field arcs.

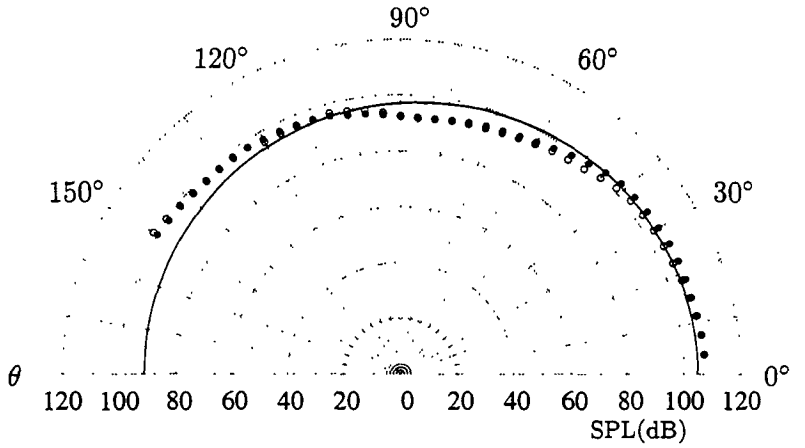

FIGURE 9. Sound pressure level along an arc in the major ○ and minor ● jet-plane of radius $60L_1/2$ around the transition area; expected Doppler-scaling ——— .

We used a five-point explicit filter in computational space with two vanishing moments in physical space. The source tensor components beyond the grid cutoff $T_{ij}^{SG}(\mathbf{u})$ cannot be recovered and must be modeled. These are not considered here. The represented part of the tensor $T_{ij}^{G}(\mathbf{u})$ is a function of $\mathbf{u}$ but can be evaluated in LES only from the filtered field $\overline{\mathbf{u}}^G$. Seror *et al.* (2001) have shown that the acoustic spectra computed from incompressible homogeneous isotropic turbulence can be improved when the Lighthill stress tensor, based on resolved velocities, is supplemented by the subgrid-scale contribution. In the present study we investigated whether the far-field spectral prediction can be improved when $\overline{\mathbf{u}}^G$ is replaced by $\mathbf{u}^\star \approx \mathbf{u}^G$, as is done for the flow computation. First, we computed the far-field sound using $T_{ij}^{G}(\overline{\mathbf{u}}^G)$ and then compared it with the prediction using deconvolved quantities $T_{ij}^{G}(\mathbf{u}^\star)$. The difference is found to be insignificant, as will

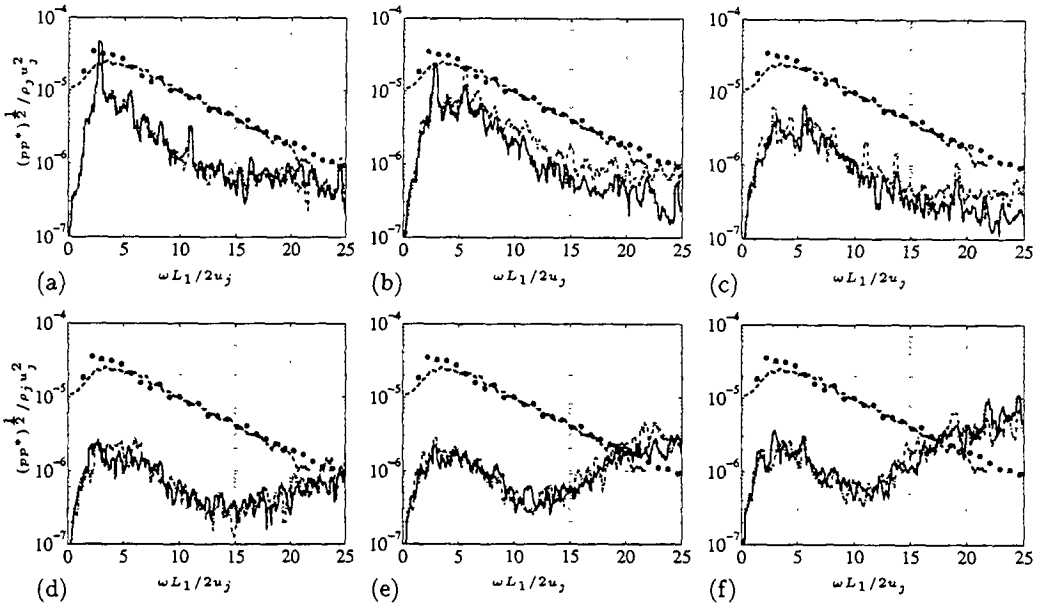

FIGURE 10. Far-field spectra at for the (a) 5°, (b) 30°, (c) 60°, (d) 90°, (e) 120°, (f) 150°, for the arc at radius $60L_1/2$ in the major ——— and minor —·— jet-plane. Spectra for a round jet of the DNS of Freund ○ and experiments of Stromberg *et al.* (1980) – – – – at an angle of 30 degrees.

be discussed later. The following results are based on the first formulation of the source term.

The instantaneous source distribution, plotted in figure 8, is seen to be very similar to the distribution in the DNS case (see figure 4) with maximum values at the edges of the jet. Quantitative analysis in the far-field, however, reveals significant discrepancies between the DNS far-field and the LES data (see figures 5 vs. 9). Whereas the directivity in the main radiation direction (at angles around 30 degrees) is well recovered, we observe spurious radiation of the LES jet at higher angles. The far-field spectra show that the spurious noise is at high frequencies, where a rapid increase in the acoustic intensity in the far-field is found, particularly at high angles. For reference the data of Freund (2001) and Stromberg *et al.* (1980) at $\theta = 30$ degrees are again plotted. Careful examination of the origin of these spurious waves is needed and ways to suppress them have to be found.

The same analysis was repeated with the source tensor based on the deconvolved velocities to include the subgrid-scale contribution. We found no significant difference between the results using the two source formulations. At this point it is not clear whether the subgrid-scale contribution is indeed small or is overwhelmed by numerical errors. In order to reliably predict the sound radiation from LES calculations and study the subgrid-scale modeling effects, the source of these spurious waves first needs to be identified and eradicated.

5. Conclusions

We have computed the far-field sound of a Mach 0.5 low-Reynolds-number rectangular jet using a DNS database and Lighthill's acoustic analogy in frequency space, and analyzed the sound pressure level and the frequency spectra along two arcs in the major and minor jet planes. The directivity is found to match the theoretical prediction and the spectra show characteristics similar to comparable data in the literature. In a second step we performed an LES of the same flow using $1/3^3$ the DNS mesh size and again computed the sound. We found that the low frequency part of the far-field spectra is well reproduced by the LES using source formulations based on both the filtered velocities and the approximately deconvolved velocities. However, spurious waves from the LES data resulted in an unphysical increase of the spectral level at higher frequencies, and no subgrid-scale contribution has been observed. For reliable prediction of the far-field sound with compressible LES this spurious effect has to be analyzed further.

REFERENCES

BASTIN, F., LAFON, P. & CANDEL, S. 1997 Computation of jet mixing noise due to coherent structures: the plane jet case. *J. Fluid Mech.* **335**, 261–304.

FREUND, J. B. 2001 Noise sources in a low-Reynolds-number turbulent jet at Mach 0.9. *J. Fluid Mech.* **438**, 277–305.

GOLDSTEIN, M. E. 1976 *Aeroacoustics*. McGraw-Hill, New York.

GRINSTEIN, F. F. 2001 Vortex dynamics and entrainment in rectangular free jets. *J. Fluid Mech.* **437**, 69–101.

KINZIE, K. W. & MCLAUGHLIN, D. K. 1999 Aeroacoustic properties of supersonic elliptic jets. *J. Fluid Mech.* **395**, 1–28.

NARAYANAN, S., BARBER, T. & POLAK, D. 2000 High subsonic jet experiments. Part II: Turbulence and noise generation studies. *AIAA Paper* 2000-2023.

REMBOLD, B., ADAMS, N. A. & KLEISER, L. 2001 Direct and large-eddy simulation of a transitional rectangular jet. In *Direct and Large-Eddy Simulation IV* (B. J. Geurts, R. Friedrich & O. Métais, eds.), pp. 197–204. Kluwer, Dordrecht.

REMBOLD, B., ADAMS, N. A. & KLEISER, L. 2002 Direct numerical simulation of a transitional rectangular jet. *Int. J. Heat and Fluid Flow* **23**, 547–553.

SEROR, C., SAGAUT, P., BAILLY, C. & JUVÉ, D. 2001 On the radiated noise computed by large-eddy simulation. *Phys. Fluids* **13**, 476–487.

STOLZ, S. & ADAMS, N. A. 1999 An approximate deconvolution procedure for large-eddy simulation. *Phys. Fluids* **11**, 1699–1701.

STOLZ, S., ADAMS, N. A. & KLEISER, L. 2001 The approximate deconvolution model for LES of compressible flows and its application to shock-turbulent-boundary-layer interaction. *Phys. Fluids* **13**, 2985–3001.

STROMBERG, J. L., MCLAUGHLIN, D. K. & TROUTT, T. R. 1980 Flow field and acoustic properties of a Mach number 0.9 jet at a low Reynolds number. *J. Sound Vibr.* **72**, 159–176.

YU, M.-H. & MONKEWITZ, P. A. 1990 The effect on nonuniform density on the absolute instability of two-dimensional inertial jets and wakes. *Phys. Fluids* **A2**, 1175–1181.

Turbulence interactions leading to far-field jet noise

By J. B. Freund,† D. J. Bodony‡ AND S. K. Lele¶

It is well understood that it is the development, not just the convection, of jet turbulence that generates fluctuations with supersonic phase velocities which radiate noise to the far acoustic field, but the mechanisms causing this mode conversion are not understood. The relative efficiency of the interactions of turbulence with the mean flow and the turbulence 'self' interactions has not been quantified. In light of this, tools are developed here to analyze the process of mode conversion (scattering of flow energy into acoustic energy) in a jet. Very large scales, with typical lengthscale between the turbulent integral length and the dominant acoustic wavelength, are thought to be capable of radiating to the far-field. Inhomogeneous linearized filtered equations for the very large scale dynamics are derived and presented. The resulting source terms are computed from a well validated DNS database, which also provides an 'ideal' subgrid-scale model for their evolution. A capability to analyze the mode conversion in streamwise frequency-wavenumber coordinates is also developed and discussed.

1. Introduction

It is widely understood that the frequency-wavenumber makeup of the turbulence in a subsonic jet is such that most of the turbulence energy does not radiate to the far-field (Ffowcs Williams 1963; Crighton 1975). Most of the energy manifests itself as evanescent near-field disturbances, which are in essence the hydrodynamic pressure fluctuations associated with the jet turbulence. Only components with supersonic phase velocity in the streamwise direction, or more specifically sonic phase velocity in the direction of radiation, are heard away from a jet. Since the flow, and the eddies in it, move at subsonic speed for a subsonic or moderately supersonic jet, it must be the evolution of the turbulence as it moves that puts energy into radiation capable modes.

A question naturally follows from this discussion: what interactions convert the great portion of the turbulence energy which cannot radiate noise into modes that can radiate? There are nominally two possible mechanisms: (i) the nonlinear interactions of the energetic turbulent eddies in the flow; or (ii) the linear interaction of the energetic motions with the background mean. At a particular frequency ω, it is only the longest wavelength (lowest streamwise wavenumber k_x) components that can have a supersonic phase velocity, $C_{\rm ph} = \omega/k_x > a_\infty$, where a_∞ is the ambient speed of sound. So the question can be posed more definitively in terms of how autonomous are the lowest-frequency modes in the jet. If the radiation dynamics of these very large scales are primarily interactions with the mean flow, this is the dominant interaction leading to radiation. However, if the smaller but energetic scales play a substantial role in the dynamics of these very

† Theoretical and Applied Mechanics, University of Illinois at Urbana-Champaign
‡ Aeronautics and Astronautics, Stanford University
¶ Mechanical Engineering and Aeronautics and Astronautics, Stanford University

large scales, then it will be clear that turbulence interactions are more important. The distinction of these mechanisms is inherent in the discussions of Goldstein (1984).

In this report we present a preliminary investigation of the modal interactions that lead to noise radiation. We do not address this question expecting to identify any particular interaction that "makes the noise." Instead, we apply a filter in physical coordinates to jet-noise simulation data, to define the very large modes. This decomposition is in turn used to see how the mean flow and the energetic turbulent scales affect the dynamics of these very large scales. Spectral analysis is used to diagnose the wavenumber-frequency makeup of different components.

The following section introduces a decomposition of the field variables into a very large scale portion and an energetic scale portion. This procedure is analogous to that of large eddy simulation, except that a substantially more restrictive filter is applied and there is an additional step of linearizing the equations about the mean flow. In section 3 we introduce the simulation database that will be used for this analysis. Section 4 illustrates the complexity of the interactions in wave space that lead to radiation capable modes by direct evaluation of convolutions in frequency-wavenumber coordinates (k,ω) that correspond to certain multiplications appearing in the flow equations. In section 5, we define and apply a low-wavenumber filter to the simulation flow fields. Its effect will be shown both qualitatively in physical coordinates with visualizations and quantitatively in k–ω coordinates. In section 6, we show some preliminary results for the evolution of the very large scales, using an ideal subgrid-scale model derived from the direct numerical simulation database. Section 7 summarizes our results and discusses the future direction of this on-going project.

2. Evolution equations for the very large scales

For a filter defined in general as

$$\tilde{q} = \int G(\mathbf{x}-\mathbf{x}')q(\mathbf{x}')\,d\mathbf{x}, \tag{2.1}$$

equations for the very-large-scale components of flow quantities, designated as $q^{(L)}$, are derived from the compressible-flow equations by following the standard procedure used for large-eddy simulation, with an additional step of linearizing about the mean flow, which is denoted as $\bar{q}$. This procedure yields

$$\frac{\partial}{\partial t}\rho^{(L)} + \frac{\partial}{\partial x_j}\left(\overline{\rho}u_j^{(L)} + \rho^{(L)}\overline{u}_j\right) = \frac{\partial}{\partial x_j}\left(\widetilde{\rho u}_j - \widetilde{\rho}\widetilde{u}_j\right) \tag{2.2}$$

$$\begin{aligned}\frac{\partial}{\partial t}\left(\overline{\rho}u_i^{(L)} + \rho^{(L)}\overline{u}_i\right) + \frac{\partial}{\partial x_j}\left(\overline{\rho}\,\overline{u}_i u_j^{(L)} + \overline{\rho}u_i^{(L)}\overline{u}_j + \rho^{(L)}\overline{u}_i\overline{u}_j + p^{(L)}\delta_{ij}\right)\\ = \frac{\partial}{\partial t}\left(\widetilde{\rho u}_j - \widetilde{\rho}\widetilde{u}_j\right) + \frac{\partial}{\partial x_j}\left(\widetilde{\rho u}_i\widetilde{u}_j - \widetilde{\rho u_i u_j}\right)\end{aligned} \tag{2.3}$$

$$\begin{aligned}\frac{\partial}{\partial t}\left(\overline{\rho}E^{(L)} + \rho^{(L)}\overline{E}\right) + \frac{\partial}{\partial x_j}\left(\left[\overline{\rho}\overline{E} + \overline{p}\right]u_j^{(L)} + \left[\rho^{(L)}\overline{E} + \overline{\rho}E^{(L)} + p^{(L)}\right]\overline{u}_j\right)\\ = \frac{\partial}{\partial t}\left(\widetilde{\rho E} - \widetilde{\rho}\widetilde{E}\right) + \frac{\partial}{\partial x_j}\left(\left[\widetilde{\rho E} + \widetilde{p}\right]\widetilde{u}_j - \left(\widetilde{\rho E u_j} + \widetilde{p u_j}\right)\right),\end{aligned} \tag{2.4}$$

with familiar 'subgrid-scale' terms appearing right of the equal sign. However, despite this similarity, these equations will be use as a diagnostic tool rather than predictive simulation tool. The missing subgrid-scale terms will be computed directly from a direct numerical solution database, thus providing an ideal turbulence model. The relatively importance of these scales and the interactions of the retained very large scales with the mean flow will be quantified.

3. Simulation database

The database we used was for a circular jet with Mach 0.9, Reynolds number 3600and constant stagnation temperature $T_j/T_\infty = 0.86$ reported in detail by Freund (2001). It was validated extensively against the corresponding experiments of Stromberg et al. (1980) and also matches turbulence statistics and mean-flow spreading rates of jets at much higher Reynolds number (Hussein et al. 1994; Panchapakesan and Lumley 1993). The mesh had $640 \times 250 \times 160$ points in the axial x, radial r, and azimuthal θ (angular) coordinates. The physical portion of the simulation domain extended $31r_o$ downstream and was surrounded by a non-physical buffer zone to absorb outgoing disturbances (Freund 2001). During the course of the entire simulation, data for all five conservative flow variables were saved every 20 numerical time steps on every other mesh point. This has been found sufficient to reconstruct nearly all relevant statistics of the turbulence and the sound field. There are 2333 such fields in all, though typically only 2304 of these are used when doing frequency analysis to facilitate fast Fourier transforms.

4. Analysis in frequency-wavenumber coordinates

4.1. *The space-time transform*

Since the wavenumber-frequency make up of the data is tied closely to its characterization as a noise source, it is instructive to transform the simulation results in both space and time and examine their structure. This is computationally challenging because it involves manipulation of the entire time resolved, three-dimensional database. Even with data saved only at every other mesh point, it involves five flow variables at over 5 billion space-time points. For this reason, the transform, which is straightforward to write analytically, is challenging to implement. The procedure for transforming the data was first developed and applied to the pressure alone (Freund 2001), but has been modified somewhat in the present study.

Each flow variable q is first transformed azimuthally as

$$\tilde{q}_n(x,r,t) = \frac{1}{N_\theta} \sum_{k=0}^{N_\theta-1} q(x,r,\theta_k,t) e^{in\theta_n} \qquad n = -N_{n_{\max}}, \ldots, -N_{n_{\max}}, \tag{4.1}$$

where $N_{n_{\max}}$ is the maximum mode number that we retain. Fortunately, the sound from this jet is dominated by the lowest azimuthal modes (Freund 1999; Freund and Colonius 2002) so we have taken $N_{n_{\max}} = 6$ in this current study.

Next, the data are interpolated onto a uniform mesh in x with $N_x = 640$ points and then padded with zeros out to $N_{xp} = 8N_x$ to minimize the implied periodicity of the discrete Fourier transform. The aperiodicity of the mean flow was removed artificially by multiplying by

$$w_x(x) = 1 + \frac{1}{2}\big(\tanh[0.06\sigma(x-x_2)] - \tanh[\sigma(x-x_1)]\big), \tag{4.2}$$

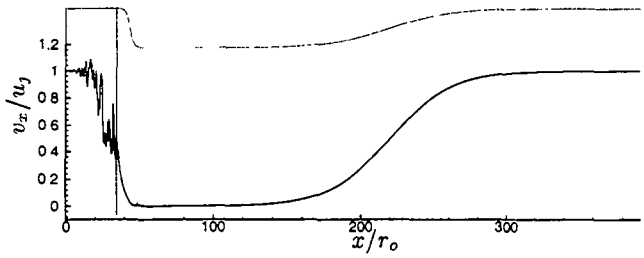

FIGURE 1. Jet velocity at $r = 0$ normalized by jet exit velocity u_j ——— . The windowing function is ····· . The vertical line indicates the extent of the physical portion of the simulation domain (Freund 2001).

where $\sigma = 0.4$, $x_1 = 44r_o$, and $x_2 = 220.3r_o$. The effect on the axial velocity at $r = 0$ at one instant is shown in figure 1. The x transform is then

$$\tilde{q}_n(k_j, r, t) = \frac{1}{N_{xp}} \sum_{i=1}^{N_{xp}} w_x(x_i) \tilde{q}_n^{(p)}(x_i, r, t) e^{ik_j x_i}; \quad k_j = \frac{2\pi j}{x_{N_{xp}}}; \; j = -N_{k_{max}}, \ldots, N_{k_{max}}, \tag{4.3}$$

where we shall see that taking $N_{k_{max}} = 640$ captures nearly all of the energy, and so is more than sufficient for our purposes.

The final step is the time transform. It is defined as

$$\hat{q}_n(k_j, r, \omega_m) = \frac{1}{N_\omega} \sum_{l=1}^{N_t} w_t(t_l) \tilde{q}_n(k_j, r, t_l) e^{i\omega_m t_l}; \quad \omega_m = \frac{2\pi m}{T}; \; m = -N_{\omega_{max}}, \ldots, N_{\omega_{max}}, \tag{4.4}$$

where taking $N_{\omega_{max}} = 200$ is sufficient for our purposes. The "window" function $w_t(t)$ was

$$w_t(t) = \frac{1}{2}\left[\tanh\left(5\frac{t - t_1}{t_1 - t_0}\right) + \tanh\left(5\frac{t_f - t}{t_f - t_2}\right)\right], \tag{4.5}$$

where t_0 and t_f in (4.5) are the time in the simulation when it was determined to be statistically stationary, and the final time, respectively. Times t_1 and t_2 are the 5 and 95 percent points in this time series. Figure 2 shows transformed velocities in (k, ω) coordinates.

4.2. *Convolution in k–ω coordinates*

The products that couple modes to put energy into radiating components are convolutions in k–ω coordinates. We can examine the modal contributions to these directly, by explicitly computing these convolutions. For example, the ρv_i products that appear in the mass equation are

$$\widehat{\rho v_i}_{k\omega} = \sum_{k'+k''=k} \sum_{\omega'+\omega''=\omega} \hat{\rho}(k', \omega') \hat{v}_i(k'', \omega''). \tag{4.6}$$

Figure 3 shows contributions of individual components to the sum for $k/\omega = a_\infty \cos\alpha$, where α is a directivity angle measured from the downstream axis. That is, if $\hat{\rho}(k', \omega')$ and $\hat{v}_i(k'', \omega'')$ combine such that $(\widehat{\rho v_i})_{k\omega}$ is indeed a component with $k/\omega = a_\infty \cos\alpha$, then the $(\widehat{\rho v_i})_{k\omega}$ from this interaction is added to the statistical 'bin' at both (k', ω')

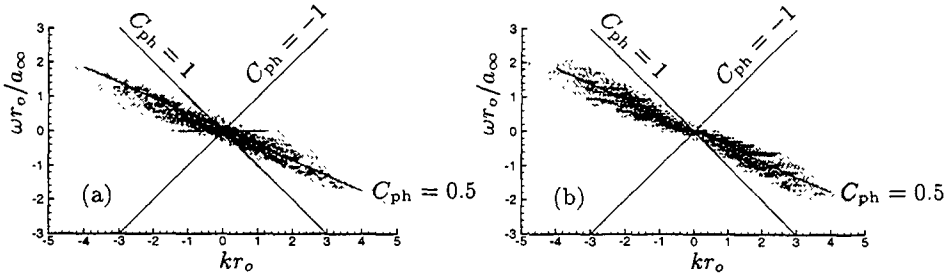

FIGURE 2. (a) and (b) show the $n = 0$ component of v_x at $r = r_o$ and the $n = 1$ component of v_r at $r = 0.5r_o$, respectively. The horizontal line at $\omega = 0$ in figure 2 (a) is the mean-flow contribution. The energy falls around a line of steeper slope in (b) than in (a) because it is at this smaller r that the convection velocity is expected to be higher. Integrating all radial contributions in r biases the slope towards lower phase velocities because of the larger volume contribution of the slower portions of the jet.

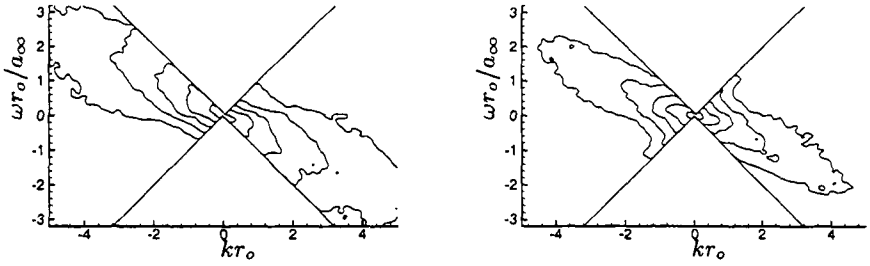

FIGURE 3. Convolution contribution (see text) for (a) $\alpha = 30°$ and (b) $\alpha = 110°$. Contours: 10^{-3}, 10^{-2}, 10^{-1}, 10^{0} and 10^{1} $\rho_\infty r_o^2$. A smoothing was applied to make the contours legible.

and (k'', ω''). Thus, we can make a contour plot that shows the contributions of different portion of the (k, ω) plane to radiation-capable components for a given product. Only non-radiation-capable components are computed, because we are most interested in the transfer of energy from non-radiation capable turbulence to that which can radiate. The contributing regions of the (k, ω) plane are differently shaped depending on the angle of radiation. The region for $\alpha = 30°$, which is the angle of peak intensity, and the region for $\alpha = 110°$ are clearly different, though most conversion comes from near the origin in both cases. These particular ρv_i products were considered because the creation of radiation capable ρ modes can be related, after subsequent manipulation, to the far-field sound,† though we have not undertaken this because of insufficient statistics.

5. Filter definition

The turbulent integral length scale, near the end of the potential core is $\lambda_{\text{int}} \approx 2.5r_o$, and the wavelength of the most intense contributions to the noise at $St \approx 0.2$ is $\Lambda = 10r_o$. Our objective is to separate these scales. A filter with a transfer function $T(\lambda)$ defined

† Applying a wave operator to ρ yields an effective noise source for the jet, which is equivalent to the Lighthill source. The far-field sound can then be computed by solving the Lighthill equation. However, this relied on us being able to differentiate in the radial coordinate, which is not possible because the convolution procedure does not preserve the smoothness of the numerical solution in physical coordinates, rendering differentiation impossible for our statistical sample.

	$\lambda_o = 2.5r_o$	$\lambda_o = 5.0r_o$
α	-0.66589224519920	-0.66665926684208
β	0.16591449129057	0.16666133194156

TABLE 1. Filter parameters for (5.1) and (5.2).

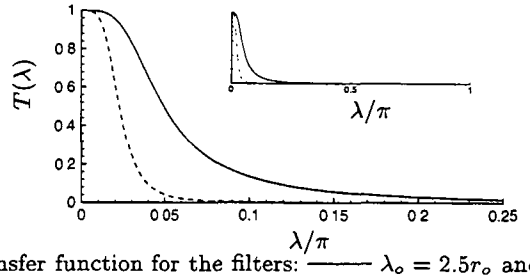

FIGURE 4. Transfer function for the filters: ——— $\lambda_o = 2.5r_o$ and - - - - $\lambda_o = 5.0r_o$.

such that $T(\lambda_o) = 0.5$ for waves with $\lambda_o = 2.5r_o$ and one that is 0.5 for wave with $\lambda_o = 5.0r_o$ were designed and applied to the data. Following Lele (1992), both filters have the form

$$\tilde{f}_i + \alpha(\tilde{f}_{i-1} + \tilde{f}_{i+1}) + \beta(\tilde{f}_{i-2} + \tilde{f}_{i+2}) = af_i + \frac{b}{2}(f_{i+1} + f_{i-1}) + \frac{c}{2}(f_{i+2} + f_{i-2}) + \frac{d}{2}(f_{i+3} + f_{i-3}), \quad (5.1)$$

where the coefficients were selected following the procedure outlined by Bodony and Lele (2002b). Requiring that the filtered field approaches the unfiltered field as Δ^6 when $\Delta \to 0$, where Δ is the grid spacing, imposes the constraints that

$$\begin{aligned} a &= (2 + 3\alpha)/4 & b &= (15 + 34\alpha + 30\beta)/32 \\ c &= (-3 + 6\alpha + 26\beta)/16 & d &= (1 - 2\alpha + 2\beta)/32 \end{aligned} \quad (5.2)$$

Values selected for α and β are given in table 1 and the transfer functions are plotted in figure 4. This filter was applied only in x. It is such a severe filtering that application in r would disrupt the quasi-parallel structure of the jet. In the θ-direction six Fourier coefficients were retained.

The effect of the filter on the streamwise and radial components of the velocity is visualized in figure 5. There is an obvious removal of scales. However, even with the substantial changes we see in the physical space visualizations brought on by the filter, the radiation-capable portion of the source in k–ω coordinates is essentially unchanged. This is shown in figure 6 for the filter of width $\lambda = 5.0r_o$.

6. Evolution of the very large scales

An assessment of the role of the 'background field' on the scattering of non-radiating fluctuations into sound is explored through the solution of equations (2.2)–(2.4), generically called the 'linearized inhomogeneous Euler' (LIE) equations by Goldstein (2002), for the large-scale fluctuations $\{\rho^{(L)}, u_i^{(L)}, p^{(L)}\}$. The inhomogeneous terms of the LIE equations are known *a priori* from the DNS database and constitute an 'ideal turbulence model' for the very large scales. Furthermore, as the filtering process defined in

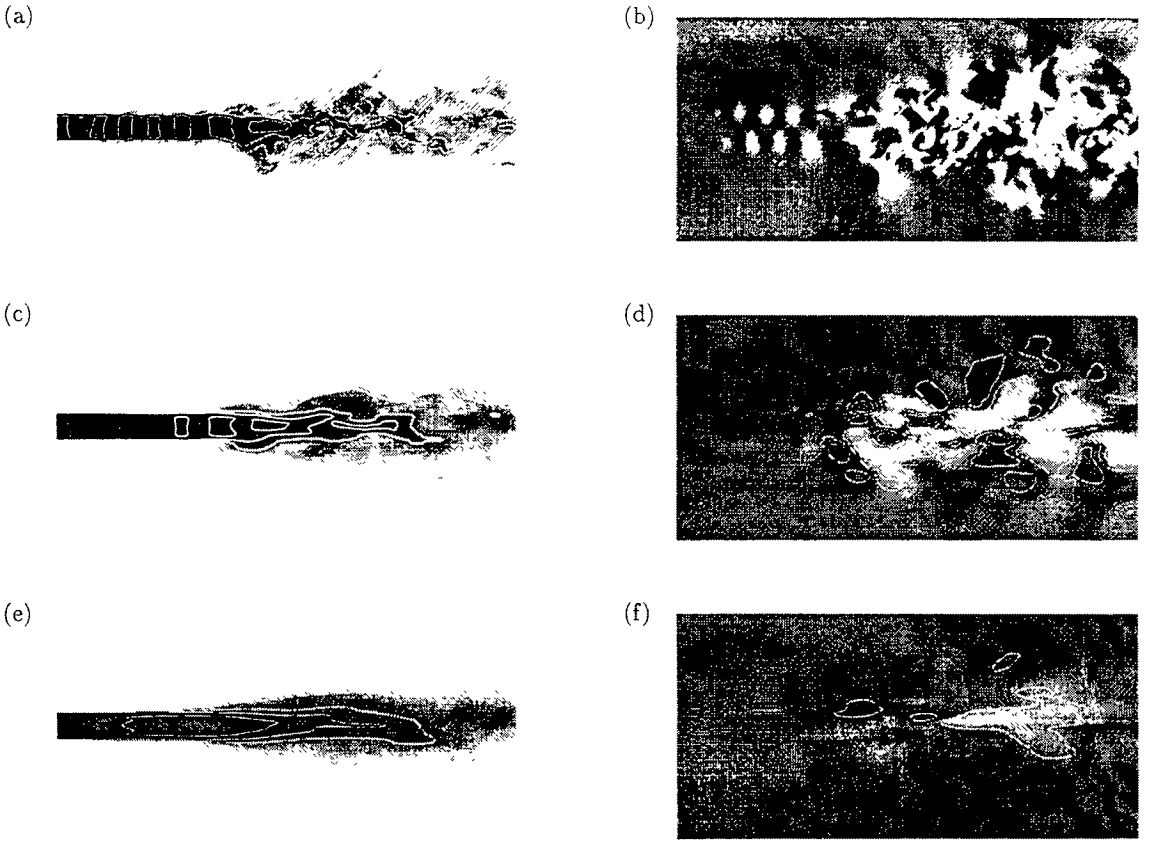

FIGURE 5. Velocity field visualization: full field (a) v_x and (b) v_r; filtered with $\lambda_o = 2.5r_o$ (c) v_x and (d) v_r; and filtered with $\lambda_o = 5.0r_o$ (e) v_x and (f) v_r. For v_x the white contours are evenly spaced between 0 and u_j; for v_r they are evenly spaced between $\pm 0.12u_j$, omitting $v_r = 0$.

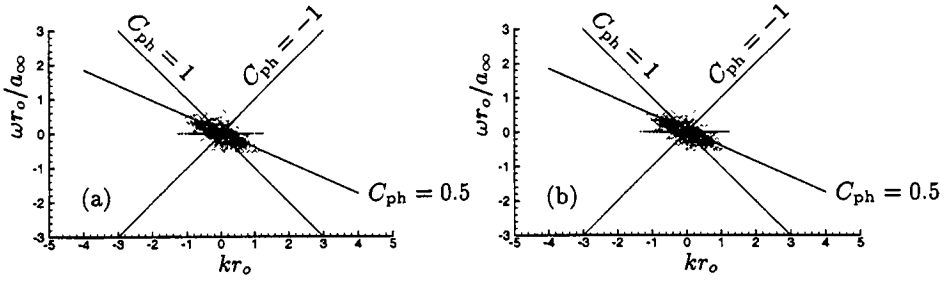

FIGURE 6. Same as figure 2 after application of the $\lambda_o = 5.0r_o$ filter.

(2.1) is purely spatial, the time-derivative terms occurring in the momentum and energy equations, (2.3) and (2.4) respectively, are smaller by an order of magnitude than the corresponding flux terms and are therefore neglected.

6.1. *Numerical Method*

The LIE equations were solved numerically using a modified larg- eddy simulation code (Bodony and Lele 2002a). Written in cylindrical coordinates, the code employs standard sixth-order Padé derivatives (Lele 1992) in the axial and radial directions, and spectral differentiation in the homogeneous direction. Time advancement is by a fourth-order explicit Runge-Kutta algorithm. Boundary conditions are non-reflecting on all computational boundaries. The source terms are stored precomputed and interpolated in time using cubic splines. Initial conditions for the simulation are taken to be the filtered, large-scale disturbance field from a particular instant in the jet. That is, if $q_o^{(L)}$ denotes an initial value of a particular conserved disturbance quantity, then $q_o^{(L)} = \tilde{q}_{\text{DNS}} - \overline{q}$.

The early development of the mean flow is laminar and therefore nearly parallel, so spatially developing instabilities can amplify substantially. If left undamped, upstream traveling disturbances couple to instabilities at the artificial inflow boundary. These quickly grow and overwhelm the solution. Thus, the inlet 'sponge' was set strong enough to damp this process completely.

6.2. *Preliminary Results*

The primary goal of the investigation of very-large-scale dynamics is to determine the role of the mean in the conversion of non-radiating hydrodynamic fluctuations into sound. For model problems, such as a 'gust' impacting the leading edge of a solid body (Crighton and Leppington 1971), the mechanism of 'scattering' vorticity into sound is well established. However, a jet is more complex because the coupling region is nonlocal, and the linear decomposition into entropy, vorticity, and acoustic fluctuations (Kovasznay 1953) is inadequate for the finite-amplitude disturbances in the jet. The current solution of the linearized equations is an attempt to examine the effect that the background flow has on the fluctuations through direct comparison with the previously known nonlinear solution. One-to-one comparisons, however, are not possible because the initial conditions described in section 6.1 are not precisely consistent with the LIE equations causing a substantial initial transient. We therefore must make statistical comparisons.

Visualizations of the large scale disturbance pressure field, of which figure 7 is a particular snapshot, do not show any distinctive large-scale motion of the jet, such as 'flapping' or 'pulsating', that can be correlated with the radiated sound. Instead, it appears that the pressure fluctuations are related to the large scale axial motion of nearly axisymmetric (low azimuthal mode number) structures through the jet. Previous experimental (Fuchs and Michalke 1975), numerical (Freund and Colonius 2002; Freund et al. 2000), and analytical work (Tam and Morris 1980) support this conjecture.

To find the radiated sound, the pressure history on a surface surrounding the jet is collected and projected onto the far-field. Beyond a radius of approximately $R_s = 5r_o$ the mean flow and its gradients are very weak so that acoustic propagation is governed by the wave equation for a stationary medium. If the pressure on the Kirchhoff surface is denoted as $p(x, R_s, \theta, t)$, then the far-field sound is found using the Fourier-transformed wave equation

$$\frac{\mathrm{d}^2\hat{p}}{\mathrm{d}r^2} + \frac{1}{r}\frac{\mathrm{d}\hat{p}}{\mathrm{d}r} + \left(\frac{\omega^2}{a_\infty^2} - k^2 - \frac{n^2}{r^2}\right)\hat{p} = 0 \tag{6.1}$$

where $\hat{p}(k, n, \omega; r)$ is the three dimensional discrete Fourier transform (in x, θ, and t) of $p(x, r, \theta, t)$ with dual variables (k, x), (n, θ), and (ω, t). Equation (6.1) is Bessel's equation

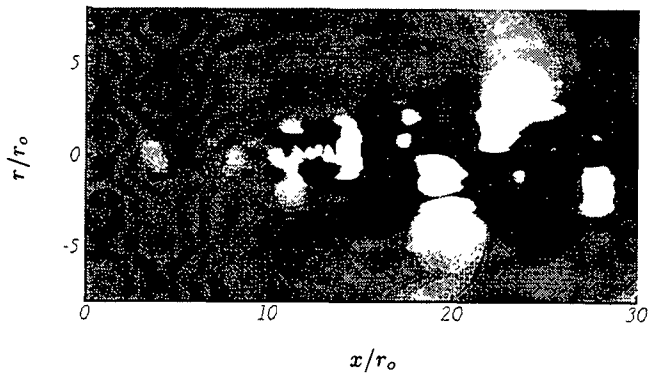

FIGURE 7. Instantaneous very-large-scale pressure-disturbance field $p^{(L)}$ obtained from solution of equations (2.2)–(2.4).

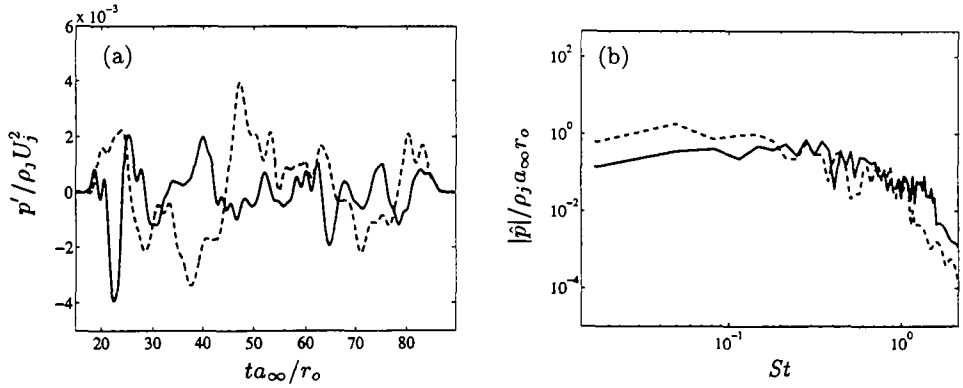

FIGURE 8. Near-field pressure data taken from Kirchhoff surface ($r = 5r_o$). (a) Pressure fluctuation traces at $x = 15r_o$ (solid) and $x = 24.4r_o$ (dashed) and (b) their Fourier coefficients.

and is subject to the boundary conditions that, for $r = R_s$, $\hat{p}(k, n, \omega; r) = \hat{p}(k, n, \omega; R_s)$, and that as $r \to \infty$ the solutions represent outgoing traveling waves.

Sample pressure traces taken from the Kirchhoff surface ($r = 5r_o$) are shown in figure 8(a) for $x = 15.0r_o$ and $x = 24.4r_o$. (The windowing of (4.5) has been applied.) Differences between the two traces are apparent. The trace at $x = 15.0r_o$ is at an angle of approximately ninety degrees from the downstream jet axis, nearly directly 'above' the end of the potential core while that at $x = 24.4r_o$ is closer to thirty degrees. From previous work (for example, Lush (1971)) the latter trace should exhibit a stronger signal, with lower frequency content relative to the former trace. This is borne out in figure 8(a) qualitatively and more quantitatively in figure 8(b). The corresponding far-field pressure signals are shown in figure 9 at a distance of $60r_o$ from the end of the potential core. (The time axes have been shifted to remove the time delay between the traces.) While the available far-field data are not sufficient to yield reliable sound pressure levels, the separation in frequency content, though minimal for this very-large-scale formulation, and in amplitude is observed.

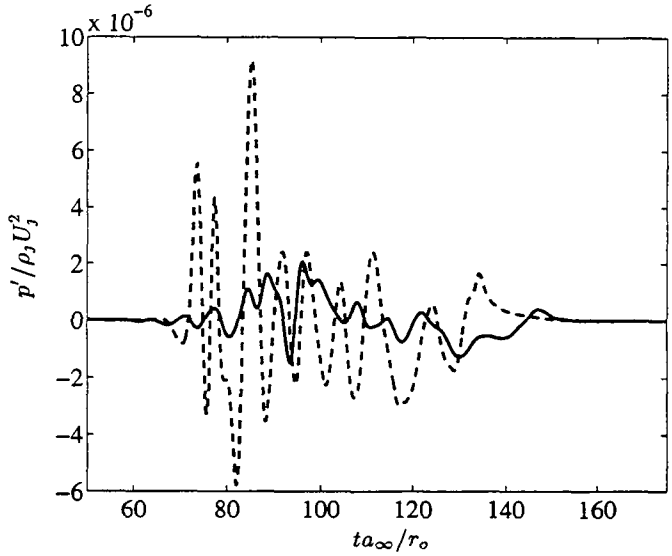

FIGURE 9. Far-field pressure levels at a distance of $60r_o$ from the end of the potential core. Legend: 90° from downstream jet axis, continuous line; 30° from downstream jet axis, dashed line. Rays drawn from the end of the potential core to the far-field observation points pass through the near-field traces of figure 8(a).

7. Conclusions

We have developed a formulation of the very-large-scale equations and the necessary filters for very large turbulence scales. The cutoff scale is larger than the integral length scale of the turbulence, but smaller than the dominant acoustic wavelength. We have also developed the tools for space-time transformation of the full flow-field data in such a way that it allows us to look at specific modal interactions. Initial observations of the very-large-scale dynamics implies that this type of investigation is warranted. Further work is planned to explore the statistical properties of the linearized dynamics and their connection to the radiated sound.

This initial effort is the starting point for a more in-depth study using the tools that we have developed. As the problem is currently defined, being the solution of the LIE equations (2.2)–(2.4), the role of the mean is masked by two factors. First, the inhomogeneous terms, collectively referred to here as S, may themselves radiate, so that the sound predicted is the sum of the scattered very-large-scale hydrodynamic field and the directly-radiated sound coming from S. To assess the importance of the mean to scattering more directly, the source terms should be appropriately filtered to remove their radiating component, leaving only that portion of S which does not radiate. The transform procedure discussed in section 4 is suitable for this. Secondly, the fact that only the mean flow has been retained in the linearization implies that the scattering efficiency is reduced relative to that if the background flow were permitted to be unsteady. The new formulation of the LIE equations would then take on an acoustic analogy quality (Goldstein 2002) as the assumption would have to be made that the very large scale hydrodynamic fluctuation field present in the DNS is independent of the radiated very large scale fluctuations. This type of study has been performed in the context of jet screech (Manning and Lele 2000) for the case of boundary sources.

REFERENCES

Bodony, D. and Lele, S. (2002a). Large eddy simulation of turbulent jets and progress towards a subgrid scale turbulence model. *Proceedings of International Workshop on LES for Acoustics, DGLR Report* 2002-03.

Bodony, D. J. and Lele, S. K. (2002b). Spatial scale decomposition of shear layer turbulence and sound sources associated with the missing scales in a large-eddy simulation. *AIAA Paper* 2002-2454.

Crighton, D. G. (1975). Basic principles of aerodynamic noise generation. *Prog. Aerospace Sci.* **16**, 31–96.

Crighton, D. G. and Leppington, F. G. (1971). On the scattering of aerodynamic noise. *J. Fluid Mech.* **46**, 577–597.

Ffowcs Williams, J. E. (1963). The noise from turbulence convected at high speed. *Phil. Trans. Roy. Soc. A* **255**, 469–503.

Freund, J. B. (1999). Acoustic sources in a turbulent jet: a direct numerical simulation study. AIAA Paper 99-1858.

Freund, J. B. (2001). Noise sources in a low-Reynolds-number turbulent jet at Mach 0.9. *J. Fluid Mech.* **438**, 277–305.

Freund, J. B. and Colonius, T. (2002). POD analysis of sound generation by a turbulent jet. *AIAA Paper* 2002-0072.

Freund, J. B., Lele, S. K., and Moin, P. (2000). Compressibility effects in a turbulent annular mixing layer. Part 1. Turbulence and growth rate. *J. Fluid Mech.* **421**, 229–267.

Fuchs, H. V. and Michalke, A. (1975). On turbulence and noise of an axisymmetric shear flow. *J. Fluid Mech.* **70**, 179–205.

Goldstein, M. (2002). A Unified Approach to Some Recent Developements in Jet Noise Theory. *Intl. J. Aeroacoustics* bf 1, 1–16.

Goldstein, M. E. (1984). Aeroacoustics of turbulent shear flows. *Ann. Rev. Fluid Mech.* **16**, 263–285.

Hussein, H. J., Capp, S. P., and George, W. K. (1994). Velocity measurements in a high-Reynolds-number, momentum-conserving, axisymmetric, turbulent jet. *J. Fluid Mech.* **258**, 31–75.

Kovasznay, L. (1953). Turbulence in supersonic flow. *J. Aero. Sci.* **20**, 657–682.

Lele, S. K. (1992). Compact finite difference schemes with spectral-like resolution. *J. Comp. Phys.* **103**, 16–42.

Lush, P. A. (1971). Measurements of subsonic jet noise and comparison with theory. *J. Fluid Mech.* **46**, 477–500.

Manning, T. A. and Lele, S. K. (2000). A numerical investigation of sound generation in supersonic jet screech. *AIAA/CEAS Paper* 2000-2081.

Panchapakesan, N. R. and Lumley, J. L. (1993). Turbulence measurements in axisymmetric jets of air and helium. Part 1. Air jets. *J. Fluid Mech.* **246**, 197–223.

Stromberg, J. L., McLaughlin, D. K., and Troutt, T. R. (1980). Flow field and acoustic properties of a Mach number 0.9 jet at a low Reynolds number. *J. Sound Vib.* **72**, 159–176.

Tam, C. K. W. and Morris, P. J. (1980). The radiation of sound by the instability waves of a compressible plane turbulent shear layer. *J. Fluid Mech.* **98**, 349–381.

Perturbation and adjoint analyses of flow-acoustic interactions in an unsteady 2D jet

By L. I. Cerviño†, T. R. Bewley†, J. B. Freund‡, AND S. K. Lele

It is well known that noise sources embedded in a jet produce sound fields which refract due to the presence of the flow. The refraction due to the mean flow has been appreciated and modeled for some time, but only occasionally is the significant refractive effect of the unsteadiness of the flow acknowledged. In the present work, perturbation and adjoint analyses of high-frequency acoustic fluctuations are performed in a numerical simulation of a cold 2D jet system at a Mach number of $M = 0.5$ and a Reynolds number based on the jet diameter of $Re_D = 5000$. The jet system is hydrodynamically excited into a sinuous mode near the jet exit at a Strouhal number of $St = 0.4$, and exhibits the classical vortex roll-up phenomenon. Acoustic perturbations to this flow system are analyzed at Strouhal numbers of $St = 0.8$, $St = 2$, and $St = 8$ (that is, $2\times$, $5\times$, and $20\times$ the vortex roll-up frequency). It is found that the unsteady effects of the flow cause a significant frequency broadening in both the perturbation and adjoint analyses.

1. Introduction

The problem of jet noise has significant engineering consequences. The far-field noise radiated by an unsteady flow system may be computed directly from a highly-accurate simulation of the compressible Navier-Stokes equation, or may be extracted from an approximate compressible flow simulation using any of several "acoustic analogies", including the celebrated Lighthill and Lilley equations. Despite their elegance and the fact that they are exact expressions, such acoustic analogies generally fail to isolate the true "sources" of far-field noise from significantly stronger noise "sources" which almost completely destructively interfere and radiate relatively little energy to the far field, as with the so-called quadrupole noise sources in a turbulent jet.

In order to better understand the physics of far-field noise and how it may be controlled, the present investigation represents one in a series of efforts to interrogate numerical databases, which capture the production of far-field sound directly, by accurate simulations of the compressible Navier-Stokes equation. The present paper focuses on the significance of acoustic scattering due to unsteady vortex roll-up in the perturbation and adjoint analyses central to this investigation.

There have been several previous investigations aimed at analyzing the effects of refraction in perturbation and adjoint analyses due to the presence of the flow. Many of them, however, consider the governing equations only after they have been linearized about the mean flow. For example, Durbin (1983a, 1983b) derived a high-frequency Green's function from an idealized steady jet profile. Tam & Auriault (1998) obtained an adjoint Green's function, using a steady jet profile obtained from a RANS calculation, and related it to the corresponding Green's function of the acoustic field at a particular point in the flow field due to additional localized sources embedded within the jet.

† Univ. of California, San Diego
‡ Univ. of Illinois, Urbana-Champaign

In a turbulent flow, however, acoustic phenomena are closely related to system unsteadiness. This was characterized in Freund & Fleischman (2001), where a refraction analysis was performed by means of ray tracing. It was observed that, when a noise source was located within the laminar jet core, the difference in the directivity calculated by the mean flow analysis and the unsteady flow analysis was rather small. However, when the source was placed farther downstream on the jet axis, the rays in the mean flow were significantly refracted by the unsteady jet shear layers, and the time average of the unsteady analysis was completely different than the corresponding analysis of the mean flow. Suzuki & Lele (1999) and Suzuki (2001) performed Green's function analyses in unsteady 2D mixing layers and boundary layers and analyzed the effects of acoustic scattering. The interaction between incoming plane waves at various angles of incidence with the unsteady vortices in the flows were investigated in detail, and the results compared with the ray-tracing procedure. A significant broadening of the frequency content of the acoustic wave after it passed through the mixing layer was observed, indicating significant flow-acoustic interaction. The present paper extends these lines of investigation with perturbation and adjoint analyses of cold 2D jets.

1.1. *Approach*

As mentioned in the Abstract, the flow system considered in this work is a Mach 0.5 cold 2D jet at a Reynolds number $Re_D = \rho D U_j/\mu = 5000$ with sinusoidal excitation near the jet exit at $S_t = f_0 D/U_j = 0.4$. Refraction effects are expected to be significantly weaker in a cold jet than in a hot jet, as the speed of sound is identical in the ambient fluid and the jet core. In fact, in sharp contrast with the perturbation and adjoint analyses of the mean of a heated jet as considered by Tam & Auriault (1998), the corresponding analyses of the refraction due to the mean of the cold jet flow studied here exhibit very little refraction. Nevertheless, as shown in this paper, the acoustic scattering due to the unsteady vortex roll-up in the present flow is quite pronounced even in this cold jet system, illustrating significant opportunities to force the hydrodynamic field (at low frequencies) in order to modify the high-frequency radiated noise.

The simulation code used in the present work implements the full compressible Navier-Stokes equation using a numerical method based closely on that developed by Freund, Moin, & Lele (1997). The present simulations do not resolve any solid boundaries. Instead, artificial "buffer zones" have been used around the domain of physical interest, coupled with characteristic-based boundary conditions on the computational boundaries. This type of *ad hoc* but effective numerical boundary conditions simulates the effect of quiescent far-field boundary conditions on the physical system, and has now become standard for this type of problem. It is discussed further in, e.g., Freund (1997) and Colonius, Lele, & Moin (1993).

As summarized in Figure 1, two types of analyses are considered in the present work. In sec. 2, perturbation analyses of the flow field are performed in order to obtain a characterization of the propagation of disturbances in the system as it evolves forward in time. In these analyses, artificial RHS forcing (to be referred to in this paper as the "control") is introduced into the jet system, and the resulting perturbation to the flow which is introduced by this forcing is computed. As depicted in Figure 1, such analyses characterize **control→effect** relationships. A representative perturbation analysis of the present system is shown in the top row of Figure 2.

In sec. 3, adjoint analyses of the flow field are performed in order to characterize the sensitivity of a particular metric measuring the flow system to additional forcing of the governing equations. In these analyses, an "adjoint system" is defined and computed in

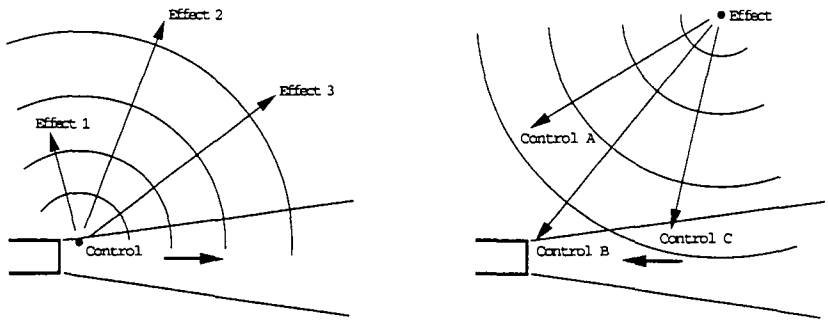

FIGURE 1. Perturbation analysis (left) and adjoint analysis (right) of the jet system.
Note that **perturbation analyses** characterize **control** → **effect** relationships:
• *If I change the "control" here, how and where will that affect the flow?*
On the other hand, **adjoint analyses** characterize **effect** → **control** relationships:
• *If I want to achieve a desired effect here, how and where should I apply "control" to the flow?*
The answer to the latter question is of particular interest when a high-dimensional forcing schedule for a complex system, such as a turbulent jet exhaust, is being optimized to achieve a desired effect, such as the reduction of radiated noise in a particular direction. Note that adjoint analyses do NOT identify the "source" of the radiated noise in such a system. Rather, they identify how and where additional forcing may be applied to the existing system to modify the radiating noise already present in a desired manner.

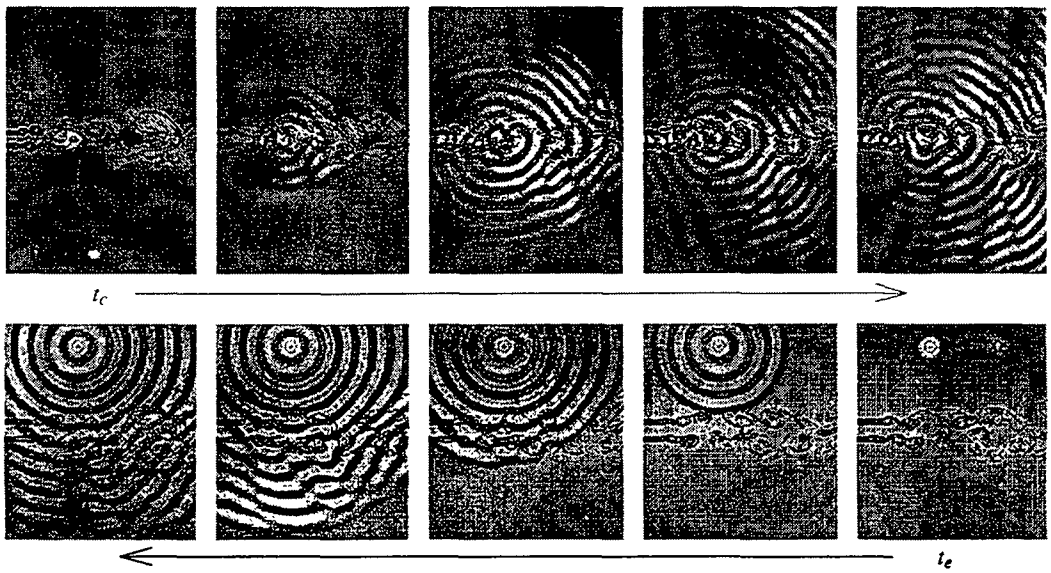

FIGURE 2. **Perturbation analysis** (top) characterizes the effect on the entire flow resulting from a small change to a particular "control" quantity, taken here to be a sinusoidally-varying mass source at point x_c. **Adjoint analysis** (bottom) characterizes the effect on a particular flow quantity, taken here to be high frequency noise at point x_e, due to small changes in the "control" applied anywhere in the flow. Note that a perturbation analysis involves marching the governing equation forward in time, whereas an adjoint analysis involves marching the corresponding adjoint equation backward in time.

order to identify the gradient of a "cost function" (which mathematically quantifies the metric of interest) to additional forcing of the jet system. As depicted in Figure 1, such analyses characterize **effect→control** relationships. A representative adjoint analysis of the present system is depicted in the bottom row of Figure 2.

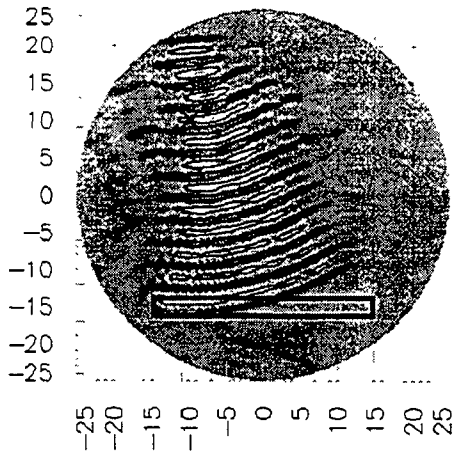

FIGURE 3. Adjoint analysis of sound waves, produced by a monopole sound source at the point marked by the X, in a stationary fluid. In the problem depicted here, the desired effect is to reduce the intensity of the sound field in the "interrogation region" outlined by the rectangular box. The corresponding adjoint field is driven by the sound waves in the box and propagates away from it, as visualized above, illustrating possible locations for "antinoise" sources where additional forcing could be applied to achieve the desired effect (namely, to reduce the sound pressure level within the box). Even though the governing system represented here is a linear, constant-coefficient PDE and the cost function is quadratic in the state variables, the adjoint field identifies a range of effective "antinoise" forcing locations, and does not accurately identify the isolated sound source. Note that the focusing of the adjoint field on the isolated sound source is found to improve when the size of the box is increased as compared with the wavelength of the sound.

It is important to note that adjoint analyses do *not* identify the "origin" or "source" of the radiated sound in such a system. This point is readily evident by considering a simpler model system (without the jet present), as depicted in Figure 3. Thus, identification of sound "sources" is not to be expected from adjoint analyses when applied to more complex systems, such as the unsteady jet considered in the present work.

Note that, in the remainder of the present work, the cost functions considered are essentially pointwise measures of the sound field, and the adjoint field computations are therefore referred to as "adjoint Green's functions".

2. Perturbation analyses

A logical starting place for this investigation is to assess the effects of hydrodynamic unsteadiness (that is, vortex roll-up) on small perturbations to the flow system. In particular, we will investigate the scattering of low-amplitude acoustic waves as they pass through the unsteady jet system. In order to perform a perturbation analysis of this sort, one approach is to calculate numerically the linearized ("perturbation") equations. The code used to solve such a problem is often referred to as a "tangent linear" code. With this approach, the perturbation field is obtained directly.

An alternative "finite-difference" approach allows us to calculate the perturbation field using the nonlinear flow solver itself, without writing a separate tangent linear code. This is achieved by computing a "nominal" flow, computing a second "perturbed" flow (with the appropriate small perturbation applied to the initial conditions, the boundary conditions, or the right-hand-side forcing), and taking their difference, dividing by the

perturbation amplitude ε. In fact, in the $\varepsilon \to 0$ limit, this is how we define the so-called "perturbation field". However, as a computational strategy, this approach presents certain difficulties. If ε is made too small, the finite-precision arithmetic of the computer leads to differencing errors, as the two fields being compared are almost identical. On the other hand, if ε is made too large, the "small" perturbation assumption breaks down, and ε^2 terms in the Taylor series expansion begin to become significant. In practice, selecting an appropriate value of ε to minimize the sum of these spurious effects is difficult. Though higher-order finite-difference approximations of the perturbation field can be proposed, they are also plagued by the competition of these two spurious effects.

In order to circumvent the difficulties cited above associated with selecting ε in a finite-difference approximation of the perturbation field, an alternative approach, referred to as the Complex Step Derivative (CSD) method, has been developed (Lyness & Moler (1967); Squire & Trapp (1998)). This method has already been applied broadly in the optimization literature (see, e.g., Martins, Sturdza, & Alonso (2001)). The basis of this method is to redefine all of the real variables in the system as complex, and to perform the nominal (real) simulation as before while introducing the small perturbation into the imaginary part of the system. It can be shown by a straightforward Taylor-series expansion of the complex fields which result that, to order ε^2, the real part of the resulting field contains the nominal flow and the imaginary part (divided by ε) contains the perturbation field sought. Further, this calculation is not plagued by the "difference of large numbers" problem, so ε may be made very small without inducing differencing errors in the calculation of the perturbation field. This provides an extremely accurate technique for computing a perturbation analysis when the simulation code nominally involves only real arithmetic (as is the case with the present 2D simulations), and is the approach selected in the present computations†.

The result of a representative perturbation analysis is shown in the top row of Figure 2. A localized mass source which oscillates sinusoidally in time (at five times the vortex roll-up frequency of the jet) has been introduced in the jet at point x_c. This has been accomplished by adding a forcing term to the right-hand side of the continuity equation. The addition of this forcing excites an acoustic wave, which is significantly refracted by the unsteady vortex roll-up. Mean-flow analyses, of course, fail to capture such scattering, which is due to the unsteadiness of the flow.

It is also straightforward to characterize acoustic waves coming from the far field. Computationally, the approach is slightly different: unsteady forcing is used along a line within the non-physical "buffer zone", and particular care must be exercised to avoid spurious effects in the corner regions of the computational domain. Physically, however, the result is qualitatively similar, and significant scattering is encountered when the acoustic field passes through the unsteady jet, as shown in Figure 4.

† In fact, it is interesting to note that it is straightforward to extend the CSD method to pseudospectral codes which nominally employ complex arithmetic. This approach was investigated briefly during the CTR summer program, and is reported in Cerviño & Bewley (2002). Unfortunately, the FFT's used in such pseudospectral extensions of the CSD approach combine the nominal (real) and perturbation (imaginary) parts of the analysis, and thus the accuracy of this approach for computing the perturbation field is found to be not significantly better than the second-order finite-difference approach.

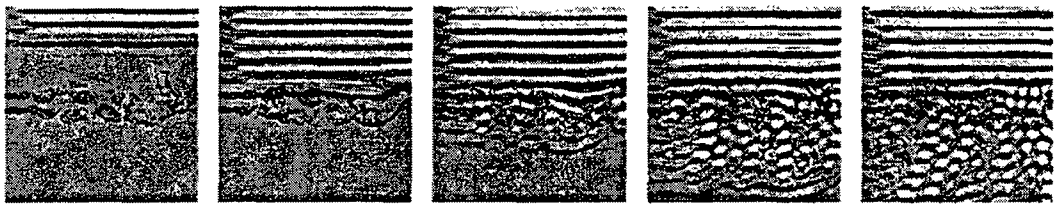

FIGURE 4. Perturbation analysis: refraction of pressure waves coming from the far-field by the unsteady 2D jet system

3. Adjoint analyses

The ultimate goal of the present research effort is to identify effective control strategies to reduce appropriate metrics of jet noise, extending the previous work reported by Wei & Freund (2002) of reducing the noise in a 2D mixing layer using a similar adjoint-based approach. Thus, though the perturbation analyses are qualitatively interesting, adjoint analyses contain significantly more relevant quantitative information related to our ultimate goal, and form the focus of the remainder of this study.

3.1. *The adjoint operator*

We now summarize briefly the adjoint formulation used in the present work. The continuous (PDE) description of the governing equation is first linearized and integrated by parts to obtain both an adjoint PDE operator useful in defining the adjoint field, and an identity that (once boundary conditions, initial conditions, and the right-hand-side forcing of the adjoint system are defined appropriately) may be used to express the required flow sensitivities in the continuous setting. As a final step before implementation in the numerical code, the state and adjoint equations are discretized in space and time in a consistent fashion.

We first define a state vector $\mathbf{q}$, a perturbation vector $\mathbf{q}'$, and adjoint vector $\mathbf{q}^*$ as

$$\mathbf{q} = \begin{pmatrix} p \\ \rho\mathbf{u} \\ \rho \end{pmatrix} = \begin{pmatrix} p \\ \mathbf{m} \\ \rho \end{pmatrix}, \qquad \mathbf{q}' = \begin{pmatrix} p' \\ \mathbf{m}' \\ \rho' \end{pmatrix}, \qquad \mathbf{q}^* = \begin{pmatrix} p^* \\ \mathbf{m}^* \\ \rho^* \end{pmatrix}. \tag{3.1}$$

We may then denote the nondimensionalized full compressible Navier-Stokes equation for an ideal gas with constant specific heats c_p and c_v and constant Prandtl number Pr as

$$\mathcal{N}(\mathbf{q}) = 0, \tag{3.2}$$

where

$$\mathcal{N}(\mathbf{q}) = \begin{pmatrix} \dfrac{\partial \rho}{\partial t} + \nabla\cdot\mathbf{m} \\ \dfrac{\partial \mathbf{m}}{\partial t} + \nabla\cdot\dfrac{\mathbf{m}\otimes\mathbf{m}}{\rho} + \nabla p - \dfrac{1}{Re}\nabla\cdot\left(\mu\nabla\dfrac{\mathbf{m}}{\rho}\right) - \dfrac{1}{Re}\nabla\left[\mu\left(\dfrac{\mu_B}{\mu}+\dfrac{1}{3}\right)\nabla\cdot\dfrac{\mathbf{m}}{\rho}\right] \\ \dfrac{\partial p}{\partial t} + \nabla\cdot\dfrac{p\mathbf{m}}{\rho} + (\gamma-1)\,p\left(\nabla\cdot\dfrac{\mathbf{m}}{\rho}\right) - \dfrac{\gamma}{RePr}\nabla\cdot\left(\mu\nabla\dfrac{p}{\rho}\right) - \Phi \end{pmatrix},$$

and Φ denotes the irreversible viscous dissipation term. Assuming appropriate expressions for μ and μ_B, the simulation code used in the present work implements the full compressible Navier-Stokes equation outlined above. In order to develop an adjoint solver, certain

additional approximations have been made, namely that $\mu =$ constant, $\mu_B =$ constant, and $\Phi = 0$. These convenient simplifications are thought to be acceptable in the approximate adjoint analysis, as the spatial and temporal variations of viscosity in the system and the irreversible viscous dissipation in the heat equation both affect the dynamics of the system only at the small length scales, and are thus thought to be relatively unimportant in terms of the mechanics of sound generation. Subject to these additional assumptions, and following the established procedure for performing an adjoint analysis [see, e.g., appendix B of Bewley, Moin, & Temam (2001) for the case of an unsteady compressible Euler system], we may take the Fréchet derivative of this governing equation to obtain a linearized equation of the form

$$\mathcal{N}'(\mathbf{q})\,\mathbf{q}' = 0. \tag{3.3}$$

Selecting an L_2 duality pairing† of the form $\langle \mathbf{q}^*, \mathbf{q}' \rangle \triangleq \int_0^T \int_\Omega \mathbf{q}^* \cdot \mathbf{q}' \, d\mathbf{x} dt$, this linearized operator is then transformed according to the identity

$$\langle \mathbf{q}^*, \mathcal{N}'(\mathbf{q})\,\mathbf{q}' \rangle = \langle \mathcal{N}'(\mathbf{q})^*\,\mathbf{q}^*, \mathbf{q}' \rangle + b. \tag{3.4}$$

After some algebra involving several integrations by parts, it is straightforward to show that the adjoint operator corresponding to the approximate linearized form of the compressible Navier-Stokes equation in this framework is:

$$\mathcal{N}'(\mathbf{q})^*\,\mathbf{q}^* = \begin{pmatrix} -\dfrac{\partial \rho^*}{\partial t} - \dfrac{\mathbf{m}}{\rho}\cdot\nabla\rho^* + (\gamma-1)\rho^*\nabla\cdot\dfrac{\mathbf{m}}{\rho} - \nabla\cdot\mathbf{m}^* - \dfrac{\gamma\mu}{\rho PrRe}\nabla^2\rho^* \\ -\dfrac{\partial \mathbf{m}^*}{\partial t} - \dfrac{\gamma p}{\rho}\nabla\rho^* - \dfrac{(\gamma-1)\rho^*}{\rho}\nabla p - \dfrac{\mathbf{m}}{\rho}\cdot\left(\nabla\otimes\mathbf{m}^* + (\nabla\otimes\mathbf{m}^*)^T\right) - \nabla p^* - \\ \qquad -\dfrac{\mu}{Re\,\rho}\left[\nabla^2\mathbf{m}^* + \left(\dfrac{\mu_B}{\mu}+\dfrac{1}{3}\right)\nabla(\nabla\cdot\mathbf{m}^*)\right] \\ -\dfrac{\partial p^*}{\partial t} + \dfrac{p\mathbf{m}}{\rho^2}\cdot\nabla\rho^* + \dfrac{(\gamma-1)\mathbf{m}}{\rho^2}\cdot\nabla(\rho^* p) + \dfrac{\mathbf{m}}{\rho}\cdot\left(\dfrac{\mathbf{m}}{\rho}\cdot\nabla\right)\mathbf{m}^* + \\ \qquad +\dfrac{\mu}{Re\,\rho^2}\left[\mathbf{m}\cdot\nabla^2\mathbf{m}^* + \left(\dfrac{\mu_B}{\mu}+\dfrac{1}{3}\right)(\mathbf{m}\cdot\nabla)(\nabla\cdot\mathbf{m}^*)\right] + \dfrac{\gamma\mu}{\rho PrRe}\dfrac{p}{\rho}\nabla^2\rho^* \end{pmatrix}.$$

It is important to note that, in the present derivation, we have associated the "adjoint pressure" with additional forcing of the continuity equation, and the "adjoint density" with additional forcing of the selected form of the energy equation. [This is in contrast with, e.g., the nomenclature selected by Tam & Auriault (1998).] The nomenclature has been defined in this manner in order to have a logical zero-Mach-number limit. In this limit, ρ and ρ^* are constant, the forward and adjoint energy equations may be dropped, and the state, perturbation, and adjoint vectors reduce to

$$\mathbf{q} = \begin{pmatrix} p \\ \rho\mathbf{u} \end{pmatrix} = \begin{pmatrix} p \\ \mathbf{m} \end{pmatrix}, \qquad \mathbf{q}' = \begin{pmatrix} p' \\ \mathbf{m}' \end{pmatrix}, \qquad \mathbf{q}^* = \begin{pmatrix} p^* \\ \mathbf{m}^* \end{pmatrix}.$$

In a domain enclosed by solid boundaries, by selecting the appropriate adjoint boundary and initial conditions, we can make the boundary term b in (3.4), which results from the several integrations by parts, equal to zero. Alternatively, as in the present analysis,

† In multiscale PDE systems such as the present, the L_2 duality pairing is not necessarily the best choice for defining the adjoint operator, and incorporating spatial or temporal derivatives into this pairing is recognized to have an important regularizing effect on the spectra of the resulting adjoint field that must be calculated. For further discussion of this important topic, see Protas, Bewley, & Hagen (2002).

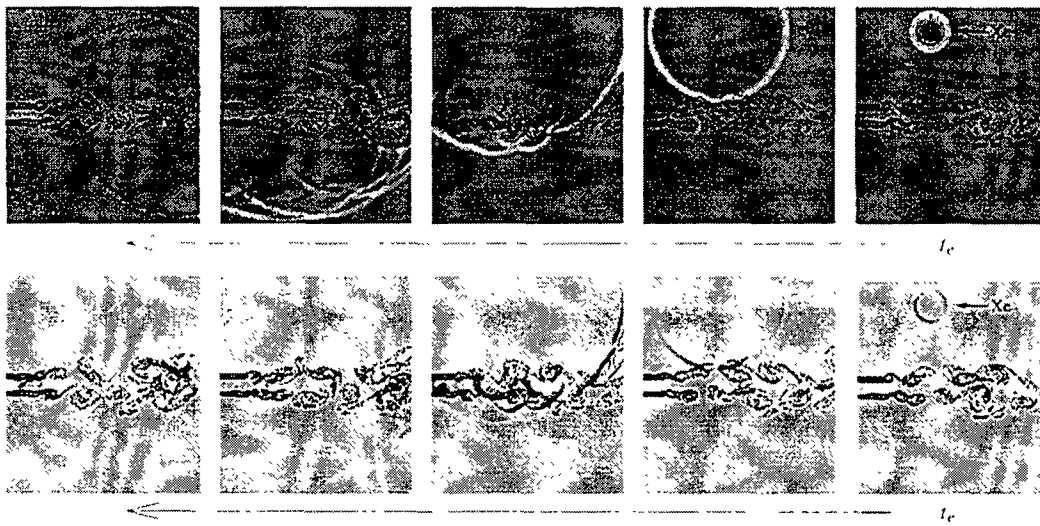

FIGURE 5. Adjoint density (top) and adjoint pressure (bottom) reveals sensitivity of the pressure component of the perturbation field at point x_e at time t_e to additional forcing of, respectively, the energy equation (top) and the continuity equation (bottom) everywhere in space x_c and for all times $t_c < t_e$. Note that, by causality, the adjoint field is zero for $t_c > t_e$; that is, the adjoint field marches backward in time from $t = t_e$.

we may surround the physical part of the domain of interest in both the flow and adjoint problems with the numerical equivalent of quiescent far-field boundary conditions which propagate no information towards the physical domain of interest; this again effectively allows us to neglect the influence of b. By so doing, the adjoint identity (3.4) then reveals that the following two analyses are equivalent:

#1) analyzing the effect on $q_i'(\mathbf{x}_e,t_e)$ (that is, the effect on the i'th component of the perturbation field at point $\mathbf{x} = \mathbf{x}_e$ and time $t = t_e$) created by applying a localized force $g_j' = \delta(\mathbf{x} - \mathbf{x}_c)\delta(t - t_c)$ to the j'th component of the perturbation equation, and

#2) analyzing the effect on $q_j^*(\mathbf{x}_c,t_c)$ created by applying a localized force $g_i^* = \delta(\mathbf{x} - \mathbf{x}_e)\delta(t - t_e)$ to the i'th component of the adjoint equation.

By the identity (3.4), we may relate the perturbation and adjoint fields in these two analyses by

$$q_i'(\mathbf{x}_e,t_e) = q_j^*(\mathbf{x}_c,t_c). \tag{3.5}$$

Note that the point $\mathbf{x}_c$ and time t_c do not appear in the formulation of the adjoint system in problem #2, but arise only in the subsequent analysis of the resulting adjoint field. Thus, a *single* adjoint calculation allows us to quantify the effect of forcing *anywhere* in the flow system (for any $\mathbf{x}_c$, t_c, and j) on the particular flow quantity $q_i'(\mathbf{x}_e,t_e)$. This relation between the perturbation and adjoint Green's functions provides an alternative but equivalent explanation of the significance of adjoint analyses to the more general "controls-oriented" explanation provided in Figure 1.

3.2. *Calculation of an adjoint Green's function*

Figure 5 illustrates a computation of the adjoint Green's function, as formulated at the end of the previous section, obtained by forcing the adjoint system $\mathcal{N}'(\mathbf{q})^*\mathbf{q}^* = \mathbf{g}^*$ with

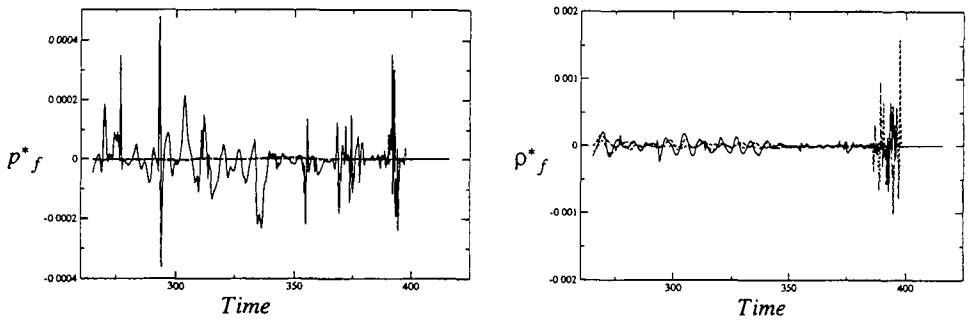

FIGURE 6. Evolution of adjoint pressure (left) and adjoint density (right) in time at the points $\{x,y\}$ of (solid) $\{5D,0\}$, (dashed) $\{5D,2.5D\}$, (dot-dashed) $\{5D,-2.5D\}$.

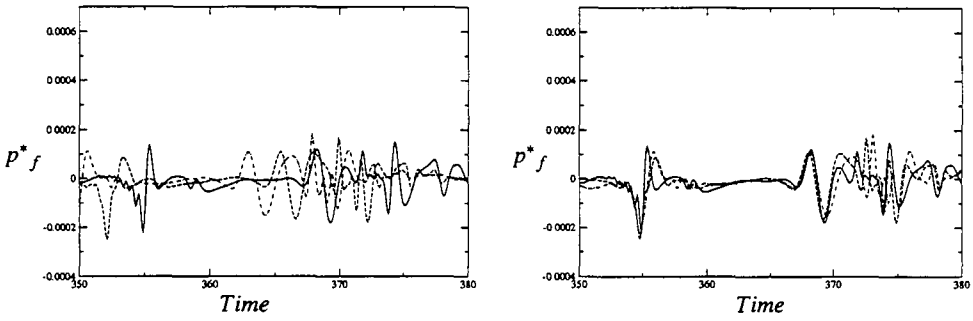

FIGURE 7. Adjoint pressure at three different locations at the centerline: at (dot-dashed) $x = 8$, (dashed) $x = 9$, and (solid) $x = 10$. When the actual evolutions of the variable (left) are shifted by the time corresponding to the convection velocity (right), there is an approximate superposition of the three lines, which indicates that these perturbations convect toward the nozzle at the convective speed.

an isolated force at a particular point in space and time, that is, $g_i^* = \delta(\mathbf{x} - \mathbf{x}_e)\delta(t - t_e)$. As discussed above, each component j of the resulting adjoint Green's function, at each point in space $\mathbf{x}_c$ and each instant in time t_c, may be interpreted as the i'th component of the perturbation to the flow at point $\mathbf{x}_e$ and time t_e that would arise due to localized forcing of the corresponding component j of the flow system at the corresponding point in space $\mathbf{x}_c$ and time t_c. The calculation reported in Figure 5 takes $i = 1$, that is, the adjoint field shown characterizes the effect on the perturbation pressure $p'(x_e,t_e)$.

It is interesting to note (see Figure 5) that the disturbance in the adjoint pressure grows rapidly as it propagates within the jet towards the nozzle at the convective velocity as the adjoint field evolves (in backwards time). In contrast, the disturbance in the adjoint density essentially propagates right through the jet, experiencing significant refraction. This behavior is quantified further in Figures 6 and 7. The component of the adjoint density that propagates at the convective speed of the jet within the jet shear layers is found to be quite small. This indicates, as one might expect, that mass sources are more efficient than energy sources in modifying the hydrodynamic field in a way which changes the radiated noise.

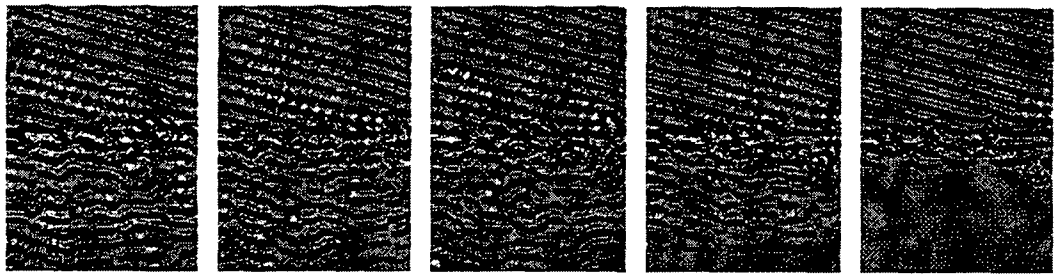

FIGURE 8. Adjoint density field due to incoming waves from the far field.

3.3. *An adjoint Green's function at temporal frequency f*

An alternative to forcing the adjoint problem at an isolated time t_e is to force it at a specific temporal frequency f. This corresponds roughly to looking at the sensitivity of the sound field at point x_e (at the frequency and phase selected) to additional forcing of the governing equations. This correspondence is only approximate, however, as the system under consideration has time-varying coefficients, and therefore frequency-based characterizations of the system's response are of limited usefulness. Note that, in systems with constant coefficients, a Bode plot completely characterizes the frequency response of the system. Such a frequency-domain analysis may only be applied to the mean flow. Nonetheless, an approximate characterization of this sort may still be developed for the present system (in the time domain) simply by forcing the adjoint system sinusoidally at the frequency of interest during the backwards march for the adjoint field. The result of such a calculation is illustrated in the bottom row of Figure 2. The scattering of the adjoint field due to the vortex roll-up is a necessary consequence of the scattering in the corresponding perturbation fields.

3.4. *An adjoint Green's function corresponding to far-field noise*

An alternative to forcing the adjoint problem at an isolated point in the computational domain x_e is to force it along a line near the boundary of the computational domain (that is, in the "buffer zone" used to approximate the far-field boundary conditions). By so doing, one may set up a propagating wave in the adjoint field which is the same as if the computational domain extended deep into the far field and the adjoint problem was forced a very long distance away. By varying the forcing along this line sinusoidally, one may simulate the arrival of a wave in the adjoint field corresponding to the effect on the far-field noise in any direction of interest. A representative example is given in Figure 8. Note that both reflection and refraction of the adjoint field are observed in this computation.

3.5. *Quantification of scattering of adjoint Green's functions*

In an attempt to quantify the scattering of a wave in the adjoint field due to the unsteady vortex roll-up, the values of the adjoint density and adjoint pressure have been measured at three different points in the representative adjoint Green's function analysis illustrated in Figure 9. The points where the adjoint density and adjoint pressure were measured are above the jet (where the scattering will be referred to as reflection), at the centerline, and below the jet (where the scattering will be referred to as refraction). The time series of these measurements were Fourier-transformed in time, and the results are plotted in Figure 10. The analysis was performed for adjoint forcing at three different Strouhal

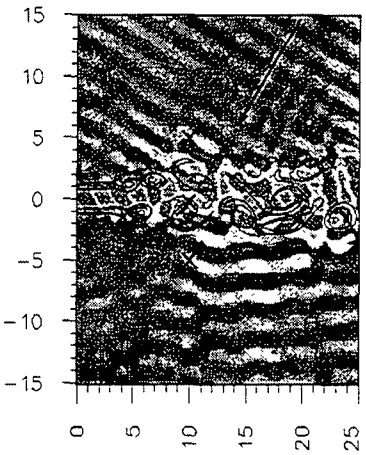

FIGURE 9. Adjoint pressure wave corresponding to far-field noise at an angle of 60° off the jet axis and at a frequency of $St = 2.0$. The Fourier transform of this field evaluated at the three points indicated is shown in Figure 10.

numbers: $St = 0.8$ (2× the vortex roll-up frequency), $St = 2.0$ (5× the vortex roll-up frequency), and $St = 8.0$ (20× the vortex roll-up frequency).

Perhaps the most important observation to make in Figure 10 is that there is very significant frequency broadening in all of the adjoint spectra measured. The adjoint systems are excited by forcing at the single frequency indicated ($St = 0.8$, 2.0, or 8.0) but, due to the time-varying coefficients (from the unsteady flow field $\mathbf{q}$) in the adjoint operator, the measurements of the adjoint field at the points indicated exhibit energy over a broad range of temporal frequencies. For comparison, the spectra of the hydrodynamic fluctuations of the base flow is shown in Figure 11. Note that the frequency broadening of the adjoint field cannot be captured by a steady-flow analysis.

The frequency broadening present when the adjoint field is forced at a high frequency is much larger than when it is forced at a low frequency. This fact was noticed by Suzuki (2001) for the direct problem, and was interpreted as "multiple scattering". In the present adjoint analysis, this suggests that high-frequency noise may be modified by a broad range of possible forcing frequencies.

Note in particular that the frequency spectrum is generally narrower at the point above the jet (dashed lines) than below the jet (dot-dashed lines), apparently because the refraction of the traveling wave in the adjoint field is stronger than the reflection of this wave for the incidence angle tested. Within the jet (solid line), it is observed that the frequency broadening is strongest.

The low-wavenumber components of the spectra of the adjoint pressure at the centerline are especially strong for all three forcing frequencies tested. This indicates that low-frequency modulation of the hydrodynamic field via mass sources within the jet can have a significant impact on the high-frequency noise in the far field, and provides impetus for further studies in jet-noise control based on such characterizations to exploit this sensitivity.

Note also that all of the spectra are somewhat jagged, and the distance between of each small peak in this jaggedness is $\Delta f = 0.2D/U$, which is exactly half of the vortex roll-up frequency. This appears to indicate (as one might expect) that the scattering of the wave in the adjoint field is closely related to its interactions with the large-scale vortex roll-up.

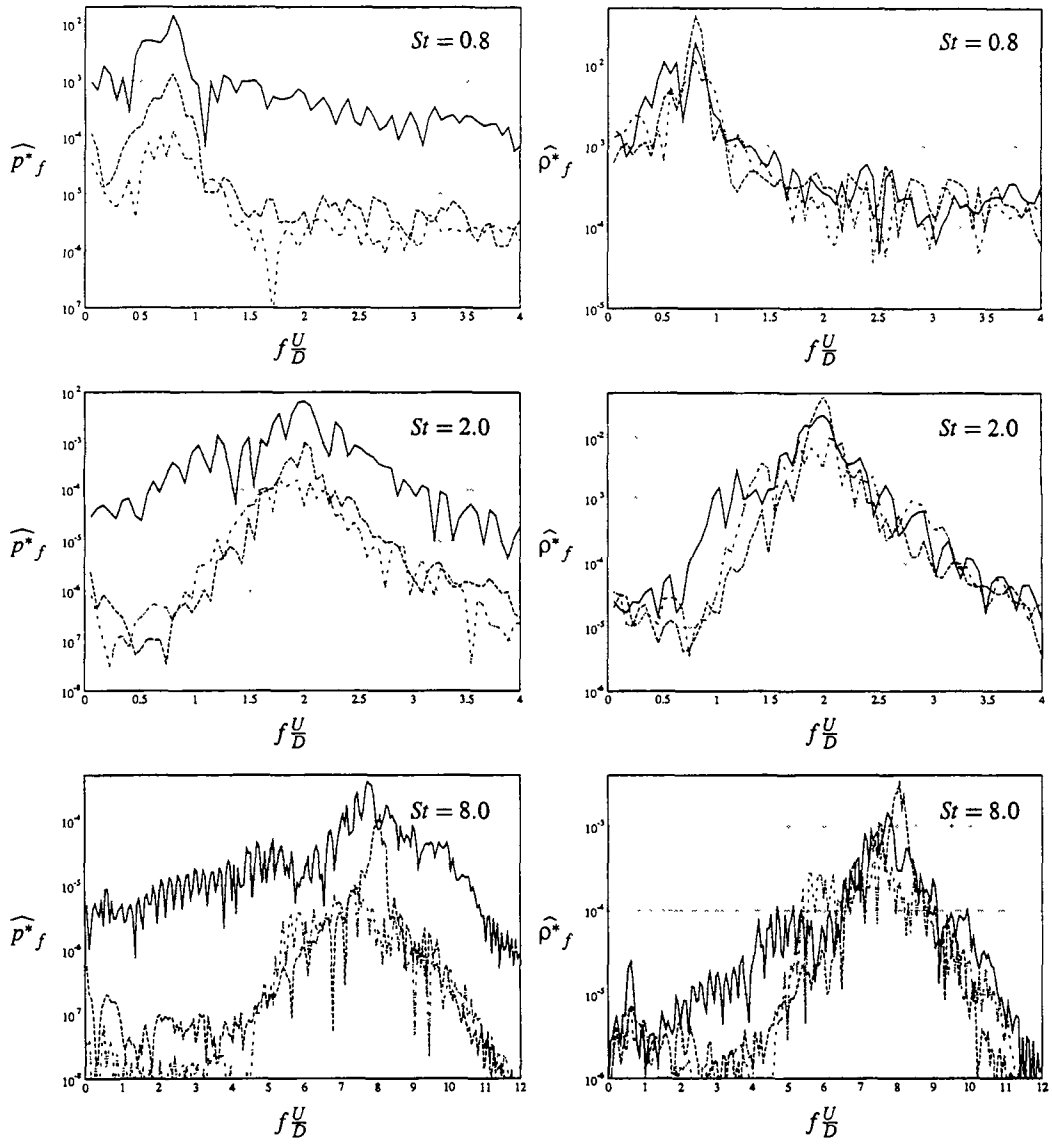

FIGURE 10. Temporal spectra of (left) the adjoint pressure $\widehat{p^*}_f$ and (right) the adjoint density $\widehat{\rho^*}_f$ for an incident wave in the adjoint field coming from above (at an angle of 60° off the jet axis), at a frequency of (top) $St = 0.8$, (middle) $St = 2.0$, and (bottom) $St = 8.0$ and measured at the points $\{x, y\}$ of (solid) $\{5D, 0\}$, (dashed) $\{5D, 2.5D\}$, (dot-dashed) $\{5D, -2.5D\}$. See Figure 9 for flow configuration.

A second set of cases was also run in which the wave in the adjoint field approaches the jet at a 90° angle off the jet axis (cf. Figure 9). The results showed very similar trends, and are thus not included here.

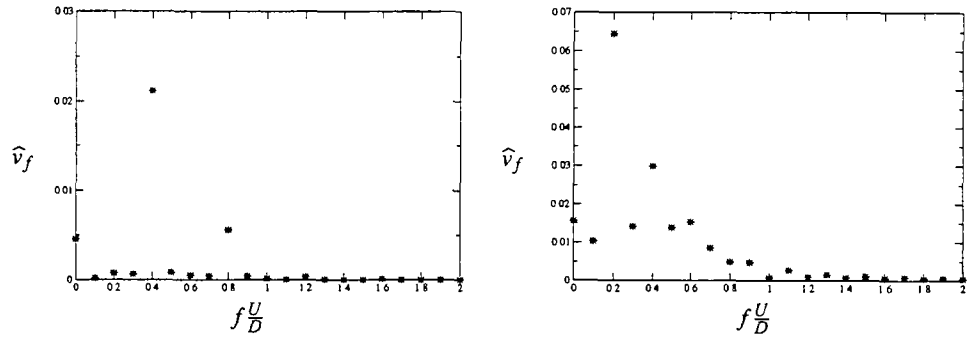

FIGURE 11. Spectra of the vertical velocity of the flow at $\{x,y\} = \{1.5D, 0.5D\}$ (left) and $\{x,y\} = \{3D, 0.5D\}$ (right). The appearance of the peak at $S_t = 0.2$ at the downstream station (right) is a result of vortex pairing (recall that the jet is forced at $S_t = 0.4$).

4. Concluding remarks

Perturbation and adjoint analyses of flow-acoustic interactions in an unsteady 2D jet have been performed. Attention has been focused on the scattering of adjoint Green's functions corresponding to far-field high-frequency noise. Significant scattering of the adjoint field is detected both above and below the jet, as quantified by a spectral analysis of the adjoint field. This scattering is a direct result of system unsteadiness (vortex roll-up), and cannot be captured by mean flow analyses.

The degree to which frequency broadening extends into the low frequencies within the jet in the adjoint analyses indicates the degree to which low-frequency alteration of the hydrodynamic field can be used to affect the high-frequency radiated acoustic field. This distinguishes promising low-frequency "hydrodynamic" control strategies from simple (but perhaps impractical) "antinoise" control strategies, which must be applied at the frequency of the radiated noise.

REFERENCES

BEWLEY, T.R., MOIN, P., & TEMAM, R. 2001 DNS-based predictive control of turbulence: an optimal benchmark for feedback algorithms. *J. Fluid Mech.* **447**, 179-225.

CERVIÑO, L.I. & BEWLEY, T.R. 2002 On the extension of the complex-step derivative technique to pseudospectral algorithms. Submitted for publication.

COLONIUS, T., LELE, S.K., & MOIN, P. 1993 Boundary conditions for direct computation of aerodynamic sound generation. *AIAA J.* **31**, 1574-1582.

DURBIN, P.A. 1983a High frequency Green function for aerodynamic noise in moving media, Part I: general theory. *J. Sound Vib.* **91**, 519-525.

DURBIN, P.A. 1983b High frequency Green function for aerodynamic noise in moving media, Part II: Noise from a spreading jet. *J. Sound Vib.* **91**, 527-538.

FREUND, J.B., MOIN, P., & LELE, S.K. 1997 Compressibility effects in a turbulent annular mixing layer. Mech. Engg. Dept., Stanford University, Tech. Rept. TF-72.

FREUND, J.B. 1997 Proposed inflow/outflow boundary condition for direct computation of aerodynamic sound. *AIAA J.* **35**, 740-742.

FREUND, J.B., & FLEISCHMAN, T.G. 2001 A numerical study of jet noise mechanisms: sound scattering by turbulence. *AIAA Paper* 2001-0375.

LYNESS, J.N. & MOLER, C.B. 1967 Numerical differentiation of analytic functions. *SIAM J. Numer. Anal.* **4**, 202-210.

MARTINS, J.R.R.A., STURDZA, P., & ALONSO, J.J. 2001 The connection between the complex-step derivative approximation and algorithmic differentiation. *AIAA Paper* 2001-0921.

PROTAS, B., BEWLEY, T.R., & HAGEN, G. 2002 A comprehensive framework for the regularization of adjoint analysis in multiscale PDE systems. Submitted.

SQUIRE, W. & TRAPP, G. 1998 Using complex variables to estimate derivatives of real functions. *SIAM Rev.* **40**, 110–112.

SUZUKI, T., & LELE, S.K. 1999 Acoustic scattering from a mixing layer: role of instability waves. *AIAA Paper* 99-0228.

SUZUKI, T. 2001 Acoustic wave propagation in transversely sheared flows. PhD Thesis, Stanford University, Department of Aeronautics and Astronautics. Also available as SUDAAR 739.

TAM, C.K.W. & AURIAULT, L. 1998 Mean flow refraction effects on sound radiated from localized sources in a jet. *J. Fluid Mech.* **370**, 149-174.

WEI, M. & FREUND, J.B. 2002 Optimal control of free shear flow. *AIAA Paper* 2002-0665.

RANS modeling

The RANS section contains two reports on three projects: RANS models have of course played a part in many other projects reported here. The work of Ooi *et al.* is addressed to Reynolds averaged analysis of flow in a ribbed duct. This configuration is used in cooling passages; the ribs enhance heat transfer. The terminology 'turbulator' is some times used to describe the role of the ribs. This project explores the possibility that the ribs function by generating strong secondary flows, not simply enhancing turbulence levels. Though experiments were done in which the secondary flow is switched off and heat transfer is compared to that of the full flow field. Swept ribs were found to produce a large amount of secondary flow heat transfer. The article by Ooi *et al.* provides some specific numbers, as well as visualizations of the secondary flow features.

Rousson *et al.* report on two projects related to fires. Reynolds averaged analysis and eddy simulation are discussed. Fires can propagate by radiative heating. Whether or not a surface will ignite can depend on whether convective cooling keeps the surface below the flash point. This group identified a benchmark data set on mixed convective cooling in a parameter range of interest to fires. They initiated a joint RANS/DNS/LES study of how well this flow can be predicted. Initial results are promising, but not definitive.

The fire group also explored the idea of time-filtered LES to simulate the puffing effect that is seen in large scale pool fires. The characterization of this phenomenon as low frequency unsteadiness suggests that one should think in terms of the time domain. It was found that puffing can be produced by LES. An auxiliary component to this and the RANS work is to further the development and application of the DOE fire prediction code called Fuego.

Paul Durbin

RANS calculations of secondary flow structures in ribbed ducts

By A. Ooi †, B.A. Petterson Reif ‡, G. Iaccarino AND P.A. Durbin

The spatial structure and effects of secondary flows in ribbed ducts are investigated using numerical data from Reynolds-averaged Navier-Stokes (RANS) calculations. Ducts with ribs placed at different angles to the mean flow are considered. The mean flow is assumed to be fully developed; therefore, only a small portion of the duct is calculated, and periodic boundary conditions are used in the streamwise direction. The computations are carried out using turbulence models based on the concept of isotropic eddy viscosity. Hence, only secondary flows (of the first kind) due to inviscid effects are predicted. Of particular interest is the effect of the secondary flow on the heat-transfer rate through the walls. It is demonstrated that, for ribs perpendicular to the flow, the secondary flow localizes the heat-transfer rate and has a direct effect on the spatial distribution of Nusselt number, Nu, on the smooth side wall of the duct. However, the value of Nu averaged over all the walls is not significantly affected by the presence of the secondary-flow structures. For ribs that are at an angle to the main flow, the presence of secondary flow influences both the spatial distribution and the average value of Nu.

1. Introduction

In order to increase the lifespan of the turbine blades in gas-turbine engines, which are subjected to high heat loads, various cooling techniques have been employed. One of the methodologies that have been used is to insert surface ribs, which act to promote turbulence and thus enhance heat transfer in the internal cooling passages of the blades. Thus, in order to improve design and produce more efficient engines, it is important that the flow and heat transfer of the internal cooling passage can be accurately predicted and understood. Using RANS methodology, Ooi, Iaccarino, Durbin & Behnia (2002) showed that accurate heat-transfer values can be obtained at the center of the ribbed walls, but the predictions get worse closer to the smooth side walls of the duct. It was suggested in that paper that this could be due to the presence of secondary-flow structures which might not have been properly predicted by simple eddy-viscosity closure schemes. The main purpose of the work presented here is to reveal the features of the predicted secondary-flow structure and to determine the role of these structures in the prediction of heat transfer in ribbed ducts.

In ribbed ducts, fluid is forced upward on the upstream side of the rib (supposed here to be on the floor of the duct) and downward downstream of the rib. This motion, caused by pressure gradients, together with the no-slip boundary condition along the side walls will generate a secondary circular motion with two cells rotating in opposite directions. Experimental observations and measurements of these secondary-flow motions have been

† The University of Melbourne, Australia
‡ Norwegian Defence Research Establishment, Norway

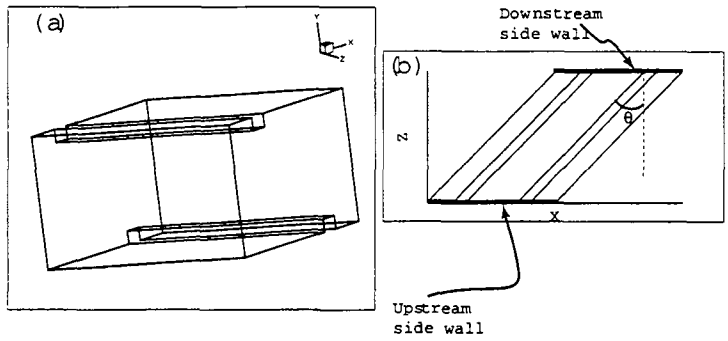

FIGURE 1. Outline of the computational domain. (a) shows a perspective view and (b) shows the top view of the computational domain.

reported by Son, Kihm & Han (1998), Rau, Cakan, Moeller & Arts (1998), Ekkad & Han (1997), Liou, Wu & Chang (1993) and Hirota, Yokosawa & Fujita (1992). The presence of these secondary-flow structures in RANS calculations has also been reported by Jang, Chen & Han (2001) and Prakash & Zerkle (1995).

'Secondary' flows allude to the currents that may arise in planes perpendicular to the primary flow direction. These flow structures may be generated by various mechanisms. Among them are pressure gradients induced by the geometry of the flow configuration, and/or by the body force associated with an imposed rotation; streamwise-aligned counter-rotating roll-cells associated with rotational or centrifugal instabilities; and turbulence-generated secondary flows. In order to capture turbulence-generated secondary flows, nonlinear or second-moment closure models must be used (see e.g. Petterson Reif & Andersson (2002)). In this study, linear eddy-viscosity models will be used, which implies that effects of turbulence-generated secondary flows are excluded. This is not a severe shortcoming *per se* since turbulence-generated secondary motions are significantly weaker than the secondary flows generated by pressure gradients. As a first step towards a more complete description of the flow in rotating ribbed passages, the present study focuses only on the non-rotating case with the ultimate objective of understanding the impact of secondary-flow structures on the overall heat transfer and on the local distribution of the Nusselt number Nu.

We have chosen to calculate the flow and heat-transfer cases investigated by Rau, Cakan, Moeller & Arts (1998). This experimental data set is unique in that heat-transfer measurements were taken both on the ribbed floor and on the smooth side walls of the duct. The data allow the effect of secondary flow on the heat-transfer distribution on all walls to be investigated. One drawback of this data set is that only the case where the ribs were placed at 90° to the mean flow was investigated. In order to investigate the effects of ribs that are at an angle to the flow, the numerical predictions were validated by the experimental data obtained by Iacovides, Kelemenis & Raisee (2003).

2. Mathematical preliminaries

In order to study the secondary-flow structures, one must first be able to detect the vortical flow structures in the numerical results. Many vortex-detection methods have been proposed in the literature, e.g. Jeong & Hussain (1995) and Chong, Perry & Cantwell (1990). In this paper, the methodology proposed by Chong, Perry & Cantwell (1990) will

be used. The vortical flow structures in the flow will be visualised by plotting isosurfaces of the second invariant of the velocity-gradient tensor, Q, defined as

$$Q = -\frac{1}{2}A_{ij}A_{ji} \tag{2.1}$$

$$= \frac{1}{2}\left(W_{ij}W_{ji} - S_{ij}S_{ji}\right). \tag{2.2}$$

A_{ij} is the local velocity-gradient tensor computed from the predicted mean-velocity field of the RANS calculations. S_{ij} and W_{ij} are the symmetric and antisymmetric parts of A_{ij} respectively. From (2.2), it is easily seen that Q measures the local strength of the rotation relative to the strain field. Positive values of Q indicate regions of the flow where rotation is dominant and negative values of Q identify regions of the flow that are strain-dominated.

To identify regions of the flow where secondary flow is important, some quantity must be used to measure the strength of the secondary flow. In this paper, the strength of the secondary flow will be measured by S, defined to be

$$S = \sqrt{\frac{V^2 + W^2}{U^2 + V^2 + W^2}}. \tag{2.3}$$

Here U is the velocity component in the direction of the main flow, and V and W are the velocity components in the plane perpedicular to U. S provides a measure of the strength of the fluid motion in the plane perpendicular to the mean flow, relative to the total velocity of the fluid. Note that S is a positive quantity which has a maximum possible value of 1 and a minimum value of 0.

3. Numerical model: assumptions and calculations

In all cases, the mean-flow field is assumed to be fully developed. Hence, only the domain extending, for example, from the leading edge of one rib to the leading edge of the next is considered. A commercial flow solver, FLUENT 6.0, is used in all calculations. The flow is assumed to be incompressible and buoyancy effects are neglected.

An outline of the computational domain is shown in figure 1. X is the streamwise direction, Y is in the vertical direction normal to the ribbed wall, and the ribs are at an angle θ to the axis of the orthogonal coordinate Z. The angle θ measures the skew of the rib relative to the main flow direction: $\theta = 0$ when the flow is perpendicular to the ribs. Walls on which the ribs are placed are called the "ribbed walls". The "side walls" are perpendicular to the "ribbed walls" and there are no ribs on these walls. The heat transfer is similar on both "side walls" for $\theta = 0$ but when $\theta \neq 0$ the heat-transfer distributions on the two "side walls" are different. In the following discussion, the part of the "side wall" upstream of the rib will be termed the "upstream side wall" and the term "downstream side wall" will be used to refer to the "side wall" downstream of the rib.

Calculations were carried out at $Re = 30,000$ with the ratio of pitch to rib height ratio, p/e, set to 9. The ribs were placed on only one of the walls, $Y = 0$. Boundary conditions of constant heat flux were implemented on all walls so that a direct comparison could be made with the experimental data of Rau, Cakan, Moeller & Arts (1998).

Another experimental data set for the flow and heat transfer in ribbed ducts can be found as case 7.3 of the 7th ERCOFTAC/IAHR Workshop. Data were obtained at

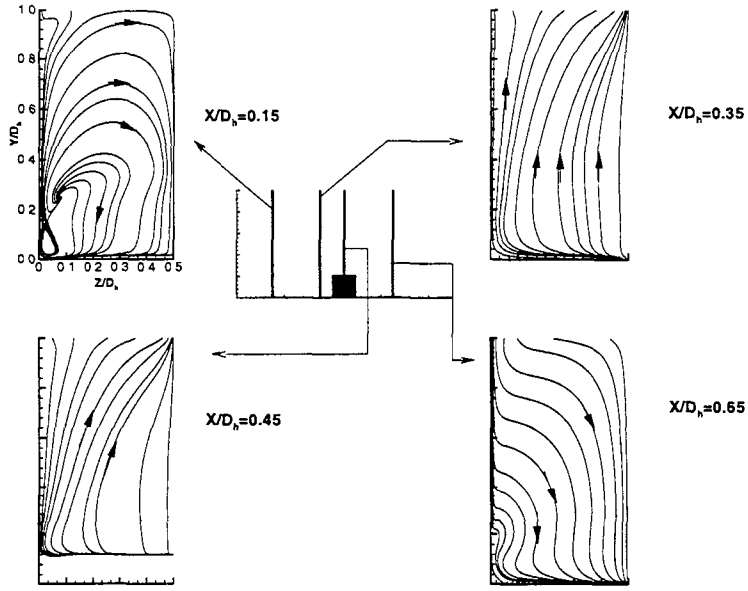

FIGURE 2. Secondary flow pattern at various streamwise stations. Calculations carried out 1s, $p/e = 9$, $Re = 30,000$, $Pr = 0.7$ with the Spalart-Allmaras model.

$Re = 100,000$ with air as the working fluid. The experiments were carried out in a square duct with the height of the ribs 10% of the width of the duct. The ribs were staggered on both the top and the bottom walls. Only the ribbed walls were heated, and the smooth side walls and the ribs themselves were insulated. In order to validate the numerical models, one set of calculations was carried out with similar thermal boundary conditions, with molecular Prandtl number $Pr = 0.71$. The results of this set of calculations can be found in Ooi, Pettersson Reif, Iaccarino & Durbin (2000). In summary, it was found that the velocity field is well predicted by all the turbulence models used, but the predicted surface heat-transfer rate differs considerably between the models. More recently, Iacovides, Kelemenis & Raisee (2003) reported measurements of the velocity field in square ducts with skewed ribs ($\theta = 45^o$) at $Re = 100,000$. Velocity fields obtained from numerical prediction are in reasonable agreement with the experimental data. No heat-transfer measurements on the side wall were reported.

As there is every likelihood that the secondary-flow structures would influence the distribution of Nusselt number Nu on the smooth side walls, further calculations were carried out with constant heat flux on the side walls in order to investigate the effects of the secondary flow on the distribution of Nu.

In order to investigate the effects of secondary-flow structures, calculations were also carried out in which the mean spanwise component of velocity, W, was set to zero at the start of the solution iterative process. Note that the value of W at the end of the iterative process is small, but finite (maximum about 10^{-5}). This is of course numerical error. This procedure eliminates all secondary-flow motion from the calculation, but still ensures mass conservation and also satisfies both the U and V momentum equations.

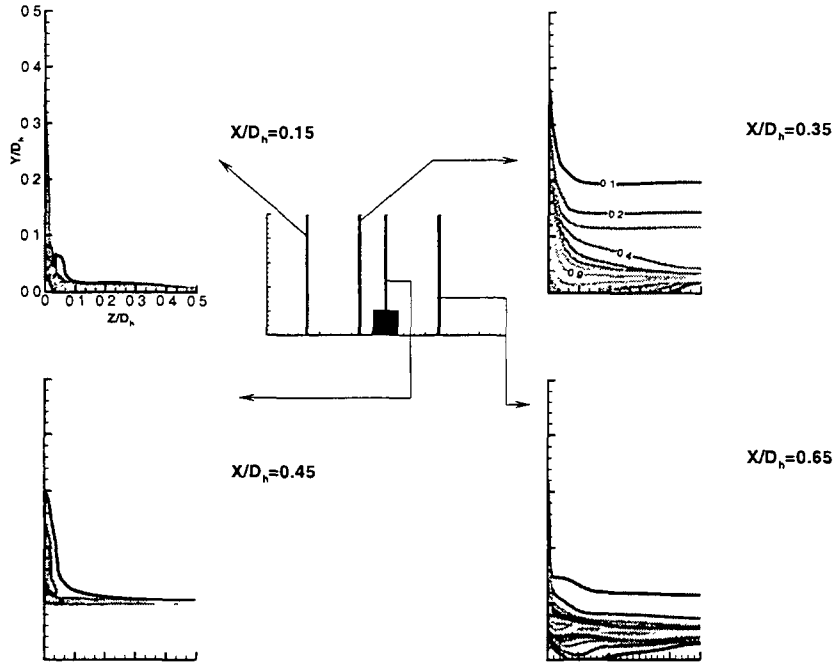

FIGURE 3. Secondary flow strength, S, at various streamwise stations. Calculations carried out at $Re = 30,000$, $p/e = 9$, $Pr = 0.71$ with the $S - A$ model.

The no-slip boundary conditions at all boundaries are also satisfied. In the discussion below, this set of calculations will be termed "no-W".

4. Results and discussion

The secondary-flow structure for calculations carried out using the Spalart-Allmaras turbulence model at $Re = 30,000$ with $p/e = 9$ is shown in figure 2. The streamlines shown are computed from the in-plane velocity components, V and W, only. Data at $X/D_h = 0.15$ and $X/D_h = 0.45$ (D_h is the hydraulic diameter) can be qualitatively compared with the sketch in the paper by Rau, Cakan, Moeller & Arts (1998). Both our predictions and the experimental data of Rau *et al.* show that on these two planes there is a general trend of fluid moving away from the smooth side wall and toward the symmetry plane. As only eddy-viscosity models are used in the calculation here, turbulence-generated secondary flow is excluded. Hence, this secondary flow must be generated by pressure gradients: this is Prandtl's secondary flow of the first kind. At $X/D_h = 0.35$ there is a general upward trend in the streamlines. This is due to the adverse pressure gradient experienced by the fluid as it approaches the rib. Further downstream, as fluid moves over the rib, a general downward movement is expected. There is a small vortex formed at the corner where the side wall meets the bottom wall. The corresponding secondary-flow strength, S, is shown in figure 3. It is clear that secondary-flow effects are more prominent close to the tip of the rib on the $Y/D_h \approx 0.1$

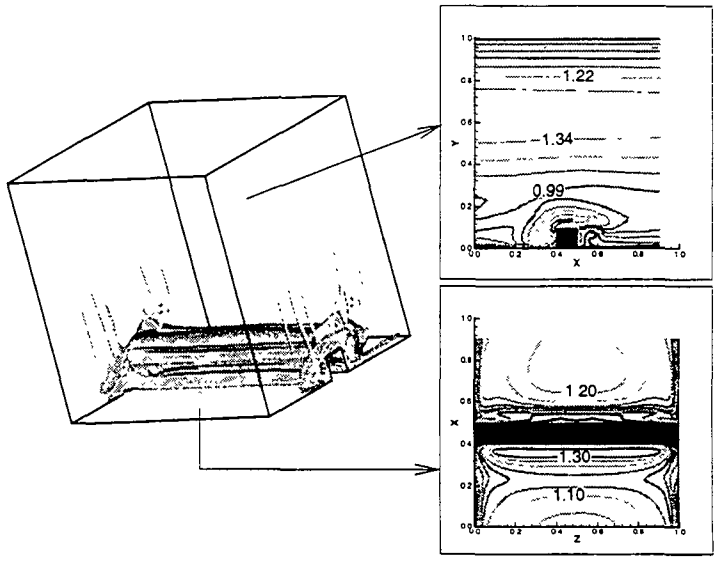

FIGURE 4. Isosurfaces of constant Q together with the spatial ditribution of Nu on the side wall of the duct. Data computed using the $S-A$ turbulence model. $Re = 30,000$, $Pr = 0.71$.

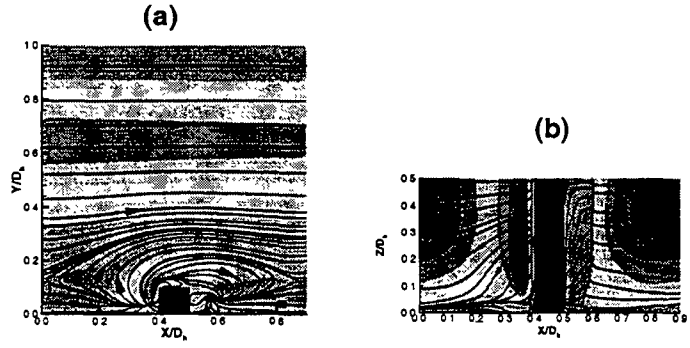

FIGURE 5. Skin friction lines on the side wall (a) and on the floor (b). Turbulent flow calculation at $Re = 30,000$ with ribs on one side ($1s$) and the Spalart-Allmaras model. Contours of Nu are also shown.

plane througout the computational domain. The secondary flow motion is stronger closer to the ribs than away from the ribs.

These secondary-flow structures can be visualised with isosurfaces of Q as shown in figure 4. As expected, spanwise structures are dominant at the center of the duct due to the recirculation bubble upstream and downstream of the rib. Close to the corners of the duct, streamwise structures are dominant. As will be shown later, these streamwise structures localize the heat-transfer rate and are responsible for the spatial distribution of Nu on the smooth side wall as shown in figure 4. From this figure, it is also clear that the spanwise flow structure is principally responsible for the spatial distribution of Nu on the bottom wall, and the streamwise flow structure is responsible for the spatial distribution of Nu on the side wall.

In order to understand the effects of the flow field on the heat-transfer distribution, skin-friction lines are shown together with the spatial distribution of Nu for the calcu-

[h]

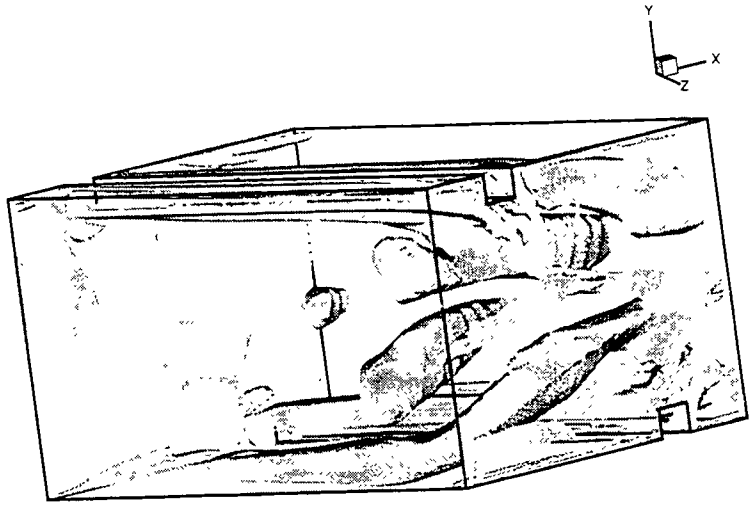

FIGURE 6. Isosurfaces of $Q = 1$. Calculations with $\theta = 45°$, $Re = 100,000$ and $Pr = 0.71$ using the $k - \epsilon$ model.

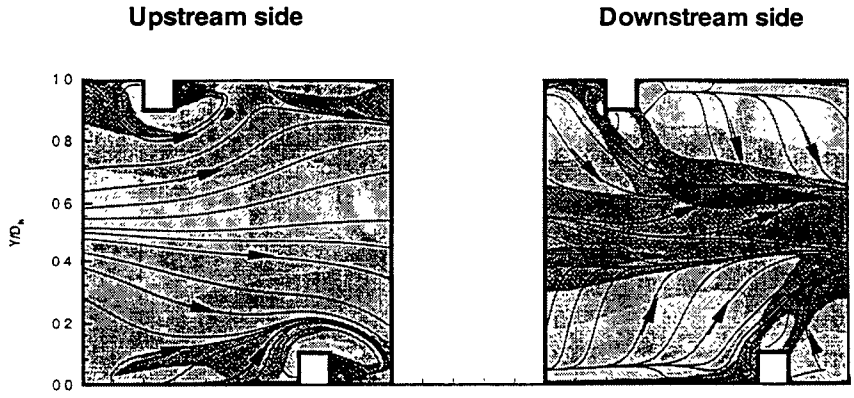

FIGURE 7. Skin friction lines and contours of Nu on the side walls of the duct. Calculations with $\theta = 45°$, $Re = 100,000$ and $Pr = 0.71$ using the $k - \epsilon$ model.

lation with $p/e = 9$ in figure 5. It is evident that flow impinges on the side wall just downstream of the rib and accelerates over the rib. This flow mechanism brings in cold fluid from the center of the duct, and this impinges on the side wall to create a region with high values of Nu. The spatial distribution of Nu on the bottom wall is influenced by the separation bubble, which is the counterpart of the spanwise vortical flow structure. The skin-friction lines show that the region of high heat transfer upstream of the rib is due to the impingement of cold fluid entrained from the center of the duct. Downstream of the rib, there are regions where relatively low values of Nu occur. This is due to the movement of fluid away from the ribbed wall towards the center of the duct.

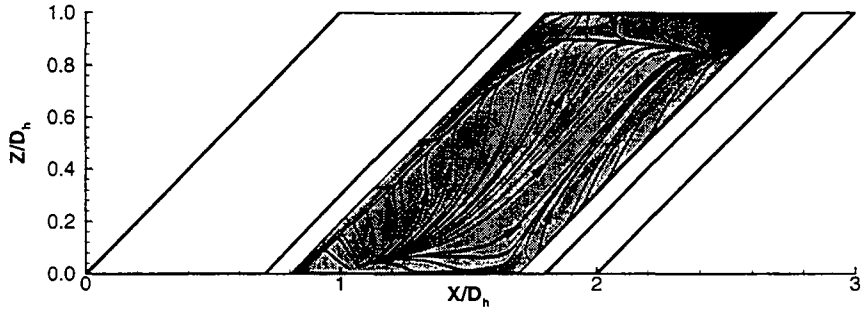

FIGURE 8. Skin friction lines and contours of Nu on the bottom wall of the duct. Calculations with $\theta = 45°$, $Re = 100,000$ and $Pr = 0.71$ using the $k - \epsilon$ model.

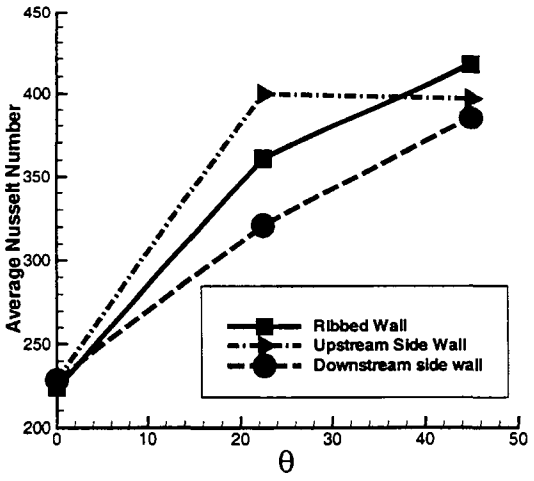

FIGURE 9. Figure showing the average Nu on the wall of the ducts. Staggered rib calculation with $Re = 100,000$ and computed using the $k - \epsilon$ turbulence model. This table shows the effects of skewing the ribs on the average values of Nu.

When the ribs are skewed, the structure of the flow field is changed dramatically. Numerical results for this case have been obtained at $Re = 100,000$ with both the two-layer $k - \epsilon$ and the Spalart-Allmaras turbulence models. The flow structure for $\theta = 45°$ is shown in figure 6. It is evident that there is much more streamwise structure in the flow field, even close to the center of the duct. This gives rise to different spatial distributions of Nu on both the smooth side walls and the ribbed walls of the duct.

The skin-friction lines and distribution of Nu on the side walls are shown in Figs. 7. On the upstream side wall, the distribution of heat-transfer rate is determined by the acceleration of flow over the ribs. On the downstream side wall, high values of Nu are found in the regions where fluid impinges on the wall. On the wall between the two ribs, the spatial distributions of Nu and skin-friction lines are shown in figure 8. It can be seen that the distribution of Nu is similar to the case where the ribs are perpendicular to the main flow.

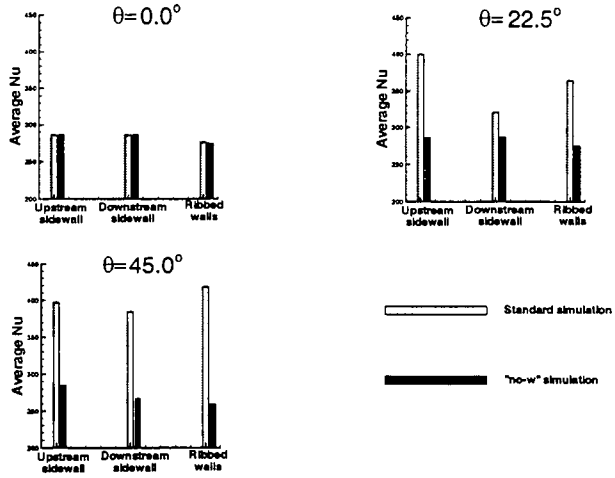

FIGURE 10. Figure showing the effects of secondary flow on the average Nu on the walls of the ducts. Staggered rib calculation with $Re = 100,000$ and computed using the $k - \epsilon$ turbulence model. This figure shows the effects of skewing the ribs on the average values of Nu.

Effects of skew angle on the heat transfer averaged all walls are shown in figure 9. In general, it can be seen that the heat transfer increases with θ. This is in agreement with experimental observation in the industry. The effects of secondary flow structures can be quantified by comparing the no-W calculations with data from the standard RANS calculations. This is shown in figure 10. The secondary flow effects on Nu_{ave} are larger for higher values of θ. For the $\theta = 0$ case, the secondary flow has very little effect on the value of Nu_{ave}. This can be understood by looking at the value of skin friction (or turbulence level) on the ribbed duct as compared to the value for a smooth duct. For higher values of skew angle, θ, the differences in the computed value of Nu between the standard and the no-W calculations is increased. This is clear evidence that the secondary flow structures that exist in the calculations for ducts with skewed ribs play an important role in the generation of heat transfer.

5. Conclusions

For a duct with surface-mounted ribs perpendicular to the mean flow, the local spatial distribution of Nusselt number Nu on the side walls is greatly affected by the presence of secondary flow structures. In agreement with the conclusions of Son, Kihm & Han (1998), it has been demonstrated that there is great enhancement of local heat-transfer rate due to flow impingement in the vicinity of the rib. Novel numerical experiments have shown that the heat-transfer rate averaged over all walls of the duct is virtually unaffected by the presence of the secondary flow structures. The average heat-transfer rate is due to the enhancement of mixing caused by turbulent diffusion.

For ducts with skewed ribs, it has been shown that the presence of secondary flow greatly increases the average heat-transfer rate. The importance of secondary flow is greater for higher values of skew angle, θ. Hence, in order to accurately predict the Nu on all walls of the duct it is critical to capture all the important physics of the secondary flow.

REFERENCES

CHONG, M. S., PERRY A.E., & CANTWELL, B. 1990 A general classification of three-dimensional flow fields. *Phys. Fluids* **2**, 765–777.

EKKAD, S. V. & HAN, J.-C. 1997 Detailed heat transfer distributions in two-pass square channels with rib turbulators. *Int. J. Heat & Mass Transfer* **40**, 2525–2537.

HIROTA M., YOKOSAWA H. AND FUJITA H.M. 1992 Turbulence kinetic energy in turbulent flows through square ducts with rib-roughened walls. *Int. J. Heat and Fluid Flow* **13**, 22–29.

IACOVIDES, H., KELEMENIS, G. AND RAISEE, M. 2003 Flow and heat transfer in straight cooling passages with inclined ribs on opposite walls; an experimental and computational study. To appear in Experimental Thermal and Fluid Science.

JANG, Y.-J., CHEN, H.-C. & HAN, J.-C. 2001 Computation of flow and heat transfer in two-pass channels with 60 deg ribs. *J. Heat Transfer* **123**, 563–575.

JEONG, J., & HUSSAIN, F. 1995 On the identification of a vortex. *J. Fluid Mech.* **285**, 69–94.

LIOU, T.-M., WU, Y.-Y. AND CHANG, Y. 1993 LDV Measurements of periodic fully developed main and secondary flows in a channel with rib-disturbed walls. *J. Fluids Engg* **115**, 109–114.

OOI, A., IACCARINO, G., DURBIN, P. & BEHNIA, M. 2002 Reynolds averaged simulation of flow and heat transfer in ribbed ducts. Accepted for publication in *Int. J. Heat and Fluid Flow.*

OOI, A., PETTERSSON REIF, B., IACCARINO, G. & BEHNIA, M. 2000 Evaluation of RANS models for rotating flows. *Proceedings of the Summer Program*, Center for Turbulence Research, NASA Ames/Stanford Univ., 229–239.

PRAKASH, C., & ZERKLE, R. 1995 Prediction of turbulent flow and heat transfer in a ribbed rectangular duct with and without rotation. *J. Turbomachinery* **117**, 255–264.

PETTERSON REIF B. A. & ANDERSSON, H. I. 2002 Prediction of turbulence-generated secondary mean flow in a square duct. *Flow, Turbulence and Combustion* **68**, 41–61.

RAU, G., CAKAN, M., MOELLER, D. & ARTS, T. 1998 The effect of periodic ribs on the local aerodynamic and heat transfer performance of a straight cooling channel. *J. Turbomachinery* **120**, 368–375.

SON, S.Y., KIHM, K.D. & HAN, J.-C. 2002 PIV flow measurements for heat transfer characterization in two-pass square channels with smooth and 90° ribbed walls. *Int. J. Heat and Mass Transfer* **45**, 4809–4822.

SPALART, P. R. & ALLMARAS, S. R. 1992 A one-equation turbulence model for aerodynamic flows. *AIAA Paper* 92-0439.

Modeling convection heat transfer and turbulence with fire applications: a high temperature vertical plate and a methane fire

By D. Rouson †, S. R. Tieszen ‡ AND G. Evans ¶

Simulations of the three-dimensional turbulent flow and heat transfer adjacent to a large (3 meter) high temperature (up to 860 K) vertical flat plate and in a large-scale methane flame have been made and compared with experimental data. Results are obtained with a Reynolds averaged Navier-Stokes (RANS) $v^2 - f$ model, a direct numerical simulation (DNS), and a detached eddy simulation (DES) model. The preliminary results are encouraging, with respect both to heat transfer and to the prediction of large-scale structures in these highly buoyant flow fields.

1. Motivation and objectives

Although radiation is the dominant heat-transfer mechanism in fires, turbulent convection to or from a surface can be significant. The convective regime typically encountered in fires is turbulent mixed convection. Due to large surfaces and large temperature differences, the Grashof number in fires can be quite high, e.g. 1.0×10^{12}, and the effects of variable properties can be significant. Turbulent mixed-convection heat transfer from a large (3 meter) vertical, high-temperature (T_{surface} up to 860K) surface was studied experimentally by Siebers, Schwind & Moffat (1983). In that study, local and average heat transfer coefficients as well as boundary layer profiles of velocity and temperature were obtained; these quantities can be used for validation of computer models of turbulent convection heat transfer dint conditions commonly encountered in fires. The present work describes three approaches that use different formulations to solve the Navier-Stokes and energy equations to predict the flow and heat transfer from a large, high temperature vertical surface. These three methods are: 1) a RANS formulation using the $v^2 - f$ model in an unstructured-control-volume finite-element code to predict the steady flow and heat transfer; 2) a DNS formulation of the unsteady free convection turbulent boundary layer on the high-temperature plate; and 3) a DES formulation that uses time filtering to allow large-scale time-dependent structures to be captured. Preliminary results were obtained during the summer program and are described in the following sections of this report.

2. RANS $v^2 - f$ modeling of mixed and forced convection

2.1. *Problem description and cases selected for simulation*

The problem studied is shown in figure 1. Air flows horizontally at constant freestream velocity parallel to the surface (xy plane) of a 3 m by 3 m vertical flat plate. In the experiment the plate surface consisted of 21 stainless steel strips oriented horizontally

† City College of the City University of New York, NY
‡ Sandia National Laboratories, Albuquerque, NM
¶ Sandia National Laboratories, Livermore, CA

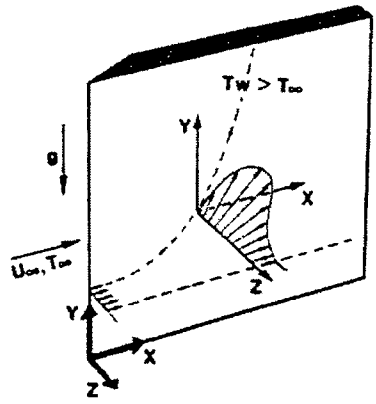

FIGURE 1. Flat plate geometry.

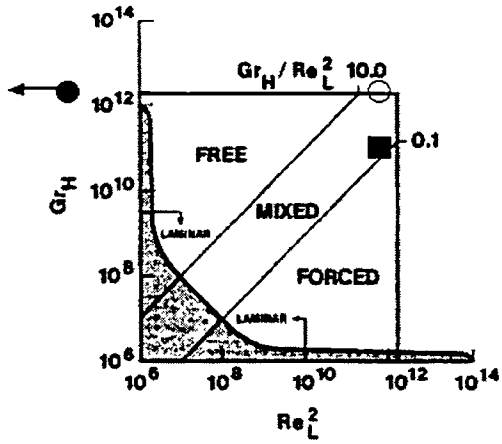

FIGURE 2. Flow regime map showing the three cases selected for simulation; filled circle: free convection ($Gr_H = 1.4 \times 10^{12}$, $Re_L = 0.0$, $Gr_H/Re_L^2 = \infty$); open circle: mixed convection ($Gr_H = 2.3 \times 10^{12}$, $Re_L = 8.7 \times 10^5$, $Gr_H/Re_L^2 = 3.06$); filled square: forced convection dominated ($Gr_H = 1.4 \times 10^{11}$, $Re_L = 8.9 \times 10^5$, $Gr_H/Re_L^2 = 0.18$).

(from x=0 to L) with an electrical current passing through each strip to give uniform heat flux through the surface. The plate surface temperature was measured at 105 locations with thermocouples. These measured surface temperatures were used in the current study as the thermal boundary condition at the surface of the plate ($z = 0$). Figure 2 shows the flow regime studied experimentally in terms of dimensionless parameters, Gr_H and Re_L, where

$$Gr_H = \frac{g\beta(T_w - T_\infty)H^3}{\nu^2} \qquad Re_L = \frac{u_\infty L}{\nu}, \tag{2.1}$$

and the cases selected for the numerical study.. The properties of air that enter these dimensionless parameters were evaluated at ambient temperature (T_∞) and pressure; H and L are the vertical and horizontal plate dimensions, respectively. The three cases selected for simulation span the range of the experiment: they are; (1) a forced-convection-

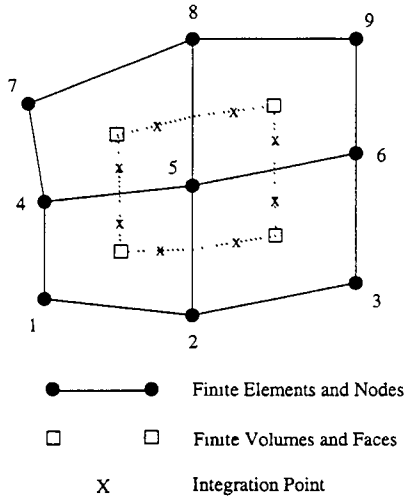

FIGURE 3. A control volume centered about a finite-element node in a collection of 2D quadrilateral elements.

dominated flow condition (ID604) with $u_\infty = 4.4\,\mathrm{m/s}$, $\mathrm{Re_L} = 8.9{\times}10^5$, $T_w \approx 323\,\mathrm{K}$, $\mathrm{Gr_H} = 1.4 \times 10^{11}$, $\mathrm{Gr_H/Re_L}^2 = 0.18$; (2) a free-convection flow condition (ID643) with $T_w \approx 698\,\mathrm{K}$, $\mathrm{Gr_H} = 1.4 \times 10^{12}$; and (3) a mixed-convection flow condition (ID648) with $u_\infty = 4.3\,\mathrm{m/s}$, $\mathrm{Re_L} = 8.7 \times 10^5$, $T_w \approx 829\,\mathrm{K}$, $\mathrm{Gr_H} = 2.3 \times 10^{12}$, $\mathrm{Gr_H/Re_L}^2 = 3.06$.

The high temperatures of the mixed- and free-convection cases result in significant property variations across the boundary layer and a radiation heat transfer that is 38% to 50% of the electrical energy dissipated in the surface. The heat transfer by radiation and by conduction through the back surface of the plate was accounted for in determining the local heat transfer coefficient, which had an experimental uncertainty ranging from 6% to 10%.

2.2. *Numerical method*

The numerical model is a low-Mach-number, variable-property formulation of the Reynolds-averaged Navier-Stokes (RANS), energy, species, and mass-conservation equations. Developed at Sandia National Laboratories as part of the Department of Energy's Accelerated Strategic Computing Initiative (ASCI) project, Fuego is a control volume finite element code for the simulation of the fluid mechanics and heat transfer in fires (Moen, Evans, Domino & Burns (2002)). Combustion is modeled with the Eddy Dissipation Concept (EDC) of Magnussen (1989); the default turbulence model is the standard $k-\epsilon$ model of Launder & Spalding (1974). Recently the $v^2 - f$ model of Durbin (1991) has been added as an option, and is used in this study. Transport equations are included for 6 species and for the nucleation, growth, and transport of soot. For fire simulations Fuego is coupled with a discrete-ordinates finite-element participating-media radiation code, Syrinx (Burns (1997)). Fuego and Syrinx are two modules of a larger suite of codes in the SIERRA framework (Edwards & Stewart (2001)) at Sandia. This framework provides a common architecture, allowing codes to be coupled to solve multi-mechanics problems. The framework provides access to linear solver packages, parallel tools, parsing tools, etc.

Variables in Fuego are collocated at the nodes of the mesh as shown in the control volume of figure 3 (shown as a 2D quadrilateral for convenience). A pressure-projection method is used together with pressure smoothing to satisfy continuity at each time step;

the equations are solved one at a time (segregated-solution method). Three-dimensional hex elements are supported currently with tetrahedral elements planned. The code is first-order accurate in time; various upwind convection discretizations yield overall spatial accuracy between first and second order. The results presented here used first-order upwind differences. Fuego runs on a variety of computing platforms including Janus, the massively-parallel computer at Sandia.

The control-volume formulation of the turbulence model is:

$$\int \frac{\partial \rho k}{\partial t} dV + \int \rho k u_j n_j dS = \int \left(\mu + \frac{\mu_t}{\sigma_k}\right) \frac{\partial k}{\partial x_j} n_j dS + \int (P - \rho\epsilon) dV \tag{2.2}$$

$$\int \frac{\partial \rho \epsilon}{\partial t} dV + \int \rho \epsilon u_j n_j dS = \int \left(\mu + \frac{\mu_t}{\sigma_\epsilon}\right) \frac{\partial \epsilon}{\partial x_j} n_j dS + \int \frac{1}{T}(C'_{\epsilon_1} P - C_{\epsilon_2} \rho\epsilon) dV \tag{2.3}$$

$$\int \frac{\partial \rho \bar{v^2}}{\partial t} dV + \int \rho \bar{v^2} u_j n_j dS = \int (\mu + \mu_t) \frac{\partial \bar{v^2}}{\partial x_j} n_j dS + \int (\rho k f - \rho N \bar{v^2} \frac{\epsilon}{k}) dV \tag{2.4}$$

$$\int \frac{f}{L^2} dV - \int \frac{\partial f}{\partial x_j} n_j dS = \int \frac{1}{L^2} \left\{ C_1 \frac{(2/3 - \bar{v^2}/k)}{T} + C_2 \frac{P}{\rho k} + \frac{(N-1)\bar{v^2}/k}{T} \right\} dV \tag{2.5}$$

$$P = 2\mu_t S^2 - \frac{2}{3}\delta_{ij} \frac{\partial u_i}{\partial x_j} \left(\rho k + \mu_t \frac{\partial u_l}{\partial x_l}\right) \tag{2.6}$$

$$S^2 = S_{ij} S_{ij} = \frac{1}{4} \left(\frac{\partial u_i}{\partial x_j} + \frac{\partial u_j}{\partial x_i}\right) \left(\frac{\partial u_i}{\partial x_j} + \frac{\partial u_j}{\partial x_i}\right) \tag{2.7}$$

$$T = \max \left[\frac{k}{\epsilon}, 6\sqrt{\frac{\nu}{\epsilon}} \right] \tag{2.8}$$

$$L = C_L \max \left[\frac{k^{3/2}}{\epsilon}, C_\eta \left(\frac{\nu^3}{\epsilon}\right)^{1/4} \right] \tag{2.9}$$

$$\mu_t = C_\mu \rho \bar{v^2} T \tag{2.10}$$

$$C'_{\epsilon_1} = C_{\epsilon_1} \left(1 + 0.045\sqrt{k/\bar{v^2}}\right) \; ; \quad C_{\epsilon_1} = 1.4, \; C_{\epsilon_2} = 1.9, \; C_\mu = 0.22 \tag{2.11}$$

$$C_1 = 0.4, \; C_2 = 0.3, \; N = 6, \; C_L = 0.23, \; C_\eta = 70, \; \sigma_\epsilon = 1.0 \tag{2.12}$$

In the above equations, $k, u_j, \rho, n_j, \mu, P, \epsilon, \bar{v^2}, f, \nu,$ and μ_t are the turbulent kinetic energy, time averaged velocity, density, unit normal, dynamic viscosity, turbulent energy production rate, turbulent energy dissipation rate, wall-normal component of turbulent kinetic energy, elliptic relaxation variable, kinematic viscosity, and turbulent viscosity, respectively. The turbulent Prandtl number is assumed to be 0.9. At the surface of the plate ($z = 0$) the boundary conditions for the turbulence variables are

$$k = \bar{v^2} = f = 0; \quad \epsilon = 2\nu k_p {y_p}^2 \tag{2.13}$$

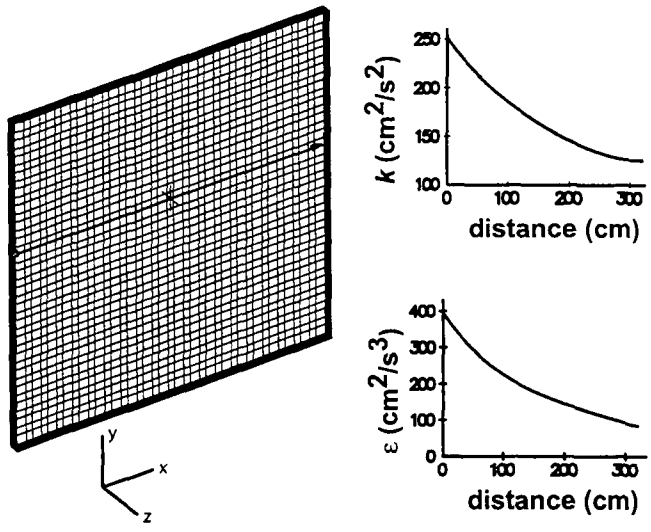

FIGURE 4. Curves of k and ϵ showing decay in the streamwise direction of the freestream values and mesh showing line along which curve data was taken (y=2 m; z=10 cm).

where variables with subscript p are assumed to be located at the centers of the surface node subcontrol volumes. For the forced and mixed convection cases, at the inflow boundary ($x = 0$), velocity, temperature, k, ϵ, and $\bar{v^2}$ are specified and $\partial f/\partial n = 0$. On the open boundaries: at y=0, H and at x=L and as $z \to \infty$, pressure is specified ($p = 0$), $\partial f/\partial n = 0$, and k, ϵ, and $\bar{v^2}$ are convected out of the domain with the calculated mass flow rate. If the flow is into the domain on the open boundaries, then k, ϵ, and $\bar{v^2}$ enter the domain with specified values.

2.3. *Forced convection dominated flow and heat transfer results*

In the forced convection dominated case selected for simulation, ID604, $\mathrm{Re_L} = 8.9\mathrm{x}10^5$ (the momentum thickness Reynolds number was approximately 1450 at x=2.75 m). In the experiment the boundary layer was tripped with a vertical wire located at x=0.65 m; effectively the upstream 30% of the boundary layer was laminar or transitional. To insure a turbulent boundary layer flow over the plate, the simulation used an inlet turbulent intensity of 3% and a length scale of 10 cm, resulting in inlet values of k and ϵ of 250 $\mathrm{cm^2/s^2}$ and 394 $\mathrm{cm^2/s^3}$, respectively; $\bar{v^2}$ was set to 70 $\mathrm{cm^2/s^2}$ at the inlet. The effects of buoyancy are small in this case ($\mathrm{Gr_H/Re_L}^2 = 0.18$). The 3D mesh used for the results shown in this report and curves showing the freestream (z=10 cm) decay of k and ϵ in the streamwise (x) direction at the height y=2 m are shown in figure 4. The mesh is $20 \times 20 \times 30$ in the (x, y, z) directions, uniform in x and y, and nonuniform in z such that $y^+ \approx 2$ at the first subcontrol volume off the surface.

Computed and measured boundary-layer profiles of temperature and the x component of velocity at x=276 cm, y=108 cm are compared in figures 5 and 6, respectively. The calculated results agree reasonably well with the data. The computed local heat-transfer coefficient is compared with experimental data in figure 7. Also shown in figure 7 is a 2D simulation result (symmetry boundary conditions were applied to the domain at y=0,

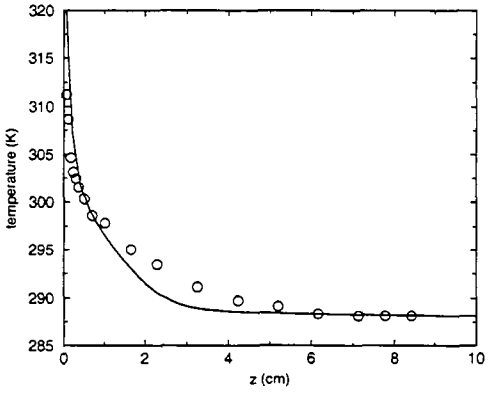

FIGURE 5. Comparison of calculated (line) and measured (symbols) boundary layer temperature profiles at x=276 cm, y=108 cm; forced convection dominated, ID604.

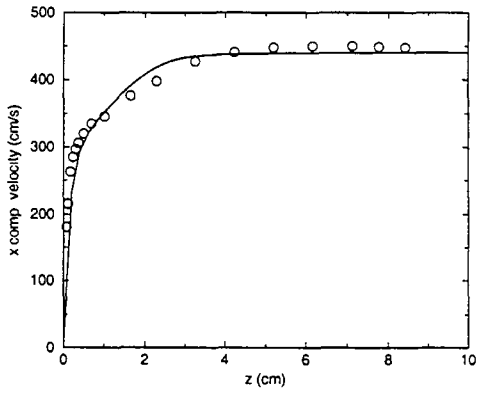

FIGURE 6. Comparison of calculated (line) and measured (symbols) boundary layer velocity profiles at x=276 cm, y=108 cm; forced convection dominated, ID604.

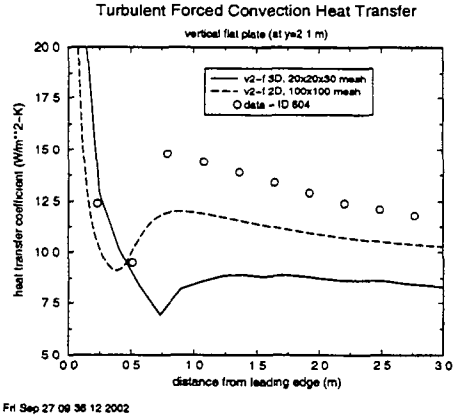

FIGURE 7. Local heat-transfer coefficient at y=2.1 m for the forced convection dominated case.

H) on a 100 × 100 mesh in the x, z plane with one element in the vertical (y) direction. Transition is evident where the heat transfer coefficient increases from a minimum value at $x \approx$60 cm. Note that the specified surface-temperature distribution implicitly includes the effects of transition; prediction of transition is not addressed here. The calculations agree qualitatively with the data. Medium- and fine-mesh 3D calculations are being made to reduce the uncertainty in the results due to mesh spacing.

2.4. *Mixed convection flow and heat transfer results*

The Reynolds number for the mixed-convection case selected for simulation, ID648, is $\mathrm{Re_L} = 8.7 \times 10^5$, similar to the forced convection dominated case. There was no trip wire in this experimental case; however there is evidence of transition at approximately the same horizontal location on the flat plate ($x \approx$0.65 m). As in the forced-convection-dominated case, the simulation used an inlet turbulent intensity of 3% and a length scale of 10 cm. The same 20 × 20 × 30 3D mesh was used for this case.

The effects of buoyancy are now significant ($\mathrm{Gr_H}/\mathrm{Re_L}^2 = 3.06$): the horizontal flow in the freestream over the plate undergoes significant turning toward the vertical (y) direction within the boundary layer. Computed and measured boundary-layer profiles

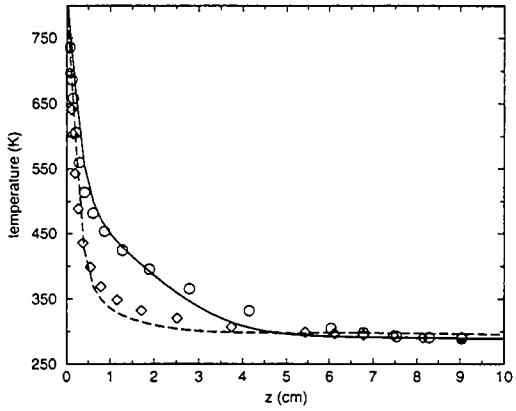

FIGURE 8. Comparison of calculated (lines) and measured (symbols) boundary layer temperature profiles at x=276 cm, y=252 cm (solid line and circles) and at x=276 cm, y=22 cm (dashed line and diamonds); mixed convection, ID648.

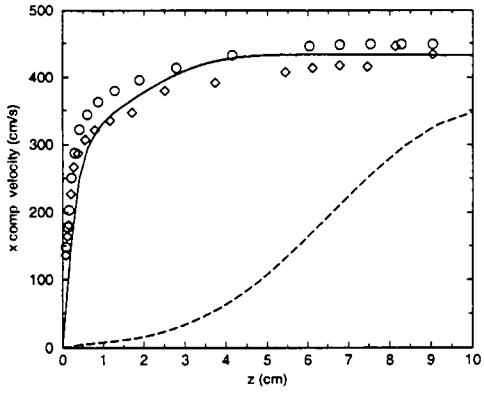

FIGURE 9. Comparison of calculated (lines) and measured (symbols) boundary layer x comp. velocity profiles at x=276 cm, y=252 cm (solid line and circles) and at x=276 cm, y=22 cm (dashed line and diamonds); mixed convection, ID648.

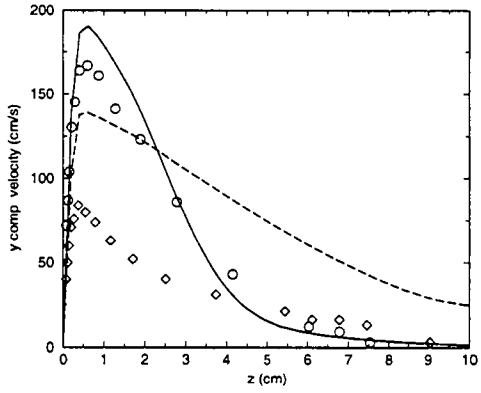

FIGURE 10. Comparison of calculated (lines) and measured (symbols) boundary layer y comp. velocity profiles at x=276 cm, y=252 cm (solid line and circles) and at x=276 cm, y=22 cm (dashed line and diamonds); mixed convection, ID648.

of temperature and x and y components of velocity near the vertical trailing edge of the plate (x=276 cm) and at two vertical locations (y=22 and 252 cm) are compared in figures 8, 9 and 10 respectively. The calculated results agree well with the data except for the velocity components at y=22 cm (near the bottom of the plate). Efforts are underway to compute this case at finer grid resolution.

The computed local heat-transfer coefficient for the mixed-convection case is compared with experimental data in figure 11 along a horizontal line on the plate at y=155 cm, and in figure 12 along a vertical line near the vertical trailing edge of the plate at $x \approx$ 270 cm. The results are in reasonable agreement with experimental data.

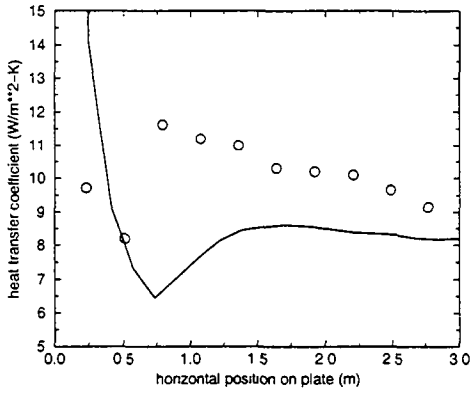

FIGURE 11. Comparison of calculated (line) and measured (symbols) local heat transfer coefficient on a horizontal line at y=1.55 m for the mixed convection case, ID648.

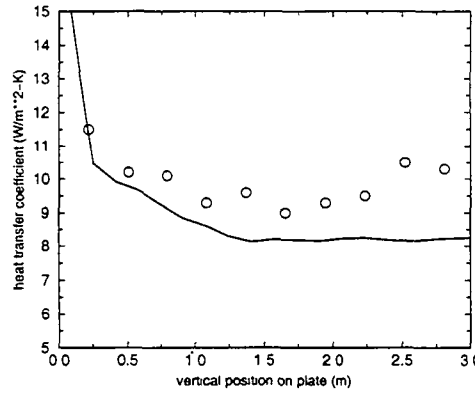

FIGURE 12. Comparison of calculated (line at x=269 cm) and measured (symbols at x=276 cm) local heat transfer coefficient on a vertical line at $x \approx$2.7m for the mixed convection case, ID648.

3. DNS of free convection

In the free-convection case of figure 1 ($Gr_H = 1.4x10^{12}$, $Re_L = 0.0$), the experimental data of Siebers, Schwind & Moffat (1983) do not include boundary layer profiles below approximately 2 m above the bottom of the plate. In such cases, the upstream flow conditions near the bottom of the plate may be difficult to predict with RANS calculations such as the forced- and mixed-convection calculations presented in the last section. In particular, it may be difficult to predict where transition to turbulence occurs. The DNS results to be presented here for *free* convection help to answer such questions and provide higher-fidelity boundary-layer statistics against which to validate the RANS calculations. Free-convection RANS calculations are still in progress.

The spatial and temporal resolution requirements of DNS restrict the size of the domain to less than 20% of the vertical extent of Siebers' plate and less than 5% of its width. However, it is expected that the DNS data will also provide a benchmark for a future LES encompassing the full vertical extent of the plate. Figure 13 shows the DNS domain geometry and instantaneous temperature contours. The opaque boundary shown encompasses a 5cm tall, unheated, free-slip surface, above which is a 50 cm tall no-slip surface heated to 424 C. Above this no-slip surface is a 5 cm tall open surface. The two 5cm tall surfaces separate the heated region from the inflow and outflow boundary conditions to prevent these conditions from affecting the statistics collected in the heated region. In the wall-normal and spanwise horizontal directions, the flow domain is 3.75 cm and 10 cm wide, respectively. The above dimensions correspond to roughly 1730, 298, and 109 wall units in the streamwise (vertical), spanwise, and wall-normal directions, respectively.

All clear boundaries in figure 13 are open and allow inflow or outflow as the problem solution dictates. The numerical implementation of these boundary conditions will be described in section 3.2.

3.1. *Mathematical model*

The DNS was performed with the Fire Dynamics Simulator (FDS) published by the National Institute of Standards and Technology (see McGrattan, Rehm & Baum (1994), McGrattan, Baum & Rehm (1998)). FDS solves the low-Mach-number form of the compress-

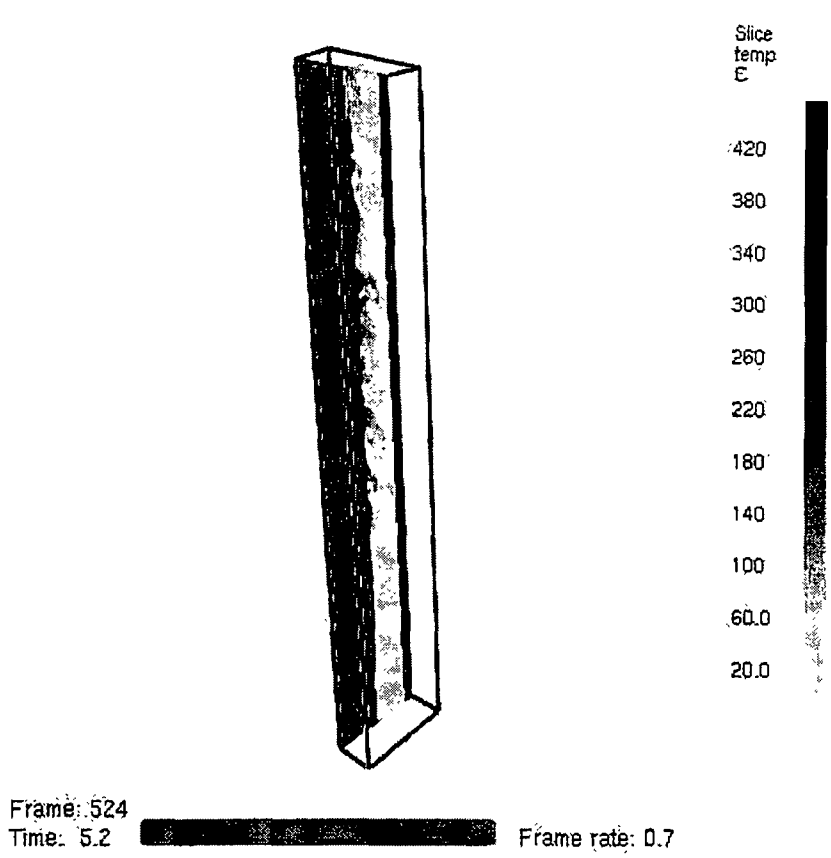

FIGURE 13. Geometry and temperature contours at the end of the DNS.

ible Navier-Stokes equations first proposed by Rehm & Baum. (1978). For a chemically -nert gas, these equations take the form

$$\frac{\partial \mathbf{u}}{\partial t} = \mathbf{u} \times \omega - \nabla \mathcal{H} + \frac{1}{\rho}(\rho - \rho_\infty)\mathbf{g} + \nabla \cdot \tau, \tag{3.1}$$

$$\frac{\partial \rho}{\partial t} + \mathbf{u} \cdot \nabla \rho = -\rho \nabla \cdot \mathbf{u}, \tag{3.2}$$

where $\mathbf{u}$, ω, and ρ are the fluid velocity, vorticity and density, respectively; ρ_∞ is a reference density; τ is the viscous-stress tensor given by

$$\tau = \mu \left[\nabla \mathbf{u} + (\nabla \mathbf{u})^T + \frac{2}{3}(\nabla \cdot \mathbf{u})\mathbf{I} \right], \tag{3.3}$$

where $\mathbf{I}$ is the identity tensor, and finally

$$\nabla \mathcal{H} \approx \frac{1}{2}\nabla |\mathbf{u}|^2 + \frac{1}{\rho}\nabla \tilde{p} \tag{3.4}$$

is an approximation that neglects baroclinic torques resulting from the non-alignment of the density and pressure gradients. In the last equation, $\tilde{p}$ is the pressure perturbation

in the following decomposition:

$$p = p_0 - \rho_\infty g z + \tilde{p}, \tag{3.5}$$

where p_0 is a background pressure,which remains constant in the present application and is given by the ideal gas law:

$$p_0 = \rho R T, \tag{3.6}$$

where T is the gas temperature and R is the gas constant divided by the molecular weight.

FDS uses fast Fourier transforms to solve the elliptic partial differential equation for $\mathcal{H}$ that results from taking the material derivative of p_0 and combining it with mass- and energy-conservation statements:

$$\nabla^2 \mathcal{H} = -\frac{\partial \nabla \cdot \mathbf{u}}{\partial t} - \nabla \cdot \mathbf{F}, \tag{3.7}$$

$$\mathbf{F} \equiv -\mathbf{u} \times \omega - \frac{1}{\rho}(\rho - \rho_\infty)\mathbf{g} + \nabla \cdot \tau, \tag{3.8}$$

$$\nabla \cdot \mathbf{u} = \frac{\gamma - 1}{\gamma p_0}(\nabla \cdot \nabla T - \nabla \cdot \mathbf{q}_r), \tag{3.9}$$

where γ is the ratio of specific heats, k is the thermal conductivity, and $\mathbf{q}_r$ is the radiative heat flux.

In all of the above equations, FDS accounts for variable properties. Since FDS is designed to model combustion, the dynamic viscosity is calculated for each species present according to

$$\mu_l = \frac{26.69 \times 10^{-7}(M_l T)^{1/2}}{\sigma_l^2 \Omega_\nu}, \tag{3.10}$$

where M_l and σ_l are the molecular weight and the Lennard-Jones hard-sphere diameter of the l^{th} species, and where Ω_ν is an empirical collision integral. Likewise, the thermal conductivity of the l^{th} species is

$$k_l = \frac{\mu_l c_{p,l}}{Pr}, \tag{3.11}$$

where the Prandtl number, Pr, is 0.7 and $c_{p,l}$ is the constant-pressure specific heat of species l.

3.2. *Numerical method*

The above equations are advanced in time using a second-order Runge-Kutta, predictor-corrector algorithm. Spatial derivatives are estimated with second-order-accurate finite differences on a rectangular grid, with scalar quantities assigned to the center of grid cells and vector quantities assigned to cell faces. Convective terms are upwind-biased, based on a CFL condition, in the predictor step and downwind-biased in the corrector step. Where the CFL number is near its upper limit, differencing is nearly fully-upwind. Where the CFL number is small, differencing is nearly centered. Diffusive terms are central-differenced. In the current problem, these differencing schemes are employed on a grid with $192 \times 96 \times 64$ points in the streamwise, spanwise and wall-normal directions resulting in spacings of 3.1, 9.0 and 1.7 wall units in these directions, respectively.

The initial condition is still air at standard temperature and pressure, to which FDS adds random vorticity perturbations resulting in velocites on the order of 1mm/s. These perturbations disrupt the flow symmetry that would othewise result from the specifi-

cation of symmetric boundary and initial conditions. As will be seen below, this has the effect of tripping the flow, causing unstable waves that decay into turbulence.

A homogeneous Neumann condition is applied to $\mathcal{H}$ at the no-slip boundary:

$$\frac{\partial \mathcal{H}}{\partial n} = 0, \tag{3.12}$$

where n is the direction normal to the boundary. At open boundaries, the boundary condition on $\mathcal{H}$ varies depending on the flow orientation:

$$\mathcal{H} = |\mathbf{u}|^2/2, \quad \text{outgoing} \tag{3.13}$$

$$\mathcal{H} = 0, \quad \text{incoming.} \tag{3.14}$$

Other implementation details are described by McGrattan *et al.* (2001).

3.3. *DNS results*

Figure 13 shows temperature contours at the final time step after 5.2 s of physical time. Smooth, laminar contours can be discerned near the bottom of the domain with a rapid transition to turbulence between 10 and 20 cm from the bottom of the heated portion. This flow pattern is established after approximately 1.5 s. It is preceded by a very orderly temporal transition, illustrated in figure 14 which shows an instantaneous isothermal surface at 200 C in a run with a slightly higher wall temperature of 462 C and a resolution of only 64 points in the wall-normal direction. Apparent in the surface at 1.2s into the simulation is a dominant mode of oscillation extending over the vertical extent of the plate with little spanwise temperature variation except near the side boundaries where cold air is entrained. This orderly instability rapidly decays into a fully three-dimensional disturbance, yielding the disorderly surface shown in figure 15 after 1.6 s. Time traces (not shown) indicate that the above unstable mode results in a persistent, periodic oscillation in the temperatures and velocities 10 cm above the bottom of the plate. This periodic variation remains at this location throughout the simulation, while just above this location, the entire flow is turbulent after 1.5 s.

Figures 16–17 show time-averaged temperature and velocity profiles at a location 40 cm above the bottom of the heated portion of the plate. Although both plots agree qualitatively with typical free-convection profiles, the RANS calculations to which these will be compared are still under way and no data were were taken this low on the plate in the experiment. Calculating a heat-transfer coefficient from the temperature profile, and evaluating all properties at freestream conditions, the ratio $Nu_x/Gr_x^{1/3}$ is 0.173, where Nu_x is the Nusselt number based on height above the bottom edge of the plate and Gr_x is the Grashof number based on the same height. This value is is 80% higher than the value measured by Siebers, Schwind & Moffat (1983) in fully-turbulent flow. However, $Nu_x = 270$ and $Gr_x = 3.8 \times 10^9$ at this location in the DNS, which falls in the middle of the turbulent transition range in the experimental data.

4. Temporal filtering

The preceding sections have addressed convection heat transfer with the broadest range of filter widths from direct numerical simulation to traditional Reynolds averaging. Approaches that implicitly or explicitly involve filter widths between these limits, including large-eddy simulation, very-large-eddy simulation, detached-eddy simulation, and unsteady RANS (cf. Speziale (2000), Spalart (2000)). All but the last are filtered

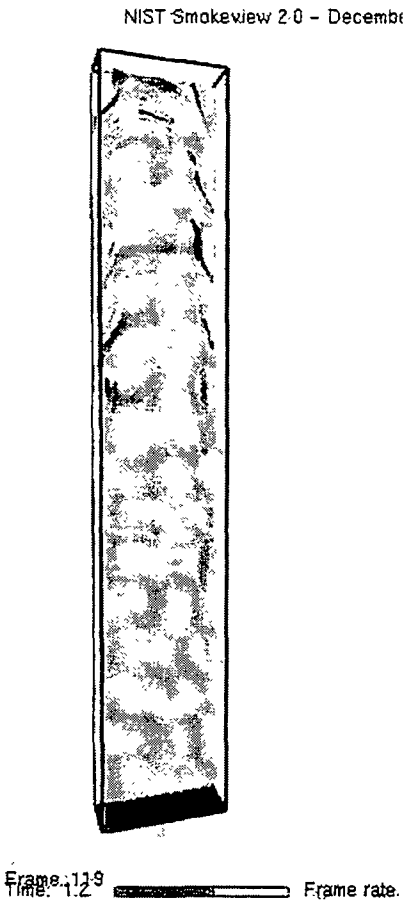

FIGURE 14. Isothermal 200 C surface 1.2 s after the initial time.

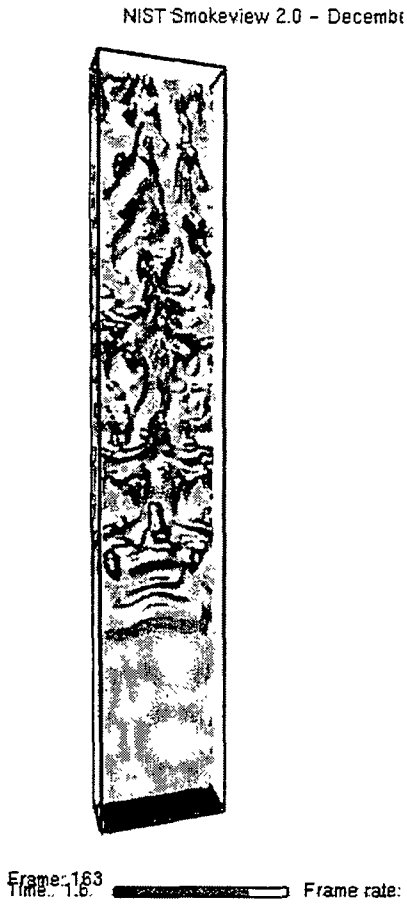

FIGURE 15. Isothermal 200 C surface 1.6 s after the initial time.

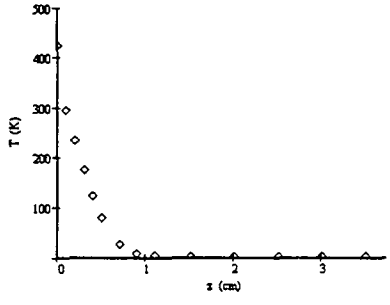

FIGURE 16. Temperature profile 40 cm above the bottom of the heated portion of the plate.

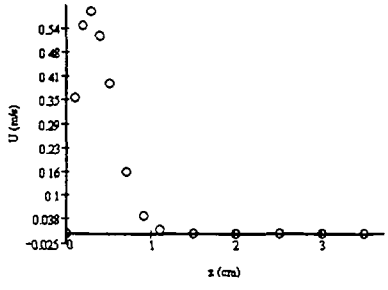

FIGURE 17. Vertical velocity profile 40 cm above the bottom of the heated portion of the plate.

in space: unsteady RANS is filtered in time. These techniques bridge the gap between fidelity and engineering practicality. The choice of method depends on application needs for these conflicting requirements.

Fire environments are strongly influenced by two modes of heat transfer, radiation and

convection, with radiation being dominant in most cases. In general, material response is dominated by conduction, and there is usually a significant separation between turbulent and material-response time scales. Thus, a substantial filter width can be employed for the reacting fluid mechanics without significant fidelity loss in material response. For this reason, it is desirable to use steady RANS approaches for maximum practicality.

On the other hand, to capture radiative emission, it is desirable to obtain as much spectral (temporal/spatial) resolution as possible from the Navier-Stokes solution because radiative emission is a highly-nonlinear process and is dominated by small-scale flame structures. Generally, the time-averaged output of a highly-nonlinear process is not strictly a function of time-averaged inputs. Specifically, the time-average flux is all that is required for material response, but the fidelity of subgrid radiative-emission models is limited by time-averaged scalar inputs. Further, fires are reacting plumes, and as such, there is strong coupling between the density and velocity fields. The coupling results in strong vorticity production, and turbulent dynamics produce large, coherent structures with a full turbulent cascade. For these reasons, it is desirable to resolve at least the large-scale, low frequency, structures within the flow.

Thus fire application requirements suggest a hybrid RANS/LES approach, retaining RANS in the near wall region of objects and LES in the bulk reacting flow. Most hybrid approaches, such as detached-eddy simulation, have employed spatial filtering of the Navier-Stokes equations, even though the RANS equations are temporally filtered. For this study, it was desired to explore temporal filtering as a means of separating the high-frequency wall boundary-layer region from the low-frequency puffing motion characteristic of fires.

Pruett (2000) explores temporal filtering for the Navier-Stokes equations and discusses its strengths and weaknesses. A strength is that temporal filters are bounded and thus the commutivity error usually associated with spatial filtering is generally avoided. Weaknesses include phase- and Doppler-shifting of the filtered signal. The phase-shifting occurs because temporal filters are by necessity causal, and hence one-sided. Doppler shifting occurs because the mean convective velocity increases the temporal frequency required to capture the signal of a given eddy size. Pruett (2000) concludes that the latter is the most serious drawback for use in applications for which it is desired to resolve eddies of a given size, i.e., traditional LES.

However, in the current application, temporal separation into structures of resolvable and unresolvable frequencies is perhaps a stronger motivation than separation of structures by size classification. Further, Courant-number limitations on numerical methods limit the time step, thus ensuring that convectively-induced Doppler shifting is minimized if the temporal filter width is some small multiple of the time step. Given the desire in current applications to employ RANS in the near-wall regions, a further advantage of temporal filtering is the consistency of the filtering operation, not requiring a shift from temporal- to spatial-filtering arguments inherent in hybrid RANS/LES approaches.

The current study represents an initial exploration of the practicality of temporal filtering within the time frame of the CTR summer program. In the next section, a simple eddy-viscosity model will be described, followed by a brief description of a test problem, comparison of model and data, and discussion.

4.1. *Implementation*

There are many possible closure models for the temporally-filtered equations. For this preliminary investigation, we chose a simple eddy-viscosity closure that retains the k-epsilon modeling in our RANS code. The definition ofintegral time scale in the standard

RANS eddy-viscosity formulation is replaced by a fixed temporal filter width which is input by the user.

$$\mu_t = \rho C_\mu k T \tag{4.1}$$

where

$$T = \min(t_f, k/\epsilon) \tag{4.2}$$

Selecting a fixed temporal time scale is analogous to selecting a fixed filter width in LES. If the selected filter width is larger than the integral scale, the min function selects the integral time scale. For this study the time step is fixed to one half the filter width.

The model has been implemented in FUEGO's predecessor, VULCAN (which is based on the KAMELEON family (cf, Holen, et al, (1990)), a staggered, block-structured grid code with second-order upwind differencing for the convective terms and a first order implicit (SIMPLE based) differencing for the transient term. In addition to the temporal filter, the k-epsilon implementation has a density based generation term (V. Nicolette, private communication). The model suite includes combustion, soot and radiation models.

4.2. *Test problem descriptions*

To test whether the current formulation will separate time scales, two problems with disparate time scales were simulated, the free convection data described earlier and recently published methane fire data Tieszen, et al, (2002). The methane data consists of a one meter high vertical plane of 2-D PIV data through the centerline of a one-meter-diameter methane fire (See citation for details). The experimental puffing frequency of the fire is 1.65 Hz.

4.3. *Model/data comparison*

Figures 18–25 show the results of the simulations, and comparisons with the methane data. The filter width for the results shown is 1/30 of the puffing period. Figure 18 shows the temperature profile at an instance in time. Figure 19 shows the simulated time history of the vertical velocity on the centerline, half a diameter above the burner. The puffing is somewhat irregular, as in the experiment, but consistent with the experimental value. Comparison of the vertical (axial) and horizontal (radial) time-averaged velocity fields is shown in figure 20 vs. figure 21, and figure 22 vs. figure 23, respectively. The width of the reacting mixing layers is somewhat underpredicted, resulting in the more-pronounced 'W' shape in the vertical velocity profile compared to the data. The transition from the 'W' shape to a Gaussian-like profile marks the end of the fuel vapor core in the fire.

Figures 24 and 25 compare the turbulent kinetic energy. The data assume that the out-of-plane fluctuations are comparable to the horizontal in-plane fluctuations. The simulation supports this assumption of the data analysis. Simulations with a filter width of 1/10 the puffing frequency (0.06 sec) still showed some dynamics, but were significantly more damped than those shown in the figures. Time-step and grid-refinement studies have yet to be conducted for a constant filter width.

Time did not permit simulations with the v^2f model for the free convection boundary layer. However, a preliminary simulation of the free convection problem using k-epsilon with no wall function with RANS mesh spacing of 7 cm parallel to the plate did not show any indication of puffing with a filter width of 0.05 sec as desired.

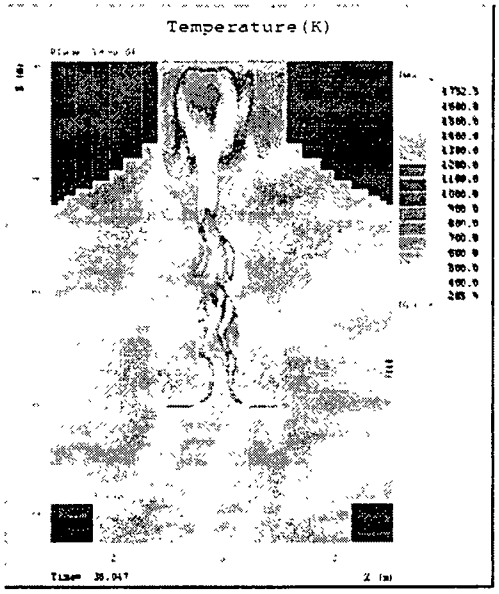

FIGURE 18. Instantaneous simulation temperature contours

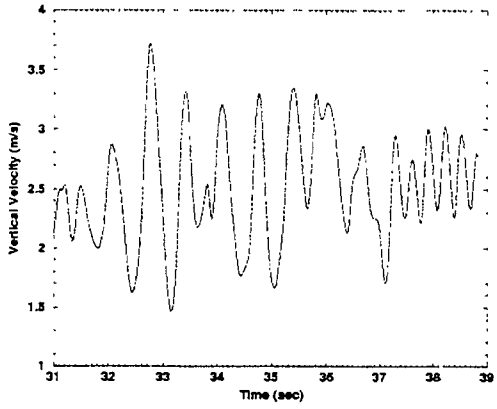

FIGURE 19. Vertical velocity vs time (Centerline at Z=0.5m)

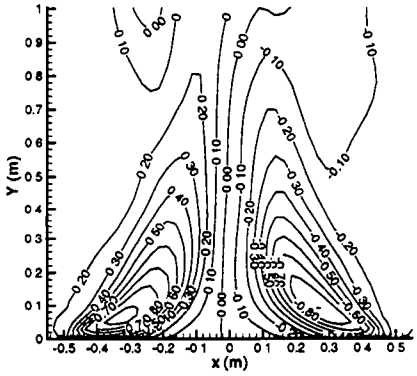

FIGURE 20. Radial Velocity (m/s) Simulation

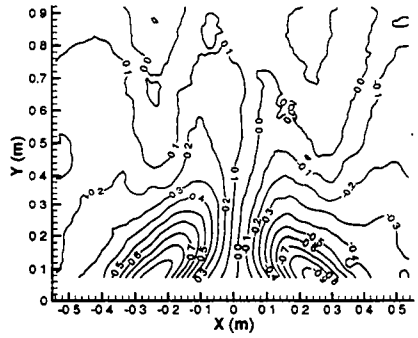

FIGURE 21. Radial Velocity (m/s) Experiment

4.4. *Discussion of temporal filtering*

Given the numerics and simple modeling closure, the preliminary comparisons are quite encouraging. Overall, the mixing is somewhat underpredicted. The underprediction may be due to an excess of numerical or model viscosity, or to physical reasons. Unlike momentum-driven flows, buoyant flows have strong coupling between the density and momentum fields. It can be argued that baroclinic vorticity production occurs at all scales in the cascade (Tieszen (2001)). Growth dynamics in the methane-fire mixing layer suggest that, via pairing, this small-scale production can result in large-scale dynamics. Eddy-viscosity models, which are designed for energy dissipation, do not capture the

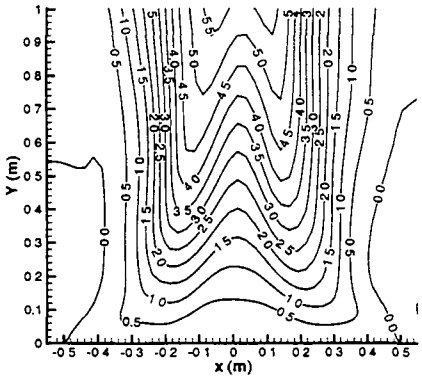

FIGURE 22. Axial Velocity (m/s) Simulation

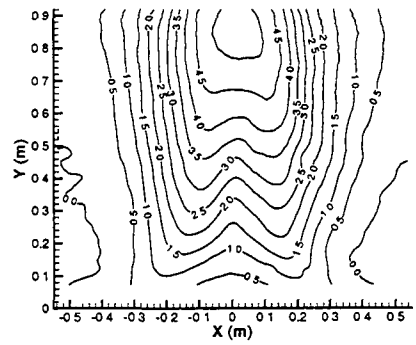

FIGURE 23. Axial Velocity (m/s) Experiment

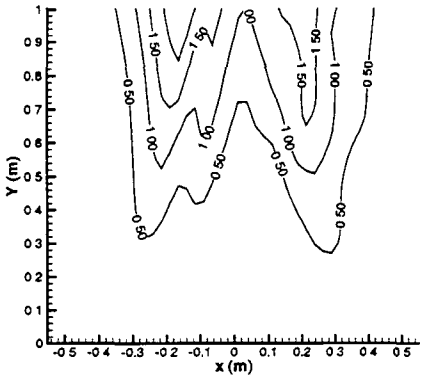

FIGURE 24. Turbulent Kinetic Energy (m^2/s^2) Simulation

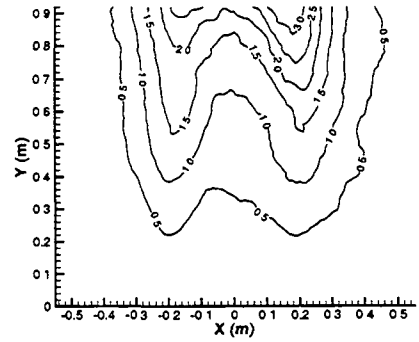

FIGURE 25. Turbulent Kinetic Energy (m^2/s^2) Experiment

vorticity production at small scales andits later appearance as vorticity at grid-resolved scales due to pairing mechanisms along the mixing layer.

5. Conclusions

Simulations of the three-dimensional turbulent flow and heat transfer adjacent to a large (3 meter) high-temperature (up to 860 K) vertical flat plate and in a large-scale methane flame have been made and compared with experimental data. Reynolds-averaged Navier-Stokes (RANS) results using the $v^2 - f$ model wall treatment of forced- and-fixed convection flow and heat transfer on a vertical flat plate with a horizontal forced flow are in qualitative agreement with experimental data, with quantitative comparisons awaiting finer-mesh results. Direct numerical simulation (DNS) results indicate that transition occurs within 10-20 cm above the bottom of the heated plate. The transition proceeds as an initially-orderly wave that convects along the entire vertical extent of the plate

before transition to turbulence. These insights have helped to inform the ongoing RANS development effort by providing a detailed picture of the upstream flow conditions where measurements were unavailable. Preliminary detached-eddy simulation (DES) comparisons for the methane fire are quite encouraging, although overall the mixing is somewhat underpredicted. For free convection on the heated plate, the preliminary DES results were steady as desired.

REFERENCES

BURNS, S. P. 1997 Application of spatial and angular domain based parallelism to a discrete ordinates formulation with unstructured spatial discretization. *2nd Int. Sympo. on Radiation Transfer* (P. Mengüç, ed.), Int. Center for Heat and Mass Transfer, Kusadasi, Turkey.

DURBIN, P. A. 1991 Near-wall turbulence closure without damping functions. *Theor. and Comp. Fluid Dyn.* **3**, 1–13.

EDWARDS, H. C. & STEWART, J. R. 2001 SIERRA: A software environment for developing complex multi-physics applications. *1st MIT Conf. on Comp. Fluid and Solid Mech.* (K. J. Bathe, ed.), Elsevier Scientific.

GRAN, I. R. & MAGNUSSEN, B. F. 1996 A numerical study of a bluff-body stabilized diffusion flame. Part 2. Influence of combustion modeling and finite-rate chemistry. *Combust. Sci. and Tech.* **119**, 191–217.

HOLEN, J., BROSTROM, M., & MAGNUSSEN, B. F. 1990 Finite difference calculation of pool fires. *23rd Sympo. (International) on Combustion*, The Combustion Institute, pp. 1677–1683.

LAUNDER, B. E. & SPALDING, D. B. 1974 The numerical computation of turbulent flows. *Computer Meth. Appl. Mech. Eng.* **3**, 269–289.

MAGNUSSEN, B. F. 1989 Modeling of NOx and soot formation by the eddy dissipation concept. *Int.Flame Res. Foundation* 1st Topical Orientation Meeting.

MCGRATTAN, K., REHM, R. G., & BAUM, H. R. 1994 Fire-driven flows in enclosures. *J. Comp. Phys.* **110**, 285–291.

MCGRATTAN, K., BAUM, H. R. & REHM, R. G. 1998 Large eddy simulation of smoke movement, *Fire Safety Journal* **30**, 161–178.

MCGRATTAN, K. B., BAUM, H. R., REHM, R. G., HAMINS, A., FORNEY, G. P., & FLOYD, J. E. 2001 Fire dynamics simulator (version 2), technical reference guide. *Natl. Inst. Standards & Tech., NISTIR* 6783.

MOEN, C. D., EVANS, G. H., DOMINO, S. P. & BURNS, S. P. 2002 A multi-mechanics approach to computational heat transfer. *proceedings IMECE2002-33098*, to be presented at 2002 ASME Int. Mech. Eng. Congress and Exhibition, November 17–22, New Orleans.

PRUETT, C. D. 2000 Eulerian time-domain filtering for spatial large-eddy simulation. *AIAA J.* **38**, 1634–1642.

REHM, R. G. & BAUM, H. R. 1978 The equations of motion for thermally driven, bouyant flows, *J. Res. NBS* **83**, 297–308.

SIEBERS, D. L.,SCHWIND, R. G., & MOFFAT, R. J. 1983 Experimental mixed convection heat transfer from a large, vertical surface in a horizontal flow. *Sandis report* SAND83-8225.

SPALART, P. R. 2000 Strategies for turbulence modelling and simulations. *Int. J. Heat and Fluid Flow.* **21**, 252–263.

SPEZIALE, C. G. 1998 Turbulence modeling for time-dependent RANS and VLES: A review. *AIAA J.* **36**, 173–184.

TIESZEN, S. R. 2001 On the fluid mechanics of fires.", *Annu. Rev. Fluid Mech.* **133**, 62–92.

TIESZEN, S. R., O'HERN T. J., SCHEFER, R.W., WECKMAN, E. J.,& BLANCHAT, T. K. 2002 Experimental study of the flow field in and around a one meter diameter methane fire. *Combust. Flame* **129**,378–391.

Large-eddy simulation

The six projects in this group aimed at developing or testing new concepts, as well as assessing existing approaches to the subgrid-scale modelling problem. Other projects in which LES is applied to complex flows or combustion and studies related to the coupling between numerics and LES modelling are reported elsewhere in this volume.

In the first project, He, Wang & Lele have evaluated the performance of several subgrid-scale models in terms of time correlations. In the past, such diagnostics have been limited to the study of the time history of pointwise quantities. Here, space-time correlations, which can be characterized by a two-time energy spectrum, have been computed in homogeneous turbulence for both DNS and LES fields. Correct predictions of the space-time correlations do not represent a purely theoretical challenge for LES since they are needed in the computation of turbulent sound sources. Various eddy-viscosity SGS models have been tested, and the results showed a systematic, though limited, over-prediction of the time correlations as compared to DNS results. This can be understood by the deterministic nature of the eddy-viscosity picture and indirectly supports the introduction of explicit random backscatter mechanisms to the models. However, Another solution is suggested by the authors: the use of a history-dependent eddy-viscosity. Although none of these approaches has been explicitly tested, the measurement of space-time correlations in turbulent fields is likely to become a new important assessment methodology in the LES community.

In the second project, Carati & Wray have explored LES formulations in which equations for nonlinear functions of the velocity are carried explicitly. Adding an evolution equation for the time derivative of the filtered velocity was first considered. This approach has however been abandoned, because the turbulence statistics appeared to depend strongly on the initial conditions chosen for the additional variable. Another, more promising, approach consisted in writing an additional equation directly for the subgrid-scale force, the divergence of the subgrid-scale stress tensor. The modelling effort is then postponed to the new equation. It contains an unknown subgrid-scale tensor for which a dynamic procedure has been developed. Preliminary runs are inconclusive as to whether this approach might be successful but tend to show that, in this formulation, the results are less sensitive to initial conditions. Interestingly, this framework could be used to implement a history-dependent eddy-viscosity as suggested in the first project.

The channel flow is the simplest LES test case of a wall bounded flow. It has been used extensively in two papers in this group. Gullbrand & Chow report on tests comparing LES of the channel flow with and without an explicit filter. In contrast to the subgrid-scale stress, which represents turbulent motions not captured on the numerical grid, the additional subfilter-scale stress generated by the explicit filter can theoretically be reconstructed exactly. In practice, however, this term is only reconstructed approximately using, for instance, the scale-similarity model or an iterative deconvolution method. Various numerical schemes have been used in this paper in order to better evaluate the effect of the numerical errors. Although the interaction of numerical errors with subfilter and subgrid models remains an open issue, a grid resolution adapted to each scheme has been determined. Comparisons between several models show that using an explicit filter improves the LES predictions as long as accurate reconstruction schemes, like high order iterative deconvolution methods, are used for the subfilter stress.

In the second paper using channel flow as a test case, Jeanmart & Winckelmans have

performed a systematic study of LES predictions for a series of dynamic models including the Smagorinsky model, a regularized version of the multiscale model, a mixed viscosity and hyperviscosity approach and an eddy viscosity acting on a modified, enhanced, velocity field. This last model is very similar in nature to the 'mixed viscosity and hyperviscosity' approach but contains a single parameter to be determined dynamically. Special attention has also been paid in this study to the consistent implementation of the test filter in the wall-normal direction in the dynamic procedure, but without significant improvement in the results. Although no model simultaneously reproduces the velocity profile and all the components of the Reynolds stress, there is a systematic trend supporting a different modelling strategy for the very large scales and for the small, but resolved, scales in LES. In particular, both the multiscale model and the Smagorinsky model acting on an artificially-enhanced velocity field appear to produce more accurate predictions.

A hyperviscosity term has also been used by Caughey & Jothiprasad in an attempt to develop a tool for assessing LES accuracy for flows at high Reynolds number. For such flows, comparison with DNS of the Navier-Stokes equations with a viscous term is usually not possible. The authors have considered an alternative way of simulating flows at high Reynolds number by artificially increasing the separation between the energetic and the dissipative scales. For this purpose, they have replaced, in a fourth order-central-difference code, the physical viscous dissipation by an artificial hyperviscous dissipation mechanism acting more in the small scales and less in the large scales. Several turbulent flows, like the freely-evolving Taylor-Green vortex, the inhomogeneous Kolmogorov flow generated by a static force periodic in space, and homogeneous decaying turbulence have been considered. Numerical results obtained using the hyperviscous dissipation mechanism on relatively modest meshes show good agreement with higher-resolution DNS.

The concepts of ideal and optimal LES have been proposed recently as strategies to reach the best possible approximations for the LES fields. Both these approaches require explicit expressions for several turbulence statistics, which are computed in the optimal LES using a stochastic estimation procedure determined from DNS. Haselbacher, Moser, Constantinescu & Mahesh have investigated the extension of optimal LES to high-Reynolds number flows using a stochastic-estimation procedure based on turbulence theory. The method has been implemented in an unstructured finite-volume code. Some of the statistics necessary to implement the optimal LES require further theoretical investigation, and predictions for the energy spectra are not fully consistent with the underlying Kolmogorov theory. However, preliminary tests of this innovative approach, coupling statistical theories of turbulence and subgrid-scale modelling, have already been performed and show a reasonable agreement for global quantities such as the total energy decay in homogeneous turbulence.

Daniele Carati

Evaluation of subgrid-scale models in terms of time correlations

By Guo-Wei He†, Meng Wang AND Sanjiva K. Lele

In certain applications such as the computation of turbulent sound sources, Large-Eddy Simulation (LES) is required to predict correctly the space-time correlations of the velocity field. A previous study (He, Rubinstein & Wang 2002) has shown that LES with the spectral eddy-viscosity model over-predicts time correlations. In this work, we evaluate the Smagorinsky model, the dynamic Smagorinsky model and the multi-scale LES method in terms of time correlations. The dynamic Smagorinsky model is shown to give better predictions on time correlations than the constant-coefficient Smagorinsky model, which gives significant over-predictions. The results from the multi-scale LES method are in between. The over-predictions are discussed according to the random backscatter and the sweeping hypothesis. Based on those discussions, a history-dependent sub-grid scale model is suggested for time correlations.

1. Motivation and objectives

The goal of this work is to evaluate and develop subgrid-scale (SGS) models for predicting time correlations in turbulent flows. Here by "time correlation" we refer to the two-time, two-point correlation of velocity fields $u_i(\mathbf{x}, t)$ in physical space

$$C(r, \tau) = \langle u_i(\mathbf{x}, t) u_i(\mathbf{x} + \mathbf{r}, t + \tau) \rangle, \tag{1.1}$$

or, equivalently, the two-time correlation of velocity Fourier modes $u_i(\mathbf{k}, t)$ in spectral space

$$C(k, \tau) = \langle u_i(\mathbf{k}, t) u_i(-\mathbf{k}, t + \tau) \rangle. \tag{1.2}$$

where $r = |\mathbf{r}|$ is the magnitude of spatial separation $\mathbf{r}$, $k = |\mathbf{k}|$ is the magnitude of wave number $\mathbf{k}$, and τ is time delay. The turbulence is assumed statistically homogeneous and isotropic, but not necessarily stationary. Hence, the correlation function also depends on t in general.

Time correlation describes temporal statistics of turbulent flows. It has been shown by previous evaluations (Meneveau & Katz 2000) that large-eddy simulation (LES) with an appropriate SGS model is capable of predicting correctly the single-time spatial statistics of turbulent flows, such as turbulent kinetic energy and Reynolds stress. The temporal statistics did not enter such evaluations. However, a major application of LES is the prediction of unsteady flows in which time accuracy, even if in the statistical sense, is important. This emphasis will impose new requirements on SGS modeling. For instance, in the computation of flow-generated sound the Lighthill acoustic analogy (Lighthill 1952) shows that the radiated sound power depends on the space-time properties of turbulence. Therefore, it is necessary to investigate the predictive power of LES in terms of time correlations. A recent study by He *et al.* (2002) has shown that LES with the spectral

† Laboratory for Nonlinear Mechanics, Institute of Mechanics, Chinese Academy of Science, Beijing 100080, China

eddy-viscosity model (Chollet & Lesieur 1981) over-predicts the time correlation relative to Direct Numerical Simulation (DNS). The over-prediction, which can be significant, alters the frequency distribution of the sound radiated by turbulence. A follow-up question to ask is then: which of the currently existing SGS models can better predict time correlations, and to what extent?

The dynamic Smagorinsky model (Germano *et al.* 1991) has been applied in many different flows, generally with good results. Therefore, this model is the first choice in our evaluations. The multi-scale LES method of Hughes, Mazzei & Oberai (2001) is also attractive in that the SGS model acts only on the small scales in the resolved field, and thus may have less impact on time-correlations, particularly at large spatial separations. We also use the classical Smagorinsky model (Smagorinsky 1963) to calculate time correlations, in order to verify our previous results and compare it with the dynamic Smagorinsky model and the multi-scale LES method.

The above SGS models are mainly based on energy balance. For example, the eddy-viscosity coefficients in the Smagorinsky models are determined by the energy-balance equation. They are not required to satisfy the governing equations for time correlations, which is the root cause of potential errors. As an extension of the present work, we incorporate the physical mechanism for time correlations into SGS modeling, and suggest a history-dependent Smagorinsky model.

2. Numerical setup

We will use a calculation of decaying homogeneous isotropic turbulence to evaluate the Smagorinsky model, the dynamic Smagorinsky model and the multi-scale LES method. The previous evaluation of He *et al.* (2002) was carried out for forced homogeneous isotropic turbulence at a moderate Taylor-scale Reynolds number (Re_λ) of 108 in a cubic box of side 2π, using DNS on a 128^3 grid and LES on a 64^3 grid. That evaluation may have been affected by the forcing scheme, the moderate Reynolds number and the relatively small grid ratio between DNS and LES. These deficiencies are rectified or reduced in the present study.

The new setting is a decaying turbulence of initial $Re_\lambda = 127.4$ in the same cube as before. It is simulated by DNS with grid size 256^3 and LES with grid size 64^3. A standard pseudo-spectral method is used, in which spatial differentiation is by the Fourier spectral method, time advancement is by a second-order Adams-Bashforth method with the same time steps for both DNS and LES, and molecular viscous effects are accounted for by an exponential integrating factor. All nonlinear terms are de-aliased with the two-thirds rule, except those involving SGS eddy viscosity.

The following SGS models are evaluated:

(1) The Smagorinsky model: the Smagorinsky constant is $C_s = 0.22$ and the filter width is set equal to the inverse of the largest effective wave number $k_c = 21$.

(2) The dynamic Smagorinsky model: the Smagorinsky coefficients are determined by the Germano identity. The grid filter width is k_c^{-1} and the test filter width is taken as $2k_c^{-1}$.

(3) The multi-scale LES method: we decompose the filtered Navier-Stokes equations into the large-scale equations for the lower one-half of the Fourier modes and the small-scale equations for the remaining half of the Fourier modes. The Smagorinsky model is applied only to the small-scale equations.

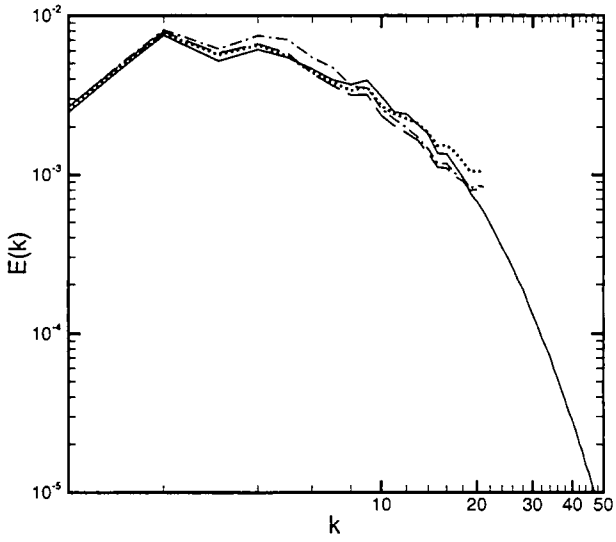

FIGURE 1. Energy spectra at $t = 2.4$. ——— DNS field; - - - - LES with dynamic Smagorinsky model; —·— Multi-scale LES; ····· LES with Smagorinsky model.

The initial condition for DNS is an isotropic Gaussian field with energy spectrum

$$E(k,0) \propto (k/k_0)^4 \exp[-2(k/k_0)^2], \tag{2.1}$$

where $k_0 = 4.68$ is the wavenumber corresponding to the peak of the energy spectrum. The shape of the energy spectrum excludes the effects of the box size. The initial condition for LES is obtained by filtering the initial DNS velocity fields with filter wavenumber $k_c = 64/3 \approx 21$. Therefore, the initial LES and filtered DNS velocity fields are exactly the same. At early stages, the LES and DNS velocity fields are highly correlated due to the same initial conditions. Therefore, the time correlations of the LES velocity field are nearly the same as those of the DNS field. As time progresses, the LES fields become decorrelated from the DNS fields. The difference in time correlations between the LES and DNS velocity fields are then observed.

3. Main results

In figure 1, energy spectra are presented at $t = 2.4$. Generally speaking, the results from the Smagorinsky model, the dynamic Smagorinsky model and the multi-scale LES method are in agreement with the DNS result. However, the multi-scale LES method over-predicts a little more than the Smagorinsky and dynamic Smagorinsky models between $k = 3$ and $k = 10$. There is also a slight under-prediction for $k \geq 10$ which is shared by the Smagorinsky model. Beyond $k = 20$, the resolution limit is exceeded, and the LES results are meaningless.

Figure 2 shows the normalized time correlations, $c(k,\tau) = C(k,\tau)/C(k,0)$, of the DNS and LES fields for wavenumbers $k = 7$, 11, 15, and 17, spanning a range of scales from the integral scale to the upper end of the resolved scale. The starting time is $t = 1.4$. The figure confirms our previous observations: LES with eddy-viscosity-type

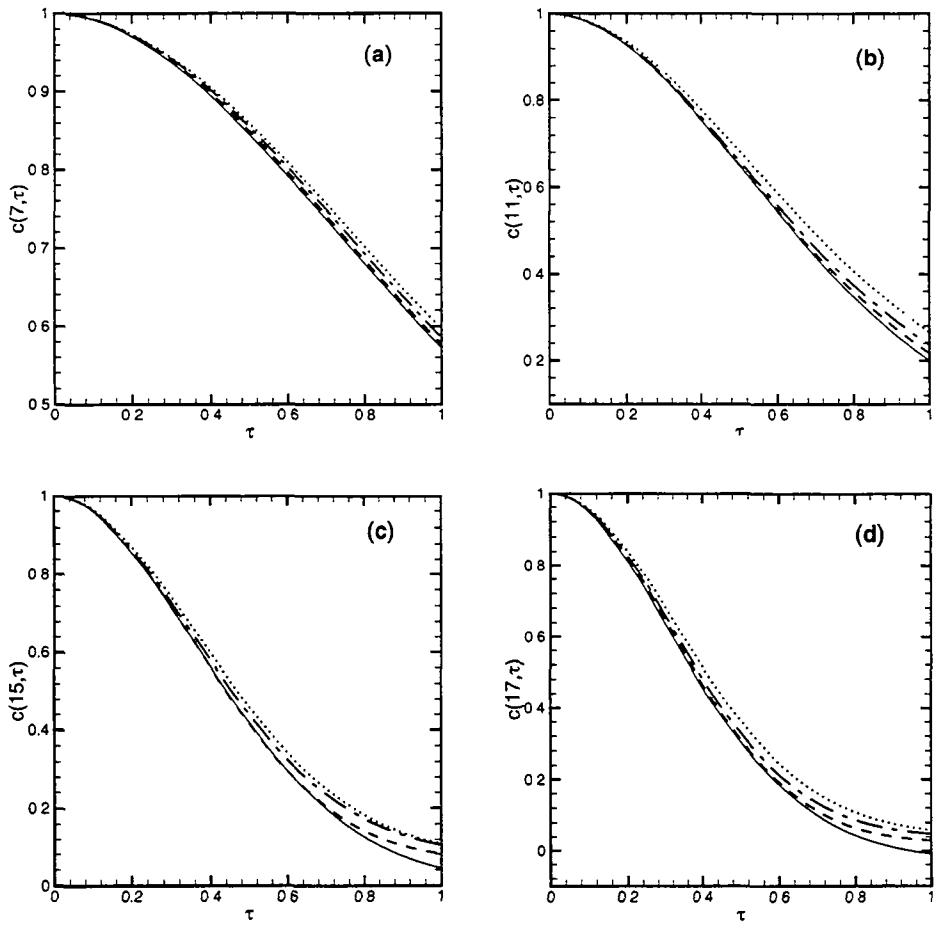

FIGURE 2. Time correlation $c(k,\tau)$ vs time lag τ (start time $t = 1.4$) for (a) $k = 7$, (b) $k = 11$, (c) $k = 15$, (d) $k = 17$. ——— DNS field; - - - - LES with dynamic Smagorinsky model; — - — Multi-scale LES; ····· LES with Smagorinsky model.

models over-predicts time correlations. The over-predictions can be understood by the following physical arguments: the contribution of unresolved scales to resolved scales can be described as energy dissipation and random backscatter. The eddy-viscosity-type SGS models are designed to model the drain of energy from resolved scales to unresolved scales, but fail to account for the random backscatter from unresolved scales to large scales. This leads to a more coherent field at resolved scales. Therefore, the LES field evolves in a more correlated fashion, in the sense that their time correlations decay more slowly. The extent of over-estimation on time correlations varies with the SGS model, as seen in figure 2. This can be understood by the sweeping effects (Kraichnan 1964): the Eulerian time correlations are dominated by the sweeping velocity. The eddy-viscosity-type models reduce the sweeping velocity by excessive dissipation, which causes the time correlations of the LES fields to decay more slowly than those of the DNS fields. It is observed from our numerical calculations that, among the SGS models evaluated,

the Smagorinsky model produces the largest dissipation and thus the smallest sweeping velocity. Therefore, it predicts the slowest correlation decay. The dynamic Smagorinsky model introduces the most appropriate amount of dissipation and hence gives the best predictions on time correlations. The dissipation produced in the multi-scale LES is smaller than the Smagorinsky model but larger than the dynamic Smagorinsky model. Therefore, its predictions for time correlation lie between those of the other two models.

Figure 2 also indicates that the time correlations of the LES fields deviate more from the DNS fields at small scales than at large scales. This is in agreement with the well-known divergence property of Eulerian time correlations discovered by Kraichnan (1964). It implies that the cutoff effects are stronger in the near range than those in the far range.

It is further noted from figure 2 that, although the dynamic Smagorinsky model and the multi-scale LES method give better overall predictions than the Smagorinsky model, all curves near $\tau = 0$ are in good agreement, implying that the Taylor microscales are well predicted by all models. The maximum time delay used in the calculations is $\tau = 1.0$, which is not long enough to catch the zero-crossing points of time correlations. Nonetheless, the relatively large differences of the LES curves relative to the DNS value at $\tau = 1.0$ are still observed, indicating that the decorrelation scales are poorly predicted.

4. Conclusions and future work

We have evaluated the Smagorinsky model, the dynamic Smagorinsky model and the multi-scale LES method in terms of time correlations. Comparatively speaking, the dynamic Smagorinsky model predictions are in better agreement with DNS fields, with some over-prediction of the decorrelation length scales. The Smagorinsky model obviously over-predicts time correlations. The results of the multi-scale LES method, using the Smagorinsky model on the small scale equations, lie in between. However, we believe that the results from the multi-scale LES method could be much improved if an appropriate SGS model is applied to the small scale equations.

Evaluations have also been made on forced turbulence, and similar results are obtained but will be presented in a forthcoming paper (He, Wang & Lele 2002). This is because the sweeping hypothesis is true for both forced and decaying turbulence. However, the sweeping hypothesis may not be valid for general unsteady flows, such as 'kicked' turbulence, where turbulence is forced periodically. In this case, the eddy viscosity coefficients should be history-dependent. Therefore, we suggest a history-dependent Smagorinsky model for time correlations

$$\tau_{ij}(\mathbf{x}, t) = \int_{-\infty}^{t} [-2\nu_r(t')\tilde{S}_{ij}(\mathbf{x}, t')]w(t')dt' \tag{4.1}$$

where τ_{ij} is the sub-grid scale stress, and $w(t')$ is a weighting function. $\nu_r(t')$ is a history-dependent-eddy-viscosity coefficient, which can be determined by either one time or two time Germano identity. This work is in progress.

Acknowledgments

We wish to thank Prof. P. Moin, Dr. A. Wray and Dr. D. Carati for helpful discussions. The first author would also like to thank Mr. Z. M. Xiong for the hospitality extended to him during his summer visit to CTR. His work was supported by the National Committee of Science and Technology, P. R. China, under the project "Nonlinear Science".

REFERENCES

CHOLLET, J.-P. & LESIEUR, M. 1981 Parameterization of small scales of three-dimensional isotropic turbulence utilizing spectral closure. *J. Atmos. Sci.* **38**, 2747–2757.

GERMANO, M., PIOMELLI, U., MOIN, P. & CABOT, W. H. 1991 A dynamic subgrid-scale eddy viscosity model. *Phys. Fluids A* **3**, 1760–1765.

HE, G.-W., RUBINSTEIN, R. & WANG, L-P. 2002 Effects of subgrid scale modeling on time correlations in large eddy simulation. *Phys. Fluids* **14**, 2186–2193.

HE, G.-W., WANG, M. & LELE, S. K. 2002 A dynamically history-dependent subgrid scale model. In preparation.

HUGHES, T. J. R., MAZZEI, L. & OBERAI, A. S. 2001 The multiscale formulation of large eddy simulation: decay of homogeneous isotropic turbulence. *Phys. Fluids* **13**, 505–512.

KRAICHNAN, R. H. 1964 Kolmogorov's hypotheses and Eulerian turbulence theory. *Phys. Fluids* **7**, 1723-1734.

LIGHTHILL, M. J. 1952 On sound generated aerodynamically; I. General theory. *Proc. R. Soc. Lond. A***211**, 564–587.

MENEVEAU, C. & KATZ, J. 2000 Scale-invariance and turbulence models for large eddy simulation. *Annu. Rev. Fluid Mech.* **32**, 1–32.

SMAGORINSKY, J. 1963 General circulation experiments with the primitive equations: I. The basic experiment. *Mon. Weather Rev.* **91**, 99–164.

Large-eddy simulations with explicit equations for subgrid-scale quantities

By Daniele Carati † AND Alan A. Wray ‡

Various alternative formulations of the LES equations have been explored in which additional evolution equations for variables such as the acceleration, the subgrid-scale stress tensor, or the subgrid-scale force are explicitly carried. Statistics of the velocity field obtained from the equation for the acceleration are shown to depend strongly on the initial conditions. This feature, which is independent of LES modeling issues, seems to prove that the velocity-acceleration formulation of the Navier-Stokes is not useful for numerical simulation. Equations for the subgrid-scale quantities appear to be much more stable. However, models required by this formulation of the LES problem still require additional study.

1. Introduction

The Navier-Stokes equation is usually written in terms of the velocity. However, it is legitimate to re-explore the turbulence problem by considering new formulations which are obtained by a change of variables. For instance, the equation for the vorticity can be considered as such an alternative formulation. The change of variables is in this case linear, and the two large-eddy simulation (LES) problems, obtained by projecting these two equations on a coarse grid, are more or less equivalent (Winckelmans *et al*, 1996). If, however, a nonlinear change of variables is considered, then the new LES problem would differ from the classical formulation of subgrid-scale modeling. The present project is devoted to the investigation of new LES formulations in which equations for certain nonlinear functions of the velocity are carried explicitly.

Our first attempt in that direction consisted in writing an explicit equation for the entire right-hand side of the velocity evolution equation, i.e., for the acceleration. In that case, the DNS formulation of the problem itself seems to be ill-conditioned since the turbulence statistics obtained from the acceleration equation appear to depend rather strongly on the initial conditions. For that reason, the related LES formulation has not been explored further.

Our second attempt in deriving a new formulation of the LES problem was to write explicit equations for the unknown subgrid-scale quantities. Equations for the Reynolds stress tensor in RANS have long been explored (Rodi, 1979), but in the LES context equations for the subgrid-scale stress have almost never been considered. One possible reason is that in LES it is a common practice to push the resolution to the limit of the available computational capacities. Consequently, carrying additional equations for the unknown subgrid-scale quantities has not been considered as a viable alternative to their modelling. Also, lack of knowledge about the phenomenology associated with the

† Université Libre de Bruxelles, Brussels, Belgium
‡ NASA Ames Research Center, Moffett Field, USA

dynamics of the subgrid-scale quantities has probably discouraged LES practitioners from exploring these equations. One exception is the equation for the trace of the subgrid-scale stress tensor, often referred to as the turbulent kinetic energy, which has been used together with the resolved velocity equation. Our objective is to generalize and systematize this approach.

2. LES based on an equation for the acceleration

In a first attempt to derive an alternative formulation of the LES problem, we have considered the incompressible Navier-Stokes equation written in terms of the acceleration variable:

$$\partial_t u_i = a_i \tag{2.1a}$$

$$a_i = -\partial_j u_i u_j - \partial_i p + \nu \nabla^2 u_i \tag{2.1b}$$

$$\nabla^2 p = -\partial_i \partial_j u_i u_j \tag{2.1c}$$

Obviously equations (2.1) are closed and there is no need for an additional evolution equation for $\vec{a}$. Nevertheless, such an evolution equation can be derived easily, and the resulting equivalent formulation of the incompressible Navier-Stokes reads:

$$\partial_t u_i = a_i \tag{2.2a}$$

$$\partial_t a_i = -\partial_j \left(u_i a_j + u_j a_i\right) + \nu \nabla^2 a_i - \partial_i p_a \tag{2.2b}$$

Here the 'pseudo pressure' p_a has been introduced to enforce incompressibility of the vector $\vec{a}$. Like the pressure in the classical formulation of the incompressible Navier-Stokes equations, it is obtained by solving a Poisson equation. Since equation (2.2a) is linear, imposing incompressibility on both $\vec{a}$ and the initial condition $\vec{u}(t_0)$ guarantees that the velocity field remains divergence free. The set of equations (2.2) is thus equivalent to the original set of equations (2.1) provided a_i is properly initialized as in (2.1b). For DNS, solving (2.2) would be more complicated that solving (2.1), and there is no reason to consider this formulation. However, filtering the two sets of equations leads to different modeling problems. Filtering the set (2.1) yields the classical LES formulation. Filtering equations (2.2) yields:

$$\partial_t \overline{u}_i = \overline{a}_i \tag{2.3a}$$

$$\partial_t \overline{a}_i = -\partial_j \left(\overline{\overline{a}_i \overline{u}_j} + \overline{\overline{a}_j \overline{u}_i}\right) + \nu \nabla^2 \overline{a}_i - \partial_i \overline{p}_a - \partial_j \overline{\phi}^a_{ij} \tag{2.3b}$$

in which a model is required for $\overline{\phi}^a_{ij} \equiv \overline{u_i a_j + a_i u_j} - \overline{\overline{u}_i \overline{a}_j} - \overline{\overline{u}_j \overline{a}_i}$. Expressing the unclosed subgrid-scale quantities in terms of $\overline{u}_i$ and $\overline{a}_i$ would constitute an entirely new approach to subgrid scale modelling. Moreover, the evolution equation for $\overline{a}_i$ carries more information on the nonlinear dynamics than the classical equation for $\overline{u}_i$.

Coding the equations (2.2) is rather straightforward. We have checked that the results produced from a standard DNS code for (2.1) and from a code for the $u_i - a_i$ formulation (2.2) yield indistinguishable results when the acceleration vector is properly initialized. Unfortunately the equations (2.2) produce results that, even in the statistical sense, depend strongly on the initial conditions. If $a_i(t_0)$ is not set exactly from (2.1b), then global statistical quantities like the total energy and the total dissipation diverge from the DNS results.

The sensitivity to the initial conditions is so high that in the example presented here, the viscous decay of energy is not at all reproduced when the phase of the initial accel-

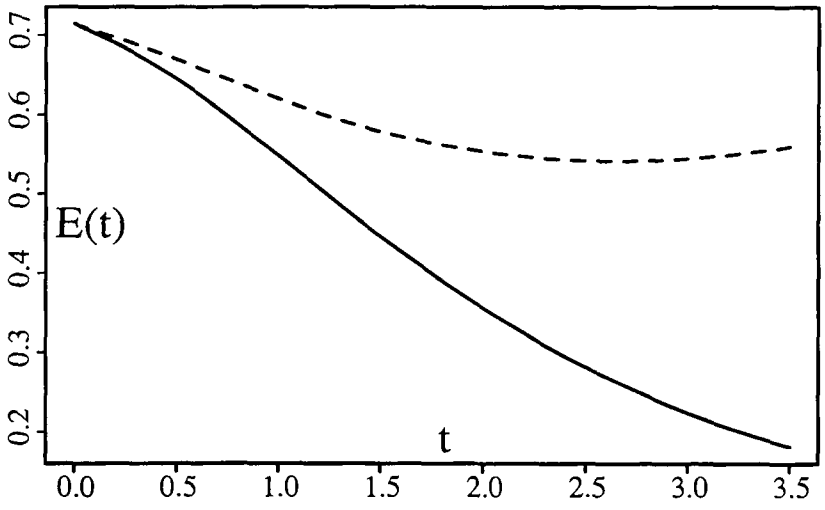

FIGURE 1. Total energy dissipation predicted by the equations (2.2) with the exact initial acceleration field (solid line) and with a field for which the phases have been slightly modified by multiplying each vector in Fourier space $a_i(\mathbf{k})$ by a factor $e^{i2\pi s}$, where $s \in [-0.1, 0.1]$ is a random variable.

eration are slightly modified. In the late stage of the computation, an increase of energy is even observed. We thus believe that the DNS velocity-acceleration formulation (2.2) is not reliable and, consequently, there is no point in further exploring the associated LES problem (2.3).

3. Equations for subgrid-scale quantities

The purpose of this section is to derive explicit evolution equations for subgrid-scale quantities. Two difficulties can immediately be anticipated. First, considering for instance the subgrid-scale stress tensor, $\tau_{ij} = \overline{u_i u_j} - \overline{u}_i \overline{u}_j$, it appears that this quantity is *not* strictly speaking a resolved variable since the product $\overline{u}_i \overline{u}_j$ cannot in general be fully captured on the same grid as the LES velocity $\overline{u}_i$. Carrying simultaneous equations for $\overline{u}_i$ and τ_{ij} thus requires two different grids, which of course is not desirable. This problem can be solved by rewriting the LES equation as follows:

$$\partial_t \overline{u}_i = -\partial_j \overline{\overline{u}_i \overline{u}_j} - \partial_i \overline{p} + \nu \nabla^2 \overline{u}_i - \partial_j \overline{\tau}_{ij}, \tag{3.1}$$

where now $\overline{\tau}_{ij} = \overline{u_i u_j} - \overline{\overline{u}_i \overline{u}_j}$. This equation implicitly assumes that the operator $\overline{\cdots}$ defining the LES field is a projection, $\overline{\cdots} = \overline{\overline{\cdots}}$, in order to ensure the Galilean invariance of the LES equations independently of the modelling approach used for representing $\overline{\tau}_{ij}$. Another obvious advantage of the formalism (3.1) is that all the terms in this equation, including the convective nonlinearity, appear as projected quantities (Carati, Winckelmans, & Jeanmart, 2001). We also note that by definition $\overline{\tau}_{ij} = \overline{\tau_{ij}}$.

The second difficulty comes from the definition of the subgrid-scale quantities. It is obvious that the time derivative of a subgrid-scale quantity is a subgrid-scale quantity as well. It might thus be argued that the evolution of $\overline{\tau}_{ij}$ is entirely driven by subgrid-scale effects that require modelling and consequently the evolution equation for $\overline{\tau}_{ij}$ might be seen as entirely arbitrary. This difficulty will be partially worked around by deriving the evolution equation directly from the definition of $\overline{\tau}_{ij}$. However, there is still some

arbitrariness in the expression of resolved and unresolved terms in this equation. Part of this arbitrariness will be removed by imposing that the evolution of any subgrid-scale quantity characteristic of a turbulent flow should be driven by an advection-dispersion equation.

3.1. *Equation for the subgrid-scale stress tensor*

The equation for $\overline{\tau}_{ij}$ is directly derived from its definition and from both the Navier-Stokes and the LES equations (3.1):

$$\partial_t \overline{\tau}_{ij} = \overline{\overline{u}_i \partial_l \overline{\tau}_{jl}} + \overline{\overline{u}_j \partial_l \overline{\tau}_{il}} + \nu \nabla^2 \overline{\tau}_{ij} - \partial_l \overline{\phi}^c_{ijl} - \overline{\Phi}^c_{ij} - \overline{\Phi}^p_{ij} - \overline{\Phi}^\nu_{ij} \tag{3.2}$$

Four unclosed terms appear in this equation. They can be related to the convective nonlinearities $\overline{\phi}^c_{ijl}$ and $\overline{\Phi}^c_{ij}$, to pressure terms $\overline{\Phi}^p_{ij}$, and to viscous terms $\overline{\Phi}^\nu_{ij}$ and are fully symmetric second and third rank tensors:

$$\overline{\phi}^c_{ijl} = \overline{u_i u_j u_l} - \overline{\overline{u}_i \overline{u}_j \overline{u}_l} \tag{3.3}$$

$$\overline{\Phi}^p_{ij} = \overline{u_i \partial_j p} + \overline{u_j \partial_i p} - \overline{\overline{u}_i \partial_j \overline{p}} - \overline{\overline{u}_j \partial_i \overline{p}} \tag{3.4}$$

$$\overline{\Phi}^c_{ij} = -\overline{\overline{u}_i \partial_l (\overline{\overline{u}_l \overline{u}_j} - \overline{u}_l \overline{u}_j)} - \overline{\overline{u}_j \partial_l (\overline{\overline{u}_l \overline{u}_i} - \overline{u}_l \overline{u}_i)} \tag{3.5}$$

$$\overline{\Phi}^\nu_{ij} = 2\nu \left(\overline{\partial_l u_i \partial_l u_j} - \overline{\partial_l \overline{u}_i \partial_l \overline{u}_j} \right) \tag{3.6}$$

The dynamic equation (3.2) for $\overline{\tau}_{ij}$ does not contain an explicit advection term, though one is presumably hidden in $\overline{\phi}^c_{ijl}$. Hence, a reasonable expansion for this fully symmetric tensor that introduces the desirable advection term would be:

$$\overline{\phi}^c_{ijl} = \overline{\overline{u}_i \overline{\tau}_{jl}} + \overline{\overline{u}_j \overline{\tau}_{il}} + \overline{\overline{u}_l \overline{\tau}_{ij}} + \overline{\Phi}^c_{ijl} \tag{3.7}$$

where $\overline{\Phi}^c_{ijl}$ is a residual tensor that remains to be modelled. This expansion yields the following dynamic equation for $\overline{\tau}_{ij}$:

$$\partial_t \overline{\tau}_{ij} = -\overline{\overline{u}_l \partial_l \overline{\tau}_{ij}} + \nu \nabla^2 \overline{\tau}_{ij} - \overline{\overline{S}^u_{jl} \overline{\tau}_{il}} - \overline{\overline{S}^u_{il} \overline{\tau}_{jl}} - \partial_l \overline{\Phi}^c_{ijl} - \overline{\Phi}^p_{ij} - \overline{\Phi}^c_{ij} - \overline{\Phi}^\nu_{ij} \tag{3.8}$$

where $\overline{S}^u_{ij} \equiv (\partial_i \overline{u}_j + \partial_j \overline{u}_i)/2$. The trace of this equation yields the evolution equation (Speziale, 1991,Ghosal *et al*, 1995) for the subgrid-scale energy $\overline{q} = \overline{\tau}_{ii}/2$:

$$\partial_t \overline{q} = -\overline{\overline{u}_l \partial_l \overline{q}} + \nu \nabla^2 \overline{q} - \overline{\overline{S}^u_{ij} \overline{\tau}_{ij}} - \partial_l \overline{\Phi}^q_l - \overline{\epsilon} \,. \tag{3.9}$$

The production term $\overline{\overline{S}^u_{ij} \overline{\tau}_{ij}}$ is independent of $\overline{q}$ since $\overline{S}^u_{ij}$ is traceless for incompressible flows. The turbulent flux $\overline{\Phi}^q_l$ originates from $\overline{\Phi}^c_{iil}$ and from $\overline{\Phi}^p_{ii}$ which can be easily written as a divergence term. The status of $\overline{\Phi}^c_{ii}$ is less obvious. However, using the property of projectors $\langle \overline{a} \overline{b} \rangle = \langle a \overline{b} \rangle$, where $\langle \cdots \rangle$ is the volume average, the following identity can be derived: $\langle \overline{\Phi}^c_{ii} \rangle = 0$. Thus it is not inconsistent to take $\overline{\Phi}^c_{ii}$ to be a divergence term which then contributes to the subgrid-scale energy flux $\overline{\Phi}^q_l$. Finally, the subgrid-scale dissipation

$$\overline{\epsilon} = \overline{\Phi}^\nu_{ii}/2 \tag{3.10}$$

is not a flux term. It represents the dissipation of subgrid-scale energy due to viscous effects and has the property of remaining finite in the limit of very small viscosity. We will not consider further the equation for $\overline{\tau}_{ij}$ but will focus in the next section on the evolution equation for the subgrid-scale force.

3.2. *Equation for the subgrid-scale force*

The subgrid-scale stress tensor $\overline{\tau}_{ij}$ represents more information than required to close the equation for the resolved velocity $\overline{u}_i$. Only the divergence-free part of $\partial_j \overline{\tau}_{ij}$, which will be denoted $\overline{h}_i$, is actually needed for incompressible flows. The dynamics of $\overline{h}_i$ can be derived immediately from the equation for $\overline{\tau}_{ij}$ and by noting that the right-hand side of the evolution equation for $\overline{h}_i$ must be the divergence of a symmetric tensor. The complete set of LES equations then reads:

$$\partial_t \overline{u}_i = -\partial_j \overline{\overline{u}_i \overline{u}_j} - \partial_i \overline{p}_{\overline{u}} + \nu \nabla^2 \overline{u}_i + \overline{h}_i + \overline{f}_i \tag{3.11}$$

$$\partial_t \overline{h}_i = -\partial_j (\overline{\overline{u}_j \overline{h}_i} + \overline{\overline{u}_i \overline{h}_j}) + \nu \nabla^2 \overline{h}_i - \partial_j \overline{\psi}_{ij} - \partial_i \overline{p}_h \tag{3.12}$$

where a pseudo pressure $\overline{p}_h$ has been introduced to ensure that the subgrid-scale force remains divergence free. An external forcing term f_i has also been added to the Navier-Stokes equation for completeness and for keeping track of the possible effect of such a forcing on the balance equations derived in the following section. The LES pressure $\overline{p}_{\overline{u}}$ is *not* $\overline{p}$ because the incompressibility of the subgrid-scale force is enforced separately. It is thus a function of the LES velocity only:

$$\nabla^2 \overline{p}_{\overline{u}} = -\partial_i \partial_j \overline{\overline{u}_i \overline{u}_j} \tag{3.13}$$

3.3. *Balance equations*

Balance equations for second order quantities based on $\overline{u}_i$ and $\overline{h}_i$ can be used to better understand the effects of the different terms entering the evolution equation for $\overline{h}_i$. The resolved kinetic energy balance is straightforwardly given by

$$\partial_t \langle \overline{u}_i \overline{u}_i / 2 \rangle = \langle \overline{u}_i \overline{f}_i \rangle + \langle \overline{u}_i \overline{h}_i \rangle - 2\nu \langle \overline{S}^u_{ij} \overline{S}^u_{ij} \rangle \tag{3.14}$$

There is nothing new in this relation. As expected the energy input rate due to the subgrid-scale force is given by the average value of the "cross-helicity" $\overline{u}_i \overline{h}_i$. In the absence of external forcing and of viscous effects, the subgrid-scale force is, as expected, the only source of variation of the resolved kinetic energy. Remarkably, in the same conditions, the evolution of the average cross-helicity depends only on the subgrid-scale force intensity $\overline{h}_i \overline{h}_i$ and on the unknown subgrid-scale tensors $\overline{\psi}_{ij}$:

$$\partial_t \langle \overline{u}_i \overline{h}_i \rangle = \langle \overline{h}_i \overline{h}_i \rangle + \langle \overline{S}^u_{ij} \overline{\psi}_{ij} \rangle + \langle \overline{f}_i \overline{h}_i \rangle - 4\nu \langle \overline{S}^u_{ij} \overline{S}^h_{ij} \rangle \tag{3.15}$$

where $\overline{S}^h_{ij} \equiv (\partial_i \overline{h}_j + \partial_j \overline{h}_i)/2$. In particular, the contributions of the nonlinear convective terms from the $\overline{u}_i$ and $\overline{h}_i$ equations cancel exactly. We can also write the balance equation for $\overline{h}_i \overline{h}_i$:

$$\partial_t \langle \overline{h}_i \overline{h}_i / 2 \rangle = -\langle \overline{h}_i \overline{h}_j \overline{S}^u_{ij} \rangle - 2\nu \langle \overline{S}^h_{ij} \overline{S}^h_{ij} \rangle + \langle \overline{S}^h_{ij} \overline{\psi}_{ij} \rangle \tag{3.16}$$

3.4. *The role of the new subgrid-scale tensor*

The unknown subgrid-scale tensor $\overline{\psi}_{ij}$ has contributions from both viscous and nonlinear effects. There is no reason here to separate these two contributions since they both appear with the same form (the divergence of a symmetric tensor) in the equation for $\overline{h}_i$. This generalized subgrid-scale stress tensor should be responsible for both the turbulent flux of $\overline{h}_i$ and the creation of $\overline{h}_i$ due to nonlinear interactions between modes from the resolved velocity field. A model for $\overline{\psi}_{ij}$ should thus have the property of remaining finite for finite $\overline{u}_i$ even when $\overline{h}_i = 0$ in order to be able to represent the creation of $\overline{h}_i$ due to the resolved velocity. However, this model should also remain finite for finite $\overline{h}_i$ when

$\overline{u}_i = 0$ in order to be able to represent the turbulent flux of $\overline{h}_i$ generated by subgrid-scale motions. Since only the projections of $\overline{\psi}_{ij}$ along the tensors $\overline{S}^u_{ij}$ and $\overline{S}^h_{ij}$ affect the global balance equations, it is tempting to model this tensor as:

$$\overline{\psi}_{ij} \approx -2\kappa_h \overline{S}^h_{ij} - 2\kappa_u \overline{S}^u_{ij} \tag{3.17}$$

Assuming that the Kolmogorov theory applies to the subgrid-scale tensor $\overline{\psi}_{ij}$, the coefficients κ_h and κ_u can be written as functions of the dissipation rate $\overline{\epsilon}$ and the projector characteristic width $\overline{\Delta}$ (or the wavenumber in Fourier space) only. Dimensional analysis then yields

$$\kappa_h = C_h \overline{\epsilon}^{1/3} \overline{\Delta}^{4/3} \tag{3.18}$$

$$\kappa_u = C_u \overline{\epsilon}^{2/3} \overline{\Delta}^{2/3} \tag{3.19}$$

where C_h and C_u are dimensionless parameters that remain to be determined.

4. Dynamic procedure for subgrid-scale quantities

The dynamic procedure (Germano *et al*, 1991; Germano, 1992), based on the introduction of a test operator $\widehat{\cdots}$, can be generalized for the pair of equations (3.11-3.12). The evolution of variables at the test level is:

$$\partial_t \widehat{\overline{u}}_i = -\partial_j \widehat{\overline{u}_i \overline{u}_j} - \partial_i \widehat{\overline{p}}_{\widehat{\overline{u}}} + \nu \nabla^2 \widehat{\overline{u}}_i + \widehat{\overline{H}}_i + \widehat{\overline{f}}_i \tag{4.1}$$

$$\partial_t \widehat{\overline{H}}_i = -\partial_j (\widehat{\overline{u}_j \overline{H}_i} + \widehat{\overline{u}_i \overline{H}_j}) + \nu \nabla^2 \widehat{\overline{H}}_i - \partial_j \widehat{\overline{\Psi}}_{ij} - \partial_i \widehat{\overline{p}}_H \tag{4.2}$$

At this stage, it is convenient to introduce the following notations for the divergence-free nonlinear terms:

$$\overline{n}_i = -\partial_j \overline{u_i u_j} - \partial_i \overline{p}_{\overline{u}}\,, \tag{4.3}$$

$$\widehat{\overline{N}}_i = -\partial_j \widehat{\overline{u}_i \overline{u}_j} - \partial_i \widehat{\overline{p}}_{\widehat{\overline{u}}}\,. \tag{4.4}$$

Because of relation (3.13), the vector $\overline{n}_i$ is known in terms of the LES velocity. Similarly, $\widehat{\overline{N}}_i$ is a function of $\widehat{\overline{u}}_i$ only. With these definitions, we can derive a generalized Germano identity between the subgrid scale force at the LES and test levels

$$\widehat{\overline{H}}_i = \widehat{\overline{h}}_i + \widehat{\overline{l}}_i \tag{4.5}$$

where $\widehat{\overline{l}}_i = \widehat{\overline{n}}_i - \widehat{\overline{N}}_i$. Because $\widehat{\overline{H}}_i \neq \widehat{\overline{h}}_i$, the comparison of $\widehat{\overline{\psi}}_{ij}$ with $\widehat{\overline{\Psi}}_{ij}$ cannot be done directly but requires an evolution equation for $\widehat{\overline{l}}_i$:

$$\begin{aligned}\partial_t \widehat{\overline{l}}_i = &-\partial_j \left(\widehat{\overline{u}_i \overline{n}_j} + \widehat{\overline{u}_j \overline{n}_i} - \widehat{\overline{u}_i \overline{N}_j} - \widehat{\overline{u}_i \overline{N}_j} \right) \\ &-\partial_j \left(\widehat{\overline{u}_i \overline{h}_j} + \widehat{\overline{u}_j \overline{h}_i} - \widehat{\overline{u}_i \overline{H}_j} - \widehat{\overline{u}_i \overline{H}_j} \right) - \partial_i \widehat{\overline{p}}_l + \nu \nabla^2 \widehat{\overline{l}}_i - \partial_j L^\nu_{ij}\end{aligned} \tag{4.6}$$

The comparison of equations (4.2-4.6) with the test-level version of equation (3.12) yields the following identity:

$$\widehat{\overline{\Psi}}_{ij} = \widehat{\overline{\psi}}_{ij} + \widehat{\overline{L}}^h_{ij} + \widehat{\overline{L}}^u_{ij} + \widehat{\overline{L}}^\nu_{ij} \tag{4.7}$$

where

$$\widehat{\overline{L}}^{\nu}_{ij} = -\nu(\widehat{\overline{\partial_l \overline{u}_i \partial_l \overline{h}_j}} - \widehat{\partial_l \widehat{\overline{u}}_i \partial_l \widehat{\overline{h}}_j}) \tag{4.8}$$

$$\widehat{\overline{L}}^{h}_{ij} = 2\left(\widehat{\overline{u}_i \overline{h}_j} + \widehat{\overline{u}_j \overline{h}_i} - \widehat{\widehat{\overline{u}}_i \widehat{\overline{h}}_j} - \widehat{\widehat{\overline{u}}_j \widehat{\overline{h}}_i}\right) \tag{4.9}$$

$$\widehat{\overline{L}}^{u}_{ij} = \widehat{\overline{u}_i \overline{n}_j} + \widehat{\overline{u}_j \overline{n}_i} + \widehat{\widehat{\overline{u}}_i \widehat{\overline{N}}_j} + \widehat{\widehat{\overline{u}}_j \widehat{\overline{N}}_i} - 2\widehat{\widehat{\overline{u}}_i \widehat{\overline{n}}_j} - 2\widehat{\widehat{\overline{u}}_j \widehat{\overline{n}}_i} \tag{4.10}$$

In order to simplify the implementation of the dynamic procedure in this preliminary study, we introduce two approximations. First, we note that, in the limit of very small molecular viscosity, $\widehat{\overline{L}}^{\nu}_{ij}$ vanishes. For this reason, we neglect this term in the present approach, assuming a high Reynolds number flow. Second, the scaling of the coefficients κ_h and κ_u depends on the dissipation rate $\overline{\epsilon}$. It will be assumed that $\overline{\epsilon}$ measured at the grid level is the same as the dissipation rate $\widehat{\overline{\epsilon}}$ measured at the test level. Again, this approximation is compatible with the large Reynolds number limit. It is thus reasonable to rewrite the coefficients κ_h and κ_u as follows:

$$\kappa_h = C_h^{\epsilon}\, \overline{\Delta}^{4/3} \tag{4.11}$$

$$\kappa_u = C_u^{\epsilon}\, \overline{\Delta}^{2/3} \tag{4.12}$$

where the coefficients $C_h^{\epsilon} = C_h \overline{\epsilon}^{1/3}$ and $C_u^{\epsilon} = C_u \overline{\epsilon}^{2/3}$ should now be the same at the grid and test levels and can be determined using the dynamic procedure. This yields the following expressions for the unknown coefficients:

$$\kappa_h = \frac{1}{2(1-\alpha^{4/3})} \frac{\langle \widehat{\overline{L}}^{tot}_{ij} \widehat{\overline{S}}^{h}_{ij} \rangle \langle \widehat{\overline{S}}^{h}_{ij} \widehat{\overline{S}}^{u}_{ij} \rangle + \langle \widehat{\overline{L}}^{tot}_{ij} \widehat{\overline{S}}^{u}_{ij} \rangle \langle \widehat{\overline{S}}^{h}_{ij} \widehat{\overline{S}}^{h}_{ij} \rangle}{\langle \widehat{\overline{S}}^{h}_{ij} \widehat{\overline{S}}^{h}_{ij} \rangle \langle \widehat{\overline{S}}^{u}_{ij} \widehat{\overline{S}}^{u}_{ij} \rangle - \langle \widehat{\overline{S}}^{u}_{ij} \widehat{\overline{S}}^{h}_{ij} \rangle \langle \widehat{\overline{S}}^{u}_{ij} \widehat{\overline{S}}^{h}_{ij} \rangle} \tag{4.13}$$

$$\kappa_u = \frac{1}{2(1-\alpha^{2/3})} \frac{\langle \widehat{\overline{L}}^{tot}_{ij} \widehat{\overline{S}}^{u}_{ij} \rangle \langle \widehat{\overline{S}}^{h}_{ij} \widehat{\overline{S}}^{u}_{ij} \rangle + \langle \widehat{\overline{L}}^{tot}_{ij} \widehat{\overline{S}}^{h}_{ij} \rangle \langle \widehat{\overline{S}}^{u}_{ij} \widehat{\overline{S}}^{u}_{ij} \rangle}{\langle \widehat{\overline{S}}^{h}_{ij} \widehat{\overline{S}}^{h}_{ij} \rangle \langle \widehat{\overline{S}}^{u}_{ij} \widehat{\overline{S}}^{u}_{ij} \rangle - \langle \widehat{\overline{S}}^{u}_{ij} \widehat{\overline{S}}^{h}_{ij} \rangle \langle \widehat{\overline{S}}^{u}_{ij} \widehat{\overline{S}}^{h}_{ij} \rangle} \tag{4.14}$$

where $\alpha \equiv \overline{\Delta}/\widehat{\overline{\Delta}}$, $\widehat{\overline{\Delta}}$ is the characteristic length of the test operator, and $\widehat{\overline{L}}^{tot}_{ij} \equiv \widehat{\overline{L}}^{u}_{ij} + \widehat{\overline{L}}^{h}_{ij}$.

These models have been implemented in a spectral code for isotropic decaying turbulence. Preliminary tests have not yet produced successful results. The equation for the $\overline{h}_i$ variable appears to be unstable without a model for $\overline{\psi}_{ij}$. However, the models described here, despite the fact that they definitely improve the behavior of the equation, do not prevent instabilities after an initial decaying stage. At least two reasons could explain these difficulties. Firstly, the approximation of neglecting $\widehat{\overline{L}}^{\nu}_{ij}$ might be too crude for the fairly modest Reynolds number considered in the present tests (the reference data base corresponds to a 256^3 DNS). Second, the very simple model we have considered so far might be inadequate to model the unclosed term.

5. Conclusion

We have considered new formulations of the LES problem based on nonlinear changes of variables in the Navier-Stokes equation. The formulation of carrying an equation for the acceleration vector appears to be ill-conditioned and produces turbulence statistics that depend strongly on the initial conditions.

We have also considered a new formulation of the LES problem based on explicit equations for the unknown subgrid-scale quantities. In particular, the equation for the subgrid-scale force has been studied in detail and implemented in a spectral code. A dynamic procedure has been proposed for the related LES equations. The results obtained in preliminary runs are inconclusive as to whether this approach might eventually be successful.

REFERENCES

CARATI, D., WINCKELMANS, G. S., & JEANMART, H. 2001 On the modelling of the subgrid-scale and filtered-scale stress tensors in large-eddy simulation. *J. Fluid Mech.* **441**, 119-138.

GERMANO, M. 1992 Turbulence: the filtering approach. *J. Fluid Mech.* **238**, 325-336.

GHOSAL, S., LUND, T. S. , MOIN, P. & AKSELVOLL, K. 1995 A dynamic localization model for large-eddy simulation of turbulent flows. *J. Fluid Mech.* **286**, 229-255.

GERMANO, M., PIOMELLI, U., MOIN, P. & CABOT, W. H. 1991 A dynamic subgrid-scale eddy-viscosity model. *Phys. Fluids A* **3**, 1760-1765.

RODI, W. 1979 Prediction methods for turbulent flows. *Lecture Series* 1979-2, Von Karman Institute.

SPEZIALE, C. G. 1991 Analytical methods for the development of Reynolds-stress closures in turbulence. *Ann. Rev. Fluid Mech.* **23**, 105-157.

WINCKELMANS, G. S., LUND, T. S., CARATI, D., & WRAY, A. A. 1996 A priori testing of subgrid-scale models for the velocity-pressure and vorticity-velocity formulations. *Proceedings of the 1996 Summer Program*, Center for Turbulence Research, NASA Ames/Stanford Univ., 309-328.

Investigation of numerical errors, subfilter-scale models, and subgrid-scale models in turbulent channel flow simulations

By Jessica Gullbrand AND Fotini Katopodes Chow †

Turbulent channel flow simulations are performed using second- and fourth-order finite difference codes. A systematic comparison of the large-eddy simulation (LES) results for different grid resolutions, finite difference schemes, and several turbulence closure models is performed. The use of explicit filtering to reduce numerical errors is compared to results from the traditional LES approach. Filter functions that are smooth in spectral space are used, as the findings of this investigation are intended for application of LES to complex domains. Explicit filtering introduces subfilter-scale (SFS) as well as subgrid-scale (SGS) turbulence terms. The former can theoretically be reconstructed; the latter must be modeled. For turbulence models, the dynamic Smagorinsky model (DSM), the dynamic mixed model (DMM), and the dynamic reconstruction model (DRM) are all studied. It is found that for explicit filtering, increasing the reconstruction levels for the SFS stress improves the mean velocity as well as the turbulence intensities. When compared to LES without explicit filtering, the difference in the mean velocity profiles is not large; however the turbulence intensities are improved for the explicit filtering case.

1. Motivation and objectives

The equations for large-eddy simulation (LES) are obtained by applying a low-pass filter to the Navier-Stokes equations. When the equations are solved on a discrete grid, a discretization operator is applied to the equations as well. These filtering and discretization operations divide the turbulent flow field into resolved, subfilter, and subgrid scales. The effect of the subfilter-scale (SFS) and subgrid-scale (SGS) motions on the resolved velocity field must be considered. The SFS contribution can theoretically be reconstructed, but the SGS stress must be modeled. The filter shape as well as the filter width and, of course, grid resolution are free parameters in LES.

For engineering purposes, second-order numerical methods are usually used when performing LES for complex flow fields. In LES the smallest resolved scales are often used to model the contribution from the unresolved scales. Therefore, it is of great importance that the former scales be resolved to high accuracy. High accuracy LES results can be achieved by high-order numerical methods and/or by explicit filtering. The complexity of implementing high-order methods, as well as the computational cost, become prohibitive when studying flow fields in complex geometries. Therefore, the use of explicit filtering may provide a favorable alternative.

In traditional LES solution methods, the computational grid and discretization operators are considered as "implicit" filtering of the Navier-Stokes equations. Using this

† Environmental Fluid Mechanics Laboratory, Civil and Environmental Engineering, Stanford University

approach, there is no need to define a filter function, but neither can the implicit filter be determined. The only actual filter that may be applied in the simulations is used in models for the SFS and/or SGS contributions. One example is the need for a test filter in the dynamic Smagorinsky SGS model to determine the model coefficient.

In contrast, when explicit filtering is applied in LES, an explicitly-defined filter function is needed. In this approach, the defined filter is used when calculating the SFS contribution. If the dynamic Smagorinsky model (DSM) is used as the SGS model, an additional filter function (with larger width than the explicit filter) must also be defined for the test filter in the dynamic procedure. Both the SFS and the SGS contributions must be included in the simulations. The differences in the implementation of the traditional LES and the explicitly-filtered LES approaches might be considered subtle; however, the effect on the LES results is considerable.

The explicit-filtering approach has recently been proposed as a method to minimize the influence of discretization error in finite-difference codes. All finite-difference approximations have a truncation error that grows with increasing wavenumber. This truncation error can be reduced or eliminated when explicit filtering with a filter width larger than the computational grid cell size is applied (Lund 1997). Several researchers have investigated explicit filtering in turbulent channel flow. Lund & Kaltenbach (1995) used sharp-cutoff filters (in spectral space) in the homogeneous directions with a second-order finite difference code (the same code used in the present work). They concluded that the explicit filtering improved the accuracy of the LES results, however, mesh refinement without explicit filtering improved the results at a greater rate. All of their simulations used the DSM with a cutoff filter, which is not applicable to general geometries. Carati *et al.* (2001) developed a useful framework for the explicit filtering approach. They proposed governing equations for LES which carefully distinguish between the discretization and filtering procedures. These equations are also used here to separate the SFS and SGS effects used in explicit filtering. Winckelmans *et al.* (2001) performed simulations with explicit filtering using a fourth-order finite-difference code (also used in the present work). However, they applied second-order filters in three dimensions, which introduce commutation errors in the wall-normal direction due to the stretched grid (Ghosal & Moin 1995). The explicit-filtering approach (with low-order SFS reconstruction) did not perform as well as DSM without explicit filtering (with a sharp-cutoff filter), though the authors suggested that higher-order reconstruction of the SFS terms could improve the results obtained with explicit filtering. Gullbrand (2001) performed explicit filtering (also with low order SFS reconstruction) in three dimensions using commutative filters with the DSM in the same fourth-order finite difference code. Results without explicit filtering showed better agreement with direct numerical simulation (DNS) data, also suggesting that higher-order reconstruction is needed for the SFS terms.

In this investigation, we study the influence of numerical errors on the LES results, as well as the influence of the filtering approach on the turbulence models. The numerical error is studied by performing simulations of a turbulent channel flow using both second-order and fourth-order finite difference codes. The advantage of studying the channel flow is that both sharp-cutoff and smooth filter functions can be used. As previously shown by Piomelli, Moin & Ferziger (1988), the DSM performs better with the sharp-cutoff filter than with a smooth filter function. In the present work, the sharp-cutoff filter is used only for comparison purposes, as our aims are to investigate approaches for LES in complex domains where sharp cutoffs cannot be used. The sharp cutoff is therefore used only for traditional LES, without explicit filtering. A smooth filter is

applied for LES with explicit filtering. Higher-order reconstruction models for the SFS stress are investigated with filters applied only in the homogeneous directions, as this avoids introducing commutation errors. The effect of three-dimensional filtering must ultimately be considered, but is left to future work. For turbulence models, the DSM, the dynamic mixed model (DMM), and the dynamic reconstruction model (DRM) are all investigated. The DSM is used as the SGS model and is applied in all the simulations presented here. The DMM is a linear combination of the scale similarity model (SSM) of Bardina *et al.* (1983) (the SFS model) and the DSM. In the DRM, the SFS stress is modeled by using an estimate of the unfiltered velocity in the unclosed term; the SGS stress is again modeled by the DSM.

2. Governing equations

The governing equations for an incompressible flow field are the continuity equation together with the Navier-Stokes equations,

$$\frac{\partial u_i}{\partial x_i} = 0\,, \qquad \frac{\partial u_i}{\partial t} + \frac{\partial u_i u_j}{\partial x_j} = -\frac{\partial p}{\partial x_i} + \frac{1}{Re_\tau}\frac{\partial^2 u_i}{\partial x_j \partial x_j}\,. \tag{2.1}$$

Here u_i denotes the velocity, p the pressure and Re_τ the Reynolds number based on the friction velocity and the channel half-width. Repeated indices indicate summation.

In computational LES, the governing equations are filtered in space and solved numerically on a grid. The traditional procedure for LES has been to treat the grid and the discretization operators as the filtering procedure of the governing equations. Here, we instead follow the approach of Carati, Winckelmans & Jeanmart (2001) and Winckelmans *et al.* (2001) where the filtering and discretization procedures are treated separately. The discretization operator is represented by a tilde and the filtering operator by an overbar. The filter function G is applied to a flow variable f in physical space as

$$\overline{f}(x,\Delta,t) = \int_{-\infty}^{\infty} G(x,x',\Delta) f(x',t) dx'\,, \tag{2.2}$$

where Δ is the filter width. Thus $\tilde{u}_i$ denotes a variable on the grid, and $\overline{\tilde{u}}_i$ denotes a filtered variable on the grid. Figure 1 shows a schematic of a typical energy spectrum from a turbulent flow. The spectrum can be separated into three parts (Carati *et al.* 2001; Zhou *et al.* 2001). The low-wavenumber portion is well-resolved on the grid, and is contained in the velocity $\overline{\tilde{u}}_i$. The shaded portion represents SFS motions; this region contains filtered information that is still resolved on the grid. The area between the dotted and solid lines is called the numerical-error (NE) region, which is present due to the discretization errors. This region would not exist if spectral methods were used; in this particular case, the complete SFS stress could be recovered. If numerical errors are present, the SFS motions cannot be fully reconstructed. The high-wavenumber portion contains SGS motions that cannot be resolved on the grid, and must be modeled.

Hence, the LES momentum equations on a discrete mesh are written as

$$\frac{\partial \overline{\tilde{u}}_i}{\partial t} + \frac{\partial \widetilde{\overline{\tilde{u}}_j \overline{\tilde{u}}_i}}{\partial x_j} = \frac{\partial \overline{\tilde{p}}}{\partial x_i} + \frac{1}{Re_\tau}\frac{\partial^2 \overline{\tilde{u}}_i}{\partial x_j \partial x_j} - \frac{\partial \widetilde{\tau_{ij}}}{\partial x_j} \tag{2.3}$$

where the turbulent stresses are defined as $\tau_{ij} = \widetilde{u_i u_j} - \overline{\tilde{u}}_i \overline{\tilde{u}}_j$. The filtered equations are not closed, due to the nonlinear term $\widetilde{u_i u_j}$. Properties of the specific filters used are described in section 4.

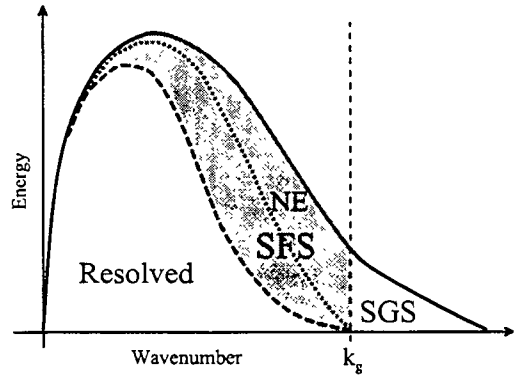

FIGURE 1. Schematic of velocity energy spectrum showing partitioning into resolved, subfilter-scale, and subgrid-scale motions. The numerical-error region is also shown. The grid is indicated by the vertical dashed line, and the filter by the curved dashed line.

Following Carati *et al.* (2001), the turbulent stresses can be separated into two parts, $\tau_{ij} = B_{ij} + \overline{A}_{ij}$, where

$$B_{ij} = \overline{\tilde{u}_i \tilde{u}_j} - \bar{\tilde{u}}_i \bar{\tilde{u}}_j \ , \qquad \overline{A}_{ij} = \overline{u_i u_j} - \overline{\tilde{u}_i \tilde{u}_j} \ . \tag{2.4}$$

$\overline{A}_{ij}$, which we call the SGS stress, depends on scales beyond the resolution domain of the LES. B_{ij}, the SFS stress, depends on the differences between the exact and filtered velocity fields within the resolution domain. As the filter width increases (with fixed grid resolution), the total turbulent stress term, consisting of the SGS and SFS terms, will increase. The SFS component can theoretically be computed, as an infinite expansion in a series model for $\tilde{u}_i$ would give the exact form (Stolz, Adams & Kleiser 2001; Katopodes, Street & Ferziger 2000). Further discussion concerning partitioning of the SFS and the SGS stresses can be found in Carati *et al.* (2001) and Winckelmans *et al.* (2001).

3. Subfilter-scale and subgrid-scale models

When an explicit filter is applied to the Navier-Stokes equations, as in Equation 2.3 above, information at the high wavenumbers is damped. In theory, this SFS information can be restored exactly by using an inverse filtering operation. Several methods have been proposed to approximate this inverse filtering operation. Stolz *et al.* (2001) use the van Cittert (1931) iterative method in their approximate deconvolution procedure to reconstruct the unfiltered velocity field $\tilde{u}_i$ from the filtered field $\bar{\tilde{u}}_i$. Chow & Street (2002) use Taylor-series expansions to obtain the unfiltered velocity. This is then substituted into the expression for B_{ij} to obtain the SFS reconstruction. The SSM (Bardina *et al.* 1983) and the tensor-diffusivity model can be derived from either of these reconstruction procedures by truncating the series expansions after a specified number of terms (Katopodes *et al.* 2000; Winckelmans *et al.* 2001). By truncating these series, a model is obtained for the SFS term B_{ij}. However, an additional term is still required to model the SGS stresses. Note that if the problem domain can be transformed into spectral space, the filter (if it is smooth) can be exactly inverted, and an exact reconstruction can be obtained. Explicit filtering is thus of no advantage when smooth filters are used in spectral methods (Winckelmans & Jeanmart 2001).

In this study, both low-order (the SSM) and higher-order reconstructions (van Cittert

iterative method) are used to model the SFS stresses. In order to do a fair comparison between the SFS models, the same SGS model (DSM) is used in all the simulations. The combinations of SFS and SGS models used are described below. Tests without explicit filtering are also performed for comparison purposes.

3.1. *Dynamic Smagorinsky Model*

The DSM is a widely-used eddy viscosity SGS model (Smagorinsky 1963):

$$\tau_{ij} = -2\tilde{\nu}_e \overline{\tilde{S}}_{ij} = -2(C\Delta)^2 |\overline{\tilde{S}}| \overline{\tilde{S}}_{ij}, \tag{3.1}$$

where ν_e is the eddy viscosity, Δ the filter width and S_{ij} the strain rate tensor. The model parameter C is calculated dynamically (Germano *et al.* 1991) using the least square approximation of Lilly (1992). The choice of the explicit filter and the test filter for the dynamic procedure greatly affects the performance of the DSM, as discussed further below. The DSM is used in our simulations with and without explicit filtering.

3.2. *Dynamic Mixed Model*

Low order reconstruction of the SFS stresses can be performed by using the scale similarity model proposed by Bardina *et al.* (1983). The SSM is obtained by substituting $\tilde{u}_i \approx \overline{\tilde{u}}_i$ into the definition of the SFS stress tensor, B_{ij}. Here the SFS stress is modeled by the scale similarity term and the DSM is used as the SGS model, in a procedure similar to that of Zang, Street & Koseff (1993):

$$\tau_{ij} = \overline{\overline{\tilde{u}}_i \overline{\tilde{u}}_j} - \overline{\overline{\tilde{u}}_i} \, \overline{\overline{\tilde{u}}_j} - 2(C\Delta)^2 |\overline{\tilde{S}}| \overline{\tilde{S}}_{ij} \,, \tag{3.2}$$

where the contribution of the SSM is taken into account in the calculation of the dynamic coefficient. In addition, the test- and explicit filters must be carefully applied in the dynamic procedure, which leads to a different form of the test-filtered equations, as described by Winckelmans *et al.* (2001). The SSM term is discretized by the same method as the convective term in each code.

3.3. *Dynamic Reconstruction Model*

Higher order reconstruction of the SFS stress tensor can be achieved by the iterative deconvolution method of van Cittert (1931). The unfiltered quantities can be derived by a series of successive filtering operations (G) applied to the filtered quantities with

$$\tilde{u}_i = \overline{\tilde{u}}_i + (I - G) * \overline{\tilde{u}}_i + (I - G) * ((I - G) * \overline{\tilde{u}}_i) + \cdots \tag{3.3}$$

where I is the identity matrix. The truncation order of the expansion determines the level of deconvolution, as discussed by Stolz *et al.* (2001). The approximate unfiltered velocity, $\tilde{u}_i^\star$ (due to the truncated series), is substituted into the first term ($\overline{\tilde{u}_i \tilde{u}_j}$) of the SFS stress which becomes $\overline{\tilde{u}_i^\star \tilde{u}^\star}_j$. This reconstruction was used by Stolz *et al.* (2001) who called the SFS model the approximate deconvolution model (ADM). Here the ADM is used together with the DSM:

$$\tau_{ij} = \overline{\tilde{u}_i^\star \tilde{u}_j^\star} - \overline{\tilde{u}}_i \overline{\tilde{u}}_j - 2(C\Delta)^2 |\overline{\tilde{S}}| \overline{\tilde{S}}_{ij} \,, \tag{3.4}$$

which we call the dynamic reconstruction model (DRM). The implementation in the code uses $\tilde{u}_i^\star$ directly in the convective term on the left-hand side of the equations (2.3), as was done by Stolz *et al.* (2001). The DSM is applied as usual to the right-hand side. The ADM with the DSM was also independently proposed and used by Winckelmans & Jeanmart (2001) for isotropic decaying turbulence. Reconstruction series of level five and ten are used in this study and they are denoted DRM5 and DRM10, respectively.

4. Filter functions

In finite-difference methods, the filter in the LES equations is important for limiting numerical errors. As shown by Ghosal (1996) and Chow & Moin (2002), numerical errors from finite-difference schemes can be larger than the entire contribution from the turbulence closure term, $\partial\tau_{ij}/\partial x_j$. To avoid this problem, the explicit filter width should be at least twice the cell size for a fourth-order-accurate finite-difference code. For a second-order finite-difference code, these studies suggest that the filter width should be four times the cell size. In this work, the filter width in the case of the second-order code is not four times the cell size, but instead is chosen to be the same as that used in the fourth-order code. The effect of this choice on the results warrants further study.

The correct use of the filter is especially important in the SFS stress models, particularly in the dynamic procedure which is based on the scale-similarity assumption in the Germano identity. To compute a quantity such as $\widehat{\overline{u}_i}$ in the dynamic procedure, the test filter ('caret' or 'hat' symbol) must be explicitly applied. To satisfy scale similarity, it is required that the caret operator be "similar" to the overbar operator. Therefore, if the filtering operator (the overbar) is a top-hat, the combined effect of the two (caret and overbar) should also be a top-hat filter. Such an operator can be obtained by following the method of Carati *et al.* (2001) and Winckelmans *et al.* (2001), described below.

A discrete approximation to a top-hat filter of twice the cell size can be obtained by trapezoidal rule integration. In one dimension the filter is

$$\overline{\phi}_i = 0.25\phi_{i-1} + 0.5\phi_i + 0.25\phi_{i+1} \,. \tag{4.1}$$

However, the effective filter width of this discrete filter is no longer twice the cell size, but rather $\sqrt{6}$. If Simpson's rule were used to derive a discrete version of the top-hat filter, the weights would instead be $(1/6, 2/3, 1/6)$, with an effective filter width of twice the cell size. Despite the inconsistency in the effective filter width for (4.1), this filter was chosen because the function goes to zero (in spectral space) at the grid cutoff, and therefore eliminates the highest wavenumber that could be sustained by the grid (see e.g. Najjar & Tafti 1996).

To construct an appropriate test filter, it is useful to write the top-hat filter in Fourier space as $\overline{G}(k) = \sin(k\Delta)/(k\Delta)$. The combined effect of the test filter (at twice the width) and the explicit filter (the overbar) should thus also be a top-hat: $\widehat{\overline{G}}(k) = \sin(2k\Delta)/(2k\Delta)$. The required test filter (acting alone), would therefore be

$$\hat{G}(k) = \sin(2k\Delta)/(2\sin(k\Delta)) = \cos(k\Delta). \tag{4.2}$$

If we now transform this back into physical space, we have a discrete filter which requires only the immediate neighboring values,

$$\hat{\phi}_i = 0.5\phi_{i-1} + 0.5\phi_{i+1} \,. \tag{4.3}$$

The combined effect of the overbar and hat filters in physical space is also a top-hat, but over a wider grid stencil, as expected:

$$\widehat{\overline{\phi}}_i = 0.125\phi_{i-2} + 0.25\phi_{i-1} + 0.25\phi_i + 0.25\phi_{i+1} + 0.125\phi_{i+2} \,. \tag{4.4}$$

In this investigation, the same top-hat explicit and test filters are used in both the second- and fourth-order finite-difference codes. The explicit and test filters are applied only in the homogeneous directions, as is commonly done in channel flow studies. Though this choice is not entirely self-consistent, it allows a direct comparison between the second-

and fourth-order LES codes without introducing commutation errors due to filtering in the wall-normal direction over a stretched grid (Gullbrand 2001). Note that the test filter in Equation 4.3 is only used in the simulations with explicit filtering, as done by Winckelmans *et al.* (2001). When no explicit filter is applied, the top-hat in Equation 4.1 is used as the test filter.

5. Solution algorithm

The second- and fourth-order codes represent spatial derivatives on a staggered grid with second- and fourth-order central difference schemes, respectively. In the second-order code, the convective terms are in divergence form, while in the fourth-order code they are in skew-symmetric form (Morinishi *et al.* 1998; Vasilyev 2000). In both codes, the equations are integrated in time using the third-order Runge-Kutta scheme described by Spalart, Moser & Rogers (1991). The diffusion terms in the wall-normal direction are treated implicitly with the Crank-Nicolson scheme. The splitting method of Dukowicz & Dvinsky (1992) is used to enforce the solenoidal condition. The resulting discrete Poisson equation for the pressure is solved in the wall-normal direction using a tri-diagonal direct matrix solver in the second-order code and a penta-diagonal matrix solver in the fourth-order code. In the homogeneous directions, the Poisson equation is solved using a discrete Fourier transform in both codes. Periodic boundary conditions are applied in the streamwise and spanwise homogeneous directions, with no-slip conditions at the channel walls. A fixed mean pressure gradient is used to drive the flow. The Reynolds number is $Re_\tau = 395$ and the computational domain is $(2\pi h, 2h, \pi h)$ in (x, y, z) where x is the streamwise direction, y the wall-normal direction, and z the spanwise direction. The computational grid is stretched in the y-direction by a hyperbolic-tangent function

$$y(j) = -\frac{\tanh(\gamma(1 - 2j/N_2))}{\tanh(\gamma)} \qquad j = 0, ..., N_2 \tag{5.1}$$

where N_2 is the number of grid points in the wall normal (j) direction and γ is the stretching parameter, which is set to 2.75. The computational codes are compared in Gullbrand (2000).

6. Turbulent channel flow simulations

6.1. *Effect of grid resolution and numerical error*

As one focus of this work is to examine the effect of numerical errors in actual LES, the resolution for the two finite-difference codes must be chosen carefully. Figure 2 shows the effect of increasing grid resolution for the second-order code, using no turbulence closure model. All results are compared to the DNS of Moser, Kim & Mansour (1999) for $Re_\tau = 395$ with a resolution of (256,193,192). It is clear that the choice of resolution can significantly alter the results of the simulation. The results in figure 2 show a minimum grid resolution of (81,65,64), where the results do not seem to be greatly affected by the numerical errors. This should be one of the necessary criteria for determining the required grid resolution. Of course, as the grid resolution is increased the solution will eventually approach the DNS of Moser *et al.* (1999). Due to increased accuracy of the fourth-order code (compared to the second-order code), the required minimum resolution was coarser at (64,49,48).

It is expected that, for a given resolution, the performance of the fourth-order code

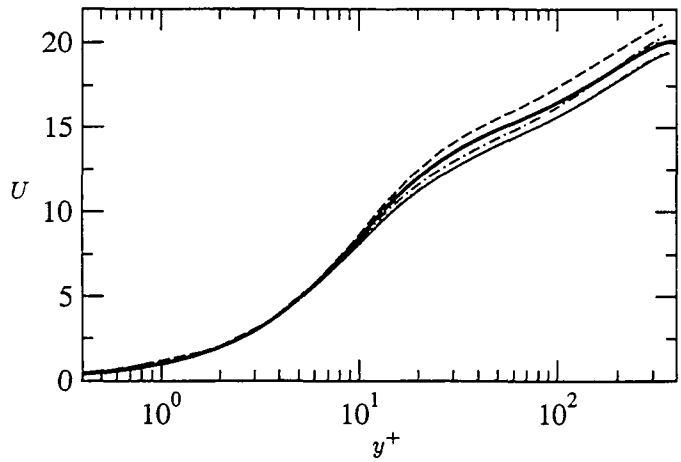

FIGURE 2. Mean velocity profiles for different grid sizes for the second-order code using no turbulence model. ---- : 48x37x36, —·— : 64x49x48, —··— : 81x65x64, ——— : 96x73x72, and ——— : DNS.

will be better than that of the second-order code, due to the higher accuracy of the finite difference schemes. Figure 3 shows results of simulations made with the same grid resolution (48,37,36) for both finite-difference codes and for the pseudo-spectral code of Jeanmart & Winckelmans (see the companion study in this volume). The pseudo-spectral code uses fourth-order compact finite differences in the vertical direction and is spectral in the horizontal directions. The simulations are performed without a closure model, so that the effect of the numerical errors can be compared. As seen in figure 2, increasing resolution (and hence decreasing numerical errors) first reduces the predicted mass flow rate (mean velocity profile) in the simulations to a level lower than the DNS results. If the resolution is further increased, the mass flow rate increases and approaches the DNS results. Similarly, it is expected that, for a given grid resolution, the pseudo-spectral code will produce the lowest mean-velocity profile of the three codes, as it has the lowest numerical errors (see figure 3). The fourth-order finite-difference code also predicts a mean velocity profile that is lower than the DNS for this resolution (but higher than the pseudo-spectral code); however the second-order code does not, due to the effect of large truncation errors.

Because of the large differences in the profiles in figure 3, different grid resolutions are chosen for each finite-difference code to make a fair comparison of results in further tests. In this way, we attempt to minimize the numerical differences at the outset of the investigation, though the interaction of these errors with different SFS and SGS models is still an issue. To choose the appropriate resolution, simulations with the DSM, using a spectral-cutoff test filter with a width of twice the grid cell size, were performed at different resolutions until good agreement was obtained. (Agreement at the two chosen resolutions can be seen in figures 4 and 5, to be described later.) We use the cutoff-filter case as the base case for comparison, because this approach does not involve explicit filtering and thus provides an independent reference. Note that the cutoff filter is more accurately termed a "cutoff projection", as it is not reversible. However, we use the term "cutoff filter" as is commonly done in the literature.

The grid resolutions for the remaining simulations are therefore as follows. The fourth-

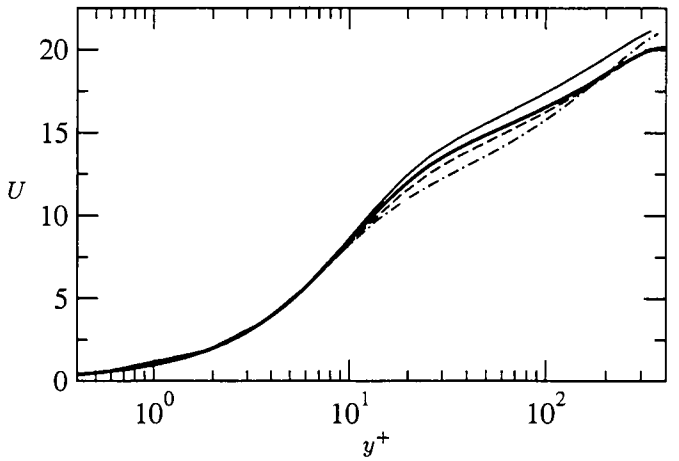

FIGURE 3. Mean velocity profiles for three different LES codes with the same grid resolution (48,37,36) using no turbulence model. ——— : second-order, - - - - : fourth-order, —·— : pseudo-spectral, ——— : DNS.

order finite-difference code resolution is chosen to be (64,49,48), which is one-quarter of the DNS resolution in each spatial direction. This resolution corresponds to a streamwise grid cell size of $\Delta x^+ = 39$, and a spanwise cell size of $\Delta z^+ = 26$. Nondimensional "plus", or "wall" units are defined as $y^+ = yu_\tau/\nu$, where u_τ is the friction velocity and ν is the kinematic viscosity. The range of cell size in the wall-normal direction is $0.4 \leq \Delta y^+ \leq 45$. In the simulations using the second-order code, a grid resolution of (81,65,64) is employed. This resolution corresponds to $\Delta x^+ = 31$, $\Delta z^+ = 19$ and $0.3 \leq \Delta y^+ \leq 34$. Thus the choice of grids for each code corresponds to the grid size which was shown to be not greatly influenced by the numerical errors for the "no model" tests mentioned previously. The time step used is 1.5×10^{-3} and is the same in both codes. A statistically-stationary solution is obtained after 30 dimensionless time units, and thereafter statistics are sampled during 15 time units. The time is normalized with the friction velocity and the channel half width.

6.2. *SGS modeling: LES without explicit filtering*

For the purpose of comparison, tests are performed using traditional SGS model formulations. These simulations do not use explicit filtering, meaning that the only filter that is actually applied is the test filter in the dynamic procedure, and this is chosen to be twice the cell size. In our test cases without explicit filtering, the reconstruction term (the SFS stress) is not considered; only the SGS stress is modeled. By using the top-hat filter (which is smooth in spectral space) as the test filter in the dynamic procedure, it is assumed that the implicit filter is also a top-hat; therefore the SFS stress should in theory be considered. However, the implicit filter cannot be determined, meaning that reconstruction of the SFS stress is questionable.

For the channel flow, the periodic lateral boundary conditions allow the use of a spectral-cutoff filter for the test filter. It is well known (Piomelli *et al.* 1988) that the Smagorinsky model performs best when used together with such a cutoff filter. The difficulty with this filter choice is that it cannot be easily applied to other geometries. The cutoff filter width in our simulations is twice the cell size, giving the filter-grid ratio

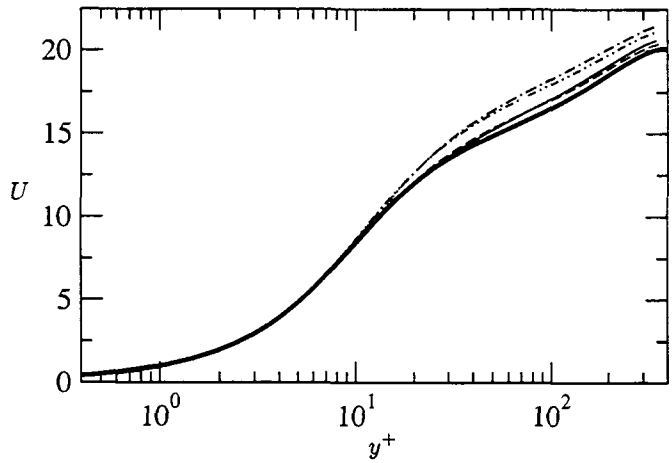

FIGURE 4. Mean velocity profiles for the second-order (81,65,64) and fourth-order (64,49,48) codes without explicit filtering. ——— : fourth-order code, DSM with sharp cutoff filter, - - - - : second-order code, DSM with sharp cutoff filter, —·— : fourth-order code, DSM with top-hat filter, —··— : second-order code, DSM with top-hat filter, and ——— : DNS.

$\alpha = \Delta/\Delta_g = 2$, where Δ and Δ_g are the filter width and grid cell size respectively. Because filtering is applied only in the x and z directions, the effective filter-grid ratio squared is $\alpha_{eff}^2 = 4^{2/3}$. Simulations with the DSM using a top-hat filter in physical space as the test filter are also performed. The test filter is applied as in Equation 4.1; the filter-grid ratio in this case is $\alpha = \sqrt{6}$ and hence $\alpha_{eff}^2 = 6^{2/3}$ (see Najjar & Tafti 1996; Lund 1997).

Figure 4 shows mean velocity profiles from both the second- and fourth-order finite difference codes, compared with DNS data. Agreement between the second- and fourth-order codes for the simulations using the cutoff filter is quite good, indicating that the chosen resolution for each code is good for comparisons. The agreement between the second- and fourth-order codes for the reduced (deviatoric) turbulent intensities for the cutoff filter case is excellent, as seen in figure 5. Note that the turbulence intensities are adjusted by removing the trace from each tensor component, as discussed by Winckelmans, Jeanmart & Carati (2002). Results for the top-hat filter are, as expected, worse than for the spectral cutoff filter. Though it is known to perform poorly with a smooth filter (Piomelli *et al.* 1988), the DSM is frequently used with the top-hat filter because spectral cutoff filters cannot be applied in domains with general geometries. Note that the profiles obtained by the second-order code in figures 4 and 5 are slightly closer than the fourth-order code to the DNS for the top-hat filter cases, which may be due to the choice of higher resolution for this code than the fourth-order code. Profiles of the SGS stress $\tilde{\tau}_{12}$ over half the channel width are shown in figure 6. The contribution of the SGS stress is smaller for the second-order code because the simulations are performed using a higher resolution, meaning that more of the turbulent motions are resolved. The SGS stress is larger for the top-hat filter cases for both codes because the effective filter width of the top-hat is larger, which therefore places more energy in the SGS terms.

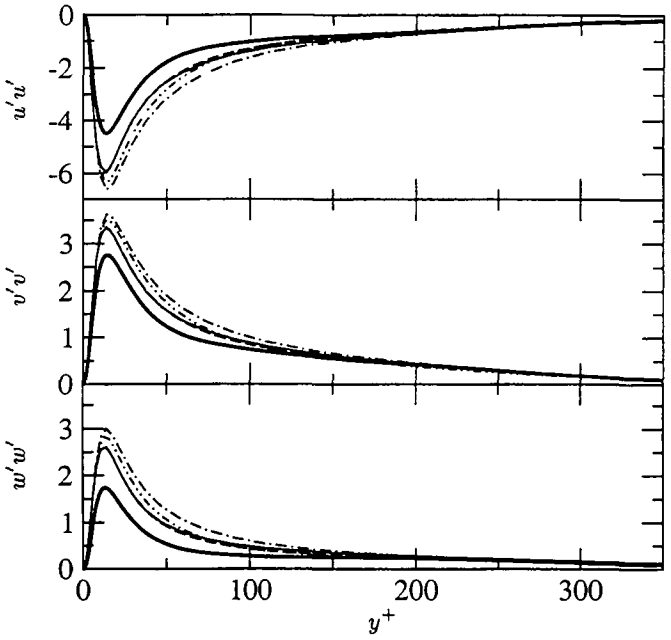

FIGURE 5. Profiles of reduced turbulence intensities in streamwise $u'u'$, wall-normal $v'v'$ and spanwise $w'w'$ directions for the second-order (81,65,64) and fourth-order (64,49,48) codes without explicit filtering. The trace is removed from each tensor component. ——— : fourth-order code, DSM with sharp cutoff filter, - - - - : second-order code, DSM with sharp cutoff filter, —·— : fourth-order code, DSM with top-hat filter, —··— : second-order code, DSM with top-hat filter, and ——— : DNS.

6.3. *SFS and SGS modeling: LES with explicit filtering*

To attempt to minimize the influence of discretization errors in finite difference codes, explicit filtering can be used. The difference between the implementation of this approach and that of section 6.2 is in the filters used in the closure models, and thus the ability to reconstruct the SFS terms. As this approach is intended for finite-difference methods in complex domains, the filters used must be smooth; the spectral-cutoff filter is not used here.

We performed several simulations using explicit filtering, using increasing levels of reconstruction for the SFS stresses. For the first case, the DSM is applied using an explicit filter of width twice the grid cell size and a test filter of four times the cell size. This case has no reconstruction terms. Then, a low-level reconstruction is added by using the DMM, followed by the DRM5 and DRM10 with five and ten levels of reconstruction, respectively (see sections 3.2 and 3.3). Figure 7 shows that the mean velocity profiles for the fourth-order code improve compared to the DNS results as the level of reconstruction increases. The improvement is very clear in the comparison of the reduced turbulent intensities in figure 8. The incremental improvement between DRM5 and DRM10 is not large, indicating that good reconstruction of the unfiltered velocity is probably already obtained by DRM5; the reconstruction series seems to have converged. The differences between the LES results (with DRM5 and DRM10) and the DNS results are therefore most probably due to numerical errors (see the NE region in figure 1) and the SGS

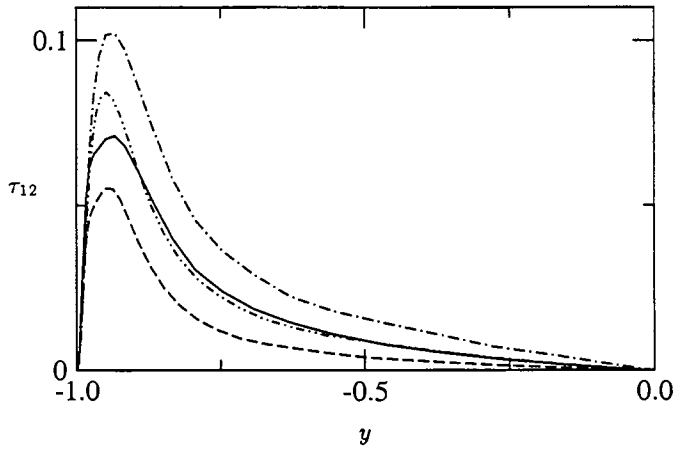

FIGURE 6. Profiles of the turbulent stress $\tilde{\tau}_{12}$ for the second-order (81,65,64) and fourth-order (64,49,48) codes without explicit filtering. ——— : fourth-order code, DSM with sharp cutoff filter, - - - - : second-order code, DSM with sharp cutoff filter, —·— : fourth-order code, DSM with top-hat filter, and —··— : second-order code, DSM with top-hat filter.

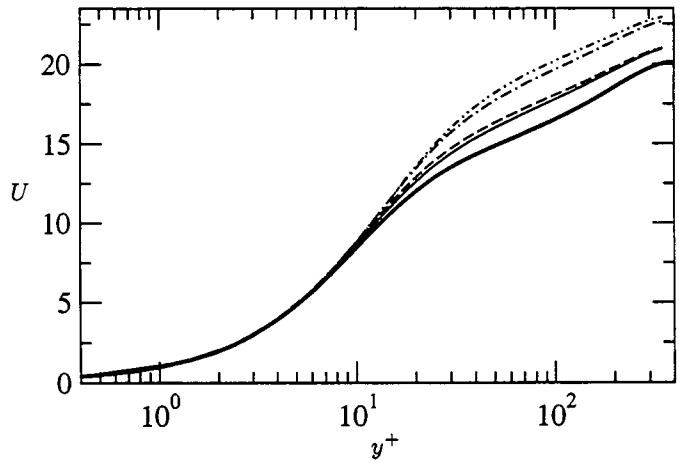

FIGURE 7. Mean velocity profiles for the fourth-order code (64,49,48) with explicit filtering (top-hat) and reconstruction. —··— : DSM, —·— : DMM, - - - - : DRM5, ——— : DRM10, and ——— : DNS.

model used. The total turbulent stress $\tilde{\tau}_{12}$ shown in Figure 9 increases considerably with increasing reconstruction level (though only slightly between DRM5 and DRM10). For each case, the contribution of the DSM portion (not shown) of the model is roughly the same, with a peak of around 0.1, so the increase of the modeled stresses is almost entirely due to the SFS model. Results for the second-order code are shown in figures 10 and 11. Turbulent intensities are not shown for the second-order code as the pattern of improvement is similar to that of the fourth-order code.

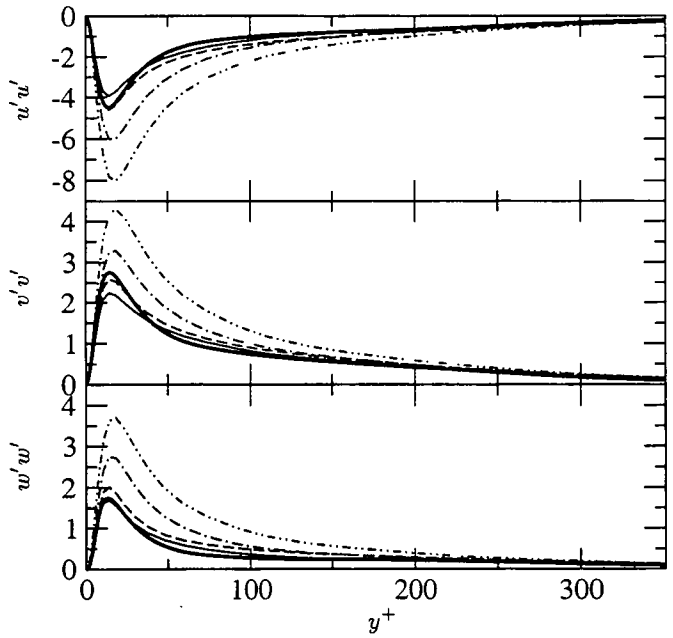

FIGURE 8. Profiles of reduced turbulence intensities in streamwise $u'u'$, wall normal $v'v'$ and spanwise $w'w'$ directions for the fourth-order (64,49,48) code with explicit filtering (top-hat) and reconstruction. The trace is removed from each tensor component. —··— : DSM, —·— : DMM, ---- : DRM5, ——— : DRM10, and ——— : DNS.

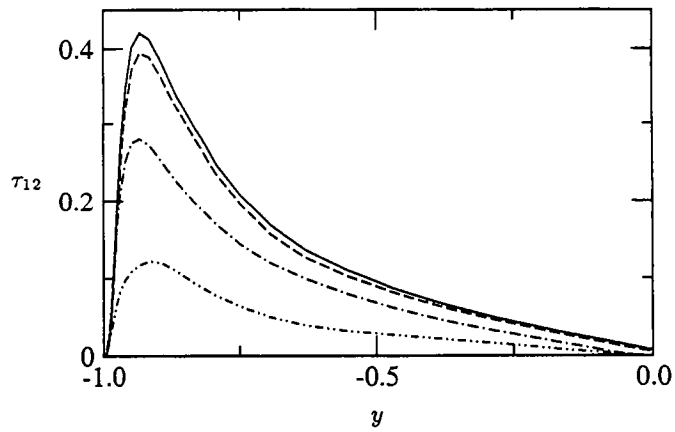

FIGURE 9. Profiles of the turbulent stress $\bar{\tau}_{12}$ for the fourth-order (64,49,48) code with explicit filtering (top-hat) and reconstruction. —··— : DSM, —·— : DMM, ---- : DRM5, and ——— : DRM10.

7. Discussion and conclusions

Despite the existing theory and previous attempts at LES using explicit filtering (Carati *et al.* 2001; Winckelmans *et al.* 2001; Lund & Kaltenbach 1995), the advantages of this method in practice remain unclear. Because of the extra filtering operations, the

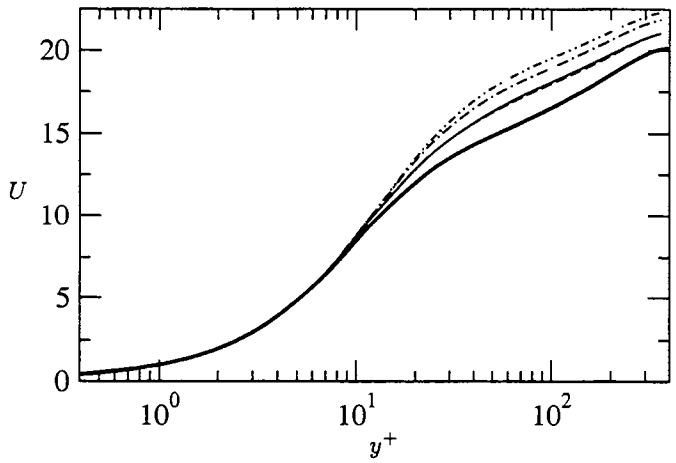

FIGURE 10. Mean velocity profiles for the second-order code (81,65,64) with explicit filtering (top-hat) and reconstruction. —··— : DSM, —·— : DMM, ---- : DRM5, ——— : DRM10, and ——— : DNS.

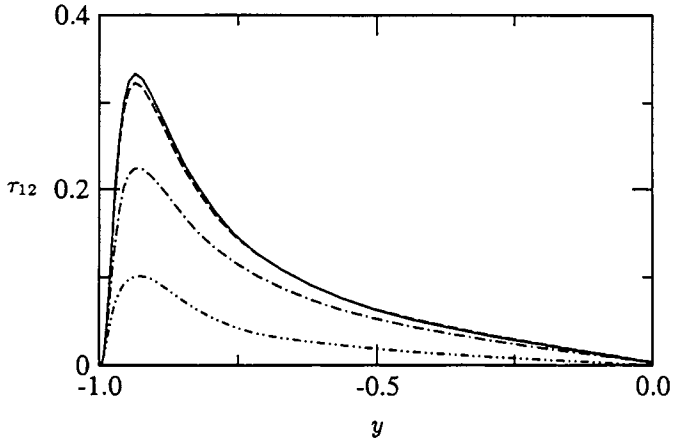

FIGURE 11. Profiles of the turbulent stress $\tilde{\tau}_{12}$ for the second-order (81,65,64) code with explicit filtering (top-hat) and reconstruction. —··— : DSM, —·— : DMM, ---- : DRM5, and ——— : DRM10.

explicit-filtering approach is necessarily more computationally expensive than traditional LES. However, explicit filtering offers the potential to limit the influence of numerical errors in finite difference schemes on the flow solution.

Figure 12 compares results from both the second- and fourth-order codes, with and without explicit filtering. The models used are the DSM with the top-hat filter (without explicit filtering, as is common in engineering applications) and the DRM10 (with explicit filtering). For both codes, there is a slight improvement in the mean flow profiles for the cases with explicit filtering and reconstruction. The largest difference is seen in the reduced turbulence intensities, shown in figure 13, where the improvements due to DRM10 are quite significant. Even the magnitudes of the reduced streamwise intensities $u'u'$ for DRM10 are smaller than the DNS values, which is the opposite of what is

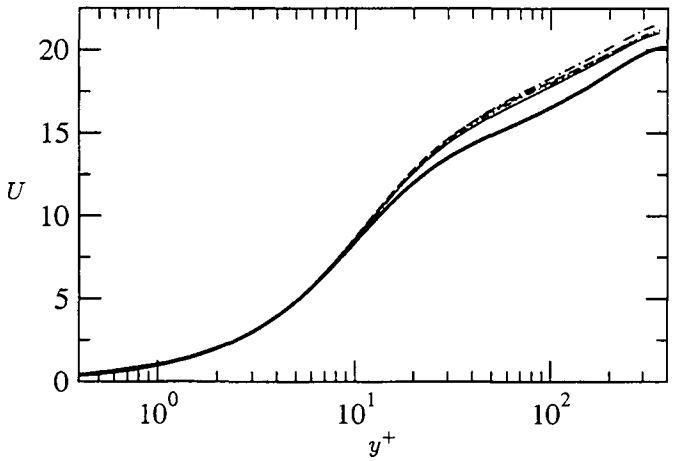

FIGURE 12. Mean velocity profiles for the second-order (81,65,64) and fourth-order (64,49,48) codes with and without explicit filtering (using top-hat filters for both). ——— : fourth-order code, DRM10, - - - - : second-order code, DRM10, —·— : fourth-order code, DSM no explicit filtering, —··— : second-order code, DSM no explicit filtering, and ——— : DNS.

usually observed with turbulence closures such as the DSM (Gullbrand 2001). Better representation of turbulent intensities is, for example, very important in applications where accurate prediction of turbulent mixing is required. These results therefore demonstrate that improvements can be obtained for a given resolution and code by using explicit filtering and reconstruction.

The implications of these results for LES for engineering applications must be considered carefully. For engineering flows, traditional LES (without explicit filtering) is commonly performed with the DSM, using a top-hat test filter. As shown in this investigation, this method poorly predicts mean velocity profiles as well as turbulence intensities. There are several choices that must be made in determining how best to improve the performance of LES in practical applications.

Choosing the appropriate grid resolution for a simulation is necessarily the first step, as our results show great discrepancies among simulations with different grid sizes. Two main concerns must be addressed when selecting the necessary grid resolution. First, the grid should be able to resolve important physical characteristics of the flow. Second, the grid must also be fine enough to obtain a solution that is not largely affected by the numerical errors.

The order of accuracy of the finite-difference scheme used also greatly affects the solution. Note, for example, that the difference between the predicted mean velocity profiles for simulations using different turbulence models was larger for the fourth-order than for the second-order code. The higher sensitivity of the fourth-order code may be due to smaller numerical errors, and/or the coarser resolution used in these simulations (compared to the resolution of the second-order code), so that the turbulence models play a larger role in the fourth-order case.

Finally, explicit filtering can be used as a means to reduce the influence of numerical errors in the high wavenumbers. Increasing the grid resolution improves the representation of the important large energy-containing scales. However, the truncation errors in the high wavenumber portion remain. It is precisely these high wavenumbers that are often

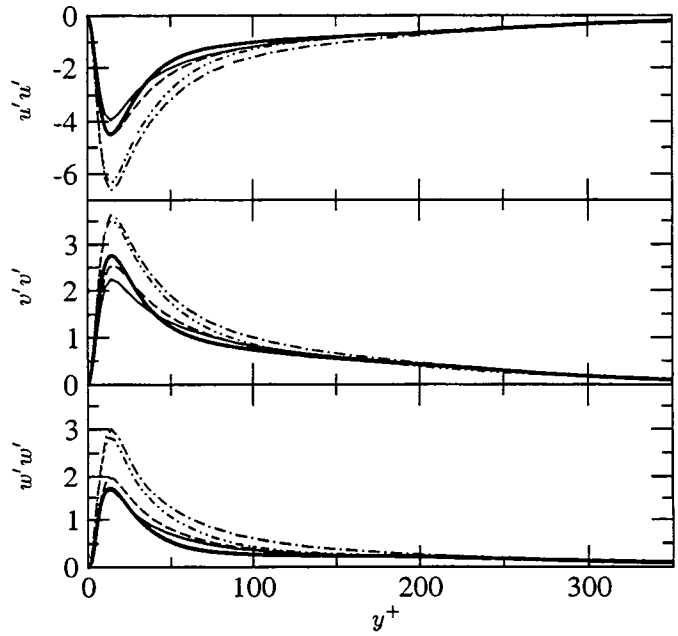

FIGURE 13. Profiles of reduced turbulence intensities in streamwise $u'u'$, wall normal $v'v'$ and spanwise $w'w'$ directions for the second-order (81,65,64) and fourth-order (64,49,48) codes with and without explicit filtering (using top-hat filters for both). The trace is removed from each tensor component. ——— : fourth-order code, DRM10, - - - - : second-order code, DRM10, —·— : fourth-order code, DSM no explicit filtering, —··— : second-order code, DSM no explicit filtering, and ——— : DNS.

used to represent SGS motions, and it is therefore imperative that they be represented as accurately as possible.

The extra computational cost of using explicit filtering to obtain increased accuracy may be worthwhile as LES continues to be applied to increasingly complex geometries and to problems where fine resolutions are not practical. The improvements resulting from use of the DRM10 (and the DRM5) model may be even more significant at coarser resolutions. Tests with DRM10 with the second-order code at a resolution of (48,37,36) show improvements over the DSM with the top-hat filter (without explicit filtering) even with such an under-resolved simulation (not shown). The turbulent intensities predicted by DRM10 are much better than those from the DSM, even though the difference in the mean velocity profiles for these two models is still small.

As this investigation has shown, the explicit-filtering approach has the potential to improve simulation results. SFS models with different levels of reconstruction were considered. The LES results with explicit filtering improve as the level of reconstruction is increased. No significant improvements were observed between DRM5 and DRM10, indicating that the reconstruction is probably adequate at level five (which is also less expensive computationally); discretization errors and poor performance of the SGS model prevent the unfiltered velocities from further approaching DNS values. The ability of the SGS (or SFS) model to account for such numerical errors due to the discretization and finite difference schemes is of course desirable. There is, therefore, a great need to develop SGS models that work well in the context of explicit filtering, where the accuracy of the

smallest scales is increased. In addition, the effect of filtering in all three directions (and the resulting commutation errors) needs to be investigated.

Acknowledgments

Thanks are extended to Dr. H. Jeanmart and Prof. G.S. Winckelmans who contributed greatly to this work through many discussions (see also their parallel project conducted during this summer program). Thanks are also due to Professors J. Ferziger, P. Moin, and R. Street for their input, as well as to Prof. O.V. Vasilyev for providing the channel flow codes. The support of NSF Grant ATM-0073395 (Physical Meteorology Program: R.R. Rogers, Program Director) for author FKC is gratefully acknowledged.

REFERENCES

BARDINA, J., FERZIGER, J. & REYNOLDS, W. 1983 Improved turbulence models based on large eddy simulation of homogeneous, incompressible, turbulent flows. *Dept. of Mech. Engg., Stanford Univ., Tech. Rept.* TF-19.

CARATI, D., WINCKELMANS, G. & JEANMART, H. 2001 On the modelling of the subgrid-scale and filtered-scale stress tensors in large-eddy simulation. *J. Fluid Mech.* **441**, 119–138.

CHOW, F. & MOIN, P. 2002 A further study of numerical errors in large-eddy simulations. *J. Comp. Phys.*(in press).

CHOW, F. & STREET, R. 2002 Modeling unresolved motions in LES of field-scale flows. In *American Meteorological Soc., 15th Sympo. on Boundary Layers and Turbulence*, pp. 432–435.

VAN CITTERT, P. 1931 Zum Einfluß der Spaltbreite auf die Intensitätsverteilung in Spektrallinien II. *Zeit. für Physik* **69**, 298.

DUKOWICZ, J. & DVINSKY, A. 1992 Approximate factorization as a high-order splitting for the implicit incompressible-flow equations. *J. Comp. Phys.* **102**, 336–347.

GERMANO, M., PIOMELLI, U., MOIN, P. & CABOT, W. 1991 A dynamic subgrid-scale eddy viscosity model. *Phys. Fluids* **3**, 1760–1765.

GHOSAL, S. 1996 An analysis of numerical errors in large-eddy simulations of turbulence. *J. Comp. Phys.* **125**, 187–206.

GHOSAL, S. & MOIN, P. 1995 The basic equations for the large eddy simulation of turbulent flows in complex geometry. *J. Comp. Phys.* **118**, 24–37.

GULLBRAND, J. 2000 An evaluation of a conservative fourth order dns code in turbulent channel flow. *Annual Research Briefs*, Center for Turbulence Research, NASA Ames/Stanford Univ.

GULLBRAND, J. 2001 Explicit filtering and subgrid-scale models in turbulent channel flow. *Annual Research Briefs*, Center for Turbulence Research, NASA Ames/Stanford Univ.

KATOPODES, F., STREET, R. & FERZIGER, J. 2000 A theory for the subfilter-scale model in large-eddy simulation. *Environmental Fluid Mech. Lab., Stanford Univ., Tech. Rept.* 2000-K1.

LILLY, D. 1992 A proposed modification of the Germano subgrid-scale closure method. *Phys. Fluids* **4**, 633–635.

LUND, T. & KALTENBACH, H.-J. 1995 Experiments with explicit filtering for LES using

a finite-difference method. *Annual Research Briefs*, Center for Turbulence Research, NASA Ames/Stanford Univ.

LUND, T. S. 1997 On the use of discrete filters for large eddy simulation. *Annual Research Briefs*, Center for Turbulence Research, NASA Ames/Stanford Univ.

MORINISHI, Y., LUND, T., VASILYEV, O. & MOIN, P. 1998 Fully conservative higher order finite difference schemes for incompressible flow. *J. Comp. Phys.* **143**, 90–124.

MOSER, R., KIM, J. & MANSOUR, N. 1999 Direct numerical simulation of turbulent channel flow up to $Re_\tau = 590$. *Phys. Fluids* **11**, 943–945.

NAJJAR, F. & TAFTI, D. 1996 Study of discrete test filters and finite difference approximations for the dynamic subgrid-scale stress model. *Phys. Fluids* **8**, 1076–1088.

PIOMELLI, U., MOIN, P. & FERZIGER, J. 1988 Model consistency in large eddy simulation of turbulent channel flows. *Phys. Fluids* **31**, 1884–1891.

SMAGORINSKY, J. 1963 General circulation experiments with the primitive equations. *Monthly Weather Rev.* **91**, 99–152.

SPALART, P., MOSER, R. & ROGERS, M. 1991 Spectral methods for the navier-stokes equations with one infinite and 2 periodic directions. *J. Comp. Phys.* **96**, 297–324.

STOLZ, S., ADAMS, N. & KLEISER, L. 2001 An approximate deconvolution model for large-eddy simulation with application to incompressible wall-bounded flows. *Phys. Fluids* **13**, 997–1015.

VASILYEV, O. 2000 High order finite difference schemes on non-uniform meshes with good conservation properties. *J. Comp. Phys.* **157**, 746–761.

WINCKELMANS, G. & JEANMART, H. 2001 Assessment of some models for les without/with explicit filtering. In *Direct and Large-Eddy Simulation IV* (B. Geurts, F. Friedrich & O. Métais, eds.), Kluwer, pp. 55–66.

WINCKELMANS, G., JEANMART, H. & CARATI, D. 2002 On the comparison of turbulence intensities from large-eddy simulation with those from experiment or direct numerical simulation. *Phys. Fluids* **14**, 1809–1811.

WINCKELMANS, G., WRAY, A., VASILYEV, O. & JEANMART, H. 2001 Explicit-filtering large-eddy simulation using the tensor-diffusivity model supplemented by a dynamic smagorinsky term. *Phys. Fluids* **13**, 1385–1403.

ZANG, Y., STREET, R. L. & KOSEFF, J. R. 1993 A dynamic mixed subgrid-scale model and its application to turbulent recirculating flows. *Phys. Fluids* **5**, 3186–3196.

ZHOU, Y., BRASSEUR, J. & JUNEJA, A. 2001 A resolvable subfilter-scale model specific to large-eddy simulation of under-resolved turbulence. *Phys. Fluids* **13**, 2602–2610.

Comparison of recent dynamic subgrid-scale models in turbulent channel flow

By H. Jeanmart † AND G. S. Winckelmans †

Some recent subgrid-scale models are evaluated in turbulent channel flow at $\mathrm{Re}_\tau = 395$. The models considered were chosen among those performing best in decaying isotropic turbulence, following the study by Winckelmans & Jeanmart (2001): the dynamic Smagorinsky model (used as a baseline); a dynamic and regularized version of the variational multiscale model of Hughes, Mazzei, Oberai & Wray (2001); a dynamic "Smagorinsky + hyperviscosity" model (here with two dynamic coefficients); and a dynamic Smagorinsky model acting on an artificially-enhanced velocity field. The last three models put more emphasis than the Smagorinsky model on the subgrid-scale (SGS) dissipation at small scales, leading to significant improvement of the results in isotropic turbulence. The last two models combine viscosity and hyperviscosity effects.

The dynamic procedure was implemented for each model, with and without adding a test projection in the wall-normal direction. The projection uses a combined "sampling + interpolation" procedure, applied in physical space.

The models are assessed and compared to the direct numerical simulation (DNS) data of Moser, Kim & Mansour (1999) on the basis of mean profiles of velocity, rms velocities and reduced (deviatoric) turbulence intensities. A main outcome is the good behavior of the multiscale model of Hughes *et al.* as compared to the Smagorinsky model. Good results are also obtained when using the Smagorinsky model acting on an artificially-enhanced velocity field. In all cases, the dynamic procedure without test "sampling + interpolation" in the wall-normal direction leads to better agreement with the DNS data. The poor performance of "sampling + interpolation" is most probably due to the interpolation part, and a possible solution to the problem is proposed.

1. Introduction

The practical approach to large-eddy simulation (LES) is concerned with modeling the effective "subgrid-scale" stress (SGS stress) due to the projection from the complete u_i field to the incomplete large-eddy field $\widetilde{u}_i$: a non-regular operation, the effect of which must be modelled. On the other hand, the mathematical approach usually assumes a regular explicit filter: a regular convolution acting on u_i to produce the filtered field $\overline{u}_i$, leading to an effective "subfilter-scale" stress (SFS stress). One can also consider practical LES with regular filtering added to the projection, thus solving for $\overline{\widetilde{u}}_i$ instead of $\widetilde{u}_i$. The effective stress is then the sum of a SFS stress (which can be reconstructed) and a SGS stress (which must be modelled).

A systematic comparison of many of the recent LES models and approaches was conducted by Winckelmans *et al.* (2001a) for the case of decay of isotropic turbulence (48^3 LES started from a truncated 256^3 DNS). The models tested were:

† Center for Systems Engineering and Applied Mechanics (CESAME), Université Catholique de Louvain, Belgium

- viscosity model (Smagorsinky (1963));
- mixed "Smagorinsky + hyperviscosity" models (similar to the model proposed in Métais *et al.* (1992), but formulated differently and with only one coefficient);
- the variational multiscale model, Hiughes *et al.* (2001a) (basically the Smagorinsky model applied to half of the wavenumbers, from $k_{\max}/2$ to $k_{\max}$);
- the Smagorinsky model acting on an artificially-enhanced velocity field (a new model);
- the approximate-deconvolution model (ADM), Stolz *et al.* (1999), Stolz *et al.* (2001).

The spectral behavior of the models was investigated numerically. Two diagnostics were used: the model dissipation spectrum and the energy spectrum. This systematic comparison work pointed out the superiority of the models combining viscosity and higher order viscosity. Models that behave as viscosity at low k and-higher order viscosity at high k can indeed reproduce the correct dissipation spectrum for the SGS stress. The best results were those with "viscosity + k^6 hyperviscosity" (also consistent with the findings reported by Métais *et al.* (1992)). The model by Hughes *et al.* performs better than the Smagorinsky model (even though it lacks the part of the SGS dissipation that occurs at low wavenumbers). The Smagorinsky model acting on an artificially-enhanced velocity field also leads to better results than the standard Smagorinsky model (Smagorsinky (1963)).

Another conclusion of this investigation was the possible uselessness, at least in pseudo-spectral methods, of using additional explicit filtering, thus requiring "deconvolution" methods augmented by "regularization" terms: either the method used in Winckelmans *et al.* (2001b) or that used in Stolz *et al.* (1999), Stolz *et al.* (2001): the results are, at best, equivalent to (and usually worse than) those obtained from LES without additional explicit filtering, using the Smagorinsky model.

LES with added explicit filtering is not considered here. The purpose of this work is to study the SGS models in a more challenging test case, the turbulent channel flow (here at $\mathrm{Re}_\tau = 395$) to see if the conclusions from isotropic turbulence still hold. All models are implemented in their dynamic version (Germano *et al.* (1991), Ghosal *et al.* (1992), Ghosal *et al.* (1995)). A more consistent test projection operator for the wall-normal direction is described in section 2. The different models investigated are detailed in section 3. The LES results are then compared to the DNS results in section 4. Comparisons are made with the profiles of mean velocity, rms velocities and reduced (deviatoric) turbulence intensities. The main conclusions are summarized in section 5.

2. Projection test operator

The operator $\tilde{}$ is the projection from DNS to the LES grid of cell size h. For the dynamic procedure, we further consider the test operator $\hat{}$: a projection from the LES grid of size h to a LES grid of size $2\,h$. The channel flow code being pseudo-spectral in x and z, and finite differences in y, we use, as projection, the sharp Fourier cutoff in x and z. In y, we can either do nothing (not fully consistent with the dynamic procedure) or apply a test projection using sampling. The sampling is done by retaining one value every two: from a sequence of field values $[f_1, f_2, f_3, \ldots]$ on the LES grid, we retain the sequence $[f_1, f_3, \ldots]$ on the twice coarser grid. Clearly, this corresponds to a projection: a loss of information. Then, in order to obtain projected values everywhere on the LES grid (we need them for the dynamic procedure, at least in its usual version), we use

interpolation. Using here linear interpolation, the projected field evaluated on the LES grid is $[f_1, (f_1 + f_3)/2, f_3, \ldots]$.

Thus, the combined operator, $\tilde{}$ followed by $\hat{}$, is also a projection: from DNS to a LES grid of size $2h$. Therefore this has nothing to do with regular explicit filtering: in that case, information is not lost and one can always recover the original field from the filtered field using a "deconvolution" method (such as the van Cittert iterative method). This point is most important: here we perform LES with projection only, and thus without regular explicit filtering and with no need for reconstruction of the effective SFS stress.

The equations for the DNS (with $\partial_i u_i = 0$) are

$$\partial_t u_i + \partial_j (u_i u_j) + \partial_i P = \nu \partial_j \partial_j u_i \,. \tag{2.1}$$

Those for the LES (with $\partial_i \widetilde{u}_i = 0$) are

$$\partial_t \widetilde{u}_i + \partial_j \left(\widetilde{\widetilde{u}_i \widetilde{u}_j}\right) + \partial_j \widetilde{a}_{ij} + \partial_i \widetilde{P} = \nu \partial_j \partial_j \widetilde{u}_i \tag{2.2}$$

with $\widetilde{a}_{ij} = \widetilde{u_i u_j} - \widetilde{\widetilde{u}_i \widetilde{u}_j}$ the SGS stress to be modelled. Thus $\widetilde{a}_{ij}$ is the projection of $u_i u_j - \widetilde{u}_i \widetilde{u}_j$, the LES resolved part of "product of complete (DNS) fields minus product of incomplete (LES) fields".

Those for the LES at the coarser level (with $\partial_i \widehat{\widetilde{u}}_i = 0$) are

$$\partial_t \widehat{\widetilde{u}}_i + \partial_j \left(\widehat{\widetilde{\widetilde{u}}_i \widetilde{\widetilde{u}}_j}\right) + \partial_j \widehat{\widetilde{A}}_{ij} + \partial_i \widehat{\widetilde{P}} = \nu \partial_j \partial_j \widehat{\widetilde{u}}_i \tag{2.3}$$

with $\widehat{\widetilde{A}}_{ij} = \widehat{\widetilde{u_i u_j}} - \widehat{\widetilde{\widetilde{u}}_i \widetilde{\widetilde{u}}_j}$ the SGS stress at the test level.

Projection, using $\hat{}$, of the equations for $\widetilde{u}_i$ leads to equations that must be consistent with those for $\widehat{\widetilde{u}}_i$. This provides the Germano's identity:

$$\widehat{\widetilde{A}}_{ij} - \widehat{\widetilde{a}}_{ij} = \widehat{\widetilde{\widetilde{u}_i \widetilde{u}_j}} - \widehat{\widetilde{\widetilde{u}}_i \widetilde{\widetilde{u}}_j} = \widehat{\widetilde{L}}_{ij} \,. \tag{2.4}$$

3. Investigated models

3.1. *Dynamic Smagorinsky model*

We first consider the dynamic Smagorinsky model. The model for the SGS stress is taken as

$$\widetilde{a}_{ij}^M = -2\, C \Delta^2 \widetilde{\left|\widetilde{S}\right|} \widetilde{S}_{ij} \tag{3.1}$$

with $\widetilde{S}_{ij} = (\partial_j \widetilde{u}_i + \partial_i \widetilde{u}_j)/2$ the rate of strain tensor and $\left|\widetilde{S}\right| = \left(2 \widetilde{\widetilde{S}_{kl} \widetilde{S}_{kl}}\right)^{1/2}$. For consistency, the model for the SGS stress at the coarser level is taken as

$$\widehat{\widetilde{A}}_{ij}^M = -2\, C (2\Delta)^2 \widehat{\widetilde{\left|\widetilde{S}\right|} \widetilde{S}}_{ij} \,. \tag{3.2}$$

The dynamic procedure consists in minimizing the error in Germano's identity,

$$\widehat{\widetilde{E}}_{ij} = \widehat{\widetilde{L}}_{ij} - \left(\widehat{\widetilde{A}}_{ij}^M - \widehat{\widetilde{a}}_{ij}^M\right) = \widehat{\widetilde{L}}_{ij} - C\Delta^2 \left(2 \widehat{\widetilde{\left|\widetilde{S}\right|} \widetilde{S}}_{ij} - 8 \widehat{\widetilde{\left|\widetilde{S}\right|} \widetilde{S}}_{ij}\right)$$

$$= \widehat{\widetilde{L}}_{ij} - C\Delta^2 \widehat{\widetilde{Q}}_{ij} \,. \tag{3.3}$$

Minimizing $\langle \widehat{\widetilde{E}}_{ij} \widehat{\widetilde{E}}_{ij} \rangle$ in the least-square sense (where $\langle\ \rangle$ stands for averaging over the homogeneous directions: x and z for the channel flow) leads to

$$(C\Delta^2)(y) = \frac{\langle \widehat{\widetilde{L}}_{ij} \widehat{\widetilde{Q}}_{ij} \rangle}{\langle \widehat{\widetilde{Q}}_{ij} \widehat{\widetilde{Q}}_{ij} \rangle} \,. \tag{3.4}$$

3.2. *Dynamic "Smagorinsky + hyperviscosity" model*

We consider a model which combines viscosity (Smagorinsky) and a fourth-order hyperviscosity. The model for the SGS stress is here taken as

$$\widetilde{a}_{ij}^M = -2\,C\Delta^2 \widetilde{|\widetilde{S}|\widetilde{S}}_{ij} + 2\,D\Delta^4 \widetilde{|\widetilde{S}|\nabla^2 \widetilde{S}}_{ij} \,. \tag{3.5}$$

The model for the SGS stress at the coarser level is thus

$$\widehat{\widetilde{A}}_{ij}^M = -2\,C(2\Delta)^2 \widehat{\widetilde{|\widetilde{S}|\widetilde{S}}}_{ij} + 2\,D(2\Delta)^4 \widehat{\widetilde{|\widetilde{S}|\nabla^2 \widetilde{S}}}_{ij} \,, \tag{3.6}$$

and the error is

$$\begin{aligned} \widehat{\widetilde{E}}_{ij} &= \widehat{\widetilde{L}}_{ij} - C\Delta^2 \left(2 \widehat{\widetilde{|\widetilde{S}|\widetilde{S}}}_{ij} - 8 \widehat{\widetilde{|\widetilde{S}|\widetilde{S}}}_{ij} \right) + D\Delta^4 \left(2 \widehat{\widetilde{|\widetilde{S}|\nabla^2 \widetilde{S}}}_{ij} - 32 \widehat{\widetilde{|\widetilde{S}|\nabla^2 \widetilde{S}}}_{ij} \right) \\ &= \widehat{\widetilde{L}}_{ij} - C\Delta^2 \widehat{\widetilde{Q}}_{ij} + D\Delta^4 \widehat{\widetilde{W}}_{ij} \,. \end{aligned} \tag{3.7}$$

Minimizing the error leads to the following system for determining $C\Delta^2$ and $D\Delta^4$ as function of y:

$$\begin{aligned} \langle \widehat{\widetilde{Q}}_{ij} \widehat{\widetilde{Q}}_{ij} \rangle\, (C\Delta^2) - \langle \widehat{\widetilde{Q}}_{ij} \widehat{\widetilde{W}}_{ij} \rangle\, (D\Delta^4) &= \langle \widehat{\widetilde{L}}_{ij} \widehat{\widetilde{Q}}_{ij} \rangle \\ -\langle \widehat{\widetilde{Q}}_{ij} \widehat{\widetilde{W}}_{ij} \rangle\, (C\Delta^2) + \langle \widehat{\widetilde{W}}_{ij} \widehat{\widetilde{W}}_{ij} \rangle\, (D\Delta^4) &= -\langle \widehat{\widetilde{L}}_{ij} \widehat{\widetilde{W}}_{ij} \rangle \,. \end{aligned} \tag{3.8}$$

3.3. *Dynamic Smagorinsky model using a "small field": a regularized multiscale model*

The model by Hiughes *et al.* (2001a) corresponds to limiting the Smagorinsky model to the small scales. The model has zero effect at large scales, and is an effective viscosity at small scales. In our regularized version of the model (Winckelmans *et al.* (2001a)), we achieve this by applying the dynamic Smagorinsky model to a regularized "small-scales field" obtained as

$$\widetilde{u}_i^s = \widetilde{u}_i - \overline{\widetilde{u}}_i \tag{3.9}$$

with $\overline{\widetilde{u}}_i = \overline{G} * \widetilde{u}$ where $\overline{G}$ is a regular smoothing filter with a Fourier transform that goes to zero at the LES cutoff wavenumber. A convenient second-order filter is the compact discrete filter (thus easily applied in physical space). In one-dimension (1-D) it reads

$$\overline{f}(x) = f(x) + \left(f(x+h) - 2f(x) + f(x-h)\right)/4 = \left(I + \delta^2/4\right) f(x) \,. \tag{3.10}$$

In Fourier space, this gives

$$\overline{\mathcal{G}}(k) = 1 - \frac{1}{2}\left(1 - \cos(kh)\right) = 1 - \sin^2(kh/2) \,. \tag{3.11}$$

In 3-D, it is applied one direction at a time,

$$\overline{\widetilde{u}}_i = \left(I + \delta_x^2/4\right)\left(I + \delta_y^2/4\right)\left(I + \delta_z^2/4\right)\widetilde{u}_i \,, \tag{3.12}$$

so that

$$\widetilde{u}_i^s = \widetilde{u}_i - \left(I + \delta_x^2/4\right)\left(I + \delta_y^2/4\right)\left(I + \delta_z^2/4\right)\widetilde{u}_i \,. \tag{3.13}$$

The model for the SGS stress is thus taken as

$$\widetilde{a}_{ij}^M = -2\,C\Delta^2\,\widetilde{\left|\widetilde{S}\right|\,\widetilde{S}_{ij}^s} \tag{3.14}$$

where $\widetilde{S}_{ij}^s = \left(\partial_j\widetilde{u}_i^s + \partial_i\widetilde{u}_j^s\right)/2$.

Notice that higher-order filters can easily be constructed by iterating the second-order filter, thus still only requiring a stencil-3 wide discrete operation in each direction; see Winckelmans *et al.* (2001a). For instance, the fourth order filter used in Stolz *et al.* (2001),

$$\overline{f}(x) = f(x) + \left(-f(x+2h) + 4f(x+h) - 6f(x) + 4f(x-h) - f(x-2h)\right)/16 \tag{3.15}$$

and

$$\overline{G}(k) = 1 - \left(3 - 4\cos(kh) + \cos(2kh)\right)/8 = 1 - \left(\sin^2(kh/2)\right)^2 \tag{3.16}$$

is also obtainable from

$$\overline{f}(x) = \left(I - \left(-\delta^2/4\right)^2\right) f(x) \,. \tag{3.17}$$

Equivalently, a filter of order $2n$ is obtained from:

$$\overline{f}(x) = \left(I - \left(-\delta^2/4\right)^n\right) f(x) \,, \tag{3.18}$$

leading to

$$\overline{G}(k) = 1 - \left(\sin^2(kh/2)\right)^n \,. \tag{3.19}$$

3.4. *Dynamic Smagorinsky model using an "enhanced field"*

Another view is to consider a model that is viscosity-like at large scales and more effective at small scales. This is easily done by using the dynamic Smagorinsky model applied to an artificial "enhanced field", see Winckelmans *et al.* (2001a). In the present implementation, $\widetilde{u}_i$ is replaced by

$$\widetilde{u}_i^e = \left[I + (I - \overline{G})\right] * \widetilde{u}_i = 2\widetilde{u}_i - \overline{\widetilde{u}}_i \,. \tag{3.20}$$

The model for the SGS stress is thus

$$\widetilde{a}_{ij}^M = -2\,C\Delta^2\,\widetilde{\left|\widetilde{S}\right|\,\widetilde{S}_{ij}^e} \tag{3.21}$$

where $\widetilde{S}_{ij}^e = \left(\partial_j\widetilde{u}_i^e + \partial_i\widetilde{u}_j^e\right)/2$. Again, we here use the discrete filter, leading to

$$\widetilde{u}_i^e = 2\widetilde{u}_i - \left(I + \delta_x^2/4\right)\left(I + \delta_y^2/4\right)\left(I + \delta_z^2/4\right)\widetilde{u}_i \,. \tag{3.22}$$

Clearly, the model essentially behaves as a a fourth-order hyperviscosity at the small scales.

4. Results

The turbulent channel flow at $\mathrm{Re}_\tau = 395$ was investigated, with the different SGS models but using the same LES code (thus allowing for self-consistent comparisons between the models). The reference DNS is that of Moser *et al.* (1999). The code is based

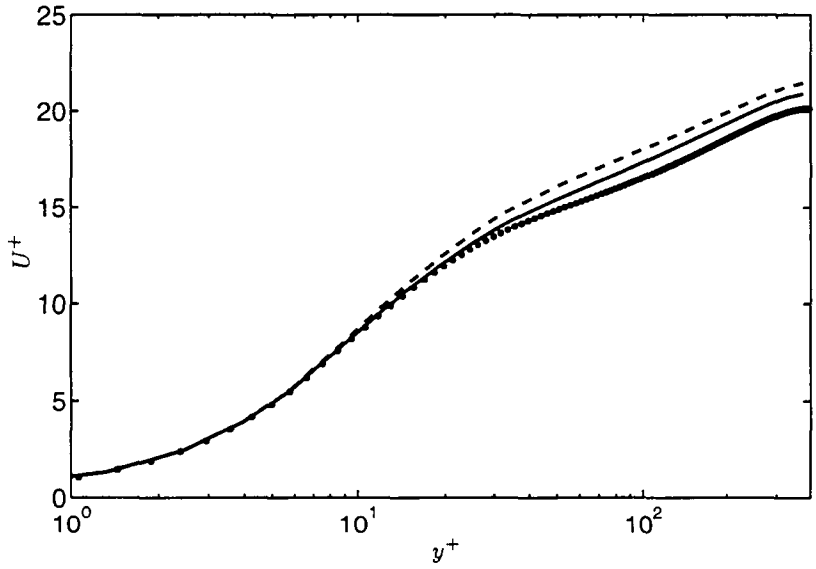

FIGURE 1. Mean velocity: dynamic Smagorinsky model without (solid) and with sampling + interpolation in y (dash); DNS data (solid circles).

on a pseudo-spectral method in the streamwise, x, and spanwise, z, directions, and on fourth-order spectral-like compact finite differences in the wall-normal direction, y. The flow is driven by a constant mean pressure gradient. A semi-implicit second order time integration scheme is used. The grid is stretched in y using a hyperbolic tangent function with a stretching factor of 2.75. The grid resolution is set to (64x49x48) giving, after de-aliasing, a resolved grid of (42x49x32). Preliminary runs were carried out with a grid of (72x37x54) points, but the resolution in the wall-normal direction proved to be too small to correctly capture the mean-velocity profile in the transition region. The x and z resolutions were here also adapted to join in an effort of comparisons between different codes on this particular flow, in collaboration with J. Gullbrand and F. K. Chow (whose work is reported elsewhere in this volume).

4.1. *Projection test operator in y*

The dynamic procedure with a sampling procedure in y at the test level is more consistent with the similarity hypothesis between the models at the LES grid and test levels. Better results were thus expected. However, the results were worse for all models when the sampling procedure in y was applied.

The results for the case of the dynamic Smagorinsky model are shown in figures 1 and 2. Both the mean velocity profile and the rms velocities are closer to the DNS data when no "sampling + interpolation" is applied in y as part of the test projection operation. This conclusion is also valid for the results obtained with the other models (not shown here).

Those results have two consequences. The first one is the ineffectiveness of the sampling + interpolation procedure as a substitute to a true coarser discretization at the test level. The interpolation applied to maintain the information datn all LES grid points creates spurious information at high wavenumbers instead of preserving the cutoff effect of the sampling procedure. This has a negative impact on the dynamic determination

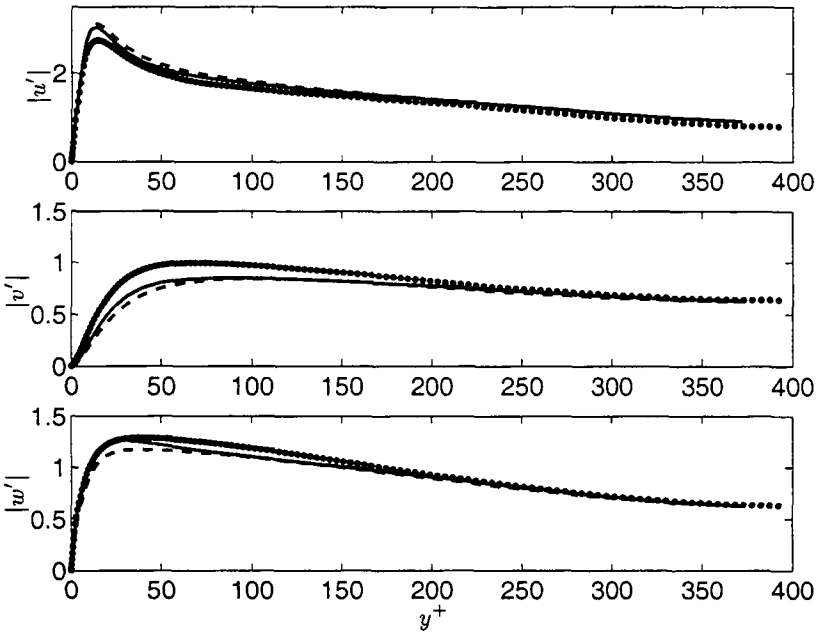

FIGURE 2. rms velocities: dynamic Smagorinsky model without (solid) and with sampling + interpolation in y (dash); DNS data (solid circles).

of the model coefficient(s), and hence on the results obtained. One way to avoid this interpolation issue would be to use sampling only, and thus to evaluate the dynamic coefficient on the test-filtered (twice coarser) grid only. One would then interpolate the dynamic coefficient back to the LES grid. This requires the definition of all the operators (derivatives, products, etc.) at both the LES and test grid levels, and was not considered in the present work (due to lack of time). The second consequence is the relatively small impact of the two dynamic implementations on the mean results. The impact on the value of the dynamic coefficient is however higher, with a maximal difference of roughly 60% in the center of the channel.

The following results all correspond to a dynamic procedure without sampling + interpolation in the wall-normal direction.

4.2. *Comparison of the models*

The mean velocity profiles obtained with the different models are presented in figures 3 and 4. The regularized version of the Hughes *et al.* model performs best. See also the good results reported in Hughes *et al.* (2001b) for decaying isotropic turbulence, and in Hiughes *et al.* (2001a) for channel flow. This conclusion is however slightly contradictory to the results obtained for more challenging (coarser grid) runs for decaying isotropic turbulence in Winckelmans *et al.* (2001a). In that case, the lack of model dissipation at the large scales was more crucial.

The results obtained with the dynamic model Smagorinsky + hyperviscosity are encouraging: the dynamic procedure was indeed successful in determining the two dynamic coefficients. They are however also disappointing: the results are no better than those obtained using the dynamic Smagorinsky model alone. This is explained by the close correspondence between the dynamic coefficients obtained for the Smagorinsky term. The

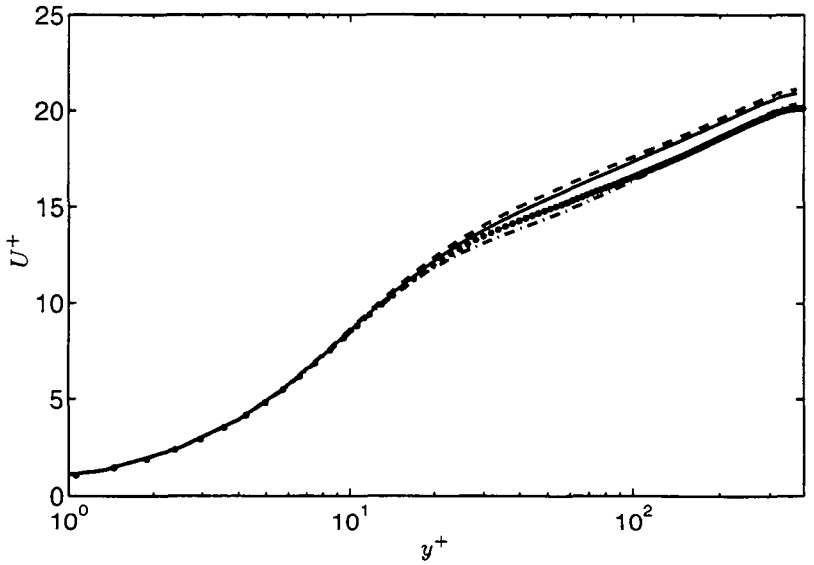

FIGURE 3. Mean velocity: dynamic Smagorinsky model (solid); dynamic Smagorinsky + hyperviscosity model (dash); regularized version of Hughes model (chained dot); DNS data (solid circles).

coefficients are similar up to $y^+ \approx 100$. The coefficient $(C\Delta^2)$ for the Smagorinky model alone goes up to 1.0×10^{-4} in the center region, while it goes to 0.6×10^{-4} with the added hyperviscosity term. This lower value is compensated by the dissipation of the hyperviscosity term, leading to nearly identical results for the mean velocity profiles.

Better results are obtained when using the Smagorinsky model applied to the artificially enhanced velocity field, see figure 4.

The conclusions drawn from the mean-velocity profiles are also valid for the rms velocities, see figures 5 and 6. The regularized Hughes model performs best. It correctly reproduces the streamwise and normal rms velocities, yet it produces an overshoot of the maximum near-wall value for the spanwise component. Similar behavior is reported by Hughes *et al.* (2001b). The results for the Smagorinsky model and the Smagorinsky + hyperviscosity model are essentially the same. Finally, the results for the Smagorinsky model applied to an enhanced field are also quite good: this new model is promising.

However, the comparison of the rms velocities from the DNS with those calculated from the LES (including the LES model contribution) is not entirely valid. Indeed, since the SGS models, $\widetilde{a}_{ij}^M$, used here have a zero trace, one can only reconstruct, and thus fairly compare with DNS, the deviatoric part of the Reynolds stress tensor, see Winckelmans *et al.* (2002). Recall also that the trace of the Reynolds stress tensor is the DNS turbulent kinetic energy, which is different from the resolved LES turbulent kinetic energy. The fair comparison, on the deviatoric components, consists in comparing $R_{ij}^{DNS^*}$ (where * means the reduced (traceless) part of the tensor) to $R_{ij}^{LES^*} - \langle \widetilde{a}_{ij}^M \rangle$. The comparison on the diagonal components (the "reduced turbulence intensities"), is presented in figure 7. The previously drawn conclusions remain unchanged. This is so because, in the present case, the resolved LES turbulent kinetic energy is still close to the DNS turbulent kinetic energy.

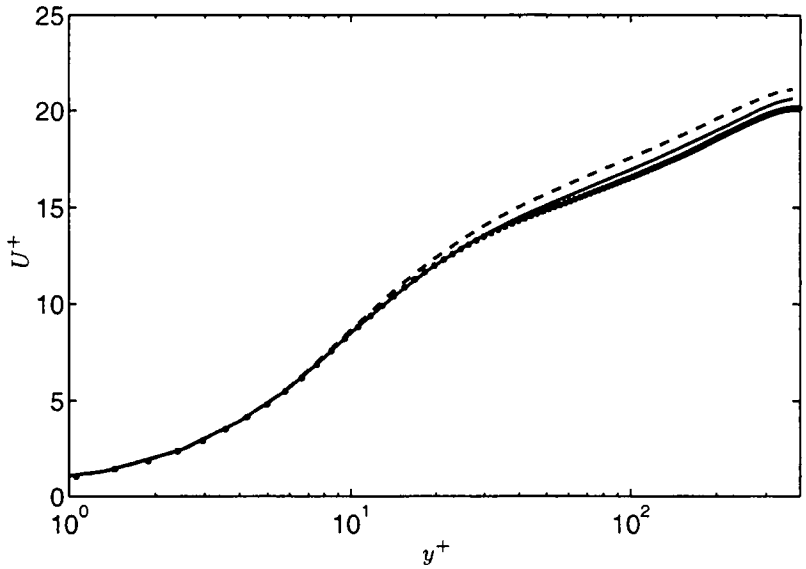

FIGURE 4. Mean velocity: dynamic Smagorisnky model applied to enhanced velocity field (solid); dynamic Smagorinsky + hyperviscosity model (dash); DNS data (solid circles).

5. Conclusions

The assessment of some recent LES models carried out for decaying isotropic turbulence was here extended to channel flow at $\mathrm{Re}_\tau = 395$.

Three models were investigated in addition to the Smagorinsky model: a regularized version of the model by Hughes *et al.*, a Smagorinsky + hyperviscosity model, and a Smagorinsky model acting on an artificially enhanced velocity field. A dynamic version of each model was developed and implemented.

A particular implementation of the dynamic procedure was also considered, where "sampling followed by interpolation" is applied as a test projection in the wall-normal direction (in addition to the usual test projection in the homogeneous directions using the sharp cutoff in spectral space). No improvement in the results was obtained. It was argued that the interpolation creates spurious information at high wavenumbers on top of the cutoff effect achieved by the sampling. Another method that avoids the interpolation part was proposed (not tested yet).

Significant improvements in the profiles of mean velocity, rms velocities, and reduced turbulence intensities, as compared to the Smagorinsky model, are obtained when using the model of Hughes et al., and when using the Smagorinsky model acting on an artificially enhanced velocity field. The results obtained using the Smagorinsky + hyperviscosity model are somewhat disappointing as no clear benefit is seen on the mean profiles. The benefit of this model could possibly lie in better agreement with DNS data on other quantities (such as two-point correlations and spectra). This deserves further investigation.

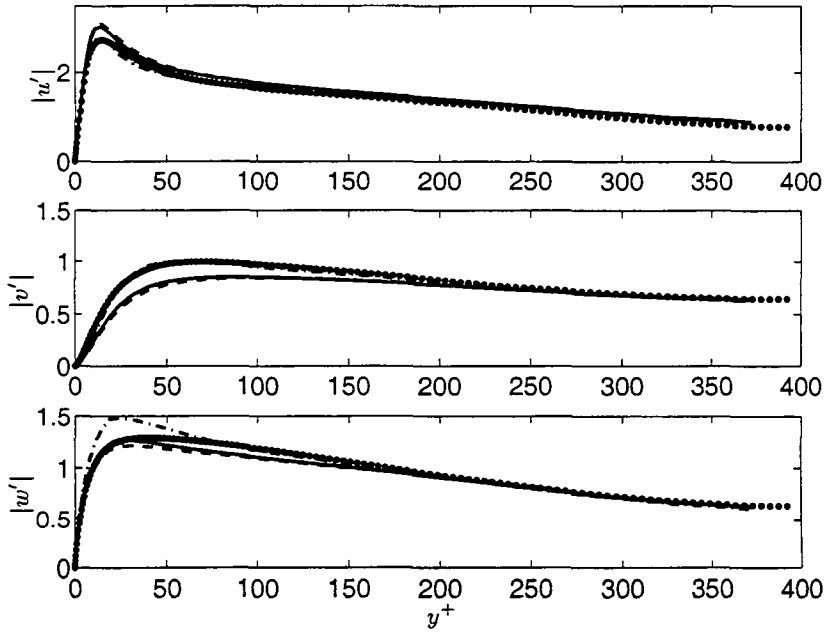

FIGURE 5. rms velocities: dynamic Smagorinsky model (solid); dynamic Smagorinsky + hyperviscosity model (dash); regularized version of Hughes model (chained dot); DNS data (solid circles).

Acknowledgments

Thanks are extended to Dr. J. Gullbrand and F. K. Chow who contributed to this work through many useful discussions (see also their paper elsewhere in this volume). Thanks are also due to Prof. J. Ferziger for his input and encouragement concerning the dynamic model "Smagorinsky + hyperviscosity", and to Prof. R. Street for useful discussions about explicit filtering in LES.

REFERENCES

CARATI, D., WINCKELMANS, G. S. & JEANMART, H. 2001 On the modelling of the subgrid-scale and filtered-scale stress tensors in large-eddy simulation. *J. Fluid Mech.* **441**, 119–138.

GERMANO, M., PIOMELLI, U., MOIN, P. & CABOT, W. 1991 A dynamic subgrid-scale eddy-viscosity model. *Phys. Fluids A* **3**, 1760–1765.

GHOSAL, S., LUND, T. S. & MOIN, P. 1992 A local dynamic model for large-eddy simulation. *Annual Research Briefs*, Center for Turbulence Research, NASA Ames/Stanford Univ., 3–25.

GHOSAL, S., LUND, T. S., MOIN, P. & AKSELVOLL, K. 1995 A dynamic localization model for large-eddy simulation of turbulent flows. *J. Fluid Mech.* **286**, 229–255.

HUGHES, T. J. R., MAZZEI, L., OBERAI, A. A. & WRAY, A. A. 2001a The multiscale formulation of large eddy simulation: Decay of homogeneous isotropic turbulence. *Phys. Fluids* **13**, 505–512.

HUGHES, T. J. R., OBERAI, A. A. & MAZZEI, L. 2001b Large eddy simulation of

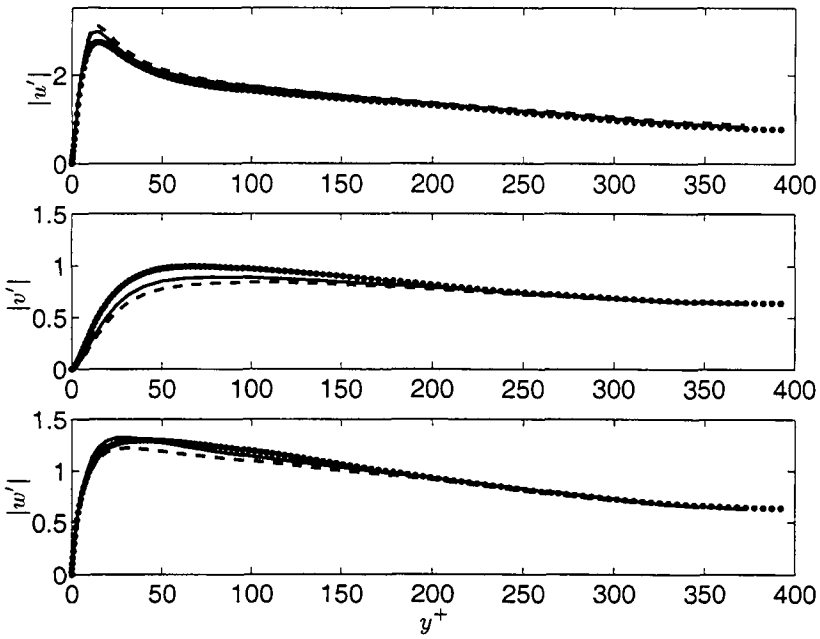

FIGURE 6. rms velocities: dynamic Smagorinsky model applied to an enhanced velocity field (solid); dynamic Smagorinsky + hyperviscosity model (dash); DNS data (solid circles).

turbulent channel flow by the variational multiscale method. *Phys. Fluids* **13**, 1784–1799.

MÉTAIS, O. & LESIEUR, M. 1992 Spectral large-eddy simulation of isotropic and stably stratified turbulence. *J. Fluid Mech.* **239**, 157–194.

MOSER, R. D., KIM, J. & MANSOUR, N. N. 1999 Direct numerical simulation of turbulent channel flow up to $\mathrm{Re}_\tau = 590$. *Phys. Fluids* **11**, 943–945.

SMAGORINSKY, J. 1963 General circulation experiments with the primitive equations. *Mon. Weather Rev.* **91**, 99–164.

STOLZ, S. & ADAMS, N. A. 1999 An approximate deconvolution procedure for large-eddy simulation. *Phys. Fluids* **11**, 1699–1701.

STOLZ, S., ADAMS, N. A. & KLEISER, L. 2001 An approximate deconvolution model for large-eddy simulation with application to incompressible wall-bounded flows. *Phys. Fluids* **13**, 997–1015.

WINCKELMANS, G. S., WRAY, A. A., VASILYEV, O. V. & JEANMART, H. 2001 Explicit-filtering large-eddy simulation using the tensor-diffusivity model supplemented by a dynamic Smagorinsky term. *Phys. Fluids* **13**, 1385-1403.

WINCKELMANS, G. S. & JEANMART, H. 2001 Assessment of some models for LES without and with explicit filtering. *Direct and Large-Eddy Simulation IV*(B.J. Geurts, R. Friedrich and O. Métais, eds.), ERCOFTAC Series **8**, Kluwer, pp. 55–66.

WINCKELMANS, G. S., CARATI, D, & JEANMART, H. 2002 On the comparison of turbulence intensities from large-eddy simulation with those from experiment or direct numerical simulation, Brief Comm., *Phys. Fluids* **14**, 1809-1811.

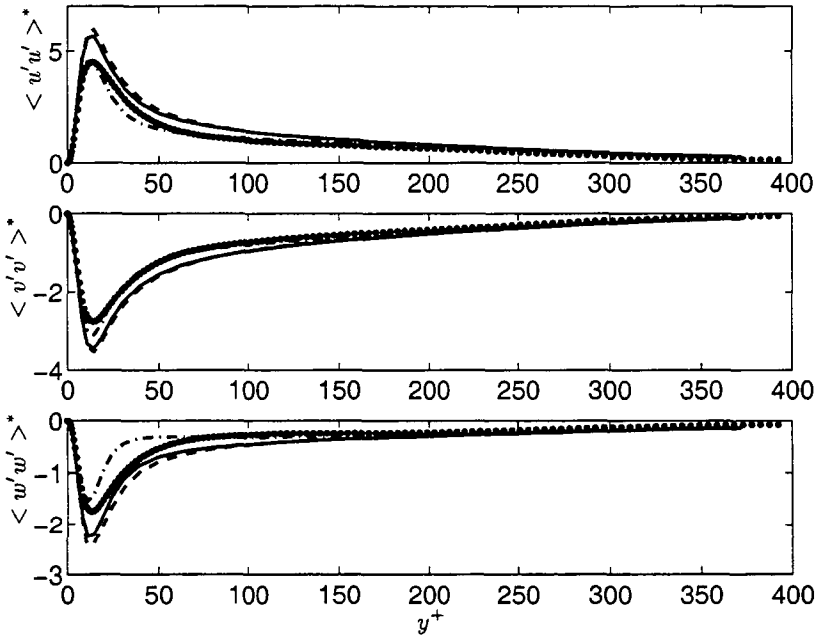

FIGURE 7. Reduced turbulence intensities: dynamic Smagorinsky model (solid); dynamic Smagorinsky + hyperviscosity model (dash); regularized version of Hughes model (chained dot); DNS data (solid circles).

Tools for large-eddy simulation

By David A. Caughey † AND Giridhar Jothiprasad †

A computer code has been developed for solving the incompressible Navier-Stokes equations for test flows that will allow the comparison of various strategies for assessing the accuracy of LES solutions for flows at large Reynolds number, where it is impractical to make direct comparisons with DNS solutions for the same flow. The code includes options for a conventional Smagorinsky subgrid model, as well as hyperviscosity dissipative terms that will allow a greater separation of scales for high Reynolds number flows. In this report, the code is validated for several simple, periodic flows, including the Taylor-Green vortex and decaying isotropic turbulence, and preliminary results are presented, showing good agreement for (forced, periodic) Kolmogorov flow in the limit of high Reynolds number, on relatively modest meshes using the hyperviscosity dissipation.

1. Introduction

Large Eddy Simulation (LES) holds the promise of improved prediction of turbulent flows at large Reynolds numbers relative to computations using the Reynolds-averaged equations, with substantially less computational cost than that required for Direct Numerical Simulation (DNS) since only the largest, most energetic, scales need to be resolved. Nevertheless, the computational resources required for LES computations for all but the simplest flows remain substantial. The required resources are so great, in fact, that most LES computations are performed at the limits of available resources, and it usually is not clear to what extent the solutions are resolved. Furthermore, since the accuracy of the computation is not assessed in any systematic way, the most frequently used metric for the performance of LES is comparison with DNS computations which, as a result of the computational resources required for DNS, necessarily limits these assessments to flows at relatively low Reynolds numbers.

In order for LES to become useful for practical engineering problems, tools must be developed that allow one to estimate the accuracy of the LES solution without having to make a direct comparison with a DNS solution for the same flow. The availability of such tools would free one from the need to make comparisons only at low Reynolds numbers where DNS solutions are feasible, and permit the evaluation of LES at the larger Reynolds numbers for which LES is most attractive, and where the separation between the energetic and dissipative scales is large enough that the LES approach has some theoretical basis.

The long-term objective of the authors' work is to develop tools suitable for assessing the accuracy of LES solutions, especially for flows at large Reynolds number. As a first step in this process, the authors have developed a computer code for solving the incompressible Navier-Stokes equations, including additional hyperviscosity dissipation, for test flows that will allow the comparison of various accuracy-assessment strategies. The incorporation of hyperviscosity dissipation (based on the biharmonic of the velocity field) is motivated by the desire to increase the separation of the energetic and dissipative

† Cornell University

scales, so that the high Reynolds number limit of solutions can be studied on meshes of relatively modest resolution.

In this report, validations of the code are presented for several simple, periodic flows, including the Taylor-Green vortex and decaying, isotropic turbulence, and preliminary results show good agreement for (forced, periodic) Kolmogorov flow in the limit of high Reynolds number, on relatively modest meshes using the hyperviscosity dissipation.

2. Algorithm

In this section we describe a variant of the fractional-step method (Chorin (1968), Temam (1969), Kim & Moin (1985)) used for the time-advancement of the incompressible Navier-Stokes equations with a Smagorinsky model and added hyperviscosity dissipation.

The constant-density Navier-Stokes equations, with an added hyperviscosity, and the continuity equation

$$\frac{\partial u_i}{\partial t} + \frac{\partial (u_i u_j)}{\partial x_j} = -\frac{\partial p}{\partial x_i} + (\nu + \nu_r)\frac{\partial^2 u_i}{\partial x_j \partial x_j} + \nu_4 \frac{\partial^4 u_i}{\partial x_j \partial x_j \partial x_l \partial x_l} \tag{2.1}$$

$$\frac{\partial u_i}{\partial x_i} = 0 \tag{2.2}$$

are discretized on a staggered grid. Velocities u_i are defined at the centers of cell faces having normals in the direction x_i, and the pressure is defined at the cell center. The equations are marched in time using an explicit approximation for the convective terms and an iterative Alternating Direction Implicit (ADI) scheme for the viscous (and hyperviscous) terms. Such a fractional-step time-advancement scheme for (2.1) and (2.2) can be written as

$$\frac{\hat{u}_i - u_i^n}{\Delta t} + \left[\frac{3}{2}H_i\left\{\mathbf{u^n}\right\} - \frac{1}{2}H_i\left\{\mathbf{u^{n-1}}\right\}\right] + G_i\left\{\phi^n\right\} = \frac{\nu + \nu_r}{2}\left[D_2\left\{\hat{u}_i\right\} + D_2\left\{u_i^n\right\}\right] + \frac{\nu_4}{2}\left[D_4\left\{\hat{u}_i\right\} + D_4\left\{u_i^n\right\}\right] \tag{2.3}$$

$$\frac{u_i^{n+1} - \hat{u}_i}{\Delta t} = -G_i\left\{\delta\phi^{n+1}\right\}, \tag{2.4}$$

with

$$C\left\{\mathbf{u^{n+1}}\right\} = 0 \tag{2.5}$$

$$\phi^{n+1} = \phi^n + \delta\phi^{n+1} \tag{2.6}$$

where

$$H_i\left\{\mathbf{u}\right\} \equiv \text{Spatial discretization of } \frac{\partial (u_i u_j)}{\partial x_j}$$

$$G_i\left\{\phi\right\} \equiv \text{Spatial discretization of } \frac{\partial \phi}{\partial x_i}$$

$$D_2\left\{u_i\right\} \equiv \text{Spatial discretization of } \frac{\partial^2 u_i}{\partial x_j \partial x_j}$$

$$D_4\left\{u_i\right\} \equiv \text{Spatial discretization of } \frac{\partial^4 u_i}{\partial x_j \partial x_j \partial x_l \partial x_l}$$

$$C\left\{\mathbf{u}\right\} \equiv \text{Spatial discretization of } \frac{\partial u_i}{\partial x_i}.$$

The convective terms $H_i\{\}$ are discretized to fourth-order spatial accuracy using central differences, and the time advancement is carried out using a second-order Adams-Bashforth approximation for the convective terms. The spatial discretization of the convective terms is designed to be energy conserving (Morinishi & Moin (1998)) in order to achieve explicit control over the dissipation introduced in the numerical scheme. The viscous diffusion terms $D_2\{\}$ are discretized to fourth order spatial accuracy, while the hyperviscous terms $D_4\{\}$ are discretized to second order spatial accuracy, both using central differences. These two terms are advanced in time using an iterative ADI scheme. It should be noted that ϕ differs from the pressure by an $O(\Delta t)$ term (Kim & Moin (1985)).

The scheme has been implemented for periodic boundary conditions on a uniform grid. Equation (2.5) can be used to eliminate u_i^{n+1} from the divergence of (2.4), giving a Poisson equation for $\delta\phi^{n+1}$

$$C\left\{\mathbf{G}\left\{\delta\phi^{n+1}\right\}\right\} = -\frac{C\{\hat{\mathbf{u}}\}}{\Delta t} \tag{2.7}$$

Further details of the spatial discretization can be found in Morinishi & Moin (1998).

The implicit equations arising at each time step are solved using an iterative ADI scheme. We first define a splitting of the operators $D_2\{\}$ and $D_4\{\}$ into differences in the x_1, x_2 and x_3 directions and cross derivatives as follows,

$$\begin{aligned}
D_2\{u_i\} &= D_{2_{x_1}}\{u_i\} + D_{2_{x_2}}\{u_i\} + D_{2_{x_3}}\{u_i\} \\
D_{2_{x_j}}\{u_i\} &\equiv \text{Spatial discretization of } \frac{\partial^2 u_i}{\partial x_j^2} \\
D_4\{u_i\} &= D_{4_{x_1}}\{u_i\} + D_{4_{x_2}}\{u_i\} + D_{4_{x_3}}\{u_i\} + D_{4_{\text{cross}}}\{u_i\} \\
D_{4_{x_j}}\{u_i\} &\equiv \text{Spatial discretization of } \frac{\partial^4 u_i}{\partial x_j^4} \\
D_{4_{\text{cross}}}\{u_i\} &\equiv \text{Spatial discretization of } 2\left[\frac{\partial^4 u_i}{\partial x_1^2 \partial x_2^2} + \frac{\partial^4 u_i}{\partial x_2^2 \partial x_3^2} + \frac{\partial^4 u_i}{\partial x_3^2 \partial x_1^2}\right].
\end{aligned}$$

Let $\hat{u}_i^{[m]}$ denote the approximation to $\hat{u}_i$ at the m^{th} iteration. Equation (2.3) can be rewritten as

$$\begin{aligned}
\frac{\hat{u}_i^{[m+1]}}{\Delta t} + \left\langle \frac{-u_i^n}{\Delta t} \right\rangle = &\left\langle \frac{3}{2} H_i\{\mathbf{u^n}\} - \frac{1}{2} H_i\{\mathbf{u^{n-1}}\} - G_i\{\phi^n\} \right\rangle + \\
&\frac{\nu+\nu_r}{2} D_2\left\{\hat{u}_i^{[m+1]}\right\} + \left\langle \frac{\nu+\nu_r}{2} D_2\{u_i^n\} \right\rangle + \\
&\frac{\nu_4}{2}\left[D_{4_{x_1}}\left\{\hat{u}_i^{[m+1]}\right\} + D_{4_{x_2}}\left\{\hat{u}_i^{[m+1]}\right\} + D_{4_{x_3}}\left\{\hat{u}_i^{[m+1]}\right\}\right] + \\
&\frac{\nu_4}{2} D_{4_{\text{cross}}}\left\{\hat{u}_i^{[m]}\right\} + \left\langle \frac{\nu_4}{2} D_4\{u_i^n\} \right\rangle
\end{aligned} \tag{2.8}$$

The terms within angle braces do not change with iteration m, and can be grouped

together to form the source term

$$S_i\{\mathbf{u^n},\mathbf{u^{n-1}}\} \equiv \frac{u_i^n}{\Delta t} + \frac{3}{2}H_i\{\mathbf{u^n}\} - \frac{1}{2}H_i\{\mathbf{u^{n-1}}\} - G_i\{\phi^n\} + \frac{\nu+\nu_r}{2}D_2\{u_i^n\} + \frac{\nu_4}{2}D_4\{u_i^n\} \tag{2.9}$$

Equation 2.8 then reduces to

$$\left(\frac{1}{\Delta t} - \frac{\nu+\nu_r}{2}\left[D_{2_{x_1}} + D_{2_{x_2}} + D_{2_{x_3}}\right] - \frac{\nu_4}{2}\left[D_{4_{x_1}} + D_{4_{x_2}} + D_{4_{x_3}}\right]\right)\left\{\hat{u}_i^{[m+1]} - \hat{u}_i^{[m]}\right\} \tag{2.10}$$

$$= S_i\{\mathbf{u^n},\mathbf{u^{n-1}}\} + \frac{-\hat{u}_i^{[m]}}{\Delta t} + \frac{\nu+\nu_r}{2}D_2\left\{\hat{u}_i^{[m]}\right\} + \frac{\nu_4}{2}D_4\left\{\hat{u}_i^{[m]}\right\}$$

$$\equiv R_i\left\{\hat{u}_i^{[m]},\mathbf{u^n},\mathbf{u^{n-1}}\right\}$$

It is easily seen that the right-hand side of (2.10) is simply the residual evaluated at $\hat{u}_i^{[m]}$. Multiplying (2.10) by Δt and approximating the left-hand side using ADI gives

$$\left(1 - \frac{\Delta t}{2}\left[(\nu+\nu_r)D_{2_{x_1}} + \nu_4 D_{4_{x_1}}\right]\right)\left(1 - \frac{\Delta t}{2}\left[(\nu+\nu_r)D_{2_{x_2}} + \nu_4 D_{4_{x_2}}\right]\right)\cdot$$
$$\left(1 - \frac{\Delta t}{2}\left[(\nu+\nu_r)D_{2_{x_3}} + \nu_4 D_{4_{x_3}}\right]\right)\left\{\hat{u}_i^{[m+1]} - \hat{u}_i^{[m]}\right\} = \Delta t R_i\left\{\hat{u}_i^{[m]},\mathbf{u^n},\mathbf{u^{n-1}}\right\} \tag{2.11}$$

Equation (2.11) requires inversions only of tridiagonal matrices, as opposed to the large sparse matrices required in (2.10). When the coefficients ν_r and ν_4 vary spatially, the left-hand side of Eq. 2.11 is further approximated by replacing the coefficients with their corresponding spatial averages, while the right-hand side is computed exactly. It has been found by numerical experimentation that three iterations are usually sufficient to reduce the residual by at least four orders of magnitude.

3. Results

Here we present results of several flows to validate the computer code described in the preceding section, and preliminary results to show its promise for computing flows at high Reynolds number. All flows considered here are periodic and are solved in a three-dimensional periodic box of edge size 2π.

3.1. *Code validation*

The periodic two-dimensional vortex problem was used extensively to validate the spatial and temporal accuracy of the code. The initial conditions for a periodic vortical flow in the x_1-x_2 plane are given by

$$\begin{aligned} u_1 &= -\cos x_1 \sin x_2\,, \\ u_2 &= \cos x_2 \sin x_1\,, \\ u_3 &= 0\,. \end{aligned} \tag{3.1}$$

The numerical solutions obtained are compared with the known analytical solutions. In order to completely validate the difference coding for all 3 directions, solutions for a

periodic vortex in the x_2–x_3 plane also were computed. Although the test problem has some symmetries, any serious error in the code could have been detected using this test case.

Mesh refinement studies were used to verify the spatial order of accuracy, which was confirmed to be fourth-order for the Navier-Stokes equations (i.e., without the hyperviscosity dissipation) and second order when the hyperviscosity terms are included. Similarly, the temporal order of accuracy was verified to be second order.

3.2. *Taylor-Green Vortex*

Next, the code was used to carry out a DNS of the Taylor-Green vortex flow (Brachet et al. (1983)). This flow is one of the simplest systems in which one can study the generation of small scales and the turbulence resulting from three-dimensional vortex stretching. The initial conditions for the Taylor-Green vortex flow are

$$\begin{aligned} u_1 &= \frac{2}{\sqrt{3}} \sin\left(\frac{2\pi}{3}\right) \sin x_1 \cos x_2 \cos x_3 \,, \\ u_2 &= -\frac{2}{\sqrt{3}} \sin\left(\frac{2\pi}{3}\right) \cos x_1 \sin x_2 \cos x_3 \,, \\ u_3 &= 0 \,. \end{aligned} \tag{3.2}$$

The Reynolds number for this flow is defined as $\mathbf{Re} \equiv 1/\nu$. The DNS of the Taylor-Green flow was carried out on a 64^3 mesh for $\mathbf{Re} = 100$, 200, 300 and 400. Since the smallest scales generated in the $\mathbf{Re} = 400$ simulation were not resolved on this mesh, the DNS was repeated on a 128^3 mesh. All computations were performed at a constant Courant number $C = 0.5$.

The time histories of the dissipation rate are compared with results of the fully-resolved spectral computations of Jeanmart (2002) in figure 1. The figure shows that the time history of the dissipation rate is well predicted in our 64^3 simulations for the lower Reynolds numbers, but that there are discrepancies between the present results on the 64^3 mesh and the reference computations in the vicinity of the maximum dissipation for the computation at $\mathbf{Re} = 400$; however, the present results agree well with the reference computation when repeated on the 128^3 mesh.

3.3. *Decaying, isotropic turbulence*

The case of decaying, isotropic turbulence allows comparison of results computed with various subgrid-scale models to those of fully-resolved DNS computations for modest Reynolds numbers. Two different subgrid-scale models were compared:

(*a*) ***Smagorinsky model***: An eddy-viscosity model of the form,

$$\nu_r = (C_r \Delta)^2 \, (S_{ij} S_{ij})^{\frac{1}{2}} \tag{3.3}$$

where S_{ij} is the local rate-of-strain tensor, Δ is the mesh spacing, and the Smagorinsky coefficient is taken to be $C_r = 0.17$, following Lilly's analysis (Lilly (1967)).

(*b*) ***Smagorinsky-type hyperviscosity model***: A hyperviscosity model of the form,

$$\nu_4 = (C_4 \Delta)^4 \, (S_{ij} S_{ij})^{\frac{1}{2}} \tag{3.4}$$

where S_{ij} is the again the local rate-of-strain tensor, Δ is the mesh spacing, and the (dimensionless) constant $C_4 \approx 0.278$ is chosen such that the flow is fully resolved on the given grid. (Note: it is clear from Eq. (2.1) that the dimensions of ν_4 are length^4/time.)

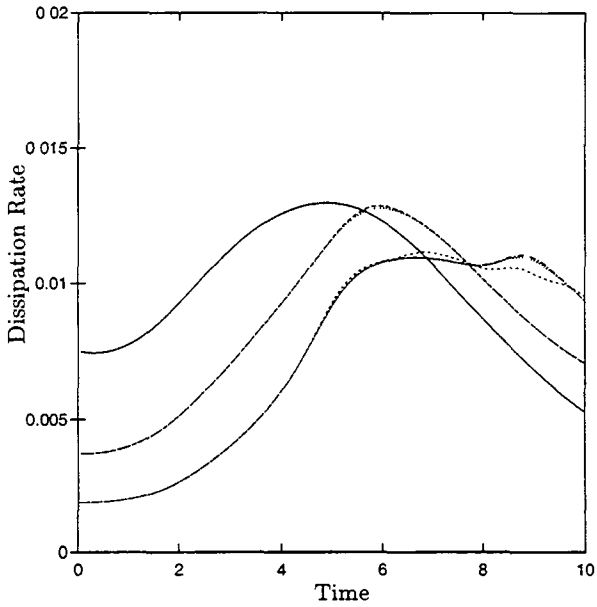

FIGURE 1. History of dissipation rate for Taylor-Green flow at various Reynolds numbers. **Re** = 100: solid line; **Re** = 200: broken line; **Re** = 400: 64^3 grid is dashed line, 128^3 grid is dash-dotted line. Comparison with spectral computations of Jeanmart, shown as dotted lines; dotted lines are invisible when overplotted with current results.

Large-eddy simulations (LES) of decaying, isotropic turbulence were performed on a 64^3 grid using both these models. An under-resolved DNS was also carried out on the 64^3 mesh. The initial conditions were provided by Alan Wray from a 256^3 spectral simulation of forced, isotropic turbulence (Wray 2002). The initial spectral field was first truncated to 64^3 spectral modes and then appropriately transformed to physical space to be used as initial conditions on the 64^3 staggered mesh. The results of the LES were compared with a direct spectral simulation for decaying turbulence carried out by Wray with the full 256^3 spectral modes, using the same initial condition. Figure 2 compares the time history of the turbulence kinetic energy for the various computations. For the purposes of this comparison, only the kinetic energy in the first 64^3 modes of Wray's full DNS are plotted. The figure shows that the results obtained using the Smagorinsky-type hyperviscosity model agree best with results of the full 256^3 simulation.

Figure 3 compares the energy spectra from the three different computations at a relatively early time in the computations. It is seen that in the case where there was no subgrid-scale model there is an accumulation of energy at the higher wavenumbers, since the physical viscosity is unable to remove energy from the small scales at a sufficiently fast rate. It is also seen that the two computations using subgrid-scale models were well resolved on the 64^3 mesh.

3.4. *Kolmogorov flow*

Kolmogorov flow is an open flow in a periodic box, driven by a large-scale steady forcing in the x_1-direction given by,

$$f_1 = -F \sin(\kappa_f x_2); \qquad \kappa_f = 1; \qquad F = 0.16 \tag{3.5}$$

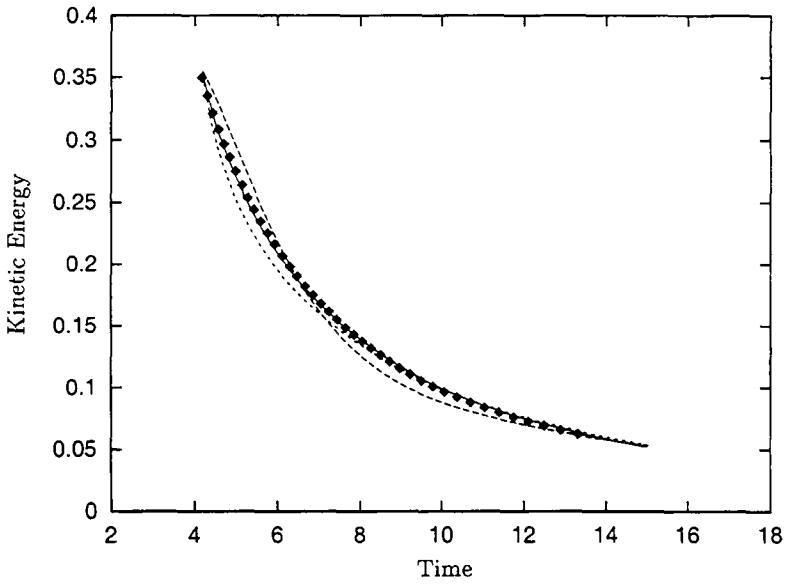

FIGURE 2. History of the kinetic energy decay for isotropic turbulence. LES computation using: no subgrid model (dotted line); Smagorinsky model (dashed line); and Smagorinsky type hyperviscosity model (solid line) carried out on a 64^3 grid. Reference DNS computation by Wray using 256^3 spectral modes (♦).

The high-Reynolds-number limit of this flow has been studied by Borue & Orszag (1996) and Shebalin & Woodruff (1997). Breaking of the symmetries imposed by the forcing has been studied by Jeanmart, Carati & Wincklemans (2002) (2002) in computations using box sizes larger than the period of the forcing.

In order effectively to increase the extent of the inertial range, we use only hyperviscous dissipation. Since the Kolmogorov flow is characterized by the amplitude of the force F, the spatial frequency of the forcing function κ_f, and the hyperviscosity ν_4, we define the following velocity and time scales and a Reynolds number based on the hyperviscosity (Borue & Orszag (1996)).

$$U_0 = 2.5\left(\frac{F}{\kappa_f}\right)^{0.5} \tag{3.6}$$

$$t_0 = \frac{1}{(F\kappa_f)^{0.5}} \tag{3.7}$$

$$\mathbf{Re} = \frac{U_0}{\kappa_f^3 \nu_4} \tag{3.8}$$

This flow is a good test case for the following reasons:

(*a*) The flow has a statistically stationary state.

(*b*) The flow is believed to have a well-defined high Reynolds number limit (Borue & Orszag (1996)), for which the turbulent intensities, energy dissipation rates, and various terms in the energy balance equations have a simple coordinate dependence, $a+b\cos 2x_2$. This makes Kolmogorov flow a good model to explore the applicability of turbulent transport approximations in open flows.

(*c*) Since the sinusoidal forcing has only one spatial frequency ($\kappa_f = 1$) and a constant

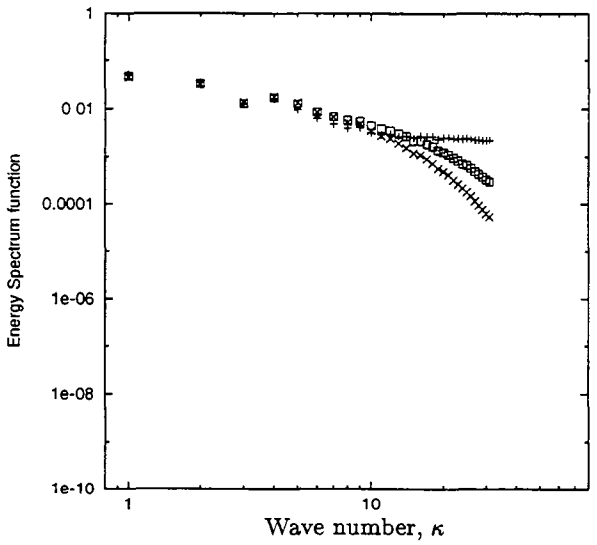

FIGURE 3. Comparison of the instantaneous energy spectra from the computations using: only molecular viscosity (+), molecular viscosity plus the Smagorinsky model (×), and molecular viscosity plus the Smagorinsky-like hyperviscosity model (□), at very early times.

amplitude F, the exact amount of energy input into the large scale can be calculated. At a sufficiently high Reynolds number, when a statistically steady state is reached, the amount of energy input into the large scales is equal to the amount of energy dissipated ϵ. This is one of the flows in which ϵ can be estimated exactly and hence enables us to estimate other length and velocity scales more accurately.

(*d*) The boundary conditions are periodic in all three directions, which means that the existing DNS code could be easily modified to include the sinusoidal forcing.
While this flow has been studied extensively using DNS, generating such a flow in the laboratory would be difficult. However, the flow in the vicinity of the inflection points of the mean profile should be similar to that for homogeneous shear flow.

In the present LES computations, the flow was initialized to the solution of an analogous laminar flow problem plus an added isotropic velocity fluctuation. The fluctuations were found to eliminate the otherwise long transient time needed for the turbulent fluctuations to develop and grow. The flow properties were averaged over planes containing the statistically-homogeneous directions (x_1 and x_3), and over time using a variant of moving averages. It was found necessary to average the flow quantities over a large number of eddy turnover times to obtain statistically reliable profiles of mean velocity, velocity autocorrelations, and Reynolds stress. The time averaging was begun only after the flow had reached a statistically-stationary state. It has been observed by Borue & Orszag (1996) that the statistically stationary state has a mean velocity profile that becomes independent of the Reynolds number for sufficiently large values of Reynolds number. The present simulations were carried out on both 64^3 and 32^3 grids. Figure 4 show the time history of turbulence kinetic energy and dissipation rate, while figure 5 shows the instantaneous energy spectra for the flow using hyperviscosity computations on the 64^3 grid. Figure 6 compares the mean velocity and velocity correlations obtained from the 64^3 hyperviscosity computation with the analytical curves found by Borue & Orszag

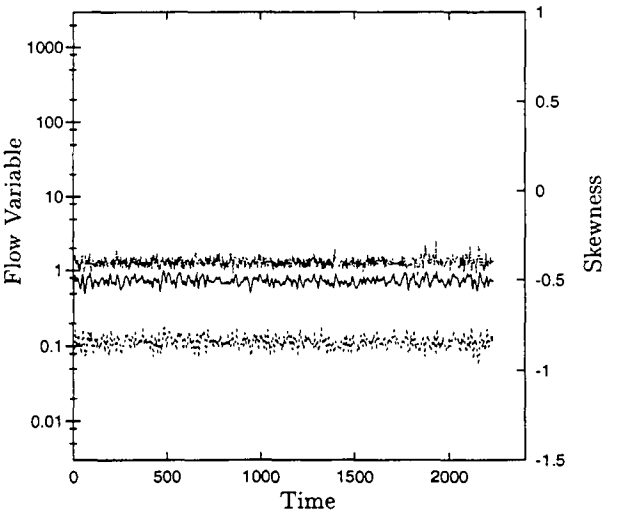

FIGURE 4. Time history of development of mean quantities for the Kolmogorov flow hyperviscosity computations on a 64^3 grid. Upper curve is skewness, middle curve is average energy, and lower curve is dissipation rate.

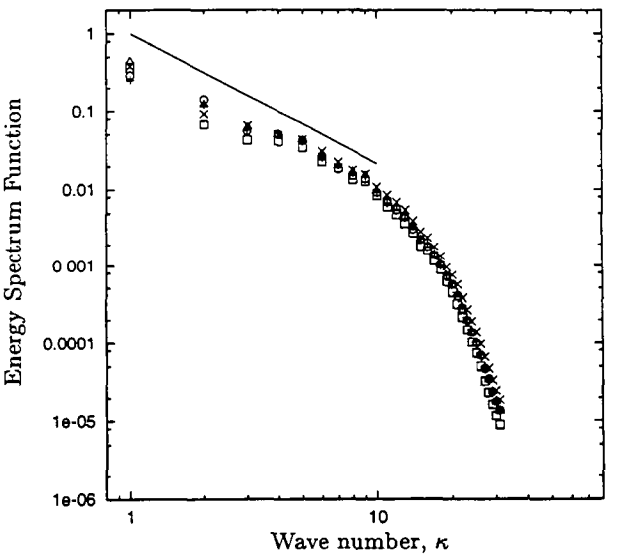

FIGURE 5. Instantaneous mean energy spectra for the Kolmogorov flow hyperviscosity computations on a 64^3 grid. Spectra are plotted at times $t = 2071$ (+), 2089 (×), 2107 (⊙), 2124 (⊡), and 2143 (Δ).

(1996) to fit the high Reynolds number limit. The agreement is quite good in spite of the relative coarseness of the grid used here.

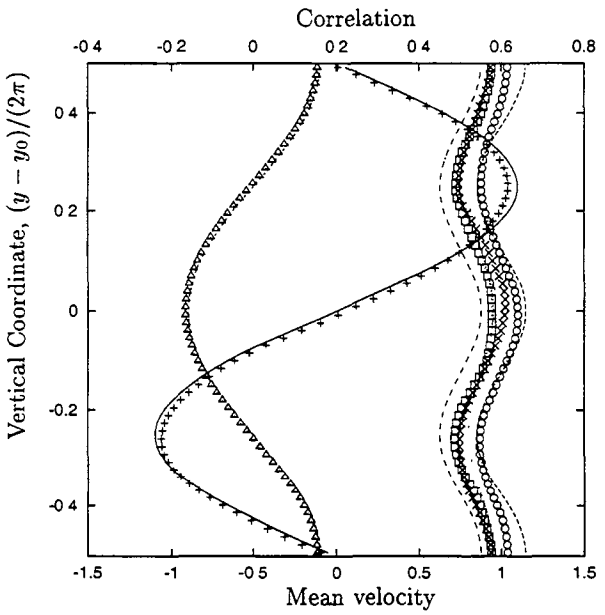

FIGURE 6. Mean velocity and velocity correlations for Kolmogorov flow; symbols are results from hyperviscosity computations on a 64^3 grid with $\nu_4 = 0.006$, and lines are high-Reynolds-number curve fits by Borue & Orszag (1996). Variables plotted are: $\langle u_1 \rangle$, + and solid line; $\langle u_1 u_2 \rangle$, Δ and short dashed line; $\langle u_1 u_1 \rangle$, $\times$ and long dashed line; $\langle u_2 u_2 \rangle$, $\odot$ and dotted line; $\langle u_3 u_3 \rangle$, $\boxdot$ and dash-dot line.

4. Conclusions

As a first step in developing tools suitable for assessing the accuracy of LES solutions for flows at large Reynolds number, the authors have developed a computer code for solving the incompressible Navier-Stokes equations for test flows that will allow the comparison of various accuracy-assessment strategies. The code includes a conventional Smagorinsky sub-grid model, as well as hyperviscosity dissipative terms that will allow greater separation of the energy-containing and dissipative scales for high Reynolds number flows. The code is validated for several simple, periodic flows, including the Taylor-Green vortex and decaying, isotropic turbulence, and preliminary results show good agreement with the high Reynolds number limit for (forced, periodic) Kolmogorov flow on relatively modest meshes using the hyperviscosity dissipation. The benefits of using the Kolmogorov flow for these studies are described, and future results will concentrate on comparisons of methods for accurately predicting the statistics of the energetic scales for this flow.

REFERENCES

BORUE, V. & ORSZAG, S. A. 1996 Numerical study of three-dimensional Kolmogorov flow at high Reynolds numbers. *J. Fluid Mech.* **306**, 293-323.

BRACHET, M. E., MEIRON, D. I., ORSZAG, S. A., NICKEL, B. G., MORF, R. H. & FRISCH, U. 1983 Small-scale structure of the Taylor-Green vortex. *J. Fluid Mech.* **130**, 411-452.

CHORIN, A. J. 1968 Numerical solution of the Navier-Stokes equations. *Math. Comput.* **22**, 745-762.

JEANMART, H. 2002 Private communication. *Centre for Systems Engineering and Applied Mechanics, Université Catholique de Louvain, 1348 Louvain-la-Neuve, Belgium.* Note: The (unpublished) results provided by Jeanmart are equivalent to those plotted in figure 7 of Brachet et al. (1983).

JEANMART, H., CARATI, D. & WINCKELMANS, G. S. 2002 Non universality and symmetry breaking in three-dimensional turbulent Kolmogorov flow. Submitted to *Phys. Fluids.*

KIM, J. & MOIN, P. 1985 Application of a fractional-step method to incompressible Navier-Stokes equations. *J. Comput. Phys.* **59**, 308-323.

LILLY, D. K. 1967 The representation of small-scale turbulence in numerical simulation experiments. *Proc. IBM Scientific Computing Symposium on Environmental Sciences* IBM Form No. **320-1951**, 195-210.

MORINISHI, Y., LUND, T. S., VASILYEV, O. V. & MOIN, P. 1998 Fully conservative higher order finite difference schemes for incompressible flow. *J. Comput. Phys.* **143**, 90-124.

SHEBALIN, J. V. & WOODRUFF, S. L. 1997 Kolmogorov flow in three dimensions. *Phys. Fluids*, **9**, 164-170.

TEMAM, R. 1969 Sur l'approximation de la solution des equations de Navier-Stokes par la méthode des pas fractionnaires. *Arch. Rational Mech. Anal.* **32**, 135-153 and **33**, 377-385.

WRAY, A. 2002 Private communication. *NASA Ames Research Center.*

Toward optimal LES on unstructured meshes

By A. Haselbacher †, R.D. Moser ‡, G. Constantinescu AND K. Mahesh ¶

A new approach for determining the correlation data required by the optimal-LES procedure of Langford and Moser (Optimal LES formulations for isotropic turbulence, *J. Fluid Mech.*, **398**, 321–346, 1999) is presented. Based on Kolmogorov's theory for isotropic turbulence, the new approach leads to stencil coefficients in terms of integrated multi-point correlations. The explicit dependence of the optimal-LES method on DNS data is thus eliminated, and its applicability is extended to high Reynolds-number flows in complex geometries. A preliminary verification of the new optimal-LES method for decaying isotropic turbulence showed good results for decay rates.

1. Introduction and Motivation

Large-Eddy Simulation (LES) is a computational technique for turbulent flows in which only large scales are resolved and the effect of the unresolved small scales is modeled. The reduced resolution makes LES an attractive approach for the analysis of engineering applications, in which the large scales often dominate momentum and heat transfer.

The separation of scales is commonly achieved through a filter operator. The lack of an unambiguous separation of the resolved and modeled scales leads to many challenging issues, including: the precise definition of the filter operator, the construction of accurate numerical methods, and, for inhomogeneous flows, the formulation of subgrid-scale models and the presence of commutation errors. These issues often involve both numerical and physical aspects and it can be difficult to isolate their effects with certainty and generality.

In an effort to address these issues, Langford & Moser (1999) introduced the concept of an "ideal LES" which is the best possible approximation, given that filtering incurs a loss of information. The ideal LES, based on the conditional average, can be proved to yield accurate large-scale one-time statistics and to minimize the error of large-scale short-time dynamics. However, the conditional average defining the ideal LES is impractical to compute because the condition is on the entire LES field. To reduce the computational cost to a practical level, the conditional average is approximated using stochastic estimation, see Adrian (1995), resulting in an approximation to the ideal LES called "optimal LES".

The optimal-LES technique was applied to forced isotropic turbulence at $\mathrm{Re}_\lambda = 164$ by Langford & Moser (1999) and to turbulent channel flow at $\mathrm{Re}_\tau = 587$ by Völker (2000). In these computations, the correlations required by the stochastic-estimation procedure were determined from Direct Numerical Simulation (DNS) data. This places an undesirable restriction on optimal LES because DNS data is available only at relatively low Reynolds numbers and for simple geometries.

† Center for Simulation of Advanced Rockets, University of Illinois at Urbana-Champaign
‡ Theoretical and Applied Mechanics, University of Illinois at Urbana-Champaign
¶ Aerospace Engineering and Mechanics, University of Minnesota

The goal of the present work is to extend the applicability of optimal LES to high-Reynolds number flows and to complex geometries. To achieve this goal, we propose a new approach in which the correlations required by the stochastic-estimation procedure are computed from turbulence theory. This approach was demonstrated for a model equation in one dimension by Balakrishnan & Moser (2001). More specifically, the present work extends the optimal-LES method to formally infinitely high Reynolds numbers by using results from Kolmogorov's theory for isotropic turbulence. This article describes this extension and presents results of a preliminary verification on unstructured grids.

The remainder of the article is structured as follows: Section 2 describes the finite-volume optimal-LES approach and explains the determination of the stencil weights using isotropic turbulence theory. The computational approach is outlined in section 3, which includes a description of the implementation of the finite-volume optimal-LES method on unstructured grids. Results are presented and discussed in section 4. Conclusions are drawn in section 5.

2. Finite-volume optimal-LES formulation

The finite-volume optimal-LES formulation was originally developed by Langford (2000) and is outlined in subsections 2.1 and 2.2. The current formulation is restricted to incompressible flows. The new approach of obtaining the correlation data from Kolmogorov's theory of isotropic turbulence is described in subsection 2.3.

2.1. *Theoretical formulation*

For incompressible flow, the momentum equations can be expressed in integral form as

$$\Delta^3 \frac{\mathrm{d}w_i}{\mathrm{d}t} + \int_s u_i u_s \,\mathrm{d}\mathbf{x} = -\int_s p n_i \,\mathrm{d}\mathbf{x} + \int_s \nu \frac{\partial u_i}{\partial x_j} n_j \,\mathrm{d}\mathbf{x}, \tag{2.1}$$

where the cell-averaged velocity is defined by

$$w_i = \frac{1}{\Delta^3} \int_v u_i(\mathbf{x}) \,\mathrm{d}\mathbf{x}, \tag{2.2}$$

and $u_s = u_i n_i$ is the velocity along the outward-directed unit normal vector with components n_i, the density has been absorbed into the pressure, ν is the kinematic viscosity, and $\mathbf{x} = \{x_1, x_2, x_3\}^t$ is the position vector. The volume of the integration region is denoted by Δ^3, so that Δ may be interpreted as the cell width for uniform hexahedral grids. The subscripts s and v indicate surface and volume integrals, respectively.

In the finite-volume optimal-LES method, the cell-averaging defined by (2.2) is regarded as the filtering operation. It is assumed that the filter width is in the inertial range. In the following, w_i and u_i are referred to as filtered and unfiltered values, respectively.

To evolve the filtered values, the fluxes of unfiltered variables appearing in (2.1) must be expressed in terms of filtered values. Thus the flux is estimated in terms of a quadratic expression of the filtered values,

$$\begin{aligned} \int_s u_i(\mathbf{x}) u_s(\mathbf{x}) \,\mathrm{d}\mathbf{x} = &\sum_v L_{ij}(s,v) \int_v u_j(\mathbf{x}) \,\mathrm{d}\mathbf{x} \\ &+ \sum_{v_1,v_2} Q_{ijk}(s,v_1,v_2) \int_{v_1} u_j(\mathbf{x}^1) \,\mathrm{d}\mathbf{x}^1 \int_{v_2} u_k(\mathbf{x}^2) \,\mathrm{d}\mathbf{x}^2, \end{aligned} \tag{2.3}$$

where the functional dependences of the velocity components were added to indicate the surfaces and volumes over which they are integrated.

Before addressing the determination of the estimation coefficients L and Q—which may also be interpreted as stencil weights—we draw attention to the following point: in contrast to conventional LES approaches, (2.1) is not space-filtered independently of the numerical discretization, the fluxes are not cast in terms of filtered values, and we do not explicitly define a subgrid-scale term. Instead, the optimal-LES method approximates the combination of fluxes and subgrid effects in an optimal way. The reasoning is that conventional finite-volume methods evaluate fluxes based on approximations derived from Taylor-series expansions, and thus require the cells to be small compared to characteristic length scales of the underlying functions. This requirement is violated in LES, so the definition of subgrid effects depends on the order of the flux approximation.

2.2. *Stencil-weights construction*

To determine the unknown stencil weights L and Q, we take moments of (2.3) and ensemble-average to obtain the system of equations,

$$I^1_{li}(v',s) = \sum_v L_{ij}(s,v) I^2_{lj}(v',v) + \sum_{v_1,v_2} Q_{ijk}(s,v_1,v_2) I^3_{ijk}(v',v_1,v_2) \tag{2.4}$$

$$I^4_{lmi}(v'_1,v'_2,s) = \sum_v L_{ij}(s,v) I^3_{lmj}(v'_1,v'_2,v) + \sum_{v_1,v_2} Q_{ijk}(s,v_1,v_2) I^5_{lmjk}(v'_1,v'_2,v_1,v_2) \tag{2.5}$$

where the integrated correlations I^1 to I^5 are given by,

$$I^1_{li}(v',s) = \int_{v'}\int_s \langle u_l(\mathbf{x}')u_i(\mathbf{x})u_s(\mathbf{x})\rangle \, d\mathbf{x}\, d\mathbf{x}' \tag{2.6}$$

$$I^2_{lj}(v',v) = \int_{v'}\int_v \langle u_l(\mathbf{x}')u_j(\mathbf{x})\rangle \, d\mathbf{x}\, d\mathbf{x}' \tag{2.7}$$

$$I^3_{ljk}(v',v_1,v_2) = \int_{v'}\int_{v_1}\int_{v_2} \langle u_l(\mathbf{x}')u_j(\mathbf{x}^1)u_k(\mathbf{x}^2)\rangle \, d\mathbf{x}^2\, d\mathbf{x}^1\, d\mathbf{x}' \tag{2.8}$$

$$I^4_{lmi}(v'_1,v'_2,s) = \int_{v'_1}\int_{v'_2}\int_s \langle u_l(\mathbf{x}^{1'})u_m(\mathbf{x}^{2'})u_i(\mathbf{x})u_s(\mathbf{x})\rangle \, d\mathbf{x}\, d\mathbf{x}^{2'}\, d\mathbf{x}^{1'} \tag{2.9}$$

$$I^5_{lmjk}(v'_1,v'_2,v_1,v_2) = \int_{v'_1}\int_{v'_2}\int_{v_1}\int_{v_2} \langle u_l(\mathbf{x}^{1'})u_m(\mathbf{x}^{2'})u_j(\mathbf{x}^1)u_k(\mathbf{x}^2)\rangle \, d\mathbf{x}^2\, d\mathbf{x}^1\, d\mathbf{x}^{2'}\, d\mathbf{x}^{1'} \tag{2.10}$$

Thus, three correlation tensors are needed to determine the estimation coefficients,

$$R_{ij}(\mathbf{r}^1) = \langle u_i(\mathbf{x})u_j(\mathbf{x}^1)\rangle, \tag{2.11}$$

$$T_{ijk}(\mathbf{r}^1,\mathbf{r}^2) = \langle u_i(\mathbf{x})u_j(\mathbf{x}^1)u_k(\mathbf{x}^2)\rangle, \tag{2.12}$$

$$F_{ijkl}(\mathbf{r}^1,\mathbf{r}^2,\mathbf{r}^3) = \langle u_i(\mathbf{x})u_j(\mathbf{x}^1)u_k(\mathbf{x}^2)u_l(\mathbf{x}^3)\rangle, \tag{2.13}$$

where homogeneity was assumed in order to express the correlations in terms of separation vectors $\mathbf{r}^i = \mathbf{x} - \mathbf{x}^i$.

2.3. *Determination of correlations*

To determine the correlations given by (2.11)-(2.13), the spatial separations are assumed to be small enough to be in the Kolmogorov inertial range of isotropic turbulence at an infinite Reynolds number. Thus the correlations are represented by isotropic tensors, and

we use the expressions for the second- and third-order longitudinal structure functions,

$$S_2(r^1) = \langle (u_{||}(\mathbf{x}) - u_{||}(\mathbf{x}^1))^2 \rangle = C_1 \epsilon^{2/3} (r^1)^{2/3}, \tag{2.14}$$

$$S_3(r^1) = \langle (u_{||}(\mathbf{x}) - u_{||}(\mathbf{x}^1))^3 \rangle = -\frac{4}{5} \epsilon r^1, \tag{2.15}$$

where $r^i = ||\mathbf{r}^i||$ is the magnitude of the separation vector, $u_{||}$ is the velocity component in the direction of the separation vector, ϵ is the rate of dissipation of turbulence kinetic energy, and $C_1 \approx 2.0$ is the Kolmogorov constant.

2.3.1. *Two-point second-order correlation*

The two-point second-order correlation is given by the well-known expression

$$R_{ij}(\mathbf{r}^1) = u^2 \left[f \delta_{ij} + \frac{1}{2} r f' \left(\delta_{ij} - \frac{r_i^1 r_j^1}{(r^1)^2} \right) \right], \tag{2.16}$$

where u^2 is the variance, $f(r^1) = \langle u_{||}(\mathbf{x}) u_{||}(\mathbf{x} + \mathbf{r}^1) \rangle / u^2$ is the longitudinal correlation coefficient, and δ_{ij} is the Kronecker delta. The longitudinal correlation coefficient can be determined from (2.14), which allows (2.16) to be rewritten as

$$R_{ij}(\mathbf{r}^1) = u^2 \delta_{ij} + \frac{C_1}{6} \epsilon^{2/3} (r^1)^{2/3} \left(\frac{r_i^1 r_j^1}{(r^1)^2} - 4 \delta_{ij} \right), \tag{2.17}$$

and hence I^2 can be computed.

2.3.2. *Two-point third-order correlation*

The most general isotropic third-order tensor which satisfies the continuity constraint and is symmetric with respect to exchanging the i and j indices is given by

$$T_{ijk}(0, \mathbf{r}^1) = h \delta_{ij} \frac{r_k^1}{r^1} - \left(\frac{r^1 h'}{2} + h \right) \left(\delta_{ik} \frac{r_j^1}{r^1} + \delta_{jk} \frac{r_i^1}{r^1} \right) + (r^1 h' - h) \frac{r_i^1 r_j^1 r_k^1}{(r^1)^3}, \tag{2.18}$$

where $h(r^1) = \langle u_{||}^2(\mathbf{x}) u_{||}(\mathbf{x} + \mathbf{r}^1) \rangle / u^3$ is the longitudinal correlation coefficient. By considering the tensor

$$B_{ijk}(\mathbf{r}^1) = \langle (u_i(\mathbf{x}^1) - u_i(\mathbf{x})) (u_j(\mathbf{x}^1) - u_j(\mathbf{x})) (u_k(\mathbf{x}^1) - u_k(\mathbf{x})) \rangle \tag{2.19}$$

$$= 2 \left(T_{ijk}(0, \mathbf{r}^1) + T_{ikj}(0, \mathbf{r}^1) + T_{jki}(0, \mathbf{r}^1) \right), \tag{2.20}$$

it can be shown that

$$S_3(r^1) = B_{ijk}(\mathbf{r}^1) \frac{r_i^1 r_j^1 r_k^1}{r^1} = -12 h(r^1). \tag{2.21}$$

Having expressed $h(r^1)$ in terms of the third-order longitudinal structure function, (2.15) can be recast as

$$T_{ijk}(0, \mathbf{r}^1) = \frac{\epsilon}{15} \left[\delta_{ij} r_k^1 - \frac{3}{2} \left(\delta_{ik} r_j^1 + \delta_{jk} r_i^1 \right) \right], \tag{2.22}$$

from which I^1 can be computed.

2.3.3. *Three-point third-order correlation*

We have so far been unable to find or derive an expression for the three-point third-order correlation. Fortunately, we can circumvent this issue by computing I^3 directly

from filtered data as

$$I^3_{ijk}(v', v_1, v_2) = \left\langle \int_{v'} u_l(\mathbf{x}')\, d\mathbf{x}' \int_{v_1} u_j(\mathbf{x}^1)\, d\mathbf{x}^1 \int_{v_2} u_k(\mathbf{x}^2)\, d\mathbf{x}^2 \right\rangle \tag{2.23}$$

$$= \langle w_l(\mathbf{x}') w_j(\mathbf{x}^1) w_k(\mathbf{x}^2) \rangle\,. \tag{2.24}$$

We thus propose to compute I^3 dynamically during the calculation from cell-averaged data. Note that this approach can in principle be applied to all pure volume integrals.

In (2.24) and all subsequent expressions involving averages of cell-averaged values, the angled brackets denote a volume average.

2.3.4. *Fourth-order correlations*

The quasi-normal approximation is invoked to determine the fourth-order correlations. The fourth-order correlations are thus expressed in terms of the second-order two-point correlations as

$$F_{ijkl}(\mathbf{r}^1, \mathbf{r}^2, \mathbf{r}^3) = R_{ij}(\mathbf{r}^1) R_{kl}(\mathbf{r}^3 - \mathbf{r}^2) + R_{ik}(\mathbf{r}^2) R_{jl}(\mathbf{r}^3 - \mathbf{r}^1) + R_{il}(\mathbf{r}^3) R_{jk}(\mathbf{r}^2 - \mathbf{r}^1). \tag{2.25}$$

Hence I^4 and I^5 can be determined from (2.25) and (2.17).

2.4. *Scaling of integrated correlations*

The integrated correlations depend on the geometric configuration of the volumes over which they are integrated, and on the flow solution via u^2 and ϵ. These dependencies can be parameterized through a scaling. However, because of the existence of two length scales, i.e., the filter width Δ and the energy-containing length scale u^3/ϵ, not all the quantities are scaled consistently.

Based on the forms of the various approximations to the correlations, the following scaled quantities are defined (dependencies and subscripts are suppressed for simplicity of notation):

$$\tilde{I}^1 = \frac{I^1}{\epsilon \Delta^6}, \tag{2.26}$$

$$\tilde{I}^2 = \frac{I^2}{u^2 \Delta^6}, \tag{2.27}$$

$$\tilde{I}^3 = \frac{I^3}{\epsilon \Delta^{10}}, \tag{2.28}$$

$$\tilde{I}^4 = \frac{I^4}{u^4 \Delta^8}, \tag{2.29}$$

$$\tilde{I}^5 = \frac{I^5}{u^4 \Delta^{12}}, \tag{2.30}$$

$$\tilde{L} = \frac{L u^2}{\epsilon}, \tag{2.31}$$

$$\tilde{Q} = Q \Delta^4. \tag{2.32}$$

Then (2.4) and (2.5) can be rewritten as

$$\tilde{I}^1_{li}(v', s) = \sum_v \tilde{L}_{ij}(s, v) \tilde{I}^2_{lj}(v', v) + \sum_{v_1, v_2} \tilde{Q}_{ijk}(s, v_1, v_2) \tilde{I}^3_{ljk}(v', v_1, v_2) \tag{2.33}$$

$$\tilde{I}^4_{lmi}(v'_1, v'_2, s) = \lambda^2 \sum_v \tilde{L}_{ij}(s, v) \tilde{I}^3_{lmj}(v'_1, v'_2, v) + \sum_{v_1, v_2} \tilde{Q}_{ijk}(s, v_1, v_2) \tilde{I}^5_{lmjk}(v'_1, v'_2, v_1, v_2) \tag{2.34}$$

where $\lambda = \Delta\epsilon/u^3$, the ratio of the filter width to the large turbulence length scale, will generally be small. In the limit $\lambda \to 0$, Q can be determined independently of L.

Furthermore, the integrated correlations depend on distances separating the surfaces and volumes over which they are integrated. Let ρ be the radius of the smallest sphere containing the volumes and surfaces over which the correlations are integrated and define $\tilde{\rho} = \rho/\Delta$. Then the integrals can be written in the following forms

$$\tilde{I}^1 = \tilde{I}^{10}\tilde{\rho} \tag{2.35}$$

$$\tilde{I}^2 = \tilde{I}^{20} + (\lambda\tilde{\rho})^{2/3}\tilde{I}^{21} \tag{2.36}$$

$$\tilde{I}^3 = \tilde{I}^{30}\tilde{\rho} \tag{2.37}$$

$$\tilde{I}^4 = \tilde{I}^{40} + (\lambda\tilde{\rho})^{2/3}\tilde{I}^{41} + (\lambda\tilde{\rho})^{4/3}\tilde{I}^{42} \tag{2.38}$$

$$\tilde{I}^5 = \tilde{I}^{50} + (\lambda\tilde{\rho})^{2/3}\tilde{I}^{51} + (\lambda\tilde{\rho})^{4/3}\tilde{I}^{52}. \tag{2.39}$$

Given the expressions for $I^{\alpha\beta}$ stated above, the expressions for $\tilde{I}^{\alpha\beta}$ are easily deduced.

2.5. *Estimation of kinetic energy and dissipation rate*

Equations (2.17) and (2.22) depend on estimates of the turbulent kinetic energy and its dissipation rate.

The turbulent kinetic energy is estimated from filtered data as

$$k \approx \frac{1}{2}\langle w_i w_i \rangle. \tag{2.40}$$

The justification for this approximation is that most of the energy is contained in the large scales. The variance is deduced from $u^2 = 2k/3$.

Two approaches to estimating the dissipation rate were investigated. The first approach is based on the observation that $\tilde{I}^2$ can be computed from

$$\tilde{I}^2_{ij}(v', v) = \frac{\langle w_l(\mathbf{x}')w_j(\mathbf{x})\rangle}{u^2}, \tag{2.41}$$

which gives, on substitution into (2.36),

$$\frac{\langle w_l(\mathbf{x}')w_j(\mathbf{x})\rangle}{u^2} = \tilde{I}^{20}_{lj} + (\lambda\tilde{\rho})^{2/3}\tilde{I}^{21}_{lj}. \tag{2.42}$$

Contracting and using the definitions of $\tilde{\rho}$ and λ leads to

$$\epsilon = \frac{1}{\rho}\left(\frac{\langle w_l(\mathbf{x}')w_l(\mathbf{x})\rangle - u^2\tilde{I}^{20}_{ll}}{\tilde{I}^{21}_{ll}}\right)^{3/2}. \tag{2.43}$$

Since ρ, $\tilde{I}^{20}$, and $\tilde{I}^{21}$ are specified by the geometric configuration of the cells over which the integrals are evaluated, ϵ as given by (2.43) is a function only of the variance and the two-point second-order correlation. The accuracy of (2.43) was evaluated *a priori* on a 32^3 grid using a single filtered velocity field of a DNS of forced isotropic turbulence at $\mathrm{Re}_\lambda = 164$. Figure 1 demonstrates that reasonably accurate approximations can be obtained if $r^1/\Delta > 3$, keeping in mind that (2.43), based on the assumption of an infinite Reynolds number, cannot be expected to reproduce the dissipation rate of the DNS exactly. It is worth noting that (2.43) exhibits the correct dynamic behavior because it can be shown that $\langle w_l(\mathbf{x}')w_l(\mathbf{x})\rangle = u^2\tilde{I}^{20}_{ll}$ for uniform flow fields, and hence the dissipation vanishes as required.

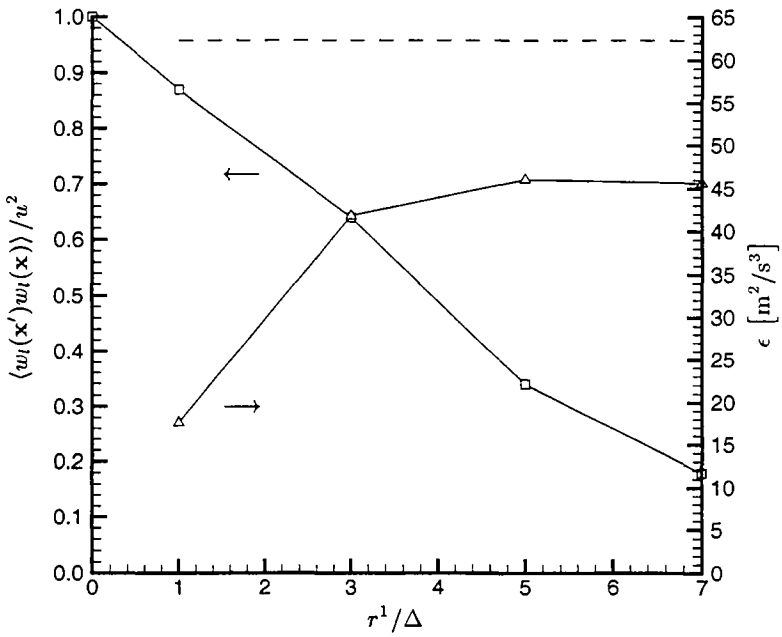

FIGURE 1. Behavior of correlation coefficient and dissipation-rate estimate given by (2.43) with non-dimensional separation distance r^1/Δ. ---- : Dissipation rate from filtered DNS of forced isotropic turbulence, □ : computed correlation coefficient $\langle w_l(\mathbf{x}')w_l(\mathbf{x})\rangle/u^2$, △ : estimated dissipation rate ϵ.

The second approach to estimating the dissipation rate is based on the relation

$$\epsilon \propto \frac{k^{3/2}}{\ell}, \tag{2.44}$$

where ℓ is a length scale of the large-scale motion.

3. Computational approach

In the present work, the optimal-LES method was implemented in a compressible unstructured-grid code based on the cell-centered finite-volume method. The unstructured code allows for grids composed of arbitrary combinations of tetrahedra, prisms, pyramids, and hexahedra, but only uniform hexahedral grids are considered in this study.

3.1. *Implementation of optimal-LES method on unstructured grids*

The implementation of the optimal-LES method on unstructured grids consists of three steps. The first step involves the construction of the stencils at each face. For stencils of only two cells per face an explicit construction is not necessary, because these cells can be obtained from the face-to-cell list used in the flux computation. If the stencils are to contain $n > 2$ cells, an Octree-based approach, see, e.g., Knuth (1998), is used to determine a set of candidate cells. The candidate cells are sorted by increasing distance from the face centroid and the closest n cells are chosen. Furthermore, stencil shapes

can be influenced depending on local cell topologies. For example, by considering the scalar product of the face normal vector and the position vector between candidate cell centroids and the face centroid, locally one-dimensional stencils may be constructed.

In the second step, the integrated correlations are evaluated using cubature. This entails the evaluation of d-dimensional integrals of tensor functions of order p. Given the restriction to hexahedral cells in the present work, the DCUHRE package of Berntsen *et al.* (1991) is used for the cubature. The computational cost of evaluating the integrals can be reduced by taking into account the symmetries of the tensors, as well as additional symmetries which arise if two or more cells coincide. On non-deforming grids, the first two steps can be completed in a preprocessing phase.

The third step concerns the actual determination of the stencil weights during a computation. This involves the estimation of the turbulence kinetic energy and its dissipation rate as described in subsection 2.5, after which the integrated correlations $\tilde{I}^{\alpha\beta}$ are computed from (2.35)-(2.39). The stencil weights follow by solving the linear system given by (2.33) and (2.34), and using (2.31) and (2.32). The fluxes are then determined from (2.3).

3.2. *Numerical method*

The Navier-Stokes equations are integrated in time using the classical fourth-order accurate Runge-Kutta method. The viscous fluxes are computed using face-gradients calculated from a least-squares reconstruction. The optimal-LES approach is applied only to the momentum equations; the continuity and energy equations are approximated with a centered discretization.

Because we simulate the decay of incompressible isotropic turbulence using the compressible Navier-Stokes equations, dilatation damping is employed to prevent density fluctuations from contributing significantly to the turbulent kinetic energy. This is achieved by modifying the viscosity multiplying the divergence in the stress tensor,

$$\tau_{ij} = 2\mu S_{ij} - \frac{2}{3}(\mu + \mu^*)\frac{\partial u_k}{\partial x_k}\delta_{ij}, \tag{3.1}$$

where μ is the dynamic viscosity, S_{ij} is the strain tensor, and μ^* is the additional viscosity used to damp acoustic waves. A value of $\mu^* = 10\mu$ is used in this study.

4. Results and discussion

The decay of isotropic incompressible turbulence was chosen for the preliminary verification of the optimal-LES approach based on the theory of isotropic turbulence. The calculation domain is a cube of edge length 2π discretized with 32^3 cells.

4.1. *Illustration of stencil weights*

It is instructive to briefly describe the stencils obtained using the finite-volume optimal-LES approach. Using the abbreviations introduced by Langford (2000), namely

$$\widetilde{w^2} = \frac{1}{2}\left[\left(w^+\right)^2 + \left(w^-\right)^2\right] \quad \text{and} \quad \overline{w^2} = w^+ w^-,$$

where the superscripts denote the cells as indicated in figure 2, an approximation of the normal momentum flux can be expressed as

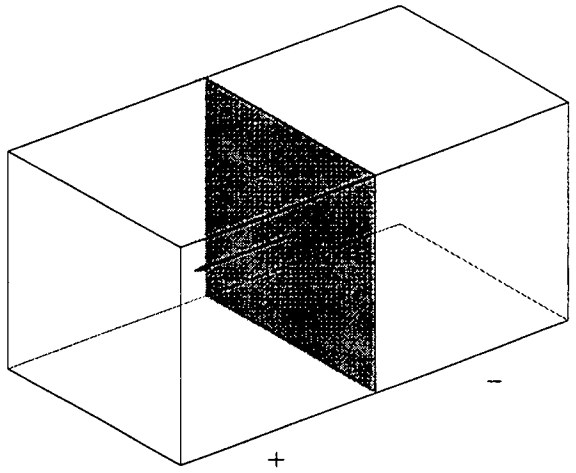

FIGURE 2. Illustration of cell configuration for stencil of two hexahedral cells. The arrow indicates the direction of the face-normal vector.

$$\frac{1}{\Delta^2}\int_s u_1^2\,d\mathbf{x} = 1.2674\,\widetilde{w_1^2} + 0.4750\,\overline{w_1^2} + 0.4200\left(\widetilde{w_2^2} + \widetilde{w_3^2}\right) - 0.0036\left(\overline{w_2^2} + \overline{w_3^2}\right) - 0.1903\,\frac{w_1^+ - w_1^-}{\Delta},$$

and an approximation of the tangential momentum flux is given by

$$\frac{1}{\Delta^2}\int_s u_2u_1\,d\mathbf{x} = 1.9468\left(\frac{w_1^+ + w_1^-}{2}\right)\left(\frac{w_2^+ + w_2^-}{2}\right) - 0.0840\left(w_1^-w_2^+ + w_1^+w_2^-\right) - 0.0785\,\frac{w_2^+ - w_2^-}{\Delta}.$$

For comparison, note that the traditional finite-volume schemes used for LES computations would probably employ a purely-centered approximation given by, for example,

$$\frac{1}{\Delta^2}\int_s u_1^2\,d\mathbf{x} = 0.5000\,\widetilde{w_1^2} + 0.5000\,\overline{w_1^2},$$

and

$$\frac{1}{\Delta^2}\int_s u_2u_1\,d\mathbf{x} = \left(\frac{w_1^+ + w_1^-}{2}\right)\left(\frac{w_2^+ + w_2^-}{2}\right).$$

The most obvious difference is that the optimal-LES stencils are not consistent. As stated in subsection 2.1, the requirement of consistency does not apply to LES because the cells are not small compared to the characteristic length scales of the turbulence. Furthermore, consistency is irrelevant because the stencil weights include the model term. The diffusive contribution to the fluxes is due to the linear term in (2.3). Langford (2000) discussed finite-volume optimal-LES stencils in detail.

4.2. *Simulation of decaying isotropic turbulence*

Before we turn to a presentation and discussion of the results, two issues merit special attention. The first issue concerns the dynamic computation of $\tilde{I}^3$ using (2.24). We have

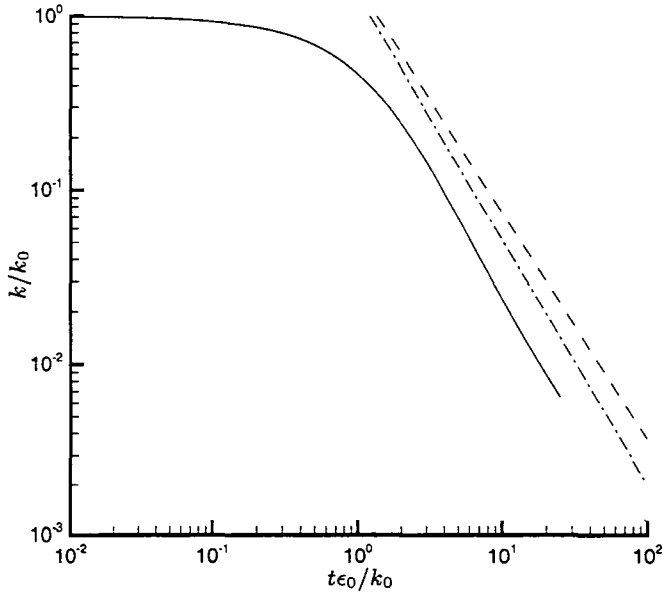

FIGURE 3. Behavior of normalized turbulent kinetic energy with normalized time. ——— : Optimal-LES result, - - - - : decay-law exponent $n = 1.3$, —·— : decay-law exponent $n = 1.4$, ····· : decay-law exponent $n = 1.5$.

thus far been unable to evaluate $\tilde{I}^3$ accurately using spatial averaging; it was not possible to discern a non-zero entry pattern reliably. The present results have therefore been obtained by setting $\tilde{I}^3 = 0$. We will revisit the dynamic computation of $\tilde{I}^3$ in the future.

The second issue is the estimation of the dissipation rate. The use of (2.43) leads to rapid growth of turbulent kinetic energy after an initial period of decay. Although the dissipation rate increased in conjunction with the growth of kinetic energy, the increase appeared to be too slow to prevent blow-up. Hence it seems that the coupling of the dissipation rate given by (2.43) to the turbulent kinetic energy is too weak. To proceed with the preliminary investigation, we have thus used (2.44) with a constant of proportionality $C = 10$ and $\ell = 2\pi$. A constant length scale is obviously a crude approximation to the growth of the integral length scale as the turbulence decays, but sufficient for this preliminary investigation. The large value of the coefficient is a consequence of the definition of ℓ.

The decay of the normalized turbulence kinetic energy and its dissipation rate is depicted in figures 3 and 4, in which the abscissae are given by the physical time normalized by the eddy-turnover time at $t = 0$. For comparison, the decay rates given by the respective analytical decay laws are indicated. It can be seen that the decay rates of both quantities are close to the typical values of the decay-law exponents after an initial adjustment period. The decay rate of the dissipation rate exhibits a gradual change toward the end of the simulation, which we attribute to the choice of a constant length scale.

The three-dimensional energy spectrum at $t\epsilon_0/k_0 = 5.6$ is depicted in figure 5. The pronounced roll-off at high wavenumbers is unexplained at present. Separate investigations have established that the roll-off is not influenced by the physical viscosity or the additional viscosity coefficient used for dilatation damping.

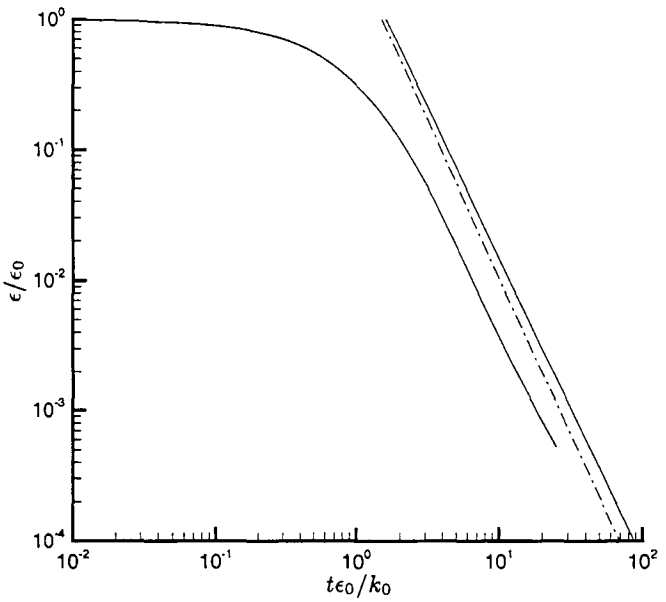

FIGURE 4. Behavior of normalized dissipation rate with normalized time. ——— : Optimal-LES result, ---- : decay-law exponent $n = 2.3$, —·— : decay-law exponent $n = 2.4$, ····· : decay-law exponent $n = 2.5$.

5. Conclusions and further work

A new method of determining the correlations required by the optimal-LES approach has been presented. The new approach is based on Kolmogorov's theory for isotropic turbulence and leads to stencil coefficients which are determined from integrated multi-point correlations. By using this approach, the explicit dependence of the optimal-LES method on DNS data is eliminated and the applicability is extended to high-Reynolds-number flows in complex geometries.

The new optimal-LES method was implemented in an unstructured finite-volume code. A preliminary verification for decaying isotropic turbulence gave satisfactory results for decay rates of the turbulence kinetic energy and its dissipation rate. The three-dimensional energy spectrum indicates that further work is required.

Further work will include the following:

- An investigation of the reasons for the pronounced roll-off in the three-dimensional energy spectrum at high wavenumbers.
- An analysis of (2.43) using DNS data.
- An investigation into averaging techniques which allow a robust and accurate dynamic determination of $\tilde{I}^3$.
- An extension of the evaluation of the integrated correlation to arbitrary unstructured grids including tetrahedral, prismatic, and pyramidal cells.
- An analysis of the accuracy of the isotropic approximations in inhomogeneous flows.
- An extension of the finite-volume optimal-LES approach to compressible flows, for which an approximation of the mass flux and correlations involving the pressure and temperature are required.

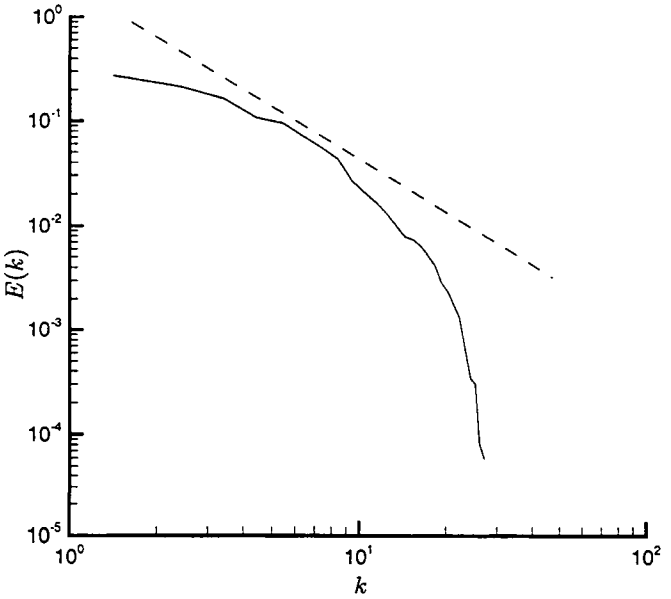

FIGURE 5. Three-dimensional energy spectrum at $t\epsilon_0/k_0 = 5.6$. □ : Optimal-LES result, ---- : $k^{-5/3}$.

Acknowledgments

The first author would like to acknowledge helpful discussions with Mr. Paulo Zandonade, Dr. Ramesh Balakrishnan, and Mr. Sofiane Benhamadouche. The first author is funded by the Department of Energy through the University of California under Subcontract number B341494.

REFERENCES

ADRIAN, R. 1995 Stochastic estimation of the structure of turbulent fields. *Theor. and Appl. Mech. Dept., Univ. of Illinois at Urbana–Champaign,* Tech. Rept. No. 800.

BALAKRISHNAN, R. AND MOSER, R.D. 2001 Optimal finite-volume stencils for large-eddy simulation of high Re turbulence. *Bull. Am. Phys. Soc.*, **46**(10), 159-160, 2001.

BERNTSEN, J., ESPELID T.O., AND GENZ A. Algorithm 698: DCUHRE: An adaptive multidimensional integration routine for a vector of integrals, *ACM Trans. Math. Softw.*, **17**(4),452-456. Software available from: `http://www.sci.wsu.edu/math/faculty/genz/homepage`.

KNUTH, D.E. 1998 *The Art of Computer Programming, Vol. 3, Sorting and Searching*, Addison Wesley.

LANGFORD, J. 2000 Toward ideal large-eddy simulation. *Ph.D. Thesis*, Univ. of Illinois at Urbana–Champaign.

LANGFORD, J. AND MOSER, R.D. 1999 Optimal LES formulations for isotropic turbulence. *J. Fluid Mech.*, **398**, 321-346.

VÖLKER, S. 2000 Optimal large-eddy simulation of turbulent channel flow. *Ph.D. Thesis*, Univ. of Illinois at Urbana–Champaign.

LES Numerics

By S. Scott Collis

In the 1990's, the advent of the dynamic procedure for subgrid-scale modeling led to the application of large eddy simulation (LES) to an increasingly wider range of problems within the research community. Likewise, the success of LES in research-type problems has encouraged industry to explore the use of LES for particularly difficult and important flow problems that cannot be accurately predicted with RANS models. As LES has moved out of the researcher's computational box to the world of industrial applications, a number of challenges with regard to accuracy, robustness, and practicality has been revealed. Discretizations, such as global spectral methods, that had before been the norm were replaced with low-order numerical methods and the interaction of numerical errors with subgrid scale models, especially when using a dynamic procedure, can prove disastrous. Practical issues that heretofore had not been of primary concern — such as grid generation, robustness, and software supportability — also become important when LES is used as a predictive tool for engineering applications. In essence, all the issues raised above are the bailiwick of **LES numerics** and the three projects in this section each strive to expand the domain of LES to more complex situations.

One approach to extend LES to complex flows is to take an existing industrial flow code that is primarily used for RANS simulations and modify it to support LES. This is the direction explored by Benhamadouche, Mahesh, and Constantinescu who have modified a collocated finite-volume code for use in LES. One of the key findings of this work is that the low-order, upwind discretizations commonly used for industrial RANS codes are not appropriate for LES since they result in excessive dissipation. To overcome this, Benhamadouche *et al.* modified their industrial code to support a convective flux treatment that is approximately energy-conserving, and found that this approach leads to significant improvements in robustness and accuracy, critical for use in LES. They also considered the influence of time discretization errors as well as errors that arise due to the use of a fractional-step procedure for enforcing incompressibility. By application of the modified code to a range of test problems, including a coaxial combustor, they demonstrate that, with modest changes, an existing industrial finite-volume code can be made suitable for LES in complex geometries using unstructured grids.

The opposite approach is taken in the second project, by Collis, who has developed a new flow solver specifically designed to support high-accuracy turbulence simulations in complex geometries using unstructured meshes. This approach utilizes a relatively new discretization, at least for turbulence simulation, called discontinuous Galerkin (DG) that offers potential advantages that can be utilized to make turbulence simulation more practical. In particular, a DG discretization provides high-order (spectral) accuracy on unstructured meshes, local *hp*-refinement, weak imposition of boundary conditions, local conservation, and orthogonal hierarchical basis that support multiscale turbulence modeling. Collis has implemented this DG method in an object-oriented software environment, which offers supportability and flexibility that are not commonly found in research codes but are of key importance for industrial applications. This implementation is applied to vortex shedding from a circular cylinder, and to fully-developed turbulent channel flow where it is shown that the weak imposition of wall boundary conditions that naturally

arises in the DG method may have significant advantages in the context of wall modeling for LES.

In the third project, Pascarelli, Iaccarino, and Fatica also extend the class of flows for which LES can be applied by developing numerical methods to support LES for submerged objects near a free surface. They accomplish this by constructing linearized boundary conditions at the free surface which are coupled with the Navier–Stokes equations for the flow variables while the submerged object is represented using an immersed boundary method. Doing so yields a numerical method that allows for both fully- and partially-submerged objects, and the technique is demonstrated both for flow over a submerged hydrofoil and flow over a partially-submerged square cylinder. While both these demonstration cases are at low Reynolds numbers, future work will apply the same techniques for turbulent flows using LES.

S. Scott Collis

Colocated finite–volume schemes for large–eddy simulation on unstructured meshes

By S. Benhamadouche †, K. Mahesh ‡ AND G. Constantinescu

Code_Saturne ® is a finite-volume, unstructured-grid code developed at Électricité De France (*EDF*), which solves the Reynolds-averaged Navier-Stokes equations for incompressible flows. The code has been extensively benchmarked for a variety of industrial applications. The solver has been extended at *EDF* to solve large-eddy simulation equations, and we found that the numerical methods used in the base RANS code are not directly applicable to LES. This paper uses *Code_Saturne* to investigate the performance of several numerical schemes for LES of different academic and industrial flows. In particular, the conservation of global kinetic energy and robustness of several numerical schemes are compared and discussed. Finally, *Code_Saturne* with non-dissipative numerical methods is validated for the swirling flow in a coaxial geometry corresponding to the experiments of Sommerfeld & Qiu (1991). Also, the role of the subgrid-scale (SGS) model is investigated through simulations without a SGS model (coarse DNS), with a constant Smagorinsky model and with a dynamic Smagorinsky model.

Introduction

The objective of this work is to use an industrial code (*Code_Saturne* ®) developed at *EDF* to perform large-eddy simulation and to test several numerical schemes for LES. We adopt the point of view that LES requires non-diffusive numerical schemes, and therefore the numerical method used in the base RANS solver cannot be directly applied to LES. Recently Mahesh *et al.* (2001) developed an algorithm for unstructured grids that is discretely energy-conserving in the absence of time-splitting errors. Good prediction for a wide range of flows, including that in a Pratt & Whitney gas-turbine combustor, was reported. Also, an LES version has been developed at EDF with *Code_Saturne* (Benhamadouche *et al.* (2002)) and several tests have been done to improve the numerical schemes (Garibian *et al.* (2001)).

In this paper, we use *Code_Saturne* to evaluate the effect of the numerical method on discrete energy conservation. The effect of discrete time steps on both convection and pressure-gradient terms is considered. Results from the evaluation are used to decide upon a suitable scheme for LES using *Code_Saturne*, which is then applied to LES of the flow in a coaxial combustor geometry.

This paper is organized as follows. Section 1 describes the numerical schemes that are evaluated. The convection and pressure-gradient terms are discussed in subsections 1.1 and 1.2 respectively. Section 2 compares the different formulations for the Taylor problem and for isotropic turbulence. *Code_Saturne* is used to simulate the flow in a coaxial combustor geometry in section 3 and the results compared to experiment and results on the same grid using CDP, the unstructured solver developed by Mahesh *et al.* (2001).

† Electricité De France / UMIST (Manchester)
‡ University of Minnesota

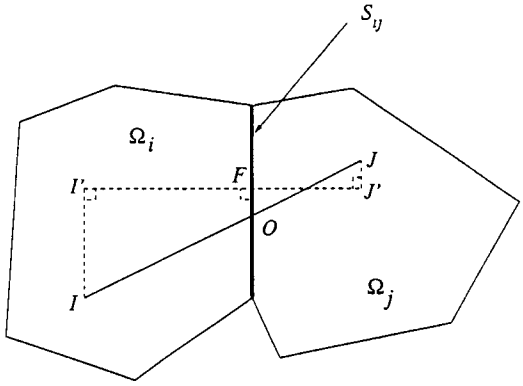

FIGURE 1. General view of a cell face

1. Numerical schemes

Code_Saturne solves the conservative form of the incompressible Navier Stokes equations (1.1). The code has the capability to use unstructured grids with cells of arbitrary shape.

$$\frac{\partial \mathbf{u}}{\partial t} + \mathrm{div}(\mathbf{u} \otimes \mathbf{u}) = -\mathbf{grad}(p) + \mathrm{div}\Big[(\nu + \nu_t)\big(\mathbf{grad}(\mathbf{u}) + \mathbf{grad}^T(\mathbf{u})\big)\Big] \tag{1.1}$$

$$\mathrm{div}(\mathbf{u}) = 0 \tag{1.2}$$

The following discussion focuses on two terms of the Navier-Stokes equations, the convection term and the pressure-gradient term.

1.1. *Convection term*

Two convection schemes have been tested. The first one is the default scheme used in *Code_Saturne* with RANS models and previous LES. It uses weighted coefficients and a reconstruction technique which is needed to account for the non-orthogonality which may occur at a cell face (figure 1). To evaluate the fluxes on the faces of a cell Ω_I, one has to compute the value of the velocity components at the center of the face F (cells Ω_I and Ω_J share face F in figure 1), $u_{i,F}$.

$$u_{i,F} = \frac{JO}{IJ}\, u_{i,I} + \frac{IO}{IJ}\, u_{i,J} + (\mathbf{grad}(u_i))_O . \overrightarrow{OF} \tag{1.3}$$

The main advantage of this scheme is that it maintains second-order accuracy in space on irregular Cartesian meshes and takes into account the geometrical non-orthogonality on unstructured meshes. However, the computation of $(\mathbf{grad}(u_i))_O$ in (1.3) is expensive if one wants to calculate this term implicitly at each time step.

The second scheme is easier to implement and has some interesting properties. It uses a symmetric formulation at the face, in which the velocity components at the face center are given by:

$$u_{i,F} = \frac{1}{2} u_{i,I} + \frac{1}{2} u_{i,J} \tag{1.4}$$

One can show, using discrete mass continuity, that the convection term which results from the discretization of the corresponding operator and use of (1.4) discretely conserves kinetic energy, provided that the transported velocity is estimated at $n+\frac{1}{2}$ with a Crank-Nicolson time-advancing scheme. This scheme, when tested for several canonical flows, shows good robustness. Note that in the algorithms where reconstruction is used for the convective term it is also used to calculate the quantities needed to estimate the other operators in the momentum equations (gradient, diffusion, ...). When the symmetric formulation for the convection term is used, no reconstruction is done for any of these fluxes. An intermediate scheme which uses the weighted coefficients (see (1.3)), but without the extrapolation with the gradient (the term $(\mathbf{grad}(u_i))_O.\overrightarrow{OF}$ in (1.3)), was found to be unstable and will not be discussed in detail.

1.2. *Pressure-gradient term*

Two algorithms have been also tested in *Code_Saturne* to insure the pressure/velocity coupling. The first algorithm is used by default in the code and employs Rhie & Chow's interpolation method. The pressure-velocity coupling is insured via the explicit pressure gradient at the previous time level in the momentum equations and by a projection method (SIMPLEC algorithm). The parameter α is set to 1 in (1.5), and $\mathbf{grad}_c$ and $\mathbf{grad}_f$ stand respectively for the cell and the face gradient in (1.5) and (1.6). This algorithm will be called **Alg1**.

$$\frac{\widetilde{\mathbf{u}}-\mathbf{u}^n}{\Delta t}+\ldots=-\mathbf{grad}_c(p^n)+\ldots \tag{1.5}$$

$$\mathrm{div}[\Delta t\ \mathbf{grad}_f(\delta p)]=\mathrm{div}\left(\widetilde{\mathbf{u}}+\alpha\ \Delta t\ \mathbf{grad}_c(p^n)-\alpha\ \Delta t\ \mathbf{grad}_f(p^n)\right) \tag{1.6}$$

The second algorithm (used also in CDP) does not take into account the explicit pressure gradient (cell gradient) in the momentum equations (see (1.7)). As the divergence of the pressure cell gradient may introduce odd-even decoupling on regular cartesian meshes, that is why this algorithm does not explicitly need the Rhie & Chow interpolation in the correction step (1.8). Odd-even decoupling will not occur as long as the Laplacian is coupling the cells (the same one used in the previous algorithm). This algorithm will be named **Alg2**.

$$\frac{\widetilde{\mathbf{u}}-\mathbf{u}^n}{\Delta t}+\ldots.=\ldots \tag{1.7}$$

$$\mathrm{div}[\Delta t\ \mathbf{grad}_f(p^{n+1})]=\mathrm{div}(\widetilde{\mathbf{u}}) \tag{1.8}$$

Moreover, for the correction step, two approaches are possible to correct the velocity. If p stands either for δp or p^{n+1} (resulting from the discrete Poisson equation), one has to correct the velocity field $\widetilde{u}$ obtained from the predictor step :

$$\mathbf{u}^{n+1} = \tilde{\mathbf{u}} - \Delta t \ \mathbf{grad}(p) \tag{1.9}$$

To compute $\mathbf{grad}(p)$, one can directly use Gauss' theorem to calculate the pressure gradient (in this case the correction step is $\mathbf{u}^{n+1} = \tilde{\mathbf{u}} - \Delta t \ \mathbf{grad}_c p$), or a least-squares method to minimize the difference between estimating the normal gradient of the pressure at the faces directly and using the pressure gradient at the cell centers. In the latter case, one has to solve (1.10) locally at each cell, where the unknown is $\delta\mathbf{u}$, S the surface of the face between the neighbors I and J, and $\mathbf{n}$ the normal to the face. In this case, the velocity is corrected with $\mathbf{u}^{n+1} = \tilde{\mathbf{u}} - \delta\mathbf{u}$.

$$\Sigma_J \Big(\delta\mathbf{u}(I).\mathbf{n}(F) - \Delta t \ \frac{\partial p}{\partial \mathbf{n}}(F) \Big) S^2 = 0 \tag{1.10}$$

2. Inviscid test cases

Several test cases have been considered. Inviscid flows have been chosen to check the conservation properties for kinetic energy and the robustness of the algorithms. The interest in inviscid flows is also motivated by the fact that high-Reynolds-number turbulent flows are close to this inviscid limit.

2.1. *Simulations on unstructured meshes with Cartesian topology*

In the case of uniform Cartesian grids, the two convection schemes give exactly the same result (because the faces are equidistant from the cell centers and the mesh is orthogonal). In addition, the two pressure-correction schemes described before are equivalent. Two test cases have been computed on Cartesian grids: 2D Taylor vortices and Homogeneous Isotropic Turbulence (HIT).

2.1.1. *Taylor vortices*

The fluid domain is a square whose side is 2π. The mesh contains 32×32 elements. Before analyzing the results obtained with the different algorithms proposed in this work, it is interesting to look at the performance of the usual algorithm used for RANS calculations. In this algorithm, the convective terms are evaluated using a blending of 20 % upwind and 80 % second-order-accurate central differences. This kind of scheme is typically used in RANS calculations but is not suitable for LES. Indeed, as one can clearly observe in figure 2, the effect of upwinding is to dramatically increase the numerical dissipation leading to a sharp decrease of the total kinetic energy. This result is obviously wrong, because for this inviscid periodic flow the total kinetic energy is supposed to be constant in time. Therefore, in the following, only fully-centered schemes will be considered.

Next, **Alg1** and **Alg2** are tested. Several time steps have been used and the total kinetic energy is plotted in figure 3 for a minimum ($\Delta t = 0.005$) and a maximum time step ($\Delta t = 0.1$). Figure 3 shows that the conservation of kinetic energy in both algorithms is not exact, due to time-splitting errors. **Alg2** is more dissipative than **Alg1** because the pressure is not included in the momentum equation during the prediction step. It is interesting to point out that simulations carried out with an explicit version of CDP showed better results for the conservation properties, comparable to those of **Alg1**. This is due to the fact that, because the convection term is treated explicitly, it contains the

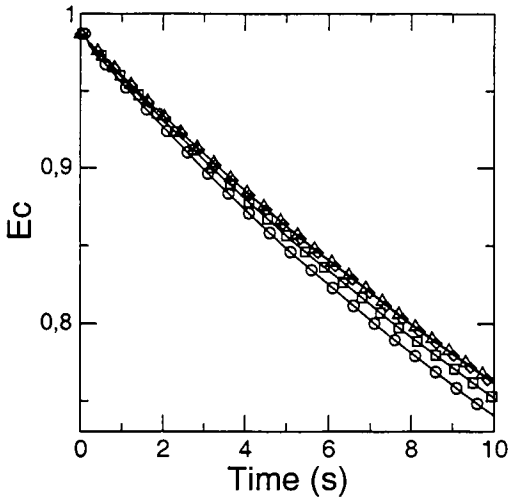

FIGURE 2. Taylor vortices - Evolution of kinetic energy with upwinding - $\Delta t = 0.1$: $\circ$, $\Delta t = 0.05$: $\square$, $\Delta t = 0.01$: $\diamond$, $\Delta t = 0.005$: $\triangle$

pressure from the previous corrector step, so in a sense the explicit version of CDP is closer to our **Alg1**. The other observation to be made is that in most LES simulations of complex flows (e.g. see section 3 and Mahesh et. al (2001)), the nondimensional time steps at which the calculations are run are considerably smaller than the time steps considered in these model problems; thus in most of these cases the time-stepping errors are not important even for **Alg2**.

Note that absolute conservation cannot be achieved in a colocated arrangement because of the Laplacian used in the Poisson equation. The mass flow contains the normal derivative (face gradient) of the corrected pressure (either δp or p^{n+1}) and the corrected velocity contains the cell gradient of this pressure. This is the case in both **Alg1** and **Alg2**. Figure 4 shows the time derivative of kinetic energy and the decay in energy due to the pressure gradient term for **Alg2**, with a very large time step $\Delta t = 0.1$. It shows that the term which is responsible for the loss in kinetic energy is the convection term, because the pressure term does not dissipate kinetic energy. Thus, the result of keeping the pressure gradient in the momentum equation even with the Rhie & Chow interpolation is to improve the conservation of the total kinetic energy. This is confirmed by the Homogeneous Isotropic Turbulence test case discussed next.

2.1.2. *Homogeneous Isotropic Turbulence*

A 32^3 mesh has been used in this case. The initial velocity field is generated using Comte-Bellot's experiment (AGARD (1998)). The viscosity is set to zero and the kinetic energy is computed at each time step. Figure 5 shows the decay of turbulent kinetic energy (which is the total kinetic energy in this case) using **Alg1** and **Alg2** and two different time steps. One can notice that the same behavior as in the previous test case is

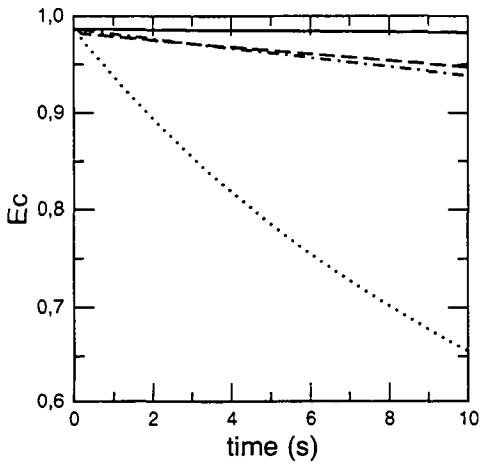

FIGURE 3. Taylor vortices - Evolution of kinetic energy - **Alg1** ($\Delta t = 0.1$) : dash, **Alg1**($\Delta t = 0.001$) : cont., **Alg2** ($\Delta t = 0.1$) : dot, **Alg2** ($\Delta t = 0.001$) : dash-dot.

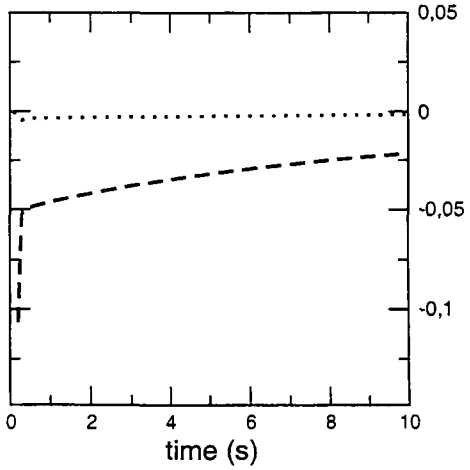

FIGURE 4. Taylor vortices - Contribution of the pressure gradient in the evolution of kinetic energy with **Alg2** and $\Delta t = 0.1$ - $\frac{\Delta E_c}{\Delta t}$: dash, $\mathbf{u}.\underline{\mathbf{grad}}(p)$: dot

observed; **Alg2** dissipates more energy than **Alg1**. The channel flow ($Re_\tau = 180$) test case has been computed with the two algorithms as well. The same behavior was observed.

2.2. *Simulations on fully-unstructured meshes*

The 2D flow corresponding to the Taylor problem has been simulated on a fully-unstructured mesh. This mesh is coarse and distorted and is representative of typical meshes used in industrial applications. In this case, both the effects of the convection scheme and of the pressure-correction algorithms described above can be tested.

In figures 6 and 7, all the cases have been run with the correction step based on the cell gradient. The effects of estimating the pressure gradient at cell centers using a least squares method will be discussed later. The simulations in figure 6 have been carried out with the reconstruction technique for the convection term - see (1.3). The calculations appear to be stable with both **Alg1** and **Alg2** when a relatively small time step is used. The numerical diffusion due to the projection step in this case is sufficient to dissipate the increase in the total kinetic energy. When the time step is decreased by a factor of 20, the calculations become unstable. This shows that for the inviscid case, the reconstruction method can entail an unstable computation.

Figure 7 shows the same case with smaller time steps, computed without any reconstruction technique - see eq. 1.4) - when the convection scheme is symmetric. The calculation is stable and visualization of the velocity field shows that the shape of the Taylor vortices is conserved in time. This proves that using this algorithm one can get robustness while maintaining accuracy, which is the main goal we want to achieve in simulations of complex flow of industrial interests using *Code_Saturne*. Note that the

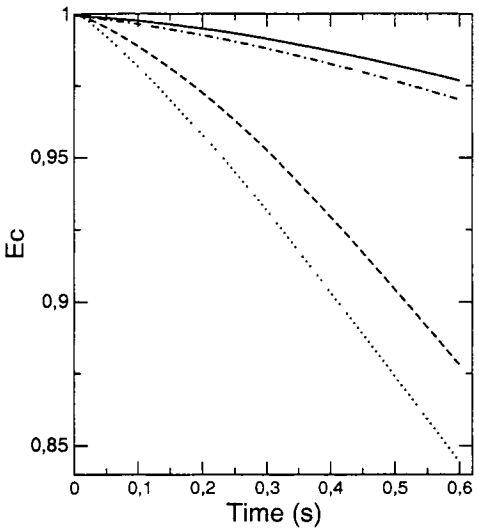

FIGURE 5. Homogemeous Isotropic Turbulence – Evolution of kinetic energy - **Alg1** ($\Delta t = 6 \times 10^{-3}$) : dash, **Alg1** ($\Delta t = 7.5 \times 10^{-4}$) : cont.,**Alg2** ($\Delta t = 6 \times 10^{-3}$) : dot, **Alg2** ($\Delta t = 7.5 \times 10^{-4}$) : dash-dot.

least-squares method used to reconstruct the pressure gradient at cell faces in the corrector step diverges, even when the symmetric formulation to compute the face velocity is used in the discretization of the convective terms. This seems to contradict the experience with CDP, which also uses this scheme and has shown good robustness when used to calculate a wide range of flows in complex geometries at high Reynolds numbers.

3. Turbulent cases – flow in a coaxial combustor geometry

The flow considered here consists of a primary jet issuing out of the core, and a swirling jet issuing out of an annular section around the core. These two streams of fluid mix as they enter the main coaxial combustor chamber. The flow is turbulent in both streams, with the Reynolds numbers around 26,000. As a result of the swirl, the streamlines diverge rapidly as they enter the main combustor chamber, and a recirculation region is set up. This is clearly visible in the contours of the instantaneous streamwise velocity component shown in figure 8. Sommerfeld & Qiu (1991) provide detailed measurements of this flow, including mean velocity components and their turbulent fluctuations at several stations inside the main combustor chamber. The inlet conditions are generated as explained in Pierce & Moin (2001) using a separate LES calculation. The inlet database, computational flow domain, mesh and the flow conditions are identical to those used in a simulation using CDP. The mesh in the present calculations contains 1.6 million cells.

The main purpose of this simulation is to show that the algorithms implemented in *Code_Saturne* can accurately simulate turbulence in complex configurations, are robust at high Reynolds numbers on fully unstructured meshes, and have an accuracy comparable to that of second-order-accurate structured codes and other unstructured solvers, in

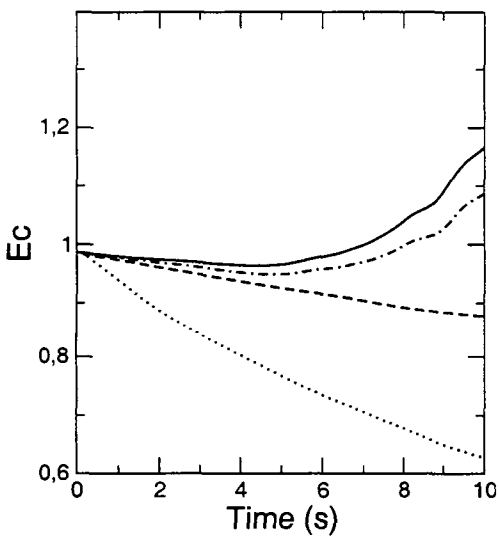

FIGURE 6. Evolution of kinetic energy - **Alg1** ($\Delta t = 0.1$) : dash, **Alg1** ($\Delta t = 0.005$) : cont., **Alg2** ($\Delta t = 0.1$) : dot, **Alg2** ($\Delta t = 0.005$) : dash-dot.

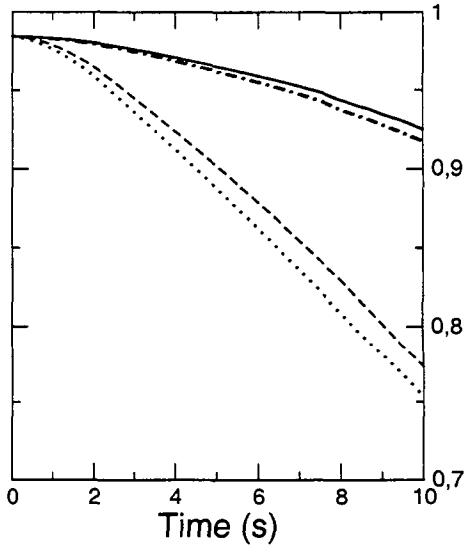

FIGURE 7. Evolution of kinetic energy - **Alg1** ($\Delta t = 0.005$) : dash, **Alg1** ($\Delta t = 6.2510^{-4}$) : cont., **Alg2** ($\Delta t = 0.005$) : dot, **Alg2** ($\Delta t = 6.2510^{-4}$) : dash-dot.

particular CDP, which uses an algorithm similar to **Alg2** and a symmetric formulation to evaluate the face velocity. In addition, sensitivity of the solution to the SGS model will be examined. Three simulations were performed using *Code_Saturne*, one in which a constant Smagorinsky SGS model with $C_s = 0.08$ was used, one in which no SGS model was used (coarse DNS) and, finally, one using a Smagorinsky SGS model with a coefficient calculated dynamically (we implemented the model described in Lilly (1992), with local averaging instead of the averaging in the homogeneous direction usually performed in structured codes). The algorithm employed in these simulations (**Alg1**) is the one that uses the Rhie & Chow interpolation and the symmetric formulation for the convection terms. No reconstruction technique was used.

A parallel version of *Code_Saturne* has been installed on an Origin 2000 machine and run on 32 processors to carry out these calculations.

The code was first run for approximately 100 nondimensional time units, defined with the mean inlet velocity in the core region and the annulus radius. Then statistics were computed over approximately the next 50 time units. Based on experience using CDP, these time intervals were found sufficient to eliminate the transients and to obtain converged statistics for this flow. As results using a second-order structured code and CDP were found to be very close (see Mahesh *et al.* 2001), we decided to plot only the experimental data, the results obtained with CDP, and the results of the three simulations performed with *Code_Saturne*. Figures 9, 10, 11, 12, 13 and 14 show, respectively, the mean

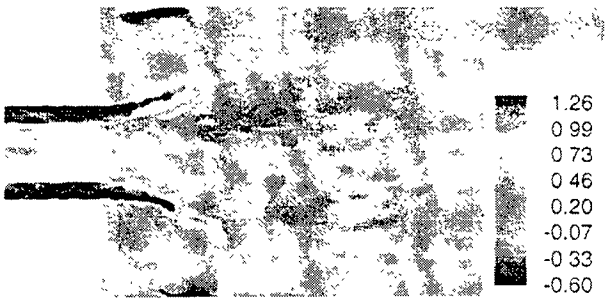

FIGURE 8. Instantaneous axial velocity with the dynamic model in *Code_Saturne* - Sommerfeld case

axial velocity, the mean fluctuations in the streamwise direction, the mean azimuthal velocity, the mean fluctuations in the azimuthal direction, the mean radial velocity, and the mean fluctuations in the radial direction.

Two-dimensional contour plots of the instantaneous and mean streamwise velocity (not shown) clearly show that in the simulation using the constant-coefficient Smagorinsky model the size of the recirculation bubble is not predicted correctly: the reattachment length of the detached shear layers is about 50% higher than that obtained from the experimental data or from the results obtained using CDP. This can be also inferred by comparing the location of the zero-velocity contour from the line plots of the streamwise velocity shown at different stations inside the main combustor chamber in figure 9. The other profiles also show a very poor level of quantitative prediction of the experimental measurements in contrast to the results using CDP.

As the prediction of this flow with CDP was shown to be very successful and the numerical methods used in the two codes are fairly similar, we suspected that the SGS model was responsible for the poor level of agreement with the experiment shown by the first calculation with *Code_Saturne*. Next we run a simulation without any SGS model (coarse DNS). This gave much better results, but a small overestimation of the recirculation zone compared to the experiment can still be observed from the line plots in figure 9. The other profiles also show a clear improvement in the prediction of the other velocity components and their turbulent fluctuations.

Finally, a calculation using a dynamic Smagorinsky model was run. Though the results show good agreement between CDP and this simulation for global quantities such as the size of the main recirculation region and the reattachment length on the lateral walls of the combustor, small differences remain when we compare the velocity statistics. Though some profiles obtained from the calculation with *Code_Saturne* are closer to the experimental data, on average CDP does a better job in predicting the flow, especially for the turbulent fluctuations. The differences between CDP and *Code_Saturne* results can be due to the different algorithms (CDP uses **Alg2** for the pressure correction) and to the somewhat different implementation of the dynamic model (explicit filtering).

4. Conclusions

Code_Saturne is an unstructured code, developed at *EDF*, which has been extensively validated using RANS models ($k-\varepsilon$ and *RSM* models). These turbulence models do

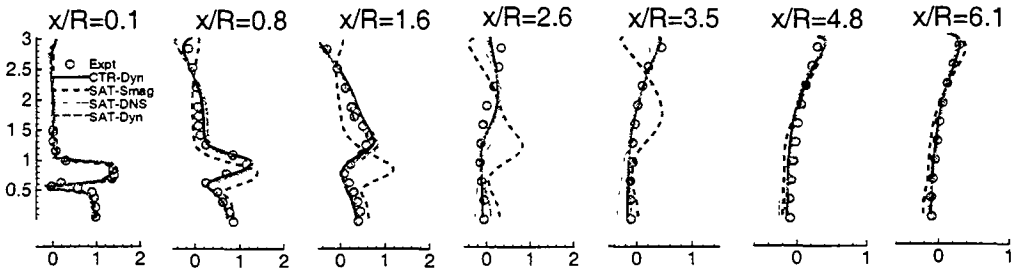

FIGURE 9. Mean axial velocity - Sommerfeld case

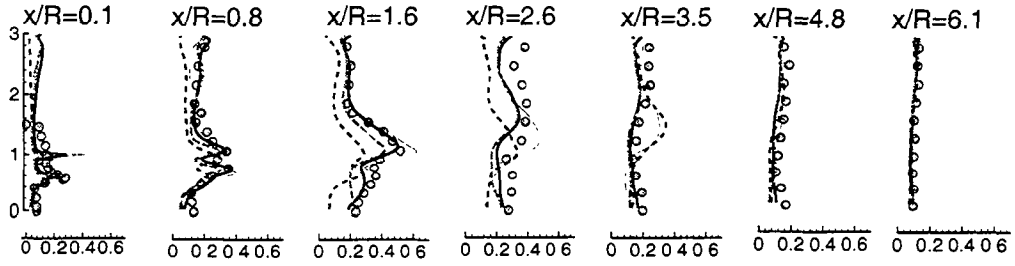

FIGURE 10. Mean axial fluctuations - Sommerfeld case

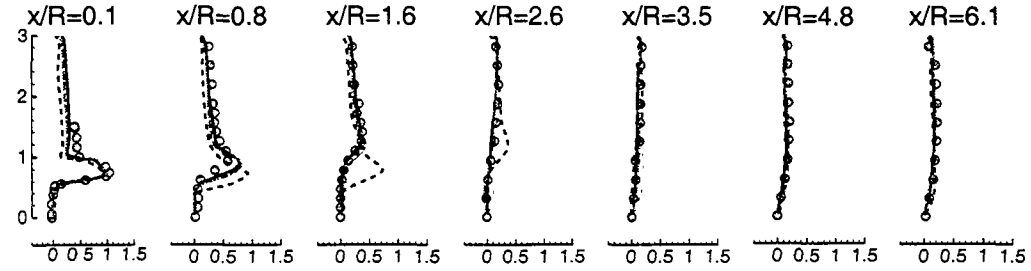

FIGURE 11. Mean tangential velocity - Sommerfeld case

not require strictly non-dissipative schemes. We extended *Code_Saturne* to solve the LES equations and noted that the numerical scheme must be non-dissipative. The use of non-dissipative schemes for high-Reynolds-number simulations is challenging because of the robustness problems. The proper way to address these problems is to try to insure conservation of kinetic energy, in a discrete sense, as accurately as possible. Several schemes have been tested in the present work, and we have shown that the usual Rhie & Chow interpolation for the pressure-gradient term is fairly acceptable for complex applications when only the mean quantities and Reynolds stresses are important. The convection term is more important; for fully-unstructured meshes, it has been shown that the use of the symmetric formulation for the convection term is more stable, as one can prove that the convection terms can be discretized in a way that fully conserves kinetic energy if the time-splitting errors are negligible. This study converged to a non-dissipative algorithm which was implemented in *Code_Saturne* and validated for several canonical flows as well as more complex turbulent flows. Future work will consist in applying this algorithm to simulate other complex flows of interest to *EDF*.

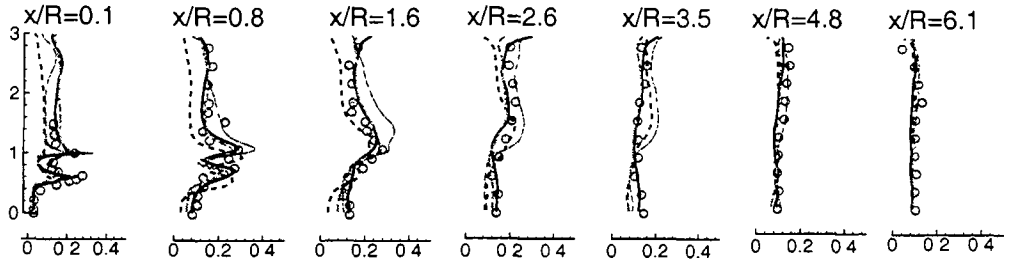

FIGURE 12. Mean tangential fluctuations - Sommerfeld case

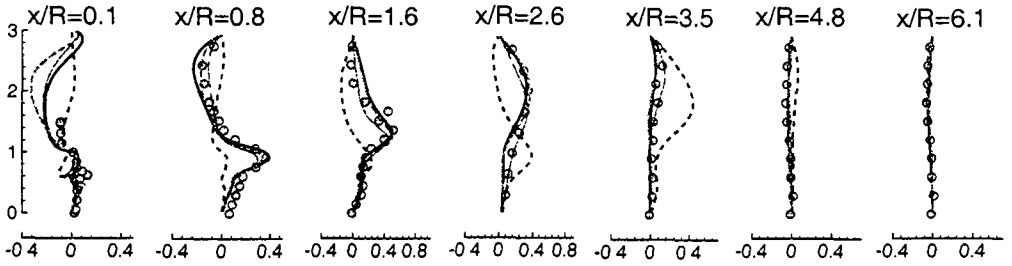

FIGURE 13. Mean radial velocity - Sommerfeld case

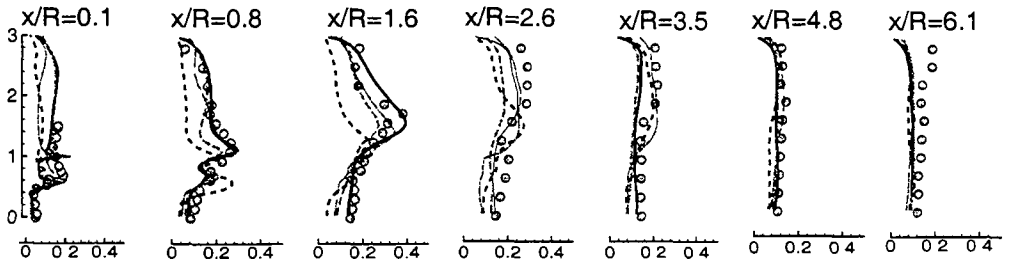

FIGURE 14. Mean radial fluctuations - Sommerfeld case

REFERENCES

ADVISORY GROUP FOR AEROSPACE RESEARCH AND DEVELOPMENT 1998 A selection of test cases for the validation of large-eddy simulation of turbulent flows. AGARD Advisory Rept. AR-345, North Atlantic Treaty Organization.

BENHAMADOUCHE, S. & LAURENCE, D. 2002 LES, COARSE LES, and transient RANS comparisons on the flow across a tube bundle. *5th International Symposium on Engineering Turbulence Modelling and Measurements Mallorca, Spain, 16-18 September 2002* (W. Rodi and N. Fueyo, eds.), Elsevier.

GARIBIAN, V., BENHAMADOUCHE, S. & LAURENCE, D. 2001 Schémas numériques conservant l'énergie cinétique avec une discrétisation colocalisée - Application à la Simulation des Grandes Échelles (LES). EDF report, HI-83/01/29.

LILLY, D. K. 1992 A proposed modification of the Germano subgrid-scale closure method. *Phys. Fluids. A* **4**, 633-635.

MAHESH, K., CONSTANTINESCU, G. & MOIN, P. 2000 Large Eddy Simulation of gas

turbine combustors. *Annual Research Briefs*, Center for Turbulence Research, NASA Ames/Stanford Univ., 219-229.

MAHESH, K., CONSTANTINESCU, G., APTE S., IACCARINO, G. & MOIN, P. 2001 Large Eddy Simulation of gas turbine combustors. *Annual Research Briefs*, Center for Turbulence Research, NASA Ames/Stanford Univ., 3-19.

PIERCE, C. D. & MOIN, P. 1998 Method for generating equilibrium swirling inflow conditions. *AIAA Journal* **36**, 1325-1330.

PIERCE, C.D. & MOIN, P. 2001 Progress variable approach for large eddy simulation of turbulent combustion. *Report TF-80*, Flow Physics and Computation Division, Mechanical Engineering Dept., Stanford University, Stanford, California.

SOMMERFELD, M. & QIU, H.H. 1991 Detailed measurements in a swirling particulate two-phase flow by a phase-Doppler anemometer *Int. J. Heat Fluid Flow* **12**, 20-28.

Discontinuous Galerkin methods for turbulence simulation

By S. Scott Collis †

A discontinuous Galerkin (DG) method is formulated, implemented, and tested for simulation of compressible turbulent flows. The method is applied to turbulent channel flow at low Reynolds number, where it is found to successfully predict low-order statistics with fewer degrees of freedom than traditional numerical methods. This reduction is achieved by utilizing local *hp*-refinement such that the computational grid is refined simultaneously in all three spatial coordinates with decreasing distance from the wall. Another advantage of DG is that Dirichlet boundary conditions can be enforced weakly through integrals of the numerical fluxes. Both for a model advection-diffusion problem and for turbulent channel flow, weak enforcement of wall boundaries is found to improve results at low resolution. Such weak boundary conditions may play a pivotal role in wall modeling for large-eddy simulation.

1. Introduction

In this paper we formulate, implement, and apply a discontinuous Galerkin (DG) method for the simulation of compressible turbulent flows. Discontinuous Galerkin can be thought of as a hybrid of finite-volume and finite-element methods that has a number of potential advantages including: high-order accuracy on unstructured meshes, local *hp*-refinement, weak imposition of boundary conditions, local conservation, and orthogonal hierarchical bases that support multiscale turbulence modeling (Hughes *et al.* 2000; Collis 2001, 2002). The interested reader should consult the review of Cockburn (1999) and Cockburn *et al.* (2000) for a recent update on the status of discontinuous Galerkin. Since the DG method is ideally suited for hyperbolic or nearly hyperbolic systems, we believe that DG may be a particularly attractive method for high-Reynolds-number *compressible* turbulent flows in complex geometries. This paper takes a first step in applying DG to turbulent flows by considering low-Reynolds-number DNS of compressible turbulent channel flow. We note, before proceeding, that there is considerable ongoing research on DG methods (see Cockburn *et al.* 2000) and we have greatly benefited from the work of Cockburn and co-workers, Karniadakis and co-workers, and Bassi and Rebay.

2. Formulation

Consider the compressible Navier–Stokes equations in strong form

$$\boldsymbol{U}_{,t} + \boldsymbol{F}_{i,i} - \boldsymbol{F}^v_{i,i} = \mathbf{S} \quad \text{in } \Omega, \tag{2.1a}$$

$$\boldsymbol{U}(\boldsymbol{x}, 0) = \boldsymbol{U}_0(\boldsymbol{x}) \quad \text{at } t = 0, \tag{2.1b}$$

where $\boldsymbol{U} = \{\rho, \rho\boldsymbol{u}, \rho e\}^T$ is the vector of conserved variables, ρ is the fluid density, $\boldsymbol{u}$ is the fluid velocity vector, and e is the total energy per unit mass. The inviscid and viscous

† Rice University, Houston, TX 77005, USA

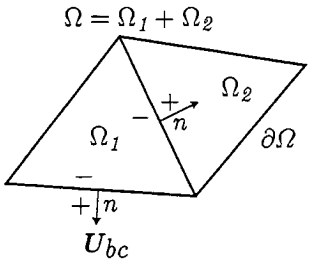

FIGURE 1. Schematic of DGM discretization

flux vectors in the ith coordinate direction are $\boldsymbol{F}_i(\boldsymbol{U})$ and $\boldsymbol{F}_i^v(\boldsymbol{U})$, and $\mathbf{S}$ is a source term, including body forces in the momentum equations and a heat source in the energy equation. Equation (2.1a) is solved subject to appropriate boundary conditions, which must be specified for each problem of interest; a state equation, such as the ideal gas equation; and constitutive laws that define fluid properties such as viscosity and thermal conductivity as functions of the conserved variables. Due to space limitations, we do not explicitly define the flux vectors, state equation, or constitutive relations, but instead refer the reader to standard texts such as Hirsch (1988).

The fixed spatial domain for the problem is denoted by Ω, which is an open, connected, bounded subset of $\mathbb{R}^d$, $d = 2$ or 3, with boundary $\partial\Omega$. Let $\mathcal{P}_h$ be a partition of the domain Ω into N subdomains Ω_e where

$$\bar{\Omega} = \bigcup_{e=1}^{N} \bar{\Omega}_e \quad \text{and} \quad \Omega_e \cap \Omega_f = \emptyset \quad \text{for} \quad e \neq f\,. \tag{2.2}$$

Starting from the strong form of the compressible Navier–Stokes equations (2.1a), we consider a single subdomain, Ω_e, multiply by a weighting function $\boldsymbol{W}$ which is continuous in Ω_e, and integrate the flux terms by parts

$$\int_{\Omega_e} \left(\boldsymbol{W}^T \boldsymbol{U}_{,t} + \boldsymbol{W}_{,i}^T (\boldsymbol{F}_i^v - \boldsymbol{F}_i) \right) dx + \int_{\partial\Omega_e} \boldsymbol{W}^T \left(\boldsymbol{F}_n - \boldsymbol{F}_n^v \right) ds = \int_{\Omega_e} \boldsymbol{W}^T \mathbf{S}\, ds \tag{2.3}$$

where $\boldsymbol{F}_n = \boldsymbol{F}_i n_i$. If the solution were assumed to be continuous and this equation were summed over all the elements in $\mathcal{P}_h$, then all the flux terms would telescope to the boundary $\partial\Omega$ and we would obtain the standard continuous Galerkin form of the compressible Navier–Stokes equations. However, in discontinuous Galerkin, one instead allows the solution and weighting functions to be discontinuous across element interfaces (see figure 1) and the solutions on each element are coupled using appropriate numerical fluxes for both the inviscid flux $\boldsymbol{F}_n(\boldsymbol{U}) \to \widehat{\boldsymbol{F}}_n(\boldsymbol{U}^-, \boldsymbol{U}^+)$ and the viscous flux, $\boldsymbol{F}_i^v(\boldsymbol{U}, \boldsymbol{U}_{,j}) \to \widehat{\boldsymbol{F}}_i^v(\boldsymbol{U}^-, \boldsymbol{U}_{,j}^-, \boldsymbol{U}^+, \boldsymbol{U}_{,j}^+)$. Introducing numerical fluxes and summing over all elements yields

$$\sum_{e=1}^{N} \int_{\Omega_e} \left(\boldsymbol{W}^T \boldsymbol{U}_{,t} + \boldsymbol{W}_{,i}^T (\boldsymbol{F}_i^v - \boldsymbol{F}_i) \right) dx + \sum_{e=1}^{N} \int_{\partial\Omega_e} \boldsymbol{W}^T \left(\widehat{\boldsymbol{F}}_n(\boldsymbol{U}^-, \boldsymbol{U}^+) - \widehat{\boldsymbol{F}}_n^v(\boldsymbol{U}^-, \boldsymbol{U}_{,j}^-, \boldsymbol{U}^+, \boldsymbol{U}_{,j}^+) \right) ds = \sum_{e=1}^{N} \int_{\Omega_e} \boldsymbol{W}^T \mathbf{S}\, ds \tag{2.4}$$

where the $\boldsymbol{U}^+$ and $\boldsymbol{U}^-$ states are defined in figure 1. For an element edge on the physical

boundary $\partial\Omega$, $\boldsymbol{U}^+ = \boldsymbol{U}_{bc}$. Likewise, for inter-element boundaries, $\boldsymbol{U}^+$ comes from the neighboring element. Thus, all interface and boundary conditions are set through the numerical fluxes. Rewriting (2.4) in a more compact notation, the discontinuous Galerkin method is:

Given $\boldsymbol{U}_0 = \boldsymbol{U}_0(\boldsymbol{x})$, for $t \in (0,T)$, find $\boldsymbol{U}(\boldsymbol{x},t) \in \mathcal{V}(\mathcal{P}_h) \times H^1(0,T)$ such that $\boldsymbol{U}(\boldsymbol{x},0) = \boldsymbol{U}_0(\boldsymbol{x})$ and

$$B_{DG}(\boldsymbol{W},\boldsymbol{U}) = (\boldsymbol{W},\mathbf{S}) \qquad \forall \boldsymbol{W} \in \mathcal{V}(\mathcal{P}_h), \tag{2.5}$$

where $\mathcal{V}(\mathcal{P}_h)$ is the broken space defined in Baumann & Oden (1999). If $\mathcal{V}(\mathcal{P}_h)$ is restricted to a space of continuous functions, then one recovers the classical continuous Galerkin approximation upon using the consistency properties of the numerical fluxes (Cockburn 1999).

While there is a wide range of choices for both the inviscid and viscous numerical fluxes (see Cockburn (1999) for a thorough review), we have initially chosen to use a Lax–Friedrichs method for the Euler flux

$$\widehat{\boldsymbol{F}}_n(\boldsymbol{U}^-,\boldsymbol{U}^+) = \frac{1}{2}\left(\boldsymbol{F}_n(\boldsymbol{U}^-) + \boldsymbol{F}_n(\boldsymbol{U}^+)\right) + \lambda_m\left(\boldsymbol{U}^- - \boldsymbol{U}^+\right) \tag{2.6}$$

where λ_m is the maximum, in absolute value, of the eigenvalues of the Euler Jacobian $\boldsymbol{A}_n = \partial \boldsymbol{F}_n / \partial \boldsymbol{U}$.

For the numerical viscous flux, we use the method of Bassi & Rebay (1997). First, a "jump savvy" gradient of the state, $\boldsymbol{\sigma}_j \sim \boldsymbol{U}_{,j}$ is computed by solving

$$\sum_{e=1}^{N} \int_{\Omega_e} \boldsymbol{V}^T \boldsymbol{\sigma}_j \, d\boldsymbol{x} = -\sum_{e=1}^{N} \int_{\Omega_e} \boldsymbol{V}_{,j}^T \boldsymbol{U} \, d\boldsymbol{x} + \sum_{e=1}^{N} \int_{\partial\Omega_e} \boldsymbol{V}^T \widehat{\boldsymbol{U}} n_j \, ds \qquad \forall \boldsymbol{V} \in \mathcal{V}(\mathcal{P}_h) \tag{2.7}$$

for each direction, j, where

$$\widehat{\boldsymbol{U}} = \frac{1}{2}\left(\boldsymbol{U}^- + \boldsymbol{U}^+\right) . \tag{2.8}$$

The Bassi–Rebay viscous flux is then computed using

$$\widehat{\boldsymbol{F}}_n^v(\boldsymbol{U}^-,\boldsymbol{\sigma}_j^-,\boldsymbol{U}^+,\boldsymbol{\sigma}_j^+) = \frac{1}{2}\left(\boldsymbol{F}_n^v(\boldsymbol{U}^-,\boldsymbol{\sigma}_j^-) + \boldsymbol{F}_n^v(\boldsymbol{U}^+,\boldsymbol{\sigma}_j^+)\right) . \tag{2.9}$$

While this method is known to be only "weakly stable," (Arnold *et al.* 2002) we have not encountered any difficulties for the problems considered here, and this method has been used successfully in the past (Bassi & Rebay 1997). In the future, we will consider other, provenly-stable, numerical fluxes for the viscous terms, and the reader is referred to Arnold *et al.* (2002) for an extensive discussion of the advantages and disadvantages of a wide range of viscous fluxes for use in discontinuous Galerkin discretizations.

In setting boundary conditions weakly through the numerical fluxes, one must construct a state, $\boldsymbol{U}_{bc}$, that enforces the appropriate boundary conditions, and Atkins (1997) provides a discussion of the important issues involved in selected $\boldsymbol{U}_{bc}$. For the Navier–Stokes calculations reported here, we use the following approach. At far-field boundaries $\boldsymbol{U}_{bc}$ is set to freestream values. At isothermal wall boundaries, we evaluate $\boldsymbol{U}_{bc}$ separately for the convective and viscous fluxes. Let $q_1 = (u^- n_y - v^- n_x) n_y$ and

$q_2 = (v^- n_x - u^- n_y) n_x$ then the reconstructed state at a wall for the convective flux is

$$\boldsymbol{U}_{bc} = \begin{Bmatrix} \rho^- \\ \rho^- q_1 \\ \rho^- q_2 \\ \rho^- e^- + 0.5\rho^-(q_1^2 + q_2^2) \end{Bmatrix} . \tag{2.10}$$

This state enforces the no-penetration condition which is appropriate for both inviscid and viscous calculations. For the viscous flux, the no-slip condition is enforced using

$$\boldsymbol{U}_{bc} = \begin{Bmatrix} \rho^- \\ 0 \\ 0 \\ \rho^- T_w/(\gamma(\gamma-1)M^2) \end{Bmatrix} \tag{2.11}$$

where T_w is the prescribed wall temperature, γ is the ratio of specific heats, and M is the reference Mach number.

By way of summary, the discontinuous Galerkin method is a hybrid of finite-element and finite-volume methods, where solutions are continuous within an element but discontinuous across element interfaces, and elements are coupled via *numerical fluxes* on element interfaces. Discontinuous Galerkin has several potential advantages including: (1) Spectral accuracy on arbitrary meshes, (2) Local *hp*-refinement, (3) Boundary conditions are imposed weakly through numerical flux, (4) Local conservation allows for different fidelity models on neighboring elements, (5) Orthonormal hierarchical basis on each element readily supports multiscale turbulence models, and (6) DG works best near the hyperbolic limit making it potentially valuable for high Reynolds number turbulence. A thorough review of the DG method is available (Cockburn 1999) while a more complete description of DG for turbulence simulation including a discussion of multi-scale turbulence modeling is given in (Collis 2002).

3. Discretization and implementation

For every element $\Omega_e \in \mathcal{P}_h$ we define the finite-dimensional space $P_{p_e}(\hat{\Omega})$ of polynomials of degree $\leq p_e$ defined on a master element $\hat{\Omega}$. Then

$$P_{p_e}(\Omega_e) = \left\{ \phi | \phi = \hat{\phi} \boldsymbol{J}_{\Omega_e}^{-1}, \hat{\phi} \in P_{p_e}(\hat{\Omega}) \right\} \tag{3.1}$$

where $\boldsymbol{J}_{\Omega_e}$ is the Jacobian of the transformation of element Ω_e to the master element and

$$\mathcal{V}_p(\mathcal{P}_h) = \left(\prod_{e=1}^{N} P_{p_e}(\Omega_e) \right)^m \subset \mathcal{V}(\mathcal{P}_h) \tag{3.2}$$

where m is the number of conserved variables; $m = 5$ in three dimensions.

Thus, the semi-discrete discontinuous Galerkin method is: Given $\boldsymbol{U}_0 = \boldsymbol{U}_0(\boldsymbol{x})$, for $t \in (0,T)$, find $\boldsymbol{U}_h(\boldsymbol{x},t) \in \mathcal{V}_p(\mathcal{P}_h) \times H^1(0,T)$ such that

$$B_{DG}(\boldsymbol{W}_h, \boldsymbol{U}_h) = (\boldsymbol{W}_h, \mathbf{S}), \qquad \forall \boldsymbol{W}_h \in \mathcal{V}_p(\mathcal{P}_h) . \tag{3.3}$$

We utilize the family of orthogonal, hierarchical bases formed from tensor products of Jacobi polynomials, as described in Karniadakis & Sherwin (1999), which are supported in a wide range of elements types in two and three dimensions. For time advancement, we currently use the third-order TVD-RK method (Shu 1988; Shu & Osher 1988)

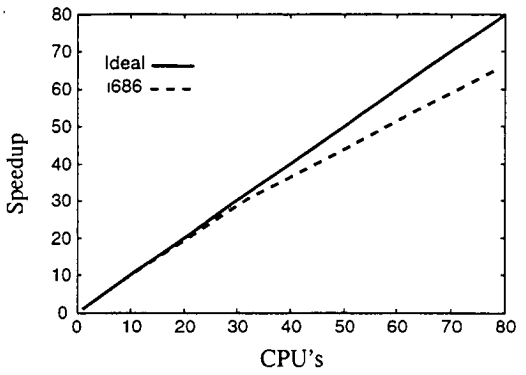

FIGURE 2. Typical parallel speedup for DG implementation on a Pentium IV Beowulf cluster.

The DG formulation presented above has been implemented using object-oriented programming (OOP) in fully modern ANSI/ISO C++ using the Standard Template Library and generic programming concepts. For efficiency, all kernel computations are performed using the ATLAS library, and the code runs on a number of operating systems including Linux, Windows, and SGI Irix. The code is implemented as an element library that supports all the operations required for discontinuous Galerkin, and we have used this library to implement specific solvers for advection-diffusion, Burgers, wave, linearized-Euler, Euler, Navier–Stokes equations. Due to the inherent locality in the discontinuous Galerkin discretization, parallel implementation is particularly easy and efficient. We use the MPI-2 library (including parallel MPI-IO) and parallel efficiency results are shown in figure 2 for our Pentium IV Beowulf cluster demonstrating excellent scaling.

4. Weak boundary conditions

One of the issues that arises in using discontinuous Galerkin methods is that Dirichlet boundary conditions are most naturally enforced weakly through the numerical fluxes. While similar "weak" boundary conditions have been used for far-field nonreflecting boundary conditions in finite-difference discretizations (see e.g. Poinsot & Lele (1992); Thompson (1987)) the use of weak boundary conditions for wall-type boundary conditions is less common, especially in the flow physics community. In the computational mechanics and applied mathematics communities there has been prior work on weak enforcement of Dirichlet boundary conditions in the continuous Galerkin method by Babuska (1973) and Nitsche (1971) and these methods are related to discontinuous Galerkin (Arnold *et al.* 2002). Likewise, the recent work of Layton (1999) provides theoretical considerations for weakly enforced Dirichlet boundary conditions for the Stokes problem that are motivated by observations of improved solution quality compared to hard Dirichlet boundary conditions.

While one can always set "hard" Dirichlet boundary conditions in any discretization (including DG), it is interesting to compare the performance of hard boundary conditions with weak enforcement through the numerical fluxes as described above. As an example, consider the simple steady forced advection-diffusion problem

$$u_{,x} = 1 + \nu u_{,xx} \tag{4.1}$$

with boundary conditions $u(0) = u(1) = 0$ and diffusivity $\nu = 0.01$. Figure 3 shows results computed using a discontinuous Galerkin discretization with two $p = 6$ elements and

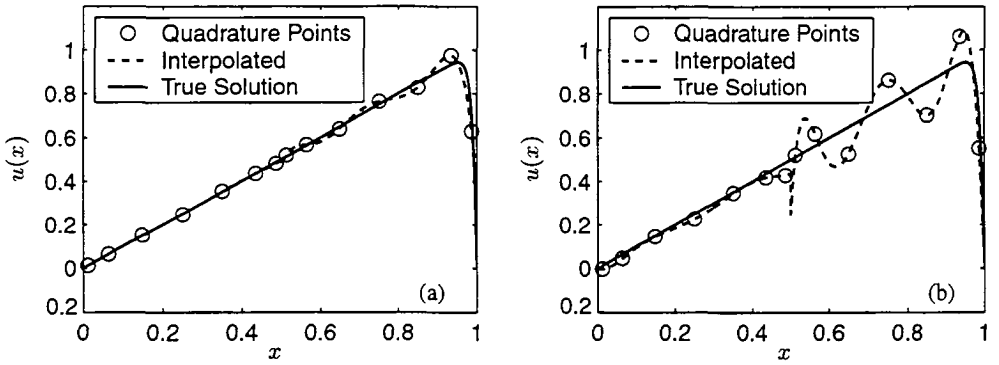

FIGURE 3. Weak (a) and hard (b) Dirichlet boundary conditions for an advection-diffusion problem

BC	L_∞	L_2	H_1
Weak	0.374	0.0198	2.00
Hard	0.251	0.0850	3.35

TABLE 1. Errors in advection diffusion solutions

both hard and weak enforcement of the Dirichlet boundary conditions. This discretization was intentionally selected to be coarse in order to highlight the differences between the two solutions. One clearly sees that oscillations are more pronounced when a hard boundary condition is used. Conversely, while oscillations are less in the weak case, the boundary condition on the right side (inside the boundary layer) is only approximately satisfied; $u(1) = 0.374$ instead of zero. Table 1 compares the error in the solution in the L_∞, L_2, and H_1 norms. Consistent with the graphical results, the solution with weak Dirichlet boundary conditions has four times less error in L_2 and is also better in H_1. However, the solution with weak boundary conditions is slightly worse in L_∞ and this is directly due to the error in the boundary value. Discarding a small region near $x = 1$, the weak solution is also better in L_∞. While these results are certainly not conclusive, they are indicative of the potential benefit to be gained from weak enforcement of Dirichlet boundary conditions that are naturally obtained from a DG discretization. Philosophically speaking, one should not enforce boundary conditions any more accurately then the error in the interior solution. Doing so tends to over-constrain the interior solution, typically leading to oscillations as seen in figure 3(b). By weakly enforcing boundary conditions one obtains solutions that still feel the influence of the boundary through the numerical fluxes, but in a manner that is consistent with the accuracy of the interior solution, leading to improved solutions away from the wall. Given the importance of wall boundary conditions for near-wall turbulence, we will pay particular attention to the success of the weak boundary condition throughout the following discussion.

5. Flow over a circular cylinder

Before applying our DG formulation to a turbulent flow, we begin by considering a benchmark problem of both steady and unsteady flow over a circular cylinder.

	DG		DG		FD		Experiment	
Re	$p = 4$		$p = 6$		6^{th} order			
	s/d	C_d	s/d	C_d	s/d	C_d	s/d	C_d
20	0.96	2.125	0.96	2.124	0.93	1.98	0.9	2.01
40	2.39	1.589	2.39	1.589	2.36	1.50	2.1	1.48

TABLE 2. Drag and separation length for laminar flow over a circular cylinder, with comparison to prior computations and experiments. The computational and experimental data are taken from Visbal (1986).

5.1. *Steady flow*

Consider the steady, laminar flow of air past an isothermal circular cylinder kept at the freestream temperature. The freestream Mach number is $M = 0.2$ and results are reported for two Reynolds numbers: 20 and 40. By considering a series of different domain sizes, we eventually selected a domain of $\Omega = [-15, 30] \times [-30, 30]$ as sufficiently large to prevent adverse influence on the net drag and length of the separation bubble. A block structured mesh using 812 quadrilaterals was generated using a special purpose grid generator (Tezduyar 1991) and each quadrilateral has polynomial order of either $p = 4$ or $p = 6$. Table 2 compares the current DG results for the total drag coefficient, C_d, and separation bubble length, s/d, with prior high-order finite-difference computations and experiments. The DG results for both $p = 4$ and $p = 6$ are nearly identical, indicating that these quantities are converged. The DG results are within about 7% of the experimental results, which is a negligible difference given the difficulty of performing measurments at such low Reynolds numbers. Comparing the DG results to the prior finite-difference calculations of Visbal (1986) yields a difference of about 6% in C_d and less than 3% in s/d. Interestingly, Morgan *et al.* (2002) recently performed simulations using a block-parallel version of the same solver used by Visbal (1986) and they report up to 3% difference in both s/d and C_d. While the source of the discrepencies between these three codes is not known, the DG results are converged with regard to both domain size and resolution.

5.2. *Vortex shedding*

Next, consider unsteady vortex shedding from a circular cylinder. The Reynolds number based on diameter and freestream velocity is $Re = 100$, the freestream Mach number is $M_\infty = 0.2$ and an isothermal condition is enforced at the cylinder surface with $T_w = T_\infty$. We have performed simulations over a range of domain sizes and have investigated both h and p-refinement to establish the convergence properties of the method. For brevity, we show results only for a relatively large rectangular domain, of size $x_1 \in [-15, 30]$ and $x_2 \in [-30, 30]$, using 812 quadrilateral elements with a tensor-product basis of Legendre polynomials on each element, where the polynomial order varies from $p = 5$ to 8. We note in passing that this domain was found to be sufficiently large to prevent far-field boundary influence on the solution. Table 3 documents the convergence of the Strouhal number St, peak-to-peak lift coefficient ΔC_l, and average drag coefficient C_d with polynomial order. We see that even with $p = 4$ all quantities are accurate to three significant figures. When $p = 8$ the average drag coefficient is converged to at least 5 significant figures. The converged Strouhal number is $St = 0.1653$ which is in excellent agreement with the experimental value of 0.165 (Williamson 1989). For both the steady and unsteady cylinder flows, the weak implementation of wall boundary conditions is found to provide excellent results, even for rather coarse discretizations.

p	St	ΔC_l	C_d
4	0.1652	0.6951	1.4104
5	0.1652	0.6953	1.4105
6	0.1653	0.6958	1.4106
7	0.1653	0.6960	1.4107
8	0.1653	0.6960	1.4107
Exp†	0.165	–	–

TABLE 3. Convergence with polynomial order for vortex shedding from a circular cylinder at $Re = 100$. †Experimental data is from Williamson (1989)

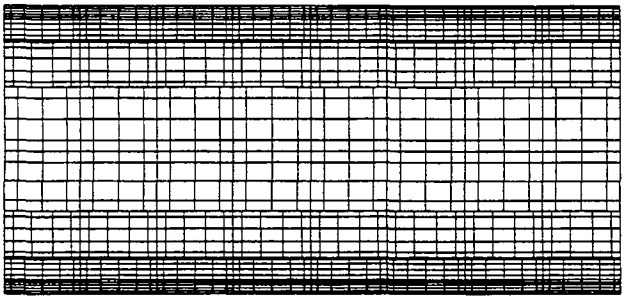

FIGURE 4. Cross-stream (z–y) quadrature grid for the stretched mesh with $p = 5, 4, 3$.

6. Fully-developed channel flow

We now consider fully-developed turbulent flow in a plane channel with coordinates $x = x_1$ in the streamwise direction, $y = x_2$ in the wall-normal direction, and $z = x_3$ in the spanwise direction. The flow is assumed to be periodic in the streamwise and spanwise directions where the box size is selected so that the turbulence is adequately decorrelated in both directions. Coleman *et al.* (1995) provide excellent documentation of DNS results for compressible channel flows at low Re_τ.

As a first step towards utilizing DG for turbulent flows, we have performed DNS at $Re_\tau = 100$ with a centerline Mach number of $M_c = 0.3$ so that comparisons can be made directly to prior incompressible results (see e.g. Kim *et al.* (1987); Moser *et al.* (1999)). Following Coleman *et al.* (1995), we use a cold, isothermal wall so that internal energy created by molecular dissipation is removed from the domain via heat transfer across the walls, allowing a statistically steady state to be achieved. The bulk mass flow is held constant by the addition of an x_1-momentum source on the right-hand side of (2.1a).

The computational domain is $(4\pi, 2, 4\pi/3)$ and this is discretized with an array of $8 \times 8 \times 8$ elements yielding a total of 512 elements. Exploiting the flexibility of the DG discretization, we use both h and p refinement to more efficiently resolve flow features near the wall. In particular, two wall-normal distributions of elements are investigated. We first use a stretched mesh in the wall-normal direction where the grid points are given by

$$y_j = \frac{\tanh(c_s(2j/N_y - 1))}{\tanh c_s} + 1\,, \qquad j = 0, 1, \ldots, N_y \tag{6.1}$$

where $N_y = 8$. For this mesh, we reduce the polynomial order away from the wall, starting with two layers of $p = 5$ elements, then a layer of $p = 4$ followed by a layer of $p = 3$ elements near the centerline. Thus, moving from the bottom wall to the top

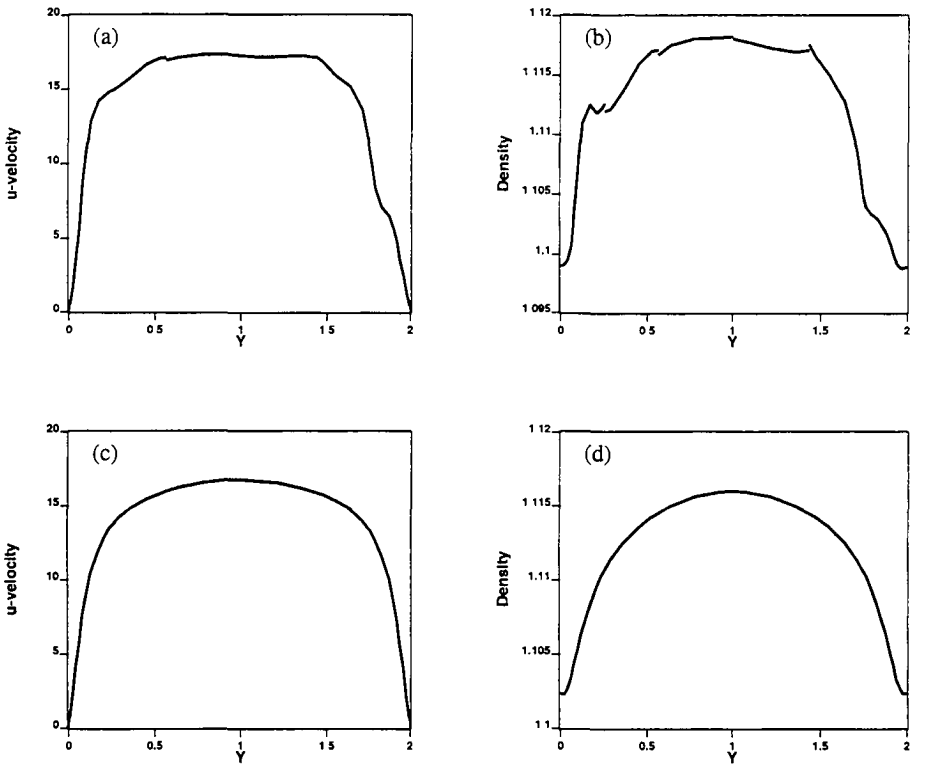

FIGURE 5. Discontinuities in instantaneous and averaged mean-flow profiles, $Re_\tau = 100$: (a) instantaneous u, (b) instantaneous ρ, (c) average u, (d) average ρ.

wall, the element order varies like: {5, 5, 4, 3, 3, 4, 5, 5} resulting in a total of 79,488 degrees of freedom. Note that the flexibility of the DG method makes it possible to coarsen simultaneously in *all three* coordinate directions as one moves away from the wall. The crossflow quadrature grid for the stretched mesh is shown in figure 4. We also have performed simulations using a uniform h mesh in the wall-normal direction but again with variable p order. For this mesh, two p distributions were considered: a low-resolution case with $p = \{5, 5, 4, 3, 3, 4, 5, 5\}$ yielding 79,488 degrees of freedom and a high-resolution case with $p = \{6, 6, 5, 4, 4, 5, 6, 6\}$ resulting in 131,456 degrees of freedom. In all cases, we use third-order TVD-RK time advancement with $\Delta t = 0.0001$. This time step is a factor of 10 smaller than that typically used in our incompressible code (Collis *et al.* 2000) because the incompressible code treats wall-normal viscous terms implicitly. We are currently enhancing our DG code to support implicit time-advancement.

We also note that computing turbulence statistics from a DG solution requires a substantial coding effort, so that currently we compute only mean and rms quantities. Higher-order statistics and spectra will be presented in the future.

We begin by plotting typical instantaneous and average u and ρ profiles for the stretched mesh solution in figure 5. In plotting all the results shown in this paper, no smoothing or other postprocessing has been done to remove the discontinuities inherent in a DG discretization. Thus, we can clearly see discontinuities in the instantaneous pro-

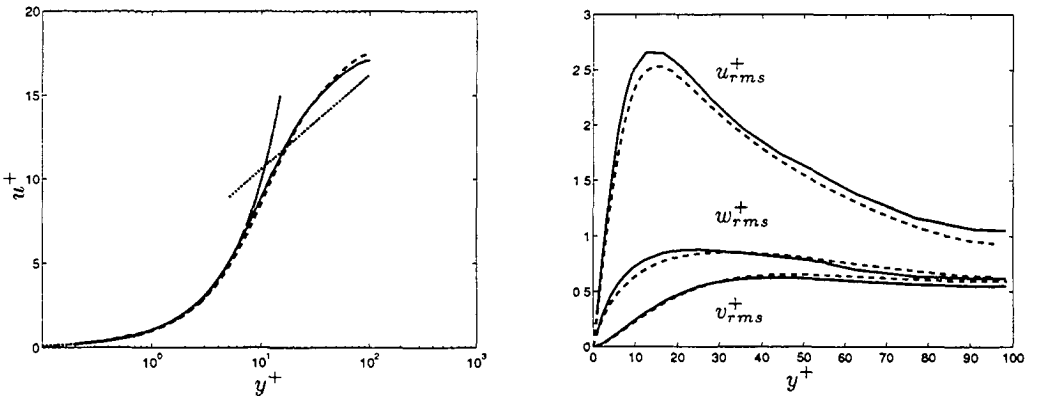

FIGURE 6. Mean and rms velocity profiles in wall units for the stretched mesh: ——— DG, - - - - incompressible DNS, ····· law of the wall.

files, especially in ρ near the center of the channel. However, after averaging, both the streamwise velocity and density profiles are smooth. One of the nice features of DG is that if the solution is known to be smooth, then visible jumps in the solution are indicative of low resolution. Thus, with the stretched mesh, the instantaneous turbulent flow near the center of the channel is only marginally resolved, although near the walls even the instantaneous profiles appear smooth, indicating good resolution there. However, it is important to note that even though the resolution near the centerline may be marginal, the mean flow is well represented.

Evidence to support this claim is given in figure 6 which shows the mean and rms velocity profiles in wall units, compared to a reference incompressible DNS at the same Re_τ (Chang 2000). Both the mean and rms velocities are in excellent agreement with the incompressible DNS. Likewise, no discernible discontinuities are observed in either the mean or the rms profiles. We recall that the DG discretization uses 79,488 degrees of freedom and is formally between 4th- and 6th-order accurate, depending on the local polynomial order. For comparison, the incompressible DNS uses a hybrid Fourier-Galerkin method in the planes and second-order finite-volume method in the wall-normal direction and uses 336,960 degrees of freedom after dealiasing. Thus, the DG solution uses a factor of 4.2 less degrees of freedom (1.9 if dealiasing is not used in the incompressible case).

On the stretched mesh, the average slip in the streamwise velocity at the wall is 0.002% of the centerline velocity where the first collocation point is $\Delta y_w^+ = 0.7$ from the wall. † To determine how the weak wall boundary condition influences the solution at coarser resolution (near the wall) we now consider results using a uniform mesh in the wall-normal direction. Figure 7 shows the mean streamwise velocity profiles in wall units as compared to the reference incompressible DNS, for both the low- and high-resolution cases. Interestingly, we see that the profiles are in excellent agreement with the reference solution. Such overlap clearly indicates that the mean shear stress is well predicted in both cases. However, careful examination of figure 7 does show that the law of the wall $u^+ = y^+$ is not perfectly satisfied at small y^+ because the flow slips at the wall. For the low resolution case, the slip velocity is 1% of the centerline velocity with $\Delta y_w^+ = 2$ while for the higher resolution case there is 0.68% slip with $\Delta y_w^+ = 1.6$. As expected, as near-wall resolution is increased, the amount of slip is reduced as the enforcement of the wall

† For reference, the centerline velocity is approximately $16u_\tau$ at $Re_\tau = 100$.

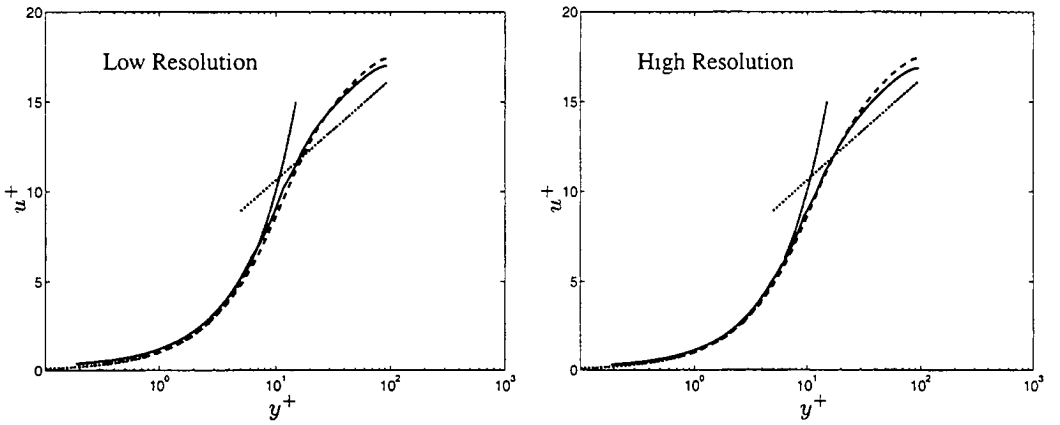

FIGURE 7. Effect of slip on mean velocity profile for the uniform mesh at two resolutions: ——— DG, - - - - incompressible DNS, ····· law of the wall.

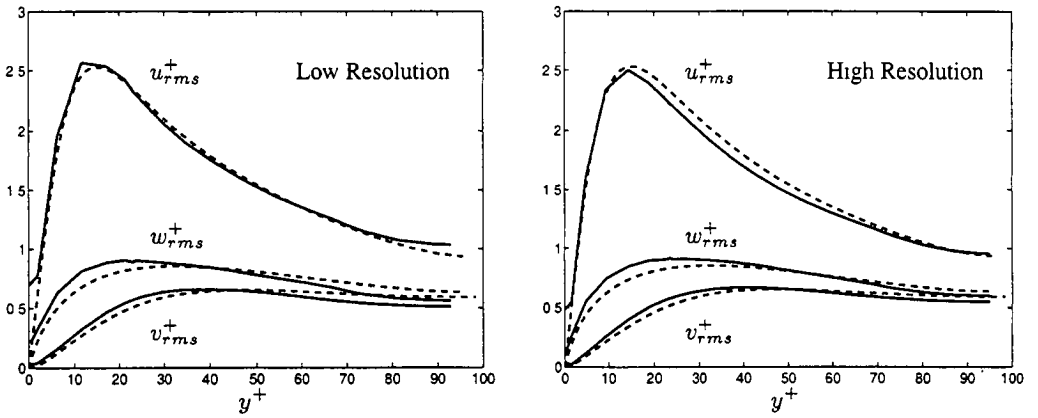

FIGURE 8. Effect of slip on rms velocity profiles for the uniform mesh at two resolutions: ——— DG, - - - - incompressible DNS.

boundary condition improves (this is especially true for the stretched mesh). Importantly, the mean shear and the majority of the mean velocity profile are well predicted even for the lowest-resolution case when $\Delta y_w^+ = 2$, which is less than many RANS models allow.

Similar behavior is found for the rms velocities, as shown in figure 8 for the low- and high-resolution uniform-mesh cases. One can clearly see the slip in the streamwise rms velocities at the wall. For the low-resolution case $u^+_{rms} = 0.65$ at the wall, while for the high-resolution case $u^+_{rms} = 0.48$ at the wall. For reference, the stretched-mesh solution has $u^+_{rms} = 0.0062$ at wall. Again, as resolution is increased in the near-wall region, the no-slip boundary condition is enforced to a higher accuracy. Importantly, with the exception of a region very close to the wall, both the mean and rms profiles throughout the channel are well predicted for all cases. Our prior experience with hard boundary conditions has shown that mean shear and rms profiles (i.e. turbulence production) are incorrectly predicted at low resolutions. Conversely, by enforcing the wall boundary conditions weakly through the numerical fluxes, the *influence* of the wall on the flow is correctly simulated in the form of net shear stress and turbulence production, even at resolutions for which the wall boundary values are inaccurate.

7. Conclusions

A discontinuous Galerkin method is formulated and implemented for simulation of complex, turbulent, compressible flows. The implementation is validated for both steady and unsteady separated flow over a circular cylinder, with results in excellent agreement with prior computations and/or experiments. An important feature of discontinuous Galerkin is the ability to enforce Dirichlet boundary conditions weakly, through numerical fluxes at the wall. The advantages of this approach are demonstrated for a simple advection-diffusion problem, where it it shown that enforcement of a weak boundary condition leads to a significant reduction in oscillations in the computed solution, resulting in a factor of 4 times less error in the L_2 norm. Applying DG to simulate fully-developed turbulent flow in a plane channel at low Reynolds number $Re_\tau = 100$ leads to results in excellent agreement with a reference incompressible DNS. The advantage of weak Dirichlet boundary enforcement is also demonstrated for this flow, where it is shown that accurate profiles of net shear stress, as well as mean and rms velocity, are obtained at low resolution—even resolution for which there is significant slip at the wall. In this context, weakly enforced wall boundary conditions may play a useful role in wall modeling for large-eddy simulation, where the wall-model is given by a particular numerical flux used at the wall.

Acknowledgments

This work was supported in part by the Stanford/NASA Center for Turbulent Research and by Texas ATP grant 003604-0011-2001. Computations were performed on an 82 processor Pentium IV Beowulf cluster that was purchased with the aid of NSF MRI grant 0116289-2001. The assistance of Guoquan Chen, Kaveh Ghayour, Eric Lee, Srinivas Ramakrishnan, and Zachary Smith is greatly appreciated as are my interactions with my CTR host, Dr. Timothy Barth of NASA Ames Research Center.

REFERENCES

ARNOLD, D. N., BREZZI, F., COCKBURN, B. & MARIN, L. D. 2002 Unified analysis of discontinuous Galerkin methods for elliptic problems. *SIAM J. Numer. Anal.* **39**, 1749–1779.

ATKINS, H. L. 1997 Continued development of the discontinuous Galerkin method for compuational aeroacoustic applications. *AIAA Paper* 97-1581.

BABUSKA, I. 1973 The finite element method with penalty. *Math. Comp.* **27**, 221–228.

BASSI, F. & REBAY, S. 1997 A high-order accurate discontinuous finite element method for the numerical solution of the compressible Navier–Stokes equations. *J. Comp. Phys.* **131**, 267–279.

BAUMANN, C. E. & ODEN, J. T. 1999 A discontinuous hp finite element method for the Euler and Navier–Stokes equations. *Inter. J. Num. Meth. Fluids* **31**, 79–95.

CHANG, Y. 2000 Reduced order methods for optimal control of turbulence. *PhD thesis*, Rice University, Mech. Engg and Matls Sci.

COCKBURN, B., ed. 1999 *High-order methods for computational applications, Lecture Notes in Computational Science and Engineering*, chap. Discontinuous Galerkin methods for convection-dominated problems. Springer, Berlin.

COCKBURN, B., KARNIADAKIS, G. & SHU, C.-W., eds. 2000 *Discontinuous Galerkin Methods: Theory, Computation, and Applications*. Springer, Berlin.

COLEMAN, G. N., KIM, J. & MOSER, R. D. 1995 A numerical study of turbulent supersonic isothermal-wall channel flow. *J. Fluid Mech.* **305**, 159–83.

COLLIS, S. S. 2001 Monitoring unresolved scales in multiscale turbulence modeling. *Phys. Fluids* **13**, 1800–1806.

COLLIS, S. S. 2002 The DG/VMS method for unified turbulence simulation. *AIAA paper* 2002-3124.

COLLIS, S. S., CHANG, Y., KELLOGG, S. & PRABHU, R. D. 2000 Large eddy simulation and turbulence control. *AIAA Paper* 2000-2564.

HIRSCH, C. 1988 *Numerical Computation of Internal and External Flows, Vol. I: Fundamentals of Numerical Discretization*. Wiley, New York.

HUGHES, T. J. R., MAZZEI, L. & JANSEN, K. E. 2000 Large eddy simulation and the variational multiscale method. *Computing and Visualization in Science* **3**, 47–59.

KARNIADAKIS, G. E. & SHERWIN, S. J. 1999 *Spectral/hp Element Methods for CFD*. Oxford University Press.

KIM, J., MOIN, P. & MOSER, R. 1987 Turbulence statistics in fully developed channel flow at low Reynolds number. *J. Fluid Mech.* **177**, 133–166.

LAYTON, W. 1999 Weak imposition of the "no-slip" conditions in finite element methods. *Comp. Math. Appl.* **38**, 129–142.

MORGAN, P., VISBAL, M. R. & RIZZETTA, D. P. 2002 A parallel high-order flow solver for large-eddy and direct numerical simulation. *AIAA Paper* 2002-3123.

MOSER, R. D., KIM, J. & MANSOUR, N. N. 1999 Direct numerical simulation of turbulent channel flow up to $Re_\tau = 590$. *Phys. Fluids* **11**, 943.

NITSCHE, J. 1971 Über ein variationsprinzip zur lösung Dirichlet-problem bei verwendung von teilräumen, die kienen randbedingungen unteworfen sind. *Abh. Math. Sem. Univ. Hamburg* **36**, 9–15.

POINSOT, T. J. & LELE, S. K. 1992 Boundary conditions for direct simulations of compressible viscous flows. *J. Comp. Phys.* **101**, 104–128.

SHU, C.-W. 1988 TVD time discretizations. *SIAM J. Sci. Stat. Comp.* **9**, 1073–1084.

SHU, C.-W. & OSHER, S. 1988 Efficient implementation of essentially non–oscillating shock–capturing schemes. *J. Comp. Phys.* **77**, 439–471.

TEZDUYAR, T. E. 1991 Stabilized finite element formulations for incompressible flow computations. *Adv. Appl. Mech.* **28**, 1–44.

THOMPSON, K. W. 1987 Time-dependent boundary conditions for hyperbolic systems. *J. Comp. Phys.* **68**, 1–24.

VISBAL, M. 1986 Evaluation of an implicit Navier–Stokes solver for some unsteady separated flows. *AIAA Paper* 86-1053.

WILLIAMSON, C. 1989 Oblique and parallel modes of vortex shedding in the wake of a cylinder at low Reynolds numbers. *J. Fluid Mech.* **206**, 579–627.

Toward the LES of flow past a submerged hydrofoil

By A. Pascarelli †, G. Iaccarino AND M. Fatica

The fluid flow past a body placed in a steady stream close to a free surface is the object of the current investigation. The viscous, incompressible Navier-Stokes equations, supplemented by linearized dynamic and kinematic boundary conditions at the free surface, are solved so that the water-surface elevation can be integrated into the solution and solved for, together with the velocity and pressure fields. The potential and limitations of the method will be illustrated and discussed.

1. Introduction

Incompressible viscous fluid flows bounded by a free surface have a number of interesting properties. The free-surface boundary is in motion, its location is part of the solution, and the relative velocity between the fluid and surface interface must vanish. In addition, the tangential stress at the surface must vanish, and the normal stress must balance the ambient pressure above the surface. As a result, when a vortex interacts with a free surface, the velocity field is significantly altered and this results in a complex structure and dynamics. For a free surface without contamination or external shear stress (idealized free surface), the vorticity at the free surface depends on the shape of the boundary (and on the assumed boundary conditions). If the free surface can be considered flat (i.e., of negligible deformation) the vortical field close to the interface is very similar to that near a free-slip plane. For a shear-free interface in which no deformations are allowed, the tangential vorticity (and its fluctuations), but not necessarily the flux of vorticity, vanishes at the free surface. The boundary condition of zero shear stress at a clean free surface requires that vortex lines which terminate at the free surface be normal to the surface. In the case of a shear-free deformed free surface, however, the vorticity at the free surface is nonzero and the surface acquires a solid body rotation due to the boundary condition allowing motion parallel to the surface. For example, in the interaction of a vortex pair with a free surface (see figure 1), the surface renewal produced by vortices with vorticity parallel to the surface already shows that the surface deformation will be an important feature of the turbulent transport at the interface. The aim of this work is to investigate the characteristics of the complex viscous interaction of the free surface with the wake of an isolated lifting hydrofoil submerged at relatively shallow depth, for moderate Froude numbers. This investigation is a precursor to a turbulent flow study at $Re = 30,000$, planned as a follow-up.

† INSEAN - Roma, ITALY

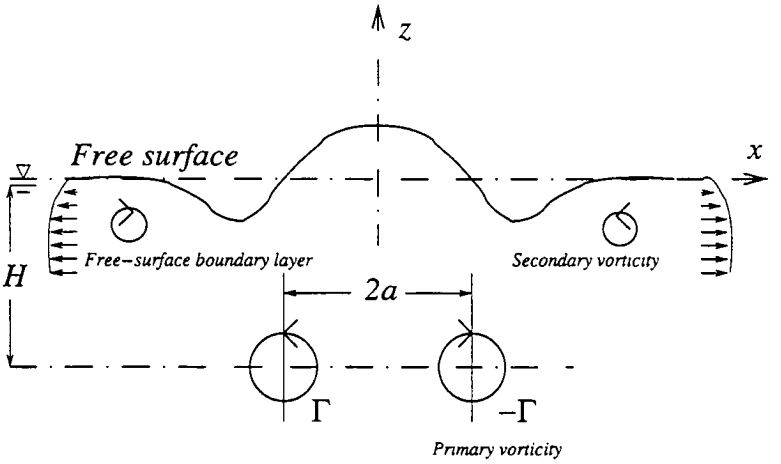

FIGURE 1. Sketch of a vortex pair impinging on a free surface.

2. Mathematical model

2.1. *Governing equations*

In Cartesian coordinates x_i $(i = 1, 2, 3) \equiv (x, y, z)$ the governing equations for an incompressible viscous flow, in the presence of body forces, of a layer of fluid of uniform depth H can be written in the following form

$$\frac{\partial u_j}{\partial x_j} = 0\,, \quad \frac{\partial u_i}{\partial t} + \frac{\partial}{\partial x_j}(u_j u_i) = -\frac{1}{\rho}\frac{\partial p}{\partial x_i} + \frac{1}{\rho}\frac{\partial \sigma_{ji}}{\partial x_j} + f_i \tag{2.1}$$

where the summation convention applies to repeated indices. Here, ρ and $\nu = \mu/\rho$ are the (constant) fluid density and kinematic viscosity respectively, t is the time, and u_i $(i = 1, 2, 3) \equiv (u, v, w)$ are the Cartesian fluid-velocity components. The vertical coordinate $z \equiv x_3$ is positive measured upwards from the flat, horizontal solid bottom surface, $z = H$ coincides with the undisturbed free surface level, while $z = 0$ corresponds to the position of the solid bottom. Let $F(x, y, z, t) = 0$ be the free-surface equation. Assuming no wave overturning or breaking, $F = F(x, y, z, t)$ is a single-valued function of x and y and can be expressed as

$$F(x, y, z, t) = \eta(x, y, t) - (z - H) = 0 \tag{2.2}$$

where η is the displacement of the free surface about the horizontal plane $z = H$. Relating the modified, or hydrodynamic, pressure p to the pressure P by $p = P + \rho g \eta$, g being the acceleration due to gravity, gravity effects appear only in the dynamic free-surface boundary condition. Like P, p appears in the equations through its gradient and is thus defined to within an arbitrary constant which is fixed by boundary conditions. The nonlinear advection term is written in conservation form. The viscous stress tensor σ_{ji} is expressed as a function of the strain-rate tensor $S_{ij} = (\partial u_i/\partial x_j + \partial u_j/\partial x_i)/2$, according to $\sigma_{ij} = 2\mu S_{ij}$. The source term f_i represents a body force per unit mass, arising from the immersed-boundary technique described below, which may vary as a function of time and space.

In flow problems involving free surfaces, part of the boundary of the computational domain (corresponding to the free surface) is unknown, and must be determined as part of the solution. On the free surface, two boundary conditions should be satisfied. The first boundary condition is determined from the balance of the stresses acting on the

interface between the upper and lower fluid layers, in the normal and tangential directions (so-called "dynamic" boundary condition). The specification of this force balance must depend on the nature of the particular physical situation being modelled. In this study, the free surface is considered as an uncontaminated free boundary between two immiscible fluids (water and air) on which no tangential stresses are imposed on its air-side. Moreover, given the water/air density ratio $\rho/\rho_a \approx 820$, we further assume the upper fluid layer light enough to cause no significant variation in hydrostatic or dynamic pressure, and both density and viscosity of the air phase are set to zero (vacuum approximation). For dynamic boundary conditions at a liquid-gas interface, with negligible viscous stresses in the gas and gradient of surface tension, we have, in general,

$$-P + \sigma_n = -P_a + \sigma_s k_s\,, \quad \sigma_t^{(l)} = 0 \quad l = 1, 2 \tag{2.3}$$

Here P_a denotes the external pressure, which we set to an arbitrary constant, say $P_a = 0$. σ_s is the (constant) surface tension coefficient (in units of force per unit length), k_s is the local interfacial curvature. $\sigma_n = n_i \sigma_{ji} n_j$ and $\sigma_t^{(l)} = t_i^{(l)} \sigma_{ji} n_j$, $l = 1, 2$ are the normal and the two tangential components of the viscous stress vector at the interface, in which n_i, $t_i^{(l)}$ are the $i-$direction components of unit vectors, the outward normal to the free surface and the two tangential to the free surface in the $(x, z)-$ and $(y, z)-$planes, respectively.

The second boundary condition at the free surface (called "kinematic") is formulated by considering that a fluid particle on the free surface remains on it, i.e. $\mathbf{u} \cdot \mathbf{n} = -(\partial F/\partial t)/|\nabla F|$ where everything is evaluated at the exact position of the free surface, $F(x, y, z, t) = 0$, and $|\nabla F| = \left[(\partial F/\partial x_i)^2\right]^{1/2}$. For a free surface given by (2.2) we have $\mathbf{n}(x, y, z) \equiv [-\eta_x, -\eta_y, 1]\left(\eta_x^2 + \eta_y^2 + 1\right)^{-1/2}$, $\mathbf{t}^x(x, y, z) \equiv [1, 0, \eta_x]\left(\eta_x^2 + 1\right)^{-1/2}$, $\mathbf{t}^y(x, y, z) \equiv [0, 1, \eta_y]\left(\eta_y^2 + 1\right)^{-1/2}$, and

$$k_s = \frac{\eta_{xx}(1 + \eta_y^2) - 2\eta_x \eta_y \eta_{xy} + \eta_{yy}(1 + \eta_x^2)}{\left(1 + \eta_x^2 + \eta_y^2\right)^{3/2}}.$$

Therefore, executing the dot product $\mathbf{u} \cdot \mathbf{n}$ the above condition can be rewritten as

$$w = \eta_t + u\eta_x + v\eta_y \quad \text{on} \quad z = \eta + H \tag{2.4}$$

Equation (2.4) represents a non-linear boundary condition; the wave elevation η is an unknown function of time and space and must be determined as part of the solution. The dynamic boundary conditions are written as

$$p = \rho g \eta + 2\rho\nu \frac{\left[w_z - (u_z + w_x)\,\eta_x - (v_z + w_y)\,\eta_y + u_x \eta_x^2 + (v_x + u_y)\,\eta_x \eta_y + v_y \eta_y^2\right]}{\left(\eta_x^2 + \eta_y^2 + 1\right)} - \sigma_s k_s \tag{2.5}$$

for the normal direction and

$$\left(1 - \eta_x^2\right)(u_z + w_x) + 2\eta_x (w_z - u_x) - \eta_y (u_y + v_x) - \eta_x \eta_y (v_z + w_y) = 0 \tag{2.6}$$

$$\left(1 - \eta_y^2\right)(v_z + w_y) + 2\eta_y (w_z - v_y) - \eta_x (u_y + v_x) - \eta_x \eta_y (u_z + w_z) = 0 \tag{2.7}$$

for the tangential directions. Again, note that each term is evaluated on the interface, $z = \eta + H$. Neglecting effects of nonlinear self-interactions of surface waves, we assume that the wave elevation in the physical region is small ($|\eta| << 1$), and the interfacial boundary conditions are linearized by assuming a free-surface deformation of order $\epsilon \sim O(Fr^2)$ and a free-surface boundary layer of thickness $\delta \sim O(Re^{-1/2})$, with $\delta^2 \ll \epsilon \ll \delta \ll 1$: see Tsai

& Yue (1995). Upon Taylor expansion about $z = H$ and using continuity we obtain the kinematic boundary condition to be enforced at the undisturbed free surface,

$$w = \eta_t + (u\eta)_x + (v\eta)_y \quad \text{on} \quad z = H. \tag{2.8}$$

Finally, for small slopes $\mathbf{n} \simeq [-\eta_x, -\eta_y, 1]$, $\mathbf{t}^{(1)} \simeq [1, 0, \eta_x]$, $\mathbf{t}^{(2)} \simeq [0, 1, \eta_y]$, and $k_s \simeq \eta_{xx} + \eta_{yy}$, so that the balance of the normal and the two tangential stress components at the unperturbed interface $z = H$ may be described conveniently by

$$p = \rho g \eta + 2\rho\nu w_z - \sigma_s (\eta_{xx} + \eta_{yy}) \text{ on } z = H \tag{2.9}$$

$$(u_z + w_x) = 0 \text{ on } z = H \tag{2.10}$$

$$(v_z + w_y) = 0 \text{ on } z = H \tag{2.11}$$

Conditions (2.9)–(2.10)–(2.11) allow a velocity across the boundary.

Usually, all the variables are made dimensionaless by a characteristic flow velocity u_{ref} and a characteristic length scale l_{ref}. The case-specific nondimensional groups in these flows are the Reynolds number, the Froude number and the Weber number. The relevant nondimensional parameter is the Reynolds number, defined as $Re = u_{ref} l_{ref}/\nu$, whereas the effect of the free-surface boundary condition is expressed in terms of the dimensionless Froude number, $Fr = u_{ref}/\sqrt{g l_{ref}}$, and Weber number, $We = \rho l_{ref} u_{ref}^2/\sigma_s$, which will appear in the condition (2.9). The Froude number is (the square root of) the ratio of inertia to gravity (or buoyancy), and, since it compares a given characteristic flow velocity to that of (long-wavelength) gravity waves, it directly relates to the speed of a surface disturbance. The Weber number represents surface-tension effects on the free surface. Capillary effects are negligible when the Weber number is large. The case of a free-slip plane surface corresponds to the limit $Fr = 0$ of the present problem. In such a flow, in which the gravity g is infinite, inviscid no-stress boundary conditions (i.e, $u_z = v_z = w = 0$, and $p_z = 0$) are imposed at the interface corresponding to the "free surface", and the physical phenomena observed there will be expected to be independent of groups such as the Froude and Weber numbers. The boundary conditions at the free surface influence quantities that involve derivatives of the velocity, which for example has interesting consequences for the vorticity at the free surface. It is of interest to note that while tangential vorticity at a flat free surface is always zero, the zero-stress boundary conditions (2.10)–(2.11) yield surface vorticity components

$$\omega_x = w_y - v_z = -2v_z = 2w_y \quad \text{on} \quad z = H \tag{2.12}$$

$$\omega_y = u_z - w_x = 2u_z = -2w_x \quad \text{on} \quad z = H. \tag{2.13}$$

2.2. *Discretization method*

The governing equations, supplemented by linearized dynamic and kinematic boundary conditions at the free surface, are solved by a fractional-step/finite-difference algorithm based on a staggered-grid formulation (Chorin 1967, Kim & Moin 1985). The overall accuracy of the method is second order in time and space. It is close to the method presented in Shen *et al.* (1999); however the equation of energy conservation has been explicitly taken into account in the numerical discretization. An immersed-boundary technique is used to handle the presence of the solid body in the fluid stream. The "direct forcing method" proposed by Fadlun *et al.* (2000) has been implemented. The discussion here is purposely kept brief because a complete description can be found in Pascarelli *et al.* (2002) and Fadlun *et al.* (2000).

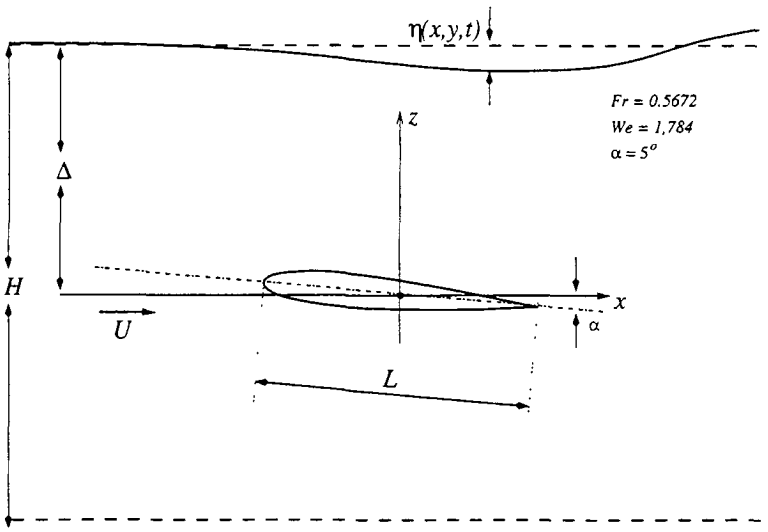

FIGURE 2. Geometry of the flow past a submerged hydrofoil.

3. Results

3.1. *Flow over a submerged hydrofoil*

We consider the flow of water around an hydrofoil which is below a free surface. The hydrofoil section considered is NACA 0012 with an angle of attack of 5°. The arrangement consists of a two-dimensional open channel whose upper boundary is a free surface. In this system, quantities are nondimenzionalized with the chord length of the body ($l_{ref} = L$) and the uniform inflow velocity ($u_{ref} = U_{in}$). Based on these scales the relevant nondimensional parameters include the Reynolds number $Re = U_{in}L/\nu$, the Froude number $Fr = U_{in}/\sqrt{gL}$, and the Weber number $We = \rho L U_{in}^2/\sigma_s$. Other geometric parameters in this problem are the upstream length L_u and the downstream length L_d. This problem reproduces the case studied experimentally (Duncan (1983)) and modelled numerically by several authors (Hino, Martinelli & Jameson (1989), Muscari & Di Mascio (2002)) at $Re = 1.624 \times 10^5$, $Fr = 0.5672$ and $We = 1784$. At any fixed dimensionless depth of submergence $\gamma = \Delta/L$, the wave amplitude (and hence wave resistance) possesses a maximum as a function of Froude number based on submergence depth $Fr_\Delta = U_{in}/(g\Delta)^{1/2}$. When that maximum is sufficiently low, linearization is justified. In our simulations the body centre is submerged at mid-chord by $\gamma = 1.034$. At this submergence the leading wave does not break. For our purposes, it is convenient to consider the situation from a frame of reference that is at rest with the body. The domain is 18.5 units in length (the upstream boundary is 6 units upstream of ht eleading edge) and 4 units in depth. In order to prevent any reflection of waves into the solution domain, an artificial damping function for η is used at the downstream boundary. The damping length is set to $l_d = 2L$. Non-uniform mesh distributions are used in both x- and z-directions, with grid clustering near the body surface. With the same Froude and Weber numbers, this flow was investigated in the Reynolds number range from 500 to 10000, far lower than the reference experimental data, but only results for the most interesting cases are reported here. Figure 3 shows the wave profiles for different Reynolds numbers. Viscous effects significantly affect the wave amplitude. Unfortunately, no experimental date are available for low Reynolds number to compare with the results. For the 2D simulations, a total of

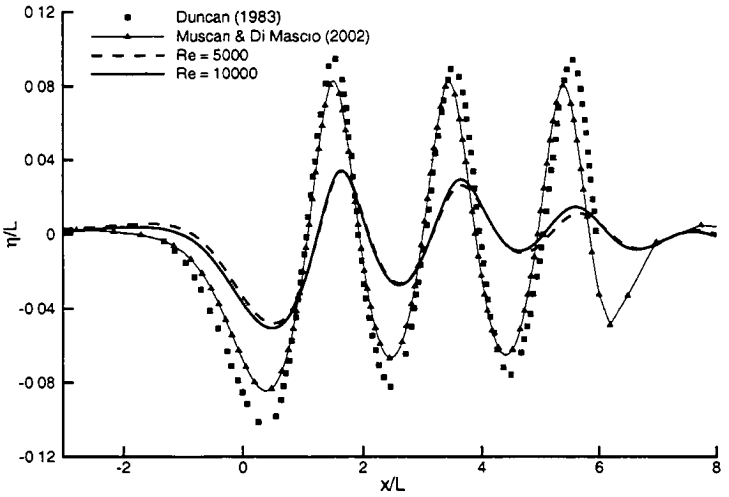

FIGURE 3. Submerged NACA 0012. Wave profiles for different Reynolds numbers.

FIGURE 4. Vorticity contours for flow over submerged NACA 0012 at $t = 45$: (a) $Re_b = 5000$; (b) $Re_b = 10000$. Only part of the domain is shown.

$nx = 780$ computational cells are used in the x-direction, while the total number of cells in the vertical direction is $nz = 200$. 4246 grid points are placed within the body. As also observed by Chen & Chwang (2002) as the Reynolds number is increased up to 5000 the von Karman street converges to an oscillatory motion. For $Re = 10000$, the flow reaches a transitional stage and transition is about to occur. The instantaneous vorticity contours for $Re = 5000$ and $Re = 10000$ are shown in figure 4 (a) and in figure 4 (b), respectively. Finally, the force coefficients for the two Reynolds numbers are plotted in figure 5. It is clear from figure 4 (b) that, despite the dense grid clustering around the body, which also

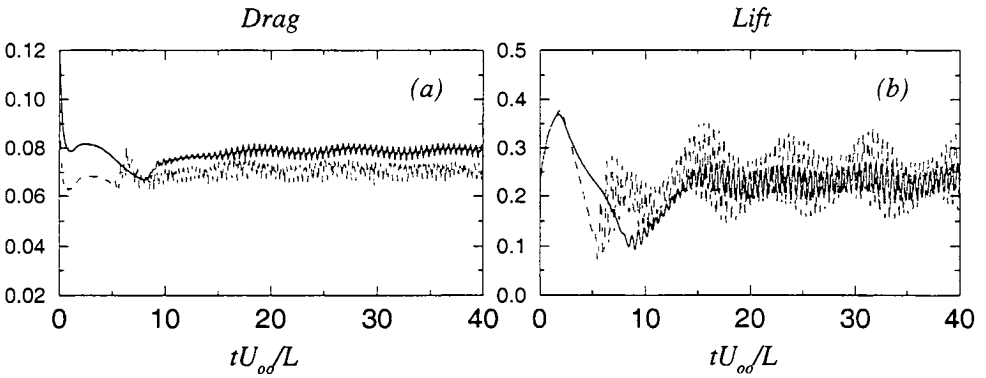

FIGURE 5. Variation of force coefficients during early wake formation with time from an impulsive start. (*a*) Drag coefficient and (*b*) lift coefficient: ——— $Re = 5000$; --- $Re = 10000$.

restricts the computational time step, the mesh resolution is not sufficient even at the moderate Reynolds number $Re = 10000$ and spurious numerical oscillations are detected. The absence of any artificial control (numerical dissipation) of the odd-even decoupling in the solution results in a serious issue when an advection equation for the free surface is solved along with the flow field. The occurence of wiggles in the velocity field at time t^n may affect the solution quality at the vnext time step through the Dirichlet boundary condition on the pressure field. We found that lack of resolution can result in numerical oscillations that can obscure the flow field.

3.2. *Flow around a free-surface-piercing square cylinder*

As an example of further applications of the present simulation technique the free–surface flow resulting from a partially-submerged square cylinder is considered.

The study of this flow is extremely complicated because of the strong interaction between the free surface and the solid object; in the previous case, only the effect of the presence of the submerged body (via the pressure and eventually the vorticity) was felt on the free surface.

The immersed-boundary technique employed here provides a very natural framework to treat problems involving partially-submerged bodies. Using the same assumptions as previously, only the part of the fluid up to the free-surace is considered. The solid body is represented through a "direct" forcing on the velocity field (in the momentum equations) whereas the pressure field is obtained solving the unmodified elliptic equation arising from the fractional-step procedure. The same treatment is applied to the kinematic boundary condition on the free surface, which accounts for the presence of the cylinder directly through the velocity field in 2.9.

Only proof-of-concept simulations have been carried out so far; a low Reynolds number ($Re = 500$) is considered and the free surface elevation is shown in figure 6.

Further analysis will be required to verify the accuracy of the present linearized free-surface boundary conditions in the presence of surface-piercing bodies.

Acknowledgments

A.P. would like to thank Dr. A. Di Mascio for his input in many useful discussions.

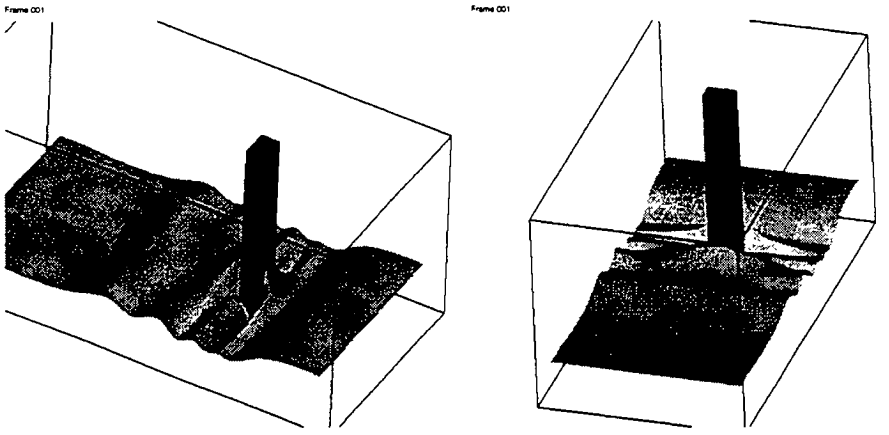

FIGURE 6. Wave elevation for a surface-piercing square cylinder: (*a*) Side View; (*b*) View from behind.

REFERENCES

CHEN, T. & CHWANG, T. 2002 Trailing vortices in a free-surface flow. *Phys. Fluids* **14**, 827–838.

CHORIN, A. J. 1967 A numerical method for solving incompressible viscous flow problems. *J. Comput. Phys.* **2**, 12–26.

DUNCAN, J. H. 1983 The breaking and non-breaking wave resistance of a two-dimensional hydrofoil. *J. Fluid Mech.* **126**, 507–520.

FADLUN, E. A., VERZICCO, R., ORLANDI, P. AND MOHD-YUSOF, J. 2000 Combined immersed-boundary finite-difference methods for three-dimensional complex flow simulations. *J. Comput. Phys.* **161**, 35–60.

HINO, T., MARTINELLI, L. & JAMESON, A. 1993 A finite volume method with unstructured grid for free-surface flow. *Proc. 6th International Conference on Num. Ship Hydrodynamics, Iowa City, IA*, 173–194.

KIM, J. & MOIN, P. 1985 Application of a fractional-step method to incompressible Navier-Stokes equations. *J. Comput. Phys.* **59**, 308–323.

MUSCARI, R. & DI MASCIO, A. 2002 A model for the simulation of spilling breaking waves. To appear in J. Ship Research

ORLANSKI, I. 1976 A simple boundary condition for unbounded hyperbolic flows. *J. Comput. Phys.* **21**, 251–269

PASCARELLI, A., BROGLIA R. & DI MASCIO, A. 2002 Numerical simulations of laminar free-surface flows. In preparation.

SHEN, L., ZHANG, X., YUE, D. K. & TRIANTAFYLLOU, G. S. 1999 The surface layer for free-surface turbulent flows. *J. Fluid Mech.* **386**, 167–212.

TSAI, W.-T. & YUE, D. K. P. 1995 Effects of soluble and insoluble surfactant on laminar interaction of vortical flows with a free surface. *J. Fluid Mech.* **289**, 315–349.

Fundamentals

By Javier Jiménez

It would be disingenuous to pretend that a section named "Fundamentals" is anything but a collection of the projects which did not easily fit anywhere else in these proceedings. A look at the titles only reinforces that impression. There is a paper on the structure of near-wall turbulence, another one on modelling magnetohydrodynamic flows, a third on the effect of wall-bounded shear turbulence on particle dispersion, a fourth on the influence of porous walls on turbulence statistics, and a final one on the dynamics and chemistry of aeroplane contrails. Besides the probably coincidental fact that three of the five papers concern themselves with wall turbulence, and the more predictable one that they all deal with turbulent flows, there is little connection among the various topics.

But it is a characteristic of human mind, probably more marked in those who have devoted time to the study of turbulence, to find patterns in seemingly chaotic situations, and we should ask ourselves whether there is something to be learned from this section as a whole, beyond what can be found in the individual papers. We should in particular reflect on why the section exists, and on why these papers are here.

A possible explanation, easily dispelled, is that these are the projects which nobody else wanted, on account of not being interesting enough, or of being marginal to turbulence research. Reading the papers shows that the opposite is true, and that they all deal with important open problems, all of which are likely to increase in importance in the future. We should also resist the assumption, implicit in the title, that this section is exclusively devoted to basic research. With the possible exception of the paper by Kawahara *el al.*, all the others start by listing the applications which motivate them, ranging from the control of hypersonic vehicles to environmental modelling.

But there is something that sets these projects apart and which prevents them from being included in other sections. A look at the proceedings of previous summer programmes gives us some historical perspective. Turbulence research has changed during the lifetime of the CTR. While exploratory papers were the norm in the first summer programmes, they are exceptional now. "Fundamental" papers were then scattered among the different topics, but are now few enough to be collected into a single "topic". Turbulence is drifting towards "big science" carried out by coordinated teams, after being during most of its history a realm of individual researchers and of personal projects.

This is not a trend that necessarily has to be resisted. As peripheral questions gradually become better understood and as we meet the harder "kernel" subjects, it is probably unavoidable that the attacks should become more focused, and that the research groups should get larger. It can in fact be argued that some activities, such as direct numerical simulations and the analysis of the resultant data, have already become too large for single teams or institutions, and that they will in the future have to be organized as cooperative projects. The Centre for Turbulence Research was actually created fifteen years ago as a first step in the direction of cooperative analysis, but it is remarkable how little DNS can be found in the latest summer proceedings.

Other scientific disciplines, notably molecular biology and particle physics, have taken that route and emerged in many ways stronger. But it is crucial to make sure that the reductionist trend does not become exclusive, and that exploration continues. Turbulence

is an aggregative science, encompassing many phenomena and applicable to many fields. It is important that, even as the subject "implodes" towards the solution of a few core questions, it continues to expand in search of new ones. Such explorations at the edges of a research field necessarily have a scattershot appearance, and it is difficult to tell whether any particular shot is aimed towards a leading or towards a marginal frontier but, as with newborn babies, one of them surely holds the keys to the future. This section is the exploratory part of the current turbulence proceedings.

Javier Jiménez

Center for Turbulence Research
Proceedings of the Summer Program 2002

Characterization of near-wall turbulence in terms of equilibrium and periodic solutions

By **Genta Kawahara †, Javier Jiménez ‡, Makoto Shiba ¶ AND Mark Simens ||**

Near-wall turbulence in the buffer region is qualitatively characterized in terms of recently-found nonlinear three-dimensional solutions to the incompressible Navier–Stokes equation for wall-bounded shear flows. Jiménez & Simens' (2001) traveling-wave solution for an autonomous wall flow, Nagata's (1990) steady and Kawahara & Kida's (2001) periodic solutions for a plane Couette flow are considered for characterization. These equilibrium and periodic solutions are classified into two families, of which one is dominated by streamwise vortices, and the other by streaks. The former family, which is composed of autonomous solutions, Nagata's upper-branch solutions and time-periodic solutions, is similar to fully-turbulent simulationss in the near-wall region.

1. Introduction

Since the famous 1883 experiments by Reynolds, wall-bounded turbulent flow has been one of the main subjects of turbulence research. The lack of a simple spatio-temporal characterization of turbulence has, however, impeded the elucidation of the structural and dynamical properties of near-wall turbulent flows.

Recently, several nonlinear equilibrium solutions of the three-dimensional Navier–Stokes equations have been obtained numerically for wall-bounded shear flows, such as plane Couette flow (Nagata 1990), plane Poiseuille flow (Toh & Itano 1999; Waleffe 2001), and an autonomous wall flow (Jiménez & Simens 2001). The equilibrium solutions of these systems exhibit a similar structure in physical space (see Waleffe 1998; Kawahara, Jiménez, Uhlmann & Pinelli 2002), which takes the form of wavy low-velocity streaks flanked by staggered streamwise vortices of alternating signs. These solutions are unstable at the Reynolds numbers where turbulence is observed, and they represent saddles in phase space, in the neighbourhood of which a turbulent state could spend a substantial fraction of time. Their structure closely resembles the spatially-coherent objects observed in the near-wall region of turbulent flows.

More recently Kawahara & Kida (2001) have numerically extracted a periodic saddle orbit embedded in low-Reynolds-number plane Couette turbulence, which well characterizes not only spatial but also temporal coherence of near-wall turbulence, i.e. a full regeneration cycle of low-velocity streaks and streamwise vortices. Besides, the mean velocity profile and the root-mean-square velocity fluctuations of plane Couette turbulence agree very well with the temporal averages of those of the periodic solution.

Of these solutions, those which are obtained as equilibrium and periodic solutions of the Navier–Stokes equations usually form parametric families, while those educed from turbulent flows have parameters which fall in definite ranges. The best-known case is

† Kyoto University
‡ Also at Universidad Politécnica de Madrid
¶ Ehime University
|| Universidad Politécnica de Madrid

of course the spanwise-wavelength selection mechanism that results in the mean streak separation of $z^+ \approx 100$, but equally intriguing is the observed $x^+ \approx 300$ streamwise separation between vortex pairs within the same streak (Jiménez & Moin 1991). Although the similarities observed between the theoretical and educed structures are striking, and definitely suggest that they are related to each other and to self-sustaining wall turbulence, the exact nature of this relation is still unclear.

The main objective of this work is to clarify this relation. We shall put together several of the known equilibrium and periodic solutions for wall-bounded shear flows. Traveling-wave solutions for an autonomous wall flow (Jiménez & Simens 2001), steady (Nagata 1990) and periodic (Kawahara & Kida 2001) solutions for a plane Couette flow will be compared and checked against those of real near-wall turbulence.

The numerical methods used to recompute some of these solutions are described in section 2. Comparisons between the different equilibrium and periodic solutions are made in section 3, and their relation with fully-developed turbulence is discussed in section 4. Finally some conclusions are offered in section 5.

2. Equilibrium and periodic solutions

2.1. *Autonomous solutions*

The permanent solutions described below as 'autonomous' are computed using a slightly modified version of the numerical scheme described by Jiménez & Pinelli (1999) and by Jiménez & Simens (2001). The Navier-Stokes equations are integrated in the form of evolution equations for the wall-normal vorticity ω_y and for $\phi = \nabla^2 v$, using a pseudospectral code with Fourier expansions in the two wall-parallel directions and Chebychev polynomials in the wall-normal direction y, as in Kim, Moin & Moser (1987). At each time step the right-hand sides of the two evolution equations are multiplied by a damping mask $1 - \Delta t\, F(y)$, where

$$F(y) = 0 \quad \text{if} \quad y \le \delta_1, \qquad F(y) = 1/T \quad \text{if} \quad y \ge \delta_2. \tag{2.1}$$

The two limits of $F(y)$ are connected smoothly by a cubic spline. For the solutions used in this paper, $\delta_2 = 1.5\,\delta_1$. This mask can be interpreted as a linear dissipation for each of the two evolution variables, acting only above $y = \delta_1$. The equations being solved are, to numerical accuracy,

$$\partial_t \omega = N - F(y)\omega. \tag{2.2}$$

where ω stands for any of the two evolution variables, and N represents the full right-hand side of the Navier–Stokes equations. The evolution equations are not modified below the mask lower limit δ_1, but F is chosen large enough for all the vorticity fluctuations to be effectively damped above $y \approx (\delta_1 + \delta_2)/2$. Irrotational fluctuations are not affected, and the outer edge of the Navier–Stokes layer is bounded by a potential core which prevents the formation of viscous boundary layers at the mask boundary.

While the flows in Jiménez & Pinelli (1999) and in Jiménez & Simens (2001) were integrated at constant mass flux in a channel, the present computations were initially carried out at constant driving stress in a 'semi-infinite' domain. No-slip, impermeable boundary conditions were imposed at $y = 0$, and the velocities were matched to outer potential fluctuations extending to infinity from the edge of the computational domain, $y = h > \delta_2$, using the method introduced by Corral & Jiménez (1995). This driving mechanism is free from the complications of a 'second wall' across the potential layer, and in particular from the effect of a mean pressure gradient, and should in principle be

L_x^+	L_z^+	δ_1^+	U_c^+	u'^+_{max}	v'^+_{max}
167	180	38.4	13.2	2.54	0.592
151	180	42.0	13.2	2.51	0.578
167	180	42.0	12.8	2.59	0.598
188	180	42.0	12.6	2.71	0.615
188	180	45.6	12.4	2.84	0.612

TABLE 1. Parameters of the autonomous simulations used in the text. L_x and L_z are the box dimensions, U_c is the phase velocity, and u'_{max}, v'_{max} are the two parameters used below to characterize solutions.

preferable to simulations involving two-walled channels. The Reynolds shear stress, for example, is constant across the Navier-Stokes layer, instead of varying linearly across the channel and the only parameter in the problem is the Reynolds number δ_1^+. In this paper the superscript $^+$ is attached to wall variables that are normalized with the kinematic viscosity ν and the friction velocity u_τ. The driving mechanism was successfully used in Jiménez, Flores & García-Villalba (2001) to simulate autonomous wall flows in a large, but shallow, computational box.

In the present case however this driving mechanism failed to reproduce the simple solutions found by Jiménez & Simens (2001). The flow passed directly from fully-chaotic (minimal) turbulence to laminar decay, upon minor changes of the mask height or of the box dimensions.

It was therefore decided to reintroduce some pressure effects. The basic structure of the code is maintained, and in particular the driving mechanism for the mean flow is still a mean shear away from the wall, instead of an imposed mean pressure gradient. The mean velocity profile tends to linear, rather than to parabolic, away from the wall. The potential fluctuations in the masked region, however, instead of being defined as decaying at $y \to \infty$, are required to match a no-stress impermeable boundary at $y = H > h$. The vertical structure of the potential wall-normal velocity Fourier mode with streamwise and spanwise wavenumbers α and β is, for example, proportional to $\sinh[(\alpha^2+\beta^2)^{1/2}(y-H)]$, instead of to $\exp[-(\alpha^2+\beta^2)^{1/2}y]$. All the cases presented in this paper were computed with $H = 2h$ and with the viscosity adjusted so that $h^+ = 120$.

This modification introduces a fluctuating pressure gradient which maintains the instantaneous mass flow constant across the domain $(0, H)$. It was found to be sufficient to restore the existence of simple solutions, with a complex bifurcation structure which will be discussed elsewhere. The significance of this observation is not clear, although it is not surprising that the dynamical properties of constant-mass and constant-stress simulations should differ in such small computational domains. Here we only use solutions which behave like permanent waves. Their computational parameters are summarized in table 1, where L_x and L_z are the box dimensions, U_c is the phase velocity, and u'_{max}, v'_{max} are the two parameters used below to characterize solutions. Because of the presence of a required fluctuation of spatially-constant pressure gradient, these flows are classified below as part of the Poiseuille family.

2.2. *Plane Couette solutions*

Here, Nagata's (1990) steady solutions of the incompressible Navier–Stokes equation for a plane Couette flow are recomputed by the Newton–Raphson method (see Shiba 2001 for detailed numerical procedures). It is well known that a laminar plane Couette flow is lin-

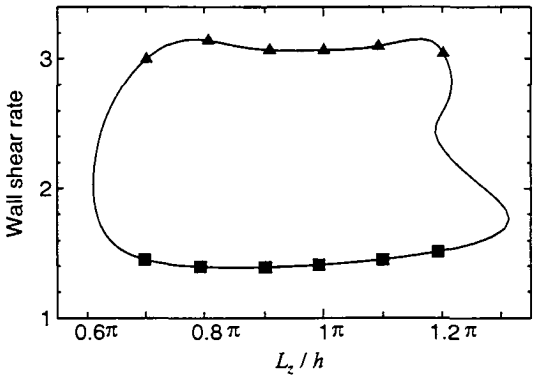

FIGURE 1. The dimensionless wall shear rate for Nagata's solution versus the spanwise period L_z. The Reynolds number Re and the streamwise period L_x are fixed as $Re = 400$ and $L_x = 2\pi h$.

early stable for all finite Reynolds numbers. Nagata's upper and lower solution branches appear subcritically at $Re \approx 125$ from saddle–node bifurcation, where $Re = Uh/\nu$ is the Reynolds number, U and h denoting half the difference of the two wall velocities and half the wall separation, respectively. In general, the upper-branch (or lower-branch) solutions generated from the bifurcation have a larger (or smaller) deviation from a laminar state.

As in Ehrenstein & Koch (1991), the flow is decomposed into a laminar part and a deviation from it, and then the latter is obtained numerically by solving steady nonlinear equations for the streamwise velocity $u_0(y)$ averaged over a plane parallel to the wall, for the wall-normal vorticity $\omega_y(x, y, z)$, and for the Laplacian of the wall-normal velocity, $\phi = \nabla^2 v(x, y, z)$. The solutions are assumed to be spatially periodic in the wall-parallel directions, and they are expressed as double Fourier expansions in these two directions. In the expansion with respect to the wall-normal dimensionless coordinate y^* $(= y/h)$, where the plane $y = 0$ is now the midplane of the channel, we use the two kinds of modified Chebychev polynomials as

$$(1 - y^{*2})\, T_l(y^*) \quad \text{for } u_0 \text{ and } \omega_y \tag{2.3}$$

and

$$(1 - y^{*2})^2\, T_l(y^*) \quad \text{for } v, \tag{2.4}$$

respectively, to satisfy the wall boundary conditions

$$u_0 = \omega_y = v = \frac{\partial v}{\partial y} = 0 \quad \text{at } y^* = \pm 1, \tag{2.5}$$

where $T_l(y^*)$ is the lth-order Chebychev polinomial. The collocation method with grid points $y^* = \cos[m\pi/(M+1)]$, $(m = 1, 2, \cdots, M)$ is used to construct a system of quadratic equations for the Fourier–Chebychev–Fourier coefficients, which is solved by the Newton–Raphson method. The arc-length method (see Ehrenstein & Koch 1991) is applied to track the nonlinear solutions, with the parameters, i.e. Re, L_x or L_z, being changed independently.

The Nagata solutions are known to have two spatial symmetries (see Nagata 1986, 1988, 1990): (i) the reflection with respect to the plane of $z = 0$ and a streamwise shift by a half period $L_x/2$

$$(u, v, w)(x, y, z) = (u, v, -w)(x + L_x/2, y, -z), \tag{2.6}$$

L_x^+	L_z^+	Re_τ	u'^+_{max}	v'^+_{max}
217	76.2	34.6	2.79	0.887
223	89.8	35.4	2.84	0.892
220	99.9	35.0	2.84	0.840
220	110	35.0	2.85	0.768
221	121	35.2	2.97	0.674
219	132	34.9	3.42	0.534

TABLE 2. Parameters of Nagata's upper-branch solutions represented by ▲ in figure 1. $Re_\tau = u_\tau h/\nu$ is the Reynolds number or half the wall separation in wall units.

L_x^+	L_z^+	Re_τ	u'^+_{max}	v'^+_{max}
151	53.5	24.1	3.20	0.302
148	58.9	23.6	3.70	0.230
156	66.7	23.6	4.16	0.194
149	74.0	23.7	4.50	0.179
151	83.3	24.1	4.85	0.170
155	92.2	24.6	5.09	0.169

TABLE 3. Same as table 2 but for the lower-branch solutions represented by ■ in figure 1.

L_x^+	L_z^+	Re_τ	T_p^+	$\overline{u'}^+_{max}$	$\overline{v'}^+_{max}$
190	130	34.4	188	3.18	0.741
154	105	27.9	299	4.62	0.231

TABLE 4. Parameters of two kinds of periodic solutions (Kawahara & Kida 2001). T_p^+ stands for the time period of the solution. $\overline{u'}^+_{max}$ and $\overline{v'}^+_{max}$ are the time averages of u'^+_{max} and v'^+_{max}.

and (ii) the 180° rotation around the line $x = y = 0$ and a spanwise shift by a half period $L_z/2$

$$(u, v, w)(x, y, z) = (-u, -v, w)(-x, -y, z + L_z/2), \tag{2.7}$$

where u and w are the streamwise and the spanwise components of the velocity deviation. Note that these two symmetries were observed to appear approximately in minimal plane Couette turbulence (Hamilton, Kim & Waleffe 1995) as well, without being imposed on the flow (Coughlin, Jiménez & Moser 1994; Kawahara & Kida 2001). These symmetries have also been imposed on the time-periodic solutions below.

Figure 1 shows the dimensionless wall shear rate, $\mathrm{d}u_0/\mathrm{d}y|_{y=\pm h}/(U/h) + 1$, averaged over the wall as a function of the spanwise period of the solution, L_z. The symmetry (2.7) implies that the averaged velocity gradients on the lower and upper walls are equal to each other. The Reynolds number Re and the streamwise period L_x have been fixed as $Re = 400$ and $L_x = 2\pi h$. Both the upper and the lower branches have a higher shear rate compared with that for a laminar state, i.e. unity. The computational parameters for the upper and the lower solutions, which will be compared with the autonomous and periodic solutions or with the turbulent solutions, are summarized in tables 2 and 3 respectively.

The two kinds of time-periodic solutions for a plane Couette flow are taken from Kawa-

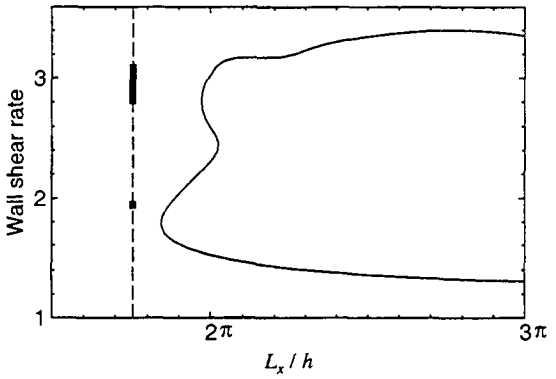

FIGURE 2. The dimensionless wall shear rate for the Nagata's solution versus the relatively small streamwise period L_x. The Reynolds number Re and the spanwise period L_z are fixed as $Re = 400$ and $L_z = 1.2\pi h$. The dashed vertical line denotes the period of $L_x = 1.755\pi h$, for which the two kinds of time-periodic solutions were found by Kawahara & Kida (2001) at the same values of Re and L_z. The upper long (or lower short) thick line on the vertical represents the wall shear variation of the time-periodic solution with the period $T_p^+ = 188$ (or $T_p^+ = 299$).

hara & Kida (2001) to be compared with the other solutions. Their periodic solutions have been obtained for the conditions $Re = 400$, $L_x = 1.755\pi h$ and $L_z = 1.2\pi h$, which are essentially the same as those of minimal plane Couette turbulence in Hamilton, Kim & Waleffe (1995). The parameters for the periodic solutions are summarized in table 4. As can be seen from figure 2, there is no Nagata steady solution at the conditions, for which time-periodic solutions were observed in Kawahara & Kida (2001). The wall shear rate of the periodic solution with period $T_p^+ = 188$ is roughly the same as that of Nagata's upper branch. The other periodic solution with $T_p^+ = 299$ has a lower wall shear rate, close to Nagata's lower branch. Hereafter, the former solution is referred to as the 'upper' periodic solution, while the latter is called the 'lower' periodic solution. The upper solution exhibits a full regeneration cycle of near-wall coherent structures, and also well represents the low-order turbulence statistics of a minimal plane Couette flow (Kawahara & Kida 2001).

3. Classification of solutions

In this section, we compare the equilibrium and periodic solutions described in the preceding section. The streamwise and wall-normal rms velocities, u' and v', for the upper solutions as well as for the autonomous solutions, are shown in figure 3, while those for the lower solutions are shown in figure 4. It can be seen that the rms velocities of the autonomous solution, Nagata's upper-branch solution and the upper-periodic solution are roughly consistent, but that they are very different from the lower-branch and lower-periodic solutions. The profiles of the autonomous and upper-periodic solutions in figure 3 seem to be qualitatively similar to those of near-wall turbulence, and the similarity will be discussed in the next section. The lower solutions, on the other hand, have stronger u'^+ and weaker v'^+, which implies that they are dominated by streaks rather than streamwise vortices and so are in a relatively quiescent state.

Since significant differences in the rms velocities are observed between the solutions, we next use the maximum rms velocities in the streamwise and wall-normal directions, u'_{max} and v'_{max}, to characterize them. It turns out from figure 5 that all the solutions are clas-

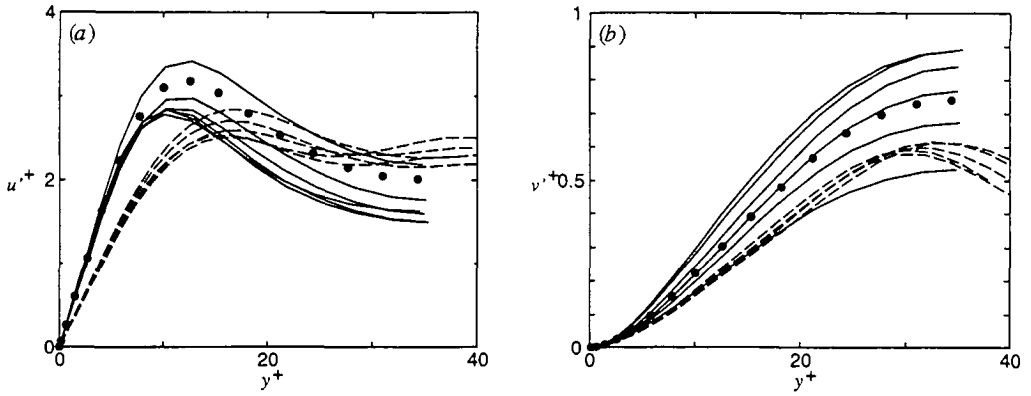

FIGURE 3. Rms velocities for the autonomous solutions, Nagata's upper branch, and the upper cycle versus y^+. (*a*) The streamwise component. (*b*) The wall-normal component. ---- , the autonomous solutions from table 1; ——— , Nagata's upper-branch solutions from table 2; • , the upper cycle with the period $T_p^+ = 188$ from table 4.

sified into two families. One of them is the vortex-dominated family, which is represented by larger v'^+_{max}, and is composed of the autonomous, upper-branch and upper-periodic solutions. The other is the streak-dominated family, which is composed of Nagata's lower branch and the lower periodic solution. The same separation into families is found if we replace v'_{max} by the maximum of the streamwise rms vorticity ω'_x (not shown here). This means that the former family is actually dominated by streamwise vortices. In this figure we have added two of Nagata's solutions for different values of Re and L_x. They have been tracked by changing L_z for fixed Re and L_x in the same way as in figure 1. The open circles and diamonds represent the upper and lower branches for $Re = 600$ and $L_x = 2\pi h$. The solid circles and diamonds represent the upper and lower branches for $Re = 400$ and $L_x = 3\pi h$. Since the separation into two branches persists even when the parameters are changed, we can assume that it is an intrinsic property of the solution.

The simple solutions discussed here have distinct natures, e.g. either (i) autonomous or Couette flow, and (ii) steady, traveling-wave, or periodic. It is remarkable that all the solutions are classified into just two families.

Let us further compare the autonomous and upper-cycle solutions, which have been classified into the same family. Figure 6 shows these solutions on the plane whose coordinates are the total turbulent production and dissipation rates, P^+ and D^+, which are respectively defined as the integrals of the turbulent production and dissipation with respect to y^+ up to $y^+ = h^+$ (up to δ_1^+ in the autonomous case). Note that the autonomous solutions, though in equilibrium, are not in energy balance because of the presence of explicit filtering (2.1). Since the filter is responsible for part of the energy dissipation, the production exceeds the dissipation in the autonomous flows themselves. The autonomous solutions are roughly aligned along the periodic orbit in the production phase in which $P^+ > D^+$. In figure 7, we compare the spanwise rms velocity for the autonomous solutions with that averaged over one whole period for the periodic solution, as well as with that averaged only in the production (or dissipation) phase, $P^+ > D^+$ (or $P^+ < D^+$). It is clear that the autonomous solutions are closer to the time average of the upper cycle solution in the production phase than to the average over the whole period. The striking difference in w' between the production and the dissipation phases is also quite interesting. No significant difference in the other two components of rms velocities is observed.

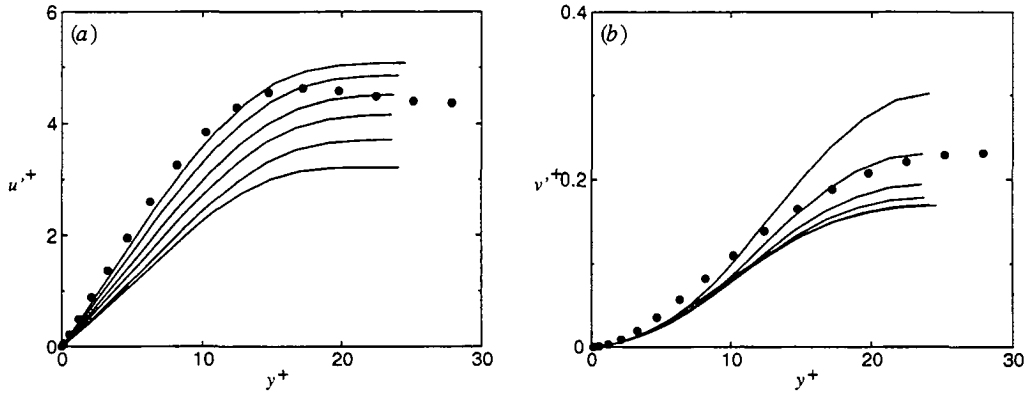

FIGURE 4. Rms velocities for Nagata's lower branch and the lower cycle against y^+. (*a*) The streamwise component. (*b*) The wall-normal component. ——— , Nagata's lower-branch solutions from table 2; • , the lower cycle with the period $T_p^+ = 299$ from table 4.

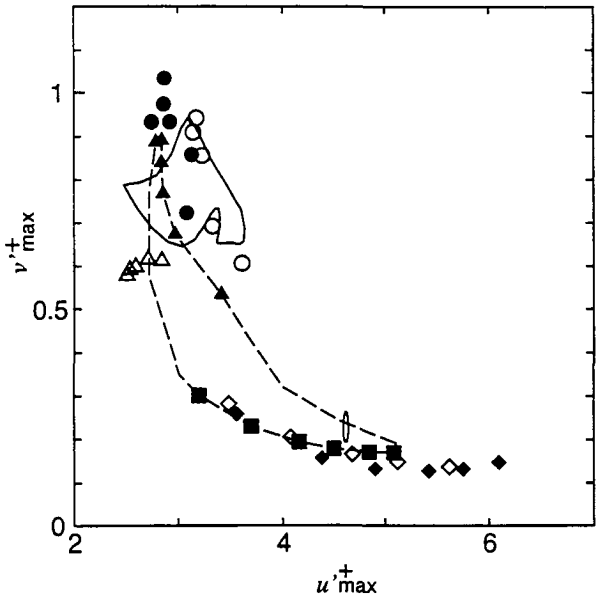

FIGURE 5. Classification into upper and lower solutions in terms of the maximum streamwise and wall-normal rms velocities, u'_{max} and v'_{max}. The solid large and small loops represent the upper and lower periodic solutions with $T_p^+ = 188$ and 299 in table 4, respectively. The dashed loop represents the Nagata steady solution for $Re = 400$ and $L_x = 2\pi h$ in figure 1. △, the autonomous solutions from table 1; ▲ , Nagata's upper-branch solutions from table 2; • , Nagata's upper-branch solutions for $Re = 400$ and $L_x = 3\pi h$; ○ , Nagata's upper-branch solutions for $Re = 600$ and $L_x = 2\pi h$. ■ , Nagata's lower-branch solutions from table 3; ◆ , Nagata's upper-branch solutions for $Re = 400$ and $L_x = 3\pi h$; ◇ , Nagata's lower-branch solutions for $Re = 600$ and $L_x = 2\pi h$.

Enhancement of the spanwise fluid motion is considered to be closely related with the sinuous instability of streaks (Kawahara, Jiménez, Uhlmann & Pinelli 2002).

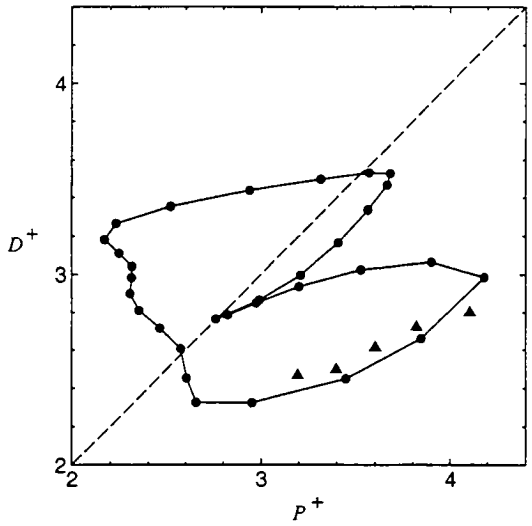

FIGURE 6. Total turbulent production and dissipation rates for the autonomous and the upper periodic solutions. ▲ , autonomous solutions from table 1; —•— , the upper periodic solution with $T_p^+ = 188$ in table 4. The production and dissipation are in balance on the dashed diagonal.

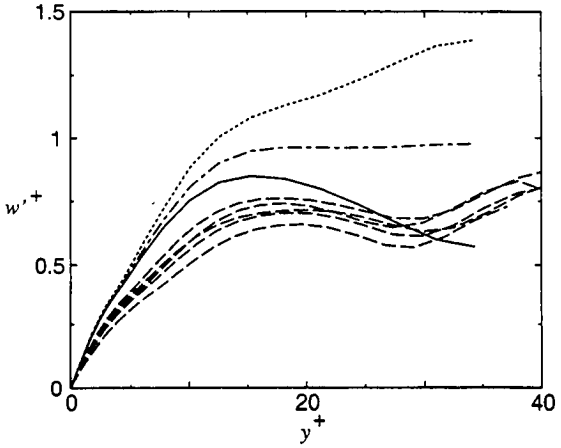

FIGURE 7. Spanwise rms velocities for the autonomous and the upper periodic solutions against y^+. - - - - , the autonomous solutions from table 1; —·— , the whole time average of the upper periodic solution with $T_p^+ = 188$ in table 4. ——— , the time average of the upper periodic solution in a production phase $P^+ > D^+$; ····· , the time average of the upper periodic solution in a dissipation phase $P^+ < D^+$.

4. Comparison with turbulent flows

After the classification in the previous section of the different simple solutions of the Navier–Stokes equations, it is interesting to inquire about their relation with fully developed turbulence in channels with large computational boxes (del Álamo & Jiménez 2001). We will use for that purpose the same two quantities u'_{max}, v'_{max} used above for the characterization of the simple solutions although, to make them comparable in both cases, we will refer them to boxes of comparable sizes. Thus, when computing the statistics of

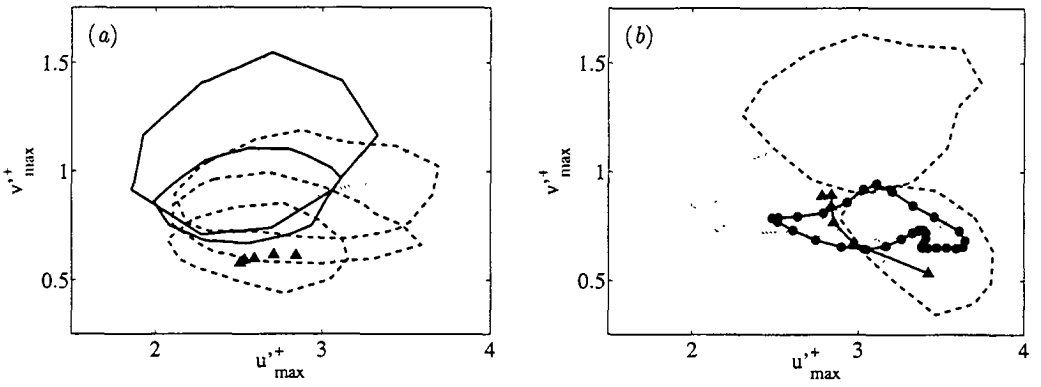

FIGURE 8. Comparison between turbulent and simple solutions. (a) Poiseuille flows. ——— , full channels from del Álamo & Jiménez (2001). The statistics are taken over sub-boxes of size $L_x^+ \times L_z^+ \approx 380 \times 180$. $Re_\tau = 550$, 180, decreasing from top to bottom; - - - - , minimal channels in boxes of approximately the same size as above. From top to bottom, $Re_\tau = 180$, 120, 85; ····· , Couette flows from (b), included for comparison; ▲ , autonomous permanent waves from table 1. (b) Couette flows. - - - - , minimal flows, $L_x^+ \times L_z^+ \approx 350 \times 150$. From top to bottom, $Re_\tau = 115$, 34. ····· , Poiseuille flows in (a); —•— , the upper cycle with $T_p^+ = 188$ from table 4; —▲— , the Nagata's upper branch from table 2.

full-sized turbulent channels, which have boxes of the order of $L_x^+ \times L_z^+ \approx 10,000 \times 5,000$, we will divide each wall of the large box into sub-boxes of size comparable to the wavelengths of the simple solutions, and the rms velocity fluctuations computed over those sub-boxes are used for the comparison.

Each sub-box is characterized by its maximum rms intensities, and the values for different sub-boxes and for different times are summarized as a joint probability density function of the two quantities. Figure 8 shows probability isolines containing 75% of the samples for each flow, compared with the single points characterizing the instantaneous values of the different upper-branch solutions. It is clear that the p.d.f.s of the full flows converge towards the simple waves as the Reynolds number decreases. Both in the Poiseuille flows in figure 8(a) and in the Couette flows in figure 8(b), the lowest Reynolds number used for the turbulent simulations is very close to the minimum value below which turbulence cannot be sustained.

It is interesting that full-sized and minimal Poiseuille flows have slightly different behaviour as the Reynolds number increases, although this may not be too significant, because the statistics are fairly sensitive to the size of the box over which they are compiled. The scatter in u'_{max} increases markedly as the box in made narrower, clearly because the samples are taken over smaller pieces of the same large streaks. The same variability does not extend to v'_{max}, probably because the scale of the v features is always smaller than the sampling boxes being used (del Álamo & Jiménez 2001). Note also that Couette and Poiseuille flows diverge at low Reynolds numbers, which is not surprising since the interactions between the two walls are substantial in that limit, but that their statistics tend to converge at higher Reynolds numbers.

Since v' peaks fairly far from the wall, the maxima in the higher-Reynolds number channel in figure 8(a) were computed only for the layer below $y^+ = 180$, despite which the maximum wall-normal velocity increases with Re_τ. Similar results are obtained by using ω'_x, instead of v', to characterize the strength of the vortices, which supports the conclusion that the vortices get stronger. This is probably independent of any interaction

with the external flow, since Jiménez & Pinelli (1999) observed that the peak vorticity fluctuations in minimal channels increased with Reynolds numbers in the range $Re_\tau = 200 - 600$, even if there was essentially no outer flow in those cases.

Note that lower-branch solutions have not been included in figure 8. Although Kawahara & Kida (2001) found that minimal Couette flow occasionally visits solutions in that branch and then becomes strongly turbulent, the same could not be confirmed here for other cases, and may be a peculiarity of flows on the verge of relaminarization.

5. Conclusions

We have shown that several known simple solutions to the Navier-Stokes equations, particularly those which correspond to permanent waves and to limit cycles in autonomous flows (Jiménez & Simens 2001), and Couette flows, can be classified into upper- and lower-branch families which agree fairly well with the corresponding branches of the Couette waves found by Nagata (1990). The velocity statistics within each branch are reasonably consistent, even though the base flows are quite different.

Although Kawahara & Kida (2001) found that minimal Couette turbulence intermittently visits the lower-branch solutions, the same does not seem to be true in flows at somewhat higher Reynolds numbers, or in larger boxes, although occasional excursions cannot be ruled out. This could be interpreted to mean that the lower branch, which should be the saddle point which Toh & Itano (1999), Itano & Toh (2001) and Kawahara & Kida (2001) found to be involved in the transition to fully turbulent states, represents an occasional tendency of minimal turbulence to relaminarize and retransition, but that these events are not allowed at higher Reynolds numbers, or in larger boxes, because of the higher level of ambient perturbations.

Fully-turbulent flows, when analyzed over sub-boxes of size consistent with the wavelengths of the permanent waves, have been shown to tend to the upper-branch solutions as the Reynolds number decreases, both in Poiseuille and in Couette flows. A reasonable interpretation is therefore that the permanent waves and cycles in that branch embody the nonlinear regeneration cycle of near-wall turbulence that has been described in the past by many investigators.

Waleffe (1998, 2001) also reported the structural similarities of his upper-branch equilibrium states with near-wall turbulence, although he presented no statistics. Because we were not able to reproduce his solutions within the time of the summer school, they are not included in the present comparison.

6. Acknowledgements

We are grateful to Professor M. Nagata for reading an early version of the manuscript. G.K. and M. Shiba appreciate helpful discussions with Professor S. Yanase in the development of a numerical code for an equilibrium solution. This work was supported in part by a Grant-in-Aid for Scientific Research (C) from Japan Society for the Promotion of Science, by the Spanish CICYT contract BFM2000-1468 and by ONR grant N0014-00-1-0146. M. Simens was supported in part by a fellowship from the TMR Intermittency network of the EC.

REFERENCES

CORRAL, R. & JIMÉNEZ, J. 1995 Fourier/Chebyshev methods for the incompressible Navier Stokes equations in infinite domains, *J. Comput. Phys.* **121**, 261–270.

COUGHLIN, K., JIMÉNEZ, J. & MOSER, R. 1994 Instability of streamwise vortices in plane channel flows. *Proc. 1994 Summer Program*, Center for Turbulence Research, NASA Ames/Stanford Univ., 229-244.

DEL ÁLAMO, J.C. & JIMÉNEZ, J. 2001 Direct numerical simulation of the very-large anisotropic scales in a turbulent channel. *Annual Research Briefs*, Center for Turbulence Research, NASA Ames/Stanford Univ., 329–342.

EHRENSTEIN, U. & KOCH, W. 1991 Three-dimensional wavelike equilibrium states in plane Poiseuille flow. *J. Fluid Mech.* **228**, 111–148.

HAMILTON, J.M., KIM, J. & WALEFFE, F. 1995 Regeneration mechanisms of near-wall turbulence structures. *J. Fluid Mech.* **287**, 317–348.

ITANO, T. & TOH, S. 2001 The dynamics of bursting process in wall turbulence. *J. Phys. Soc. Jpn.* **70**, 701–714.

JIMÉNEZ, J., FLORES, O. & GARCÍA-VILLALBA, M. 2001 The large scale organization of autonomous turbulent walls, *Annual Research Briefs*, Center for Turbulence Research, NASA Ames/Stanford Univ., 317–329.

JIMÉNEZ, J. & MOIN, P. 1991 The minimal flow unit in near wall turbulence. *J. Fluid Mech.* **225**, 221–240.

JIMÉNEZ, J. & PINELLI A. 1999 The autonomous cycle of near wall turbulence, *J. Fluid Mech.* **389**, 335–359.

JIMÉNEZ, J. & SIMENS, M.P. 2001 Low-dimensional dynamics in a turbulent wall, *J. Fluid Mech.* **435**, 81–91.

KAWAHARA, G., JIMÉMENZ, J., UHLMANN, M. & PINELLI, A. 2002 Linear instability of a corrugated vortex sheet – a model for streak instability. Submitted to *J. Fluid Mech.*

KAWAHARA, G. & KIDA, S. 2001 Periodic motion embedded in plane Couette turbulence: regeneration cycle and burst. *J. Fluid Mech.* **449**, 291–300.

KIM, J., MOIN, P. & MOSER, R. 1987 Turbulence statistics in fully developed channel flow at low Reynolds number. *J. Fluid Mech.* **177**, 133–166.

NAGATA, M. 1986 Bifurcations in Couette flow between almost corotating cylinders. *J. Fluid Mech.* **169**, 229–250.

NAGATA, M. 1988 On wavy instabilities of the Taylor-vortex flow between corotating cylinders. *J. Fluid Mech.* **188**, 585–598.

NAGATA, M. 1990 Three-dimensional finite-amplitude solutions in plane Couette flow: bifurcation from infinity. *J. Fluid Mech.* **217**, 519–527.

SHIBA, M. 2001 Equiliburium and turbulent solutions for a wall-bounded shear flow. *Master's thesis*, Ehime Univ. (in Japanese).

TOH, S. & ITANO, T. 1999 Low-dimensional dynamics embedded in a plane Poiseuille flow turbulence. Traveling-wave solution is a saddle point? preprint. physics/9905012.

WALEFFE, F. 1998 Three-dimensional coherent states in plane shear flows. *Phys. Rev. Letters* **81**, 4140–4143.

WALEFFE, F. 2001 Exact coherent structures in channel flow. *J. Fluid Mech.* **435**, 93–102.

Center for Turbulence Research
Proceedings of the Summer Program 2002

MHD turbulence in the presence of a strong magnetic field

By S. C. Kassinos, B. Knaepen AND D. Carati

We consider the case of homogeneous turbulence in a conducting fluid that is exposed to a uniform external magnetic field. When the magnetic Reynolds number is vanishingly small ($R_m \ll 1$), the induced magnetic fluctuations are much weaker than the applied field, and in addition, their characteristic time scale based on their diffusion is much shorter than the eddy turnover time. In this case, it is customary to simplify the governing MHD equations using what is known as the quasi-static (QS) approximation. In practice, the QS approximation is often used even when R_m is moderately high, where its validity is unclear. Here we introduce a new approximation, which we have called the Quasi-Linear (QL) approximation, which is designed to be valid for both small and moderate R_m. The accuracy of both approximations is systematically studied in a series of direct numerical simulations (DNS) of decaying MHD turbulence, in which their predictions are compared with those of the full system of MHD equations. Both approximations are satisfactory for $R_m \lesssim 1$, but the QL approximation is clearly shown to be much more accurate for moderately high values, $1 \lesssim R_m \lesssim 10$.

1. Introduction

1.1. *Motivation and objectives*

The interaction of the turbulence in a conducting fluid with an externally-applied magnetic field at low magnetic Reynolds numbers is important in both Magnetohydrodynamic (MHD) and Magnetogasdynamic (MGD) applications. MHD applications include the use of electromagnetic brakes to control flow unsteadiness during continuous steel casting, and flow-control schemes for submarines. MGD applications involve advanced flow control and propulsion schemes for hypersonic vehicles. In MGD applications, fluid conductivity arises due to thermal ionization of the incoming flow, which in addition can be seeded if desired.

CFD codes used for the prediction of MHD and MGD flows rely on simple turbulence models, like k-ϵ models, with additional *ad hoc* modifications to account for the effects of the magnetic field. This approach neglects the important dynamical role that the structure of the turbulence plays in the interaction between the turbulence and the applied magnetic field. Unfortunately, simple closures using *ad hoc* MHD modifications cannot account for structural effects and, as a result, they tend to be flow-specific, lacking any degree of generality.

Structure-Based Models (SBM) are by construction able to account for the dynamical effects of the energy-containing turbulence structure. Preliminary work in the case of homogeneous unstrained MHD turbulence (Kassinos & Reynolds 1999), has shown that SBM are well suited for use in the prediction of MHD and MGD applications. The task of developing turbulence SBM or other closures for MHD and MGD applications can be simplified by taking advantage of approximations to the governing equations that are valid for the flow regimes that are typically encountered in technological applications.

The objective of this work is to explore two different approximations that can be used for flow regimes of relevance to MHD and MGD applications. For vanishingly small magnetic Reynolds numbers ($R_m \ll 1$), the induced magnetic fluctuations are much weaker than the applied field and their characteristic time scale, based on their diffusion, is much shorter than the eddy turnover time. A classical approximation for decaying MHD turbulence at low R_m is the Quasi-Static (QS) approximation. As recalled in section 3.1, in this approximation, the induced magnetic field fluctuations become a linear function of the velocity filed. In practice, the QS approximation is often used for the prediction of flows even where $1 \lesssim R_m \lesssim 10$, and therefore here we seek to establish the exact range of validity of the QS approximation. In section 4.1, we also introduce a new approximation, which we have called the Quasi-Linear approximation (QL). The QL approximation is designed to be valid even when the Re_m is moderately high. Thus, we seek to establish the range of validity of the QL approximation and also to compare the relative accuracy of the two approximations.

We start by discussing the relevant dimensionless parameters that characterize MHD and MGD flows in greater detail. In section 3.1 we introduce the governing equations and the simplifications associated with the QS approximation. The numerical code and initial conditions used for the numerical experiments are described in section 3.2, while section 3.3 is devoted to a discussion of the results pertaining to the QS approximation. This is followed in section 4.1 by a detailed description of the QL approximation and in section 4.2 by the description of its predictions. A concluding summary is given in section 5.

2. Dimensionless parameters

The effects of a uniform magnetic field applied to unstrained homogeneous turbulence in an electrically conductive fluid are characterized by two dimensionless parameters, the first being the magnetic Reynolds number

$$R_m = \frac{vL}{\eta} = (\frac{v}{L})(\frac{L^2}{\eta}). \tag{2.1}$$

Here v is the r.m.s. fluctuating velocity

$$v = \sqrt{R_{ii}/3}, \qquad R_{ij} = \overline{u_i u_j}\,, \tag{2.2}$$

where u_i is the fluctuating velocity, and L is the integral length scale. η is the magnetic diffusivity

$$\eta = 1/(\sigma\mu^*) \tag{2.3}$$

where σ is the electric conductivity of the fluid, and μ^* is the fluid magnetic permeability (here we use μ^* for the magnetic permeability and reserve μ for the dynamic viscosity). Thus the magnetic Reynolds number represents the ratio of the characteristic time scale for diffusion of the magnetic field to the time scale of the turbulence. In the case of vanishingly small R_m, the distortion of the magnetic field lines by the fluid turbulence is sufficiently small that the induced magnetic fluctuations $\mathbf{b}$ around the mean (imposed) magnetic field $\mathbf{B}$ are also small.

One can also define a magnetic Prandtl number representing the ratio of R_m to the

hydrodynamic Reynolds number Re_L

$$P_m \equiv \frac{\nu}{\eta} = \frac{R_m}{Re_L}, \qquad Re_L = \frac{vL}{\nu}. \tag{2.4}$$

The second relevant dimensionless parameter is the magnetic-interaction number (or Stuart number),

$$N \equiv \frac{\sigma B^2 L}{\rho v} = \frac{\tau}{\tau_m} \tag{2.5}$$

where B is the magnitude of the magnetic field and ρ is the fluid density. N represents the ratio of the large-eddy turnover time τ to the Joule time τ_m, i.e. the characteristic time scale for dissipation of turbulent kinetic energy by the action of the Lorentz force. N parametrizes the ability of an imposed magnetic field to drive the turbulence to a two-dimensional three-component state. Under the continuous action of the Lorentz force, energy becomes increasingly concentrated in modes independent of the coordinate direction aligned with **B**. As a two-dimensional state is approached, Joule dissipation decreases because fewer and fewer modes with gradients in the direction of **B** are left available. In addition, the tendency towards two-dimensionality and anisotropy is continuously opposed by non-linear angular energy transfer from modes perpendicular to **B** to other modes, which tends to restore isotropy. If N is larger than some critical value N_c, the Lorentz force is able to drive the turbulence to a state of complete two-dimensionality. For smaller N, the Joule dissipation is balanced by non-linear transfer before a complete two-dimensionality is reached. For very small N ($N \leq 1$), the anisotropy induced by the Joule dissipation is negligible. Here we consider N in the range $1 - 50$.

In MGD applications relying on thermal ionization without artificial flow seeding, the magnetic Reynolds number ranges from $R_m \sim 10^{-3}$ to $R_m \sim 5$ depending on the vehicle speed. The magnetic-interaction or Stuart number is typically of order unity.

3. The Quasi-Static approximation

3.1. *Equations and assumptions*

If the external magnetic field B_i^{ext} is explicitly separated from the fluctuations b_i, the MHD equations can be written as

$$\partial_t u_i = -\partial_i(p/\rho) - u_j \partial_j u_i + \frac{1}{(\mu^* \rho)}(B_j^{ext} + b_j)\partial_j(B_i^{ext} + b_i) + \nu \Delta u_i, \tag{3.1}$$

$$\partial_t(B_i^{ext} + b_i) = -u_j \partial_j(B_i^{ext} + b_i) + (B_j^{ext} + b_j)\partial_j u_i + \eta \Delta(B_i^{ext} + b_i), \tag{3.2}$$

where p is the sum of the kinematic and magnetic pressures, ν is the kinematic viscosity, ρ is the fluid density, μ^* is the magnetic permeability and η is the magnetic resistivity.

Since here we only consider homogeneous and stationary external magnetic fields, (3.1) and (3.2) reduce to

$$\partial_t u_i = -\partial_i(p/\rho) - u_j \partial_j u_i + \frac{1}{(\mu^* \rho)} b_j \partial_j b_i + \frac{1}{(\mu^* \rho)} B_j^{ext} \partial_j b_i + \nu \Delta u_i, \tag{3.3}$$

$$\partial_t b_i = -u_j \partial_j b_i + b_j \partial_j u_i + B_j^{ext} \partial_j u_i + \eta \Delta b_i. \tag{3.4}$$

For flows at low magnetic Reynolds number, (3.4) can be simplified considerably (see e.g. Roberts 1967). Indeed, by definition, the limit $R_m \ll 1$ describes flows for which

non-linear terms resulting from magnetic fluctuations are negligible when compared to the dissipative term in (3.4). This is easily seen by adopting the traditional scalings,

$$\|u_j\partial_j b_i\| = \frac{vb}{L}, \quad \|b_j\partial_j u_i\| = \frac{vb}{L}, \quad \|\eta\Delta b_i\| = \frac{\eta b}{L^2}, \tag{3.5}$$

where $b = \sqrt{\frac{2}{3}b_i b_i}$, and noting that

$$R_m = \frac{vL}{\eta} = \frac{\|u_j\partial_j b_i\|}{\|\eta\Delta b_i\|} = \frac{\|b_j\partial_j u_i\|}{\|\eta\Delta b_i\|}. \tag{3.6}$$

In place of (3.4) we thus have, in the limit $R_m \ll 1$,

$$\partial_t b_i = B_j^{ext}\partial_j u_i + \eta\Delta b_i. \tag{3.7}$$

The so-called *quasi-static* (QS) *approximation* (Roberts 1967) is obtained by further assuming that $\partial_t b_i \approx 0$ in (3.7). To understand how this comes about, let us consider the time scales of the two terms on the right-hand side of (3.7). Since B^{ext} is independent of time, the time scale of $B_j^{ext}\partial_j u_i$ is $\mathcal{T} = L/v$, while the time scale of the diffusion term can be identified with the damping time $\mathcal{T}^* = L^2/\eta$. The ratio of these two time scales is then

$$\frac{\mathcal{T}^*}{\mathcal{T}} = R_m, \tag{3.8}$$

indicating that at low magnetic Reynolds number, diffusion time is much smaller than large-eddy turnover time. This justifies the assumption $\partial_t b_i \approx 0$ since the magnetic fluctuations then adapt instantaneously to the slowly varying velocity field and reach their asymptotic values for which $\partial_t b_i \approx 0$ (see section 4.1 for more details). In the QS approximation, we thus have

$$\eta\Delta b_i = -B_j^{ext}\partial_j u_i. \tag{3.9}$$

Using a Fourier representation for u_i and b_i, this equation is readily solved and yields

$$b_i(\mathbf{k},t) = i\frac{(B_j^{ext}k_j)}{\eta k^2}u_i(\mathbf{k},t), \tag{3.10}$$

where we have defined

$$u_i(\mathbf{k},t) = \sum u_i(\mathbf{x},t)e^{-i\mathbf{k}\cdot\mathbf{x}}, \quad b_i(\mathbf{k},t) = \sum b_i(\mathbf{x},t)e^{-i\mathbf{k}\cdot\mathbf{x}}. \tag{3.11}$$

Since b_i is now expressed completely in terms of u_i, the evolution equation for the velocity field can be explicitly closed. In Fourier representation one gets,

$$\partial_t u_i(\mathbf{k},t) = -\partial_i p'(\mathbf{k},t) - [u_j\partial_j u_i](\mathbf{k},t) - \sigma\frac{(\mathbf{B}^{ext}\cdot\mathbf{k})^2}{\rho k^2}u_i(\mathbf{k},t) - \nu k^2 u_i(\mathbf{k},t), \tag{3.12}$$

where $p' = p/\rho$ (consistently with the small magnetic fluctuations assumption, the second-order term $b_j\partial_j b_i$ does not appear in (3.12)).

To summarize, two simplifications are needed in order to reach (3.12). The first consists in neglecting the non-linear terms $u_j\partial_j b_i$ and $b_j\partial_j b_i$ in (3.4). The second is obtained by discarding the time derivative of b_i in (3.7). These two simplifications are consequences of the assumption $R_m \ll 1$ and one should thus expect them to break down when the magnetic Reynolds number is increased. In the next sections, we test the QS approximation by comparing its predictions to those obtained using the full MHD equations (3.3) and (3.4).

3.2. *Numerical code and initial condition*

To test the range of validity of the QS approximation, we have used two different pseudo-spectral codes. The first one simulates the full MHD equations (3.3) and (3.4), while the second one simulates (3.12). All the runs presented here have a resolution of 128^3 cube Fourier modes in a $(2\pi)^3$ computational domain.

The initial condition for the velocity field is common to both codes. The field is initialized in Fourier space and the mode amplitudes are set to match the spectra (see Rogallo 1981 for details),

$$E(k) = 16\left(\frac{2}{\pi}\right)^{.5} \frac{v_0^2}{{k_p}^5} k^4 \exp(-2k^2/{k_p}^2), \tag{3.13}$$

where we have arbitrarily set $v_0 = 1$ and $k_p = 3$. In order to let the higher-order statistics develop, the flow is then evolved (without any external magnetic field) until the skewness reaches its peak value. At that time, hereafter referred to as t_0, the external magnetic field is switched on.

For the full MHD case, an initial condition for b_i has to be chosen at $t = t_0$. Here we have made the choice $b_i(t_0) = 0$. In other words, our simulations describe the response of an initially non-magnetized turbulent conductive fluid to the application of a strong magnetic field. The corresponding completely-linearized problem has been described in detail in Moffatt (1967). For the QS approximation case, an initial condition for b_i is of course not required since the equation for the velocity field is completely closed. In this case, the initial condition is in fact implicitly given by (3.10) at $t = t_0$. One could then argue that the two codes do not simulate the same flow since they do not have the same initial condition for the magnetic field. However, the independence of the QS approximation of the initial magnetic field is precisely one aspect that is interesting to test. If the flow behaves according to the QS approximation, the magnetic field (using full MHD) should very rapidly converge to the value given by (3.10).

The only free parameters that remain to be specified are the kinematic viscosity ν, magnetic diffusivity η and external 'magnetic field' strength $B^{ext}/\sqrt{\mu^* \rho}$ (by convention we chose the magnetic field to be orientated in the z direction). The kinematic viscosity is $\nu = 0.003$ for all the runs and the rest of the parameters are specified in table 1, along with the corresponding values of the interaction number and magnetic Reynolds number at $t = t_0$. These last two quantities are calculated using (2.1) and (2.5), taking into account the fact that at $t = t_0$ (i. e. at the end of the initial decay during which $B^{ext} = 0$), we have $v(t_0) = 0.984$ and $L(t_0) = 0.787$.

All the runs can be grouped according to the initial value of the Stuart number. For the first five runs we have $N(t_0) = 1$; for the next five $N(t_0) = 10$ and finally for runs 11-15 we have $N(t_0) = 50$.

3.3. *Results*

In this section we present some results obtained by performing the simulations detailed in section 3.2.

3.3.1. *Kinetic energy decay*

In figure 1 we present the time evolution of the normalized kinetic energy,

$$E_K = \frac{1}{E_K(0)} \int d\mathbf{x} \frac{1}{2} u_i(\mathbf{x}) u_i(\mathbf{x}). \tag{3.14}$$

#	η	$\frac{B^{ext}}{\sqrt{\mu^* \rho}}$	$N(t_0)$	$R_m(t_0)$
1	7.75	3.11	1	0.1
2	.387	.696	1	2.0
3	.258	.568	1	3.0
4	.155	.440	1	5.0
5	.0775	.311	1	10.0
6	7.75	9.84	10	0.1
7	.387	2.20	10	2.0
8	.258	1.80	10	3.0
9	.155	1.39	10	5.0
10	.0775	.984	10	10.0
11	7.75	22.0	50	0.1
12	.387	4.92	50	2.0
13	.258	4.02	50	3.0
14	.155	3.11	50	5.0
15	.0775	2.20	50	10.0

TABLE 1. Summary of the parameters for the different runs performed

From (3.12), it is clear that the behavior of u_i in the QS approximation does not depend on the magnetic Reynolds number but only on the Stuart number (all other parameters being constant). The reason for this is of course that the QS approximation corresponds to the implicit limit $R_m \to 0$. As expected, in each set of runs at fixed $N(t_0)$ the agreement between full MHD and the QS approximation gets better as the Reynolds decreases. At $R_m = 0.1$ the agreement is nearly perfect. At intermediate values, $R_m = 2$ and above, there is a quite severe discrepancy: the rate at which the QS approximation dissipates kinetic energy is too high.

It is also interesting to note that the difference between full MHD and the quasi-static approximation at higher magnetic Reynolds numbers is not very sensitive to the value of the Stuart number.

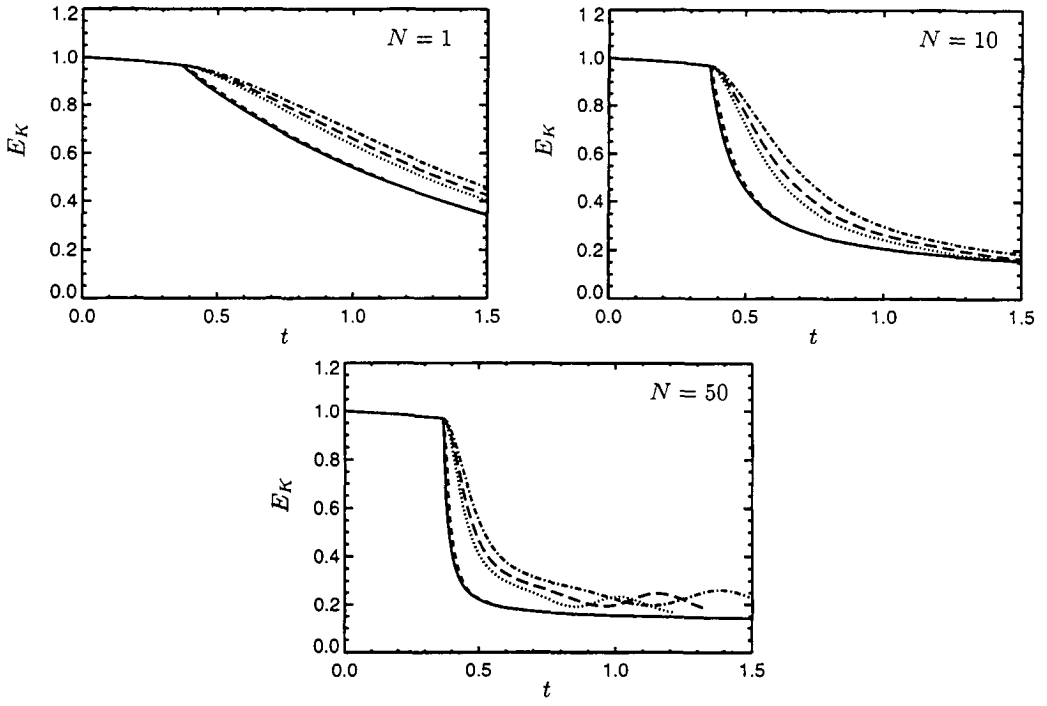

FIGURE 1. Evolution with time of the kinetic energy at different Stuart number and magnetic Reynolds number. ——— quasi-static approximation; ------ $R_m = 0.1$; ····· $R_m = 2$; - - - - $R_m = 3$; —·— $R_m = 5$.

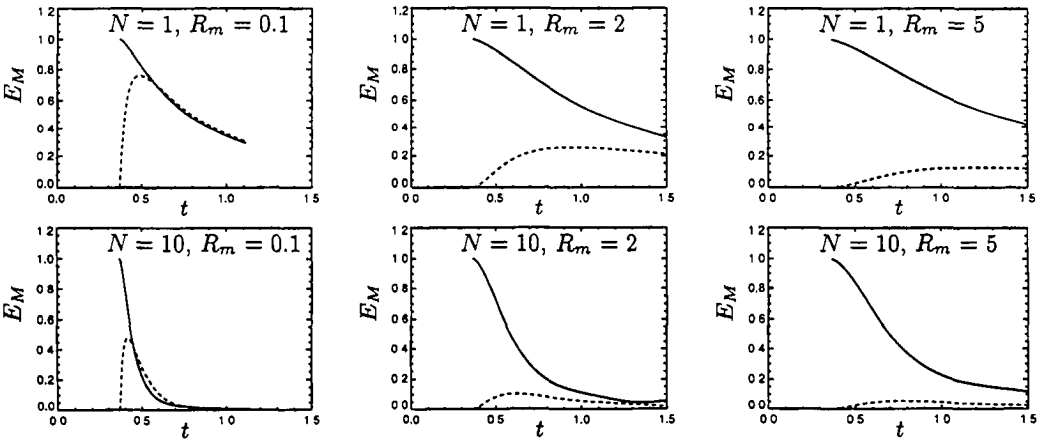

FIGURE 2. Evolution with time of the magnetic energy. ——— 'quasi-static' approximation computed from (3.15); ------ full MHD computed from (3.16).

3.3.2. *Magnetic energy decay*

The difference between full MHD and the QS approximation can result only from the fact that the quasi-static approximation predicts the magnetic fluctuations incorrectly. In order to assess this, we can define two normalized magnetic energies for each full-MHD

run: one obtained from the velocity field through (3.10),

$$E_{M1} = \frac{1}{E_{M1}(t_0)} \int d\mathbf{k} \frac{1}{2} \frac{(B_j^{ext} k_j)^2}{\eta^2 k^4} |u_i(\mathbf{k}, t)|^2, \tag{3.15}$$

and one computed directly from the magnetic fluctuations.

$$E_{M2} = \frac{1}{E_{M1}(t_0)} \int d\mathbf{k} \frac{1}{2} |b_i(\mathbf{k}, t)|^2. \tag{3.16}$$

Ideally, we should have $E_{M1} = E_{M2}$.

The comparison between (3.15) and (3.16) for different runs is displayed in figure 2. We observe that at magnetic Reynolds number $R_m = 0.1$, (3.15) and (3.16) predict similar values soon after the field is switched on. This indicates that, in a very short time, the magnetic fluctuations forget their initial state and 'align' with the predictions of the QS approximation (3.10). This is entirely in the spirit of the assumption that at low magnetic Reynolds number the time derivative in (3.7) can be neglected (or rather that it is significant only during a very short transient time). At higher values of the magnetic Reynolds number the transient time becomes longer and the 'true' energy content of the fluctuations never reaches values comparable to those predicted by the QS expression. The same conclusions hold for the runs at Stuart number $N = 50$ (not displayed).

As one expects, this discussion indicates that neglecting the time derivative of b in the induction equation is problematic when the magnetic Reynolds number is increased. In the next section we study this question in more detail.

4. The Quasi-Linear approximation

4.1. *Governing equations*

As was recalled in section 3.1, the final quasi-static induction equation is obtained by dropping the time derivative of the magnetic field in (3.7). The discussion of the previous section suggests that keeping this time derivative might be crucial when the magnetic Reynolds number is increased.

We thus introduce an intermediate approximation which is obtained by considering the following simplified MHD equations:

$$\partial_t u_i = -\partial_i (p/\rho) - u_j \partial_j u_i + \frac{1}{(\mu^* \rho)} B_j^{ext} \partial_j b_i + \nu \Delta u_i, \tag{4.1}$$

$$\partial_t b_i = B_j^{ext} \partial_j u_i + \eta \Delta b_i. \tag{4.2}$$

We call this approximation the *quasi-linear* (QL) *approximation* since we discard only the non-linear terms involving the magnetic field and keep the non-linear convective term in the velocity equation.

If $\partial_t b_i$ is neglected in (4.2) one immediately recovers the quasi-static approximation. In fact, (4.2) is nothing else than a 'heat' equation for the magnetic field with a source term given by $B_j^{ext} \partial_j u_i$. In Fourier space the solution of this equation is easily obtained and reads,

$$b_i(\mathbf{k}, t) = b_i(\mathbf{k}, 0) e^{-\eta k^2 t} + i \int_0^t d\tau k_j B_j^{ext} u_i(\mathbf{k}, \tau) e^{-\eta k^2 (t-\tau)}. \tag{4.3}$$

From the first term on the right-hand side of (4.3), we see that the initial condition for b_i gets damped more rapidly with increasing magnetic diffusivity (if v and L are

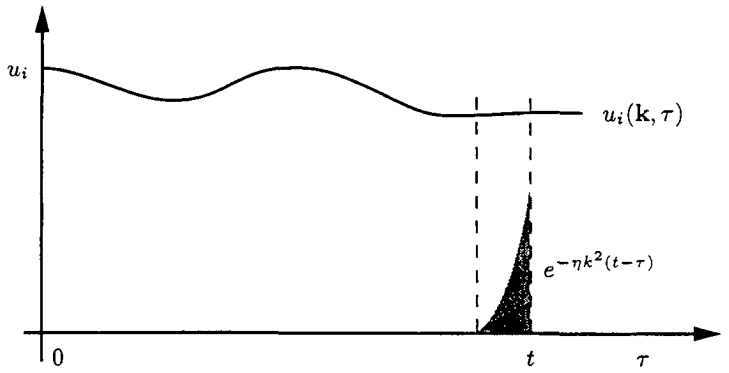

FIGURE 3. Evaluation of $b_i(\mathbf{k},t)$ in the quasi-linear approximation.

constant this is equivalent to a decrease in the magnetic Reynolds number). Note that with the initial condition we have chosen for the magnetic field, i.e. $b_i(0) = 0$, this first term vanishes. At high magnetic diffusivity the integral in (4.3) converges to (3.10) and the QS approximation holds. More explicitly, we have the situation depicted in figure 3. The interval between the dashed lines represents the support in which $\exp^{-\eta k^2(t-\tau)}$ is significant and thus where there is some contribution to the integral of (4.3). As η increases, this interval gets smaller, and $u_i(\mathbf{k},t)$ may be assumed constant in that short period of time. The integration is then immediate and one gets (3.10). Thus, the time history of $u_i(\mathbf{k},t)$ plays a role only when η is small, in which case the exponential has a wider support.

4.2. *Results*

In order to compare the QL approximation with full MHD, we have performed the same numerical simulations as described in section 3, but this time using (4.1) and (4.2) instead of the QS approximation. The only points we mention here are first, that (4.2) needs an initial condition, so to be consistent with the full MHD case we have set $b_i(0) = 0$; and secondly, we have increased the magnetic Reynolds number as far as $R_m = 10$ for the results presented in this section.

4.2.1. *Kinetic energy decay*

In figure 4 we present the time history of the kinetic energy (as defined by (3.14)) obtained from both full MHD and the QL approximation. As is obvious from the graphs, the quasi-linear theory predicts this diagnostic extremely well, even at magnetic Reynolds number up to $R_m = 10$. The improvement over the quasi-static approximation (also shown in the graphs) is evident.

4.2.2. *Magnetic energy decay*

Figure 5 represents the time evolution of the energy of the magnetic fluctuations (defined by (3.16) without the normalization factor) for various values of the Stuart number and magnetic Reynolds number. Each graph contains one curve for the full MHD case and another for the QL approximation case. The agreement is excellent at magnetic Reynolds number $R_m = 2$ and degrades only slightly for higher values. It is interesting to note that, as the Stuart number is increased, the agreement between full MHD and the QL approximation gets better. As in the case of classical homogeneous sheared flows, we thus see that the further away from equilibrium the flow is, the better it is described

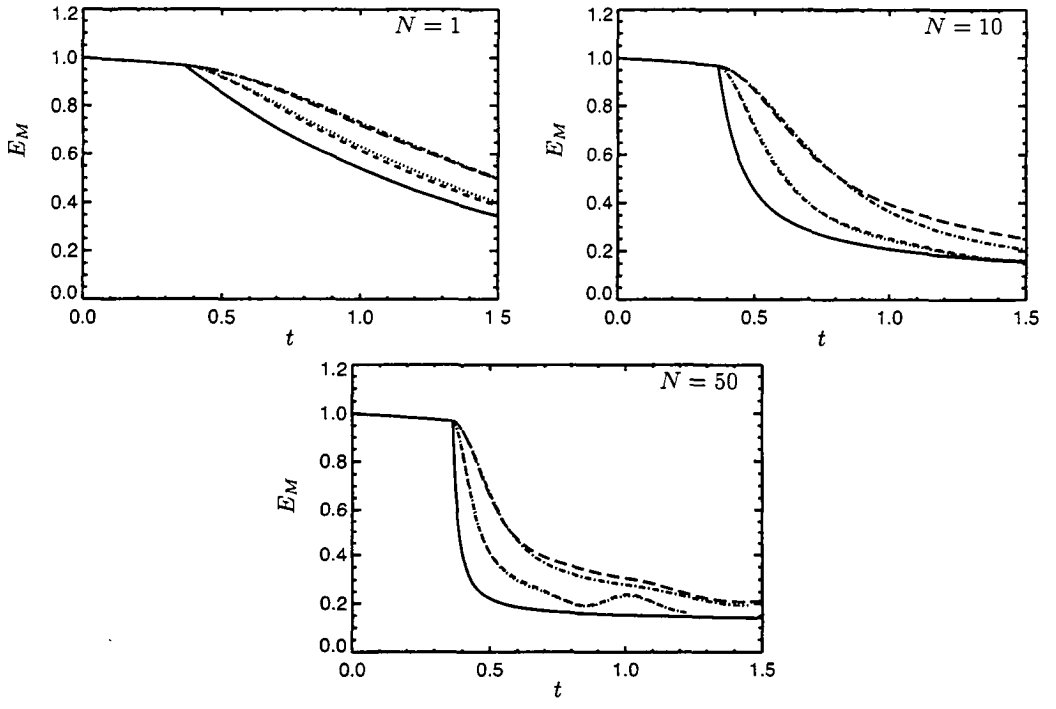

FIGURE 4. Evolution with time of the kinetic energy. ——— quasi-static approx.; ····· $R_m = 2$ full MHD; ------ $R_m = 2$ QL approx.; —·— $R_m = 10$ full MHD; - - - - $R_m = 10$ QL approx.

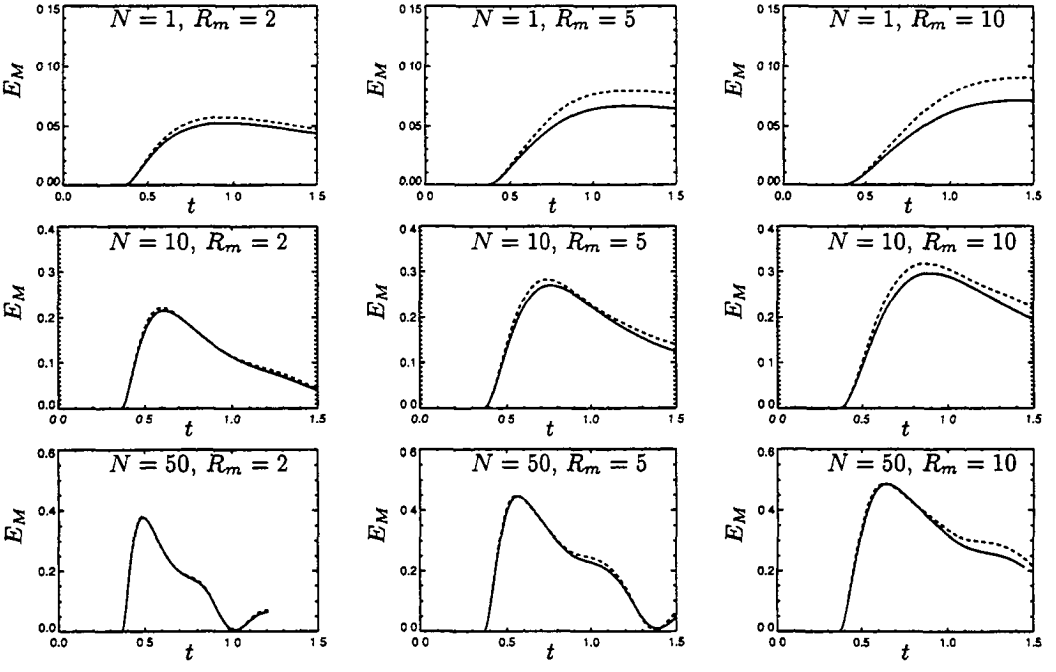

FIGURE 5. Evolution with time of the magnetic energy. ——— full MHD; ------ QL approx.

by a linear theory. The role of increased shear is played here by the increasing external magnetic field.

5. Conclusions and future plans

By studying the case of decaying homogeneous MHD turbulence, we have established that the Quasi-Static (QS) approximation is valid for $R_m \lesssim 1$, but progressively deteriorates as R_m is increased beyond 1. The magnetic Stuart number does not seem to have a strong effect on the accuracy of the QS approximation. That is, at a given R_m, the accuracy of the QS approximation is roughly the same for $N = 1$ as it is for $N = 50$. The QL approximation, as we expected when we proposed it during the Summer Program, performs like the QS approximation for $R_m \lesssim 1$, but has the advantage that it retains excellent agreement with full MHD for $0 \lesssim R_m \lesssim 10$ at least. It should be noted that $R_m = 10$ is the highest value of the magnetic Reynolds number that we tested during the Summer Program.

In terms of computational costs, the QS approximation is clearly the cheapest of the three methods used during our study. It has fewer non-linear terms to evaluate, and the time step needed to advance the flow is governed by the time scale of the velocity field which, for most industrial cases involving liquid metal, is significantly longer than the time scale of the underlying magnetic field.

However, as we have demonstrated, the QS approximation becomes inadequate for conductive flows with moderate magnetic Reynolds numbers such as are, for instance, encountered in MGD applications involving hypersonic vehicles. We have studied another approximation, the *QL approximation*, for use at higher R_m. As with the QS approximation, this approximation assumes small magnetic fluctuations but it tries to resolve the time dependence of these fluctuations explicitly. Our numerical simulations indicate that the QL approximation should be adopted in place of the quasi-static approximation for flows with a moderate value of the magnetic Reynolds number, since in those cases it compares much better with full MHD. In terms of computational cost the QL approximation does not depart enormously from full MHD, but nevertheless allows a reasonable gain since fewer non-linear terms need to be evaluated. The appeal of the QL approximation lies more in the prospect of simpler turbulence models for conductive flows at moderate magnetic Reynolds number. Indeed, the structure of equations (4.1) and (4.2) is simpler than that of the full MHD equations. We thus have a strong hope that devising turbulence models in the framework of the QL approximation should be an easier task. This question will be examined in the coming months and will undoubtedly benefit significantly from the work we have produced during this 2002 Summer Program.

REFERENCES

KASSINOS, S. C. & REYNOLDS, W. C. 1999 Structure-based modeling for homogeneous MHD turbulence. *Annual Research Briefs*, Center for Turbulence Research, NASA Ames/Stanford Univ., 301–315.

MOFFATT, H.K. 1967 On the suppression of turbulence by a uniform magnetic field. *J. Fluid Mech.* **28**, 571–592.

ROBERTS, P. H. 1967 *An Introduction to Magnetohydrodynamics.* Elsevier, New York.

ROGALLO, R.S. 1981 Numerical experiments in homogeneous turbulence. *NASA TM* 81315.

Characteristics of scalar dispersion in turbulent-channel flow

By Juan C. del Álamo † AND Javier Jiménez ‡

The dispersion of a passive scalar by wall turbulence, in the limit of infinite Peclét number, is analyzed using frozen velocity fields from the DNS of del Álamo & Jiménez (2001). The Lagrangian trajectories of fluid particles in these fields are integrated and used to compute the first- and second-order moments of the distribution of fluid-particle displacements. It is shown that the largest scales in the flow dominate turbulent diffusion, and the computed dispersion is in good agreement with measurements in the atmospheric boundary layer. This agreement can be understood by noting that the lifetimes of the large structures are much longer than the time scale of the transition from linear to Gaussian particle spreading in the cross-stream plane. Numerical experiments on computing the Lagrangian trajectories in reference frames moving at different velocities suggest that this transition is controlled by the difference between the mean streamwise velocity and the phase speed of the large-scale structures of the cross-stream velocity field. In the streamwise direction, the effect of the mean shear dominates and produces elongated scalar patches, with dispersion exponents which are different from the transverse ones.

1. Introduction

The prediction of diffusion characteristics in turbulent shear flows, particularly in those near walls, is a notoriously difficult problem. While, for example, the width of a contaminant plume follows a Gaussian spreading law relatively well in isotropic turbulence, or even in wall-bounded flows far enough from the source, this is not true closer to the source (Nokes & Wood 1988), near the wall, or in atmospheric flows. This is an important consideration in many practical applications, such as the prediction of dispersal of pollution from industrial plants, or of hazardous substances from either accidental or malicious releases. There are many other problems in which this subject is important, apart from the ones already mentioned. For instance, the diffusion of odors in the atmosphere is known to affect the migrational patterns of some insects, and it is not known whether similar effects occur in other anisotropic flows, such as near-surface ocean turbulence, where it could influence the rate of decay of the thermal wake of vehicles. The solution to these problems is typically estimated using empirical laws (Brown *et al.* 1997), or computed from semi-empirical models (Hanna *et al.* 1999). Many of these models are used for regulatory purposes, and the fact that some of them produce different results for the same input data is an indication of the difficulty of the problem. This has led to the development of standardization programs (Olesen 1995) with the purpose of establishing systematic procedures for the development and testing of dispersion models, based on compilations of meteorological data from field experiments. However, due to the inherent difficulty of performing such experiments, the data sets are scarce, the number

† School of Aeronautics UPM, 28040 Madrid, Spain.
‡ Also at School of Aeronautics UPM, 28040 Madrid, Spain.

Case	U_{adv}/U_b	Spatial Resolution	No. of Fields	No. of Particles per Field
1	0	full	1	2×10^5
2	0.84	full	1	2×10^5
3	0	$\lambda_x, \lambda_z > 0.25\,h$	3	2×10^5
4	0.84	$\lambda_x, \lambda_z > 0.25\,h$	3	2×10^5

TABLE 1. Summary of computed cases.

of measured magnitudes is limited, and some of the data sets are of doubtful accuracy (Olesen 1994).

Since the atmospheric effects are observed over scales of hundreds of meters, and there are sound theoretical reasons to expect small-scale turbulence to produce Gaussian diffusion at such long distances, it is tempting to conclude that the reason for the anomalous spreading is the presence of very large anisotropic scales (VLAS) in turbulent wall flows. Recently we have performed a direct numerical simulation of turbulent channel flow at moderate Reynolds number, which we believe to be the first which has both a Reynolds number high enough to observe some scale separation and a computational domain large enough not to interfere with the dynamics of the largest scales. The present work, which used flow data from this simulation, is intended to be a first step in using direct numerical simulation in research on atmospheric dispersion, which might contribute to diminishing the current experimental uncertainties.

2. Computing dispersion from frozen fields

We will consider the release of a passive scalar into turbulent channel flow in the limit of infinite Peclét number $U_b h/D$ (here U_b is the bulk mean velocity in the channel, h is the channel half-width, and D is the kinematic diffusivity of the scalar). In that case the dispersion of the scalar is controlled by the Lagrangian trajectories $\mathbf{x}$ of the fluid elements that transport it, given by

$$\frac{\mathrm{d}\mathbf{x}}{\mathrm{d}t} = \mathbf{u}(\mathbf{x}(t), t). \tag{2.1}$$

The main difficulty of computing the Lagrangian trajectories of fluid particles lies in knowing the unsteady three-dimensional velocity field $\mathbf{u}(\mathbf{x}, \mathbf{t})$, which has to be computed from the continuity and Navier-Stokes equations, leading to a problem much more expensive than the integration of (2.1) itself. Due to the preliminary nature of this work, and in order to avoid the computational expense of integrating in time the Lagrangian trajectories coupled with the velocity field, we have decided to calculate the former using frozen velocity fields which were already available from the DNS of turbulent channel flow by del Álamo & Jiménez (2001). This simulation was performed at a Reynolds number $Re_\tau = 550$ based on the friction velocity u_τ and on the channel half-width h, and its most important characteristic is that the computational domain is large enough not to interfere with the largest scales in the flow, which will allow us to study their effect on the scalar dispersion. The size of the numerical box is $L_x \times L_y \times L_z = 8\pi h \times 2h \times 4\pi h$ in the streamwise, wall-normal and spanwise directions, respectively. In isotropic turbulence the frozen-field approximation would be reasonable for times much shorter than the char-

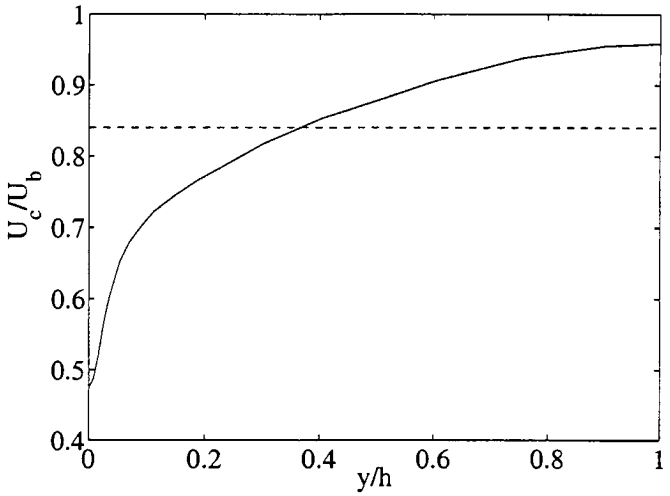

FIGURE 1. ——— , phase velocity U_c of the large-scale spanwise velocity component as a function of wall distance. Only structures such that $\lambda_x, \lambda_z \geq 0.25\,h$ are taken into account. ····· , advection velocity U_{adv} of the frozen fields.

acteristic lifetime of the eddies, which is proportional to their turnover time. However, this might not be true in wall turbulence, where the flow features are known to travel in the streamwise direction with an advection velocity of the order of U_b (Wills, 1964). This advection velocity, acting on scales of length λ, introduces a convective time scale $T_c \sim \lambda/U_b$ which is always shorter that the eddy-turnover time $T_L \sim \lambda/u_\tau$. We have tried to take into account the effect of the mean advection by integrating the Lagrangian trajectories from the frozen velocity fields in a moving reference frame,

$$\frac{d\mathbf{x}}{d\tau} = \mathbf{u}\left(\mathbf{x}(\tau) - \tau \mathbf{U_{adv}},\, t_0\right). \tag{2.2}$$

Here $\mathbf{u}(\mathbf{x}, \mathbf{t_0})$ is the instantaneous frozen velocity field at $t = t_0$, and $\mathbf{U_{adv}} = (U_{adv}, 0, 0)$ is the velocity of the reference frame, which can be interpreted physically as a choice for the convection or 'advection' velocity of the frozen fields. This choice affects the paths of fluid particles by modifying their velocities relative to the turbulent structures. In order to evaluate the effect of the convection velocity of the frozen fields in scalar dispersion, we have integrated (2.2) for two different values of U_{adv}. In one case we have chosen $U_{adv} = 0$, while in the other we have set it equal to the representative phase velocity of the large energetic scales in the flow, which have widths and lengths of the order of or larger than h (del Álamo & Jiménez 2001). There are several possible ways to compute the phase velocity of a flow variable (Wills, 1964; Hussain & Clark 1981; del Álamo & Jiménez 2002): this is the usual definition of convection velocity. Here we have computed it from the frequency-wavenumber power spectrum $P(\omega, k_x, y)$ as in Wills (1964), where the phase velocity is defined as the velocity $U_c(y)$ of the moving reference frame for which the integral time scale

$$T_L(k_x, y) = \frac{P(-U_c k_x, k_x, y)}{\int_{-\infty}^{\infty} P(\omega, k_x, y)\mathrm{d}\omega} \tag{2.3}$$

is a maximum. The frequency-wavenumber power spectrum has been computed using time histories of velocity fields that were available from the DNS, as was done by Choi

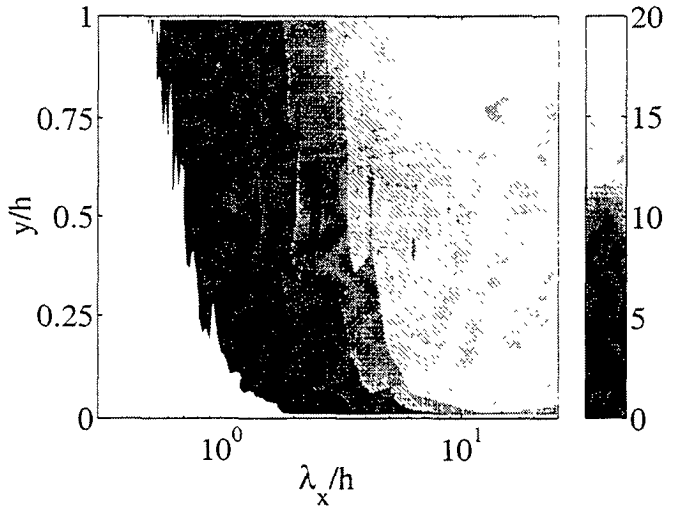

FIGURE 2. Lagrangian time scale $U_b T_L/h$ of the spanwise velocity, low-pass filtered in z ($\lambda_z > 0.25\,h$), as a function of the streamwise wavelength λ_x and wall distance y.

& Moin (1990). In the present case, the minimum and maximum frequencies imposed by the temporal sampling are $\omega_{min} = 0.14\,U_b/h$ and $\omega_{max} = 71\,U_b/h$. Due to storage limitations, the time histories of the velocity field were spatially filtered by removing all the length scales either shorter or narrower than $0.25\,h$ using a Fourier cut-off filter. Figure 1 displays the average phase speed of the low-pass-filtered spanwise-velocity fluctuations as a function of wall distance, and non-dimensionalized with the bulk mean velocity U_b (solid line), together with its average across the channel width (dashed line)

$$U_{adv} = \frac{1}{2h}\int_0^{2h} U_c(y)\mathrm{dy} = 0.84\,\mathrm{U_b}.$$

We have chosen this value as the advection velocity of the frozen fields to be used in (2.2) for our second set of numerical experiments. Kim & Hussain (1993) computed the propagation speeds of several turbulent magnitudes, including the velocity components, in a fully-resolved $Re_\tau = 180$ channel. They obtained a phase velocity of w in the near-wall region approximately equal to $10\,u_\tau$, which is the same as we have measured in the low-pass-filtered $Re_\tau = 550$ channel. In the outer region, however, they obtain convection velocities approximately 10% higher than we do, and which are closer to the local mean velocity in their case than in ours. This is not surprising. If we believe that turbulent structures propagate roughly at the average streamwise velocity that they feel, then the smaller scales should follow the local mean velocity better than the large ones.

The integral time scale T_L in (2.3) measures the characteristic time associated to the turbulent fluctuations of a given magnitude with a certain length $\lambda_x = 2\pi/k_x$ at a given wall-distance, and in a reference frame moving with their local advection velocity. This magnitude can be interpreted as the Lagrangian time scale seen by an observer following the mean trajectories of the eddies or, in other words, as the typical lifetime of the structures of a given length. The Lagrangian time scale of the fluctuations of spanwise velocity has been represented in figure 2, low-pass filtered in z, as a function of streamwise wavelength λ_x and wall distance y. The figure shows that the lifetimes of the large scales of w can be very long, even comparable to a 'wash-out' or 'through-flow' time $8\pi\,h/U_b$.

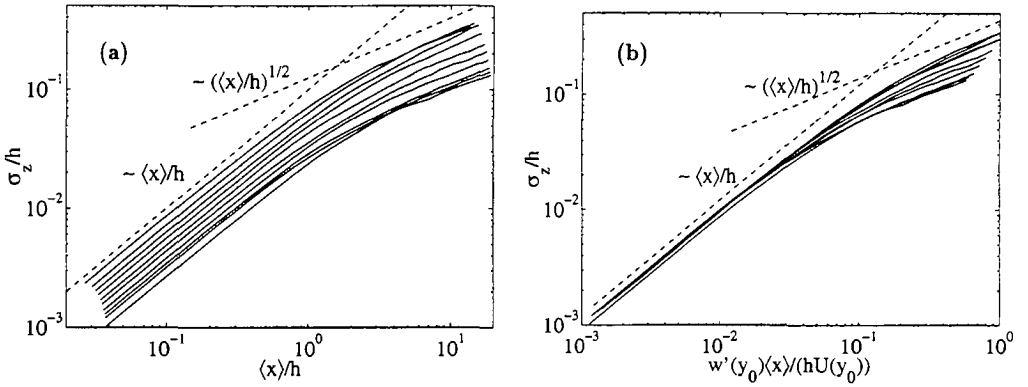

FIGURE 3. R.m.s. of the spanwise displacement σ_z of fluid particles as a function of their mean streamwise displacement $\langle x \rangle$. The different curves correspond to $y_0/h = 0.1(0.1)1$ from bottom to top. The dashed lines have logarithmic slopes 1 and 1/2. (a), using h as the scale of σ_z and $\langle x \rangle$; (b), using $w'(y_0)t$ as the scale of σ_z and $U(y_0)t$ as the scale of $\langle x \rangle$.

The values of T_L for the other two components of velocity, not shown here, are similar, and give an *a priori* estimate of the longest intervals of time for which we can expect the integration of (2.2) to provide reasonably accurate results. Note that this prediction would only be true if the large scales controlled the characteristics of dispersion. In order to analyze their importance in this phenomenon, we have solved (2.2) using both fully-resolved and low-pass-filtered fields. Overall, we have integrated (2.2) in four different cases, depending on the choice of U_{adv} and of the spatial resolution. These cases have been summarized in table 1, indicating the number of different fields that have been used for each case, as well as the number of trajectories that have been computed per field. The time discretization is fourth-order Runge-Kutta, and third-order B-splines have been used to interpolate the velocity field from the collocation points of the DNS.

3. Results. One-point statistics

The single-particle statistics $\langle x_i \rangle$ and $\sigma_i = \langle (x_i - \langle x_i \rangle)^2 \rangle^{1/2}$ are of great interest because they indicate respectively the mean displacement of the center of a typical scalar patch and its size in the three spatial directions, and also because the latter is often measured as a function of the former in field experiments, which will allow us to test the approximation (2.2). These magnitudes are functions of the initial position y_0 of the fluid element, of its instantaneous position y, and of time. Operating on (2.1) it is possible to obtain (Hunt 1985) that

$$\partial_t \sigma_i^2 = u_i'(y) u_i'(y_0) \int_0^t \rho_{ii}(r_x - \tau U_{adv}, r_z, y_0, y, t - \tau) \mathrm{d}\tau, \tag{3.1}$$

where ρ_{ii} is the two-point autocorrelation coefficient of the ith-component of the velocity vector. This magnitude is a function of the streamwise and spanwise separations r_x and r_z, of the initial and instantaneous wall distances, and of time. Note that the frozen-field approximation is equivalent to setting $t - \tau = 0$ in ρ_{ii} in (3.1). For times and spatial separations short compared with the corresponding integral scales, the velocity field is almost fully correlated, $\rho_{ii} \approx 1$, and $y_0 \approx y$. We then have

$$\sigma_i \approx u_i'(y_0) t \sim \langle x \rangle \approx U(y_0) t. \tag{3.2}$$

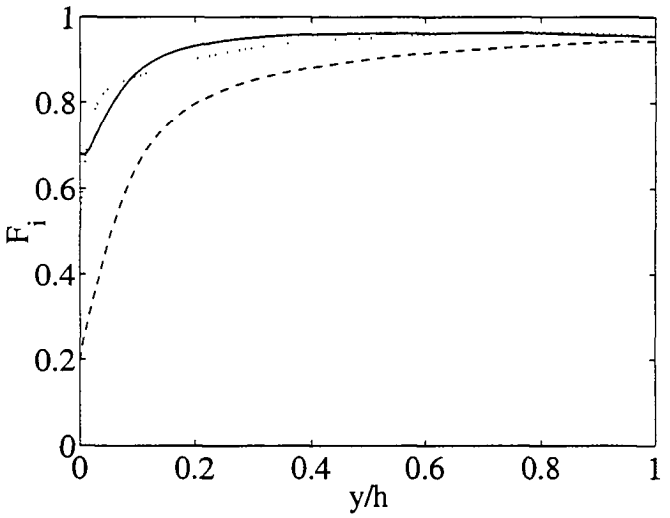

FIGURE 4. Fraction F_i of the ith-contribution to turbulent kinetic energy contained in the cut-off filtered fields as a function of wall-distance. ——— , u; - - - - , v; ····· , w.

On the other hand, for very long temporal and spatial separations the velocity field is approximately decorrelated, $\rho_{ii} \approx 0$, and the integral on the right-hand side of (3.1) is roughly independent of its upper limit. We then obtain the Gaussian spreading law $\sigma_i \sim (\langle x \rangle h)^{1/2}$. Both asymptotic behaviors can be observed in figure 3, where the solid curves show σ_z from case 2 as a function of the mean streamwise displacement for ten equispaced intervals of initial wall distance, from the wall to the center of the channel. In figure 3(a) we have used the channel half-width as the length scale for σ_z and $\langle x \rangle$, while in figure 3(b) we have scaled σ_z with $w'(y_0)t$ and $\langle x \rangle$ with $U(y_0)t$. The figures show that in the short-range limit, the curves representing σ_z are parallel to the dashed line with logarithmic slope 1, while far away from the release point the curves are roughly parallel to the dashed line with logarithmic slope 1/2. It can be observed in figure 3(b) that the scaling (3.2) gives a good collapse of the plume widths corresponding to different release points, at least at short distances from the source. As expected, the collapse worsens beyond the turning point in the curves, where their slope starts decreasing and (3.2) is no longer valid. The characteristic position of this turning point is a measure of the shortest integral scale involved in the dispersion process.

Equation (3.1) also suggests that the large scales may play an important role in turbulent dispersion. Coherent structures with $\lambda_x/h > 2$ and $\lambda_z/h \approx 1 - 2$ are known to be correlated right across the channel half-width and to contain a large fraction of the turbulent kinetic energy (del Álamo & Jiménez 2002), which suggests that they should contribute substantially to the right-hand side of (3.1). Figure 4 displays the fraction F of the total streamwise (solid line), wall-normal (dashed line) and spanwise (dotted line) contributions to kinetic energy contained in the cut-off filtered fields, as a function of wall distance. The figure shows that the structures which are longer and wider than $0.25\,h$ contain most of the kinetic-energy contributions of u and w in the outer region of the flow, and hence could be expected to produce values of σ_x and σ_z similar to the ones generated by the full fields. On the other hand, the small scales of v contain relatively more kinetic energy than those of u and w, suggesting that the value of σ_y computed from the filtered fields will be less accurate than that obtained from the full fields. This

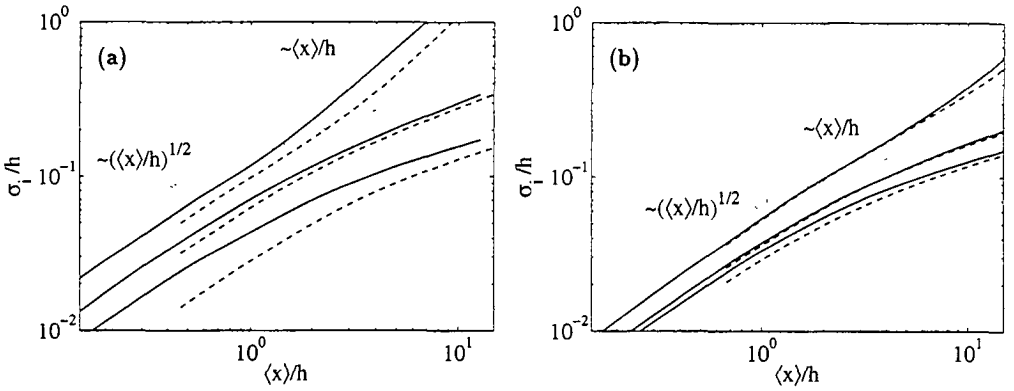

FIGURE 5. R.m.s. of the displacement of fluid particles in the ith-direction as a function of their mean streamwise displacement $\langle x \rangle$. Top, σ_x; middle, σ_z; bottom, σ_y. ——— , full DNS fields (case 2); ····· , cut-off filtered DNS fields (case 4). In all the cases $U_{adv} = 0.84\,U_b$. (a), $y_0^+ < 100$; (b), $0.2 < y_0/h < 1$.

is actually what is observed in figure 5, where we have plotted the three components of σ (from top to bottom σ_x, σ_z and σ_y) computed from the full (case 2, solid lines) and the filtered (case 4, dashed lines) moving frozen DNS fields. In figure 5(a) the patch size has been averaged for fluid particles released in the near-wall region ($y_0^+ < 100$), while in figure 5(b) the average has been performed for initial positions in the outer region ($0.2 < y_0/h < 1$). The results from the filtered fields compare fairly well with those from the fully resolved ones in the outer region, while they underestimate the different components of the r.m.s. in the near-wall region. Note that the agreement between the different sets of data is better wherever F is higher, and *vice versa*, supporting the argument above. These observations agree with the previous work of Armenio *et al.* (1999), who performed a similar analysis using time-evolving velocity fields, with application to LES modeling. The results from the stationary frozen DNS fields (cases 1 and 3), not shown here, behave in the same way as those we have presented in figure 5.

Note that the standard deviations in figure 5 are always much smaller than $\langle x \rangle$, implying that the basic motion of the particles is advection by the local mean velocity, $\langle r_x \rangle \approx U(y_0)\tau$, while the spreading around that position is slow.

Figure 5 also shows the relative magnitudes of σ along the different axes, which give an idea of the evolution of the shape of a typical scalar patch with distance from the source. In the short-range region the three standard deviations grow at the same rate, and a typical cloud of scalar would initially conserve its original shape as it moved away from the release point. However, after the cloud has traveled a certain distance it would start elongating very rapidly, as we can deduce from the increase in the slope of σ_x that takes place at large distances, seen in the figure. Comparison of figures 5(a) and 5(b) indicates that this phenomenon occurs at a smaller distance from the source for lower values of y_0, and this is more apparent in figure 6. This figure displays the logarithmic slope of σ_x (from case 2) as a function of time for ten equispaced intervals of y_0. The slope of σ_x increases and reaches a maximum value after times which are longer as the curves move from the left to the right, corresponding to increasing values of y_0. There are strong reasons for believing that this effect is due to the mean shear. Scaling the time with $\partial_y U$, as in figure 6(b), collapses the position of the maxima of the different curves, indicating

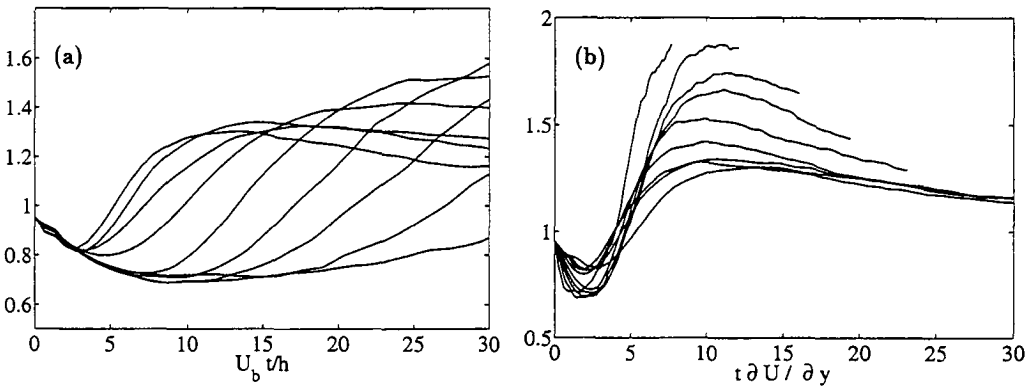

FIGURE 6. Logarithmic slope of σ_x (case 2) as a function of time t for $y_0/h = 0.1(0.1)1$. (a), using time non-dimensionalized with U_b/h. The curves peak at longer times as we move away from the wall; (b), using time non-dimensionalized with $\partial_y U$. The values of the maxima increase as we move away from the wall.

that the time scale associated with this phenomenon is the inverse of the mean shear. Also, in a different numerical experiment, we integrated (2.2) using fields from which we had removed the mean velocity profile, and the resulting σ_x behaved in the same way as σ_y and σ_z, without the transient increase in slope. Tennekes & Lumley (1972) show that in a flow subjected to a uniform shear S, the dispersion in the streamwise direction increases asymptotically with time as $(St)^{3/2}$. This value of the logarithmic slope lies roughly in the center of the set of different maximum values that we obtained from the DNS fields, and the scatter in the numerical values might be explained by the fact that $\partial_y U$ is not uniform in a turbulent channel.

3.1. *Comparison with atmospheric data*

In section 2 we discussed the *a priori* validity of our study, obtaining a rough estimate of the longest time intervals for which we could expect reasonable results from the model problem (2.2). Here we analyze the frozen-turbulence approximation *a posteriori*, by comparing the computed dispersion characteristics with those measured in the atmospheric boundary layer. Figure 7 shows the r.m.s. spanwise displacement of fluid particles as a function of their mean streamwise displacement. The symbols come from field experiments, most of which were compiled by Nielsen *et al.* (2002) and Olesen (1995). The atmospheric data sets are difficult to compare among themselves and with the numerical results. In general, the experiments consist of releasing a passive tracer from a smokestack and measuring its near-ground concentration along arcs situated at increasing distances from the release point. However, neither the releases nor the measurements were performed at the same ground distances in the different experiments; the monitoring procedures also differed, and so did the topological and meteorological conditions. Thus, any quantitative conclusion from the observations of figure 7 should be taken only as a guideline, as is also suggested by the scatter of the data in the figure. The solid line comes from our numerical results with $U_{adv} = 0.84\,U_b$, while the dashed line corresponds to $U_{adv} = 0$. In both cases we have represented the average values over the interval of particle positions $y/h < 0.1$, in order to compare with the atmospheric near-ground measurements. It should be noted however, that the numerical results contain the contributions from particles released at all possible wall distances across the

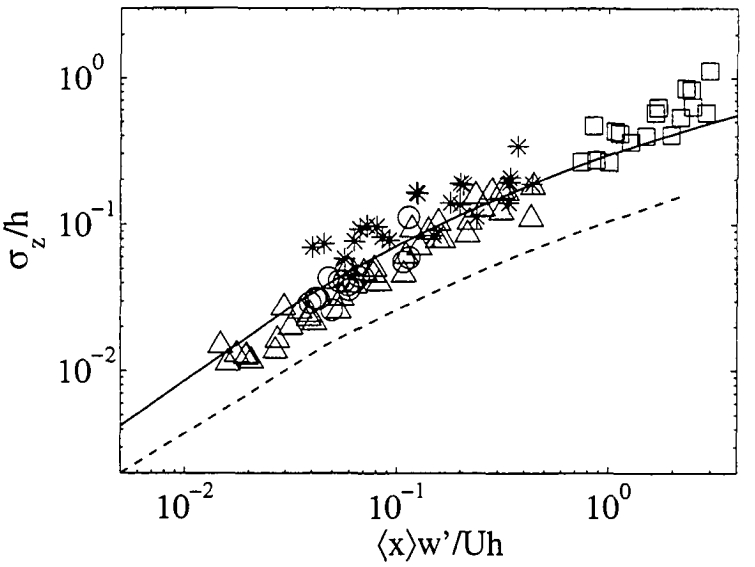

FIGURE 7. R.m.s. of the spanwise displacement of fluid particles, σ_z/h, as a function of their mean streamwise displacement $\langle x\rangle w'/(Uh)$. Lines, data from DNS fields; ——— , $U_{adv} = 0.84\,U_b$; ···· , $U_{adv} = 0$. Symbols, atmospheric experiments; ○, Ecofin Project (Nielsen *et al.* 2002); △ , Prairie Grass (Olesen 1995); ∗, Lillestrøm; □ , Copenhagen (Olesen 1995).

channel, while in the experiments the particles were released at a single distance above the ground. Even so, the agreement between the numerical and the experimental results is reasonably good for the results from the moving fields. They somewhat underestimate σ_z at large streamwise distances, but this could be because the atmospheric data in the corresponding experiment (the Copenhagen data set, represented by squares) were taken under unstably-stratified atmospheric conditions, with Monin-Obukhov lengths of the order of -100 m (Olesen 1994). The results from the stationary fields look qualitatively correct, but they predict widths smaller than the experimental values. This is understandable considering that, since the particles move approximately with the mean flow velocity, the mean streamwise separation that enters the correlation function in (3.1) is $\langle r_x\rangle \approx U(y_0)\tau$, so that the first argument in the autocorrelation coefficient of w is

$$\langle r_x\rangle - \tau U_{adv} \approx (U(y_0) - U_{adv})\tau.$$

In the stationary fields, fluid elements separate faster from their initial positions with respect to the flow structures than in the moving fields, because the difference between the mean velocity and that of the reference frame is higher in the former than in the latter. This is true all across the channel, except in the near-wall region where $U(y_0)$ is small. The fluid particles in the stationary 'snapshots' therefore feel a less-correlated velocity field than in the advecting cases, leading to lower values of σ_z. This argument is supported by figure 8, which shows the logarithmic slope of σ_z as a function of time (figure 8 (a)) and as a function of $|\langle r_x\rangle - \tau U_{adv}|$ (figure 8(b)), for five equispaced intervals of y_0 from the wall to the center of the channel. In figure 8(a) the logarithmic slope of σ_z decreases faster with time for the stationary fields (case 1), plotted with dotted lines, than for the moving ones (case 2), represented by solid lines. On the other hand, the curves in figure 8 (b) collapse fairly well, except for the curve on the left-hand side of

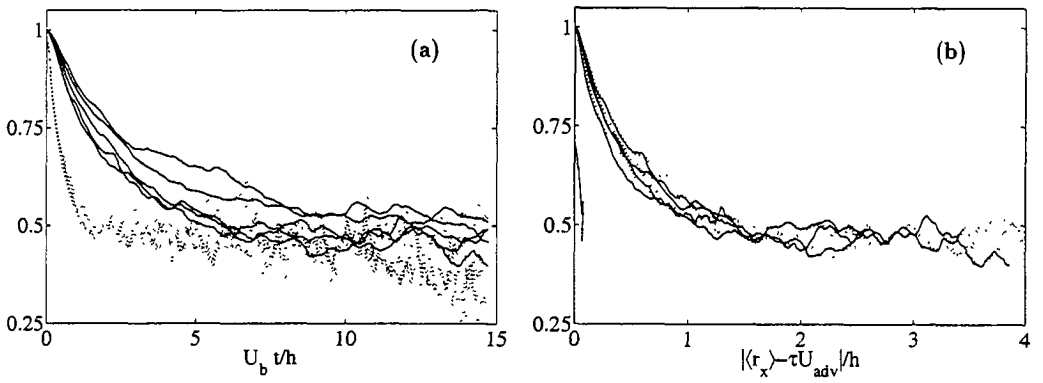

FIGURE 8. Logarithmic slope of σ_z for $y_0/h = 0.2(0.2)1$. (a), as a function of time $U_b t/h$. (b), as a function of the separation $|\langle r_x \rangle - \tau U_{adv}|/h$. ——— , $U_{adv} = 0.84\,U_b$. ····· , $U_{adv} = 0$. The solid line that does not collapse well in the left-hand side of (b) corresponds to $y_0 = 0.2\,h$, near the critical layer at $y_c = 0.23\,h$;

the plot which corresponds to $y_0/h = 0.2$. This position is near the critical layer at $y_c = 0.23\,h$, where $U(y_c) = U_{adv}$. In that region, the mechanism that we have just described is weaker, and it is reasonable to think that the dispersion is dominated by the turbulent velocity fluctuations and not by the mean advection. Note that in the case of the stationary fields the critical layer is located at the walls, which may explain why all the dotted lines collapse well in figure 8(b). The behavior that we have observed in figure 8 is common to the results from both the fully-resolved and the cut-off filtered fields.

As we have mentioned, the location of the point where the logarithmic slopes of $\sigma_{y,z}$ decay from 1 to their asymptotic value of 1/2 is a measure of the integral scale most relevant to turbulent dispersion in the cross-stream plane. The fact that the results from the moving frozen fields, which neglect the time evolution of turbulent structures, are able to predict the position of the turning region in the data from the field experiments, can help us identify that integral scale. The large scales of w have lifetimes (see figure 2) which are approximately 4 times longer than the time scale of to the decay of the slope of σ_z from the moving fields (figure 8(a)). This suggests that the temporal decay of the turbulent structures may not be important in the decorrelation that the particles feel as they move in the flow. On the other hand, the streamwise separation corresponding to the transition of σ_z shown in figure 8(b), is $r_x \approx h$. This length is essentially equal to the position of the peak of the premultiplied energy spectrum of w (del Álamo & Jiménez 2001), which is a measure of its streamwise integral scale. These observations also apply to the wall-normal direction, for which the experimental information is much scarcer than for the spanwise direction. They suggest that the transition in $\sigma_{y,z}$ may be caused by the difference between the mean velocity of the flow, and the phase speed of the velocity components in the cross-stream plane.

4. Conclusions

The results show that the large scales of turbulent channel flow play a very important role in turbulent dispersion in the outer region of the flow, especially in the streamwise and spanwise directions. These structures contain a large fraction of the turbulent kinetic energy, and they are correlated across the full channel (del Álamo & Jiménez 2002), so

they are expected to contribute substantially to the standard deviations in (3.1). Filtered velocity fields, retaining only structures with λ_x, $\lambda_z > 0.25\,h$, produce more than 90% of $\sigma_{x,z}$ and roughly 80% of σ_y in the outer region. These results indicate that LES should be a valuable tool in the study of scalar dispersion.

The transition from linear to Gaussian spreading is due to the decorrelation of the velocity field along the Lagrangian trajectories of the particles. The lifetimes of the large scales of the spanwise velocity are roughly four times longer than the time scale of the decay in the slope of the plume width from 1 to 1/2. Thus, the time evolution of turbulent structures does not seem to be significant in the decorrelation process that leads to Gaussian spreading and, to a first approximation, it may be possible to study turbulent diffusion using frozen velocity fields. In fact, we have integrated the Lagrangian trajectories of fluid particles from frozen velocity fields, obtaining values of σ_z that agree well with atmospheric measurements. The agreement is better when the trajectories are computed in a reference frame moving with the average phase velocity of the large scales. The stationary frozen fields, on the other hand, produce values of σ_z smaller than those from the field experiments. This is because the decorrelation times experienced by the fluid elements in the stationary fields are shorter than those in the moving ones. In both cases, the decay in the slope of σ_z takes place when the streamwise separation of the particles relative to the velocity fields, $\langle r_x \rangle - \tau U_{adv}$, is roughly equal to the streamwise integral scale of w. Since the particles move in the x direction approximately following the mean velocity profile, their separation with respect to their initial positions is given by $(U(y_0) - U_{adv})\tau$, suggesting that the main cause of the transition from linear to Gaussian spreading is the difference between the mean streamwise velocity and the phase speeds of the velocity components in the cross-stream plane.

The mean shear is the dominating mechanism in the streamwise direction. It generates values of σ_x much greater than σ_y or σ_z, and leads to very elongated patch shapes. Although this consideration is not important in the case of the dispersion of contaminants from a continuous source, it may be fundamental in the case of discrete releases.

Acknowledgements

This work was supported by grant BFM 2000-1468 of CICYT. J.C.A. was supported by the CTR and by the Spanish Ministry of Education. The authors would like to thank Helge R. Olesen at NERI, Denmark for providing a digital version of the atmospheric data sets collected by the Harmonisation Group. We are also indebted to Julian C. R. Hunt, with whom we had fruitful discussions related to the subject of this work.

REFERENCES

ARMENIO, V., PIOMELLI, U. & FIOROTTO, V. 1999 Effect of the subgrid scales on particle motion. *Phys. Fluids* **11**, 3030–3042.

BROWN, M. J., ARYA, S. P. & SNYDER, W. H. 1997 Plume descriptors derived from a non-Gaussian concentration model. *Atmospheric Environment* **31**, 183–189.

CHOI, H., MOIN, P. 1990 On the space-time characteristics of wall-pressure fluctuations. *Phys. Fluids A* **2**, 1450–1460.

DEL ÁLAMO, J. C. & JIMÉNEZ, J. 2001 Direct numerical simulation of the largest scales in a turbulent channel. *Annual Research Briefs*, Center for Turbulence Research,

NASA Ames/Stanford Univ., 329–341. Also in *Advances in Turbulence IX*, (Castro, I. P., Hancock, P. E. & Thomas, T. G., eds.) CIMNE, 403-406.

DEL ÁLAMO, J. C. & JIMÉNEZ, J. 2002 The organization of the outer region of turbulent channels. *In preparation.*

HANNA, S. R., EGAN, B. A., PURDUM, J. & WAGLER J. 1999 Evaluation of the ADMS, AERMOD and ISC3 Models with the Optex, Duke Forest, Kincaid, Indianapolis and Lovett Field Data Sets. *Proc. of Rouen Conference 11–14 October 1999.*

HUNT, J. C. R. 1985 Turbulent diffusion in complex flows. *Ann Rev. Fluid Mech.* **17**, 447–485.

HUSSAIN, A. K. M. F. & CLARK, A. R. 1981 Measurements of wavenumber-celerity spectrum in plane and axisymmetric jets. *AIAA J.* **19**, 51-55.

KIM, J. & HUSSAIN, A. K. M. F. 1993 Propagation velocity of perturbations in turbulent channel flow. *Phys. Fluids A* **5**, 695–706.

NIELSEN, M., CHATWIN, P. C., JØRGENSEN, H. E., MOLE, N., MUNRO, R. J. & OTT, S. 2002 Concentration Fluctuations in Gas Releases by Industrial Accidents. *RisøReport* **R-1329 (EN)**.

NOKES, R. I. & WOOD, I. R. 1988 Vertical and lateral turbulent dispersion: some experimental results. *J. Fluid Mech.* **187**, 373–394.

OLESEN, H. R. 1994 Model Validation Kit for the workshop on Operational Atmospheric Dispersion Models for Environmental Impact Assessments in Europe. *Report of the NERI, Denmark.*

OLESEN, H. R. 1995 The model validation exercise at Mol: overview of results. *Int. J. Environment and Pollution* **5, Nos. 4–6**, 781–784.

TENNEKES, H. & LUMLEY, J. L. 1972 *A First Course in Turbulence.* The MIT Press, p. 232.

WILLS, J. A. B. 1964 On convection velocities in turbulent shear flows. *J. Fluid Mech.* **20**, 419–432.

The turbulent flow over a permeable wall

By W.P. Breugem † AND B.J. Boersma †

In this paper we discuss some turbulence statistics that are obtained from a Direct Numerical Simulation (DNS) of a turbulent flow in a channel of which one wall is permeable (porous, with zero net transpiration) and the other is impermeable. The flow within the porous wall is modeled using the Volume-Averaged Navier-Stokes equations (VANS). Among others, it is shown that wall permeability causes a considerable increase in the total drag, and an increased production of all Reynolds stresses when compared to an impermeable wall.

1. Introduction

There are many real-life cases of turbulent flows over porous media. Examples of this are flows over plant canopies, Finnigan (2000), and over river beds. In general it is assumed that these porous media increase the drag that the flow experiences, and enhance turbulent mixing near the wall. Not much is known about the physical mechanism that causes the drag increase.

In the present paper we study the flow over porous media in simple, two-dimensional geometries. First, we investigate the flow in a channel, which has one permeable and one impermeable wall. The second case is the spatially-developing boundary layer over a permeable wall. For the first case we will present statistics including the budgets in the transport equations for all Reynolds stresses. For the second case we will present only some preliminary results.

In the literature a porous medium is often represented simply by specifying boundary conditions at the wall, see e.g. Jiménez *et al.* (2001) and Hahn *et al.* (2002). In the paper of Jiménez *et al.* (2001), the wall-normal velocity component is assumed to be proportional to the wall-pressure fluctuation, whereas a no-slip condition is imposed for both the streamwise and the spanwise velocity components. In the paper of Hahn *et al.* (2002), the wall-normal velocity is assumed to be zero, and a slip velocity in both the streamwise and spanwise direction is imposed as given by the model of Beavers & Joseph (1967). In the present study we directly solve the governing equations for the flow within the porous medium together with the Navier-Stokes equations for the flow in the channel. The flow field is continuous over the interface between the porous medium and the channel, and hence no boundary conditions need to be prescribed at the interface. A fifth-order polynomial in the wall-normal coordinate is adopted to model the rapid variation of the porosity in a thin layer near the interface. Of course our approach results in a more complicated set of equations and larger computational costs than in the studies of Jiménez *et al.* (2001) and Hahn *et al.* (2002).

The organization of the paper is as follows. In section 2 we discuss the governing equations for the porous medium and give a short outline of the numerical method that

† Address: Laboratory for Aero and Hydrodynamics, J.M. Burgers Center, Leeghwaterstraat 21, 2628 CA Delft, The Netherlands.

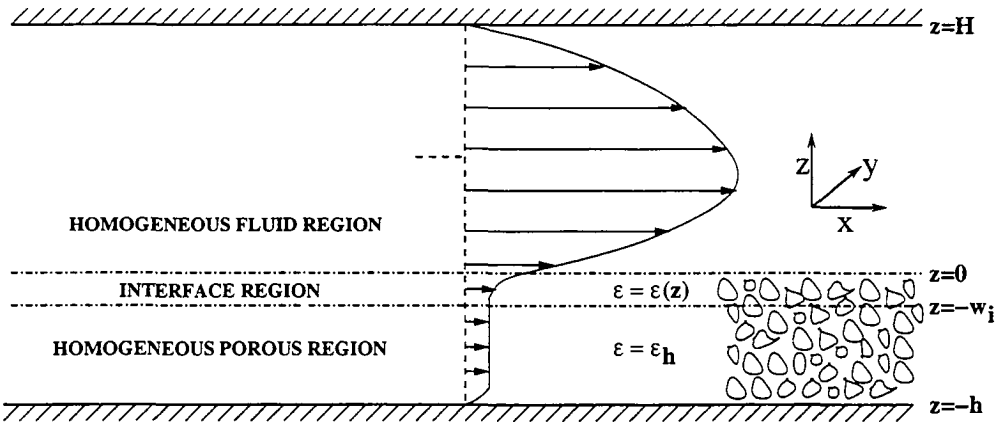

FIGURE 1. A sketch of the channel flow geometry (not on scale).

we use to solve these equations. In section 3 we present turbulence statistics obtained from a simulation such as mean-profiles, rms-profiles and Reynolds-stress budgets. Finally, in section 4 some conclusions are given.

2. Governing equations and numerical method

In this section we present the flow geometry, the governing equations for the flow along and through a porous medium, and the numerical method that we use to solve these equations.

2.1. *Governing equations*

In figure 1 we show the geometry of the channel flow. The flow is bounded by two impermeable walls located respectively on top of the two-dimensional channel (at $z = H$) and below the porous medium (at $z = -h$). Following Ochoa-Tapia & Whitaker (1995a), we distinguish between three regions:

(a) The homogeneous fluid region between $z = 0$ and $z = H$.

(b) The interface region between $z = -w_i$ and $z = 0$, which is characterized by rapid changes in the porous structure and the permeability.

(c) The homogeneous porous region between $z = -h$ and $z = -w_i$, with a constant porosity ($\epsilon = \epsilon_h$) and an isotropic permeability.

In the studies performed by Jiménez *et al.* (2001) and Hahn *et al.* (2002), the porous medium is modeled by specifying boundary conditions at the interface ($z = 0$). In contrast to their approaches, in our study we directly describe the flow inside the porous medium by means of the Volume-Averaged Navier-Stokes equations. These equations can be derived by averaging the standard Navier-Stokes equations for the flow inside the pores, over a small spatial volume. Figure 2 gives an illustration of the volume-averaging procedure. The constraints for the length scale R of the averaging volume are that it has to be much larger than the typical length scale l_β of the flow inside the pores, but also much smaller than the characteristic length scale of the volume-averaged flow.

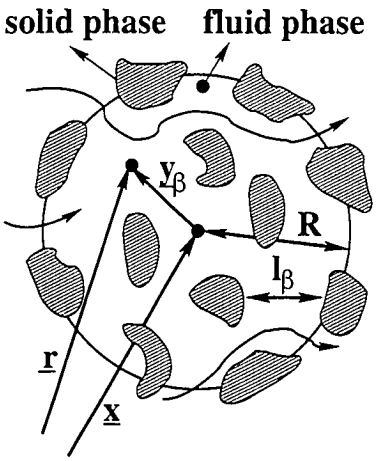

FIGURE 2. An illustration of the volume-averaging procedure.

It is important to distinguish between superficial and intrinsic volume-averages. The intrinsic velocity is denoted by square brackets and defined according to

$$<\underline{u}(\underline{x},t)>\equiv \frac{1}{V_\beta}\int_{V_\beta}\underline{u}(\underline{x}+\underline{y}_\beta,t)dV \tag{2.1}$$

where V_β is the part of the averaging volume V that is occupied by fluid. The vector $\underline{x}$ points to the centroid of the volume, and $\underline{y}_\beta$ is the position vector with respect to the centroid of V and points only into the fluid phase β (see figure 2). The subscript β refers to the fluid or β–phase, in distinction to the solid or σ–phase. The superficial velocity is related to the intrinsic velocity according to

$$<\underline{u}(\underline{x},t)>^s\equiv \frac{1}{V}\int_{V_\beta}\underline{u}(\underline{x}+\underline{y}_\beta,t)dV=\epsilon<\underline{u}(\underline{x},t)> \tag{2.2}$$

where the superscript s refers to the superficial instead of the intrinsic average. The porosity ϵ is the ratio of the volume taken up by the fluid phase to the total averaging volume, i.e.

$$\epsilon\equiv\frac{V_\beta}{V}$$

Notice that the superficial and intrinsic averages are defined everywhere inside the porous medium, in the β-phase as well as in the σ-phase.

The local deviations of the velocity and pressure insides the pores from the corresponding volume-averaged quantities are denoted by a tilde and defined as respectively

$$\tilde{\underline{u}}\equiv\underline{u}-<\underline{u}>$$

$$\tilde{p}\equiv p-<p>$$

By applying the volume-averaging procedure to the Navier-Stokes equations for the incompressible flow inside the pores, Whitaker (1996) gives a formal derivation of the Volume-Averaged Navier-Stokes equations. The result reads:

$$\frac{D<\underline{u}>}{Dt}+\epsilon^{-1}\nabla\cdot<\tilde{\underline{u}}\tilde{\underline{u}}>^s=-\frac{1}{\rho}\nabla<p>+\nu\nabla^2<\underline{u}>+$$

$$\nu\frac{\nabla\epsilon}{\epsilon}\nabla<\underline{u}>+\nu\frac{\nabla^2\epsilon}{\epsilon}<\underline{u}>+$$
$$\frac{1}{\rho}\frac{1}{V_\beta}\int_{A_{\beta\sigma}}\underline{n}_{\beta\sigma}\cdot(-\underline{\underline{I}}\tilde{p}+\mu\nabla\tilde{\underline{u}})dA \tag{2.3}$$

$$\nabla\cdot(\epsilon<\underline{u}>)=0 \tag{2.4}$$

where $A_{\beta\sigma}$ is the contact area between the β– and σ–phase within the averaging volume, $\underline{n}_{\beta\sigma}$ the normal vector pointing into the σ–phase, and $\underline{\underline{I}}$ the unity tensor. For homogeneous porous media (ϵ = constant) the terms containing derivatives of the porosity are zero, and so these terms are significant only in the interface region (see figure 1). Notice from equation (2.4) that when the porosity is varying in space, only the superficial and not the intrinsic velocity is divergence-free.

We need closures for the second term at the left-hand-side and the last term at the right-hand-side of equation (2.3). The second term on the left-hand-side of equation (2.3) is a dispersive flux term. It represents the effect of spatial correlations between flow variations inside the pores, on the volume-averaged flow. In the literature it is often implicitly assumed that this term can be neglected, as we will do in the present study. For the last term on the right-hand-side of equation (2.3), Whitaker (1996) formulates a closure problem in which the surface integral is replaced by the following expression

$$\frac{1}{\rho}\frac{1}{V_\beta}\int_{A_{\beta\sigma}}\underline{n}_{\beta\sigma}\cdot(-\underline{\underline{I}}\tilde{p}+\nu\nabla\tilde{\underline{u}})dA=-\nu\epsilon\underline{\underline{K}}^{-1}\cdot<\underline{u}>^\beta-\nu\epsilon(\underline{\underline{K}}^{-1}\cdot\underline{\underline{F}})\cdot<\underline{u}>^\beta \tag{2.5}$$

where $\underline{\underline{K}}$ and $\underline{\underline{F}}$ are referred to as respectively the (yet unknown) permeability and the Forchheimer tensor. The first term on the right-hand side of equation (2.5) is known as the Darcy term, and it basically represents the effect of the viscous drag that the flow inside the pores encounters. The second term on the right-hand side represents the effect of pressure drag on the flow inside the pores. In the literature semi–empirical relationships are available for the tensors $\underline{\underline{K}}$ and $\underline{\underline{F}}$ for homogeneous porous media. Based on one of these relations, known as the Ergun equation - see MacDonald *et al.* (1979) - the Forchheimer and permeability parameters can then be expressed by the following scalars

$$F=\frac{1}{100(1-\epsilon)}\frac{d_p||<\underline{u}>^s||}{\nu} \tag{2.6}$$

$$K=\frac{{d_p}^2\epsilon^3}{180(1-\epsilon)^2} \tag{2.7}$$

with the mean particle diameter d_p defined as six times the ratio of the total volume V_p to the total surface area A_p of the σ–phase

$$d_p\equiv\frac{6V_p}{A_p} \tag{2.8}$$

The major advantage of a direct description of the flow inside the porous medium is that we do not need to prescribe any boundary conditions at the interface, because the flow field is continuous over the interface. Yet we have to deal with another problem as strictly speaking the closure (2.5) is not valid in the interface region. The thickness of the interface region is on the order of the mean particle diameter, and inside this region the flow field is very complicated due to roughness. In our present study we use a variable-porosity-model for the interface region, see Ochoa-Tapia & Whitaker (1995b), and still assume the validity of the closure in this region. The porosity is described by a fifth-order

polynomial in the wall-normal coordinate, such that it satisfies the requirements that its derivatives are zero at $z = 0$ and $z = -w_i$, that at $z = 0$ the porosity equals 1, and that at $z = -w_i$ its value is equal to ϵ_h.

2.2. *Numerical method*

The governing equations (2.3) and (2.4) are discretized with a pseudo-spectral method in the x- and y-directions and with a second-order finite-difference method in the direction perpendicular to the porous medium, i.e. the z-direction. The (staggered) grid in this direction is non-uniform with points clustered around the interface ($z = 0$) between the clear fluid and the porous medium. The solution is advanced in time with a second-order explicit Adams-Bashforth method. The pressure-correction method is used to ensure conservation of mass. The flow in both the porous medium and the channel is forced in the x-direction by a constant pressure gradient dp/dx.

3. Results

In this section we present some turbulence statistics that are obtained from a fully developed channel flow simulation over a permeable wall. The simulation is one of the first that we performed to test our DNS code. The porosity in the homogeneous porous region is high and equal to $\epsilon_h = 0.95$. In table 1 some characteristics of the simulation are listed. As the flow in the channel is asymmetric, the Reynolds number based on the friction velocity at the upper wall is different from the corresponding Reynolds number based on the square root of the total stress at the interface with the lower wall. The Reynolds number based on the bulk velocity in the channel is 4517. The thickness of the porous medium is 1/16 of the channel height. In this simulation the thickness of the interface region is set equal to the thickness of the porous medium as this requires less grid points in the porous medium. The numerical resolution of this test-simulation is coarse with grid spacings in (upper) wall-units of $dx^+ = 33.9$, $dy^+ = 20.3$, $dz^+_{min} = 1.0$ and $dz^+_{max} = 5.1$ for the streamwise, spanwise and wall-normal directions, respectively. The stretch factor for the grid spacing in the wall-normal direction is 2.5 % for both the porous medium and the channel. Unfortunately, there is a jump in the grid spacing over the interface where the first grid cell above the interface is a factor 2.2 smaller than the first grid cell below the interface. The simulation is run until the bulk velocity reached a steady state. Once the flow reached a steady state, 60 data fields were stored each equally separated in time by H/u_*, with u_* the friction velocity at the upper wall. The statistics in this study are obtained from these 60 data fields. The simulation has been performed on a AMD-Athlon with 1Gb of core memory.

To start with we show the mean-velocity profile. (figure 3). The dashed line marks the interface with the permeable wall. Clearly, there is a non-zero velocity (slip-velocity) at the interface. The velocity profile has its maximum above the centerline of the channel, already indicating a higher total shear stress at the permeable wall.

In figure 4 we show the root-mean-square profiles of the three velocity components and of the pressure, normalized with the friction velocity at the upper wall. Near the upper wall, the rms-profiles behave as expected and are similar to the profiles for standard channel flow. The rms-profiles near the lower wall are clearly altered by wall permeability. A strong increase can be observed in the spanwise and wall-normal velocity fluctuations, and in the pressure fluctuations. The axial rms has its peak just at the interface, with a value slightly smaller than at the peak near the upper impermeable wall.

In figure 5 the turbulent and viscous stresses as a function of the channel height are

$Re_*(top)$	325.
$Re_*(bottom)$	393.
Re_b	4517.
$N_x \times N_y \times N_z$	$48 \times 48 \times (128 + 8)$
$L_x \times L_y \times L_z$	$5 \times 3 \times (1 + 1/16)$
ϵ_h	0.95
d_p	1/125
w_t	1/16

TABLE 1. Characteristics of the channel flow simulation.

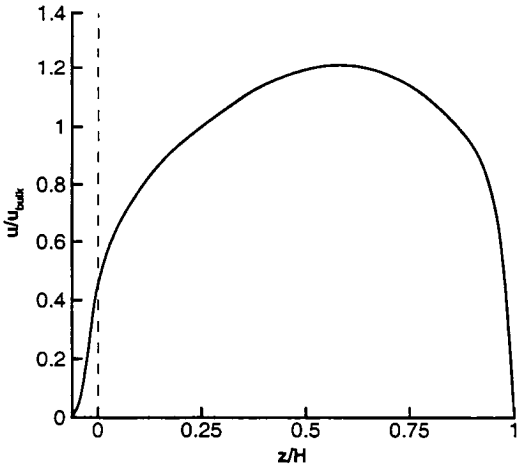

FIGURE 3. The mean velocity profile as function of the channel height. The dashed line marks the position of the interface between the porous medium and the clear fluid.

plotted. The total stress (sum of the viscous plus the turbulent stress) is linear, which is a direct consequence of the constant pressure gradient that drives the flow. We clearly observe a strong increase in drag on the lower permeable wall compared to the upper solid wall. In this simulation the drag increase is almost 50 %. This increase in drag is caused by the exchange of momentum between the clear fluid and the porous medium. In engineering appliances porous materials are sometimes used as heat-exchanger. From the results presented in figures 4 and 5, it is clear that a porous wall aligned parallel to the mean-flow direction will indeed give a very efficient turbulent heat exchange between the flow over and the flow in the porous medium (the behavior of the turbulent heat flux $\overline{<u'><T'>}$ will be very similar to that of the turbulent stress $\overline{<u'><w'>}$).

To get a better insight into the mechanisms behind the drag increase we have calculated the budgets of the transport equations of all the individual Reynolds stresses. The terms are made dimensionless with u_*^4/ν, where u_* is the friction velocity at the upper wall. The exact equations are given in Appendix A. In figure 6 the budgets of the transport equation for the streamwise normal stress (streamwise contribution to turbulent kinetic

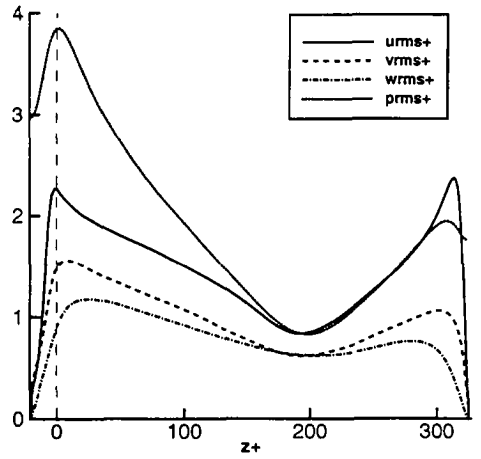

FIGURE 4. The rms-profiles of the streamwise, spanwise and wall-normal velocity fluctuations together with the rms-profile of the pressure, all normalized by friction velocity.

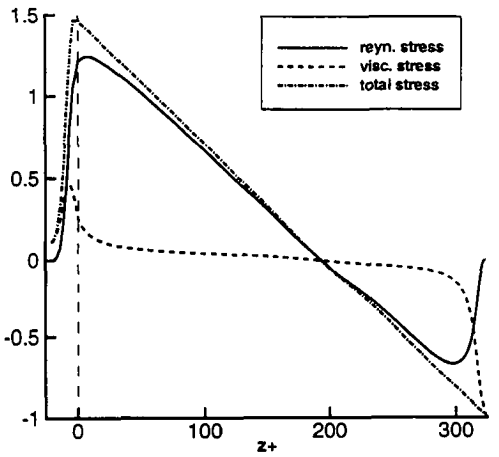

FIGURE 5. The turbulent, viscous and total stress profiles as a function of the channel height.

energy) are shown. The left part of the figure gives the budgets near the permeable wall and the right part the budgets near the upper impermeable wall. The budgets in the upper part of the channel are similar to the budgets calculated by Mansour *et al.* (1988) for standard channel flow between two impermeable walls. Very close to the upper wall the dissipation term (uuDISS) is balanced by the transport term (uuTRANS). At more than about 40 wall units from the upper wall, the pressure-strain term (uuPS) is on the order of the dissipation term and their sum balances the production term (uuPROD). At the lower permeable wall the budgets have changed dramatically. Just above the interface the production term is balanced by the sum of the transport term, the pressure-strain term and the dissipation term. Within the porous wall, the Forchheimer

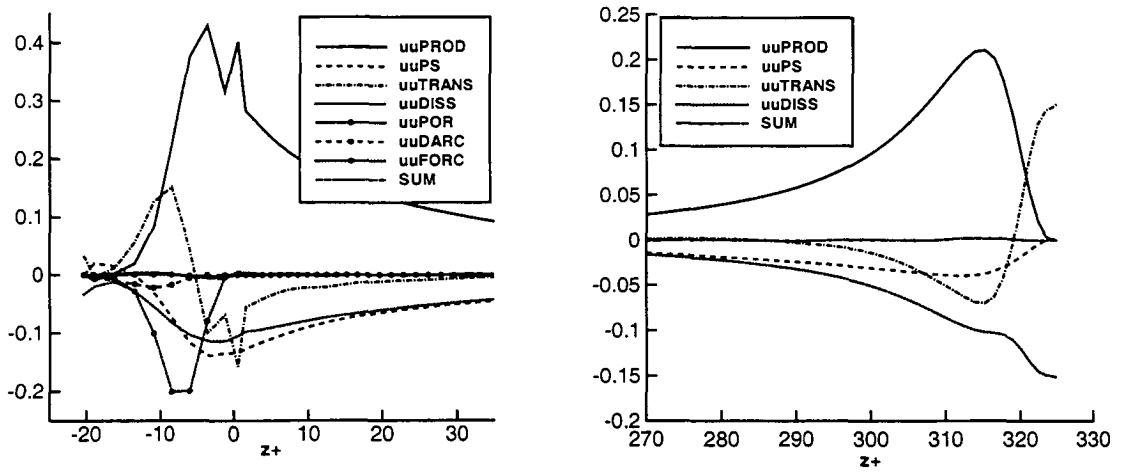

FIGURE 6. The budget of the transport equation for the streamwise contribution to turbulent kinetic energy. Left: the budget at the lower permeable wall (the interface is located at $z = 0$). Right: the budget at the upper wall. (The 'kink' in the production term (uuPROD) and in the transport term (uuTRANS) is a consequence of the jump in the wall-normal grid spacing over the interface, as mentioned before at the beginning of this section.)

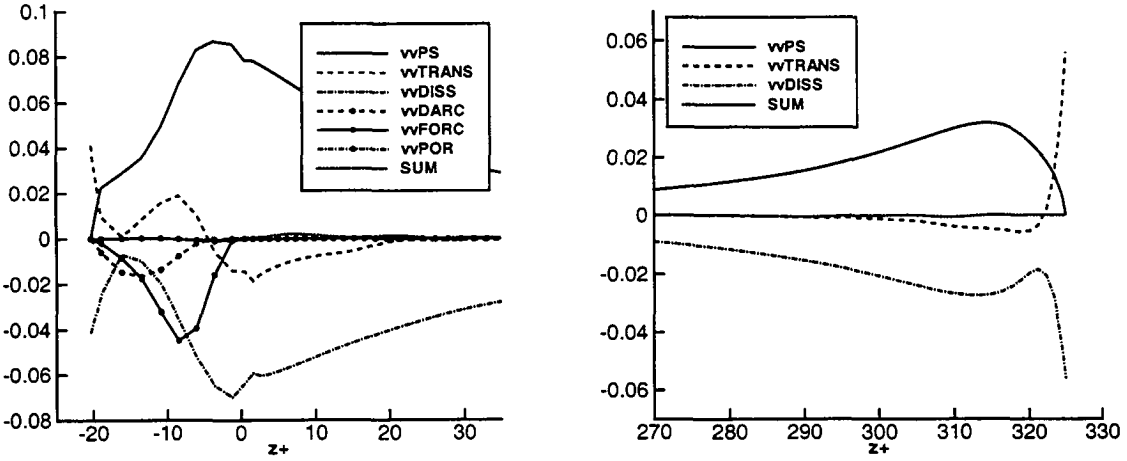

FIGURE 7. The budget of the transport equation for the spanwise contribution to turbulent kinetic energy. Left: The budget at the lower permeable wall (the interface is located at $z = 0$). Right: The budget at the upper wall.

term (uuFORC) becomes the dominant loss term, but it vanishes again close to the impermeable wall below the porous medium. The Darcy term (uuDARC) is of minor importance, a consequence of the high porosity of the wall. The porosity term (uuPOR) basically represents the sum of the advection and the production/dissipation of kinetic energy by changes in the porous structure. It appears to be negligible in this simulation,

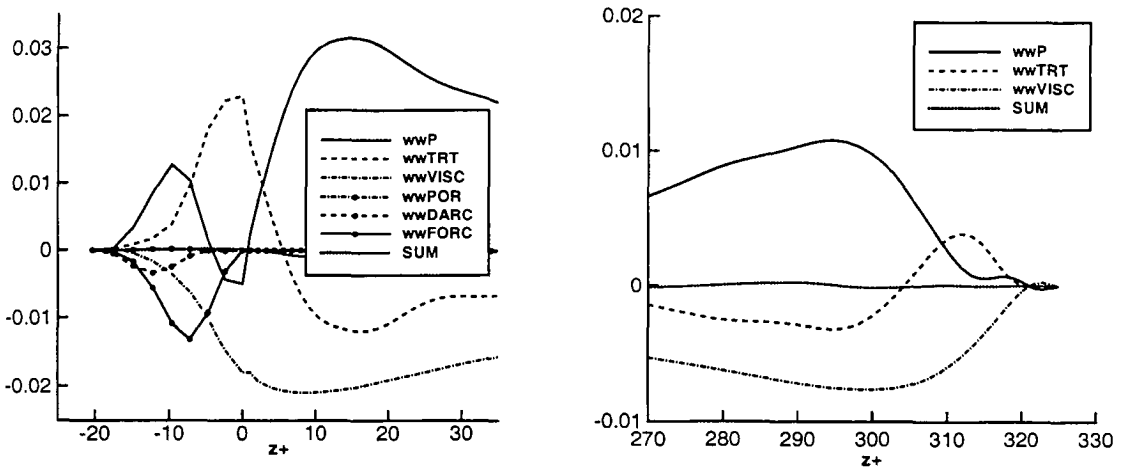

FIGURE 8. The budget of the transport equation for the wall-normal contribution to turbulent kinetic energy. Left: The budgets at the lower permeable wall (the interface is located at $z = 0$). Right: The budgets at the upper wall.

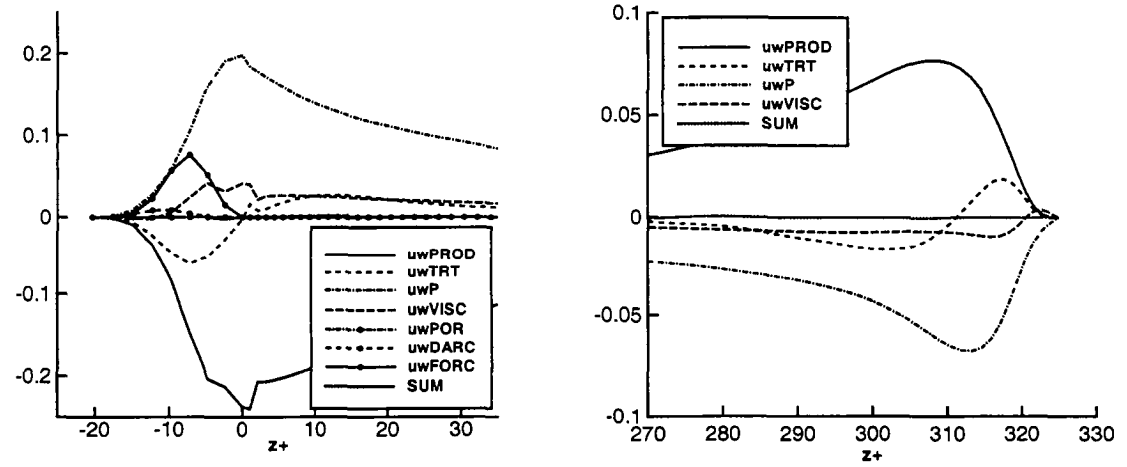

FIGURE 9. The budget of the transport equation for the Reynolds stress $\overline{<u'><w'>}$. Left: the budgets at the lower permeable wall (the interface is located at $z = 0$). Right: the budgets at the upper wall.

because of the high porosity and the large width of the interface region over which the porosity is varying. Notice also from figure 6 that the peak in the production term just below the permeable interface is roughly twice as large as the corresponding peak near the upper wall.

In figure 7 the budgets of the transport equation for the spanwise kinetic energy are shown. Again the left graph shows the budgets near the permeable wall, and the right graph the budgets near the upper wall. At the upper wall the pressure-strain term (vvPS)

balances the dissipation term (vvDISS), except in a region less than about 5 wall units from the wall. In this small region the pressure-strain term falls off to zero and the transport of energy (vvTRANS) by viscous diffusion balances the dissipation. Above the interface with the lower permeable wall, the transport term remains small and there is basically a balance between only the pressure-strain term and the dissipation term. Inside the porous wall, the Forchheimer term becomes the dominant loss term in a small region. The porosity term (vvPOR) is not significant, and the Darcy term (vvDARC) is only of importance in a region of roughly 10 wall units close to the impermeable wall below the porous medium. As we saw before for the production term in the axial case, in the spanwise case the pressure-strain term has a peak inside the porous medium which is more than twice as large as the corresponding peak near the upper wall. The pressure-strain term is a redistribution term, which is responsible for the transfer of axial kinetic energy into spanwise and wall-normal kinetic energies. The enormous increase in this term near the permeable wall explains the increase in the rms of the spanwise velocity fluctuations near the permeable wall as compared to the peak at the upper wall.

In figure 8 the budgets in the transport equation for the wall-normal kinetic energy are shown. Close to the upper wall, the velocity-pressure-gradient term (wwP) becomes smaller than the turbulent-transport term (wwTRT). This behavior is slightly different from that of a standard channel flow described by Mansour *et al.* (1988), where close to the wall the turbulent-transport term is still smaller than the velocity-pressure-gradient term. The reason for this discrepancy might be a matter of grid resolution, as we have in our simulation a coarse grid. In the region just above the interface with the permeable wall, the turbulent-transport term changes of sign and is responsible for a flux of wall-normal kinetic energy into the porous medium. Strangely enough, the velocity-pressure-gradient term is negative in a small region around the interface. In this region the only source of wall-normal kinetic energy comes from the turbulent-transport term. Inside the porous medium there is again a region where the Forchheimer term (wwFORC) is the most important loss term. The Darcyterm (wwDARC) is of minor importance except close to the impermeable wall below the porous medium. The porosity term (wwPOR) is everywhere negligible. Notice that the velocity-pressure-gradientterm has a peak above the permeable interface, which is almost three times larger than the corresponding peak near the upper wall. This energy-redistribution term is responsible for the increase in the rms of the wall-normal velocity fluctuations near the permeable wall as compared to the peak at the upper wall.

In figure 9 the budgets of the transport equation for the turbulent stress ($\overline{<u'><w'>}$) are shown. At the upper as well as near the lower permeable wall, the leading terms are the production term (uwPROD) and the velocity-pressure-gradient term (uwP). Different from the case for the kinetic energies, the Forchheimer term is nowhere the leading loss term. The Darcy term (uwDARC) and the porosity term (uwPOR) are negligible. It is striking that near the permeable interface, the peak values of the production termg and the velocity-pressure-gradient term are more than twice as large as the corresponding peak values near the upper wall. The increase in the production term is caused solely by the enormous increase in the wall-normal velocity fluctuations as the gradient of the mean velocity near the permeable interface is reduced as compared to the upper wall.

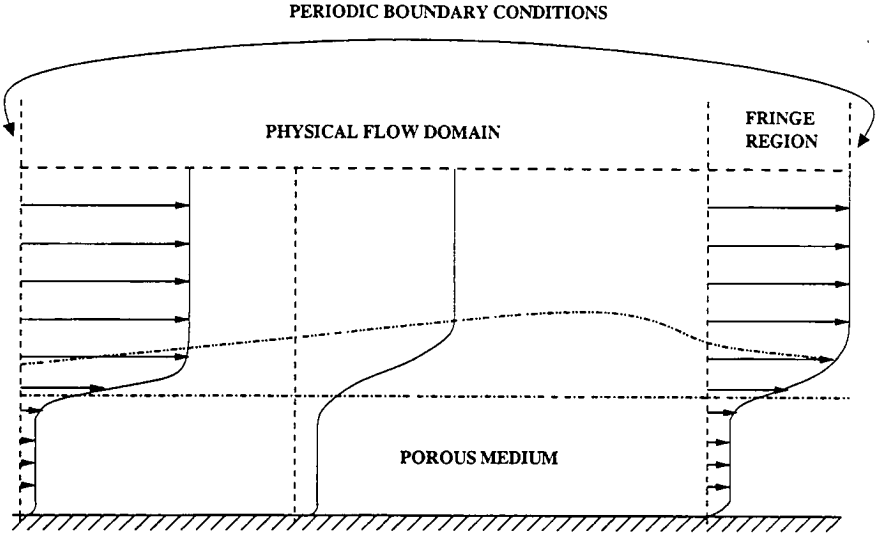

FIGURE 10. A sketch of the computational domain for the simulation of the spatially developing boundary layer over a permeable wall.

4. The turbulent boundary layer over a permeable wall.

In the previous section we presented some results for the flow over a porous channel wall. It was assumed that the flow in the channel was fully developed. In this section we will give some preliminary results for a turbulent, spatially-developing boundary layer over a permeable wall.

The boundary layer is not periodic in the streamwise direction. However, we would like to use the pseudo-spectral method as outlined in the previous section. This method requires that the flow field can be considered as periodic in the streamwise direction. In order to make the problem periodic we have added a 'fringe' region to our domain in which an artificial force drives the velocity field to a specified target. This is illustrated in figure 10. This fringe region can also be seen as a region in which the mean flow in the boundary layer is accelerated and where turbulent kinetic energy is dissipated. A first result of these simulations is shown in figure 11. The porosity in the homogeneous porous region is 0.8. The thickness w_i of the interface region is equal to $1/25\ H$, where H is the height of the flow domain above the permeable interface. The thickness of the porous medium is $0.4\ H$. The mean particle diameter associated with the porous medium is $1/62.5\ H$. The dimensions of the flow domain are $L_x \times L_y \times L_z = 20 \times 3 \times (1 + 0.4)$ for respectively the streamwise, spanwise and wall-normal direction. The artificial force in the fringe region is a smooth function of the streamwise coordinate and has a significant value over a length of about $2\ H$. The number of grid points is $192 \times 64 \times (82 + 24)$ for respectively the streamwise, spanwise and wall-normal direction.

5. Conclusions

In this paper we have presented results from a direct numerical simulation of the flow over and through a permeable wall forming one wall of a channel with fully-developed turbuloent flow. In contrast to the simulations presented in the literature, Jiménez *et al.* (2001) and Hahn *et al.* (2002), we have solved for the flow in the channel coupled with

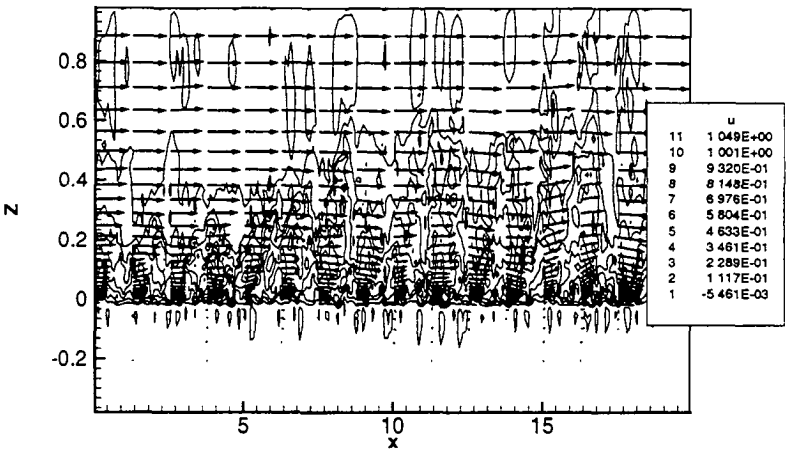

FIGURE 11. A preliminary result of a simulation of the spatially developing boundary layer over a permeable wall. The graph shows an instantaneous snapshot of the velocity field (u, w) in plane with y=constant, where the solid lines are contours of constant streamwise velocity.

the flow in the porous medium. Over the interface with the permeable wall, the flow is continuous and hence no boundary conditions need to be prescribed at the interface. From the simulation we observe a considerable increase in the total drag at the permeable wall. This is caused by the exchange of wall-normal momentum through the interface with the wall, resulting in a higher Reynolds stress $\overline{<u'><w'>}$ as compared to the impermeable wall. The budgets in the transport equations for all the Reynolds stresses have demonstrated that for the evaluated simulation with a porosity of 0.95, the Darcy term is small compared to the Forchheimer term. The Darcy term represents the loss of Reynolds stresses by the viscous drag that the flow inside the pores encounters. The Forchheimer term represents losses due to the pressure drag acting on the flow inside the pores. The porosity term, which represents the advection and production/dissipation of Reynolds stresses by porosity variations, appears to be negligible throughout the porous medium. Furthermore, a start has been made with the simulation of a spatially developing boundary layer over a permeable wall.

Appendix A. transport equations for all the Reynolds stresses

In the following equations, the velocity components and the pressure are all intrinsic volume-averages, but for clarity we have omitted the square brackets.

- transport equation for the axial kinetic energy $\frac{1}{2}\overline{u'^2}$.

$$0 = \underbrace{-\overline{u'w'}\frac{\partial \overline{u}}{\partial z}}_{uuPROD} + \underbrace{\overline{p'\frac{\partial u'}{\partial x}}}_{uuPS} + \underbrace{\frac{\partial}{\partial z}\left(\frac{1}{Re}\frac{1}{2}\frac{\partial \overline{u'^2}}{\partial z}\right) - \frac{1}{\epsilon}\frac{\partial}{\partial z}\left(\epsilon\frac{1}{2}\overline{u'^2 w'}\right)}_{uuTRANS}$$

$$\underbrace{-\frac{1}{Re}\overline{\left(\frac{\partial u'}{\partial x}\right)^2+\left(\frac{\partial u'}{\partial y}\right)^2+\left(\frac{\partial u'}{\partial z}\right)^2}}_{uuDISS}$$

$$+\underbrace{\frac{1}{2}\frac{1}{Re}\frac{1}{\epsilon}\frac{\partial\epsilon}{\partial z}\frac{\partial\overline{u'^2}}{\partial z}+\frac{1}{Re}\frac{1}{\epsilon}\frac{\partial^2\epsilon}{\partial z^2}\overline{u'^2}}_{uuPOR}-\underbrace{\frac{1}{Re}\frac{\epsilon}{Da}\overline{u'^2}}_{uuDARC}-\underbrace{\frac{1}{Re}\frac{\epsilon}{Da}\overline{u'\left[F\cdot u-\overline{F\cdot u}\right]}}_{uuFORC}$$

- transport equation for the spanwise kinetic energy $\frac{1}{2}\overline{v'^2}$.

$$0=\underbrace{\overline{p'\frac{\partial v'}{\partial x}}}_{vvPS}+\underbrace{\frac{\partial}{\partial z}\left(\frac{1}{Re}\frac{1}{2}\frac{\partial\overline{v'^2}}{\partial z}\right)-\frac{1}{\epsilon}\frac{\partial}{\partial z}\left(\epsilon\frac{1}{2}\overline{v'^2w'}\right)}_{vvTRANS}$$

$$\underbrace{-\frac{1}{Re}\overline{\left(\frac{\partial v'}{\partial x}\right)^2+\left(\frac{\partial v'}{\partial y}\right)^2+\left(\frac{\partial v'}{\partial z}\right)^2}}_{vvDISS}$$

$$+\underbrace{\frac{1}{2}\frac{1}{Re}\frac{1}{\epsilon}\frac{\partial\epsilon}{\partial z}\frac{\partial\overline{v'^2}}{\partial z}+\frac{1}{Re}\frac{1}{\epsilon}\frac{\partial^2\epsilon}{\partial z^2}\overline{v'^2}}_{vvPOR}-\underbrace{\frac{1}{Re}\frac{\epsilon}{Da}\overline{v'^2}}_{vvDARC}-\underbrace{\frac{1}{Re}\frac{\epsilon}{Da}\overline{v'\left[F\cdot v-\overline{F\cdot v}\right]}}_{vvFORC}$$

- transport equation for the wall-normal kinetic energy $\frac{1}{2}\overline{w'^2}$.

$$0=\underbrace{\overline{p'\frac{\partial w'}{\partial z}}-\frac{\partial}{\partial z}\overline{p'w'}}_{wwP}-\underbrace{\frac{1}{\epsilon}\frac{\partial}{\partial z}\left(\epsilon\frac{1}{2}\overline{w'^2w'}\right)}_{wwTRT}$$

$$\underbrace{+\frac{\partial}{\partial z}\left(\frac{1}{Re}\frac{1}{2}\frac{\partial\overline{w'^2}}{\partial z}\right)-\frac{1}{Re}\overline{\left(\frac{\partial w'}{\partial x}\right)^2+\left(\frac{\partial w'}{\partial y}\right)^2+\left(\frac{\partial w'}{\partial z}\right)^2}}_{wwVISC}$$

$$+\underbrace{\frac{1}{2}\frac{1}{Re}\frac{1}{\epsilon}\frac{\partial\epsilon}{\partial z}\frac{\partial\overline{w'^2}}{\partial z}+\frac{1}{Re}\frac{1}{\epsilon}\frac{\partial^2\epsilon}{\partial z^2}\overline{w'^2}}_{wwPOR}-\underbrace{\frac{1}{Re}\frac{\epsilon}{Da}\overline{w'^2}}_{wwDARC}-\underbrace{\frac{1}{Re}\frac{\epsilon}{Da}\overline{w'\left[F\cdot w'-\overline{F\cdot w'}\right]}}_{wwFORC}$$

- Tranport equation for the turbulent stress $\overline{u'w'}$.

$$0=\underbrace{-\overline{w'^2}\frac{\partial\overline{u}}{\partial z}}_{uwPROD}\underbrace{-\frac{1}{\epsilon}\frac{\partial}{\partial z}\left(\epsilon\overline{w'^2u'}\right)}_{uwTRT}\underbrace{+\overline{p'\left(\frac{\partial u'}{\partial z}+\frac{\partial w'}{\partial x}\right)}-\frac{\partial\overline{p'u'}}{\partial z}}_{uwP}$$

$$\underbrace{-\frac{2}{Re}\overline{\left(\frac{\partial u'}{\partial x}\frac{\partial w'}{\partial x}\right)+\left(\frac{\partial u'}{\partial y}\frac{\partial w'}{\partial y}\right)+\left(\frac{\partial u'}{\partial z}\frac{\partial w'}{\partial z}\right)}+\frac{1}{R}\frac{\partial^2\overline{u'w'}}{\partial z^2}}_{uwVISC}$$

$$+\underbrace{\frac{1}{Re}\frac{1}{\epsilon}\frac{\partial\epsilon}{\partial z}\frac{\partial\overline{u'w'}}{\partial z}+\frac{2}{Re}\frac{1}{\epsilon}\frac{\partial^2\epsilon}{\partial z^2}\overline{u'w'}}_{uwPOR}-\underbrace{\frac{1}{Re}\frac{\epsilon}{Da}\overline{u'w'}}_{uwDARC}$$

$$\underbrace{-\frac{1}{Re}\frac{\epsilon}{Da}\overline{w'\left[F\cdot u-\overline{F\cdot u}\right]}-\frac{1}{Re}\frac{\epsilon}{Da}\overline{u'\left[F\cdot w'-\overline{F\cdot w'}\right]}}_{uwFORC}$$

REFERENCES

MacDonald, I.F., El-Sayed, M.S., Mow, K. & Dullien, F.A.L. 1979 Flow through porous media: The Ergun equation revisited. *Ind. and Eng. Chemistry* **18**, 199-208.

Whitaker, S. 1996 The Forchheimer equation: a theoretical development. *Transport in Porous Media* **25**, 27-61.

Finnigan, J. 2000 Turbulence in plant canopies. *Annu. Review Fluid Mech.* **32** 519-571.

Beavers, G.S., & Joseph, D.D. 1967 Boundary conditions at a naturally permeable wall. *J. Fluid Mech.* **30**, 197-207.

Mansour, N.N., Kim,J. & Moin, P. 1988 Reynolds-stress and dissipation-rate budgets in a turbulent channel flow. *J. Fluid Mech.* **194**. 15-44.

Hahn, S., Je, J. & Choi, H. 2002 Direct numerical simulation of turbulent channel flow with permeable walls. *J. Fluid Mech.* **450**, 259-285.

Jiménez, J., Uhlmann, M., Pinelli, A. & Kawahara, G. 2001 Turbulent shear flow over active and passive porous surfaces. *J. Fluid Mech.* **442**, 89-117.

Spalart, P.R. 1988 Direct simulation of a turbulent boundary layer up to $Re_\theta = 1410$. *J. Fluid Mech.* **187**, 61-98.

Ochoa-Tapia, J.A. & Whitaker, S. 1995a Momentum transfer at the boundary between a porous medium and a homogeneous fluid – I. Theoretical development. *Int. J. Heat Mass Transfer* **38**, 2635-2646.

Ochoa-Tapia, J.A. & Whitaker, S. 1995b Momentum transfer at the boundary between a porous medium and a homogeneous fluid – II. Comparison with experiment. *Int. J. Heat Mass Transfer* **38**, 2647-2655.

Contrail formation in aircraft wakes using large-eddy simulations

By R. Paoli †, J. Hélie ‡, T. J. Poinsot ¶ AND S. Ghosal ||

In this work we analyze the issue of the formation of condensation trails ("contrails") in the near-field of an aircraft wake. The basic configuration consists in an exhaust engine jet interacting with a wing-tip trailing vortex. The procedure adopted relies on a mixed Eulerian/Lagrangian two-phase flow approach; a simple micro-physics model for ice growth has been used to couple ice and vapor phases. Large eddy simulations have carried out at a realistic flight Reynolds number to evaluate the effects of turbulent mixing and wake vortex dynamics on ice-growth characteristics and vapor thermodynamic properties.

1. Introduction

Contrails are ice clouds generated by water in the exhaust from aircraft engines, forming the common visible white lines in the sky. As assessed in the special report of the Intergovernmental Panel on Climate Change (IPCC report (1999)), they have an important environmental impact because they artificially increase cloudiness and trigger the formation of cirrus clouds, thus altering climate both on local and regional/global scales (see figure 1). This was confirmed in a recent climate study (Travis *et al.* (2002)) performed in the three days following the 11th of September 2001, when all american aircraft were grounded and there were no contrails over the USA. During this period, abnormal and significant temperature differences between day and night (namely, "daily temperature range" or DTR) were observed in the USA. This confirms that contrails are of major importance for global climate change by artificial clouds formation.

Contrails consist of ice crystals which form mainly by condensation of exhaust water vapor over suitable nucleation sites, like soot particles and sulfur aerosols, emitted by aircraft engines (Schumann (1996), Karcher & *al.* (1996)). Background atmospheric vapor, which eventually adds to the exhaust content, is responsible for the persistence of contrails (Gierens (1996)). Contrails form when the air surrounding a nucleation site becomes supersaturated with respect to ice (Appleman (1953), Schumann (1996)). For certain atmospheric conditions, this may occur somewhere in the jet plume, as the result of the increased humidity due to mixing between hot and moist exhaust gases with cold and less humid ambient air. In a temperature/vapor-pressure plane (see figure 2), assuming that vapor and heat diffuse at the same rate ($(Sc = Pr)$ and that the flow is adiabatic, pure mixing can be graphically represented by a straight ("mixing") line which is completely defined by the two states A (ambient air) and B (exhaust gas). In figure 2, supersaturation corresponds to the thermodynamic states lying between S_1 and

† CERFACS
‡ IMFT
¶ CERFACS and IMFT
|| Northwestern University

FIGURE 1. Contrails in South-Eastern France sky (http://eol.jsc.nasa.gov).

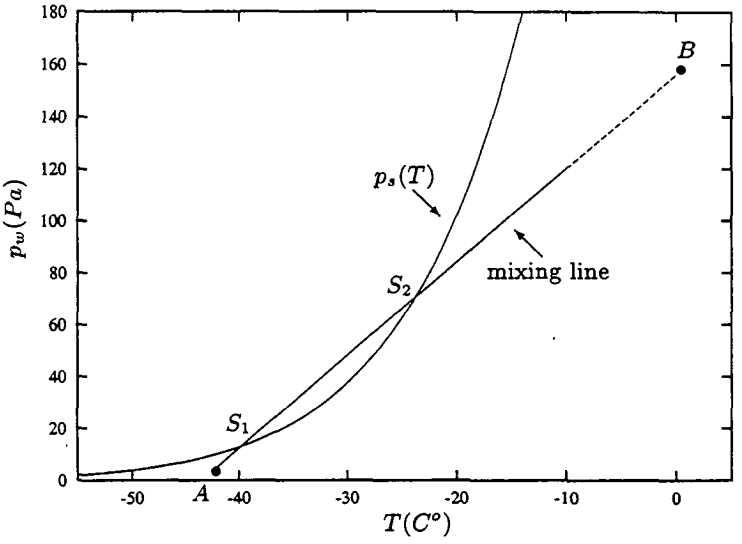

FIGURE 2. Thermodynamic conditions for ice formation: $p_s(T)$ is the saturation curve with respect to ice. State A represents (cold) atmospheric conditions; state B, (hot) exhaust conditions (for the sake of representation, we placed it much closer to p_s than what it really is). States S_1 and S_2 define the range of supersaturation, $p_w > p_s(T)$.

S_2, where $p_w > p_s(T)$. An ice crystal forms when such a condition is locally satisfied in the jet plume and, at the same time, a nucleation particle is present. A two-phase flow solver, using a Lagrangian solver for nucleation particles, then represents the most suitable approach to deal with ice formation in the contrails.

Formation and persistence of contrails have been studied during last years, mostly in geophysical and atmospheric science literature, through *in situ* measurements and numerical simulations with different level of complexity (see IPCC report (1999) and references therein). The main intent there was to characterize the general features of the phenomenon on time scales up to minutes from the emission time. Other authors

investigated in detail the micro-physics of ice formation (the initial composition of the jet contrail, the mechanism of water uptake on the nucleation site, homogeneous versus heterogeneous nucleation, etc. see Pruppacher & Klett (1997) for a complete review).

In the present work we have focused on the simulation of contrail formation and early-stage evolution in the near-field of an aircraft wake, i.e., up to a few seconds from the emission time. The basic configuration consists of an exhaust jet interacting with a wing-tip trailing vortex. This represents a complex issue because of the different phenomena involved, such as jet and wake-vortex instabilities, transition to turbulence, two-phase flow and ice micro-physics. Large-eddy simulations are well suited to deal with all these inherently unsteady processes, at realistic flight Reynolds numbers, and have been used in this work. The object of the study is two-fold. First, we aim to characterize: (i) the spatial distribution of supersaturation around particles, in the jet plume; and (ii) the effects of wake vortex. Then, we test a simple micro-physics model for ice-growth to account for (iii) the early stage of contrail evolution and (iv) its influence on the thermodynamic properties of water vapor. Governing equations for the two-phase flow model are detailed in section 2, results are presented in section 3. In section 4 an alternative approach is proposed to account for a general (initial) distribution of soot particles.

2. Governing equations and ice micro-physics model

Large-eddy simulations of ice formation are carried out through an Eulerian/Lagrangian two-phase flow approach. For the gaseous (carrier) phase we solve fully-compressible Navier-Stokes equations together with a transport equation for a scalar field, representing the exhaust water vapor, Y_w. These equations are filtered spatially so that any variable $\phi(x) = [\rho, \rho u, \rho v, \rho w, \rho E, \rho Y_w]$ is decomposed into a resolved part $\overline{\phi(x)}$ and a non-resolved (or subgrid-scale) part $\phi''(x)$, with $\phi(x) = \overline{\phi(x)} + \phi''(x)$. For compressible flows, we use Favre-filtered variables, defined as $\phi(x) = \tilde{\phi}(x) + \phi'(x)$, with $\tilde{\phi} = \overline{\rho\phi}/\overline{\rho}$. Using this approach, dimensionless Favre-averaged equations are

$$\frac{\partial \overline{\rho}}{\partial t} + \frac{\partial(\overline{\rho}\tilde{u}_j)}{\partial x_j} = \dot{\omega}, \tag{2.1}$$

$$\frac{\partial(\overline{\rho}\tilde{u}_i)}{\partial t} + \frac{\partial(\overline{\rho}\tilde{u}_i\tilde{u}_j)}{\partial x_j} + \frac{\partial \overline{p}}{\partial x_i} = \frac{1}{Re}\frac{\partial \tilde{\tau}_{ij}}{\partial x_j} + \frac{\partial \sigma_{ij}}{\partial x_j}, \tag{2.2}$$

$$\frac{\partial(\overline{\rho}\tilde{E})}{\partial t} + \frac{\partial[(\overline{\rho}\tilde{E} + \overline{p})\tilde{u}_j]}{\partial x_j} = \frac{1}{Re}\frac{\partial \tilde{\tau}_{ij}\tilde{u}_i}{\partial x_j} + \frac{\partial \sigma_{ij}\tilde{u}_i}{\partial x_j} - \frac{1}{Re\,Pr}C_p\frac{\partial \tilde{q}_j}{\partial x_j} - \frac{\partial Q_j}{\partial x_j}, \tag{2.3}$$

$$\frac{\partial(\overline{\rho}\tilde{Y}_w)}{\partial t} + \frac{\partial(\overline{\rho}\tilde{Y}_w\tilde{u}_j)}{\partial x_j} = \frac{1}{Re\,Sc}\frac{\partial}{\partial x_j}\left(\mu\frac{\partial \tilde{Y}_w}{\partial x_j}\right) + \frac{\partial \xi_j}{\partial x_j} + \dot{\omega}. \tag{2.4}$$

The sub-grid scale (SGS) stress tensor $\sigma_{ij} = -(\overline{\rho u_i u_j} - \overline{\rho}\tilde{u}_i\tilde{u}_j)$, the SGS heat flux $Q_j = \overline{\rho C_p T u_j} - \overline{\rho} C_p \tilde{T}\tilde{u}_j$ and the SGS scalar flux $\xi_j = -(\overline{\rho Y_w u_j} - \overline{\rho}\tilde{Y}_w\tilde{u}_j)$ are modeled through the subgrid-scale eddy-viscosity concept

$$\sigma_{ij} - \frac{1}{3}\sigma_{kk}\delta_{ij} = -2\mu_{sgs}\left(\tilde{S}_{ij} - \frac{1}{3}\delta_{ij}\tilde{S}_{kk}\right),\ Q_j = -\frac{\mu_{sgs}\,C_p}{Pr_t}\frac{\partial \Theta}{\partial x_j},\ \xi_j = -\frac{\mu_{sgs}}{Sc_t}\frac{\partial \tilde{Y}_w}{\partial x_j}, \tag{2.5}$$

where $\Theta = \tilde{T} - \frac{1}{2\overline{\rho}C_v}\sigma_{kk}$ is the modified temperature (Métais & Lesieur (1992)) while turbulent Prandtl and Schmidt numbers are assumed to be constant. In the present simulations, we assumed $Pr_t = 0.3$ and $Sc_t = 0.3$. Sub-grid scale viscosity μ_{sgs} is obtained

through the Filtered Structure Function model (Métais & Lesieur (1992), Ducros & al. (1996)), initially developed in spectral space and then transposed into physical space. This model was found to be well suited for the simulation of transitional flows, due to the property of insuring no SGS viscosity when there is no energy at the cutoff wavelength (Ducros & al. (1996)). Vapor/ice mass coupling in the continuity and scalar equations, $\dot{\omega}$ is discussed in the next section.

2.1. *Particles treatment and ice-growth model*

Soot-ice particles are tracked through a Lagrangian solver with point force approximation (see Boivin & *al.* (1998) for details). Due to their small size (from tens of nanometers to a few microns, see Karcher & *al.* (1996)) their relaxation time is negligible compared to the characteristic times of the filtered gas variables. This allows them to be treated as tracers. In addition, due to their high number density (varying approximately between 10^9 and $10^{11}\,m^{-3}$ (Karcher & *al.* (1996)), we can carry only packets of particles, or "numerical particles", each one containing a large number n_{trans} of real soot-ice kernels. A numerical particle is defined as the center of mass, $\underline{x}_p$, of n_{trans} physical particles. In the tracer limit, its motion is completely described by

$$\frac{d\underline{x}_p}{dt} = \tilde{\underline{u}}(\underline{x})\,\delta(\underline{x} = \underline{x}_p) \tag{2.6}$$

where $\tilde{\underline{u}}$ is the (filtered) gas velocity. Using filtered quantities instead of exact un-filtered ones is equivalent to neglecting sub-grid dispersion, compared to the resolved, large-scale dispersion. This assumption is justified because the Reynolds number is high. Gas sources are estimated at the numerical particle positions; afterwards they are projected on the Eulerian grid, inversely proportional to the mesh-point distance. This numerical method can be viewed as a spatial filtering (Boivin & *al.* (1998), Hélie & al. (2002)). Exchange between phases is allowed by the code (two-way coupling). Nevertheless, due to the tracer limit and solid/gas mass ratio, drag momentum exchange is negligible. Temperature cannot be modified by ice growth by more than a few Kelvin (Schumann (1996)), so that thermal coupling is also neglected. Therefore, we only consider mass exchange, i.e. vapor condensation on the soot particle. The term $\dot{\omega}$ can be neglected in (2.1) because of the small amount (order of a few percent) of water vapor in the exhaust gases. On the other hand, in (2.4) it accounts for vapor/ice phase exchange and is related to the rate of growth of a single ice crystal, through the quasi-stationary model (Karcher & *al.* (1996))

$$\frac{dr_p}{dt} = \frac{J_w}{\tilde{\rho} S_p}, \tag{2.7}$$

$$\dot{\omega} = -\sum_{p=1}^{n_p} \delta(\underline{x} = \underline{x}_p) n_{trans} \frac{dr_p}{dt} \rho_p\, S_p. \tag{2.8}$$

$S_p = 4\pi r_p^2$ and ρ_p are the area of the particle (supposed spherical) and its density, while J_w is the mass flux of water vapor on the particle surface

$$J_w = 4\pi r_p D\, G(r_p)(\tilde{Y}_w - Y_s) \tag{2.9}$$

where $D = \mu/(\rho Sc)$ is the molecular diffusivity of water vaporin air, Y_s is the mass fraction of gaseous water at ice saturation. The dimensionless collision factor $G(r_p)$ is

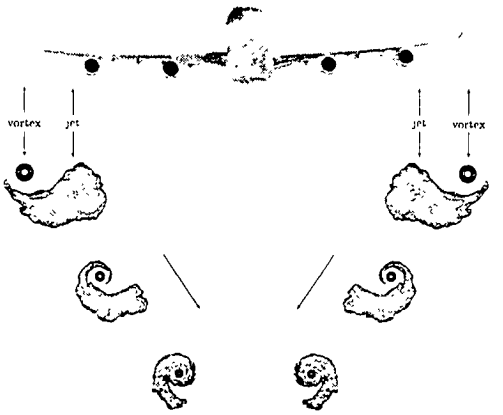

FIGURE 3. Basic configuration of a jet/vortex interaction in the near-field of an aircraft wake.

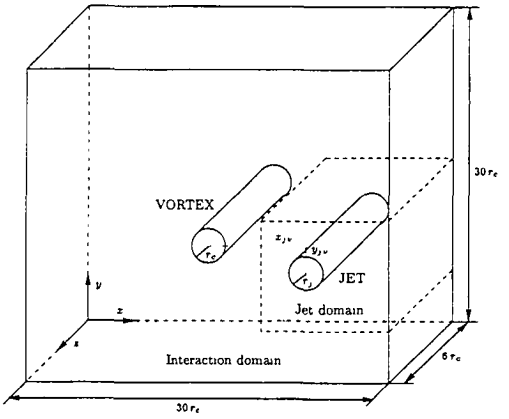

FIGURE 4. Sketch of the computational domains for the jet and the interaction phases.

given by the semi-theoretical correlation

$$G(r_p) = \left(\frac{1}{1+K_n} + \frac{4K_n}{3\alpha} \right)^{-1} . \tag{2.10}$$

It depends on the Knudsen number $K_n = \lambda / r_p$ (ratio of the vapor mean free path to the particle radius) and the empirical constant $\alpha = 0.1$, and was found to give good results for quasi-isothermal flows and cases with low heat transfer (see Qu & Davis (2001) for details). Saturation conditions are estimated by Sonntag (1994) as

$$p_s = p\, X_s = \exp\Big(\frac{6024.5282}{\tilde{T}} + 29.32707 + 1.0613868\, 10^{-2} \tilde{T} - 1.3198825\, 10^{-5} \tilde{T}^2 - 0.49382577 \ln \tilde{T} \Big) \tag{2.11}$$

where $\tilde{T}$ is the filtered gas temperature (heat inertia of particles is neglected). Mass and molar fractions at saturation conditions are related by $Y_s = X_s / (X_s + (1 - X_s)\, W_{air}/W_w)$, with $W_{air} = 28.85$ kg/Kmole, $W_w = 18.01$ kg/Kmole.

The numerical code, NTMIX3D, is a three-dimensional, two-phase flow, finite-difference solver. For the gas phase, space discretization is performed by a sixth-order compact scheme (Lele (1992)). Time integration is performed by means of a three-stage Runge-Kutta method, for both the two phases. The solver is fully parallel, using domain decomposition. Simulations are performed using 16 processors on CINES O3000 machine.

3. Results

This section describes the results of the simulation of ice formation in the near-field of an aircraft wake. The basic configuration is an exhaust jet interacting with a (single) wing-tip trailing vortex (Fig 3). We adopted a two-stage simulation which consists in first simulating a temporally-evolving jet ("jet phase") and then its interaction with the vortex ("interaction phase"). This procedure has been used previously (Paoli & *al.* (2002), Garnier & *al.* (2002)) and its validity has been recently discussed by some of the authors (Paoli & *al.* (2002)). A sketch of the computational domain for the two phases is shown in figure 4. For the jet phase it has dimensions $L_x = L_y = 16\, r_j$ and $L_z = 6\, r_j$

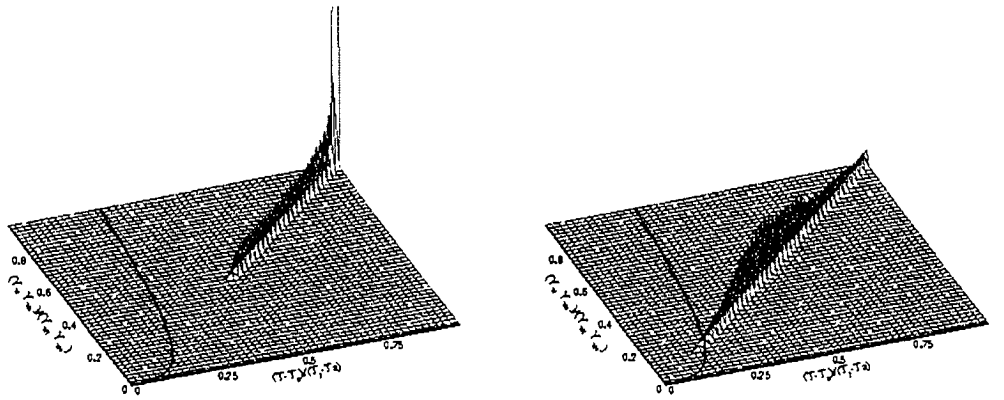

FIGURE 5. Joint PDF of temperature and water vapor partial pressure around passive particles, during the jet phase (saturation curve is also displayed); left, $t = 0.16\,s$; right $t = 0.56\,s$.

(z being the jet axis and r_j the exhaust jet radius) and consists of $161 \times 161 \times 61$ grid points; for the interaction phase, the dimensions are $L_x = L_y = 30\,r_j$ and $L_z = 6\,r_j$ with $301 \times 301 \times 61$ grid points. The Reynolds number, based on the radius, $r_j = 1\,m$, and the exhaust jet velocity, $w_j = 60\,\mathrm{m/s}$, is $Re_j = 3.2 \times 10^6$, while the exhaust Mach number is $M_j = 0.2$. Axial velocity, temperature and vapor mass fraction are initialized according to a tanh law (for simplicity, all bars and tildes are omitted)

$$w_0(r) = \frac{1}{2}\Big[(w_j + w_a) - (w_j - w_a)\,F(r)\Big]; \quad F(r) = \tanh\left[\frac{1}{4}\frac{r_j}{\theta}\left(\frac{r}{r_j} - \frac{r_j}{r}\right)\right] \tag{3.1}$$

where r is the radial distance from the center; $r_j/\theta = 10$; while subscripts j and a indicate exhaust jet and ambient air, respectively (see Paoli & *al.* (2002) for details). Initial temperature and water vapor mass fraction follow the same law

$$T_0(r) = \frac{1}{2}\Big[(T_j + T_a) - (T_j - T_a)\,F(r)\Big], \tag{3.2}$$

$$Y_{w_0}(r) = \frac{1}{2}\Big[(Y_{w_j} + Y_{w_a}) - (Y_{w_j} - Y_{w_a})\,F(r)\Big]. \tag{3.3}$$

In the present simulations we assume no coflow, $w_a = 0$, and no background water content, $Y_{w_a} = 0$; the exhaust water content, taken from available data (Garnier & *al.* (1997)), is $Y_{w_j} = 0.03$. Ambient temperature is $T_a = 225\,K$ and exhaust-to-ambient temperature ratio is $T_j/T_a = 2$ which gives $T_j = 450\,K$, a reasonable value for the exhaust temperature. The jet is loaded with $n_p = 250000$ (numerical) soot particles with the same radius $r_p = 0.02\,\mu m$. They behave as tracers and each one represents a packet of $n_{trans} = 10^6$ physical particles. Particle number density is then 2.5×10^{11}, in agreement with literature data (Karcher & *al.* (1996)).

A random-noise perturbation δw is added to the base flow w_0 in (3.1) (with $\delta w_{max} = 0.005\,w_0(r)$), to trigger jet instability and transition to turbulence. When the maximum jet velocity has decreased to half the initial value, the domain is enlarged and a vortex inserted (the relative position is $x_{jv} = 5\,r_j$ and $y_{jv} = -r_j$, see figure 4), according to the

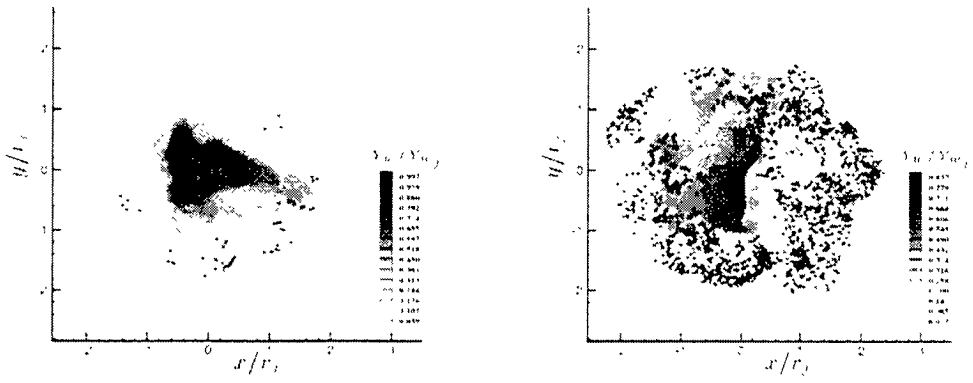

FIGURE 6. Passive particles case (jet phase). Plane cut of vapor content and distribution of supersaturated particles; left, $t = 0.56\,s$; right, $t = 0.7\,s$.

Lamb-Oseen model ($\alpha = 1.4$, $\beta = 1.2544$)

$$v_\theta(r) = \alpha\, v_c \frac{r_c}{r}\left\{1 - exp\left[-\beta\left(\frac{r}{r_c}\right)^2\right]\right\}; \qquad \frac{dp}{dr} = \rho\frac{v_\theta^2}{r} \tag{3.4}$$

where $r_c = r_j$ is the vortex core radius and $v_c = 1.5\, w_j(t_{jv})$ is the core velocity (t_{jv} being the time at the end of the jet phase simulations; see Paoli & *al.* (2002)).

3.1. *Passive-particle results*

A first set of simulations was performed with the ice-growth model switched off. The object was to obtain a reference mixing case at high Reynolds numberss typical of aircraft wake configurations. It was also useful to analyze the spatial distribution of supersaturated particles and identify the regions where ice formation is most likely to occur. Basic diagnostics consists in analyzing the thermodynamic properties of the exhaust gas during mixing with ambient air. Probability Density Function (PDF) is a convenient diagnostic because it provides the additional information on the fraction of particles that supersaturate with respect to ice. Figure 5 shows the joint PDF of normalized temperature, $(T - T_a)/(T_j - T_a)$, and the partial pressure of water vapor, $(p_w - p_{w_a})/(p_{w_j} - p_{w_a})$, around soot particles. The PDF follows a straight line which indicates pure mixing between hot jet and cold air. This is a consequence of the assumptions of low Mach number and $Le = Sc/Pr = 1.$. The first assumption implies small pressure fluctuations and kinetic energy negligible compared to internal energy in (2.3). The second implies that the diffusion terms in Eqs. (2.3) and (2.4) are the same. Therefore, T and p_w are given by the same transport equations and evolve along a mixing line (obtained by elimination of r in the initial conditions, Eqs. (3.2) and (3.3))

$$\frac{p_w}{p_{w_j} - p_{w_a}} = \frac{T}{T_j - T_a} + \frac{1}{2}\left(\frac{p_{w_j} + p_{w_a}}{p_{w_j} - p_{w_a}} - \frac{T_j + T_a}{T_j - T_a}\right). \tag{3.5}$$

All particles are initially (at $t = 0.16\,s$) placed below the saturation curve p_s because they are still concentrated inside the hot jet region. Due to the mixing with cold air, particles cool, moving along the mixing line, until some of them become supersaturated (crossing of p_s curve at $t = 0.56\,s$). The spatial distribution of supersaturated particles is given in

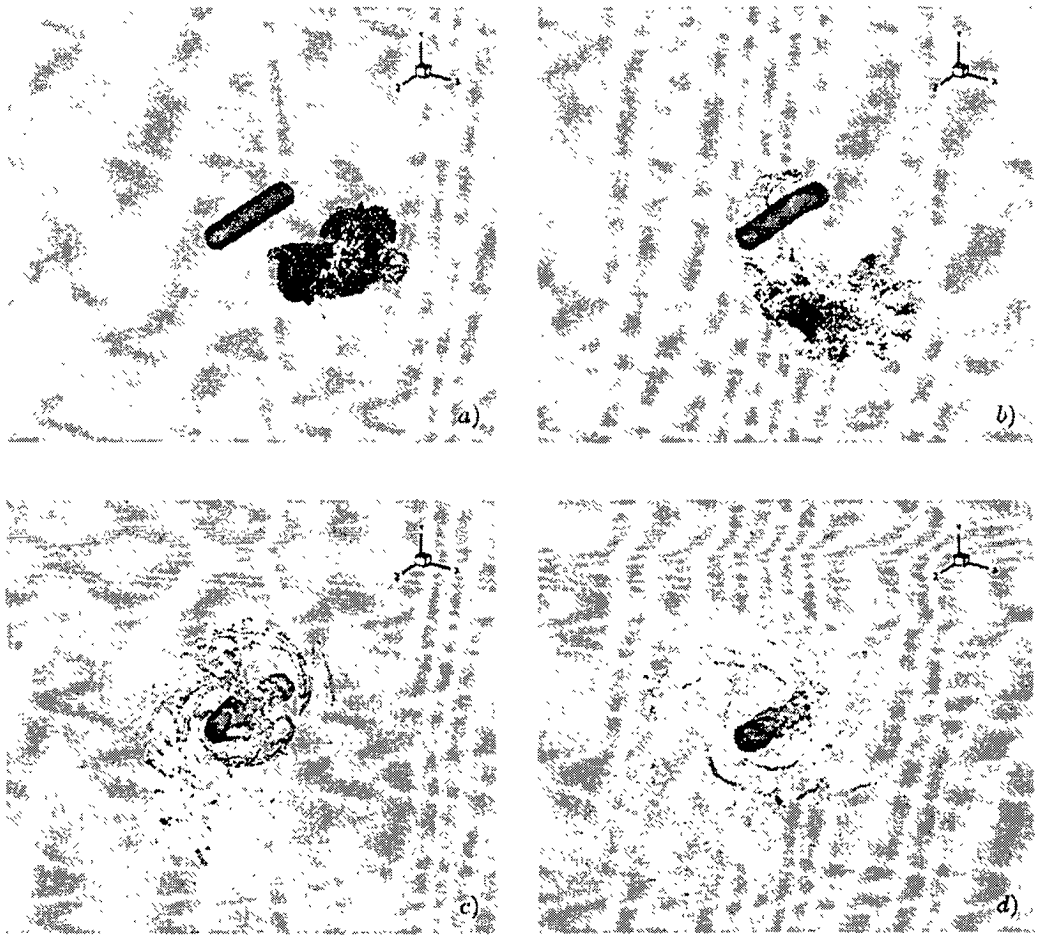

FIGURE 7. Passive particles distribution during the jet/vortex interaction phase. Dry soot particles are represented in black, iced supersaturated particles in white. Total vorticity iso-surface identifies the vortex core and the secondary vortical structures due to the interaction with the jet; *a*), $t = 0.7\,s$; *b*), $t = 1\,s$; *c*), $t = 1.5\,s$; *d*), $t = 2\,s$.

figure 6, together with a plane cut of water vapor content at two times during the jet phase. The figure shows that air first saturates around the particles placed at the edges of the jet where the temperature has fallen and there is sufficient vapor to condense.
The dynamics of the jet/vortex interaction phase are dominated by the entrainment of the jet inside the vortex field. Nevertheless, other phenomena occur, as shown in figure 7: when the jet is close enough to the vortex core, its axial velocity strongly interacts with the vortex tangential velocity, causing the formation of three-dimensional structures of azimuthal vorticity. These structures progrssively decay ($t = 2\,s$, see figure 7(d)), corresponding to complete entrainment of the jet (Paoli & *al.* (2002)). This mechanism of entrainment enhances mixing with external air: therefore, exhaust cooling and vapor condensation are favored by the presence of the vortex. Figure 7 shows that at $t = 2\,s$ all particles are supersaturated and contrail can form everywhere in the wake.

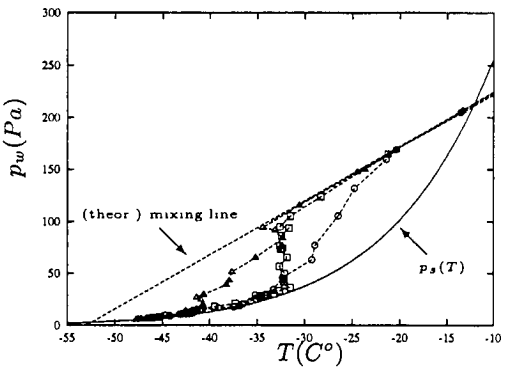

FIGURE 8. Trajectories of three sample particles in a $T - p_w$ plane.

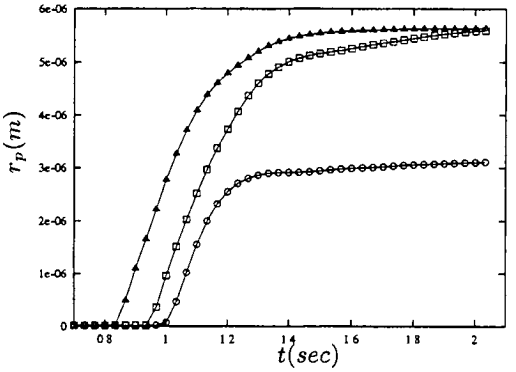

FIGURE 9. Time evolution of three sample particles radius.

3.2. *Freezing-particle results*

This section presents the results of the simulations with the ice-growth model activated. The goal is to analyze the early-stage evolution of the contrail and how it influences mixing and the thermodynamic properties of the vapor. The simulation procedure is the same as in the previous calculations, i.e., we first simulate the jet alone and then its interaction with the vortex. The key point is that the ice and vapor phases are coupled through Eqs. (2.7) and (2.8). Figure 8 displays the trajectories of three sample ice particles in the temperature/vapor-pressure plane (results are reported only during the interaction phase when ice/vapor coupling is significative). The figure shows that condensation causes large deviations from the mixing line because of vapor removal and the consequent decrease in p_w. In addition, all the particles finally collapse on the saturation curve, $p_s(T)$, which indicates the thermodynamic equilibrium between vapor and ice phases. This is confirmed in figure 9 by the evolution of ice-particle radii which attain plateau values between 3 and 6 μm. The distribution of ice crystals size is provided in figure 10 in terms of radius PDF. The peak around $r_p = r_p$ at $t = 0.7$ s (end of the jet phase) indicates that only a small amount of ice has formed. As long as ice nucleation proceeds, such a peak decreases and finally disappears, and the shape of the PDF finally approaches a Gaussian at approximatively $t = 2$ s. A remarkable result is the high variance of the PDF with $r_p'/ < r_p > \approx 0.5$. This indicates high polydispersion whereas the temperature and partial pressure around particles have become approximately uniform.

4. Future directions

The particle-tracking approach adopted in this work is an attempt to approximate the behavior of a cloud of particles by attributing the properties of a "representative" particle to all members of the cluster. In reality, however, every fluid element contains particles of many different radii due to different amounts of ice-condensation on each of them. Indeed, due to the chaotic nature of particle trajectories in a turbulent flow, particles experience quite different ambient conditions during their history. Therefore, the appropriate variable that describes the current state of the system is the distribution function of particles $n_p(r, \mathbf{x}, t)$: the number of particles of radius between 'r' and '$r + dr$' that are contained in an elementary volume '$d\mathbf{x}$' around location '$\mathbf{x}$' at time t. If the law

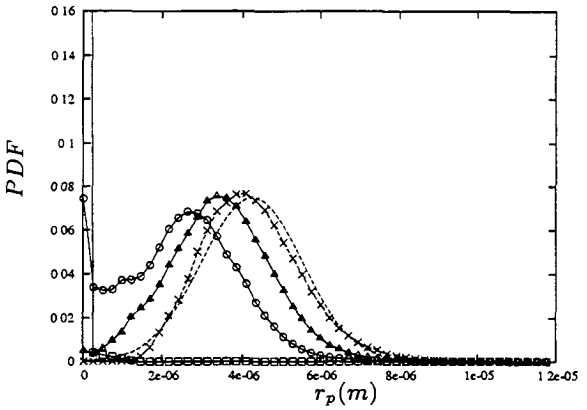

FIGURE 10. PDF of particles radius during the interaction phase; —□— , $t = 0.7\,s$; —○— , $t = 1\,s$; —△— , $t = 1.5\,s$; --×--, $t = 2\,s$; ---- , $t = 2\,s$ (Gaussian curve).

of growth of an ice crystal, (2.7) is known, an evolution equation may be written for n_p

$$\frac{\partial n_p}{\partial t} + \nabla \cdot (n_p \mathbf{u}) = -\frac{\partial}{\partial r}(n_p \dot{r}). \tag{4.1}$$

This is essentially a Liouville equation for particle conservation in the four-dimensional phase space (x, y, z, r). The term on the right-hand side represents losses or gains from each "bin" $(r, r+dr)$ due to evaporation or condensation. The source term in the equations for mass/momentum/energy are of the form $\int_0^\infty (...) n_p\, dr$ where (....) denotes the flux of the appropriate quantity onto a particle of size 'r'. In principle, one needs to simulate (4.1) for n_p, together with the equations of compressible flow. However, since solving partial differential equations in four-dimensional space involves a large increase in computational cost, it would be prudent to look for simplifying approximations. This is discussed next.

4.1. *Method of moments*

Let us assume that the size distribution of particles at a given location may be written as $n_p = F(r; m_0, m_1, \cdots)$, where m_0, m_1, $\cdots$ are parameters, which without loss of generality, may be taken as the moments of the distribution. The functional form of 'F' is presumed known. It then remains to determine evolution equations for the moments of the distribution, defined as $m_k(\mathbf{x}, t) = \int_0^\infty r^k n_p(r, \mathbf{x}, t)\, dr$. The first few moments are familiar, for example, $m_0 = N_p$, the total concentration of particles $m_1 = N_p \langle r \rangle$, where $\langle r \rangle$ is the mean size of particles; $m_2/m_0 - m_1^2/m_0^2 = \langle \Delta r^2 \rangle$, the variance of particle size distribution about the mean. If we integrate both sides of (4.1) with respect to r, we get the following equation for $m_0 = N_p$

$$\frac{\partial N_p}{\partial t} + \nabla \cdot (\mathbf{u} N_p) = 0. \tag{4.2}$$

This may also be written as $D/Dt(N_p/\rho) = 0$ using the continuity equation (D/Dt is the material derivative). It simply expresses the conservation law for the number of particles (irrespective of size). In general, on taking the r-th moment of both sides of (4.1) and using integration by parts, we have

$$\frac{\partial m_k}{\partial t} + \nabla \cdot (m_k \mathbf{u}) = \int_0^\infty n_p r^{k-1} \dot{r}\, dr. \tag{4.3}$$

The right-hand side may be evaluated if a differential equation for particle growth $\dot{r}$, and the form of the "presumed pdf" $n_p = F(r; \cdots, m_i, \cdots)$ is known. If F is assumed to be a distribution with 'n' parameters, then 'n' moment equations need to be retained.

Example 1 Let us assume the following distribution function; $n_p = N_p \delta(r - r_p)$, that is, all particles in a given fluid element at a particular time instant are identical in size. Then $m_1 \equiv N_p \langle r \rangle = N_p r_p$, and on substituting this in the moment equation (4.3) we have $\partial(N_p r_p)/\partial t + \nabla \cdot (N_p r_p \mathbf{u}) = N_p \, \dot{r} \mid_{r=r_p}$ which, using (4.2), may be put in the form

$$\frac{Dr_p}{Dt} = \dot{r} \mid_{r=r_p} . \tag{4.4}$$

Solving (4.4) together with $D/Dt(N_p/\rho) = 0$ is exactly equivalent to tracking a certain number of representative Lagrangian particles released into the fluid (of course, in order to obtain the exact solution an infinite number of such particles must be tracked). Particle tracking is therefore a special case of our approach.

Example 2 A more realistic model may be $n_p = N_p \phi(r; m_1, m_2)$, that is, the particle size distribution at any location is parametrized by its mean and variance. An appropriate form for ϕ may be chosen on examining the available data in the atmospheric sciences literature. Using the growth model (2.7) in (4.3) we then have the following coupled equations for determining m_1 and m_2

$$\frac{\partial m_1}{\partial t} + \nabla \cdot (m_1 \mathbf{u}) = \frac{D}{\rho_I}(Y_w - Y_s) J_1(m_1, m_2), \tag{4.5}$$

$$\frac{\partial m_2}{\partial t} + \nabla \cdot (m_2 \mathbf{u}) = \frac{D}{\rho_I}(Y_w - Y_s) J_2(m_1, m_2) \tag{4.6}$$

where ρ_I is the density of ice and J_1, J_2 are functions of m_1 and m_2 defined by

$$J_1(m_1, m_2) = \int_{r_0}^{\infty} \frac{G(r)}{r} \phi(r; m_1, m_2)\, dr, \; J_2(m_1, m_2) = \int_{r_0}^{\infty} G(r) \phi(r; m_1, m_2)\, dr. \tag{4.7}$$

Once the form of the presumed pdf 'ϕ', and the initial radius of soot particles, r_0, is selected, the integrals can be evaluated. Clearly, Eqs. (4.2), (4.5) and (4.6) may also be put in the Lagrangian form using the continuity equation

$$\frac{D}{Dt}\left(\frac{N_p}{\rho}\right) = 0, \tag{4.8}$$

$$\frac{D}{Dt}\left(\frac{m_1}{\rho}\right) = \frac{D}{\rho_I} \frac{Y_w - Y_s}{\rho} J_1(m_1, m_2), \tag{4.9}$$

$$\frac{D}{Dt}\left(\frac{m_2}{\rho}\right) = \frac{D}{\rho_I} \frac{Y_w - Y_s}{\rho} J_2(m_1, m_2). \tag{4.10}$$

In these equations, $\mathbf{u}$ is the velocity vector and all variables denote the physical field. In order to obtain the filtered fields, one should apply Favre averages on both sides of Eqs. (4.8) - (4.10) and introduce appropriate subgrid modeling assumptions (such as neglect of the fluctuating terms and introduction of "eddy" diffusivities) to achieve closure.

5. Conclusions

In this work, we studied the process of formation and early evolution of a contrail in the near-field of an aircraft wake. The basic tool was a two-phase flow code; the basic

configuration, an engine exhaust jet, loaded with soot particles, and interacting with a wing-tip trailing vortex. Large-eddy simulations were carried out at high Reynolds numbers, typical of wake configurations. A simple micro-physics model was used to account for nucleation of water vapor on the soot particles. A first set of simulations was carried out without any ice-growth model, to analyze the spatial distribution of supersaturation around soot particles. Results showed that particles first saturate at the edges of the exhaust jet. Vortex-induced entrainment in the wake enhances mixing of exhaust gases with cold air and favor water vapor supersaturation and condensation. A second set of simulations was carried out with the ice-growth model activated. The results showed that the radii of the frozen particles reach asymptotic values which depend on the local supersaturation. This corresponds to local thermodynamic equilibrium state between vapor and ice phases. Taking vapor depletion into account results in significant deviation from the classical mixing line. This justifies the need for two-phase flow simulations to deal with contrail formation.

6. Acknowledgments

The support of CINES is gratefully acknowledged. One of us (S.G.) was supported by the NASA-ASEE-SJSU Faculty Fellowship Program (NFFP). R.P. thanks Dr. K. Shariff for helpful discussions at NASA Ames.

REFERENCES

APPLEMAN, H. 1953 The formation of exhaust condensation trails by jet aircraft. *Bull. Amer. Meteor. Soc.* **34**, 14–20.

BOIVIN, M., SIMONIN O. & SQUIRES K. D. 1998 Direct numerical simulations of turbulence modulation by particles in isotropic turbulence. *J. Fluid Mech.* **375**, 235–263.

DUCROS F., COMTE P. & LESIEUR M. 1996 Large-Eddy Simulation of transition to turbulence in a boundary layer spatially developing over a flat plate. *J. Fluid. Mech.* **326**, 1–36.

GARNIER, F., BAUDOIN, C., WOODS P., & LOUISNARD, N. 1997 Engine emission alteration in the nearfield of an aircraft. *Atmos. Environ.* **31**, 1767–1781.

GARNIER, F., FERREIRA-GAGO, C. & UTHEZA, F. 2002 Numerical Investigation of turbulent mixing in a jet/wake vortex interaction. *AIAA J.* **40**, 276–284.

GIERENS, K. M. 1996 Numerical simulations of persistent contrails. *J. Atmos. Sci.* **53**, 3333–3348.

HÉLIE, J., BEDAT, B., SIMONIN, O. & POINSOT, T. J. 2002 Analysis of mixture fraction fluctuations generated by spray vaporisation. *Proc. ICNC Conference.* Sorrento (Italy). Society of Industrial and Applied Mathematics.

INTERGOVERNMENTAL PANEL OF CLIMATE CHANGE 1999 *Aviation and the Global Atmosphere.* Cambridge Univ. Press.

KARCHER, B., PETER, T., BIERMANN, U. & SCHUMANN, U. 1996 The initial composition of jet condensation trails. *J. Atmos. Sci.* **53**, 3066–3083.

LELE, S. K. 1992 Compact finite difference scheme with spectral-like resolution. *J. Comp. Phys.* **103**, 16–42.

MÉTAIS, O. & LESIEUR M. 1992 Spectral large-eddy simulation of isotropic and stably stratified turbulence. *J. Fluid Mech.* **239**, 157–194.

PAOLI, R., LAPORTE, F., CUENOT, B., & POINSOT, T. J. 2002 Dynamics and mixing in a simple configuration of Jet/Vortex interaction. Submitted to Phys. Fluids.

PRUPPACHER, H. R. & J. D. KLETT 1997 *Microphysics of Clouds and Precipitation.* Kluwer, Dordrecht.

QU, X. & DAVIS E. J. 2001 Droplet evaporation and condensation in the near-continuum regime. *J. Aerosol Sci.* **32**, 861–875.

SCHUMANN, U. 1996 On the conditions for contrail formation from aircraft exhausts. *Meteorol. Zeitsch.* **5**, 4–23.

SONNTAG, D. 1994 Advancements in the field of hygrometry. *Meteorol. Zeitsch.* **3**, 51–66.

TRAVIS, D. J., CARLETON A. M. & LAURITSEN R. G. 2002 Contrails reduce daily temperature range. *Nature* **418**, 601.

Stratified flows

Stable stratification impacts geophysical and astrophysical fluid dynamics across a spectrum of space and time scales, ranging from rapidly-evolving shear layers only tens of centemeters in depth in the ocean thermocline (Woods & Wiley 1972) to residual circulation and mixing due to gravity-wave dynamics in the Earth's middle and upper atmosphere (Andrews, Holton & Leovy 1987) and in the solar interior (e.g. Fritts, Vadas & Andreassen 1988).

Unique features of turbulence in stratified environments complicate the modeling of these flows: e.g.
1) vertical mixing is impeded by gravity's restoring force, while horizontal mixing is less constrained, resulting in the formation of layers that extend in the horizontal and are confined in the vertical;
2) such layers can be subgrid-scale in the vertical direction, and in some cases nearly all of the dynamics must be modeled;
3) the persistent damping of vertical motion leads to, in the absence of continuous external forcing, eventual turbulence decay and restratification, leaving the fossil remnants of dynamically-inactive (or only weakly-interacting) 'frozen-in' flow features;
4) these fossil remnants of past turbulence events can serve to precondition future turbulence outbreaks when external forcing reappears, resulting in preferred locations where turbulence nucleation recurs;
5) gravity-wave radiation from flow over topographic or layered-turbulence features can propagate great distances before succumbing to overturning; when the wavelengths of the waves are not resolved, non-local mixing must be incorporated in the sub-grid model of such flows. The three papers included in this section individually examine aspects of stably-stratified dynamics. The first two are basic studies, involving analysis of direct numerical simulations (DNS) of turbulence in stratified environments. The paper titled "Entrainment-zone restratification and flow structures in stratified shear turbulence" by Reif et al. investigates the late-time dynamics and morphology of a stratified turbulent shear layer using turbulence budgets, single-point structure tensors, and 3D flow visualization. The paper "Waves in turbulent stably-stratified shear flow" by Jacobitz, Rogers & Ferziger explores attempts to partition flow fields into gravity-wave and turbulence components. The authors caution against the identification of gravity waves via the phase angle between density and vertical velocity, and examine the utility of projecting the flow onto the linearized inviscid equations of motion when stratification is present. Though their results (and others they cite) show some promise, the authors point out a fundamental difficulty with this approach ,and conclude that turbulence and waves in stratified environments may be inextricably entangled.

The third paper "Adriatic simulations by DieCAST" by Dietrich, Carnevale, & Orlandi endeavors to identify the root cause(s) of and influences on the cross-Adriatic current flowing from the Croatian coast to the Italian coast. At the outset of the CTR Summer Program, their study identified several influences on this current, including the topography of the Mid-Adriatic Pit and seasonal variations in stratification due to near-surface solar radiation, air-sea exchanges, freshwater river plumes and the saltier water entering through the Strait of Otranto. The work reported here focuses on the dominant

influence of topography, laying the groundwork for future detailed studies of the influence of stratification.

REFERENCES

Woods, J. D. & R. L. Wiley 1972 Billow turbulence and ocean microstructure. *Deep-Sea Research* **19**, 87–121.

Andrews, D. G., J. R. Holton & C. B. Leovy 1987 *Middle Atmosphere Dynamics.* Academic Press.

Fritts, D. C., S. L. Vadas & Ø. Andreassen 1998 Gravity wave excitation and momentum transport in the solar interior: implications for a residual circulation and lithium depletion. *Astronomy & Astrophysics*, **333**, 343–361.

Joseph Werne

Center for Turbulence Research
Proceedings of the Summer Program 2002

Entrainment-zone restratification and flow structures in stratified shear turbulence

By **B. Anders Pettersson Reif †, Joseph Werne ‡, Øyvind Andreassen†, Christian Meyer ‡, AND Melissa Davis-Mansour‡**

Late-time dynamics and morphology of a stratified turbulent shear layer are examined using 1) Reynolds-stress and heat-flux budgets, 2) the single-point structure tensors introduced by Kassinos *et al.* (2001), and 3) flow visualization via 3D volume rendering. Flux reversal is observed during restratification in the edges of the turbulent layer. We present a first attempt to quantify the turbulence-mean-flow interaction and to characterize the predominant flow structures. Future work will extend this analysis to earlier times and different values of the Reynolds and Richardson numbers.

1. Introduction

Stable density stratification poses several significant challenges for turbulence modeling. Unlike the case of unstable stratification (for which numerous potential turbulence nucleation sites may trigger volume-filling motion), turbulence in stable stratification must satisfy more difficult onset conditions, and once initiated, must combat the damping effects of the background density gradient, which acts to confine the turbulence in the vertical direction and eventually to suppress it.

There are two primary mechanisms by which naturally-occurring turbulent motion may be initiated in stably-stratified fluids: 1) shear instability and 2) internal gravity-wave breaking. In both cases conditions for onset are satisfied by wind-driven forcing, either such that a) local Richardson-number criteria are met or b) propagating waves are generated which travel into regions of favorable shear or density variation for overturning. Once overturning and the consequent turbulent mixing occurs and subsides, the resulting background velocity and density profiles are left in a restratified state that is only marginally unstable, optimally configured to act as a nucleation site for the next turbulence-instigating event, even if that event does not occur for a significant period of time.

The challenge for modeling turbulence in stable environments is that the confinement in the vertical direction is often severe (e.g., a few hundred meters in the troposphere and stratosphere and only tens of meters in the ocean thermocline); hence the entire process (i.e., not just the smallest scales) can be sub-grid in scale. Nevertheless, the impact on mixing and mean flows can be significant, and because the restratified layer is marginally unstable and will therefore probably become unstable again at some time in the future, potential subgrid-scale (SGS) temporal coherence over very long periods of time is possible. Even more challenging is the characterization of SGS wave transport processes and distant overturning (possibly in remote restratification zones), implying the necessity for non-local SGS descriptions of wave dynamics and transport and coupling to restratified layers which will likely also be sub-grid in scale.

† Norwegian Defence Research Establishment (NDRE)
‡ Colorado Research Associates Div., Boulder, CO, NorthWest Research Associates, Inc.

In this report we examine some of the aspects of restratification in a turbulent mixing layer generated by the Kelvin-Helmholtz (KH) instability. Because restratification occurs first in the edges of the layer, much of our interest during this initial effort is focused on the dynamics in the layer edges and in comparisons between the edges and the middle of the layer. Our near-term goals are to characterize the dynamics of the fluctuating fields and the flow structures during restratification, and to examine the ramifications for modeling. To this end, we begin by making a detailed exploration of the budgets for the Reynolds stress and heat flux and by exploring the potential of the single-point structure tensors introduced by Kassinos *et al.* (2001) for describing the flow features and morphology. If this latter effort is successful, we anticipate these structure tensors may 1) provide a means to characterize the energy-containing structures and 2) be a valuable component in future modeling efforts. More work is necessary to expand on the work we begin here.

2. Numerical simulations

2.1. *Problem formulation*

To simulate the non-linear evolution of the Kelvin-Helmholtz instability and subsequent turbulence dynamics, we begin with the Boussinesq approximation in a Cartesian geometry. A streamwise background flow $u = U_o \tanh(z/h)$ is initiated with constant velocity U_o and length scale h; z is the vertical dimension. The background temperature is initially linear: $T = \beta z$, where β is the constant mean gradient.

The equations of motion describing momentum, heat, and mass conservation are

$$\partial_t \vec{u} + \vec{\omega} \times \vec{u} = Re^{-1} \nabla^2 \vec{u} - \vec{\nabla} (P + \vec{u} \cdot \vec{u} \,/\, 2) + \vec{Ri}\, T \ , \tag{2.1}$$

$$\partial_t T + \vec{u} \cdot \vec{\nabla} T = Pe^{-1} \nabla^2 T \ , \text{ and} \tag{2.2}$$

$$\vec{\nabla} \cdot \vec{u} = 0 \ . \tag{2.3}$$

Here $\vec{u} = (u, v, w)$ and $\vec{x} = (x, y, z)$ are velocity and position vectors; $\vec{\omega} = \vec{\nabla} \times \vec{u}$. All quantities are non-dimensional, using characteristic time h/U_o, length h, velocity U_o, and temperature βh scales. The non-dimensional parameters $Ri = N^2 / \max(\partial_z u)^2$, $Re = U_o h/\nu$, and $Pe = U_o h/\kappa$ are the Richardson, Reynolds, and Peclet numbers, and $\vec{Ri} = Ri\ \hat{z}$. $N^2 = g\alpha\beta$ is the square of the buoyancy frequency, and ν and κ are the kinematic viscosity and thermal diffusivity. g and α are the acceleration due to gravity and the thermal expansion coefficient, respectively. $Ri = 0.05$ and $Re = Pe = 2500$ are used for the 3D solutions presented below. Equality of Re and Pe implies $Pr = \nu/\kappa = 1$, which is near the value for air ($Pr_{air} \approx 0.7$), while $Ri < 0.25$ indicates dynamic instability (Miles (1960)).

To obtain numerical solutions we proceed as follows. First, the solenoidal condition (2.3) is satisfied exactly by employing a two-streamfunction decomposition:

$$\vec{u} \ = \ \vec{\nabla} \times \vec{\psi} \ + \ \vec{\nabla} \times \vec{\nabla} \times \vec{\phi} \ + \ \vec{U}(z) \ . \tag{2.4}$$

Here $\vec{\psi}$ and $\vec{\phi}$ are given by $\vec{\psi} = \psi \hat{z}$ and $\vec{\phi} = \phi \hat{z}$. $\vec{U}(z)$ refers to the mean velocity in the x and y directions (the mean vertical velocity $U_3(z)$ is identically zero).

We numerically integrate evolution equations for the scalar fields ψ, ϕ, and θ, which we obtain by 1) substituting $T = z + \theta$ into (2.2) and by 2) retaining the vertical components of the equations that result when the operators $\vec{\nabla}\times$ and $\vec{\nabla} \times \vec{\nabla}\times$ are applied to (2.1). Note that this eliminates the pressure from the system of equations, since $\vec{\nabla} \times \vec{\nabla} P \equiv 0$.

The boundary conditions are periodic in the horizontal directions, and stress-free with fixed-temperature on the top and bottom boundaries. Solutions are obtained with a pseudo-spectral Galerkin algorithm, with field variables represented horizontally by Fourier series and vertically by either sine or cosine expansions. Nonlinear terms are evaluated in physical space, while differentiation operations and time advancement are carried out in spectral space. Linear terms are treated implicitly, while nonlinear terms are handled explicitly, using the mixed implicit/explicit third-order Runge-Kutta scheme developed by Spalart *et al.* (1991) with a CFL number of 0.68.

We initiate the motion with the most-rapidly-growing asymptotic linear eigenmode ($\lambda \approx 4\pi$) with a Kolmogorov noise spectrum added to the velocity field. Vorticity amplitudes for these perturbations are 0.07 and 0.014, respectively. To accommodate the eigenmode and the anticipated "secondary instability" (Klaassen & Peltier (1985), Klaassen & Peltier (1991), Palmer *et al.* (1994), Smyth & Moum (2000a), Smyth & Moum (2000b)), horizontal dimensions of $x_o \times y_o = 12.56 \times 4.2$ are used. Sufficient remoteness of top and bottom boundaries is established with 2D tests, and $z_o = 25$ is chosen.

Spatial resolution (i.e., number of spectral modes) is varied during the evolution so that small-scale features are always properly represented; this includes thermal and viscous dissipation scales. With $Re = 2500$, as many as $1200 \times 400 \times 2400$ modes are required.

2.2. *Basic flow evolution*

Plate 1 shows the flow morphology with $Re = 2500$. The lower left panel shows the dissipation fields at $t = 77$ when the primary Kelvin vortex is well formed. At this time the depth of the mixing layer (at its deepest) is roughly $6h$, and the velocity difference is $2U_o$, so the layer Reynolds number is $Re_L \approx 30,000$. The initially-stable density stratification is inverted by the primary vortex so that the flow becomes unstable in the vortex-edge regions, and secondary rolls aligned with the streamwise direction develop (Klaassen & Peltier (1985), Klaassen & Peltier (1991), Palmer *et al.* (1994), Smyth & Moum (2000a), Smyth & Moum (2000b)). These secondary rolls are evident in the view from above (middle left panel), which shows tongues of intense thermal gradients in upflow regions at the edge of the mixing layer, interleaved with downflow regions with reduced thermal gradients. The top left panel clearly shows the secondary rolls, using the vortex visualization technique of Jeong & Hussain (1995). The center and right panels show the evolution of the flow at later times, when the vortex tubes interact and trigger the development of small-scale turbulence (Fritts *et al.* (1998)). Note that despite the reflection symmetry of (2.1)-(2.3), e.g., $(\vec{x}, \vec{u}, T) \rightarrow -(\vec{x}, \vec{u}, T)$, asymmetries in flow perturbations can produce apparent spontaneous symmetry breaking in the solutions (e.g., note differences in the upper and lower edges in the lower right panel).

Figure 1 shows the total kinetic energy KE and maximum vorticity for the velocity field with the horizontal mean removed. Oscillations in KE reveal interactions between the primary billow and the horizontal mean. Fluctuations in the vorticity maxima indicate the turbulence intensity of the small scales of motion (Werne & Fritts (1999)).

For the study presented here, we examine the turbulence budgets and statistics during the turbulence-decay phase of the flow evolution ($t > 175$) when the mean fields undergo restratification. Figure 2 shows mean profiles for streamwise velocity and temperature for $t = 240$, i.e. well into the turbulence-decay phase. We can see from the figure that mixing in the interior of the layer has homogenized the velocity and temperature fields there, compressing the initial mean gradients into the edge regions. Despite the enhanced shear that results in the edge of the layer, the combined action of shear and temperature-gradient increase results in a larger Richardson number in the edge of the layer than in

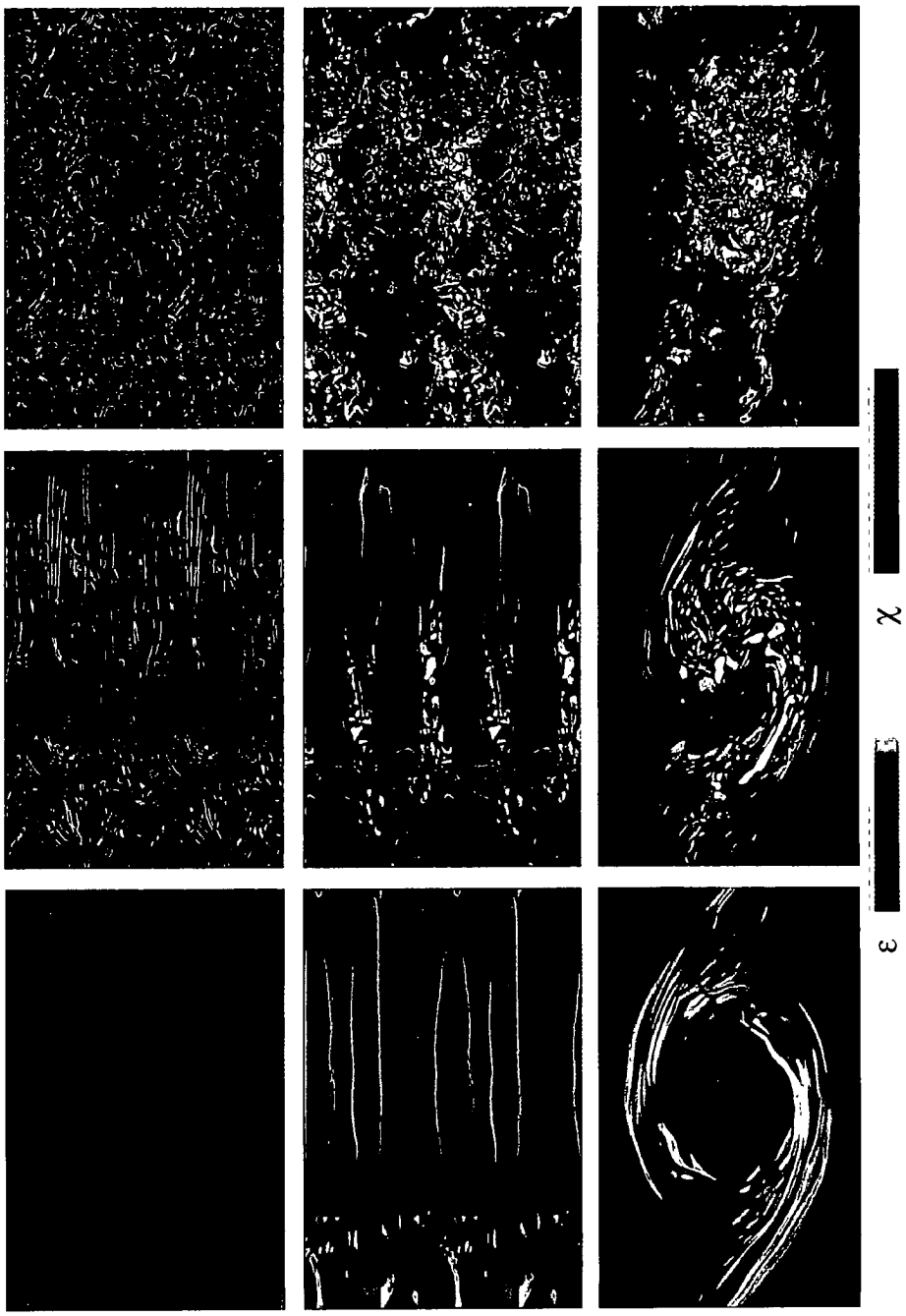

Plate 1: DNS of the Kelvin-Helmholtz instability. Bottom (middle) row shows thermal χ and viscous ε dissipation viewed from the side (above) at $t = 77$, 103, and 164. The top row depicts vortex tubes viewed from above.

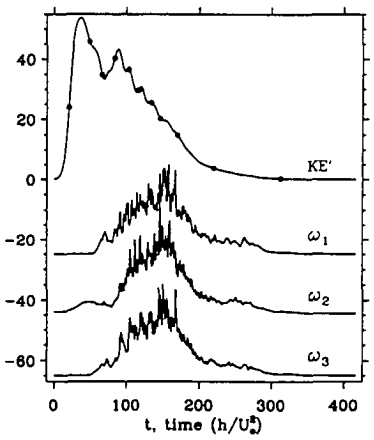

FIGURE 1. Billow and fluctuation kinetic energy (KE) and max(ω_i) versus time. ω_1 (ω_2) [ω_3] has been shifted down by 25 (45) [65].

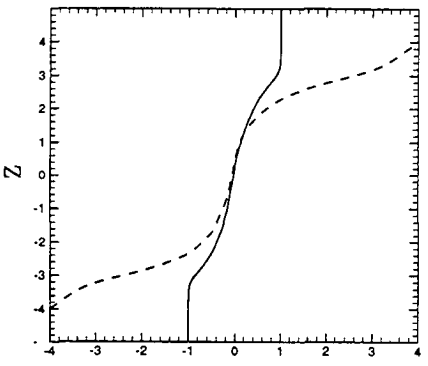

FIGURE 2. Mean velocity (——) and temperature (- - -) profiles.

the middle, and, as a result, the motion in the edge regions is more effectively damped than in the layer interior.

2.3. *Flow decomposition and averaging procedure*

For purposes of analysis we follow Palmer *et al.* (1996) and decompose the flow fields, e.g., θ, into mean $\overline{\theta}$, residual spanwise average $\tilde{\theta}$, and fluctuating components θ': $\theta = \overline{\theta} + \tilde{\theta} + \theta'$. We identify horizontal averages, e.g., $\overline{\theta}$, with the mean field and residual spanwise averages, e.g., $\tilde{\theta}$, with the primary Kelvin vortex. Both $\overline{\theta}$ and $\tilde{\theta}$ contribute to the background environment of θ', and in what follows we lump these together into what we will refer to as the 'background field', which we denote with upper-case symbols. To simplify our notation, we will drop the use of primes for the 'fluctuating' fields, denoting them by lower-case symbols; hence, $\overline{\theta} + \tilde{\theta} = \Theta$ and $\theta' \to \theta$.

3. Statistical analysis: mathematical framework

The mathematical framework for the analysis in section4 and section 5 is developed here.

3.1. *Turbulence transport equations*

The budgets for the equations governing the evolution of the Reynolds stress, heat flux and temperature variance are given by

$$\frac{D\overline{u_iu_j}}{Dt} = \underbrace{-\left(\overline{u_ju_k}\partial_kU_i + \overline{u_iu_k}\partial_kU_j\right)}_{P_{ij}} + \underbrace{\left(Ri_i\,\overline{u_j\theta} + Ri_j\,\overline{u_i\theta}\right)}_{G_{ij}} - \underbrace{2Re^{-1}\overline{\partial_ku_i\partial_ku_j}}_{\epsilon_{ij}} + \underbrace{\overline{p\left(\partial_ju_i + \partial_iu_j\right)}}_{\phi_{ij}} + \mathcal{D}_{ij} \tag{3.1}$$

$$\frac{D\overline{u_i\theta}}{Dt} = \underbrace{-\left(\overline{u_k\theta}\partial_kU_i + \overline{u_ku_i}\partial_k\Theta\right)}_{P_{i\theta}} - \underbrace{\left(Pe^{-1} + Re^{-1}\right)\overline{\partial_ku_i\partial_k\theta}}_{\epsilon_{i\theta}} - \overline{p\partial_i\theta} + Ri_i\,\overline{\theta^2} + \mathcal{D}_{i\theta} \tag{3.2}$$

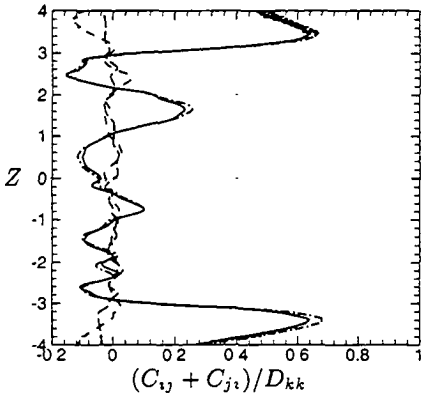

FIGURE 3. Normalized $C_{ij} + C_{ji}$; – – i=j=1; – · – i=j=2; —— i=j=3; - - - i=1, j=3.

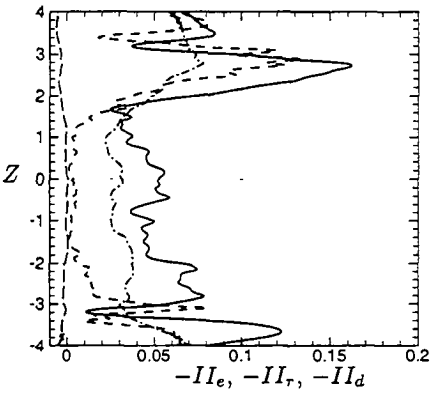

FIGURE 4. Invariants of $\overline{u_i u_j}$, ε_{ij}, and D_{ij}; - - - $(-II_e)$; —— $(-II_r)$; – · – $(-II_d)$; – – III_d.

$$\frac{D\overline{\theta^2}}{Dt} = \underbrace{-2\overline{u_k\theta}\partial_k\Theta}_{P_{\theta\theta}} \underbrace{-2Pe^{-1}\overline{\partial_k\theta\partial_k\theta}}_{\epsilon_{\theta\theta}} + \mathcal{D}_{\theta\theta} \tag{3.3}$$

respectively, where $D/Dt \equiv \partial_t + U_k\,\partial_k$ is the total rate of change and $\mathcal{D}_{ij}$, $\mathcal{D}_{i\theta}$ and $\mathcal{D}_{\theta\theta}$ denote diffusion terms.

3.2. *Structure-based tensors*

The components of the single-point Reynolds-stress tensor $\overline{u_i u_j}$ describe the 'componentality' of the turbulence field, i.e., the strengths of different fluctuating velocity components. This, however, is insufficient to completely quantify the state of turbulence because structural information characterizing flow morphology is absent from $\overline{u_i u_j}$. It is straightforward to describe such information with two-point or spectral descriptions; however, because of their inherent complexity, such approaches are currently impractical for predictive modeling efforts. Kassinos *et al.* (2001) point out that an adequate one-point description may be possible by utilizing the so-called structure-based tensors. These are second- and third-rank tensors derived from correlations of gradients of a turbulence vector streamfunction Ψ_i: $\nabla^2\Psi_i = -\omega_i$, where ω_i is the fluctuating vorticity. The velocity is simply $u_i = \epsilon_{ijk}\partial_j\Psi_k$, and continuity imposes the free condition $\partial_k\Psi_k = 0$.

Using Ψ_i, Kassinos *et al.* (2001) introduce the following set of single-point tensors: $D_{ij} \equiv \overline{\partial_i\Psi_k\partial_j\Psi_k}$ (Dimensionality); $F_{ij} \equiv \overline{\partial_k\Psi_i\partial_k\Psi_j}$ (Circulicity); $C_{ij} \equiv \overline{\partial_k\Psi_i\partial_j\Psi_k}$ (Inhomogeneity); and $Q_{ijk} \equiv -\overline{u_j\partial_k\Psi_i}$ (Stropholysis). These tensors characterize the large-scale turbulence field. Together with $\overline{u_i u_j}$ they form a minimal tensorial base for a complete single-point turbulence theory. Members of the subset $\overline{u_i u_j}$, D_{ij}, F_{ij}, and C_{ij} are linearly independent and can be related to the trace of $\overline{u_i u_j}$ through $\overline{u_i u_j} + D_{ij} + F_{ij} - (C_{ij} + C_{ji}) = \overline{u_k u_k}\delta_{ij}$.

The information content of the individual tensors is most easily understood by considering the special case of homogeneous turbulence. Here we just mention the highlights: see Kassinos *et al.* (2001) for details.

The dimensionality tensor D_{ij} describes the anisotropy of wave-vectors in spectral space, i.e., it contains information that is distinct from that in $\overline{u_i u_j}$; if, e.g., $D_{11} = 0$, then the large-scale turbulence field is independent of the streamwise direction x. The

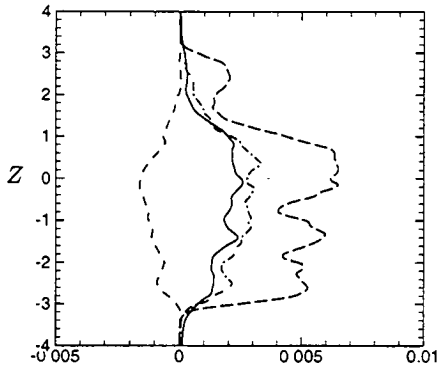

FIGURE 5. Unnormalized $\overline{u_i u_j}$; – – – $\overline{u^2}$; – · – $\overline{v^2}$; —— $\overline{w^2}$; - - - $\overline{uw}$.

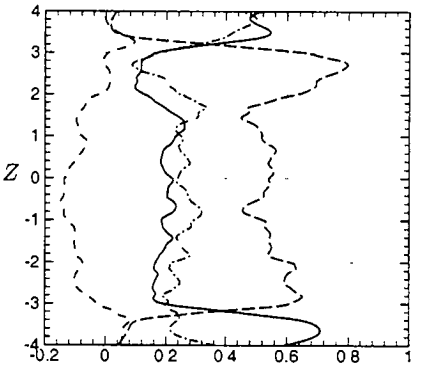

FIGURE 6. Normalized $\overline{u_i u_j}$; – – – $\overline{u^2}/\overline{u_k u_k}$; – · – $\overline{v^2}/\overline{u_k u_k}$; —— $\overline{w^2}/\overline{u_k u_k}$; - - - $\overline{uw}/\overline{u_k u_k}$.

inhomogeneity tensor C_{ij} is a measure of departure from local homogeneity. For homogeneous turbulence, $C_{ij} \equiv 0$. The circulicity tensor F_{ij} describes the large-scale vorticity field. If one of the diagonal components dominates the others, then the largest turbulence scales create rotation predominantly about that direction. Finally, the third-rank stropholysis tensor Q_{ijk} contains information that is distinct from the other structure tensors. It relates to the pressure-strain correlation ϕ_{ij} appearing in (3.1) and is of particular importance in situations where there are significant contributions from mean or frame rotations.

4. Dynamics in the near-edge region

4.1. *Shear-layer-interior homogeneity*

We begin by examining the flow inhomogeneity $C_{ij} + C_{ji}$ during turbulence decay and restratification in figure 3. Here we see from $C_{11}/D_{kk} \approx 0$ that the flow is nearly homogeneous in the streamwise direction across the layer, justifying the streamwise-averaging procedure we have adopted. The two other diagonal components, C_{22}/D_{kk} and C_{33}/D_{kk}, are also nearly zero in the core region, indicating local homogeneity in these directions as well when $|z| < 3$.

4.2. *Edge-region flux suppression*

Figure 5 shows the shear-stress components for the same time shown in figure 3. Note the reduction in the fluctuation KE near the edges of the layer where density stratification is elevated (*cf.* figure 2). Note also the significant asymmetry that has appeared between the upper and lower edges due to the relatively larger density stratification which has developed spontaneously in the upper edge region. Animations reveal that this asymmetry results when reminants of the primary KH billow descend (by random advection), increasing the turbulence intensity of the lower edge relative to the upper edge and triggering the early collapse and restratification of the upper edge.

The enhanced stratification in the upper edge leads to the development of a significant region of flux suppression (see $\overline{uw}$ for $z > 2$ in figures 5 and 6), with flux reversal being observed momentarily. Much of the discussion that follows concentrates on the nature

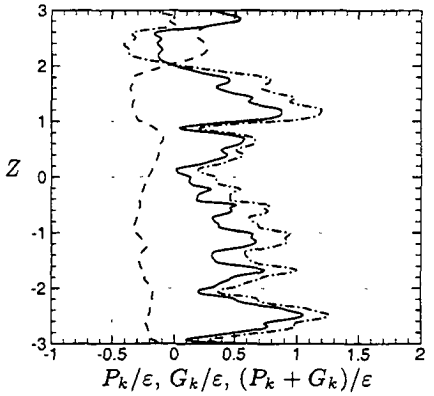

FIGURE 7. Production/dissipation rate ratio; $-\cdot-P_k/\varepsilon$; - - - G_k/ε. —— $(P_k+G_k)/\varepsilon$.

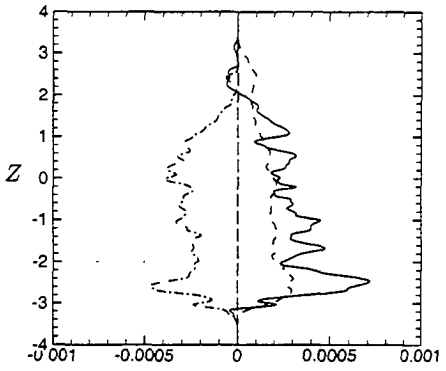

FIGURE 8. Incomplete budget for $\overline{uu}$; $-\ -\ G_{11}$; $-\cdot-\phi_{11}$; —— P_{11}; - - - ε_{11}.

and consequences of the edge-region flux reduction as a case study in the impact of stratification. We will extend this analysis in future work to examine the behavior at earlier time and for varied Ri and Re.

4.3. *Turbulence production and mean-field evolution*

As a result of the more rapid restratification near the upper edge of the shear layer, the background Richardson number is higher here and the turbulence kinetic energy is reduced. We see from the turbulence-kinetic-energy production terms

$$\mathcal{P}_k = P_k + G_k \approx \underbrace{-\overline{uw}\partial_3 U}_{\frac{1}{2}P_{11}} + \underbrace{Ri\overline{w\theta}}_{\frac{1}{2}G_{33}}, \tag{4.1}$$

which we obtain from the trace of (3.1), that reduction in turbulence kinetic energy is intimately tied to flux suppression. We also note that the shear production term P_k is normally positive, and the buoyancy production term $G_k = Ri\overline{w\theta}$ usually acts to enhance the background temperature field Θ at the expense of the turbulence. This is the behavior near midlayer. However, when flux reversal occurs, as it does for a period of time near the upper edge of the layer, the terms exchange roles, with buoyancy acting as a source in the $\overline{w^2}$ equation and shear behaving as a sink for $\overline{u^2}$. Figure 7 shows the relative contributions of P_k and G_k for kinetic energy production, demonstrating that, despite the exchange in roles for the two terms during flux reversal, shear consistently dominates buoyancy effects throughout the layer; i.e., $|P_k| > |G_k|$. The shift in the turbulence kinetic energy production from P_{11} in $\overline{u^2}$ to G_{33} in $\overline{w^2}$ has interesting consequences for stably-stratified shear-flow dynamics when flux suppression and reversal occur. First, when $P_{11} \lesssim 0$, energy transfer from the background flow is abruptly shut off; see figure 8. Secondly and perhaps more interestingly, the intercomponent energy transfer in (3.1) between $\overline{u^2}$, $\overline{v^2}$, and $\overline{w^2}$ (via pressure-strain correlations ϕ_{ij}) is fundamentally different from homogeneous shear flow. Figure 9 demonstrates this by showing the normal components of ϕ_{ij}. The majority of the layer exhibits $\phi_{11} < 0$ and $\phi_{22}, \phi_{33} > 0$, consistent with homogeneous shear-flow dynamics; however the upper edge region, where flux reversal is occuring, exhibits a change in sign of the vertical component, with the other two components retaining their midlayer signs; i.e. $\phi_{11} < 0$, $\phi_{22} > 0$, and $\phi_{33} < 0$. The peculiarity of this

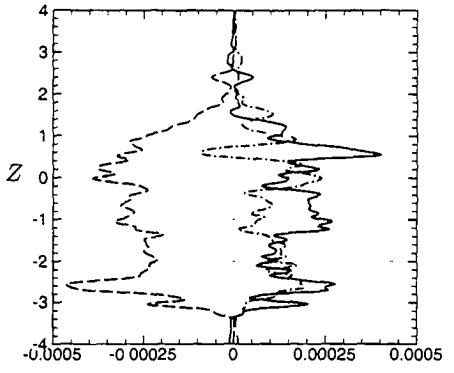

FIGURE 9. ϕ_{ij}; − − − ϕ_{11}; − · − ϕ_{22}; —— ϕ_{33}

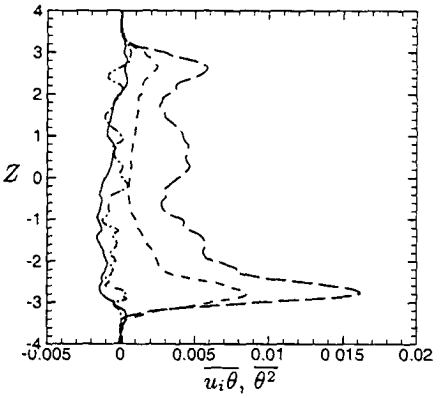

FIGURE 10. $\overline{\theta^2}$ and $\overline{u_i\theta}$; − − $\overline{u\theta}$; − · − $\overline{v\theta}$; —— $\overline{w\theta}$; - - - $\overline{\theta^2}/10$.

behavior is not that ϕ_{33} has changed sign, but rather that ϕ_{11} has not. To understand the ramifications, consider the case of homogeneous shear flow unaffected by body forcing. In this case $P_{11} > 0$ and $P_{22} = P_{33} = 0$, and $\phi_{11} < 0$, $\phi_{22}, \phi_{33} > 0$. Background-flow energy is thus transferred directly to the streamwise stress componen,t and orthogonal components are subsequently fed via pressure-strain correlations. In contrast, for the case near the upper portion of the shear layer presented in figures 8 and 9, pressure-strain correlations redistribute energy into $\overline{v^2}$ from both $\overline{u^2}$ and $\overline{w^2}$, despite the fact that $P_{11} + G_{11}$ is negative. The importance of this result is that pressure-strain models employed by traditional RANS closures fail in this situation because they cannot predict $\text{sign}(P_{ij} + G_{ij}) = \text{sign}(\phi_{ij})$. This is similar to the blocking effect in turbulent boundary layers, except in that case wall-normal- and shear-stress components are affected, see e.g. Durbin & Pettersson Reif (2001).

4.4. *Turbulence production and $\overline{u^2}$ damping*

An apparent oddity of the normalized Reynolds-stress components (figure 6) near the edges of the shear layer is the sharp reduction in $\overline{u^2}$ relative to $\overline{v^2}$ and $\overline{w^2}$ as the far field is approached. This is particularly striking given the well-established damping of $\overline{w^2}$ in stable stratification when background shear is not present (Thoroddsen & Van Atta (1992)). Clearly, background shear introduces a fundamental change in the dynamics.

In order to explain the reduction of $\overline{u^2}$ and demonstrate its relation to flux suppression (and possible reversal), we must examine the dominant production terms for $\overline{u^2}$, $\overline{uw}$ and $\overline{w\theta}$:

$$\mathcal{P}_{11} = P_{11} + G_{11} \approx -\overline{uw}\partial_3 U \tag{4.2}$$

$$\mathcal{P}_{13} = P_{13} + G_{13} \approx -\overline{w^2}\partial_3 U + Ri\,\overline{u\theta} \tag{4.3}$$

$$\mathcal{P}_{3\theta} = P_{3\theta} + Ri\overline{\theta^2} \approx -\overline{w^2}\partial_3\Theta + Ri\overline{\theta^2}. \tag{4.4}$$

We see that it is also instructive to consider the generation terms for $\overline{u\theta}$, $\overline{\theta^2}$, and $\overline{w^2}$:

$$P_{1\theta} \approx -\overline{w\theta}\partial_3 U - \overline{uw}\partial_3\Theta, \quad P_{\theta\theta} = -2\overline{w\theta}\partial_3\Theta, \quad \mathcal{P}_{33} = P_{33} + G_{33} \approx Ri\overline{w\theta}. \tag{4.5}$$

From (4.3) we see that $\overline{u\theta}$ and a reduction in $\overline{w^2}$ will act to reduce $-\overline{uw}$, which in turn through (4.2) will decrease $\overline{u^2}$. As $-\overline{uw}$ decreases, the background shear generation of

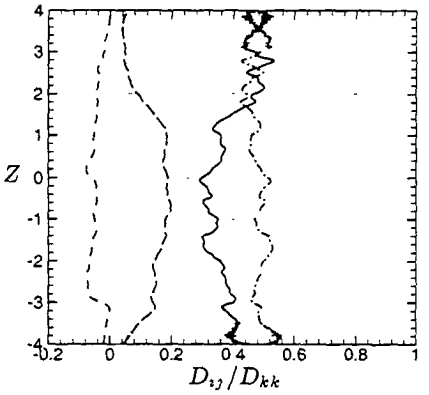

FIGURE 11. Normalized D_{ij}; – – i=j=1; – · – i=j=2; —— i=j=3; - - - i=1, j=3.

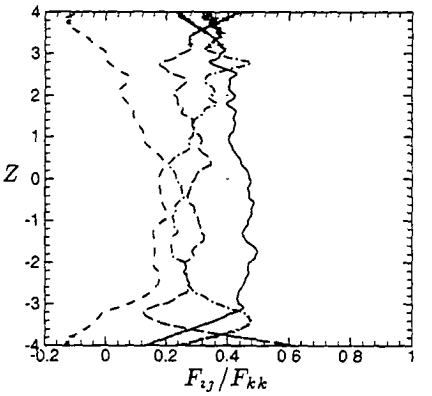

FIGURE 12. Normalized F_{ij}; – – i=j=1; – · – i=j=2; —— i=j=3; - - - i=1, j=3.

turbulence kinetic energy is reduced, and therefore so is $\overline{w^2}$. It is important to note however that a change in sign of $\overline{uw}$ does *not* promote high positive levels of $\overline{u\theta}$ due to the second term $P_{1\theta}$ (4.5), suggesting that high levels of $\overline{u\theta}$ alone cannot be responsible for flux reversal when it occurs. Nevertheless, from $P_{1\theta}$ (4.5) we see that for fixed or slowly-varying values of $-\overline{w\theta}$ and $-\overline{uw}$, increases in the background gradients do result in elevated values of $\overline{u\theta}$, which can participate in reducing $-\overline{uw}$ and $\overline{u^2}$.

Similarly we can understand the suppression (and possible reversal) of $\overline{w\theta}$ by noting that for relatively fixed values of $-\overline{w\theta}$ an elevated value of $\partial_3\Theta$ will result in enhanced $\overline{\theta^2}$, which combined with a reduction in $\overline{w^2}$ will reduce $-\overline{w\theta}$ via (4.4). But, as can be seen from $P_{\theta\theta}$ (4.5), and similar to the case for $-\overline{uw}$, reduced $-\overline{w\theta}$ acts to decrease $\overline{\theta^2}$, suggesting that high levels of $\overline{\theta^2}$ alone cannot be responsible for a reversal in $-\overline{w\theta}$ when it occurs. This suggests that a reduction in $\overline{w^2}$ is the most important instigator for flux reversals, both $\overline{w\theta}$ and $\overline{uw}$.

5. Anisotropies and large-scale structures

The second invariant $II_x = -\frac{1}{2}x_{ij}x_{ij}$ of a second-rank tensor x_{ij} quantifies the departure from isotropy ($II_x = 0$). In particular $x_{ij} + \delta_{ij}/3 = \overline{u_iu_j}/\overline{u_ku_k}$ (II_r), D_{ij}/D_{kk} (II_d), and $\varepsilon_{ij}/\varepsilon_{kk}$ (II_e) reflect the character of the large ($\overline{u_iu_j}$, D_{ij}) and dissipative (ε_{ij}) scales, respectively. The profiles displayed in figure 4 reveal that the small-scale anisotropy can be comparable to, or even larger than, the integral-scale anisotropy in the strongly inhomogeneous edges of the shear layer, whereas the small-scale motion is significantly more isotropic near mid-layer. D_{ij} is less anisotropic than $\overline{u_iu_j}$ throughout the layer, and $III_d = \frac{1}{3}x_{ij}x_{jk}x_{ki} < 0$ indicates cigar-shaped features near the layer edges.

By examining the individual components of $\overline{u_iu_j}$, D_{ij}, and F_{ij} (figures 6–12), we can gain further insight into the large-scale turbulence structures (Kassinos *et al.* (2001)). For example, in the upper near-edge region with $D_{22} \approx D_{33}$ and $D_{11} \approx D_{22}/6$, we anticipate that the cigar-shaped features are aligned in the streamwise direction, are roughly six times longer in the x direction than in the other directions, and since $\overline{u^2} >> \overline{v^2} \approx \overline{w^2}$, these features are strongly 'jetal' in character. At mid-layer the diagonal components of D_{ij} are roughly in the ratio $(D_{11} : D_{22} : D_{33}) \approx (2 : 5 : 3.4)$ and we expect less elongated structures here, extending roughly 2.5 times in the streamwise direction as in

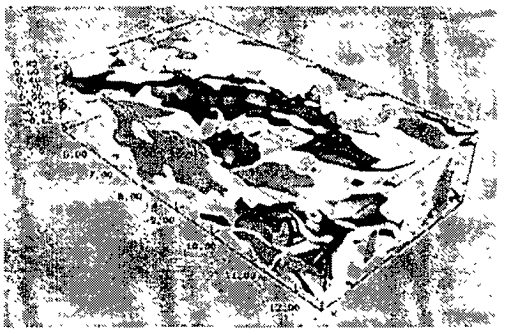

FIGURE 13. Streamwise fluctuations in the center of the layer. Dark (light) regions with light (dark) cores represent $u > 0$ ($u < 0$).

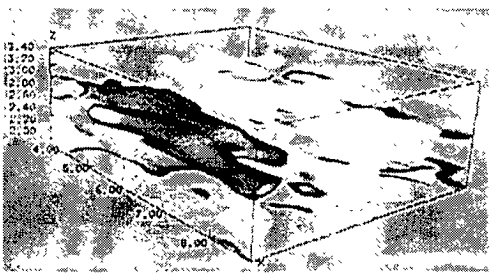

FIGURE 14. Streamwise fluctuations at the edge of the layer. Dark (light) regions with light (dark) cores represent $u > 0$ ($u < 0$).

the spanwise, and possessing $\sim 30\%$ greater height than spanwise extent. Figures 13 and 14 support these expectations. In particular, note the nearly circular (spanwise-flattened) $y-z$ cross-sections of features at the $x = 12.56$ ($x = 9.0$) cutting plane in the upper-edge (mid-layer) region.

The circulicity tensor (figure 12), which quantifies large-scale turbulence circulation, exhibits a tendency for large-scale vertical vorticity at mid-layer with $F_{33} > F_{11} \gtrsim F_{22}$. This results from jetal motions in the horizontal plane and is identical to the behavior in the unstratified case (Kassinos *et al.* (2001)). Near the edges of the layer F_{11} decreases while F_{22} grows until $F_{22} \approx F_{33}$, and just outside the layer F_{22} surpasses F_{33} to become the dominant circulation direction. This behavior results from the strong vortex sheet adjacent to the turbulent layer which acts as the transition interface between turbulent and irrotational flow.

6. Conclusions

We have presented Reynolds-stress and heat-flux budgets for stratified shear flow during layer restratification. During this time the outer regions of the shear layer exhibit flux suppression and reversal, both for $\overline{uw}$ and $\overline{w\theta}$; we offer an explanation for this behavior. The reversals are most pronounced at the top of the layer where turbulence kinetic energy is severely damped by the action of stable stratification.

We also examined the ability of single-point structure tensors to describe the features exhibited by 3D volume-rendered depictions of the flow. The structure tensors appear to capture and quantify the relevant flow morphology.

We will extend this analysis to earlier times and different Re and Ri so we can evaluate the robustness of the result. Furthermore, because the edges of the shear layer appear to pose important challenges for modeling, it is imperative that we insure that quantification of the edge regions is reliable. For this reason future characterization will adopt the conditional-sampling technique of Bisset *et al.* (2002).

Acknowledgment

The authors acknowledge discussions with Professors P. A. Durbin, J. H. Ferziger and J. C. R. Hunt, and with Drs F. Jacobitz, S. C. Kassinos, N. N. Mansour and M. M. Rogers. Plate 1 was created using OGLE, a 3D visualization package written by Dr. Michael

Gourlay. Figures 13 and 14 were created using Viz, a volume-rendering tool maintained at the Norwegian Defence Research Establishment. JW is partially supported by AFRL F19628-02-C-0037, DOE (Environmental Meteorology Program) DE-FG03-99ER62839, and NASA NASW-99026. Simulations were conducted on Cray T3E's at the U.S. Army Engineer Research Development Center and at the Naval Oceanographic Office as part of the DoD Airborne Laser Challenge program.

REFERENCES

BISSET, D. K., HUNT, J. C. R., & ROGERS, M. M. 2002 The turbulent/non-turbulent interface bounding a far wake. *J. Fluid Mech.* **451**, 183–410.

DUDA, R. O. & HART, P. E. 1973 *Pattern Classification and Scene Analysis.* Wiley, New York.

DURBIN, P. A. & PETTERSSON REIF, B. A. 2001 *Statistical Theory and Modeling for Turbulent Flows.* Wiley, New York.

FRITTS, D. C., ARENDT, S. & ANDREASSEN, Ø. 1998 Vorticity dynamics in a breaking internal gravity wave, 2. Vortex interactions and transition to turbulence. *J. Fluid Mech.* **367**, 47–65.

JANG, P. S., BENNEY, D. J. & GRAN, R. L. 1986 On the origin of streamwise vortices in a turbulent boundary layer. *J. Fluid Mech.* **169**, 109–123.

JEONG, J. & HUSSAIN, F. 1995 On the identification of a vortex. *J. Fluid Mech.* **285**, 69–94.

KASSINOS, S. C., REYNOLDS, W. C. & ROGERS, M. M. 2001 One-point turbulence structure tensors. *J. Fluid Mech.* **428**, 213–248.

KLAASSEN, G. P. & PELTIER, W. R. 1985 The onset of turbulence in finite-amplitude Kelvin-Helmholtz billows. *J. Fluid Mech.* **155**, 1–35.

KLAASSEN, G. P. & PELTIER, W. R. 1991 The influence of stratification on secondary instability in free shear layers. *J. Fluid Mech.* **227**, 71–106.

MILES, J. W. 1960 On the stability of heterogeneous shear flows. *J. Fluid Mech.* **10**, 496–508.

PALMER, T. L., FRITTS, D. C., ANDREASSEN, Ø. & LIE, I. 1994 Three-dimensional evolution of Kelvin-Helmholtz billows in stratified compressible flow. *Geophys. Res. Letters* **21**, 2287–2290.

PALMER, T. L., FRITTS, D. C. & ANDREASSEN, Ø. 1996 Evolution and breakdown of Kelvin-Helmholtz billows in stratified compressible flows, II: Instability structure, evolution and energetics. *J. Atmos. Sci.* **53**, 3192–3212.

SMYTH, W. D. & MOUM, J. N. 2000a Length scales of turbulence in stably stratified mixing layers. *Phys. Fluids* **12**, 1327–1342.

SMYTH, W. D. & MOUM, J. N. 2000b Anisotropy of turbulence in stably stratified mixing layers. *Phys. Fluids* **12**, 1343–1362.

SPALART, P. R., MOSER, R. D. & ROGERS, M. M. 1991 Spectral methods for the Navier-Stokes equations with one infinite and two periodic directions. *J. Comput. Phys.* **96**, 297–324.

THORODDSEN, S. & VAN ATTA, C. W. 1992 The influence of stable stratification on small-scale anisotropy and dissipation in turbulence *J. Geophys. Res.* **97**, 3647–3658.

WERNE, J. & FRITTS, D. C. 1999 Stratified shear turbulence: evolution and statistics. *Geophys. Res. Letters* **26**, 439–442.

Waves in turbulent stably-stratified shear flow

By F. G. Jacobitz †, M. M. Rogers ‡ AND J. H. Ferziger ¶

Two approaches for the identification of internal gravity waves in sheared and unsheared homogeneous stratified turbulence are investigated. First, the phase angle between the vertical velocity and density fluctuations is considered. It is found, however, that a continuous distribution of the phase angle is present in weakly and strongly stratified flow. Second, a projection onto the solution of the linearized inviscid equations of motion of unsheared stratified flow is investigated. It is found that a solution of the fully nonlinear viscous Navier-Stokes equations can be represented by the linearized inviscid solution. The projection yields a decomposition into vertical wave modes and horizontal vortical modes.

1. Introduction

An important problem in geophysical fluid mechanics is the characterization of turbulence and wave motion in stably-stratified flows. Fluid motion can occur as a result of either of these phenomena, and the ability to separate the motions associated with each should lead to better understanding and predictability of the flow. Stewart (1969) listed criteria that might be used to distinguish between internal wave motion and turbulence. The first distinction noted was that wave motion satisfies linear equations, whereas turbulence is inherently nonlinear. However, when both waves and turbulence are present, the motions are coupled nonlinearly and it is unclear how to extract the wave component of the flow. Secondly, the processes by which energy is transported are different. In turbulence, energy is advected at the speed of the motion, whereas waves transport energy via pressure-velocity correlations, usually at a group velocity that is greater than the particle velocity. Lastly, Stewart noted the difference between turbulence and waves with regard to mixing. Except when they break, waves do not produce mixing. Although they can transport momentum, they cannot transport scalars. Thus the scalar flux $\overline{u_2\rho}$, where u_2 is the vertical velocity component, should be large in regions dominated by turbulence and small where waves predominate. Furthermore, the relative phase of vertical velocity fluctuations u_2 and density fluctuations ρ is different for waves and turbulence. For stably-stratified flows, in-phase motion between u_2 and ρ corresponds to down-gradient turbulent transport, while 180° out-of-phase motion is associated with counter-gradient turbulent transport. For wave motions, u_2 and ρ have a phase difference of 90° and there is no mean correlation between them.

Stewart (1969) concluded that this last distinction held the greatest promise for distinguishing waves and turbulence and this criterion has been used extensively ever since. For example, Stillinger, Helland, & Van Atta (1983) felt that their unsheared stably-stratified decaying turbulence "had been completely converted to random internal wave motions" when $\overline{u_2\rho}$ became zero. However, Lienhard & Van Atta (1990) pointed out that $\overline{u_2\rho}$ can be zero as a result of co-gradient and counter-gradient fluxes at different scales of motion

† University of California, Riverside
‡ NASA Ames Research Center
¶ Stanford University

cancelling each other out. More careful diagnosis requires examination of the cospectrum of $\overline{u_2\rho}$ as a function of wavenumber, as originally proposed by Stewart (1969). Defining the cospectrum Co and quadrature spectrum Qu as

$$Co_{u_2\rho}(k_1, x_2) = Re\left(\Sigma_{k_3}\tilde{u}_2^*(k_1, x_2, k_3)\tilde{\rho}(k_1, x_2, k_3)\right) \tag{1.1}$$

$$Qu_{u_2\rho}(k_1, x_2) = Im\left(\Sigma_{k_3}\tilde{u}_2^*(k_1, x_2, k_3)\tilde{\rho}(k_1, x_2, k_3)\right) , \tag{1.2}$$

where the tildes indicate Fourier transformed quantities, the phase angle $\phi_{u_2\rho}$ between vertical velocity u_2 and density ρ is given by

$$\phi_{u_2\rho} = \arctan\left(\frac{Qu_{u_2\rho}}{Co_{u_2\rho}}\right) . \tag{1.3}$$

The above spectral quantities (or similar measures in terms of other wavenumber components) have been used in evaluating both experimental and computational data on stratified flows. McBean & Miyake (1972) used measurements in the atmospheric surface layer to tentatively conclude that wave motions may be important at low frequencies in stably stratified flow. Komori, Ueda, Ogino & Mizushina (1983) felt that a significant fraction of the motion in their stably stratified open-channel flow experiment was wavelike based on the phase angles measured. In contrast, data from experiments in both unsheared (Lienhard & Van Atta 1990) and sheared (Piccirillo & Van Atta 1997) stably stratified homogeneous turbulence indicate no evidence of wavelike motion based on examination of the phase angle. Analysis of direct numerical simulations of similar sheared homogeneous stratified turbulence (Holt, Koseff & Ferziger 1992) also indicates that even for strong stratification there is no band of wavenumbers with $\phi_{u_2\rho} \approx 90°$.

Riley, Metcalfe, and Weissman (1981) proposed a different method for separating wavelike and turbulent motions. They used the Craya (1958) decomposition to split the turbulent velocity field associated with each wavenumber into two solenoidal components, one normal to the wavenumber vector and to the gravity vector, and the other orthogonal to the first component and to the wavenumber vector. For small amplitudes, this second component satisfies the linear propagation equation for internal gravity waves, and is thus identified as the "wave" component of the motion. The other component consists of quasi-horizontal motions containing all the vertical vorticity and is identified as "turbulence". This decomposition splits the flow into propagating and non-propagating parts only in the limit of zero Froude number. For small but finite Froude number Staquet and Riley (1989) proposed a generalization of this decomposition using Ertel's (1942) Theorem for potential vorticity. However, this generalization is invalid when the density gradient is zero or unbounded, and therefore cannot be used for turbulent flows.

Despite this shortcoming, Herring and Métais (1989) and Métais and Herring (1989) used the original Riley *et al.* decomposition to split their numerically-simulated turbulent flow fields into "wave" and "turbulent" components. They acknowledge the deficiencies of this approximation, noting 1) that "a proper definition of waves should include the density field, and its phase relative to the 'wave'-component of the velocity" and 2) their non-zero Froude number. However, the "turbulent" components of their flows do not show oscillations that scale with the Brunt–Väisälä frequency; such oscillations are observed in the wave component of the flows. This suggests a weak interaction between the components, and perhaps the adequacy of the decomposition.

The prototypical example of homogeneous turbulent stratified shear flow with uniform stable vertical stratification $S_\rho = \partial\rho/\partial x_2$ and uniform vertical shear $S = \partial U/\partial x_2$ is the simplest flow that contains both shear and stratification. It has been studied extensively

in the past due to its geophysical significance. Experimental investigations include Rohr, Itsweire, Helland & Van Atta (1988) and Piccirillo & Van Atta (1997). Numerical simulations include the work by Gerz, Schumann & Elghobashi (1989), Holt, Koseff & Ferziger (1992), Jacobitz, Sarkar & Van Atta (1997), Jacobitz (2000) and Shah, Koseff & Ferziger (2000). Turbulence in decaying stratified turbulence without shear has been investigated by Métais & Herring (1989), Lienhard & Van Atta (1990), Yoon & Warhaft (1990) and Briggs, Ferziger, Koseff & Monismith (1998).

In this study, possible ways to decompose the fluid motion into turbulence and wave components are investigated in direct numerical simulations of both sheared and unsheared homogeneous stratified turbulence. Both the phase angle between the vertical velocity and density and projections onto eigensolutions of the linearized governing equations are examined.

In the following section, the numerical simulations used in the present study are introduced. In sections 3 and 4, the phase angle results in sheared and unsheared stably stratified turbulence are presented. In section 5, a turbulence-wave decomposition based on the linear inviscid equations of motion is applied to the numerical data. Results are summarized in section 6.

2. The numerical simulations

The current study is based on the results of five direct numerical simulations of sheared, homogeneous stably-stratified turbulence and two direct numerical simulations of unsheared, decaying homogeneous stably-stratified turbulence.

In the direct numerical simulations, all dynamically-important scales of the velocity, density and pressure fields are resolved and no turbulence models are introduced. A spatial discretization is first performed to obtain a semi-discrete system of ordinary differential equations from the original system of partial differential equations. An integration of the system of ordinary differential equations is then performed to advance the solution in time. The spatial discretization is accomplished by a spectral collocation method. The temporal advancement is accomplished by a fourth-order Runge-Kutta scheme. A computational grid overlaying a cube of length 2π was used with 256^3 points. The initial conditions are taken from a separate simulation of isotropic turbulence without density fluctuations, which was allowed to develop for approximately one eddy turnover time. The energy spectrum of the initial field peaks at a wavenumber $k = 13$ and the resulting vertical integral scale, computed as the vertical integral of the autocorrelation of the vertical velocity component, is $L = 0.174$, compared to the box size 2π. The initial value of the Taylor microscale Reynolds number is taken as $Re_\lambda = 45$ in all simulations.

Figure 1 shows the evolution of the normalized turbulent kinetic energy K/K_0 for sheared stably-stratified turbulence with Richardson numbers $Ri = 0$, $Ri = 0.1$, $Ri = 0.2$, $Ri = 0.5$, and $Ri = 1.0$. Here the Richardson number is given by N^2/S^2, where N is the Brunt-Väisälä frequency, given by $\sqrt{(-g/\rho_0)\partial\overline{\rho}/\partial y}$. Initially, the turbulent kinetic energy decays as a result of the absence of Reynolds shear stress $\overline{u_1 u_2}$ in the isotropic initial condition. For simulations with small values of the Richardson number, the turbulent kinetic energy eventually grows with nondimensional time St. For simulations with large values of the Richardson number, however, the turbulent kinetic energy continues to decay, with the stratification overwhelming the turbulence production by the mean shear.

Figure 2 shows the evolution of the normalized turbulent kinetic energy K/K_0 for unsheared stably stratified turbulence with initial Froude numbers $Fr = 64$ and $Fr = 6.4$,

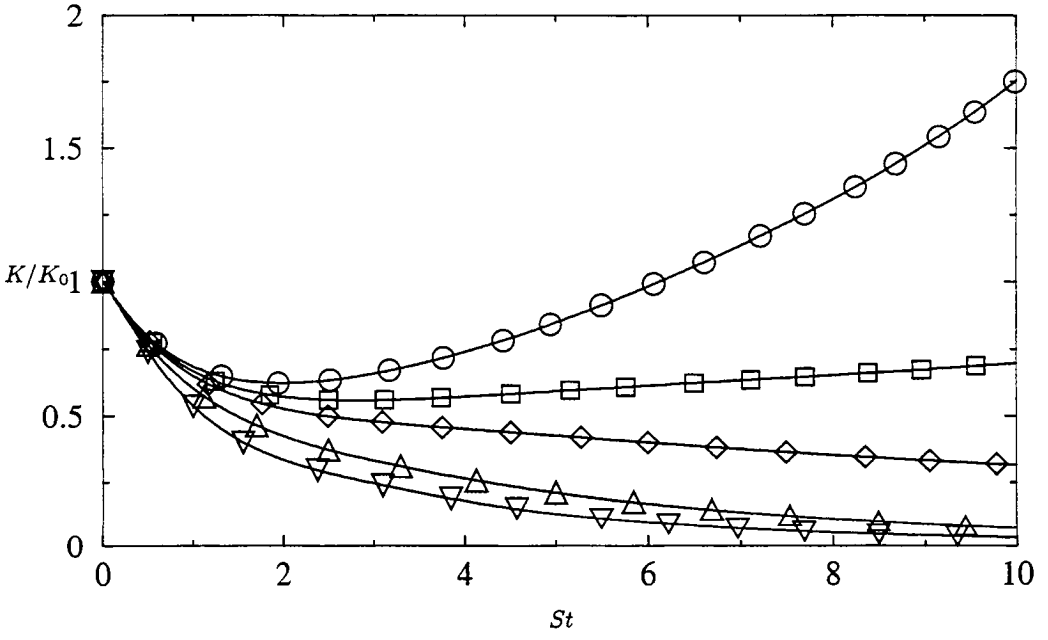

FIGURE 1. Evolution of the normalized turbulent kinetic energy K/K_0 in sheared stratified turbulence with Richardson numbers 0 (○), 0.1 (□), 0.2 (◇), 0.5 (△), and 1.0 (▽).

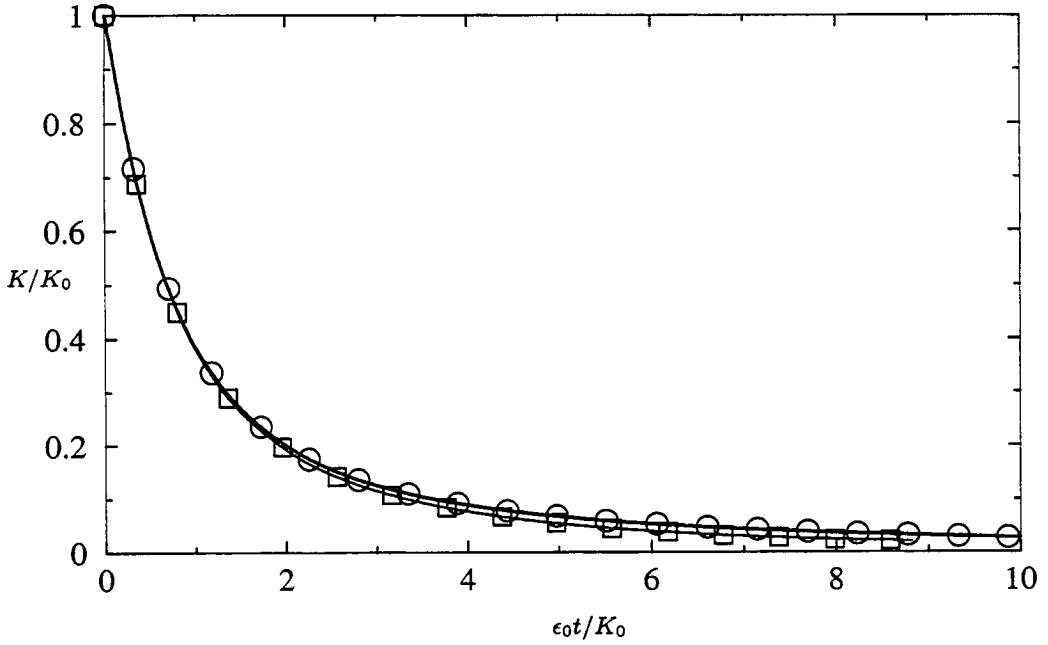

FIGURE 2. Evolution of the normalized turbulent kinetic energy K/K_0 in unsheared stratified turbulence with initial Froude numbers 64 (○) and 6.4 (□).

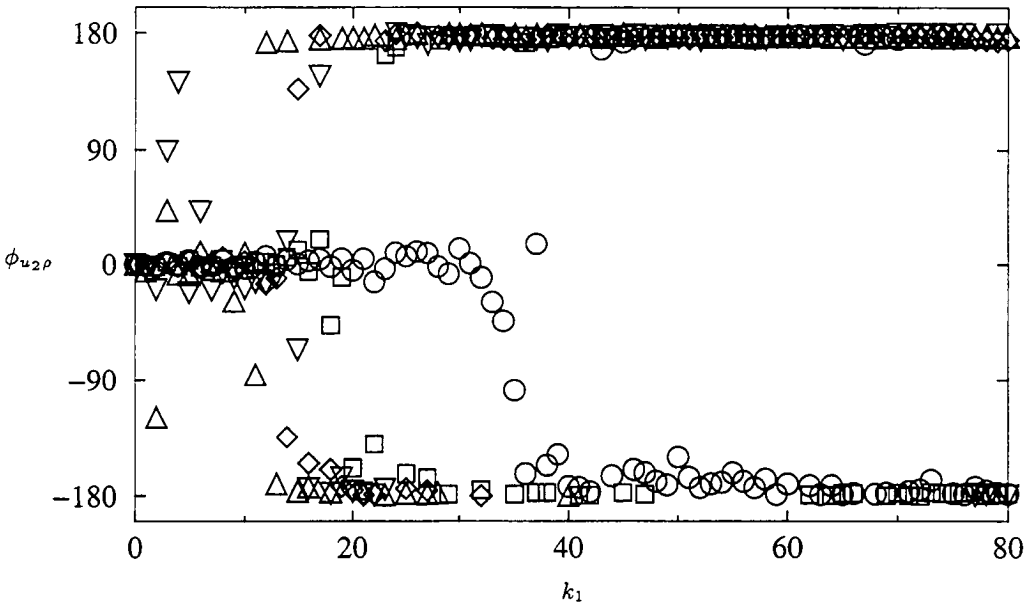

FIGURE 3. Spectrum of the phase angle $\phi_{u_2\rho}$ in sheared stratified turbulence at $St = 5$ with Richardson numbers 0 (○), 0.1 (□), 0.2 (◇), 0.5 (△), and 1.0 (▽).

where $Fr = \sqrt{\overline{u_2^2}}/(LN)$. A slightly stronger decay of the turbulent kinetic energy is found for the more strongly-stratified simulation.

3. Phase angle in sheared stably stratified turbulence

In this section, the phase angle in sheared stably-stratified turbulence is discussed. The Richardson number Ri is varied from $Ri = 0$, corresponding to unstratified shear flow, to $Ri = 1$, corresponding to strongly-stratified shear flow.

Figure 3 shows the spectrum of the phase angle $\phi_{u_2\rho}$ between the vertical velocity u_2 and the density ρ at non-dimensional time $St = 5$. In the unstratified simulation with $Ri = 0$ (○ symbols), phase angles $\phi_{u_2\rho} \approx 0$ are found for small wavenumbers k_1, and phase angles $\phi_{u_2\rho} \approx \pm 180°$ are found for large values of k_1. The transition from $\phi_{u_2\rho} \approx 0$ to $\phi_{u_2\rho} \approx \pm 180°$ occurs at a wavenumber $k_1 \approx 35$. At this wavenumber, the cospectrum $Co_{u_2\rho}$ crosses zero and changes sign. As the Richardson number is increased, the transition wavenumber decreases to about $k_1 \approx 20$ for $Ri = 0.1$, $k_1 \approx 17$ for $Ri = 0.2$, $k_1 \approx 10$ for $Ri = 0.5$, and $k_1 \approx 5$ for $Ri = 1$. Phase angles $\phi_{u_2\rho} \approx \pm 90°$, indicating possible internal wave motion, are observed only in the strongly stratified simulations with $Ri = 0.5$ and $Ri = 1$ and only for a few scattered wavenumbers, not over a region of wave-space. Again, these isolated instances of 90° phase angles are associated with zero-crossings of the associated cospectrum, rather than a region in wavespace exhibiting wavelike behavior.

Figure 4 shows the probability distribution of the phase angle $\phi_{u_2\rho}$ over an instantaneous flow field. The phase angle distribution of the unstratified simulation with $Ri = 0$ has a slight maximum at $\phi_{u_2\rho} = 0$, indicating a very modest predominance of down-gradient mixing. As the Richardson number is increased, the maximum of the phase angle distribution is found at $\phi_{u_2\rho} = \pm 180°$, corresponding to counter-gradient mixing.

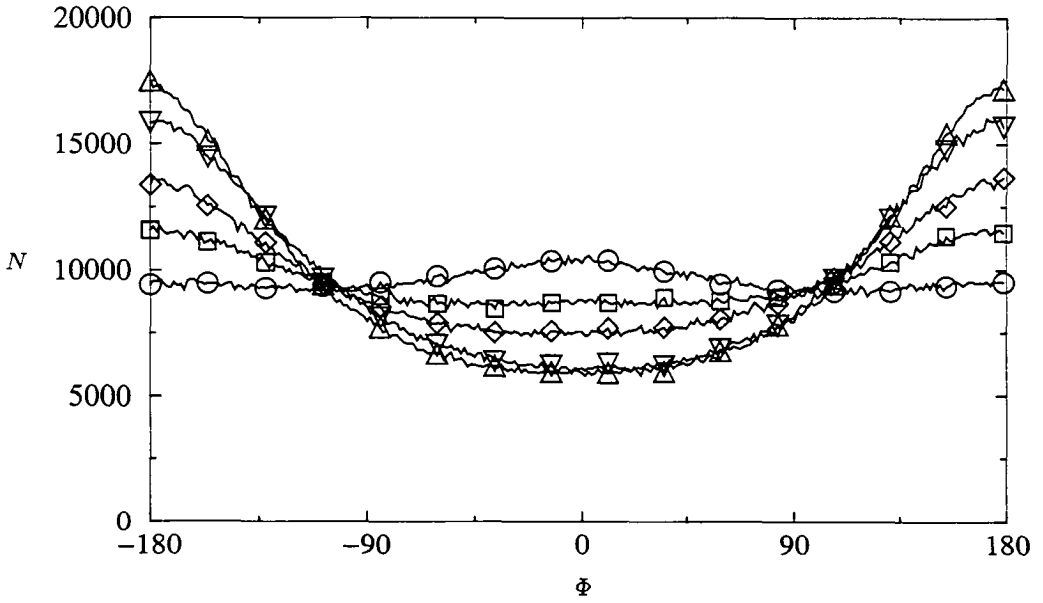

FIGURE 4. Distribution of the phase angle $\phi_{u_2\rho}$ in sheared stratified turbulence at $St = 5$ with Richardson numbers 0 (○), 0.1 (□), 0.2 (◇), 0.5 (△), and 1.0 (▽).

The largest contribution to $\phi_{u_2\rho} = \pm 180°$ is found in the $Ri = 0.5$ case, which also shows the strongest counter-gradient mixing coefficient. For all cases, a continuous phase angle distribution is observed. There are no local peaks apparent around $\phi_{u_2\rho} = \pm 90°$ that would suggest regions of wavelike behavior distinct from the background turbulence.

In order to obtain a more complete picture of phase angle distributions in turbulent stratified flow, figure 5 shows the distribution of the phase angle $\phi_{u_1u_2}$ between downstream, u_1, and vertical, u_2, velocity components, again at $St = 5$. The distribution is relatively unaffected by the Richardson-number variation. It shows strong peaks around $\phi_{u_1u_2} = 0$ and around $\phi_{u_1u_2} = \pm 180°$ that can be explained using the continuity equation. For modes with $k_3 = 0$, the continuity equation in wave space requires that the Fourier coefficients $\tilde{u}_1$ and $\tilde{u}_2$ are in the same direction, corresponding to $\phi_{u_1u_2} = 0$, or in opposite directions, corresponding to $\phi_{u_1u_2} = \pm 180°$. The peaks are therefore a result of two-dimensional modes.

4. Phase angle in unsheared stably-stratified turbulence

In this section, the phase angle in unsheared decaying stably stratified turbulence is discussed. A weakly-stratified case with initial Froude number $Fr = 64$ is compared to a more strongly stratified case with $Fr = 6.4$.

The spectrum of the phase angle $\phi_{u_2\rho}$ after about 10 eddy-turnover times is shown in figure 6. The weakly-stratified case with $Fr = 64$ has $\phi_{u_2\rho} \approx 0$ for all k_1, corresponding to down-gradient flux. The case with $Fr = 6.4$, however, shows $\phi_{u_2\rho} \approx \pm 180°$ for wave numbers larger than about $k_1 = 30$, corresponding to counter-gradient mixing. As in the sheared cases, there is no band in wavespace with wavelike behavior.

The phase-angle distribution over the instantaneous field at the same time as in figure 6 is shown in figure 7. The distribution in the weakly-stratified case shows a clear maximum

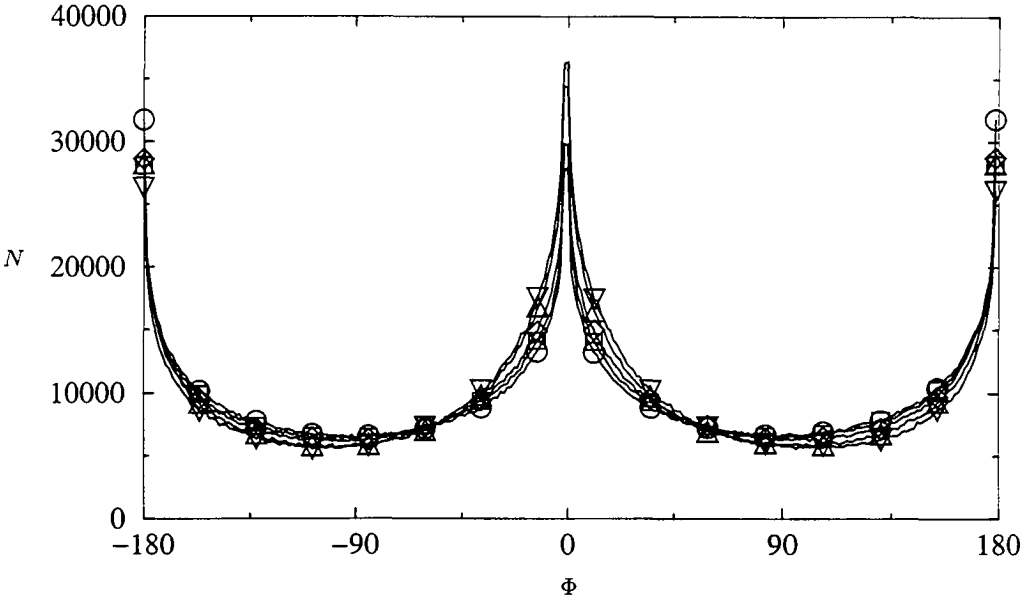

FIGURE 5. Distribution of the phase angle $\phi_{u_1u_2}$ in sheared stratified turbulence at $St = 5$ with Richardson numbers 0 (○), 0.1 (□), 0.2 (◇), 0.5 (△), and 1.0 (▽).

around $\phi_{u_2\rho} = 0$. However, the phase angles are widely distributed, which perhaps would not have been anticipated given the distribution in figure 6, which shows averaged phase angles at a given wavenumber. The distribution in the $Fr = 6.4$ case shows a maximum around $\phi_{u_2\rho} = \pm 180°$, corresponding to counter-gradient mixing. The distribution of phase angles between downstream velocity u_1 and vertical velocity u_2 is very similar to that of the sheared case, with strong peaks at 0° and ±180° and a weak dependence on the strength of the stratification.

5. Normal-mode analysis

A normal-mode analysis of the linearized inviscid equations of motion for the unsheared flow is performed. The direct numerical simulation results are then projected onto the eigensolution in order to extract a possible linear wave motion present in these results .

The analysis is based on the following linearized inviscid equations of motion:

$$\frac{\partial \rho}{\partial t} = -S_\rho u_2$$

$$\frac{\partial u_i}{\partial t} = -\frac{1}{\rho_0}\frac{\partial p}{\partial x_i} - \frac{g}{\rho_0}\rho\delta_{i2}$$

The pressure is eliminated from the equations using the continuity equation. The equations are transformed into Fourier space and take the following form:

$$\frac{\partial \tilde{\rho}}{\partial t} = -\frac{g}{\rho_0}S_\rho \tilde{u}_2 = N^2\tilde{u}_2$$

$$\frac{\partial \tilde{u}_i}{\partial t} = \tilde{p}\left(\frac{k_i k_2}{k^2} - \delta_{i2}\right) .$$

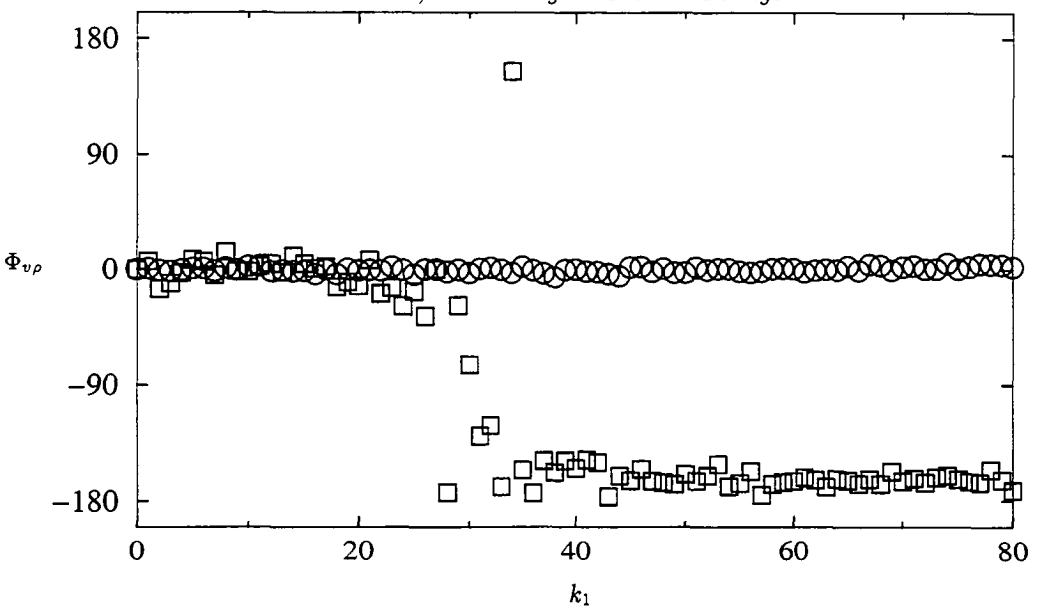

FIGURE 6. Spectrum of the phase angle $\phi_{u_2\rho}$ in unsheared stratified turbulence after about 10 eddy-turnover times with initial Froude numbers 64 (○) and 6.4 (□).

Normal modes of the form

$$\begin{pmatrix} \tilde{\rho} \\ \tilde{u}_1 \\ \tilde{u}_2 \\ \tilde{u}_3 \end{pmatrix} = \begin{pmatrix} \hat{\rho} \\ \hat{u}_1 \\ \hat{u}_2 \\ \hat{u}_3 \end{pmatrix} \exp i(k_j x_j + \omega t)$$

are introduced and lead to the following system of equations:

$$\begin{pmatrix} i\omega & 0 & S_\rho & 0 \\ -\frac{g}{\rho_0}\frac{k_1 k_2}{k^2} & i\omega & 0 & 0 \\ -\frac{g}{\rho_0}\left(\frac{k_2^2}{k^2}-1\right) & 0 & i\omega & 0 \\ -\frac{g}{\rho_0}\frac{k_2 k_3}{k^2} & 0 & 0 & i\omega \end{pmatrix} \begin{pmatrix} \hat{\rho} \\ \hat{u}_1 \\ \hat{u}_2 \\ \hat{u}_3 \end{pmatrix} = 0$$

From this system of equations, the following dispersion relation is obtained:

$$\omega^2 = 0 \qquad \omega = \pm\sqrt{D}$$

Here, D takes the following value:

$$D = N^2 \frac{k_1^2 + k_3^2}{k^2}$$

The following eigenvectors are obtained:

$$\mathbf{e}_{1,3} = \begin{pmatrix} S_\rho(k_1^2+k_3^2) \\ \mp i k_1 k_2 \sqrt{D} \\ \pm i(k_1^2+k_3^2)\sqrt{D} \\ \mp i k_2 k_3 \sqrt{D} \end{pmatrix} \qquad \mathbf{e}_2 = \begin{pmatrix} 0 \\ 1 \\ 0 \\ 0 \end{pmatrix} \qquad \mathbf{e}_4 = \begin{pmatrix} 0 \\ 0 \\ 0 \\ 1 \end{pmatrix}$$

The solution from direct numerical simulations can now be expressed in terms of the

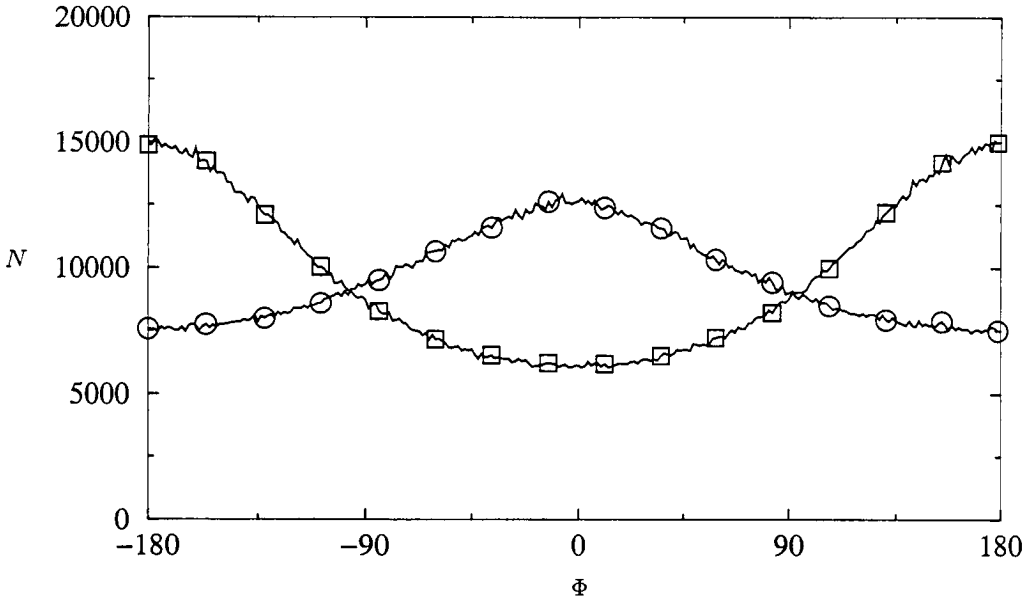

FIGURE 7. Distribution of the phase angle $\phi_{u_2\rho}$ in unsheared stratified turbulence after about 10 eddy-turnover times with initial Froude numbers 64 (○) and 6.4 (□).

eigenvectors:

$$\mathbf{a}_{DNS} = a_1\mathbf{e}_1 + a_2\mathbf{e}_2 + a_3\mathbf{e}_3 + a_4\mathbf{e}_4$$

Here, the components a_2 and a_4 describe horizontal vortical motion. The components a_1 and a_3 define an upper bound for the wave motion present in the field. Note that any DNS data, except that for k_1 and k_3 both zero, can be represented by a choice of complex a_1, a_2, a_3, and a_4. The coefficients are found by multiplication with the complex conjugate of the eigenvectors of the adjoint problem.

Note that the solution to the linearized governing equations is also used in Rapid Distortion Theory. The analytical solution to the equations presented at the beginning of this section was developed by Hanazaki and Hunt (1996). The solutions of these linearized equations show an impressive degree of similarity to solutions of the full nonlinear problem and capture much of the distinctive behavior of stably-stratified turbulence. Remarkably, Hanazaki and Hunt (2002) have extended this analysis to include the case of uniformly-sheared stratified turbulence as well. Presumably this solution could be used to provide guidance on how to decompose the sheared flow fields, but the difficulties encountered above would still be present (that is, all of the turbulent motion could be represented by the eigenvectors of the linearized system and, even after eliminating horizontal motions containing the vertical vorticity, the remaining "wave" motion could still contain a turbulent component).

6. Summary

In this study, the phase angle $\phi_{u_2\rho}$ between vertical velocity u_2 and density ρ was computed from direct numerical simulations of sheared and unsheared homogeneous stratified turbulence. A broad distribution of the phase angle was found that is consistent with

the observed down-gradient mixing for weakly stratified flow and counter-gradient mixing for strongly stratified flow. However, the broad distribution hides any internal wave signature that may be present in the flow.

A decomposition based on linear analysis has been proposed for unsheared decaying stratified turbulence. The flow fields are decomposed into horizontal vortical motions and vertical wave motions. However, there may still be some turbulent motion contained in the wave field. In agreement with Stewart (1969) we find that "there is probably no really clear-cut distinction between turbulence and waves".

REFERENCES

BRIGGS, D. A., FERZIGER, J. H., KOSEFF, J. R. & MONISMITH, S. G. 1998 Turbulent mixing in a shear-free stably stratified two-layer fluid. *J. Fluid Mech.* **354**, 175–208.

CRAYA, A. 1958 Contribution à l'analyse de la turbulence associée à des vitesses moyennes. Pub. Sci et Tech. du Ministère de l'Air (France) No. 345.

ERTEL, H. 1942 Ein neuer hydrodynamischer Wirbelsatz. Meteorol. Z., **59**, 271–281.

GERZ, T., SCHUMANN, U. & ELGHOBASHI, S. E. 1989 Direct numerical simulation of stratified homogeneous turbulent shear flows. *J. Fluid Mech.* **200**, 563–594.

HANAZAKI, H. & HUNT, J. C. R. 1996 Linear processes in unsteady stably stratified turbulence. *J. Fluid Mech.* **318**, 303–337.

HANAZAKI, H. & HUNT, J. C. R. 2002 Structure of unsteady stably stratified turbulence with mean shear. Submitted to J. Fluid Mech.

HERRING, J. R. & MÉTAIS, O. 1989 Numerical experiments in forced stably stratified turbulence. *J. Fluid Mech.* **202**, 97–115.

HOLT, S. E., KOSEFF, J. R. & FERZIGER, J. H. 1992 A numerical study of the evolution and structure of homogeneous stably stratified sheared turbulence. *J. Fluid Mech.* **237**, 499–539.

JACOBITZ, F. G., SARKAR, S. & VAN ATTA, C. W. 1997 Direct numerical simulations of the turbulence evolution in a uniformly sheared and stably stratified flow. *J. Fluid Mech.* **342**, 231–261.

JACOBITZ, F. G. 2000 Scalar transport and mixing in turbulent stratified shear flow. *Int. J. Heat Fluid Flow* **21**, 535–541.

KOMORI, S., UEDA, H., OGINO, F. & MIZUSHINA, T. 1983 Turbulence structure in stably stratified open-channel flow. *J. Fluid Mech.* **130**, 13–26.

LIENHARD, J. H. & VAN ATTA, C. W. 1990 The decay of turbulence in thermally stratified flow. *J. Fluid Mech.* **210**, 57–112.

MCBEAN, G. A. & MIYAKE, M. (1972) Turbulent transfer mechanisms in the atmospheric surface layer. *Quart. J. R. Met. Soc.* **98**, 383–398.

MÉTAIS, O. & HERRING, J. R. 1989 Numerical simulations of freely evolving turbulence in stably stratified fluids. *J. Fluid Mech.* **202**, 117–148.

PICCIRILLO, P. S. & VAN ATTA, C. W. 1997 The evolution of a uniformly sheared thermally stratified turbulent flow. *J. Fluid Mech.* **334**, 61–86.

RILEY, J. J., METCALFE, R. W. & WEISSMAN, M. A. 1981 Direct numerical simulations of homogeneous turbulence in density-stratified fluids. In *Nonlinear Properties of Waves* (B. J. West, ed.), 79–112.

ROHR, J. J., ITSWEIRE, E. C., HELLAND, K. N. & VAN ATTA, C. W. 1988 Growth and decay of turbulence in a stably stratified shear flow. *J. Fluid Mech.* **195**, 77–111.

STAQUET, C. & RILEY, J. J. 1989 On the velocity field associated with potential vorticity. *Dyn. Atmos. and Oceans* **14**, 93–123.

SHIH, L.H., KOSEFF, J.R., FERZIGER, J.H. & REHMANN, C.R. 2000 Scaling and parameterization of stratified homogeneous turbulent shear flow. *J. Fluid Mech.* **412**, 1–20.

STEWART, R. W. 1969 Turbulence and waves in a stratified atmosphere. *Radio Sci.* **4**, 1269–1278.

STILLINGER, D. C., HELLAND, K. N. & VAN ATTA, C. W. 1983 Experiments on the transition of homogeneous turbulence to internal waves in a stratified fluid. *J. Fluid Mech.* **131**, 91–122.

YOON, K. & WARHAFT, Z. 1990 The evolution of grid generated turbulence under conditions of stable thermal stratification. *J. Fluid Mech.* **215**, 601–638.

Adriatic simulations by DieCAST

By D. Dietrich †, G.F. Carnevale ‡ AND P. Orlandi ¶

The DieCAST model is modified for simulations of flow in the Adriatic Sea. A ten-year simulation is performed and the ability of the model to capture important features of the Adriatic circulation is demonstrated. A series of numerical experiments on the importance of the Mid Adriatic Pit (MAP) on the circulation is performed. It is demonstrated that the cross-Adriatic current over the northern flank of the MAP, which flows from the Croatian to the Italian coast, is primarily a topographic current and that such a current would reverse direction if the gradient of the bathymetry were reversed.

1. DieCAST Model Background:

The DieCAST ocean model (Dietrich 1997; Dietrich *et al.* 1997; Staneva *et al.* 2001; Haney *et al.* 2001) is applied to study the circulation of the Adriatic Sea. The hydrostatic, Boussinesq primitive continuum equations are derivable as an infinitesimal control-volume limit of the discrete conservation equations solved by DieCAST. A free-slip quasi-rigid-lid approximation is used. (The "lid" is weakly porous due to evaporation, precipitation and river source treatments; Staneva *et al.* 2001.) However, efficient free-surface and non-hydrostatic options are available; the former uses a shallow-water equations submodel forced by vertically-averaged baroclinic-mode terms; the latter uses an efficient iteration on the non-hydrostatic vertical acceleration terms (Dietrich *et al.* 1987, Appendix 1; Dietrich & Lin 2001).

The DieCAST lineage began with the Sandia Ocean Modeling System (Dietrich, *et al.* 1987), which included a two-way-coupled three- dimensional bottom boundary layer (bbl) submodel designed for risk assessment under the DOE sponsored Subseabed Waste Disposal Program. By confining sloping coordinates to the thin bbl, such approach avoids inaccuracies and associated numerical problems (e.g. Haney 1991) of baroclinic pressure gradient evaluation in a sloping bottom-fit (e.g. "sigma") coordinate system outside the bbl, while allowing accurate specialized (e.g. having sophisticated subgrid-scale turbulence submodel for Reynolds stress parameterization) treatment of the bbl in a full ocean modeling system.

Resolution sensitivity studies (Roache 1998a,b) (Dietrich *et al.* 1990; Dietrich 1993) verify model numerics and show that higher-order treatment of numerically-dispersive interpolations, used to evaluate the large Coriolis terms on the original staggered Arakawa "c" grid, greatly improves accuracy. Although included in these resolution sensitivity studies, the present DieCAST semi-collocated grid approach avoids such numerical dispersion of the large Coriolis terms. The original semi-collocated approach was improved (Dietrich 1997) by:

a) RDA (reduced dispersion advection)
b) MIA (modified incompressibility algorithm)

† Mississippi State University
‡ Scripps Institution of Oceanography
¶ University of Rome

MIA reduces numerical dispersion associated with two-way interpolations used by the incompressibility step. The original RDA is, effectively, 3.5-order-accurate. Following Sanderson (1998) and Sanderson & Brassington (1998), a slightly-modified RDA is used in recent versions: this is formally fourth-order-accurate on a collocated control volume grid. Third-order-upwind advection is a reasonable alternative, but there are advantages to our present fourth-order-accurate approach.

The present DieCAST model is fourth-order-accurate, except for subgrid- scale diffusive parameterization and vertical integration of the vertical momentum (hydrostatic) equation and in zones adjacent to lateral boundaries, where second-order-accuracy is used.

Dietrich & Mehra (1998) introduced a robust one-way nesting approach, which has been upgraded in a two-way-coupled nearly seamless duo grid North Atlantic/Gulf of Mexico/Caribbean Sea model that is one-way-nested in a global version of DieCAST (Dietrich, Haney & Mehra 2002); for more details on the basic grid coupling and nesting approach, see:

http://www.maths.unsw.edu.au/ bxs/DieCAST/MANUAL/.

Results include: highly-inertial realistic Gulf Stream separation and dynamics; difficult-to-model warm core rings (pinched off northern meanders of the GS); cold core rings; and a robust Deep Western Boundary Current, not resolved by the initialization climatology, that develops over a time scale O(10) years and significantly affects the GS separation and underlying fields.

Accuracy — including low numerical dispersion — and robustness with low numerical dissipation are extremely desirable features in numerical models. These features, and algorithmic simplicity and numerical efficiency, are serious goals in the DieCAST lineage. However, it is noteworthy that other versions exist which include advanced features such as partial bottom cells and more sophisticated advection and turbulence closure algorithms (e.g. the Canadian version of DieCAST, CANDIE; Sheng *et al.* 1998).

2. Present Adriatic Sea implementation of DieCAST

The present 30-layer, 2.5 min longitudinal resolution DieCAST adaptation is one-way-nested inside a 7.5 min resolution full Mediterranean Sea adaptation with a spatial resolution of 7.5 min. of arc (open southern boundary conditions are derived from the latter). Latitudinal resolution is such that horizontal cell aspect ratio is 1.0 (dy=dx). Unfiltered etop05 bathymetry truncated at depth 2750m is used. This is NOAA database and details can be found at: http://www.ngdc.noaa.gov/mgg/global/etopo5.HTML. Annual cycle Hellerman climatological winds are used (additional details can be found at http://ingrid.ldeo.columbia.edu/SOURCES/.HELLERMAN).

The bathymetry of the Adriatic with 1 min. resolution is shown in figure 1. This figure indicates the position of two important basins in the Adriatic called the South Adriatic Pit and the Mid Adriatic Pit (MAP, also called the Jabuka or Pomo Pit). Also indicated is the important Italian promontory called the Gargano. All of these structure are very important in determining the circulation of the Adriatic. With the resolution of the current model the bathymetry takes on the form shown in figure 2.

Thermodynamic surface boundary conditions (heat flux, evaporation, precipitation) are derived from more accurate annual cycle climatological data for surface temperature and salinity, combined with model internal dynamics. In contrast to conventional Haney restoring (Haney 1971) approaches, this physically motivated new approach (Di-

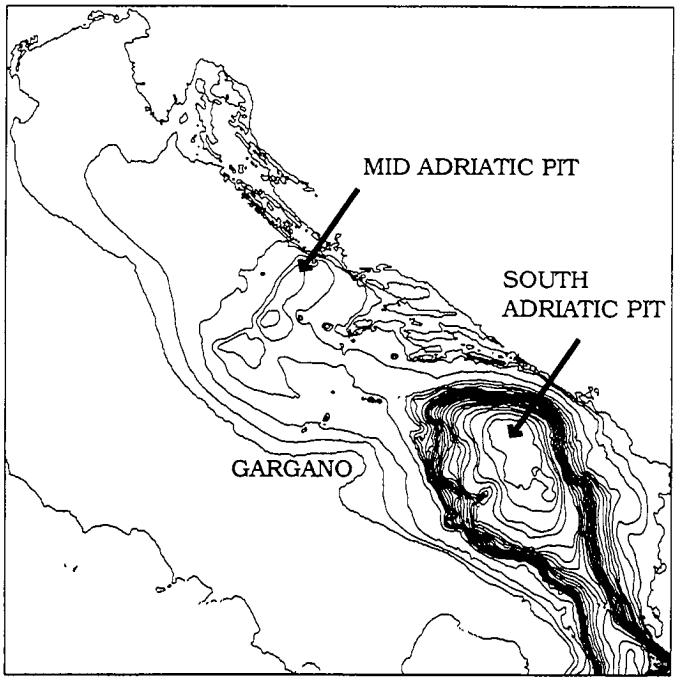

FIGURE 1. Contour plot of the bathymetry of the Adriatic Sea with horizontal resolution of 1 min. The Mid Adriatic Pit is the relatively deep region which nearly transects the Adriatic. The contour interval is 50 m.

etrich, Haney, Fernandez & Tintore 2002) has no phase lag or amplitude damping of the ensemble (multi-year) average annual cycle and does not artificially damp surface fronts. River sources may alternatively be specified directly, as done for 11 rivers in the Black Sea DieCAST adaptation (Staneva *et al.* 2001), but are implicitly included in the climatological data when using the new surface boundary conditions approach.

Vertical mixing, described in detail by Staneva *et al.* 2001, is represented by adding a Pacanowski & Philander (1981) surface mixed layer parameterization to background near-molecular-level viscosity (0.02 cm-cm/sec) and diffusivities (0.004 cm-cm/sec) plus a numerically and physically motivated component based on the vertical cell Reynolds number and Richardson number. During the summer and in deeper layers, especially near the pycnocline, the mixing is near the laminar values. Lateral viscosity and diffusivities are specified constants (5 m-m/sec), sufficiently small to allow realistic fronts and eddies, and wake recirculations downstream from major coastal abutments.

3. Model Performance

From a ten year run of this Adriatic Sea implementation of DieCAST, we observed a number of features that verified the ability of the model to capture realistic features of the Adriatic Sea dynamics. Among these are:

a) realistic triple-gyre major general-circulation features as shown in the streakline plot of figure 3 (discussed further in the next section);

b) realistic annual-cycle surface T and S. The ten-year run showed convergence of the mean statistics to climatology. In figure 4, we show the evolution of the horizontally-

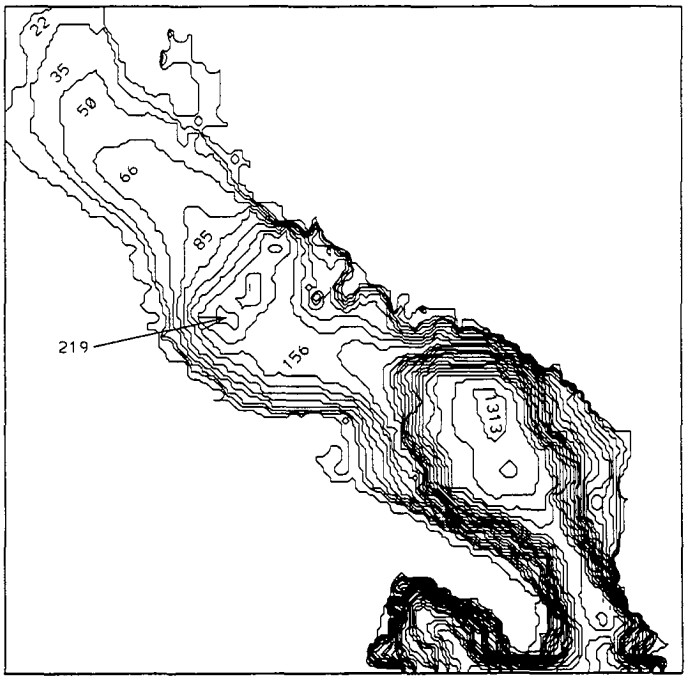

FIGURE 2. Contour plot of the model bathymetry used in our implementation of the DieCAST model with 2.5 min. horizontal resolution. The bathymetry is represented as 30 discrete steps in the model. Here we label the depth of some of these steps in meters.

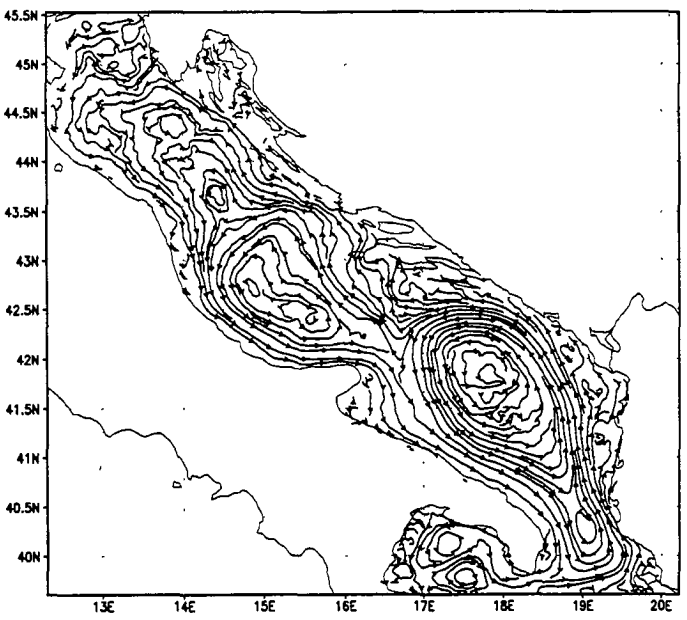

FIGURE 3. Streak plot for the velocity averaged over the fourth year of the simulation.

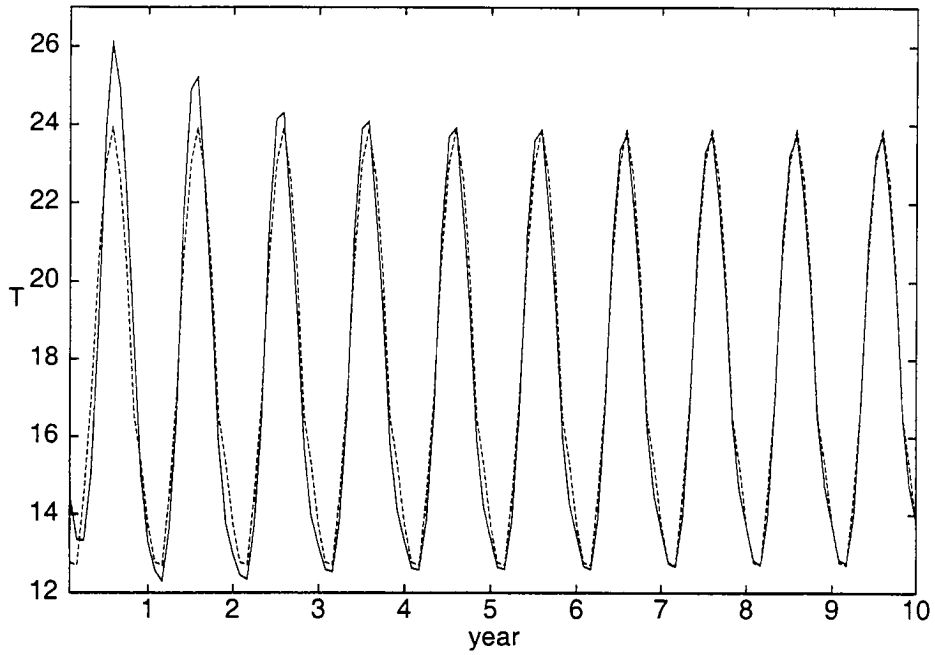

FIGURE 4. Graph of the ten-year history of the horizontally-averaged surface temperature from the simulation of the Adriatic. The model data is represented by the solid line while the climatological cycle is the dashed line.

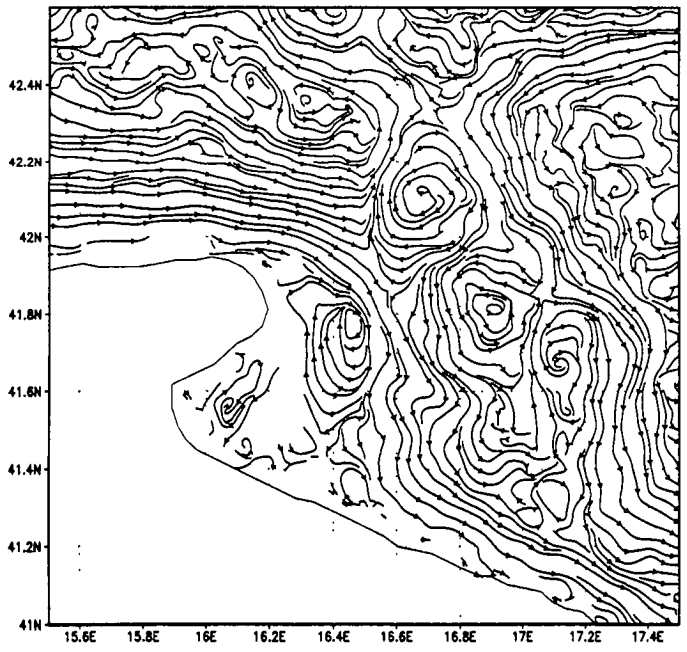

FIGURE 5. Streakline plot showing a recirculation eddy in the lee of the Gargano Peninsula from the end of February in year 10.

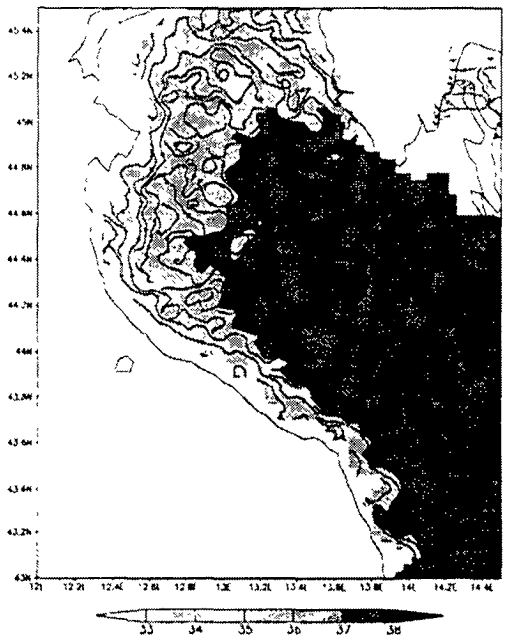

FIGURE 6. Surface salinity at the beginning of January year 10 with superposed streakline plot. This figure indicates the extent of the low salinity Po river plume at the beginning of winter. Values are grams of salt per kilogram of water.

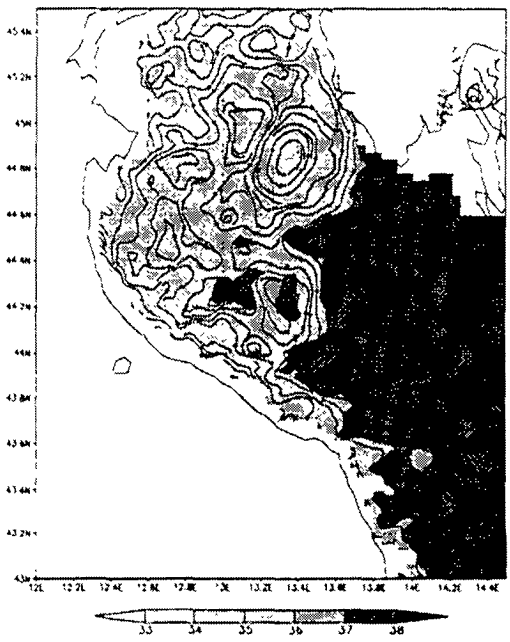

FIGURE 7. Surface salinity at the end of March year 10 with superposed streakline plot. This figure indicates the extent of the low salinity Po river plume in late winter. Values are grams of salt per kilogram of water.

averaged temperature and the annual cycle of this statistic taken from climatology. Notice that after just a few years the model mean temperature tracks the climatology very well, save for some small interannual variation due to the expected continuing temperature fluctuations.;

c) Cross-Adriatic southwestward current over the northern flank of the Mid Adriatic Pit (discussed further in the next section);

d) detailed fronts and eddies especially strong during the winter, with wintertime relative vorticity locally exceeding the earth's vertical rotation component; these intense eddies are energized by vigorous resolved slantwise convection that occurs due to weak or negative stratification during the winter;

e) recirculation in the wake of the major Gargano Peninsula, especially during winter when reduced stratification allows finer-scale features to develop; (figure 5 shows a recirculation eddy in the lee of the Gargano Peninsula at the end of February in year 10); such recirculations require a highly inertial model to be addressed realistically; frontal eddies associated with the dominant southern gyre (see figure 5) also interact with the flow near the Gargano;

f) the eastward mixing of the Po River plume during the late winter leading to a southward transport, well offshore, associated with the laterally-mixed buoyant region (see contour plots of salinity for the beginning of January and the end of March in figures 6 and 7), similar to the Danube River dynamics in the Black Sea adaptation of

DieCAST (Staneva *et al.* 2001); during the stable summer stratification periods, the plume is much closer to shore.

4. Topographic effects

The circulation of the Adriatic Sea is strongly affected by various influences such as bottom bathymetry, surface winds, inflow from the Mediterranean through the Otranto strait, etc. With our numerical model, we can begin to assess the importance of such effects. The influence of bottom bathymetry is particularly important, and, in considering it here, we will make some contact with our previous analytical work on the bifurcations of coastal currents due to the presence of bottom bathymetry (Carnevale *et al.* 1999).

The bathymetry of the Adriatic with horizontal contours from a data base of 1 min. horizontal resolution is shown in figure 1. The depth contours are drawn at 50 m intervals. The northern end of the Adriatic is much shallower than the southern end. Features of particular note are the South Adriatic Pit, reaching depths of over 1300 m, and the Mid Adriatic Pit, reaching depths of over 250 m, as we now explain.

For various theoretical reasons (cf. Carnevale and Frederiksen 1987, Salmon *et al.* 1976) there should be a strong tendency for the flow in a deep basin to be cyclonic (e.g. counter-clockwise in the northern hemisphere), and, indeed, the flow in the South Adriatic Pit is rather persistently cyclonic. Basically the argument is that fluid constrained to move in a thin layer and subject to strong rotation should behave in a nearly two-dimensional fashion. Fluid parcels can then be considered columns of fluid aligned along the vertical direction. Such columns moving from shallow to deep regions would be stretched while those moving from deep to shallow would be compressed. The conservation of angular momentum with realistically weak dissipation (largest in shallow regions) thus results in creation of cyclonic/anticyclonic relative vorticity (that is a rotation that is faster or slower than the background rotation rate). This is consistent with northern-hemisphere mid-size basins, which usually have offshore cyclonic mean circulation and coastal anti-cyclonic features enhanced by interactions with coastal abutments (e.g. the Black Sea: Staneva *et al.* 2001): random horizontal motions over a basin tend to create a region of mean cyclonic vorticity in the center of the basin and anticyclonic on the rim. The net result is cyclonic flow around the basin.

The effect of the Mid Adriatic Pit is a bit more subtle. Note that this pit has a rather steep northern flank while the topographic gradient on the southern flank is relatively mild. The flow in the vicinity of the Mid Adriatic Pit fluctuates considerably, but is often along the northern flank from the Croatian toward the Italian coast (southwestward). Arguments similar to those used to establish the cyclonic circulation around basins can be used to explain this trans-Adriatic flow. Motions across the step would tend to produce cyclonic circulation on the deep side and anticyclonic motion on the shallow side of the step. The net result would be motion along the step in the direction facing forward with the shallow fluid on the right and the deep on the left. This tendency to produce anticyclonic flow north of the step seems to be barely over-compensated, except in the vicinity of the step, by the tendency to produce cyclonic flow in the northern shallow region by coastal region mixing, and is further complicated by the locally strong influence of the Po River plume. Thus, the central and northern Adriatic Sea are modified significantly by the MAP, in spite of its much shallower nature than the dominant Southern Adriatic Basin, showing the important influence of shallow bathymetric features.

Furthermore, Carnevale *et al.* (1999), in a study of the effects of a step aligned perpen-

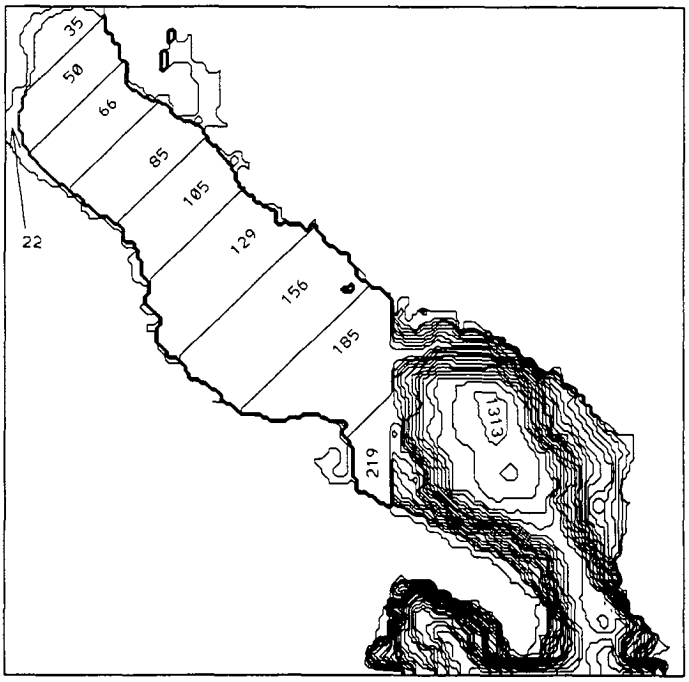

FIGURE 8. Contour plot of the smoothed bathymetry used to demonstrate the effect of removing the Mid Adriatic Pit. Step depths are given in meters for select steps.

dicular to the shore, found an analytic solution for the current that runs along the step topographic contours. In accordance with the above principles, this analytic solution has the topographic current flowing away from the coast when the step is such that in looking across the step from deep to shallow water the coast is on the right, while the flow is toward the shore if the coast is on the left. To a certain extent, the northwestern flank of the MAP forms a step running almost from the eastern to the western boundaries of the Adriatic. Thus, according to the above, there should be a tendency to establish a current along the northwestern flank of the MAP from the eastern to the western boundary, that is, from the coast of Croatia to that of Italy. Indeed such a current is often indicated by drifter data (Falco *et al.* 2000) and in satellite images. The reason for this MAP current has alternatively been suggested to be the result of strong winds that are funneled by coastal bathymetry and blow in a narrow band at this location. Our goal here is to present a few simple simulations that demonstrate the topographic nature of this current in the framework of a full ocean general circulation model.

First, we demonstrate that the MAP current flowing southwestward along the steep gradient of the MAP is found in our simulation of the Adriatic. In the time span allotted for this project, we needed to strike a balance between the desire to sufficiently resolve the steep gradient of the MAP, and the speed of computation. We decided to use a 2.5 min resolution in these runs. This spreads the 'step' out to some extent, as shown in figure 2, where we display the actual levels used in the computation; however, given the small diffusivity associated with the DieCAST model, this resolution proved adequate for a preliminary study.

We made an average of the velocity field over the 4th year of our simulation. This mean velocity field was then used to generate streaklines to give an indication of the mean

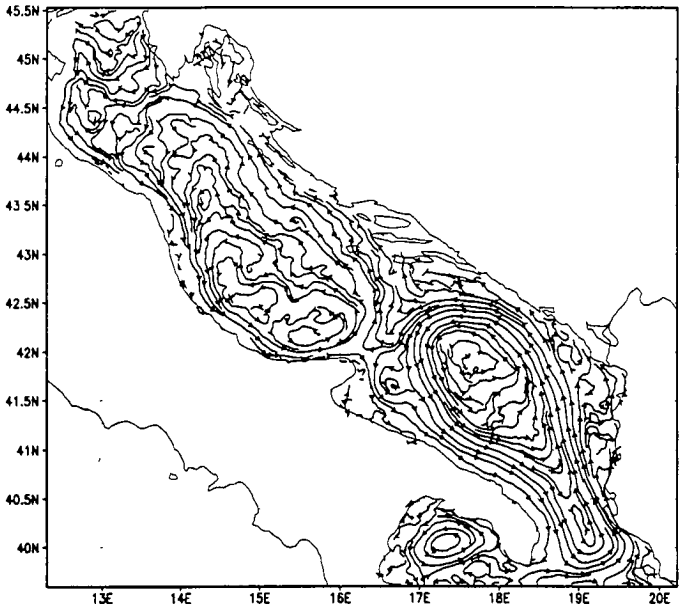

FIGURE 9. Streak line plot based on the mean field for the rerun of the fourth year but with the bathymetry shown in 8, that is without the Mid Adriatic Pit.

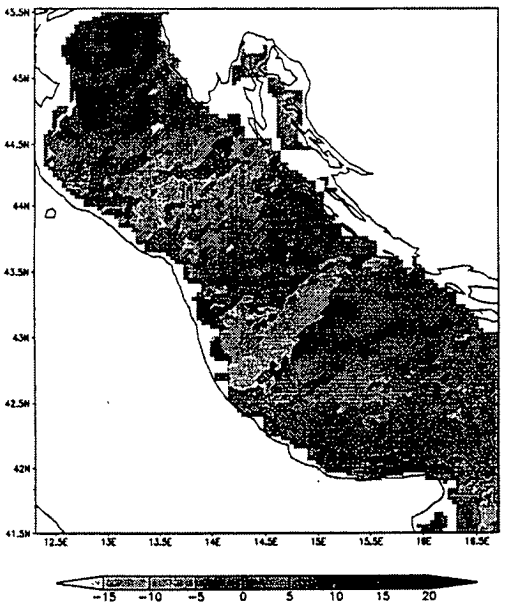

FIGURE 10. Mean velocity in the northeast direction from the fourth year of the run with the bathymetry shown in figure 2 (including the MAP)

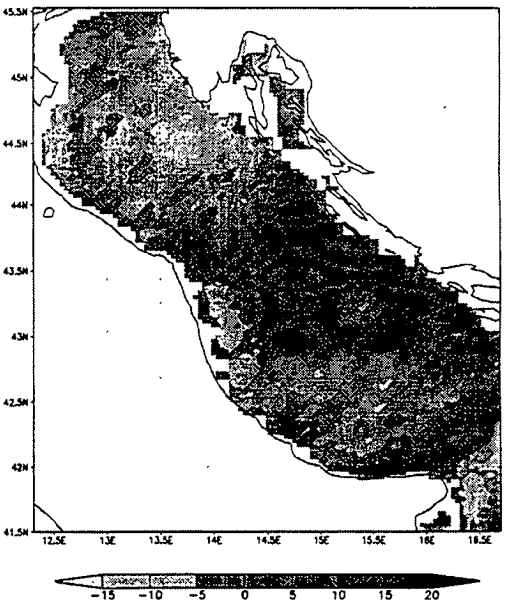

FIGURE 11. Mean velocity in the northeast direction from the rerun of the fourth year with the bathymetry shown in figure 8 (with no MAP).

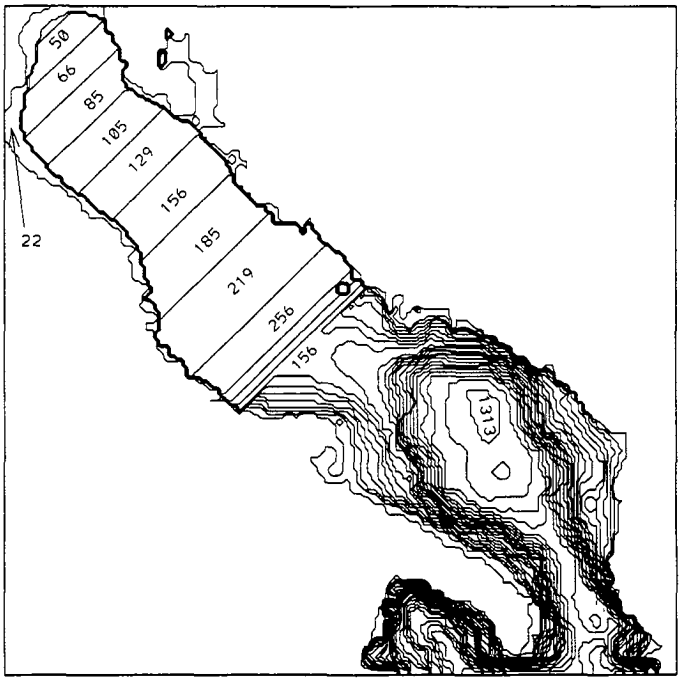

FIGURE 12. Contour plot of the bathymetry used to demonstrate the effect of a steep gradient in in the opposite sense of that on the northern flank of the the Mid Adriatic Pit. Step depths are given in meters for select steps.

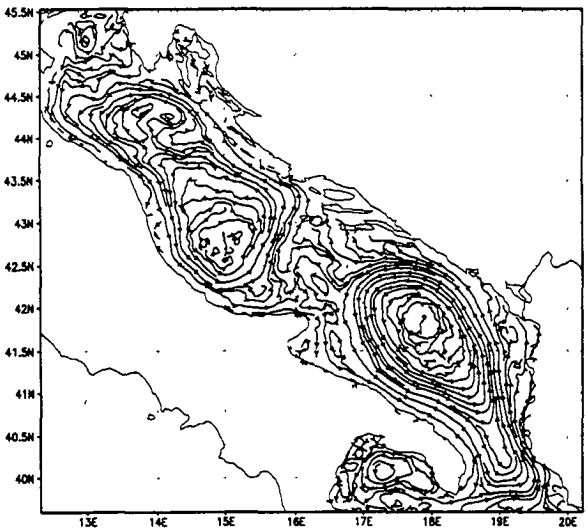

FIGURE 13. Streak line plot based on the mean field for the rerun of the fourth year but with the bathymetry shown in figure 12. The steep slope in the mid Adriatic is now oriented in such a way as to produce a concentrated northeastward current and such a current results.

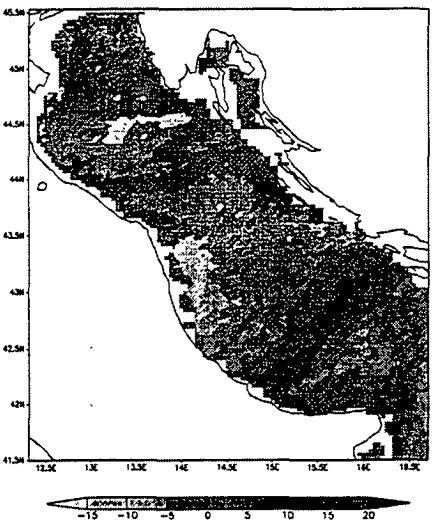

FIGURE 14. Mean velocity in the northeast direction from the rerun of the fourth year with the bathymetry shown in figure 12 (with no MAP).

current directions. This mean streakline pattern is shown in figure 3. Notice first of all the 'three-gyre' cyclonic pattern of the mean current. As mentioned above, there is the rather robust cyclonic gyre over the SAP. Further north there is a cyclonic gyre with its northern side following the northern flank of the MAP in the anticipated direction. Finally, there is the weaker northern cyclonic circulation, extending almost to the northernmost reaches of the shallow end of the Adriatic. Instantaneous figures often show the northern flank MAP current, but sometimes this is obscured by the eddying field. The MAP current appears to be the strongest and best-organized in May and June, and weakest in the winter.

In order to emphasize the importance of the bathymetry in establishing the current on the northern flank of the MAP, we performed another simulation for the same year four, with everything exactly the same except for the bottom bathymetry. In this run we eliminated the MAP and replaced the 'real' bathymetry with a smooth slope from the northern rim of the SAP to the northern end of the Adriatic. This bathymetry is shown in figure 9. The flow with this bathymetry, averaged over the year, results in the streakline plot shown in figure 9. Now the circulation has only two large cyclonic gyres instead of the original three. The northern gyre now covers the area originally occupied by the MAP gyre and the northernmost gyre. This result establishes the importance of the MAP in determining the 3-gyre circulation of the Adriatic.

If there were a steep step crossing the Adriatic with a gradient opposite that of the northern flank of the MAP, then that should induce an intense current along the topographic contours in the opposite direction of that seen in figure 10. To demonstrate this, we created another model bathymetry with such a 'reverse' step. This is shown in figure 12. The mean circulation for a year long flow over this bathymetry is shown in figure 13 as a streakline plot. Here we see that although the SAP gyre is relatively unaffected, the two northern gyres have practically merged into one and the southern edge of this combined gyre is now sharply defined by an intense *northeastward* flow along the steep gradient of the southern flank of the MAP. Finally, in figure 14, we again show the mean velocity component in the northeast direction. This is the counterpart to figure 10. There is a nice contrast between the two cases showing the direction of the induced narrow cross Adriatic currents depends on the sign of the topographic gradient.

5. Conclusions

We created a 2.5 min. resolution model of the Adriatic based on the DieCAST code. A simulation representing ten years of evolution was performed. The behavior of the model was found to be optimal. The general-circulation pattern was correctly reproduced, and the overall temperature and heat balances maintained over the period of evolution. Furthermore, the surface temperature distribution was found to be in accord with typical observations. In addition, the low viscosity of the model allowed the representation of realistic eddies generated by the flow past the Gargano peninsula, as well as the frontal eddies generated by the South Adriatic Pit current.

Given the overall success of the model, we turned to questions concerning the effect of the topographic feature known as the Mid Adriatic Pit on the Adriatic circulation. Observations had shown a distinct southwestward flow along the northwest flank of this pit. The topographic slope on this flank is considerably steeper than on the opposite flank, so it was natural to conjecture that the current over it is topographically generated, as discussed in previous work (Carnevale *et al.* 1999). Nevertheless, a competing

view, suggesting that intense winds in the area were responsible for this current, made it important to test our hypothesis. First, we demonstrated that our 2.5 min. resolution model was capable of reproducing this current. Then we showed that if the steep slope were smoothed over, then the coherent, relatively intense, narrow current would be replaced by a broad weak current. This indicates the topographic nature of this current. In addition, we demonstrated that the direction of the current is determined by the sign of the topographic gradient (and the direction of the rotation of the earth) by running a simulation with a deformed topography containing a topographic step with the opposite sign of slope, and in that case the resulting current flowed in the opposite direction, that is to the northeast. These results were predicted by our quasi-geostrophic theory (Carnevale *et al.* 1999) for the much simpler system of a single-layer barotropic flow. Quantitative comparison with such a theory is difficult given the stratified nature of the actual flow.

Acknowledgments

P.O. was partially supported by ONR through the grant N00014-02-1-4047 G.F.C. has been partially supported by Office of Naval Research grants N00014-97-1-0095 and N00014-96-1-0065 and National Science Foundation grant OCE 01-28991 and OCE 01-29301. We also thank P. Giannini, R. Purini, N. Rachev for their help in this project, and G.F.C. thanks the University of Rome and the Istituto Talassografico (CNR-Trieste) for their hospitality.

REFERENCES

CARNEVALE, G. F. & FREDERIKSEN, J. S. 1987 Stability and statistical mechanics of flow over topography. *J. Fluid Mech.* **175,** 157–181.

CARNEVALE, G. F., LLEWELLYN SMITH, S. G., CRISCIANI, F., PURINI, R. & SERRAVALL, R. 1999 Bifurcation of a coastal current at an escarpment. *J. Physical Oceanography* **29,** 969–985.

DIETRICH, D. E. 1993 On modeling geophysical flows having low Rossby number. *Atmosphere-Ocean* **31,** 57–71.

DIETRICH, D. E. 1997 Application of a modified "a" grid ocean model having reduced numerical dispersion to the Gulf of Mexico circulation. *Dynamics of Atmospheres and Oceans* **27,** 201–217.

DIETRICH, D. E., HANEY, R. L. & MEHRA, A. 2002 Progress in modeling the North Atlantic Ocean system. *Oceans 2002,* Oct 29-31, Biloxi, MS.

DIETRICH, D. E., HANEY, R. L., FERNANDEZ, V. & TINTORE, J. , 2002 Model-determined suface heating and freshwater sources using a precise, non-damping zero-phase-lag approach. *Under review.*

DIETRICH, D. E. & MEHRA, A. 1998 Sensitivity studies in the Santa Barbara Channel using the DieCAST ocean model. *Proceedings of the Santa Barbara Channel Quality Review Board Meeding, San Diego, February, 1998.*

DIETRICH, D. E., LIN, C. A., MESTAS-NUNEZ, A. & D.-S. KO, 1997 A high resolution numerical study of Gulf of Mexico fronts and eddies. *Meteorol. Atmos. Phys.,* **64,** 187–201.

DIETRICH, D. E., ROACHE, P. J. & MARIETTA, M.G. 1990 Convergence studies with the Sandia Ocean Modeling System. *Int. J. Numer. Methods Fluids,* **11,** 127–150.

DIETRICH, D.E., MARIETTA, M. G. & ROACHE, P. J. 1987 An ocean modeling system with turbulent boundary layers and bathymetry, Part 1: Numerical Description. *Int. J. Numer. Methods Fluids,* **7**, 833–855.

FALCO, P., GRIFFA, A., POULAIN, P.-M. & ZAMBIANCHI, E. 2000 Transport properties in the Adriatic Sea as deduced from drifter data. *J. Phys. Oceanogr.,* **30**, 2055–2071.

HANEY, R. L., HALE, R. A. & DIETRICH, D. E. 2001 Offshore propagation of eddy kinetic energy in the California Current. *JGR-Oceans* **106, C6,** 11,709–11,717.

HANEY, R. L. 1991 On the pressure gradient force over steep bathymetry in sigma coordinate ocean models. *J. Phys. Oceanogr.,* **21**, 610–619.

HANEY, R.L., 1971. Surface thermal boundary condition for ocean circulation models. *J. Phys. Oceanogr.,* **1**, 241–248.

PACANOWSKI, R. C. & PHILANDER, S. G. H. 1981 Parameterization of vertical mixing in numerical models of tropical oceans. *J. Phys. Oceanogr.,* **30**, 1069–1082.

ROACHE, P. J. 1998A *Verification and Validation in Computational Science and Engineering.* Hermosa Publishers, ISBN 0-913478-08-3.

ROACHE, P. J. 1998 *Fundamentals of Computational Fluid Dynamics.* Hermosa Publishers, ISBN 0-913478-09-1.

SALMON, R., HOLLOWAY, G. & HENDERSHOTT, M. C. 1976 The equilibrium statistical mechanics of simple quasi-geostrophic models. *J. Fluid Mech.,* **75**, 691–703.

SANDERSON, B. G. 1998 Order and resolution for computational ocean dynamics. *J. Phys. Oceanogr.,* **28**, 1271–1286.

SANDERSON, B. G. & BRASSINGTON, G. 1998 Accuracy in the context of a control-volume model. *Atmosphere-Ocean,* **36**, 355–384.

SHENG, J., WRIGHT, D. G. GREATBACH, R. J. & DIETRICH, D. E. 1998 CANDIE: A new version of the DieCAST ocean circulation model. *JAOT,* **15**, 1414–1432.

STANEVA, E., DIETRICH, D. E., STANEV, E. & BOWMAN, M. 2001 Rim Current and coastal eddy mechanisms in an eddy-resolving Black Sea general circulation model. *J. Marine Systems, special issue on the Black Sea,* **31**, 137–157.

Optimization

In the past two decades, numerical tools have been refined for the accurate modeling of a wide variety of laminar and turbulent flow systems. In several cases of engineering relevance, we are now confident in the predictive capability of these numerical tools for determining the bulk quantities characterizing such systems, such as the drag, the lift, the far-field noise, the mixing of fuels and oxidizers, the heat transfer, etc. We are also confident, in many cases, that we can capture accurately the variation of these flow quantities with the variation of the near- and far-field boundary conditions and the forcing of the system by actuators providing either steady or unsteady control inputs. In such systems, optimization strategies are playing an increasingly important role in the selection of effective shape and surface compliance parameters, open-loop control forcing schedules, and closed-loop control feedback rules to achieve desired effects on the flow quantities of interest while respecting a variety of constraints related to insuring the feasibility of the engineering design. The present section focuses on a few such efforts in the simulation-based optimization of flow systems.

Mohammadi reports on recent advances in the development of the so-called "incomplete sensitivity" method to provide approximate gradient information in a shape optimization problem related to the minimization of the sonic boom created by a supersonic transport. The incomplete sensitivity method is designed to calculate approximate gradient information for optimization of the flow system at significantly reduced cost as compared with calculating the full expression for the gradient. The utility of such a method is clear, as the determination of accurate gradient information (via an adjoint analysis) can sometimes be quite difficult, both in terms of the human time required to write and debug the appropriate numerical code and the computation time required to execute such a code. The accuracy of the approximate gradient information provided by the incomplete sensitivity approach varies greatly from problem to problem, and has recently been a topic of active interest in the optimization community.

Catalano *et al.* report on the application of a direct search method, referred to as the "response surface" technique, applied to minimize the drag of the flow past a cylinder. The response surface technique first develops a local approximation of the surface of the cost function in the space of the control parameters based on recent function evaluations alone (that is, it does not require gradient or approximate gradient information). It then minimizes this approximating surface using analytical or gradient-based methods in order to obtain the next candidate point in the optimization of the full system. Such an approach provides an attractive alternative to the more expensive gradient-based optimization strategies, and is tractable when the number of control parameters is relatively low.

Sbalzarini *et al.* report on the application of several so-called "machine learning" algorithms to classify the trajectories of moving cells with regard to their mean and minimum speeds in order to quantify the response of the mobility of such cells to changes in environmental conditions. This represents a problem in system identification based on experimental observation and post-processing of large amounts of experimental data. Note that the system identification problem is in fact closely related to the problem of system optimization, and similar concepts and techniques may be applied to both.

Also included in the present section is a report on the molecular dynamics simulations of Walther *et al.* This paper studies the effect of both hydrophobic and hydrophilic

boundary conditions on simulations of both planar Couette flow and the flow of past carbon nanotubes, using water as the operating fluid in both cases. A comparison of molecular dynamics simulations and conventional Navier-Stokes simulations is also made for the flow past an array of carbon nanotubes, and the two types of simulations are found to be in good agreement.

Thomas R. Bewley

Optimization of aerodynamic and acoustic performance of supersonic civil transports

By Bijan Mohammadi †

We present a shape-optimization problem under acoustic, aerodynamic and geometric constraints. The acoustic specification concerns the generated sonic boom. The aim is to see the validity of incomplete sensitivities when a nonlinear CFD model is coupled with a nonlinear wave-transport model to define pressure rise on the ground.

1. Motivation and objectives

In shape design for transonic aircraft under cruise conditions, multi-criteria aspects mainly concern the aerodynamic and elastic characteristics of the aircraft. For instance, the aim can be to reduce the drag at given lift and with given maximum cross-section thickness, which would ensure structural realizability. Shape optimization for civil supersonic transports includes another main ingredient: the control of the sonic boom (Whitham 1952). This makes the problem harder than in the transonic case, as drag and sonic boom reductions are by nature incompatible (in supersonic regime low drag geometries are sharp and have high boom level as shocks are attached then).

A large effort is currently being made on the improvement of the potential of supersonic transport. As an example, in the United States, the DARPA Quiet Supersonic Platform (QSP) program is directed towards development and validation of critical technology for long-range advanced supersonic aircraft with substantially reduced sonic boom, reduced takeoff and landing noise, and increased efficiency relative to current generation supersonic aircraft. Improved capabilities include supersonic flight over land without adverse sonic boom consequences with boom overpressure rising less than 0.3 pounds per square foot (psf) (about 14 Pa), increased unrefueled range approaching 6,000 nmi, gross take-off weight approaching 1,000,000 pounds, increased area coverage and lower overall operational

Similar efforts are made in Europe. In France, the Committee for Scientific Orientation for Supersonic Transport directs studies on the feasibility of the next generation of the Concorde jetliner.

2. Sonic boom

The sound heard on the ground as a "sonic boom" is the sudden onset and release of pressure after the buildup by the shock wave or "peak overpressure." The change in pressure caused by a sonic boom is only a few pounds per square foot – about the same pressure change we experience in an elevator as it descends two or three floors, but in a much shorter time period. It is the magnitude of this peak overpressure that describes a sonic boom.

There are two types of booms: N-waves and U-waves. The N-wave is generated from steady flight conditions, and its pressure wave is shaped like the letter "N". N-waves have a front shock to a positive peak overpressure, which is followed by a linear decrease in

† University of Montpellier, Mathematics, CC51, 34095 Montpellier, France

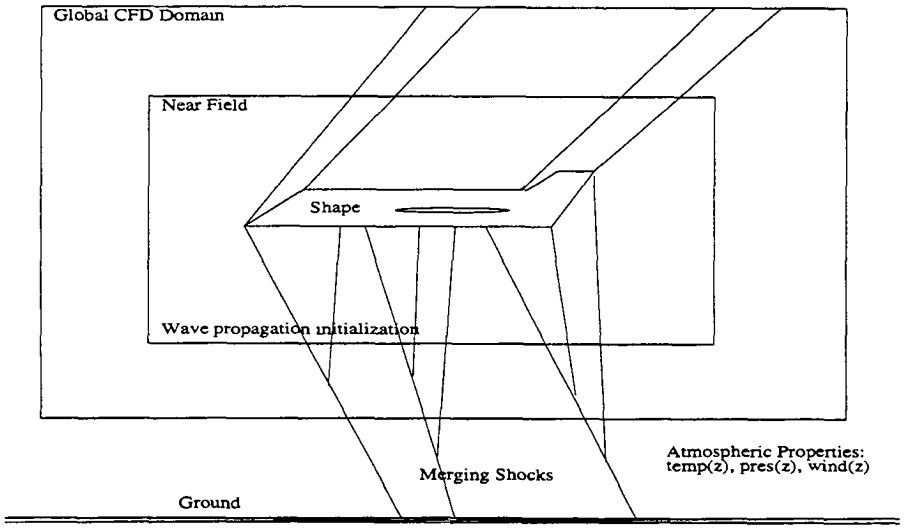

FIGURE 1. Shock-wave pattern and illustration of the near-field CFD computation domain and the initialization of the wave-propagation method with CFD predictions.

pressure until the rear shock returns to ambient pressure. In principle, a supersonic civil transport in cruise condition produces only N-waves.

For today's supersonic aircraft in normal operating conditions, the peak overpressure varies from less than one pound to about 10 pounds per square foot for an N-wave boom (15 to 150 Pascal).

3. Governing equations

In this work, the flow in the regions close to the aircraft, or the near field, is computed using the Euler equations for gas dynamics in conservation form. The solution method is based on a finite-volume Galerkin method and is described in Mohammadi (1994). The variables at the lower boundary of this domain are then used to define waveform parameters which are propagated to the ground using the waveform parameter method (Thomas 1972). A schematic of the approach is shown in figure 1. As the propagation in this work is performed only in post-processing, the use of a more complete propagation tool does not change the current optimization methodology.

4. CAD-Free shape parameterization

We use a CAD-Free control space to specify shape deformations (Mohammadi & Pironneau 2001). In this approach all the nodes of the surface mesh over the shape are control parameters. One particular property of this parameterization comes from the fact that, unlike the case of a CAD-based parameter space, regularity requirements have to be specified and handled by the user (see figure 2). Indeed, if the shape is described using a CAD tool and if we use the same parameterization to specify the deformations, the two entities belong to the same space in term of regularity.

From a practical point of view, this inconvenience is compensated by the fact that a CAD-based parameter space might not be suitable for optimization. In fact, our experience shows that optimization in the CAD-Free framework helps improve the CAD

FIGURE 2. Sketch of a CAD-Free deformation without and with the regularization operator. The initial deformation is only $C^0(\Gamma)$, and to have a $C^1(\Gamma)$ variation we need to project it, for instance, into $H^{5/2}(\Gamma)$ if Γ is a surface in $\mathbb{R}^3$.

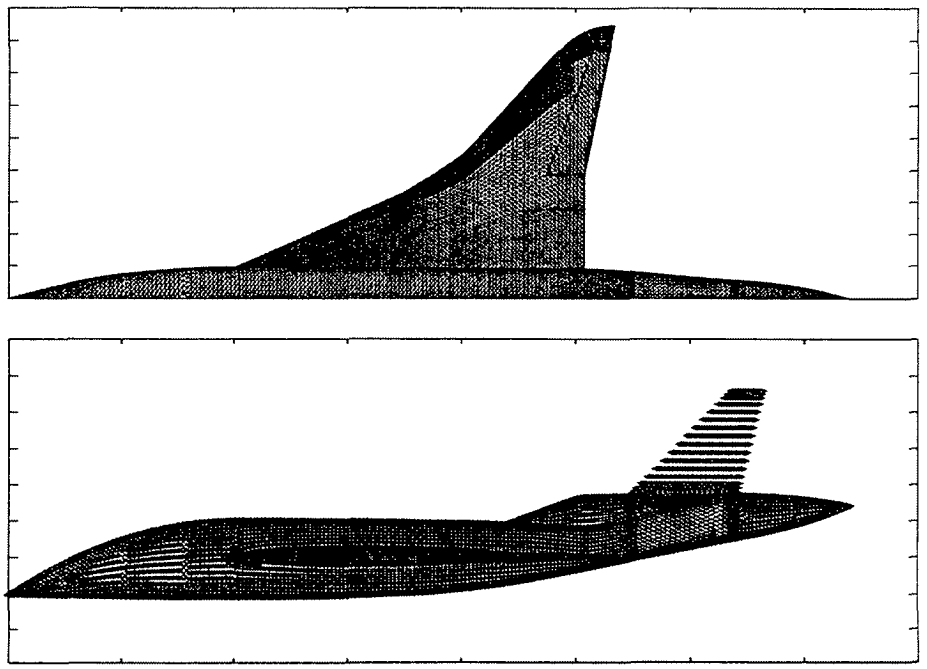

FIGURE 3. Upper and side views of the SSBJ discretization; all these nodes are control parameters.

definition of the shape. This is interesting, as the final shape has to be expressed through CAD in all cases. Concerning mesh-dependence of the optimization, the same remark holds when using a CAD-based parameter space. Indeed, it is obvious that the optimization might converge to different shapes in different CAD-based parameter spaces. Finally, the new generation of CAD tools are able to fit CAD parameters into a surface mesh if the initial correspondence between CAD parameters and surface mesh is known. Theoretical justification for the introduction of smoothing operators for the CAD-Free parameter space comes from the consistent approximation theory (Polack 1997).

5. Gradient evaluation

We consider two types of functionals: those using shape-based information and those involving information away from the surface. Examples are, for the first type, aerody-

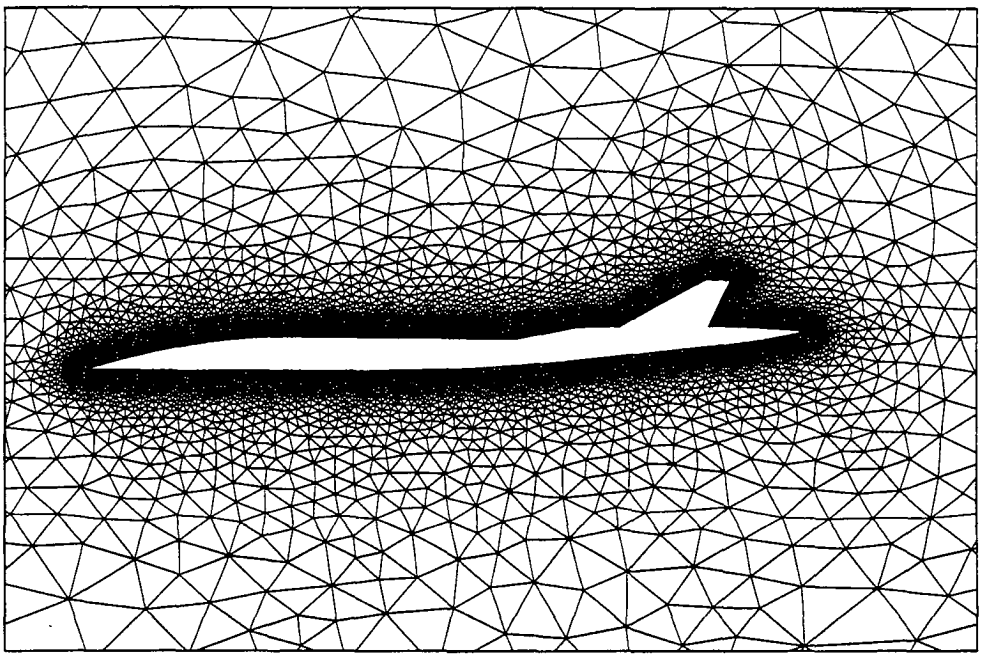

FIGURE 4. Partial view of the CFD mesh in the symmetry plane.

namic coefficients such as lift and drag coefficients, or geometric quantities such as the volume and the maximum cross-section of the aircraft, and for the second type the sonic boom defined by the ground-pressure signature.

There is a major difference between these two classes concerning the evaluation of sensitivities. Indeed, we will see that the first class is suitable for the use of the so-called incomplete sensitivity technique while a functional involving information on the ground requires the linearization of state equations.

5.1. *Incomplete sensitivities*

One of the main purposes of this paper is to see if we can use, for sonic boom reduction, a redefinition of the cost function compatible with incomplete sensitivity evaluations. Indeed, in the past we have applied this approximation to functionals involving aerodynamic coefficients. The redefinition is designed to be used only for sensitivity evaluation.

We briefly recall the incomplete-sensitivity approach. Consider a general simulation loop linking the control parameter x to a functional J:

$$J(x) : x \to q(x) \to U(q(x)) \to J(x, q(x), U(q(x))), \tag{5.1}$$

where q represents all geometrical entities and U all state-related variables. The gradient of J with respect to x is:

$$\frac{dJ}{dx} = \frac{\partial J}{\partial x} + \frac{\partial J}{\partial q}\frac{\partial q}{\partial x} + \frac{\partial J}{\partial U}\frac{\partial U}{\partial x}. \tag{5.2}$$

The major part of the cost of this evaluation is due to $\partial U/\partial x$ in the last term.

Consider the following context for shape optimization:

- 1. both the cost function and the control space are defined on the shape (or on some part of it),
- 2. J is of the form

$$J(x) = \int_{\text{shape}} f(x)g(U)d\gamma,$$

- 3. the local curvature of the shape is not too large (this needs to be quantified for each case: for a wing we typically consider regions away from leading and trailing edges).

If these requirements hold, we can use an incomplete evaluation of this gradient, neglecting the sensitivity with respect to the state in (5.2). This does not mean that a precise evaluation of the state is unnecessary, but that for a small change in the shape the state will remain almost unchanged, while geometrical quantities have variations of the same order as the shape variation.

5.1.1. *Illustrations of incomplete sensitivities*

A first simple example concerns the application of the incomplete sensitivity technique to the evaluation of the sensitivity of functionals involving the solution of the following Burgers equation:

$$u_t + 0.5(u^2)_x = \mu x u, \quad \text{on }]a, 1[, \quad u(a) = 1, \quad u(1) = -0.8. \tag{5.3}$$

We consider the steady solution of (5.3) and take the left hand side frontier a as control parameter. Suppose the functional is $J(a) = au_x(a)$; then the gradient is given by

$$J_a(a) = u_x(a) + au_{xa}(a).$$

We are in the validity domain for incomplete sensitivities. Without computing the solution, it is clear from the equation that in regions where the solution is regular, $u_x = \mu x$. The exact gradient is therefore $J_a(a) = \mu a + a\mu$, to be compared with the incomplete gradient μa. We see that the sign of the incomplete gradient is always correct, and there is only a factor of 2 missing; something which is not important when using an optimal descent step size in minimization. Obviously, the condition for this analysis to hold for any functional of the form $f(a)g(u)$, where u is a solution of (5.3), is that there exists $\epsilon > 0$ such that $(log(g))_a = \epsilon(log(f))_a$. This is something we can verify *a priori* before using the incomplete sensitivity in optimization.

Another interesting example is to consider the sensitivity analysis for an expression of the form $p(x)u_\infty n(x)$ with respect to a parameterization x (for the sake of simplicity, we formally consider the case of scalar quantities). This expression appears in the definition of the aerodynamic drag coefficient, for instance. Suppose the pressure is given by the Newton formula $p = p_\infty(u_\infty.n)^2$. We have therefore $pu_\infty n = p_\infty(u_\infty n)^3$. The gradient of this expression with respect to x is

$$\frac{d(pu_\infty n)}{dx} = (pu_\infty)\frac{dn}{dx} + \frac{dp}{dx}(u_\infty n) = 3p_\infty u_\infty(u_\infty.n)^2\frac{dn}{dx}.$$

On the other hand, the incomplete sensitivity is given by

$$\frac{d(pu_\infty n)}{dx} = (pu_\infty)\frac{dn}{dx} = p_\infty u_\infty(u_\infty n)^2\frac{dn}{dx}.$$

We see that the two gradients have the same sign, but that there is a factor of 3 missing in the incomplete sensitivity. From a fluid-dynamic point of view this is a worst case, as we know that small changes in the geometry in high-curvature area where the Newton model is valid (leading edges for instance) have important effects on the flow, much

more than changes in area where the shape is flat. Below, we reconsider this analysis for the sensitivity of sonic boom with respect to the shape. Other analytical examples of the comparison of incomplete and exact sensitivities are shown in (Mohammadi & Pironneau 2001).

5.2. *Reduced-complexity models and incomplete sensitivities*

One cheap way to improve the incomplete evaluation of sensitivities is to use the linearization of models of reduced complexity to approximate the last term in (5.2). In other words, consider the following reduced model for the definition of $\tilde{U}(x) \sim U(x)$. Suppose for instance $\tilde{U}$ is the Newton formula for the pressure and U the pressure from the Euler system. Consider the following approximate simulation loop:

$$x \to q(x) \to \tilde{U}(q(x))(\frac{U(x)}{\tilde{U}(x)}). \tag{5.4}$$

The incomplete gradient of J with respect to x can be improved by evaluating the last term in (5.2) linearizing (5.4) instead of (5.1) freezing $U/\tilde{U}$.

$$\frac{dJ}{dx} \sim \frac{\partial J(U)}{\partial x} + \frac{\partial J(U)}{\partial q}\frac{\partial q}{\partial x} + \frac{\partial J(U)}{\partial U}\frac{\partial \tilde{U}}{\partial x}\frac{U(x)}{\tilde{U}(x)}. \tag{5.5}$$

$\tilde{U}$ is used only in the definition of the gradient and not the state. The reduced model need be valid only over the support of the control parameters.

A simple example shows the importance of the scaling introduced in (5.4). Consider $U = \log(1+x)$ scalar for simplicity and $j = U^2$ with $dj/dx = 2UU' = 2\log(1+x)/(1+x) \sim 2\log(1+x)(1-x+x^2...)$ and consider $\tilde{U} = x$ as the reduced complexity model, valid around $x = 0$. Without the scaling factor incomplete sensitivity gives $j' \sim 2U\tilde{U}' = 2\log(1+x)$ while after introducing the local correction $j' \sim 2U\tilde{U}'(U/\tilde{U}) = 2\log(1+x)(\log(1+x)/x) \sim 2\log(1+x)(1-x/2+x^2/3...)$. Here the scaling is taken linear in U but higher order approximations can be introduced as well.

5.3. *Sensitivity of sonic boom to the near field pressure*

Consider the simulation loop for the calculation of a cost function to measure the sonic boom for a given parameterization x of the shape:

$$B(x) : x \to q(x) \to p_H \to p_g(p_H, \text{atmosphere prop.}) \to B(p_g),$$

where p_H is the near-field pressure distribution at altitude H, which is a function of the state variables (solution of the Euler equations), and p_g is the solution of the waveform-propagation method on the ground.

The gradient of B with respect to x requires the linearization of the different operators involved:

$$\frac{dB}{dx} = \frac{\partial B}{\partial p_g}\frac{\partial p_g}{\partial p_H}\frac{\partial p_H}{\partial q}\frac{\partial q}{\partial x}. \tag{5.6}$$

This evaluation is of course expensive when the dimension of the control space is large. Usually an adjoint approach is used to make the cost of the evaluation independent of the size of the control space (Alonso *et al.* 2002; Mohammadi & Pironneau 2001). This is done in particular in the case of steady flows, where the storage of intermediate states is not required and the adjoint is developed around the steady solution. This can be done in either continuous or discrete forms using automatic differentiation (AD).

In the context of sonic-boom evaluation using the waveform-propagation method, due

to coalescing shocks, one would prefer to perform the adjoint development at the discrete, not the continuous level, using automatic differentiation in reverse mode. Indeed, the non-differentiability of some operators involved and the presence of discontinuity are naturally taken into account in this approach. This is because in discrete form a discontinuity is always represented by a continuous function. In any event, it would be necessary to save all intermediate solutions of the waveform parameter method between the flight altitude and the ground to be able to integrate backward for the adjoint using the reverse mode of automatic differentiation (Gilbert et al 1991, Griewank 2001, Faure 1996, Rostaing *et al.* 1993, Mohammadi & Pironneau 2001).

Sonic boom can be monitored minimizing, for instance, one of the following functionals:

$$B_{min} = \left(\frac{I(p_g) - aI(p_g^0)}{I(p_g^0)} \right)^2, \quad I = \int_{\text{ground}} |\Delta p_g| d\gamma, \tag{5.7}$$

with $0 < a < 1$ and p_g^0 the pressure signature on the ground for the original shape and

$$B_{inv} = \alpha \int_{\text{ground}} (p_g - p_g^{target})^2 d\gamma + \beta \int_{\text{ground}} (p_g - p_g^{target})^\delta d\gamma,$$

$$\alpha > 0, \quad \beta > 0, \quad \alpha + \beta = 1.$$

where p_g^{target} is a user-specified target pressure distribution on the ground. But the target pressure might be unrealizable and the optimization problem without solution.

B_{min} is a measure of the accumulation of pressure jumps on the ground and the aim is to reduce these jumps. a cannot be 0 as we cannot completely remove the boom.

On the other hand, by minimizing B_{inv}, we realize a target pressure signature on the ground having less boom. In B_{inv}, the second integral in the cost function is used to avoid the functional being flat close to the minimum. $0 < \delta < 1$ is also an optimization parameter and has to be chosen. In this work, we consider $\delta = 0.3$. We studied the importance of such functionals in Cabot & Mohammadi (2002) and Mohammadi & Saiac (2002) for a model problem.

The difficulty with B_{inv} is that the prescribed ground pressure might not be associated to a feasible flow field while B_{min} does not involve an *a priori* ground-pressure distribution. In addition, we will see that $\partial B_{min}/\partial p_H$ is less sensitive to discrepancies in the near-field flow prediction, due for instance to the mesh quality.

Once $\partial B/\partial p_H$ is computed (for either B_{min} or B_{inv}, see figure 5), we evaluate its product with the operator $\partial p_H/\partial x$. This latter evaluation requires the linearization of the Euler system which we would like to avoid. We have two alternatives:

- to use reduced complexity models for sensitivity analysis,
- to redefine the functional and adapt the problem to the context of incomplete sensitivities.

5.3.1. *Reduced-complexity models*

The first approach to reduce the complexity of the sensitivity analysis is to replace, only for sensitivity analysis, the Euler system by the waveform-propagation method, propagating the wall pressure distribution (p_x) directly to the ground (instead of just from altitude H). We require p_x to be a solution of the Euler equations:

$$x \to q(x) \to p_x \to p_g.$$

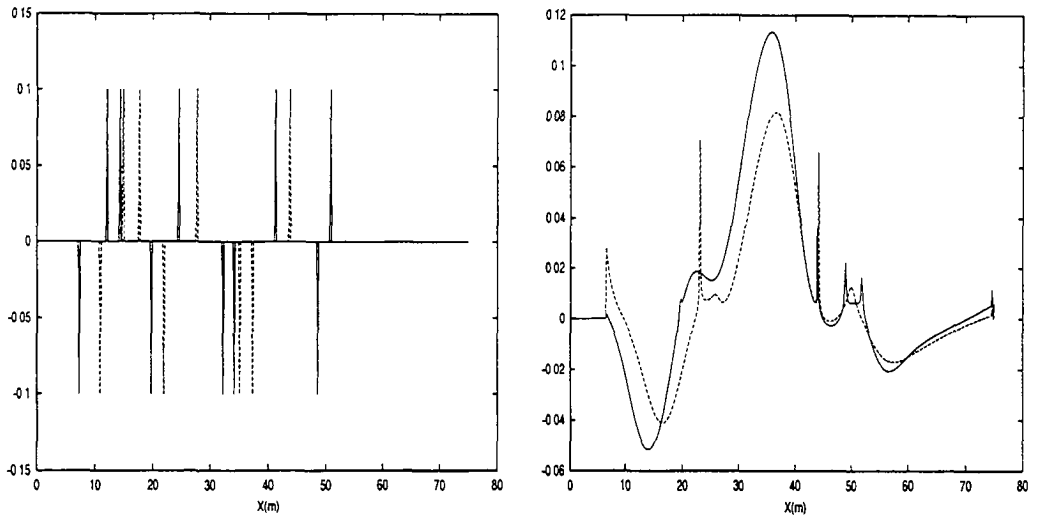

FIGURE 5. $\partial B_{min}/\partial p_H$ (left) and $\partial B_{inv}/\partial p_H$ (right) in the plane of symmetry close to (plane curves) and far from (dashed curves) from the aircraft. We see that $\partial B_{min}/\partial p_H$ is less sensitive to the altitude (only a shift is observed in the location of the delta functions). This also shows that the waveform-propagation model is a suitable reduced-complexity model, to be considered instead of the Euler system in the analysis of the sensitivity of the sonic boom to the aircraft shape.

To compute dp_g/dx we need finally to find an approximation linking p_x and the shape x to be used in the linearization (instead of the Euler system). For inviscid flows, in regions of high curvature, a good approximation is given by the Newton formula for the pressure distribution over walls. We therefore account only for the effect of the pressure distribution on the shape of the near-field pressure signature. We therefore have to account for the part of the boom coming from the shocks away from the wall. By keeping the shocks bow and the leading edges as smooth as possible, this requirement is satisfied.

6. Cost function definition

The functionals B_{min} and B_{inv} accounting for the sonic boom have been introduced above. In this work, we also consider constraints on aerodynamic coefficients as well as geometric characteristics of the aircraft.

More precisely, we consider the problem of drag (C_d) minimization with constraints on the lift (C_l), volume (V) and maximum cross-section thickness (d) defined for each node. In our approach the mesh is unstructured and the surface mesh is made of triangles. In the cross-sectional definition of the shape the number of sections is arbitrary and depends on the complexity of the geometry. The sections are obtained by intersecting vertical planes with the shape. The maximum thickness d of each section is evaluated. Then, each node in the surface mesh is associated with two sections and linear interpolation is used to define the maximum cross-section thickness associated with this node (see figure 6). The cost function is given by:

$$J(x) = |C_d - C_d^{des}| + (C_l^0 - C_l)_+ + (\mathrm{V}^0 - \mathrm{V})_+ + \int_{\text{shape}} |d - d_0| d\gamma + B(x).$$

Notation 0 denotes initial shape values. $C_d^{des} \leq C_d^0$ is the target value for the drag

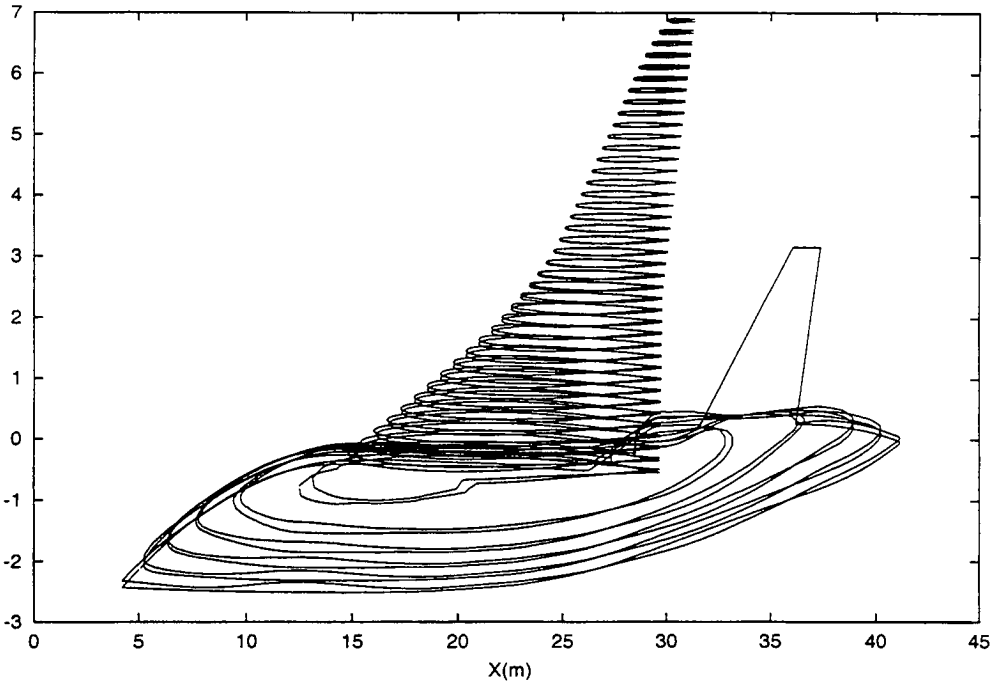

FIGURE 6. Cross-section definition of the shape used to enforce the maximum cross-section thickness constraint for the original and optimized aircraft.

coefficient. $B(x)$ is either B_{min} or B_{inv} from (5.7). $(.)_+ = \max_r(0,.)$ where $\max_r$ is a regularized max. The aim is to avoid the volume and lift coefficient from decreasing.

6.1. *Redefinition of J for incomplete sensitivity evaluation*

We said that a cost function based on informations away from the wall is not suitable for incomplete sensitivity evaluation. In particular, since B_{inv} and B_{min} are defined on the ground and not on the shape, we propose a reformulation of the functional linking the pressure signature on the ground to wall-based quantities. This is done together with the use of the waveform propagation method for the evaluation of $\partial p_g/\partial x$ as seen above.

We think that bow shocks introduce less pressure jump than attached shocks. Bow shocks are usually associated with smooth geometries. On the other hand, shape optimization based on drag reduction in supersonic regime leads to sharp leading edges. Therefore, to avoid an increase in the boom, it is important to keep the leading edges of the aircraft smooth while doing drag reduction. We introduce the following requirements:

- Specify that the wall near leading edges has to remain smooth. This is monitored through the smoother in the CAD-free framework see above.
- Ask for the local drag force C_d^{loc} due to the leading edge to remain unchanged or to increase while the global drag force decreases.

The cost function therefore becomes:

$$\tilde{J}(x) = |C_d - C_d^{des}| + (C_l^0 - C_l)_+ + (\mathrm{V}^0 - \mathrm{V})_+ + \int_{\text{shape}} |d - d_0| d\gamma + ((C_d^{loc})^0 - (C_d^{loc}))_+,$$

where C_d^{loc} is the measure of the drag force over regions where $\vec{n}.\vec{u}_\infty < 0$ ($\vec{n}$ being the

local outward normal to the shape). Introducing a differentiable localization function $f(s^+)$ such that $(0 \leq f(s^+) \leq 1)$, C_d^{loc} is defined as:

$$C_d^{loc} = \frac{2}{\rho_\infty |\vec{u}_\infty|^2} \int_{shape} p.\vec{n}.\vec{u}_\infty f(s^+) d\Gamma, \quad s^+ = \frac{\vec{n}.\vec{u}_\infty}{|\vec{n}.\vec{u}_\infty|}.$$

This differentiable localization term is used to avoid non-differentiability for C_d^{loc} and to allow for integration over the whole shape.

In addition to the previous modification of the functional, we introduce regularity requirements for areas where $(f(s^+) \neq 0)$. This is also monitored through the smoothing operator available in the CAD-free parameterization.

7. Full aircraft optimization

We consider a supersonic business jet geometry provided by Dassault Aviation company (see figure 4 and 4). The cruise speed is Mach 1.8 at zero incidence and the flight altitude is 55000 ft. The results show the performance of the optimization method including the validity of the incomplete sensitivity approach and the reformulation of the functional we use for this configuration.

We performed 1000 steepest-descent minimization iterations. At each iteration, an incomplete evaluation of the state (10 explicit Runge-Kutta iterations of the Euler solver) is performed. The global cost of this optimization is comparable to one flow analysis with this code (about 10000 explicit RK iterations) and takes about 4 hours on a 1GHz PC with 500 MB of RAM. In figure (7) we show a cross-section of the close field CFD pressure signature close to the aircraft in the symmetry plane and a the ground pressure signature for the initial and optimized shapes. Figure (8) shows upper and lateral views of aircraft surface iso-Mach contours. Picture (9) shows iso-contours of normal deformations with respect to the original shape. During optimization, the drag has been reduced by 20 percent while the lift has been increased by 10 percent. Geometric constraint on the volume and maximum cross-section thickness has been satisfied and the value of C_d^{loc} maintained.

8. Conclusions

Shape optimization in a CAD-Free framework using incomplete state and gradient evaluations has been presented for a multi-criteria optimization problem involving requirements for the acoustic, aerodynamic and geometric characteristics of jetliners. It has been shown that this platform is suitable for such a realistic design and that the complexities of the optimization and simulation are now comparable. In particular, it has been shown that incomplete sensitivities give satisfactory results after a reformulation of the cost functional. This allows a better understanding of sonic boom origins and mechanisms, and provides useful input to the design of future supersonic civil transports with a controlled boom and reduced drag.

9. Acknowledgements

This work has been supported by the French Committee for Scientific Orientation for Supersonic Transport and the Center for Turbulence Research at Stanford University. The geometry of the SSBJ was provided by Dassault Aviation Company. I would like

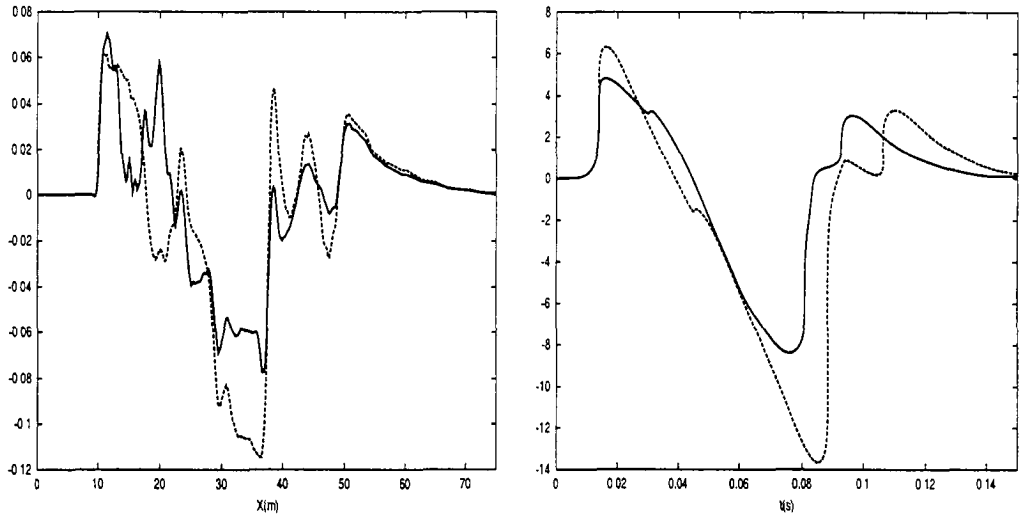

FIGURE 7. Cross-section of the near-field CFD pressure variations ($\frac{p-p_\infty}{p_\infty}$) in the symmetry plane (left) and the corresponding ground pressure signatures (right) for the initial (dashed curves) and optimized (continuous curves) shapes. We observe a non trivial impact of the modification of the near-field pressure distribution on the ground pressure.

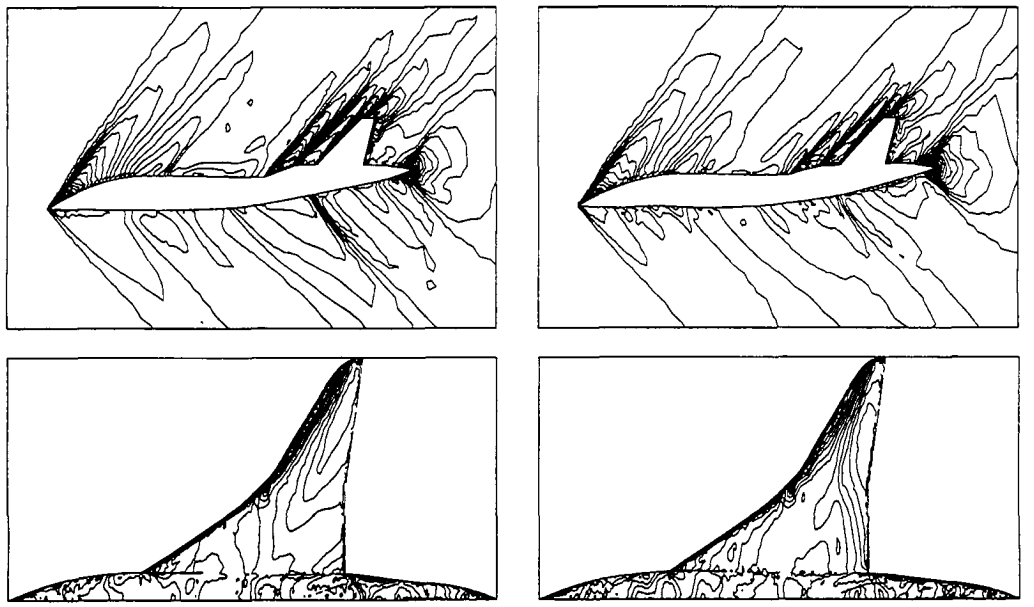

FIGURE 8. Upper: near-field iso-Mach contours for the initial and optimized aircraft in the symmetry plane. Lower: Upper surface iso-Mach contours for the initial and optimized aircraft.

to thank in particular B. Stoufflet, M. Mallet, Ph. Rostand and G. Rogé of Dassault Aviation for their suggestions. I would like also to thank Prof. S. Candel, A. Dervieux, D. Jeandel, P. Moin and O. Pironneau for their interest in this work realization. Thanks also to Dr. J. Alonso, M. Fatica and B. Koobus for the scientific interactions we had on

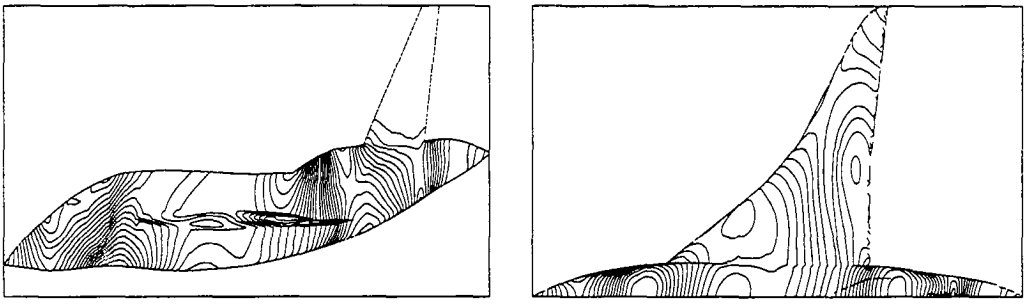

FIGURE 9. Iso-contours of normal deformation with respect to the original shape.

this subject. Many thanks to Dr. M. Wang for his helpful feedback on this manuscript. I am grateful to M. Chethik, C. Gichane-Bell, M. Lomuljo-Bautista and D. Michael for their assistance during my stay at CTR.

REFERENCES

ALONSO, J.J. & KROO, I. M. & JAMESON, A. 2002 Advanced algorithms for design and optimization of QSP, *AIAA Paper* 2002–0144.

CABOT, A. & MOHAMMADI, B. 2002 Incomplete sensitivities and cost function reformulation leading to multi-criteria investigation of inverse problems: Application to a Model Problem. *Optimization, theory and control* (to appear).

FAURE C. 1996 Splitting of algebraic expressions for automatic differentiation. *Proc. of the Second SIAM Workshop on Computational Differentiation,* Santa Fe, NM.

GILBERT J.C., LE VEY G. & MASSE J. 1991 La différentiation automatique de fonctions représentées par des programmes. *INRIA research report,* Rocquencourt, France.

GRIEWANK A. 2001 *Computational differentiation.* Springer, New York.

MOHAMMADI, B. 1994 CFD with NSC2KE : user-guide. *INRIA Tech. note* 164, Rocquencourt, France.

MOHAMMADI, B. & SAIAC, J. H. 2002 *Pratique de la simulation numérique.* Dunod, Paris.

MOHAMMADI, B. & PIRONNEAU, O. 2001 *Applied shape optimization for fluids.* Oxford Univ. Press.

POLAK E. 1997 *Optimization: algorithms and consistent approximations.* Springer, New York.

ROSTAING N., DALMAS S. & GALLIGO A. 1993, Automatic differentiation in Odyssee, *Tellus,* **45a**, *558–568.*

THOMAS, C. L. 1972 *Extrapolation of sonic boom pressure signatures by the waveform parameter method. NASA TN* D-6832.

WITHAM, G. B. 1952, The flow pattern of a supersonic projectile, *Comm. Pure and Appl. Math.* **5–3**, 301–348.

Optimization of cylinder flow control via actuators with zero net mass flux

By P. Catalano†, M. Wang, G. Iaccarino, Ivo F. Sbalzarini‡, AND P. Koumoutsakos¶

A direct search method in combination with a DNS/LES numerical approach is applied to optimize the control of the flow around a circular cylinder. The objective is the minimization of the drag coefficient and control is achieved via actuators with zero net mass flux. The optimization process has been first evaluated and validated at Reynolds number 500 and then the more demanding flow at Reynolds number 3900 has been considered. The search of the optimum has been carried out in 2D simulations, and a 3D simulation, indicating similar drag reduction, has been performed using the parameters of the 2D optimization.

1. Introduction

Flow control has the potential of manipulating flow fields in order to achieve transition delay/advancement, separation prevention/provocation, and turbulence suppression/enhancement. The modifications of these flow properties can lead to large benefits in aeronautical applications, such as increased aerodynamic efficiency, reduced structural weight, reduced operating costs and reduced emissions. In addition flow control techniques are employed to improve the aerodynamic capabilities of wings at off-design conditions, and to maintain performance throughout the flight envelope of vehicles whose design is driven by mission requirements (i.e. unmanned, stealth) and not by aerodynamic considerations.

Flow-control methods can be classified as passive or active. Passive control devices, such as riblets, vortex generators, and boundary-layer trips, have been shown to be quite effective in delaying flow separation, but cannot adapt to changes of the incoming flow, and introduce a drag penalty if the flow does not separate. Active-control approaches, such as external and internal acoustic excitation, vibrating ribbons or flaps, and steady and unsteady blowing and suction, couple the control input to the flow instabilities and can operate in a broad range of conditions. However, so far, active flow-control methods have relied on sophisticated and complicated support systems that require their own power supply devices.

A novel concept for active flow control is the use of Micro Electronic Mechanical Systems (MEMS). The MEMS couple sensors, control and logic electronics, and actuators into a single low-weight compact device. Several low-power MEMS such as microflaps, surface heating elements and synthetic jets have been used for flow control. Synthetic jets (Glezer & Amitay 2002) are active control devices with zero net mass flux which do not require internal fluid supply lines. They consist of an oscillating membrane located at the bottom of a cavity having small orifices in the face opposite the membrane. When

† CIRA Italian Aerospace Research Center, Via Maiorise 81043 Capua (CE), Italy
‡ Institute of Computational Science, ETH Zürich, Switzerland
¶ Institute of Computational Science, ETH Zürich, Switzerland

the membrane moves upwards fluid is expelled through the orifice, and a shear layer is formed at the orifice edge. The shear layer rolls up to form a vortex ring that moves away from the orifice under its own momentum. When the membrane moves downwards fluid enters into the cavity. This entrainment process is not affected by the vortex ring, which is supposed to be sufficiently far from the cavity. Over one period of oscillation of the membrane the net mass flux is zero.

Actuators based on synthetic-jet techniques have been shown to be very effective for several applications of aerodynamic flow control. The modification of the global forces on a circular cylinder induced by applying synthetic jets has been investigated experimentally at Reynolds numbers of up to 1.3×10^5 by Amitay *et al.* (1997) and Amitay, Smith & Glezer (1998). They found that the interaction between the jet and the main flow induces a local separation bubble that acts as a virtual surface and displaces the streamlines outside the undisturbed boundary layer. Drag increase and decrease can be achieved depending on the azimuthal location of the actuators. The control of the separated flow over an unconventional airfoil (cylindrical leading edge plus the aft portion of a NACA 4-digits serie) at Reynolds number 3×10^5 has been investigated experimentally by Smith *et al.* (1998) and Amitay *et al.* (1999, 2001). The airfoil without control stalls at $\alpha = 5°$, while with control fully-attached flow was achieved up to $\alpha = 15°$, and partial reattachment and recovery of lift were found up to $\alpha = 25°$.

In the present work, the synthetic jet is numerically modeled as time-periodic blowing and suction of fluid at the cylinder surface. The peak velocity, operating frequency, and location are the defining parameters of a synthetic jet actuator. The objective is to explore the use of a direct search technique, namely the response-surface method (Grigoriu 1982, Rackwitz 1982), to optimize the synthetic jet parameters. To this end, two-dimensional, unsteady laminar flows are first considered, with the expectation of future extension to turbulent flows at high Reynolds number, such as those in the experiment of Amitay, Smith & Glezer (1998). The drag coefficient of the flow at Reynolds numbers 500 and 3900 has been chosen as cost function. The optimization process has been carried out in 2D, and a 3D simulation using the 2D "optimum" actuator parameters has been performed for comparison.

2. Optimization techniques and numerical set-up

We implement a response-surface technique (Grigoriu 1982, Rackwitz 1982) in order to identify the optimal parameters for the control actuators. The response-surface method belongs to a class of optimization techniques which are called direct techniques because they do not use gradient information for the function minimization. Key advantages of such methods include their portability and robustness and their capability of escaping local minima. Disadvantages include relatively slow convergence rates as compared with gradient-based techniques, and and inefficiency in large dimensional spaces.

The response-surface technique relies on the iterative reconstruction of the initially-unknown cost function using the values acquired during the optimization. A surface is fitted to a set of function values obtained from an set of parameters chosen initiallly, and the minimum of this surface is found using analytical or gradient-based methods. The surface constitutes a model of the "true" cost function and the minimum found serves as the next candidate point for the iterative procedure. An extensive description of the method can be found in Booker *et al.* (1998).

The response-surface method, in combination with a LES/DNS numerical approach,

has been applied to find the minimum drag coefficient of the circular cylinder subject to control via synthetic jets. The optimization process has been first evaluated at Reynolds number 500 and then the flow at Reynolds number 3900 has been considered. The search of the optimum has been limited to the 2D flow, although a 3D simulation using the 2D optimal control parameters has also been carried out to investigate if the cost function reduction still exists.

An energy conserving Navier-Stokes flow solver (Choi 1993) of hybrid finite difference/spectral type using C meshes (Mittal & Moin 1997) has been employed in the numerical simulations. The equations are advanced in time using the fractional step approach, in combination with the Crank-Nicolson method for viscous terms and the third order Runge-Kutta algorithm for the convective terms. The continuity constraint is imposed at each Runge-Kutta substep by solving a pressure Poisson equation employing a multigrid iterative method. The dynamic procedure (Germano *et al.* 1991) together with a least-square contraction and spanwise averaging (Lilly 1992) is used to model the subgrid scale stress tensor. The numerical simulations have been performed in 3D using LES, and in 2D with the subgrid model switched off.

The actuator is modeled by imposing a velocity normal to the surface as

$$V_j = g(\theta_j) V_{jA} \sin\left(2\pi f_j \frac{V_\infty t}{D}\right) \tag{2.1}$$

where V_∞ is the free-stream velocity, θ_j is the jet location, and D is the cylinder diameter. The frequency is made proportional to the natural shedding frequency of the flow

$$f_j = k_j f_s \tag{2.2}$$

and $g(\theta_j)$ is assumed to be a top-hat function whose width b is that of the jet orifice (Rizzetta *et al.* 1998).

The momentum transferred by the jet to the main flow is measured by the following coefficient defined as

$$C_\mu = \frac{2\rho_j V_{jA}^2 b}{\rho_\infty V_\infty^2 D} \tag{2.3}$$

where ρ_j the density of the jet.

The parameters that define the synthetic jet model are the amplitude, the frequency, and the location. The objective of this work is to apply a direct search method to find the values of V_{jA}, k_j, and θ_j that minimize the drag coefficient C_D of a circular cylinder.

3. Results

3.1. *Flow at Reynolds number* 500

First, two simulations without control, on meshes of 201×60 points and 401×80 points, have been performed to compute the reference value of the drag coefficient. The resulting C_{D0} was 1.390 on the coarse mesh and differed by only 0.5% on the fine mesh, suggesting that the coarse mesh is sufficient for the optimization iterations. The computed flow exhibits vortex shedding with a Strouhal number of about 0.2, and with the flow separating from the rear part of the cylinder at about $\theta = 105°$.

A first search for the minimum drag coefficient has been performed keeping the amplitude V_{jA} constant with a momentum coefficient C_μ of 6.5×10^{-3} and varying the jet location and the frequency. The surface $C_D = f(\theta_j, k_j)$ has been computed by means of a series of 2D simulations. To initialize the optimization process, four additional points

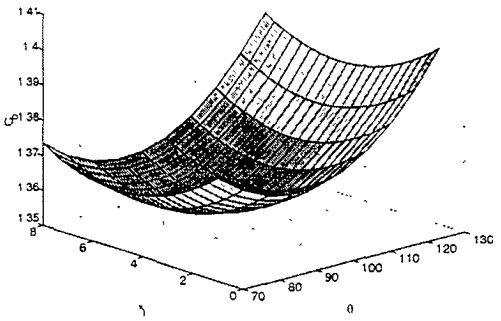

FIGURE 1. Approximate surface $C_D = f(\theta_j, k_j)$ at $Re = 500$, at the last iteration.

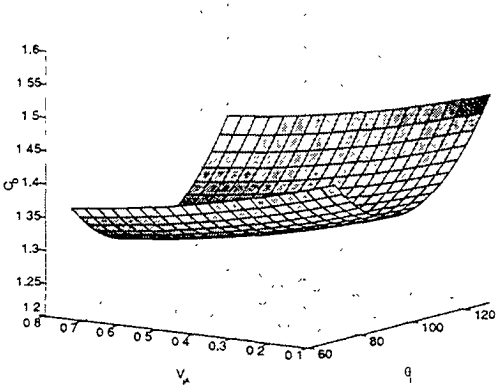

FIGURE 2. Approximate surface $C_D = f(\theta_j, V_{jA})$ at $Re = 500$, at the last iteration.

in the $(\theta_j,\ k_j)$ parameter space are obtained. The optimization process has been carried out iteratively, evaluating the minimum of the response surface at each iteration. Convergence is reached in six steps and the response surface at the final iteration is shown in Figure 1. The optimum values found for θ_j and k_j, and the resulting reduction in drag coefficient with respect to the unforced flow

$$\Delta C_D = \frac{C_{D0} - C_D}{C_{D0}}, \tag{3.1}$$

are reported in the first row of table 1.

From figure 1, it can be seen that the drag coefficient depends more strongly on θ_j than on k_j. Hence, another search with the frequency constant and θ_j and V_{jA} variable has been performed. The final response surface is shown in figure 2, and the optimum parameters found are reported in the second row of the table 1. A decrease of about 6% in C_D has been achieved.

To check if the reduction in C_D persists when the flow is three-dimensional, a 3D LES using the optimum parameters (second row of table 1) found in 2D is performed. A mesh of $401 \times 120 \times 49$ points with a spanwise domain size of four times the cylinder diameter is used. The simulation has been advanced for about 300 time units (based on D/V_∞) and the value obtained for the mean C_D is 1.104. This is about 8% lower than the experimental value for the unforced flow (as given by Zdravkovich 1997).

In an attempt to reduce the drag coefficient further, a spanwise variation of the jet amplitude has been introduced. The jet is modeled as

$$V_j = g(\theta_j) V_{jA} \sin\left(2\pi k_z z\right) \sin\left(2\pi f_j \frac{V_\infty t}{D}\right) \tag{3.2}$$

where $k_z = 0.5$, and V_{jA}, k_j and θ_j are the values reported in table 1 (second row). The C_D obtained was 1.130, lower than the experimental unforced value but higher than the drag coefficient found with a jet with constant V_{jA}. However an optimization using k_z as an additional parameter has not been performed.

The flow at this Reynolds number is seen to be fairly insensitive to the control applied, and the decrease obtained for the cost function has been quite small. In order to achieve a larger reduction of the cost function, and to further validate the methodology used, two

TABLE 1. Optimum synthetic jet parameters at $Re = 500$

	V_{JA}	θ_j	k_j	ϕ	$\Delta C_D\%$
One jet	0.14	89.8°	4.4	-	4
One jet	0.59	93.9°	5.0	-	6
Two jets	0.62	93.9°	4.18	132°	12

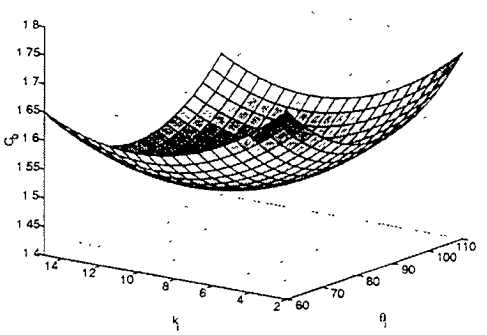

FIGURE 3. Approximate surface $C_D = f(\theta_j, k_j)$ at $Re = 3900$ at the last iteration.

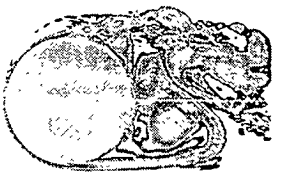

FIGURE 4. 2D Flow at $Re = 3900$ forced by a synthetic jet located at $\theta = 85.12°$ with $C_\mu = 6.5 \times 10^{-3}$. 50 contours (levels from 1 to 50 with exponential distribution) of the instantaneous vorticity magnitude are plotted.

jets located symmetrically with respect to the streamwise direction and with different phase ϕ have been considered. The amplitude and the location are kept fixed, while the frequency and the phase are chosen as the parameters to optimize. The reduction in C_D is 12% and the optimal k_j and ϕ are reported in the third row of table 1.

3.2. *Flow at Reynolds number* 3900

The drag coefficient of the unforced flow has been obtained by employing a mesh of 401×120 points. Its value of 1.719 compares well with the C_D for instantaneously-2D flow computed by Beaudan & Moin (1994). The mean flow exhibits two symmetrical recirculation bubbles from about $\theta = 105°$ to $\theta = 120°$, and coherent vortex shedding with a Strouhal number of about 0.22.

The search for the minimum drag coefficient has been performed taking the location and the frequency as parameters to optimize, while keeping the amplitude fixed with a momentum coefficient of 6.5×10^{-3}. The response surface at the last iteration is shown in figure 3 and the optimum values found are reported in table 2. The reduction in drag coefficient is about 13%. The instantaneous vorticity field of the 2D flow forced by a synthetic jet using the optimum values is presented in figure 4. The small-scale vortices due to the interaction of the jet with the boundary layer are clearly visible.

A 3D LES, with the optimum jet parameters found in 2D, has also been performed. The mesh used has $401 \times 120 \times 49$ points and the spanwise width of the computational

TABLE 2. Optimum synthetic jet parameters at $Re = 3900$

V_{JA}	θ_j	k_j	$\Delta C_D\%$
0.14	85.12°	9.21	13

domain is πD. The simulation has been advanced for about 270 time units and the resulting mean C_D is 1.01. The unforced flow around a circular cylinder at $Re = 3900$ has been investigated numerically using LES by Beaudan & Moin (1994), who found a mean drag coefficient of 1.00. The unforced experimental value (Norberg 1987) is 0.98 ± 0.05.

Evidently, the optimized jet parameters found from the (admittedly artificial) 2D simulation does not work for the 3D turbulent flow. This is not unexpected since the flow structures are different. In particular, the points of boundary layer separation, which affects the optimal location of the actuator, are more advanced in the 3d case than in 2D. It has not been possible, due to lack of time, to carry out the optimization using 3D simulations during the summer program. However this remains our longer-term objective.

4. Conclusions

A response-surface method, in combination with a LES/DNS numerical approach, has been applied to minimize the drag coefficient of the flow over a circular cylinder controlled via synthetic jet actuators. The optimization process has been evaluated and validated in 2D model problems at Reynolds numbers of 500 and 3900. 3D simulations using optimal parameters obtained from 2D have also been performed.

The process has been successful, although the flow is shown to be quite insensitive to the controls applied, and the decrease in cost function is quite small at Reynolds number 500. At Reynolds number 3900, the drag coefficient reduction is more significant according to 2D computations, but this result is not reproduced in 3D with the same set of control parameters. Overall, we have demonstrated the robustness of the technique for this type of control problems. Optimization using 3D simulations at higher Reynolds number will be of longer-term interest beyond the summer program.

5. Acknowledgments

The authors wish to thank Dr. A. Crook for the many fruitful discussions held during the Summer Program.

REFERENCES

AMITAY, M., HONOBAN, A., TRAUTMAN, M. & GLEZER, A. 1997 Modification of the aerodynamic characteristics of bluff bodies using fluidic actuators. *AIAA Paper* 97-2004.

AMITAY, M., SMITH, B. L. & GLEZER A. 1998 Aerodynamic flow control using synthetic jet technology. *AIAA Paper* 98-0208.

AMITAY, M., KIBENS, V., PAREKH, D. & GLEZER, A. 1999 The dynamics of flow reattachment over a thick airfoil controlled by synthetic jet actuators. *AIAA Paper* 99-1001.

AMITAY, M., SMITH, D. R., KIBENS, V. & GLEZER A. 2001 Aerodynamic flow control over an unconventional airfoil using synthetic jet actuators. *AIAA J.* **39**, 361–370.

BEAUDAN, P. & MOIN, P. 1994 Numerical experiments on the flow past a circular cylinder at sub-critical Reynolds number. *Mech. Engg Dept., Stanford Univ. Rept.* TF-62.

BOOKER, A. J., DENNIS, J.E., FRANK, P.D., SERAFINI, D. B., TORCZON, V. & TROSSET, M. 1998 A rigorous framework for optimization of expensive functions by surrogates. *ICASE Rept.* 98-47.

CHOI, H. 1993 Toward large eddy simulation of turbulent flow over an airfoil. *Annual Research Briefs*, Center for Turbulence Research, NASA Ames/Stanford Univ., 145–149.

GERMANO, M., PIOMELLI, U., MOIN, P. & CABOT, W. H. 1991 A dynamic subgrid-scale eddy viscosity model. *Phys. Fluids A* **3**, 1760–1765.

GLEZER, A. & AMITAY, M. 2002 Synthetic jets. *Annu. Rev. Fluid Mech.* **34**, 503–529.

GRIGORIU, M. 1982 Methods for approximate reliability analysis. *Structural Safety* **1**, 155-165.

LILLY, D. K. 1992 A proposed modification of the Germano subgrid scale closure method. *Phys. Fluids A* **3**, 2746–2757.

MITTAL, R. & MOIN, P. 1997 Suitability of upwind-biased finite difference schemes for large eddy simulation of turbulent flows. *AIAA J.* **35**, 1415–1417.

NORBERG, C. 1987 Effects of Reynolds number and a low-intensity free-stream turbulence on the flow around a circular cylinder. *Dept. of Appl. Thermodynamics and Fluid Mech., Chalmers Univ. of Tech., Gothenburg, Sweden, Publ. No.* 87/2.

RACKWITZ, R. 1982 Response surfaces in structural reliability. *Berichte zur Zuverlässigkeitstheorie der Bauwerke* **67**, TU München.

RIZZETTA, D. P., VISBAL, M. R. & STANEK, J. 1998 Numerical investigation of synthetic jet flowfields. *AIAA Paper* 98-2910.

SMITH, D., AMITAY, M., KIBENS, V., PAREKH, D. & GLEZER, A. 1998 Modification of lifting body aerodynamics using synthetic jet actuators. *AIAA Paper* 98-0209.

ZDRAVKOVICH, M. M. 1997 *Flow around circular cylinders. Vol 1 : Fundamentals.* Oxford University Press.

Machine learning for biological trajectory classification applications

By Ivo F. Sbalzarini†, Julie Theriot ‡ AND Petros Koumoutsakos ¶

Machine-learning techniques, including clustering algorithms, support vector machines and hidden Markov models, are applied to the task of classifying trajectories of moving keratocyte cells. The different algorithms are compared to each other as well as to expert and non-expert test persons, using concepts from signal-detection theory. The algorithms performed very well as compared to humans, suggesting a robust tool for trajectory classification in biological applications.

1. Motivation and Objectives

Empirical sciences create new knowledge by inductive learning from experimental observations (*data*). Biology, or life science in general, is a prime example for a field that is facing a rapidly growing amount of data from continuously more sophisticated and efficient experimental assays. The general lack of predictive models makes quantitative evaluation and learning from the data one of the core processes in the creation of new knowledge. Trajectories of moving cells, viruses or whole organisms are a particularly interesting example, as they represent dynamic processes. The application of machine-learning techniques for automatic classification of data mainly serves 3 goals: First, one wishes to learn more about the biological or biochemical processes behind the observed phenomenon by identifying the parameters in the observation that are significantly influenced by a certain change in experimental conditions (*causality detection*). Second, the information contents of a given data set with respect to a certain property of interest may be estimated (*capacity estimation*) and third, automatic identification and classification of vast amounts of experimental data (*data mining*) could facilitate the process of interpretation. The paper starts by formally stating the problem of classification and introducing the notation. Then, different machine-learning techniques are summarized, starting from clustering methods in the d-dimensional real space $\mathbb{R}^d$ and proceeding to risk-optimal separation in $\mathbb{R}^d$ and dynamic signal source models in $\mathbb{R}^d \times \mathbb{T}$. Finally, the results of two automatic classification experiments of keratocyte cell trajectories are presented and compared to the performance of human test subjects on the same task.

2. The classification problem

Classification is one of the fundamental problems in machine-learning theory. Suppose we are given n classes of objects. When we are faced with a new, previously unseen object, we have to assign it to one of the classes. The problem can be formalized as follows: we are given m empirical data points

† Institute of Computational Science, ETH Zürich, 8092 Zürich, Switzerland
‡ Department of Biochemistry, Stanford University
¶ Institute of Computational Science, ETH Zürich and CTR/NASA Ames

$$(x_1, y_1), \ldots, (x_m, y_m) \in \mathcal{X} \times \mathcal{Y} \tag{2.1}$$

where $\mathcal{X}$ is a non-empty set from which the *observations* (sometimes called *patterns*) are taken and in the present context $\mathcal{Y} = \{1, \ldots, n\}$. The $y_i \in \mathcal{Y}$ are are called *labels* and contain information about which class a particular pattern belongs to. Classification means *generalization* to unseen data points (x, y), i.e. we want to predict the $y \in \mathcal{Y}$ given some new observation $x \in \mathcal{X}$. Formally, this amounts to the *estimation* of a function $f : \mathcal{X} \mapsto \mathcal{Y}$ using the input-output *training data* (2.1), generated independent and identically distributed (i.i.d.) according to an unknown probability distribution $P(x, y)$, such that f will optimally classify unseen patterns $x \in \mathcal{X}$. The criterion of optimality is to minimize the *expected risk*

$$R[f] = \int_{\mathcal{X} \times \mathcal{Y}} l\,(f(x), y)\; dP(x, y) \tag{2.2}$$

where l denotes a suitably chosen *cost function*. A common choice is the *0/1-loss*, for which $l(f(x), y)$ is 0 if (x, y) is a correct classification and 1 otherwise. Unfortunately, the expected risk cannot be minimized directly, since the underlying probability distribution $P(x, y)$ is unknown. Therefore, machine-learning algorithms try to *approximate* $R[f]$ based on the available information from the training data. The most common approximation is the *empirical risk*

$$R_{emp}[f] = \frac{1}{m} \sum_{i=1}^{m} l\,(f(x_i), y_i) \tag{2.3}$$

Different classifiers use different approximations to (2.2) as well as different methods to minimize those approximations.

3. Machine-learning methods used

3.1. *k-nearest neighbors (KNN)*

One of the simplest classifiers if $\mathcal{X} = \mathbb{R}^d$ is the k–nearest neighbor (KNN) algorithm. A previously unseen pattern x is simply assigned to the same class $y \in \mathcal{Y}$ to which the majority of its k (to be chosen) nearest neighbors belongs. The algorithm can be seen as a very simple form of a self-organizing map (Kohonen (2001)) with fixed connections.

3.2. *Gaussian mixtures with expectation maximization (GMM)*

Gaussian mixture models (GMM) are more sophisticated clustering algorithms in $\mathcal{X} = \mathbb{R}^d$. They make use of Gaussian probability distributions on $\mathbb{R}^d$ and try to approximate the unknown distribution $P(x, y)$ on $\mathcal{X} \times \mathcal{Y}$ by a mixture of n Gaussians $\mathcal{N}_i(x, y, \mu_i, \Sigma_i)$ with means $\mu_i \in \mathbb{R}^d$, $i = 1, \ldots, n$ and covariance matrices $\Sigma_i \in \mathbb{R}^{d \times d}$, $i = 1, \ldots, n$. The parameters μ_i and Σ_i are chosen so as to maximize the *log-likelihood* that the given training data has actually been drawn i.i.d. from the probability distribution $P(x, y) = \sum_{i=1}^{n} \mathcal{N}_i(x, y, \mu_i, \Sigma_i)$. The algorithm can be written as follows:

Step 1: Choose a set of initial means $\mu_1, \ldots, \mu_n$ using the *k–means* clustering algorithm (Hartigan & Wong (1979)); all covariances are initialized to identity: $\Sigma_i = I_d$.

Step 2: Assign the m training samples to the n clusters Γ_i using the *minimum Mahalanobis distance rule*: Sample x belongs to cluster Γ_i if the corresponding log-likelihood measure becomes minimum, i.e. $i = \arg\min_i \left[\log\left(\det\left(\Sigma_i\right)\right) + \left(x - \mu_i\right)^\top \left(\Sigma_i\right)^{-1} \left(x - \mu_i\right)\right]$.

Step 3: Compute new means $\mu_i \leftarrow \sum_{x \in \Gamma_i} x / \#\{\Gamma_i\}$ and new covariance estimates $\Sigma_i \leftarrow \sum_{x \in \Gamma_i} \left(x - \mu_i\right)\left(x - \mu_i\right)^\top / \#\{\Gamma_i\}$, where $\#\{\Gamma_i\}$ denotes the number of vectors x assigned to cluster Γ_i in step 2.

Step 4: If the changes in the means and covariances are smaller than a certain tolerance, stop; otherwise go to step 2.

3.3. *Support Vector Machines (SVM)*

Support vector machines (SVM) are kernel-based classifiers (Müller *et al.* (2001)) for binary classification in $\mathcal{X} = \mathbb{R}^d$. Past applications included time-series prediction (Mukherjee *et al.* (1997)), gene expression analysis (Brown *et al.* (2000)) as well as DNA and protein analysis (Zien *et al.* (2000)). SVM make use of the following theorem of *statistical learning theory* by Vapnik (1998) that gives an upper bound for the expected risk:

Theorem 1: Let h denote the Vapnik-Chervonenkis (VC) dimension of the function class $\mathcal{F}$ and let $R_{emp}[f]$ be the empirical risk for the 0/1-loss of a given classifier function $f \in \mathcal{F}$. It holds, with probability of at least $1 - \delta$, that:

$$R[f] \leq R_{emp}[f] + \sqrt{\frac{h\left(\log\frac{2m}{h} + 1\right) - \log\left(\frac{\delta}{4}\right)}{m}} \tag{3.1}$$

for all $\delta > 0$, for $f \in \mathcal{F}$ and $m > h$.

The VC dimension h of a function class $\mathcal{F}$ measures how many points $x \in \mathcal{X}$ can be separated in all possible ways using only functions of the class $\mathcal{F}$. Kernel methods use a mapping $\Phi(x)$ of the training data x into a higher-dimensional *feature space* $\mathcal{H}$ in which it can be separated by a hyper-plane $f(\mathbf{x}) = (\mathbf{w} \cdot \Phi(\mathbf{x})) + b$. In $\mathcal{H}$, the optimal separating hyper-plane is determined such that the points $\Phi(x)$ closest to it (called the *support vectors*) have maximum distance from it, i.e. such that the "safety margin" is maximized. This is done by solving the quadratic optimization problem $(\mathbf{w}, b) = \arg\min_{\mathbf{w},b} \frac{1}{2}||\mathbf{w}||_2^2$ subject to the condition that $\mathbf{w} \cdot \Phi(\mathbf{x}) + b$ is a separating hyper-plane. Solving the dual optimization problem, the Lagrange multipliers α_i, $i = 1, \ldots, s$ are obtained, where s is the number of support vectors. The classifier function f in $\mathcal{H}$ is then given by:

$$f(x) = \frac{3}{2} + \frac{1}{2} \cdot sign\left(\sum_{i=1}^{s} y_i \alpha_i \left(\Phi(x) \cdot \Phi(x_i)\right) + b\right)$$

Since this depends only on the scalar product of the data in feature space, the mapping Φ does not need to be explicitly known. Instead, a *kernel function* $k(x, x_i)$ is introduced such that $k(x, x_i) = \Phi(x) \cdot \Phi(x_i)$. The support vector classifier $f : \mathcal{X} \mapsto \{1, 2\}$ to be evaluated for any new observation thus is:

$$f(x) = \frac{3}{2} + \frac{1}{2} \cdot sign\left(\sum_{i=1}^{s} y_i \alpha_i k(x, x_i) + b\right) \tag{3.2}$$

Notice that the sum runs only over all support vectors. Since generally $s \ll m$, this allows efficient classification of a new observation by comparing it to a small relevant subset of the training data.

3.4. *Hidden Markov models (HMM)*

Hidden Markov models (HMM) are stochastic signal source models, i.e. they do not require observations $x \in \mathbb{R}^d$ but can treat discrete dynamic time series $x = \{O_1, \ldots, O_T\} \in \mathcal{X}$, $O_i \in \mathbb{R}$. In the past, their most successful application was in speech recognition (Rabiner (1989)). An HMM attempts to model the source producing the signal x as a dynamic system which can be described at any time t as being in one of r distinct discrete states, $Q_1, \ldots, Q_r$, which are hidden, i.e. cannot be observed. At regularly-spaced discrete times $t_i = i\delta t$, $i = 1, \ldots, T$, the system changes its internal state, possibly back to the same state. The process is assumed to be Markovian, i.e. its probabilistic description is completely determined by the present and the predecessor state. Let q_i denote the actual state of the system at time t_i. The Markov property thus states that $P[q_i = Q_j | q_{i-1} = Q_k, q_{i-2} = Q_l, \ldots] = P[q_i = Q_j | q_{i-1} = Q_k]$ where $P[E|F]$ denotes the probability of an event E given that F occurred. The state transitions are described by probabilities $a_{jk} = P[q_i = Q_k | q_{i-1} = Q_j]$ forming the elements of the state transition matrix A and obeying the constraints $a_{jk} \geq 0 \; \forall \; j, k$ and $\sum_{k=1}^{r} a_{jk} = 1$. At each time point t_i the system produces an observable output O_i, drawn from the output probability distribution $b_{Q_i}(O)$ associated with state Q_i; $B = \{b_{Q_j}\}_{j=1}^{r}$. The model is completed with the initial state probabilities $\pi = \{\pi_j = P[q_1 = Q_j]\}_{j=1}^{r}$ and the complete HMM is denoted by $\lambda = (A, B, \pi)$.

Given the form of HMM described above, there are three basic problems of interest that must be solved (Rabiner (1989)):

(1) Given an observation $x = \{O_1, \ldots, O_T\}$ and a model $\lambda = (A, B, \pi)$, compute the probability $P[x|\lambda]$ that the observation x has been produced by a source described by λ.

(2) Given an output sequence $x = \{O_1, \ldots, O_T\}$ and a model $\lambda = (A, B, \pi)$, determine the most probable internal state sequence $\{q_1, \ldots, q_T\}$ of the model λ that produced x.

(3) Determine the model parameters $\lambda = (A, B, \pi)$ to maximize $P[x|\lambda]$ for a given observation x.

3.4.1. *Discrete hidden Markov models (dHMM)*

If the set of possible distinct values $\{v_k\}$ of any output O_i is finite, the HMM is called *discrete* (dHMM). The output probability distribution of any state Q_j is thus discrete: $b_{Q_j} = \{b_{Q_j}(k) = P[O_i = v_k | q_i = Q_j]\}$ for $k = 1, \ldots, M$.
Direct solution of problem (1) would involve a sum over all possible state sequences: $P[x|\lambda] = \sum_{\forall\{q_1,\ldots,q_T\}} P[x|\{q_1, \ldots, q_T\}, \lambda] P[\{q_1, \ldots, q_T\}|\lambda]$. The computational cost of this evaluation is $\mathcal{O}(2Tr^T)$, which is about 10^{50} for an average dHMM and thus clearly unfeasible. The *forward-backward algorithm*, as stated by Baum & Egon (1967), Baum & Sell (1968), solves this problem efficiently in $\mathcal{O}(r^2 T)$. The solution of problem (2) is given by the *Viterbi algorithm* (Viterbi (1967), Forney (1973)) and the "training problem" (3) is solved using the iterative *Baum-Welch expectation maximization method* (Dempster *et al.* (1977)).

3.4.2. *Continuous hidden Markov models (cHMM)*

If the observations O_i are drawn from a continuum, b_{Q_i} is a continuous probability density function and the HMM is called *continuous* (cHMM). The most general case for which the above three problems have been solved is a finite mixture of M Gaussians $\mathcal{N}_k$, thus $b_{Q_j}(O) = \sum_{k=1}^{M} c_{jk} \mathcal{N}_k(O, \mu_{jk}, \Sigma_{jk})$ (see Liporace (1982), Juang *et al.* (1985)).

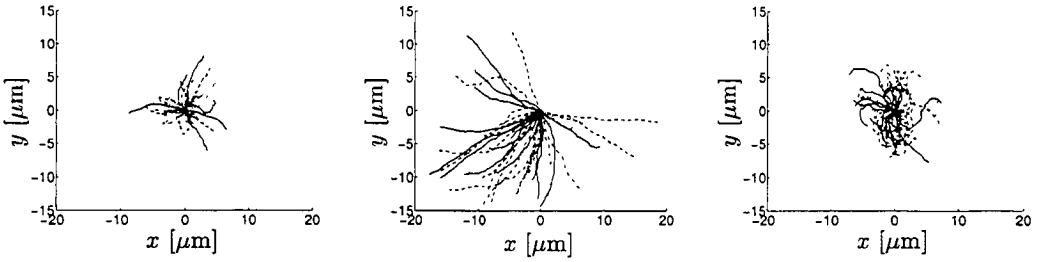

10°C observation 20°C observation 30°C observation

FIGURE 1. Temperature data set. 46 trajectories of moving keratocytes were used per class. The 3 classes are defined by the 3 temperatures at which the observations were made. All trajectories are shifted such that they start at the origin of the coordinate system.

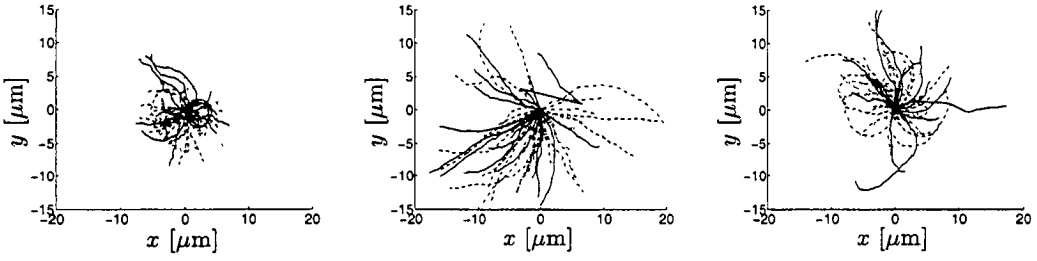

10°C acclimation 16°C acclimation 25°C acclimation

FIGURE 2. Acclimation data set. 58 trajectories of moving keratocytes were used per class. The 3 classes are defined by the 3 temperatures at which the fish were acclimated for 3 weeks prior to the experiment. All trajectories are shifted such that they start at the origin of the coordinate system.

4. Application to trajectory classification

4.1. *The data*

All machine-learning classifiers described in the previous section were applied to the task of classifying trajectories of living cells. The cells were keratocytes taken from the scales of the fish *Gillichthys mirabilis* (commonly called longjawed mudsucker). Isolated cells cultured on glass coverslips were observed using an inverted phase-contrast microscope connected to a video camera. The 2D trajectories of the moving cells were then extracted from the movies using the semi-automatic tracking software Metamorph (Universal Imaging, Inc.) yielding position readings at equidistant sampling intervals of $\delta t = 15\,\mathrm{s}$. The observations x in the present case were position/time data sets, thus $\mathcal{X} = \mathbb{R}^2 \times \mathbb{T}$ where $\mathbb{T}$ denotes the discrete ordered time space. Two different experiments were performed: For the *temperature data set*, fish were acclimated at 16°C, i.e. they were kept in water of this temperature for at least 3 weeks† prior to cell isolation. The movement of the isolated cells was then recorded at 10°C, 20°C and 30°C using a temperature-controlled microscope stage. 167 trajectories (46 at 10°C, 63 at 20°C and 58 at 30°C) from 60 different cells were collected. To make all classes the same size, 46 trajectories were used from each making a total of $N = 138$. Figure 1 shows them for the 3 temperature classes. For the *acclimation data set* all cells were observed at 20°C but they were taken from three different fish populations acclimated at 10°C, 16°C and 25°C, respectively. From

† After this time the adaptive changes in liver lipid content are complete.

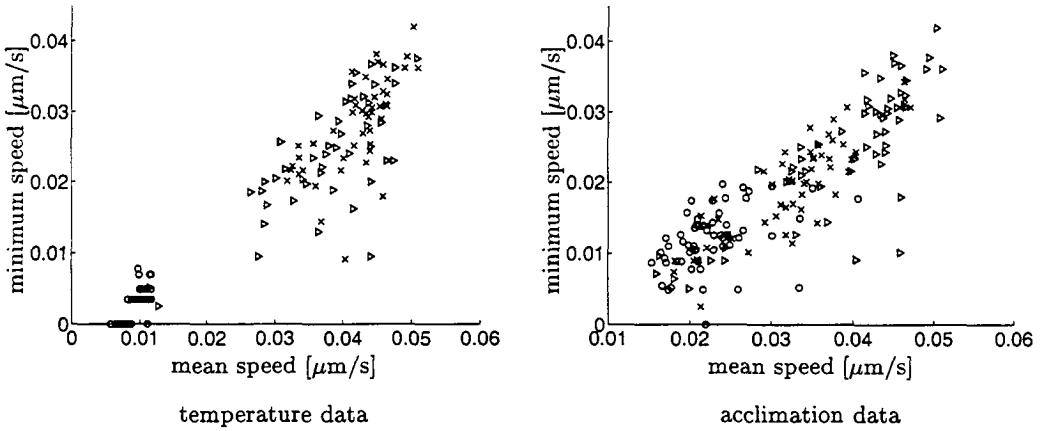

FIGURE 3. Encoded data sets. Both the temperature data set (left) and the acclimation data set (right) were encoded using the average and the minimum of the speed along a trajectory. Data points from the 10°C temperature and 10°C acclimation classes are denoted by circles (○), those from the 20°C temperature and 16°C acclimation classes by triangles (▷) and those from the 30°C temperature and 25°C acclimation classes by crosses (×).

the recorded 184 trajectories (58 for 10°C, 63 for 16°C, 63 for 25°C) of 60 different cells a total of $N = 174$ (58 in each class) was used as shown in figure 2. Both data sets have $n = 3$ classes.

4.2. *Data preprocessing and encoding*

Since the trajectories $x \in \mathbb{R}^2 \times \mathbb{T}$ are not vectors in $\mathbb{R}^d$, encoding is necessary for all machine-learning algorithms considered. HMM are capable of handling dynamic data in $\mathbb{R} \times \mathbb{T}$ and thus need the least encoding. Since the reaction rates of many biochemical processes that contribute to cell movement depend on temperature, the latter is suspected to influence the speed of the movement. The encoding for the cHMM was thus chosen to be the momentary speed of the movement along the trajectory. For dHMM the speed was discretized into 4 equidistant bins. One HMM was trained for each of the 3 classes. After evaluating the probability $P[x|\lambda_i]$ of a new observation x against the models λ_i for all classes $i = 1, 2, 3$, x is assigned to the class which has the highest probability. For all other algorithms, a quasi-static representation in $\mathbb{R}^d$ has to be found. The following properties were calculated for all trajectories: average speed, standard deviation of speed, mean angle of direction hange between 2 subsequent measurement points, standard deviation of those angles, distance between first and last point of trajectory compared to its total path length, decay of autocorrelation functions of speed and direction-change angle, minimum and maximum occurring speed and angle change. Histograms of the distribution of these properties among the different classes of trajectories gave evidence about which are the most discriminating properties. For the following considerations, the mean and the minimum of the speed of a trajectory over time were taken as encoding properties. The trajectories were thus represented as vectors in $\mathbb{R}^2$. Figure 3 shows the encoded data sets for both the temperature and the acclimation cases. It can be seen that the clusters mostly overlap, making the data non-separable in this encoding space.

4.3. *Classification and evaluation of the results*

The different classification algorithms were trained on a subset of $m = N/2$ data points from each set and then tested on the remainder of the data. For the KNN we set $k = 5$

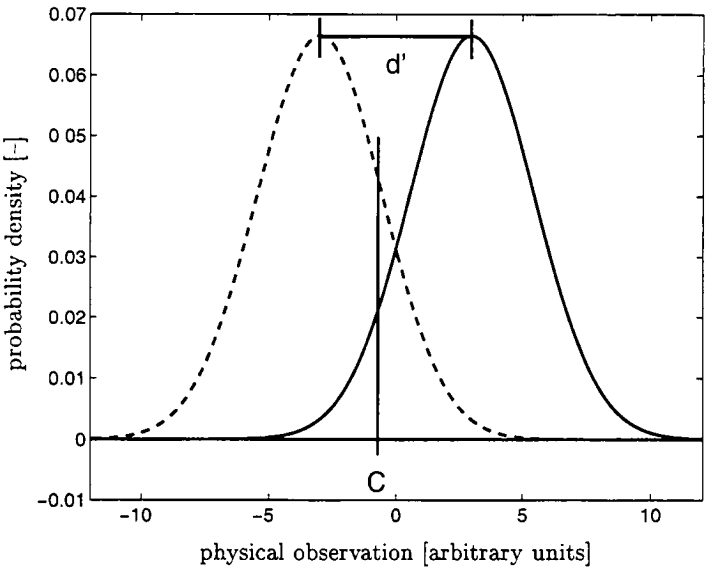

FIGURE 4. Schematic of the theory of signal detection. Observations that belong to a class i of interest occur at a certain probability (———) and observations that do not belong to that class occur at a different probability (- - - -). The classifier chooses a threshold C and will assign all future observations above C to the class of interest. The discrimination capability of the classifier is given by the normalized distance measure d'.

and for the SVM a Gaussian kernel with standard deviation $\sigma = 0.05$ was used. To reduce the random influence of which particular data points are taken for training and which for testing, the whole procedure was repeated 4 times for different partitioning of the data into training and test sets. Let $\mathcal{D} = \{(x_j, y_j),\ j = 1, \ldots, N\}$ be the complete data set of all N recorded trajectories x_j with corresponding class labels y_j, a random $\mathcal{T} \subset \mathcal{D}$ with $\#\{\mathcal{T}\} = m$ the *training set* and $\mathcal{E} \subset \mathcal{D}$ with $\#\{\mathcal{E}\} = N - m$ and $\mathcal{E} \cap \mathcal{T} = \emptyset$ the *test set*. An algorithm, trained on $\mathcal{T}$, classifies the trajectories $x_j \in \mathcal{E}$ without knowing the correct y_j. The outcome of this classification is $\widetilde{y}_j$. The *hit rate* for class i is then defined as $h_i = \#\{x_j \in \mathcal{E} : \widetilde{y}_j = y_j = i\}/\#\{x_j \in \mathcal{E} : y_j = i\}$ where $\#\{\mathcal{A}\}$ denotes the number of elements in a set $\mathcal{A}$. The *false-alarm rate* (sometimes also called "false positives") for class i is given by $f_i = \#\{x_j \in \mathcal{E} : \widetilde{y}_j = i \wedge y_j \neq i\}/\#\{x_j \in \mathcal{E} : y_j \neq i\}$. The complementary quantities $m_i = 1 - h_i$ and $r_i = 1 - f_i$ are termed *miss rate* and *correct rejection rate*, respectively. In each classification experiment, both the hit rate and the false-alarm rate were recorded for each temperature class since they compose the minimal sufficient set of properties.

Using the *theory of signal detection* (Green & Sweets (1966)), which was originally developed in psychophysics and is widely used in today's experimental psychology, two characteristic parameters were calculated from h_i and f_i. Figure 4 depicts the basic idea: the occurrence of observations that belong to class i and such that they do not belong to class i is assumed to be governed by 2 different Gaussian probability distributions. During training, the classifier determines a threshold C above which it will assign all future observations to class i. If, after transformation to standard normal distributions, $C = 0$, the classifier is said to be "neutral"; for $C < 0$ it is called "progressive" and for $C > 0$ "conservative". The discrimination capability of the classifier is given by the separation distance d' of the two normalized (by their standard deviation) distributions.

class	hit [%]	f.a. [%]	d'	C
10°C	100.0	2.2	∞	-
20°C	54.4	24.5	0.8	0.29
30°C	46.7	22.9	0.7	0.41

TABLE 1. KNN on temperature data

class	hit [%]	f.a. [%]	d'	C
10°C	100.0	2.2	∞	-
20°C	54.3	15.7	1.1	0.46
30°C	68.5	20.7	1.3	0.15

TABLE 2. GMM on temperature data

class	hit [%]	f.a. [%]	d'	C
10°C	100.0	2.2	∞	-
20°C	51.1	27.2	0.6	0.29
30°C	41.3	24.4	0.5	0.46

TABLE 3. SVM on temperature data

class	hit [%]	f.a. [%]	d'	C
10°C	100.0	3.3	∞	-
20°C	77.2	28.3	1.3	-0.09
30°C	37.0	11.4	0.9	0.77

TABLE 4. dHMM on temperature data

class	hit [%]	f.a. [%]	d'	C
10°C	100.0	2.2	∞	-
20°C	76.1	30.5	1.2	-0.10
30°C	34.8	11.9	0.8	0.79

TABLE 5. cHMM on temperature data

$d' = 0$ corresponds to "pure random guessing" where hits and false alarms grow at equal rates and $d' = \infty$ characterizes a "perfect classifier". Since the hit rate is given by the area under the solid curve above C and the false-alarm rate is the area under the dashed curve above C, both C and d' can be calculated from h_i and f_i and the latter two completely describe the situation. Classifiers were compared based on d', since algorithms that are capable of better separating the two probability distributions will have a lower expected risk R.

5. Results

5.1. *Temperature data set*

The temperature data set as introduced in section 4.1 was classified using all the algorithms presented in section 3 and the results were evaluated according to section 4.3. Tables 1 to 5 state the average percentage of hits and false alarms (over all different partitioning of the data into training and test sets) as well as the normalized discrimination capabilities d' and thresholds C of the classifiers for each temperature class.

Figure 5 graphically displays the hit and false-alarm rates of the classifiers for the 3 temperature classes. The averages over all data partitionings are depicted by solid bars,

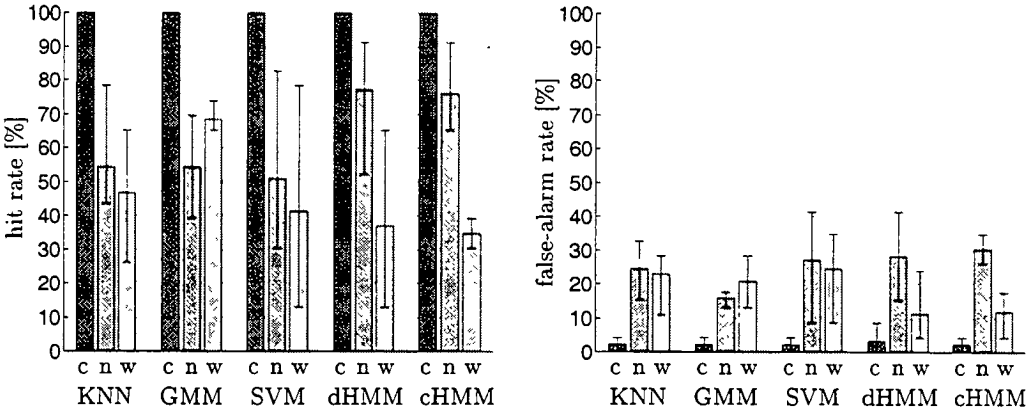

FIGURE 5. Hit and false-alarm rates for all classifiers. The percentage of hits (left) and false alarms (right) on the temperature data set is shown for each classifier in each of the 3 temperature classes: 10°C ("c"), 20°C ("n") and 30°C ("w"). The error bars range from the smallest observed rate to the largest one (min–max bars).

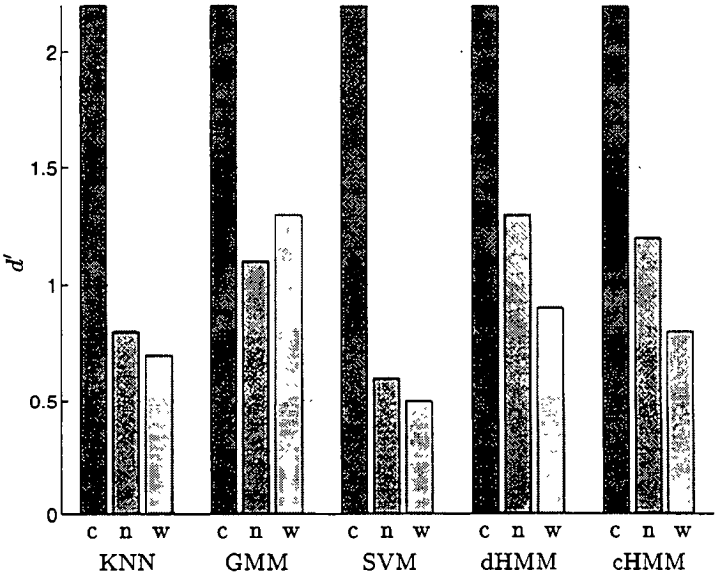

FIGURE 6. d' values for all classifiers. The value of the discrimination sensitivity on the temperature data set is shown for each classifier in each of the 3 temperature classes: 10°C ("c"), 20°C ("n") and 30°C ("w").

the error bars indicate the minima and maxima in the measurements. The d' values of the different classification methods are compared in figure 6.

5.2. *Acclimation data set*

The same classification experiments were also performed using the acclimation data set as introduced in section 4.1. The results are summarized in tables 6 to 10 using the same format as in the previous section. Figure 7 shows the average hit and false-alarm rates of the classifiers for the 3 temperature classes along with the min–max bars. Again the classifiers are compared against each other in figure 8 based on their d'.

class	hit [%]	f.a. [%]	d'	C
10°C	77.6	23.3	1.5	-0.02
16°C	59.5	15.5	1.3	0.39
25°C	41.4	22.0	0.6	0.50

TABLE 6. KNN on acclimation data

class	hit [%]	f.a. [%]	d'	C
10°C	88.0	21.1	2.0	-0.19
16°C	58.6	4.3	1.9	0.75
25°C	61.2	20.68	1.1	0.27

TABLE 7. GMM on acclimation data

class	hit [%]	f.a. [%]	d'	C
10°C	86.2	20.3	1.9	-0.13
16°C	62.9	9.9	1.6	0.48
25°C	54.3	18.1	1.0	0.40

TABLE 8. SVM on acclimation data

class	hit [%]	f.a. [%]	d'	C
10°C	84.5	20.3	1.8	-0.09
16°C	71.6	22.4	1.3	0.09
25°C	35.3	11.6	0.8	0.79

TABLE 9. dHMM on acclimation data

class	hit [%]	f.a. [%]	d'	C
10°C	75.0	19.4	1.5	0.09
16°C	56.0	6.9	1.6	0.67
25°C	61.9	27.2	0.9	0.15

TABLE 10. cHMM on acclimation data

class	hit [%]	f.a. [%]	d'	C
10°C	88.5	24.8	1.9	-0.26
16°C	47.3	16.5	0.9	0.52
25°C	33.8	23.8	0.3	0.57

TABLE 11. Humans on acclimation data

In addition to machine-learning algorithms, the acclimation data set was also classified by humans. After training on a set of 30 trajectories and their labels, the test subjects were presented with one unknown trajectory at a time. Individual position measurement points were symbolized by circles along the trajectory. Since they are equidistant in time, this includes information about the speed. All trajectories were shifted such as to start at $(0,0)$ and they were rotated by a random angle prior to presentation. Each person classified 174 trajectories appearing in random order. The average result over 5 test subjects is given in table 11. The best-performing person who declared after the experiment to have looked at speed information reached only $d' = 2.0$ for the 10°C class, $d' = 1.6$ for the 16°C class and $d' = 0.7$ for the 25°C class. The best person of all reached $d' = 2.1$, $d' = 1.9$ and $d' = 1.0$, respectively by taking into account both speed and shape (curvature) information. The lowest result of the test group was $d' = 1.9$, $d' = 0.1$, $d' = -0.6$.

6. Conclusions and future work

Considering the results of section 5, the following conclusions can be made: (1) All methods perform equally well in the case of separable clusters (10°C temperature class). (2) On the acclimation data set, GMM perform best, closely followed by SVM. This is evidence that the data is actually normally distributed. (3) All classifiers have relatively

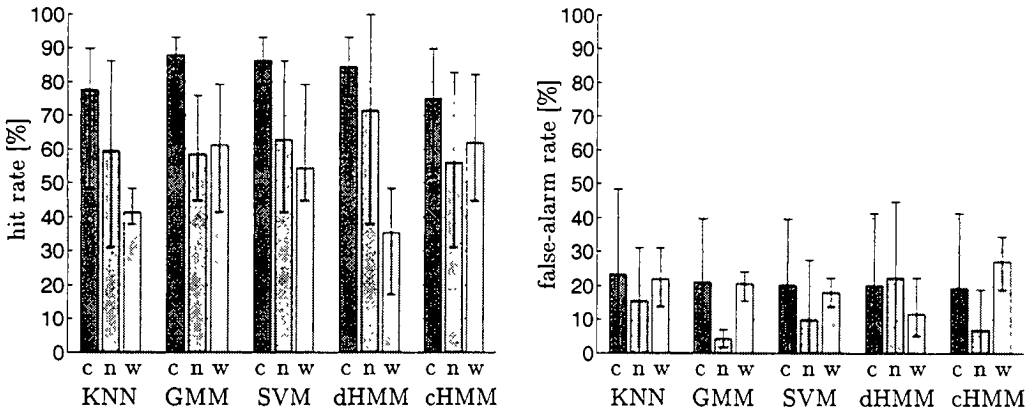

FIGURE 7. Hit and false-alarm rates for all classifiers. The percentage of hits (left) and false alarms (right) on the acclimation data set is shown for each classifier in each of the 3 temperature classes: 10°C ("c"), 16°C ("n") and 25°C ("w"). The error bars range from the smallest observed rate to the largest one (min–max bars).

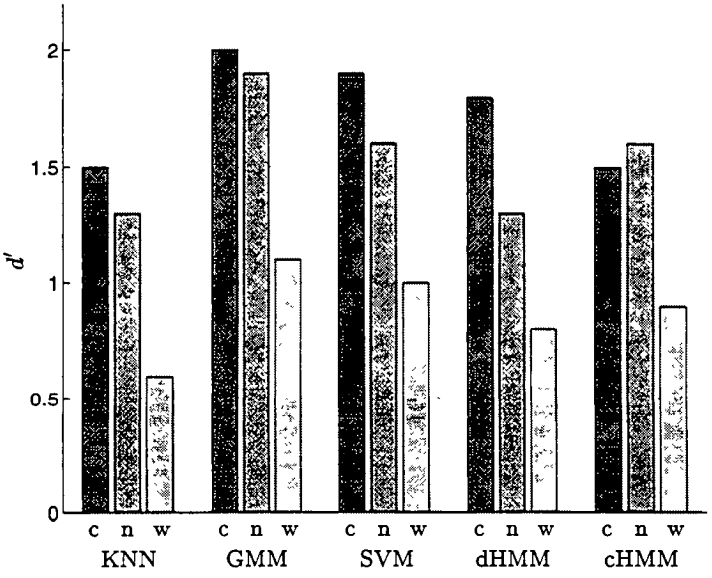

FIGURE 8. d' values for all classifiers. The value of the discrimination sensitivity on the acclimation data set is shown for each classifier in each of the 3 temperature classes: 10°C ("c"), 16°C ("n") and 25°C ("w").

low values of C, thus being more or less neutral. (4) The HMM methods are the least robust due to their dynamic character. The dHMM and the cHMM have comparable performance. (5) Humans on average perform less well than the algorithms. This could be due to bias based on prior information or expectations, fatigue effects or inaccuracy. (6) The best test person performs about equally well as the best machine-learning algorithm, indicating that the latter was able to extract and use all the information contained in the data set. In summary, it has been demonstrated that automatic classification of biological trajectories is possible with near-maximum accuracy and that machine-learning techniques can be a useful tool in estimating the information content and the relevant

parameters in a data set. Future work will be concerned with implementing a general-purpose framework code for classification of dynamic data sets in multiple dimensions. A modular approach will allow different classification algorithms to be used, and a preprocessor is envisaged that automatically detects those properties that best cluster (separate) the data at hand. Future applications will include the analysis of *Listeria* and *Shigella* movement inside host cells as well as virus movement and automatic virus detection and identification systems.

REFERENCES

BAUM, L. E. & EGON, J. A. 1967 An inequality with applications to statistical estimation for probabilistic functions of a Markov process and to a model for ecology. *Bull. Amer. Meteorol. Soc.* **73**, 360–363.

BAUM, L. E.&SELL, G. R. 1968 Growth functions for transformations on manifolds. *Pac. J. Math.* **27**, 211–227.

BROWN, M. P. S., GRUNDY, W. N., LIN, D., CRISTIANINI, N., SUGNET, C., FUREY, T. S., ARES, M.& HAUSSLER, D. 2000 Knowledge-based analysis of microarray gene expression data using support vector machines. *Proc. Natl. Acad. Sci. USA* **97**, 262–267.

DEMPSTER, A. P., LAIRD, N. M. & RUBIN, D. B. 1977 Maximum likelihood from incomplete data via the EM algorithm. *J. Roy. Stat. Soc.* **39**, 1–38.

FORNEY, G. D. 1973 The Viterbi algorithm. *Proc. IEEE* **61**, 268–278.

GREEN, D. M. & SWEETS, J. A. 1966 *Signal Detection Theory and Psychophysics*. Krieger, New York.

HARTIGAN, J. & WONG, M. 1979 A k-means clustering algorithm. *Appl. Stat.* **28**, 100–108.

JUANG, B. H., LEVINSON, S. E. & SONDHI, M. M. 1985 Maximum likelihood estimation for multivariate mixture observations of Markov chains. *IEEE Trans. Informat. Theory* **IT–32**, 307–309.

KOHONEN, T. 2001 *Self-Organizing Maps*, 3rd edn. Springer-Verlag, New York.

LIPORACE, L. A. 1982 Maximum likelihood estimation for multivariate observations of Markov sources. *IEEE Trans. Informat. Theory* **IT–28**, 729–734.

MUKHERJEE, S., OSUNA, E. & GIROSI, F. 1997 Nonlinear prediction of chaotic time series using a support vector machine. In *Neural Networks for Signal Processing VII – Proceedings of the 1997 IEEE Workshop* (J. Principe, L. Gile, N. Morgan and E. Wilson, eds.), pp. 511–520. IEEE.

MÜLLER, K.-R., MIKA, S., RÄTSCH, G., TSUDA, K. & SCHÖLKOPF, B. 2001 An introduction to kernel-based learning algorithms. *IEEE Trans. on Neural Networks* **12**, 181–202.

RABINER, L. R. 1989 A tutorial on hidden Markov models and selected applications in speech recognition. *Proc. IEEE* **77**, 257–286.

VAPNIK, V. N. 1998 *Statistical Learning Theory*. Wiley, New York.

VITERBI, A. J. 1967 Error bounds for convolutional codes and an asymptotically optimal decoding algorithm. *IEEE Trans. Informat. Theory* **IT–13**, 260–269.

ZIEN, A., RÄTSCH, G., MIKA, S., SCHÖLKOPF, B., LENGAUER, T. AND MÜLLER, K.-R. 2000 Engineering support vector machine kernels that recognize translation initiation sites in DNA. *Bioinformatics* **16**, 799–807.

On the boundary condition for water at a hydrophobic, dense surface

By J. H. Walther†, R. L. Jaffe‡, T. Werder†, T. Halicioglu‡
AND P. Koumoutsakos¶

We study the no-slip boundary conditions for water at a hydrophobic (graphite) surface using non-equilibrium molecular-dynamics simulations. For the planar Couette flow, we find a slip length of 64 nm at 1 bar and 300 K, decreasing with increasing system pressure to a value of 31 nm at 1000 bar. Changing the properties of the interface to from hydrophobic to strongly hydrophilic reduces the slip to 14 nm. Finally, we study the flow of water past an array of carbon nanotubes mounted in an inline configuration with a spacing of 16.4×16.4 nm. For tube diameters of 1.25 and 2.50 nm we find drag coefficients in good agreement with the macroscopic, Navier-Stokes values. For carbon nanotubes, the no-slip condition is valid to within the definition of the position of the interface.

1. Motivation and objectives

Macroscopic, Navier-Stokes modeling of problems in nano-fluidics may prove a computationally cost-effective alternative to themolecular-dynamics simulations usually employed at these length scales (Koplik & Banavar 1995) provided the complex fluid-solid interactions can find a suitable macroscopic model. At hydrophobic interfaces these interactions typically result in strong density fluctuations, anisotropic orientation of the water molecules (Lee *et al.* 1984), and, for solids with a high density, a finite fluid velocity (ΔU) at the interface (Helmholtz & von Piotrowski 1860; Schnell 1956; Churaev *et al.* 1984; Baudry *et al.* 2001). Thus while the kinematic boundary condition of impermability follows naturally from the definition of a fluid-solid interface, the issues relating to momentum transfer at the interface determining the dynamics of the problem is less clear. At moderate shear rates ($\partial u/\partial y$) the fluid remains Newtonian (Loose & Hess 1989), and the slip velocity may be described by the linear relation:

$$\Delta U = L_s \frac{\partial u}{\partial y}, \tag{1.1}$$

where L_s is the slip length. Experimental evidence of slip has been demonstrated in studies of water in hydrophobized quartz capillaries (Churaev *et al.* 1984) and in drainage experiments (Baudry *et al.* 2001) with slip lengths of 30 ± 10 nm and 38 ± 2 nm, respectively. While most experiments have focused on the presence of slip at hydrophobic surfaces and on the possible validity of the no-slip condition at hydrophilic surfaces, recent colloid probe experiments with water on mica and glass have indicated a persistent slip of 8–9 nm at these hydrophilic surfaces (Bonaccurso *et al.* 2002). Molecular dynamics-simulations of Poiseuille flow (Barrat & Bocquet 1999; Travis *et al.* 1997; Travis & Gub-

† Institute of Computational Science, ETH Zürich, Switzerland
‡ NASA Ames Research Center, USA
¶ Institute of Computational Science, ETH Zürich, Switzerland and CTR/NASA Ames

1997; Cieplak *et al.* 2001) of simple Lennard-Jones fluids confined between Lennard-Jones solids have demonstrated the presence of both slip, no-slip and locking (negative slip length) depending on the "corrugation" of the surface. Thus, no-slip and locking are observed for low-density solids, and slip is found to occur at strongly non-wetting interfaces, or for high-density solids. In a recent study of methane confined between dense, graphite surfaces Sokhan *et al.* (2001) found the slip to be fairly insensitive to the wetting properties of the surface, but to depend strongly on the density of the solid.

In this paper we present detailed non-equilibrium molecular dynamics (NEMD) simulations of water confined between hydrophobic, dense (graphite) surfaces. For the planar Couette flow, we study the influence of the system pressure on the slip length, and on the wetting behaviour of the interface, by artificially increasing the carbon-water Lennard-Jones interaction. To study the effect of geometry on the slip, we consider simulations of water flowing past an array of carbon nanotubes. This flow configuration furthermore serves as a preliminary study of carbon nanotubes as sensing devices in aqueous environments.

2. Governing equations and solution procedure

The present study employs non-equilibrium molecular-dynamics (NEMD) simulations of water-graphite and carbon nanotube-water systems. In these simulations the graphite and the carbon nanotubes are treated as rigid structures, to permit the maximum time step of 2 fs imposed by the SPC/E water model. The influence of modelling the solids as rigid structures is expected to be minor, as demonstrated in the recent work of Sokhan *et al.* (2001). However, for the flow past carbon nanotubes, the deformation of the tubes imposed by the motion of the water may prove significant and will be included in later studies. The governing Newton's equations are integrated in time using the leapfrog scheme, subject to periodic or quasi-periodic boundary conditions for the Couette and carbon nanotube flow problems, respectively. The algorithm has been parallelized using a domain decomposition technique and explicit message passing (MPI). The computational domain is distributed onto the processors and the atoms mapped accordingly. Atoms leaving their host processor during the simulation is are sent to the receiving processor. The bond topology is described through global pointers, and mapped onto a local pointer set on the host processor. A decomposition onto 16 processors of the flow past a carbon nanotube is shown in figure 1. The simulations were performed on the SGI Origin 2000 cluster at NASA Ames.

2.1. *Potentials*

The water is modelled using the standard SPC/E model which involves a Lennard-Jones term between the oxygen atoms

$$U(r_{ij}) = 4\epsilon_{OO}\left[\left(\frac{\sigma_{OO}}{r_{ij}}\right)^{12} - \left(\frac{\sigma_{OO}}{r_{ij}}\right)^{6}\right], \text{ for } r_{ij} < r_c, \tag{2.1}$$

where r_c is the radius of truncation ($U(r_{ij}) = 0$ for $r_{ij} > r_c$), and a Coulomb potential acting between all atom pairs from different water molecules

$$U(r_{ij}) = \frac{q_i q_j}{4\pi\epsilon_0}\frac{1}{r_{ij}}, \tag{2.2}$$

where ϵ_0 is the permittivity in vacuum, and q_i is the partial charge, $q_O = -0.8476$ and $q_H = 0.4238$, respectively (Berendsen *et al.* 1987). The Coulomb interaction is computed

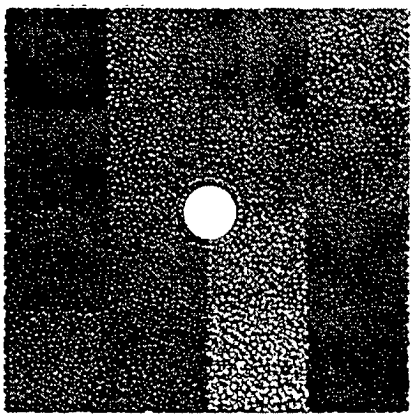

FIGURE 1. The parallel decomposition onto 16 processors for the NEMD simulations of the flow past a carbon nanotube. The different gray scale indicate the processor affiliation of the molecules.

using a smooth truncation as

$$U(r_{ij}) = \frac{q_i q_j}{4\pi\epsilon_0}\left(\frac{1}{r_{ij}} - E_s(r_{ij})\right), \text{ for } r_{ij} < r_c, \tag{2.3}$$

where $E_s(r_{ij})$ is a smoothing function (Levitt *et al.* 1997)

$$E_s(r_{ij}) = \frac{1}{r_c}\left(1 - \frac{r_{ij} - r_c}{r_c}\right), \tag{2.4}$$

and $U(r_{ij}) = 0$ for $r_{ij} > r_c$. The truncation of the Coulomb potential has been shown to have little effect on the thermodynamic and structural properties of bulk water (Andrea *et al.* 1984), and for water at interfaces (Walther *et al.* 2001; Werder *et al.* 2002). In this study we employ a cutoff of 1.0 nm, throughout. The bond length (r_W) and bond angle (θ_W) of the water are constrained using SHAKE (van Gunsteren & Berendsen 1977).

The carbon-water interaction consists of a Lennard-Jones term between the carbon and oxygen atoms

$$U(r_{ij}) = 4\epsilon_{CO}\left[\left(\frac{\sigma_{CO}}{r_{ij}}\right)^{12} - \left(\frac{\sigma_{CO}}{r_{ij}}\right)^{6}\right], \text{ for } r_{ij} < r_c, \tag{2.5}$$

and $U(r_{ij}) = 0$, for $r_{ij} > r_c$, and the parameters of the potential ϵ_{CO} and σ_{CO} are obtained from the experiments by Bojan & Steele (1987), with a modified ϵ_{CO} parameter obtained from molecular-dynamics simulations of the contact angle of water droplets on graphite (Werder *et al.* 2002). The parameters of the potentials are summarized in table 1.

3. Results

The results from the Couette and carbon nanotube studies are presented in terms of the time average profiles of the density

$$\rho_k = \frac{1}{V_k}\sum_{i}^{n_k} m_i, \tag{3.1}$$

r_W	=	1.000 Å	θ_W	=	109.47°	ϵ_{OO}	=	0.6502 kJ mol^{-1}
σ_{OO}	=	3.166 Å	q_O	=	−0.8486 e	q_H	=	0.4238 e
ϵ_{CO}	=	0.4389 kJ mol^{-1}	σ_{CO}	=	3.190 Å			

TABLE 1. Parameters for the SPC/E water model (Berendsen *et al.* 1987), and for the carbon-water interaction potentials cf. (Bojan & Steele 1987) and (Werder *et al.* 2002). r_W, and θ_W denote the water bond length and angle, respectively, and q_O and q_H the partial charges. ϵ_{OO} and σ_{OO} are the SPC/E Lennard-Jones parameters, and ϵ_{CO} and σ_{CO} the carbon-water (oxygen) Lennard-Jones parameters.

and streaming velocity

$$v_k = \frac{\sum_i^{n_k} m_i u_i}{\sum_i^{n_k} m_i}, \tag{3.2}$$

where m_i and u_i are the mass and velocity of the i-th atom, and n_k denotes the number of atoms in the k-th bin of volume V_k. The statistics for the Couette flow are sampled in Cartesian bins with a spacing in y-direction of 0.100 nm and 0.025 nm for the velocity and density profiles, respectively. A polar binning is used for the flow past a carbon nanotube with a radial bin resolution of 200 and 800 (a spacing of 0.32 and 0.08 nm) for the velocity and density profiles, respectively. The radial bins are subdivided in 6 bins in the circumferential direction. The slip length is extracted from the time average velocity profiles using a least square fit.

3.1. *Couette flow*

The simulations of the Couette flow involve from 240 to 1040 water molecules confined between a pair of (single) graphite sheets with a spacing of 1.35 nm to 4.72 nm depending on the system size and pressure. The size of the system in the streamwise (L_x) and spanwise (L_z) directions is 2.98 × 2.46 nm: see figure 2. The water molecules are initially placed on a regular lattice and the system is equilibrated for 40 ps to obtain a system temperature of 300 K and the desired pressure. Periodic boundary conditions are imposed in the streamwise and spanwise directions, and free space conditions are assumed in the wall-normal (y) direction. A Berendsen thermostat (Berendsen *et al.* 1984) is applied to adjust both the temperature and pressure, thus

$$L_y^{n+1} = L_y^n \left(1 - \frac{3\delta t}{\tau_p}(P_0 - P^n)\right), \tag{3.3}$$

where L_y^n denotes the spacing between the graphite sheets at the n-th time step, τ_p is the time constant of the thermostat (here $\tau_p = 0.1$ ps), and P_0 and P^n are the target and instantaneous pressure, respectively. The pressure is measured from the total normal forces acting on the graphite sheets as

$$P^n = \frac{1}{2L_xL_z}\sum_i^{n_c} f_i^n \cdot n_i, \tag{3.4}$$

where f_i^n denotes the force acting on the i-th carbon atom, n_c is the total number of carbon atoms, and n_i is the surface normal; see figure 2. The pressure bath is switched off after 40 ps, while maintaining the heat bath until 42 ps. The upper graphite wall is set into motion after 50 ps with a constant velocity (U) of 100 m s^{-1} throughout the 6 ns

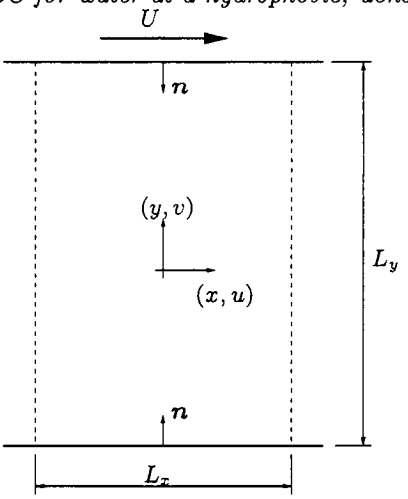

FIGURE 2. Sketch of the planar Couette flow problem. L_x and L_y denote the length of the unit cell in the streamwise (x) and wall-normal direction (y). The upper wall is forced to move with a constant velocity (U) and periodic boundary conditions are enforced in the streamwise and the spanwise (z) directions.

case	n_w	ϵ_{CO} kJ mol^{-1}	P (bar)	H (nm)	L_s (nm)
1	1040	ref.	10	4.72	63
2	1040	ref.	200	4.71	63
3	1040	ref.	500	4.60	42
4	1040	ref.	1000	4.50	31
5	1040	+50 %	200	4.66	33
6	1040	+100 %	200	4.59	14
7	800	ref.	200	3.70	41
8	240	ref.	200	1.35	∞

TABLE 2. Simulation cases for the planar Couette flow conducted at 300 K and pressures (P) of 10, 200, 500, and 1000 bar, respectively. The reference water-graphite van der Waals interaction given by ϵ_{CO} is 0.4389 kJ mol^{-1} (Werder *et al.* 2002). H denotes the spacing between the graphite surfaces, and L_s the slip length. n_w is the number of water molecules, and 560 carbon atoms were used in all the cases.

of simulation. The system did not experience any appreciable viscous heating during the course of the simulation. The results are summarized in table 2.

We first consider the influence of the system pressure on the amount of slip for system pressures of 10, 200, 500, and 1000 bar using the reference carbon-water interaction potential. At these pressures the time-average profiles of the streaming velocity shown in figure 3 reveal a decreasing slip length for increasing pressure, resulting in a slip of 63, 63, 42, and 31 nm, respectively. The peaks in the profiles for $|x| > 2$ nm are caused by the poor sampling at the interfaces. The large fluctuations in the pressure typical of these small systems lead to similar results for the 10 and 200 bar system. The tendency for decreasing slip with increasing system pressure is in agreement with the recent NEMD simulations of Lennard-Jones fluids confined between Lennard-Jones solids by Barrat & Bocquet (1999). Moreover, the magnitude of the slip is in good agreement with the experimental values of 30–40 nm: see Churaev *et al.* (1984) and Baudry *et al.* (2001).

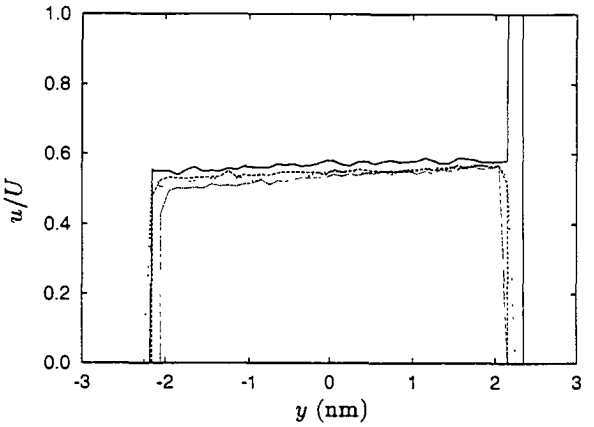

FIGURE 3. Time average streaming velocity profiles in a Couette flow as function of the system pressure: —: 10 bar (case 1); – –: 200 bar (case 2); - -: 500 bar (case 4); · · ·: 1000 bar (case 4).

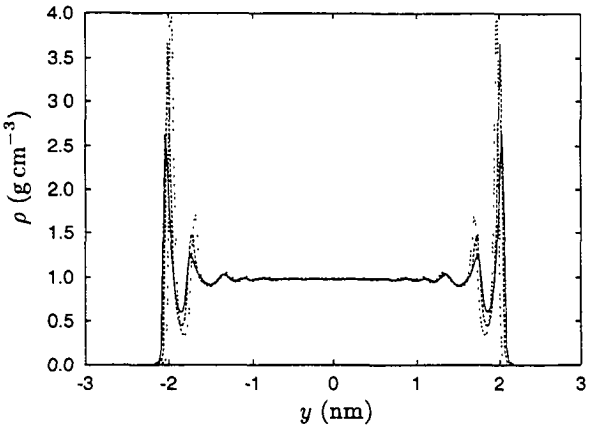

FIGURE 4. Time average density profile in a Couette flow as function of the wetting properties of the fluid-solid interface: —: $\epsilon_{CO} = 0.4389\,\mathrm{kJ\,mol^{-1}}$ (case 2); – –: $\epsilon_{CO} = 0.6594\,\mathrm{kJ\,mol^{-1}}$ (case 5); - -: $\epsilon_{CO} = 0.8778\,\mathrm{kJ\,mol^{-1}}$ (case 6).

Next we consider the influence of the wetting properties of the graphite-water interface by varying the strength of the Lennard-Jones interaction potential through an increase of the ϵ_{CO} parameter from the reference value of $0.4389\,\mathrm{kJ\,mol^{-1}}$ by 50 % ($0.6594\,\mathrm{kJ\,mol^{-1}}$) and 100 % ($0.8778\,\mathrm{kJ\,mol^{-1}}$). The corresponding macroscopic contact angle for these interaction potentials for water droplets on graphite is 85°, 30°, and 0°, respectively (Werder *et al.* 2002). The time average density profiles shown in figure 4 display the characteristic fluctuations at a solid surface with increased peak values for increased wetting. The corresponding streaming velocity shown in figure 5 reveals a marked influence on the slip length. Thus, the slip decreases from 63 nm for the reference interaction potential to 33 and 12 nm for the 50 % and 100 % systems, the latter in good agreement with the experimental value of 8–9 nm for water at a hydrophilic surface (Bonaccurso *et al.* 2002).

Finally, we consider the influence of the size of the system by changing the distance between the graphite sheets from 4.71 to 3.70 and 1.35 nm. The density profiles shown in

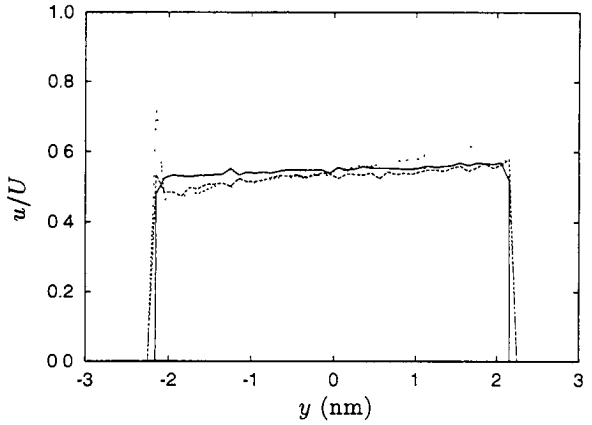

FIGURE 5. Time average streaming velocity profiles in a Couette flow as function of the wetting properties of the fluid-solid interface: —: $\epsilon_{CO} = 0.4389\,\mathrm{kJ\,mol^{-1}}$ (case 2); – –: $\epsilon_{CO} = 0.6594\,\mathrm{kJ\,mol^{-1}}$ (case 5); - -: $\epsilon_{CO} = 0.8778\,\mathrm{kJ\,mol^{-1}}$ (case 6).

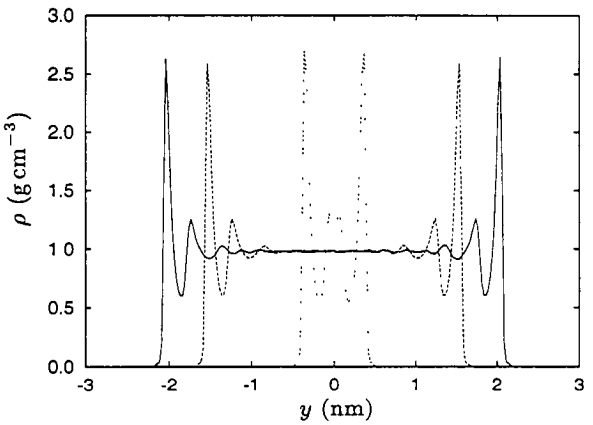

FIGURE 6. Time average density profile in a Couette flow as function of the size of the channel: —: $L_y = 4.71\,\mathrm{nm}$ (case 2); – –: $L_y = 3.70\,\mathrm{nm}$ (case 7); - -: $L_y = 1.35\,\mathrm{nm}$ (case 8).

figure 6 indicate the presence of bulk water at the center of the system for the 4.71 and 3.70 nm cases, whereas the density variations in the 1.35 nm case persist throughout the system. The velocity of the upper graphite sheet is $100\,\mathrm{m\,s^{-1}}$ for all systems, with an imposed shear of 2.0×10^{10}, 2.7×10^{10} and $7.4 \times 10^{10}\,\mathrm{s^{-1}}$, respectively, all below the critical value for water of approximately $12 \times 10^{10}\,\mathrm{s^{-1}}$ (Rahman & Stillinger 1971; Eisenberg & Kauzmann 1969). The results from the 3.70 nm system indicate a reduced slip length of 41 nm, and a very large slip for the 1.35 nm system. However, for the 1.35 nm system a longer sampling time appears to be required to determine the slip length with sufficient accuracy. The amount of thermal noise, and the presence of low-frequency oscillations in the system is demonstrated by the time history of the centerline velocity ($u(\frac{1}{2}L_y)$) as shown in figure 8. The centerline velocity is presented as a running mean with a time window of 40 ps for the 4.71 nm and 1.35 nm cases. The signals clearly contain low-frequency oscillations, with a period of approximately 0.5 ns, and similar to the fluctuations observed by Sokhan *et al.* (2001). Longer simulations including extended equilibration of

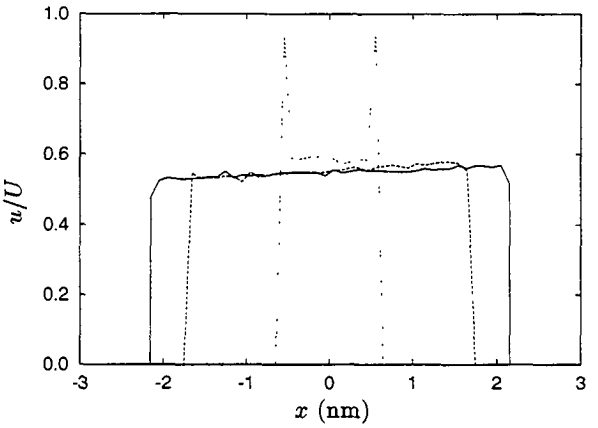

FIGURE 7. Time average streaming velocity profiles in a Couette flow as function of the size of the channel: —: $L_y = 4.71\,\mathrm{nm}$ (case 2); – –: $L_y = 3.70\,\mathrm{nm}$ (case 7); - -: $L_y = 1.35\,\mathrm{nm}$ (case 8).

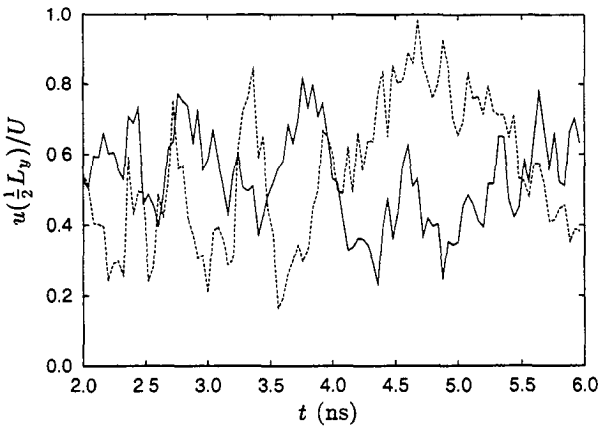

FIGURE 8. The time history of the running mean (40 ps averages) center line velocity in a Couette flow at different system sizes (L_y) —: 4.71 nm (case 2); – –: 1.35 nm (case 8).

the system are currently being conducted to allow more accurate definition of the system pressure and of the slip length.

3.2. *Flow past an array of carbon nanotubes*

The flow past an array of carbon nanotubes is computed for tube diameters of 1.25 nm and 2.50 nm, to study the effect of curvature on the no-slip boundary condition and to compare the fluid forces acting on the array with macroscale Navier-Stokes models. The carbon nanotubes are (16,0) and (32,0) zigzag tubes, located at the center of the computational box with dimensions of $16.4 \times 16.4 \times 2.1\,\mathrm{nm}$. The total number of water molecules is approximately 18500, and the carbon nanotubes consist of 320 and 640 atoms for the 1.25 nm and 2.50 nm tubes, respectively.

The onset flow speed ($U = 50\,\mathrm{m\,s^{-1}}$) is chosen sufficiently above the thermal noise to allow efficient sampling, but yet corresponding to a low Mach number (Ma < 0.05). During the first 4 ps of the 8 ps equilibration, the volume of the computational box is adjusted to match the target density of water (here $\rho = 0.997\,\mathrm{g\,cm^{-3}}$) in the far-field, i.e.

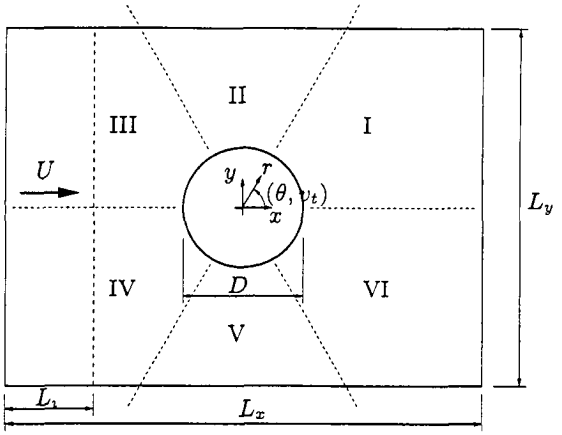

FIGURE 9. Sketch of the carbon nanotube-water system. D denotes the diameter of the carbon nanotube, L_x the size of the system in the streamwise direction, and L_y and L_z the height and width, respectively. The velocity of the center of mass of the water molecules contained in the "inlet" region (L_i) of the computational box is fixed to the desired value (U).

in the region defined by $r > R + \delta$, where $R = D/2$ is the tube radius, and $\delta = 0.8\,\text{nm}$ is chosen to exclude the region containing the density variations in the vicinity of the carbon nanotube (Walther *et al.* 2001). The regulation of the volume is performed by scaling the computational box in the x-y plane (see figure 9), while keeping the extent of the box in the z-direction fixed. The carbon nanotube is excluded from the scaling to preserve the radius of the tube. The flow is initially quiescent and impulsively turned on after 6 ps while maintaining the thermostat for the remaining 2 ps of the equilibration. The spatially-averaged streaming velocity is computed during the simulation and subtracted to allow equilibration of the peculiar velocities (i.e. the thermal component) only. The viscous heating during the 0.76 ns simulation was less than 8 K.

The flow speed is adjusted by monitoring the velocity of the center of mass of the water in the 3 nm (L_i) wide inlet region upstream of the carbon nanotube: see figure 9. In a leapfrog approximation, the velocity of the molecules is updated according to

$$\boldsymbol{v}^{n+1/2} = \boldsymbol{v}^{n-1/2} + \frac{\delta t}{m}(\boldsymbol{f} + \boldsymbol{b}), \tag{3.5}$$

where δt is the time step, m the mass of the molecule, and $\boldsymbol{f}$ and $\boldsymbol{b}$ denote the force and body force on the molecule, respectively. Thus, the center of mass velocity of the water molecules in the inlet region is updated accordingly

$$\boldsymbol{v}_{com}^{n+1/2} = \boldsymbol{v}_{com}^{n-1/2} + \frac{\delta t}{m_{tot}}(\boldsymbol{f}_{tot} + \boldsymbol{b}_{tot}), \tag{3.6}$$

where $\boldsymbol{f}_{tot}$ is the total force acting on the center of mass of the molecules in the inlet region, and $\boldsymbol{b}_{tot}$ is the total body force. In equation (3.6), $\boldsymbol{b}_{tot}$ is adjusted to yield the desired center of mass velocity ($\boldsymbol{v}_{com}^{n+1/2} = \boldsymbol{U}$), thus

$$\boldsymbol{b}_{tot} = \frac{m_{tot}}{\delta t}\left(\boldsymbol{U} - \boldsymbol{v}_{com}^{n-1/2}\right) - \boldsymbol{f}_{tot}. \tag{3.7}$$

This boundary condition is equivalent to a prescribed total mass flow through the system and allows a non-uniform inlet velocity profile, and effectively modelling the flow past an array of carbon nanotubes arranged in an inline configuration.

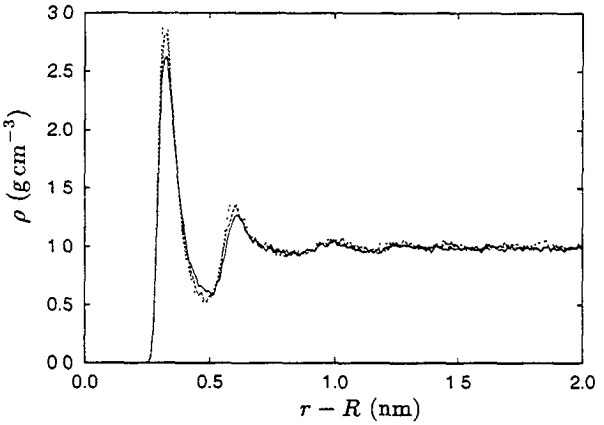

FIGURE 10. The time-average radial density profile for the flow past an array of 2.50 nm carbon nanotube. The profiles are sampled upstream, at the mid-section and downstream sections: —: section I; – –: section II; - -: section III.

The simulations involve approximately 380000 time steps corresponding to 0.76 ns, with snapshots collected every 100 time steps (0.2 ps) starting at 0.4 ns for subsequent analysis. The time average density and streaming velocity profiles are sampled along the 6 radial bins as shown in figure 9. Both profiles exhibit symmetry across the x-axis, whereas asymmetries are discernable in the density profiles in the streamwise direction, in the vicinity of the carbon nanotube: see figure 10. The locations of the density extrema are similar for the three profiles, with the first peak located at $r - R = 0.32$ nm coinciding with the van der Waals equilibrium distance (σ_{CO}). However, the peak values decrease from 3.0 g cm^{-3} at the upstream direction (section III) to 2.8 g cm^{-3} and 2.6 g cm^{-3} for the sections II and I, respectively. Since the far-field density is constant with a value of approximately 1.0 g cm^{-3}, the observed asymmetry is ascribed to a local compression near the surface.

The amount of slip experienced in these systems is extracted from the tangential component (v_t) of the streaming velocity for the sections II and V shown in figure 11. The velocity profiles are similar but reach different free-stream values due to the different blockage ($(D - L_y)/L_y$) experienced by the flow. Since the Reynolds number (Re) based on the tube diameter and the fluid viscosity (ν) is less than unity, the velocity profile is fitted to the Stokes velocity field for a single circular cylinder (Batchelor 1967)

$$v_t = a \log\left(\frac{r}{R}\right) + b + c\frac{R^2}{r^2}, \tag{3.8}$$

where a, b, and c, are parameters of the fit. The fit is performed for the data shown in figure 11 in the interval $r \in [R + \sigma_{CO} : 7\,\text{nm}]$. We find, within the uncertainty of the fit and to within the accuracy of the definition of the location of the surface, that the no-slip condition is satisfied, i.e., $L_s < \sigma_{CO}$. We speculate that the difference dbetweenn the amount of slip found in the planar Couette flow and in the flow past an array of carbon nanotubes is related to the amount of time the water is exposed to the solid surface ($\approx D/U = 25 - 50$ ps), and to the difference in the imposed external boundary conditions. Specifically, the driving mechanism of the Couette flow is the imposed shear, while for the Poiseuille flow (see e.g., Travis *et al.* (1997)) it is an imposed gravity (body) force. Since the present flow is driven by a body force imposed at the inlet section only,

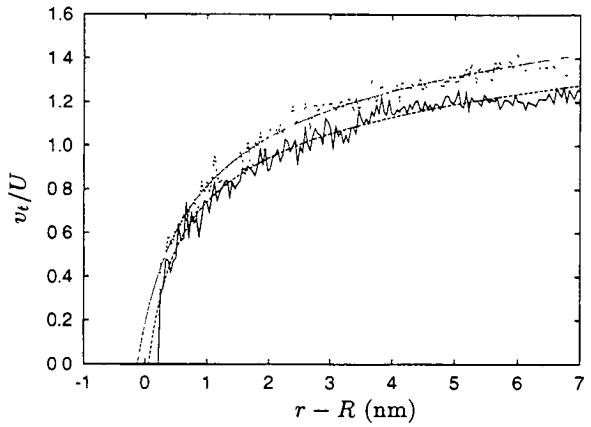

FIGURE 11. The time average tangential component of the streaming velocity for the flow past an array of carbon nanotubes. The profiles are sampled from section II and V and compared with equation (3.8) the for the 1.25 nm tube: —: measured; – –: fit and the 2.50 nm tube: - -: measured; · · ·: fit.

the remaining part of the flow is driven by a pressure gradient. To validate this conjecture we are currently performing simulations of Poiseuille flow driven by a pressure gradient, i.e. by imposing a body force in a limited inlet region similar to the present carbon nanotube study.

Finally, we consider the fluid forces (f_{fl}) acting on the carbon nanotube array by computing the total force on the carbon atoms

$$f_{fl} = \sum_{i}^{n_c} f_i. \tag{3.9}$$

The streamwise component of the force is compared with the Stokes-Oseen drag for the flow past an array of two-dimensional circular cylinders (Probstein 1994)

$$C_d = C_d^{cc} \frac{3 + 2\phi^{5/3}}{3 - \frac{9}{2}\phi^{1/3} + \frac{9}{2}\phi^{5/3} - 3\phi^2}, \tag{3.10}$$

where ϕ is the volume fraction (here $\phi = \pi R^2 (L_x L_y)^{-1}$), and C_d^{cc} is the drag coefficient ($C_d = f_x(\frac{1}{2}\rho U^2 D)^{-1}$) on a single circular cylinder given by (Batchelor 1967)

$$C_d^{cc} = \frac{8\pi}{\mathrm{Re}\log(7.4/\mathrm{Re})}. \tag{3.11}$$

For the two cases $\phi_{1.25\,\mathrm{nm}} = 0.0047$ and $\phi_{2.50\,\mathrm{nm}} = 0.0183$, the Reynolds numbers are $\mathrm{Re}_{1.25\,\mathrm{nm}} = 0.063$, and $\mathrm{Re}_{2.50\,\mathrm{nm}} = 0.125$, resulting in drag coefficients (see equations 3.10 and 3.11) of 112 and 81 for the 1.25 nm and 2.50 nm tubes respectively. The measured forces are sampled from 0.40 ns to 0.66 ns using 13 samples of 20 ps each. The force components per unit length of the tube are $(126 \pm 19,\ 0 \pm 15,\ 0 \pm 4)$ kJ mol^{-1} nm^{-1} and $(159 \pm 19,\ 0 \pm 21,\ 0 \pm 5)$ kJ mol^{-1} nm^{-1}, for the 1.25 nm and 2.50 nm tubes, respectively. The corresponding drag coefficients are 134 ± 20 and 85 ± 20, both in good agreement with the Stokes-Oseen values. Thus, the hydrodynamic diameter of the carbon nanotube appears to be represented by the atomic center-to-center diameter of the carbon nanotube rather than an "effective diameter" based on the water density profile.

4. Summary and conclusions

We have presented non-equilibrium molecular dynamics simulations of water in a planar Couette flow and water flowing past an array of carbon nanotubes. For the planar Couette flow, we find a slip length of 63 nm at 300 K and 1 bar, decreasing to a value of 31 nm at higher pressures (1000 bar). By changing the properties of the interface from hydrophobic (contact angle of 85°) to hydrophilic (zero contact angle), the slip persists with a value of 14 nm. The values for both the hydrophobic and the hydrophilic interfaces are in good agreement with experimental values of 30-38 nm and 8-9 nm, respectively. Low frequency oscillations were observed in the velocity field and the simulations are currently being extended to secure a more accurate sampling.

Studies of the flow past an array of carbon nanotubes were also conducted to determine the effect of curvature on the amount of slip, and to compare the fluid forces with that of macroscopic Navier-Stokes models. For the two cases considered, with 1.25 nm and 2.50 nm zigzag carbon nanotubes mounted in an inline arrangement with a spacing of 16.4 × 16.4 nm, the no-slip condition appears to be valid. The extracted slip length is less than the van der Waals radius of the interface (< 0.3 nm). The hydrodynamic forces acting on the arrays are found to be in good agreement with macroscopic Navier-Stokes models, hence indicating that the integral fluid-dynamic properties of the system can be estimated using traditional fluid dynamics tools.

REFERENCES

ANDREA, T. A., SWOPE, W. C. & ANDERSEN, H. C. 1984 The role of long ranged forces in determining the structure and properties of liquid water. *J. Chem. Phys.* **79**, 4576–4584.

BARRAT, J.-L. & BOCQUET, L. 1999 Large slip effect at a nonwetting fluid-solid interface. *Phys. Rev. Lett.* **82**, 4671–4674.

BATCHELOR, G. K. 1967 *An Introduction To Fluid Dynamics*, 1st edn. Cambridge University Press.

BAUDRY, J., CHARLAIX, E., TONCK, A. & MAZUYER, D. 2001 Experimental evidence for a large slip effect at a nonwetting fluid-solid interface. *Langmuir* **17**, 5232–5236.

BERENDSEN, H. J. C., GRIGERA, J. R. & STRAATSMA, T. P. 1987 The missing term in effective pair potentials. *J. Phys. Chem.* **91**, 6269–6271.

BERENDSEN, H. J. C., POSTMA, J. P. M., VAN GUNSTEREN, W. F., DINOLA, A. & HAAK, J. R. 1984 Molecular dynamics with coupling to an external bath. *J. Chem. Phys.* **81**, 3684–3684.

BOJAN, M. J. & STEELE, W. A. 1987 Interactions of diatomic molecules with graphite. *Langmuir* **3**, 1123–1127.

BONACCURSO, E., KAPPL, M. & BUTT, H.-J. 2002 Hydrodynamic force measurements: Boundary slip of water on hydrophilic surfaces and electrokinetic effects. *Phys. Rev. Lett.* **88**, 076103-1–076103-4.

CHURAEV, N. V., SOBOLEV, V. D. & SOMOV, A. N. 1984 Slippage of liquids over lyophobic solid surfaces. *J. Coll. Interface Sci.* **97**, 574–581.

CIEPLAK, M., KOPLIK, J. & BANAVAR, J. R. 2001 Boundary conditions at a fluid-solid interface. *Phys. Rev. Lett.* **86**, 803–806.

EISENBERG, D. & KAUZMANN, W. 1969 *The Structure and Properties of Water*. Oxford University Press.

VAN GUNSTEREN, W. F. & BERENDSEN, H. J. C. 1977 Algorithms for macromolecular dynamics and constraint dynamics. *Mol. Phys.* **37**, 1311–1327.

HELMHOLTZ, H. & VON PIOTROWSKI, G. 1860 Über reibung tropfbarer flussigkeiten. *Sitzungsberichte der Kaiserlich Akademie der Wissenschaften* **40**, 607–658.

KOPLIK, J. & BANAVAR, J. R. 1995 Continuum deductions from molecular hydrodynamics. *Annu. Rev. Fluid Mech.* **27**, 257–292.

LEE, C. Y., MCCAMMON, J. A. & ROSSKY, P. J. 1984 The structure of liquid water at an extended hydrophobic surface. *J. Chem. Phys.* **80** (9), 4448–4455.

LEVITT, M., HIRSHBERG, M., LAIDIG, K. E. & DAGGETT, V. 1997 Calibration and testing of a water model for simulation of the molecular dynamics of proteins and nucleic acids in solution. *J. Phys. Chem. B* **101**, 5051–5061.

LOOSE, W. & HESS, S. 1989 Rheology of dense model fluids via nonequilibrium molecular dynamics: shear thinning and ordering transition. *Rheol. Acta* **28**, 91–101.

PROBSTEIN, R. F. 1994 *Physicochemical Hydrodynamics*. 2nd edition. Wiley, New York.

RAHMAN, A. & STILLINGER, F. H. 1971 Molecular dynamics study of liquid water. *J. Chem. Phys.* **55**, 3336–3359.

SCHNELL, E. 1956 Slippage of water over nonwettable surfaces. *J. Appl. Phys.* **27**, 1149–1152.

SOKHAN, V. P., NICHOLSON, D. & QUIRKE, N. 2001 Fluid flow in nanopores: An examination of hydrodynamic boundary conditions. *J. Chem. Phys.* **115**, 3878–3887.

THOMPSON, P. A. & ROBBINS, M. O. 1990 Shear flow near solids: Epitaxial order and flow boundary conditions. *Phys. Rev. A* **41**, 6830–6841.

THOMPSON, P. A. & TROIAN, S. M. 1997 A general boundary condition for liquid flow at solid surfaces. *Nature* **389**, 360–362.

TRAVIS, K. P. & GUBBINS, K. E. 2000 Poiseuille flow of Lennard-Jones fluids in narrow slit pores. *J. Chem. Phys.* **112**, 1984–1994.

TRAVIS, K. P., TODD, B. D. & EVANS, D. J. 1997 Departure from Navier-Stokes hydrodynamics in confined liquids. *Phys. Rev. E* **55**, 4288–4295.

WALTHER, J. H., JAFFE, R., HALICIOGLU, T. & KOUMOUTSAKOS, P. 2001 Carbon nanotubes in water: Structural characteristics and energetics. *J. Phys. Chem. B* **105**, 9980–9987.

WERDER, T., WALTHER, J. H., KOUMOUTSAKOS, P., JAFFE, R. L. & HALICIOGLU, T. 2002 On the water-graphite interaction for use in MD simulations. To appear in *J. Phys. Chem. B*.

Combustion

While during the 2000 CTR summer program the combustion group had strong participation from industry, assessing the merits of large-eddy simulation (LES) of combustion problems, both the feasibility and the benefits of combustion LES now seem to be well-established facts. The combustion and sprays group of the 2002 CTR Summer Program was largely dominated by projects addressing theoretical and modeling questions with relevance to applications in complex systems. This section includes reports on six projects, four related to combustion modeling and two on multiphase flows.

Selle *et al.* report on the LES of an industrial power-generation gas-turbine combustor using the so-called Thickened Flame combustion model. Since CO is a major concern in gas-turbine combustion, this model, which was based on one-step global chemistry, has been extended to account for a two-step chemical scheme including carbon monoxide and validated with flame/vortex interaction DNS data. Simulations are performed for the non-reactive and reactive cases and results are compared with velocity and temperature measurements.

Also related to combustion of stationary gas turbines is the project of Polifke and Wall. An efficient alternative to performing CFD for an entire engine in studying combustion instabilities, is the use of acoustic multi-port or network representations of the thermo-acoustic system. For this approach, the thermo-acoustic transfer matrices of individual components of the network have to be known. Here it is suggested that these matrices could be determined from LES of generic components, and simulations are performed for a simple geometry without heat release. It is shown that the formulation of inflow and outflow boundary conditions is a critical aspect of this work and a new formulation is proposed.

The physics of large-scale fires are dominated by the strong coupling of fluid dynamics, soot formation, and radiation. In numerical simulations these complex interactions are usually not adequately accounted for. As a first step towards fully-coupled simulations Rawat *et al.* performed an LES of a pool fire of one meter diameter, employing an unsteady flamelet model including a kinetically-based soot model and a simplified description of radiative transport. The effect of using a simplified model for radiation is assessed by post-processing the LES results with a detailed radiation model.

Models for scalar mixing are formulated and evaluated with DNS data in the project of Fox *et al.*. The Lagrangian Spectral Relaxation model to describe scalar dissipation rates, and the Lagrangian Fokker-Planck (LFP) model, describing the scalar mixing process of two scalars given the dissipation rates, have been developed by Fox in recent years. Here, the LFP model is extended to account for multi-scalar mixing and chemical reactions. The model is validated with DNS data for three-component mixing and for reactive scalars.

In practical combustion devices, fuel is often supplied as liquid spray or as solid particles. In numerical simulations it is usual to apply Lagrangian particle methods describe the evolution of droplets and particles. In both the projects of Kaufmann *et al.* and of Réveillon *et al.*, Eulerian formulations for a dispersed phase are developed. Kaufmann *et al.* develop a formulation for mono-disperse particles, containing a newly-appearing sub-grid stress term, which is demonstrated to be of importance. The formulation with the modeled stress term is applied in a DNS of particle dispersion in isotropic turbulence. Results are compared with a DNS using a Lagrangian formulation.

The main difference in the formulation of Réveillon *et al.* is that it is for polydisperse evaporating sprays. A multi-fluid method is developed, in which equations for number density, droplet momentum, and droplet kinetic energy are solved for each individual size class. Two-dimensional DNS for two-phase flows with evaporation are performed using a Lagrangian and the multi-fluid method. In a comparison with the DNS results, the model is shown to perform well in predicting spray dynamics and evaporation.

Heinz Pitsch

Large-eddy simulation of turbulent combustion for gas turbines with reduced chemistry

By L. Selle†, G. Lartigue† T. Poinsot‡, P. Kaufmann¶, W. Krebs¶ AND D. Veynante||

An LES computation has been performed for the complete burner of a partially- premixed gas turbine, for both non-reacting and reacting cases. The flame is described using a two-step chemical scheme combined with the thickened-flame (TF) model. Results show that the inlet boundary conditions (especially the swirl level) have a very large effect on flow topology. With the correct inlet conditions, the overall agreement with experiment is very good, for both cold flow and reacting flows.

1. Introduction

Large-eddy simulation (LES) is becoming a standard tool to study the dynamics of turbulent flames (see for example recent Summer Programs at CTR, the special issue of *Flow Turbulence and Combustion* (vol. 65, 2000) on LES of reacting flows, and recent books on turbulent combustion (Peters (2000)) and Poinsot & Veynante (2000)). Many recent papers have demonstrated the power of LES methods (Pierce & Moin (1998), Desjardins & Frankel (1999), Légier *et al.* (2000),5 Colin *et al.* (2000), Angelberger *et al.* (2000), Pitsch and Duchamp de Lageneste (2002)). For example, LES appears as one of the key tools for predicting and studying the combustion instabilities encountered in many modern combustion devices, such as aero or industrial gas turbines, rocket engines or industrial furnaces.

Up to now, most LES of reacting flows in complex geometries has been limited to fairly simple chemical schemes (single-step chemistry) for obvious reasons of reduction of cost and complexity. In the same way, thermodynamic and transport properties are often simplified (constant heat capacity for all species, equal Lewis numbers).

This study presents a computation of a fairly complex industrial burner, developed at Siemens Power Generation, using an unstructured LES compressible solver. The main objectives are to:

- investigate the capacities of LES in a realistic configuration,
- extend the existing flame-interaction model (called the Thickened Flame model) to a two-step chemical scheme and
- compare the LES results to experimental data obtained at University of Karlsruhe.

Section 2 presents the LES solver used for the study. The TF (Thickened Flame) model is discussed in section 3. A two-step chemical mechanism, incorporating CO as the main intermediate species, was tuned for the conditions of the Siemens burner and tested in section 4. Specific DNS were performed to check the possible effects of reduced

† CERFACS, CFD team, 42 Av. G. Coriolis, 31057 Toulouse Cedex
‡ IMF Toulouse, INP de Toulouse and CNRS, 31400 Toulouse CEDEX, France
¶ Siemens PG, Mullheim, Germany
|| Ecole Centrale de Paris and CNRS, 92295 Châtenay Malabry CEDEX, France

chemistry on the efficiency function which characterizes the subgrid scale wrinkling in the TF model (section 5). The configuration used for the Siemens burner installed in the Karlsruhe combustion chamber is described in section 6. The specification of inlet conditions is discussed in section 7, while cold-flow results are presented in section 8. Finally, results with combustion are discussed in section 9.

2. The LES solver

The LES solver AVBP (see `www.cerfacs.fr/cfd/CFDWeb.html`) is used here. The full compressible Navier-Stokes equations are solved on hybrid (structured and unstructured) grids. Subgrid stresses are described by the WALE model (Nicoud & Ducros (1999)). The flame / turbulence interaction is modeled by the Thickened Flame (TF) model: see Angelberger *et al.* (1998), Angelberger *et al.* (2000), Colin *et al.* (2000), Légier *et al.* (2000) and Légier (2001). The numerical scheme has second- or third-order spatial accuracy and third-order time accuracy (Colin & Rydgyard(2000)). The AVBP version (AVBP 5.1) used here also handles variable heat capacities. Species enthalpies are tabulated and the mean heat capacity is determined as a function of temperature and species mass fractions Y_k. Therefore, local quantities such as the mean molecular weight W or the ratio of heat capacities γ are not constant. This introduces significant additional complexities in the numerical method, especially near boundaries, where classical characteristic methods such as NSCBC (Poinsot & Lele (1992)) must be replaced by a more complex technique (Baum, Poinsot and Thévenin (1994)).

3. The Thickened-Flame model

Modelling the interaction between flame and turbulence in partially premixed combustion systems is a major present challenge for turbulent combustion research. Possible paths are to address this issue using probability density functions (pdf) or flamelet concepts (Poinsot & Veynante (2000)). Pdf methods do not rely on any assumption on the flame topology but are limited by the accuracy of mixing models and by the required computing efforts.

On the other hand, flamelet models need assumptions for the flame topology: the flamelet approach is typically applicable when flame fronts are either of diffusion type or of premixed type. Laminar flamelet libraries are then constructed, and combined with pdf or flame-surface densities to determine species mass fractions or reaction rates in turbulent flames. When this formalism is valid, flamelet approaches offer a powerful way to incorporate complex kinetics into LES. But the flame structure type, either premixed or non-premixed, should be known *a priori* or determined from a sensor as proposed, for example, by Domingo *et al.* (2002). Unfortunately, in many practical applications such as gas turbine combustors, the flame front generally does not correspond to a pure premixed flame, separating premixed fresh gases and burnt gases perfectly, or to the usual non-premixed flame between pure fuel and pure oxidizer streams (Légier *et al.* (2000)). These situations are difficult to handle with flamelet models, even though recent work at CTR shows promising results (Pitsch and Duchamp de Lageneste (2002)).

Another path is followed here: the Thickened-Flame (TF) model initiated during the previous summer programs and continued in France (Veynante & Poinsot (1997), Angelberger *et al.* (1998), Légier *et al.* (2000), Charlette *et al.* (2002)) is now able to compute reacting flows in gas turbine combustors in complex geometries. Unsteady com-

bustion mechanisms are captured with no assumption for the flame structure: chemistry and transport are modified to offer larger reaction zones, which can be resolved on LES meshes. In this approach, the balance equation for the Y_k mass fraction in a one-dimensional flame,

$$\frac{\partial \rho Y_k}{\partial t} + \frac{\partial \rho u Y_k}{\partial x} = \frac{\partial}{\partial x}\left(\rho D_k \frac{\partial Y_k}{\partial x}\right) + \dot{\omega}_k\left(Y_j, T\right) \tag{3.1}$$

is modified as:

$$\frac{\partial \rho Y_k^{th}}{\partial t} + \frac{\partial \rho u Y_k^{th}}{\partial x} = \frac{\partial}{\partial x}\left(\rho F D_k \frac{\partial Y_k^{th}}{\partial x}\right) + \frac{1}{F}\dot{\omega}_k\left(Y_j^{th}, T^{th}\right) \tag{3.2}$$

where F is the thickening factor and superscript th stands for thickened quantities. Introducing the variable changes $X = x/F$; $\Theta = t/F$ leads to:

$$\frac{\partial \rho Y_k^{th}}{\partial \Theta} + \frac{\partial \rho u Y_k^{th}}{\partial X} = \frac{\partial}{\partial X}\left(\rho D_k \frac{\partial Y_k^{th}}{\partial X}\right) + \dot{\omega}_k\left(Y_j^{th}, T^{th}\right) \tag{3.3}$$

which has the same solution as (3.1). Then, $Y_k^{th}(x,t) = Y_k(x/F, t/F)$ showing that the flame is thickened by a factor F. The time response is also modified but this point is neglected in a first step assuming that the flame front is in equilibrium. The integrated reaction rate is kept constant:

$$\dot{\Omega}_k^{th}(t) = \int_{-\infty}^{+\infty} \frac{1}{F}\dot{\omega}_k\left(Y_j^{th}(x,t), T^{th}(x,t)\right)\, dx = \dot{\Omega}\left(\frac{t}{F}\right) \tag{3.4}$$

and, accordingly, the laminar flame speed s_L is conserved. This approach has some advantages: the flame propagation, for example, is due to the combination of diffusive and reactive terms so that quenching and ignition may be simulated. Fully-compressible equations may also be used as required to study combustion instabilities. Obvious drawbacks also exist: subgrid scale wrinkling must be modeled using an efficiency function E derived from DNS results, as shown by Veynante & Poinsot (1997), Angelberger *et al.* (1998) or Colin *et al.* (2000). Using the same DNS, a more refined efficiency function E has been recently derived by Charlette *et al.* (2002). In practice, the diffusion coefficient D_k is replaced by $E\,F\,D_k$ and the pre-exponential constant A by $A\,E/F$. The flame front is then thickened by a factor F and propagates at the subgrid-scale turbulent flame speed Es_L. Furthermore, the complexity of the chemical scheme must remain limited. Up to now, only simple one-step chemical schemes have been used. In the present study, a two-step scheme is introduced to capture CO and predict more accurate flame temperatures, as an intermediate step towards more complex schemes (typically four-step schemes such as that of Jones & Lindstedt (1988)). In fact, the approach is questionable when intermediate species are present. According to (3.4), the overall reaction rate of these species is conserved (and is close to zero), but, as the mass fraction profiles are thickened, their total amount is increased. For a one dimensional flame, this increase has no effects but could lead to some difficulties for wrinkled or/and stretched flame fronts. This point is investigated, using DNS, in section 5.

A_1	n_{1F}	n_{1O}	E_{a1}	A_2	n_{2CO}	n_{2O}	n_{2CO_2}	E_{a2}
$2E15$	0.9	1.1	34500	$2E9$	1	0.5	1	12000

TABLE 1. Rate constants for scheme 2S-CM2. The activation energies are in cal/moles and the preexponential constants in cgs units.

CH_4	CO_2	CO	O_2	H_2O	N_2
0.68	0.98	0.76	0.76	0.6	0.75

TABLE 2. Schmidt numbers used with the 2S-CM2 scheme.

4. Two-step chemistry

The chemical scheme used for this study, called 2S-CM2, takes into account six species (CH_4, O_2, CO_2, CO, H_2O and N_2) and two reactions:

$$CH_4 + \frac{3}{2}O_2 \longrightarrow CO + 2H_2O \tag{4.1}$$

$$CO + \frac{1}{2}O_2 \longleftrightarrow CO_2 \tag{4.2}$$

The first reaction (4.1) is irreversible, whereas the second one (4.2) is reversible and leads to an equilibrium between CO and CO_2 in the burnt gases. The rates of reaction (4.1) and (4.2) are given respectively by:

$$q_1 = A_1 \left(\frac{\rho Y_{CH_4}}{W_{CH_4}}\right)^{n_{1F}} \left(\frac{\rho Y_{O_2}}{W_{O_2}}\right)^{n_{1O}} \exp\left(-\frac{E_{a1}}{RT}\right) \tag{4.3}$$

$$q_2 = A_2 \left[\left(\frac{\rho Y_{CO}}{W_{CO}}\right)^{n_{2CO}} \left(\frac{\rho Y_{O_2}}{W_{O_2}}\right)^{n_{2O}} - \left(\frac{\rho Y_{CO_2}}{W_{CO_2}}\right)^{n_{2CO_2}}\right] \exp\left(-\frac{E_{a2}}{RT}\right) \tag{4.4}$$

where the parameters are given in table 1.

Transport by molecular diffusion also requires some attention: PREMIX uses polynomial fits for diffusion coefficients D_k. This technique is accurate but expensive, and may be replaced by a simpler approximation based on the observation that the individual Schmidt numbers of species $S_c^k = \nu/D_k$ are almost constant in these flames. Therefore, in AVBP 5.1, the diffusion coefficient D_k of species k is obtained as $D_k = \nu/S_c^k$ where ν is the viscosity and S_c^k the fixed Schmidt number of species k. The Schmidt number values used in the present simulations are given in table 2. In most cases, these values correspond to the PREMIX values measured in the burnt gases. The Prandtl number is set to 0.68. With this parameter set, the agreement between flame profiles obtained using AVBP 5.1 or PREMIX with the same chemical scheme is excellent.

The 2S-CM2 scheme is directly implemented into the LES code. Its first advantage compared to a single-step scheme is to provide more accurate adiabatic flame tempera-

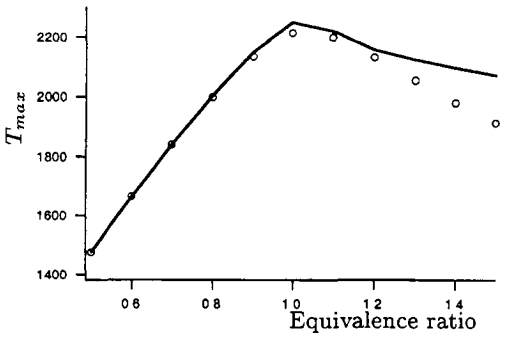

FIGURE 1. Maximum temperature T_{max} (K)
2S-CM2: ——— ; GRI mech: o

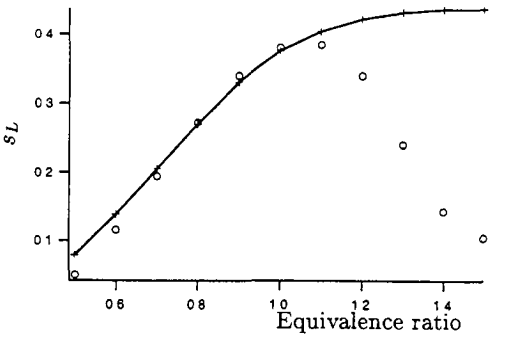

FIGURE 2. Flame speed s_L (m/s)
2S-CM2: ——— ; GRI mech: o

tures. Figure 1 compares the maximum flame temperatures obtained with 2S-CM2 and the full GRI mech scheme. The laminar flame speeds are also well predicted on the lean side, (figure 2) but deviate from the exact results for rich cases. This drawback is not a problem for the Siemens burner investigated here: the axial burner injects pure air, while the diagonal burner feeds premixed air with an equivalence ratio of 0.5 so that combustion proceeds everywhere under lean conditions.

5. Efficiency function for reduced chemistry

The thickened-flame model is theoretically able to handle complex chemical schemes but, as described in section 3, possible drawbacks may occur because of intermediate species. Direct numerical simulations of laminar premixed flame / vortex interactions were conducted to study the thickened-flame approach combined with the 2S-CM2 chemical scheme (section 4) and to check whether the existing efficiency functions proposed by Angelberger *et al.* (1998), Colin *et al.* (2000) or Charlette *et al.* (2002) could be used without modification. This point is investigated using a pair of counter-rotating vortices interacting with a perfectly premixed flame thickened with a factor F from $F = 1$ to $F = 20$. The vortex size r is kept constant ($r/\delta_l^0 = 26.3$, where δ_l^0 is the thermal thickness of the actual laminar flame) but the vortex strength is changed (see Angelberger *et al.* (1998) or Colin *et al.* (2000) for details of the numerical configuration). A typical DNS result is displayed in figure 3. The total reaction rates of the two reactions (4.1) and (4.2) are plotted as a function of time during the interaction for various thickening factors F. The counter-rotating vortices wrinkle the flame front and increase both the flame surface and the total reaction rate. However, when the thickening factor F increases, the flame surface and the total reaction rate are underpredicted (Meneveau & Poinsot (1991)), in agreement with Angelberger *et al.* (1998) and Colin *et al.* (2000). This effect corresponds to a subgrid-scale wrinkling which must be parametrized through the efficiency function.

The main result is that the two chemical reaction rates (4.3) and (4.4) follow exactly the same evolution, although the overall quantity of carbon monoxide CO increases with increasing values of the thickening factor F. For the range of parameters investigated in the present simulations, the premixed flame acts as a flamelet distorted by the flow, even for low values of the length-scale ratio $r/(F\delta_l^0)$. No differences are found between the two reactions. Moreover, the effective strain rates induced by the vortices on the flame front, as derived from the present DNS, are in close agreement with the findings of Angelberger *et al.* (1998) and Colin *et al.* (2000). Accordingly, the efficiency functions

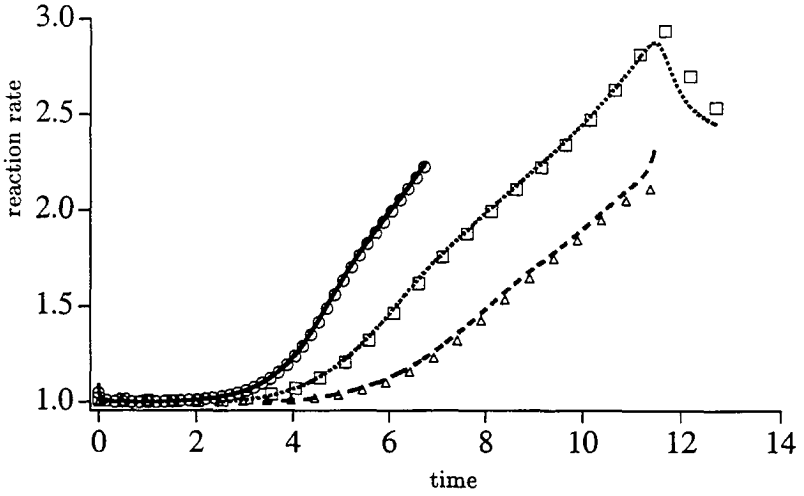

FIGURE 3. Typical flame / vortex interaction DNS results. The reduced total rates of reactions 4.1 (lines) and 4.2 (symbols) are displayed as functions of time for various thickening factors F. $F = 1$ (——— , ○); $F = 10$ (····· □); $F = 20$ (---- , △). Reaction rates are made non-dimensional using the reaction rate of the planar flame whereas times are reduced using the flame time δ_l^0/s_l^0. $u'/s_l^0 = 11.4$ where u' denotes the maximum vortex speed.

derived by Angelberger *et al.* (1998), Colin *et al.* (2000) and Charlette *et al.* (2002) may be used without any modifications with the present 2S-CM2 chemical scheme.

6. The Siemens burner geometry

Another objective of this study was to investigate the limits of present computer capabilities to perform LES of combustion in realistic geometries. An industrial gas turbine is considered here. The CAD data was provided by Siemens PG and meshed at CERFACS using CFD GEOM. The grid contains 306240 points and 1739695 cells. Figure 4 shows the main features of the burner: a central axial swirler (colored in dark) is used to inject and swirl air and, for certain regimes, non premixed fuel. In addition, six small tubes (not visible on this figure) can be used to generate pilot flames but they were not fed during the present computation. Most of the combustion air as well as fuel is injected by the diagonal swirler (the fuel entering through holes located on both sides of the swirlvanes). The external surface of the swirler is visualized in figure 4 by a wireframe surface.

7. Inlet conditions

As a first step, the non-reacting flow in the burner is computed and compared to LDV velocity measurements at the University of Karlsruhe. A major issue in such calculations is to specify boundary conditions. Since the axial burner flow is fully computed, the flow in Section 1a is introduced along the x axis only, without swirl. The main problem is then to specify inlet conditions for the diagonal swirler (Section 1b in figure 5). The inlet velocity profiles are adjusted to match the first measurement section in the burner under non-reacting cases. Velocity measurements have been made at various sections as shown in figure 5. The swirl velocity W and the velocity U_{22} normal to a plane parallel to the diagonal swirler exit plane (at an angle of 22 degrees compared to the vertical

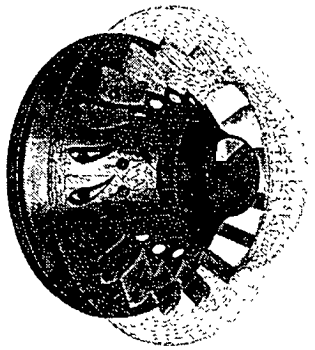

FIGURE 4. Burner: the vanes of the diagonal swirler are not computed

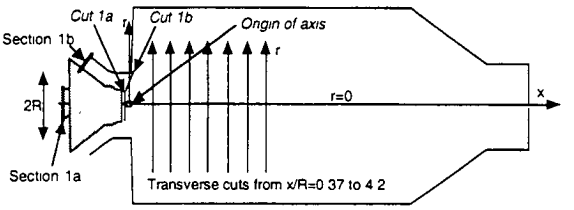

FIGURE 5. Burner mounted on ITS combustion chamber: location of LDV measurements

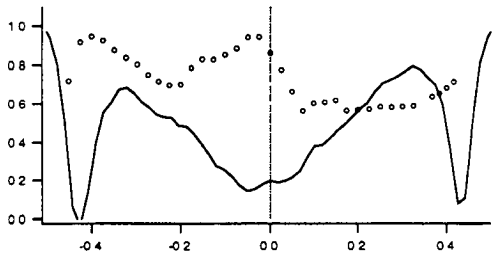

FIGURE 6. Normalized velocity U_{22}/U_{bulk} at the exit of the axial swirler (Cut 1a) LES: ——— ; Experiments: o

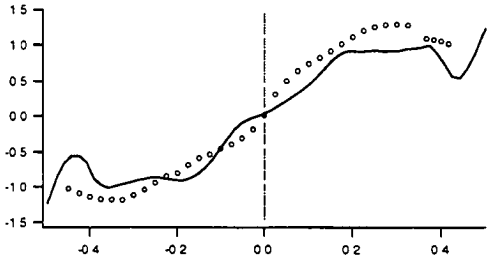

FIGURE 7. Normalized swirl velocity W/U_{bulk} at the exit of the axial swirler (Cut 1a) LES: ——— ; Experiments: o

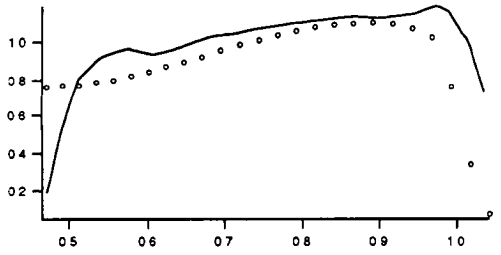

FIGURE 8. Normalized velocity U_{22}/U_{bulk} at the exit of the diagonal swirler (Cut 1b) LES: ——— ; Experiments: o

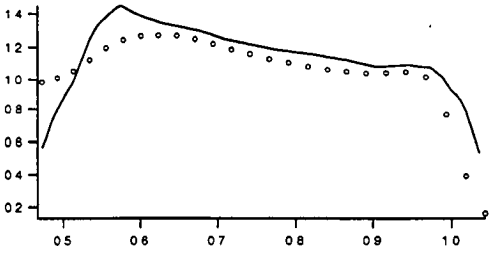

FIGURE 9. Normalized swirl velocity W/U_{bulk} at the exit of the diagonal swirler (Cut 1b) LES: ——— ; Experiments: o

axis) are measured in the test section located close to the burner nozzle (cuts 1a and 1b). Distances and velocities are respectively scaled by the burner radius R and the bulk velocity U_{bulk} defined by $U_{bulk} = \dot{V}/\pi R^2$ where $\dot{V}$ is the total volume flow rate through the burner.

Average profiles of axial and radial velocities at the exit of the axial burner are shown in figure 6 and 7 (cut 1a in figure 5) and at the exit of the diagonal burner in figure 8 and 9 (cut 1b in figure 5). Measurements along cut 2 start at location R_0. In the figures, symbols (o) denote experimental data while LES results are plotted as continuous lines.

The differences in axial velocity between LES and experimental results at the exit of

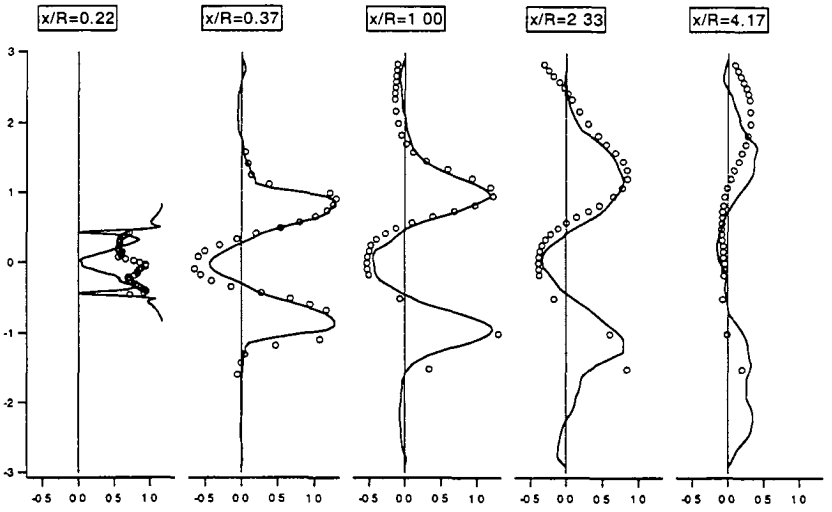

FIGURE 10. Cold flow mean axial velocities: experiment (o) and LES (———) data.

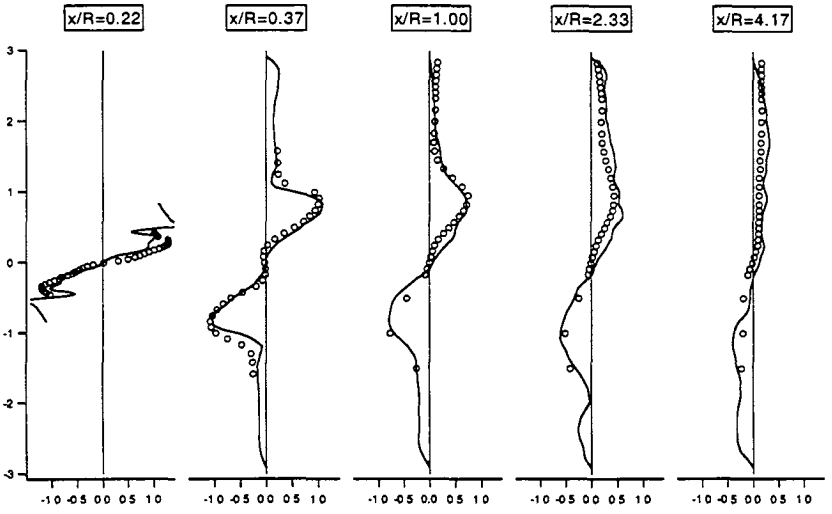

FIGURE 11. Cold flow mean swirling velocities: experiment (o) and LES (———) data.

the axial swirler (figure 6) are thought to be due to experimental uncertainties, and are being discussed with the Karlsruhe group.

8. Non-reacting flow results

Once the inlet conditions have been set, LDV measurements are compared to averaged LES results at different downstream locations x in the combustor, as shown in figures 10 (axial velocity profiles) and 11 (swirling velocities). LES results are averaged over about 36 ms corresponding to twice the flow time through the entire combustion chamber at the bulk velocity. Only five downstream locations are shown for clarity but 16 were investigated.

The overall agreement between LES and experimental data is excellent. Similar lev-

els of agreement are found for RMS values (not shown here). All results are shown for the complete combustion chamber, not just for one half chamber, to show up any departures from symmetry. Since the chamber is square and the injection device axisymmetric, average velocities are expected to be symmetrical with respect to the x-axis. Both experimental data and LES results are not symmetric, especially downstream. This finding may indicate a lack of sampling of LES data, but may also be due to an intrinsic inability of the flow to follow the symmetry of the geometry.

9. Reacting-flow results

Reacting cases are computed starting from a cold-flow solution. Fresh premixed gases (equivalence ratio $\phi = 0.5$) are injected through the diagonal swirler, while pure air is injected through the axial swirler. Both flows, which come from the compressor in the real gas turbine, enter the combustion chamber of the ITS burner after being preheated electrically. As the actual ignition process is not described here, the chemical reaction is started numerically by filling the combustion chamber with hot fully-burned gases. Note however that the pressure increases by 25 % and the exit velocity Mach number goes up to 0.4 in the outlet contraction during the transient.

Three-dimensional visualizations of the flow field are shown for five consecutive times in figure 12. A two-dimensional cut in the vertical plane at the last time is also provided, to show the fuel mass-fraction and reaction-rate fields, together with the recirculation zones. The premixed stream injected by the diagonal swirler is mixed with the pure air fed by the axial swirler and consumed by the flame front. The flame appears to be stabilized by the hot gases, both from the sides of the combustion chamber and from the recirculation zone downstream of the injector lips. A strong swirling motion is clearly apparent (rotating clockwise as seen from downstream, as in the figure. Note that a misleading analysis may be developed from two-dimensional visualizations only: the swirling motion is viewed as a flapping of the fresh reactant jets inducing "pockets" of burned gases.

Mean temperature profiles obtained from LES are compared to experimental data in figure 13. The agreement is very good: the downstream profiles, which are important for the turbine design, are very well reproduced. The slight discrepancy between experimental data and numerical results is due mainly to an underestimatden of the lateral flame expansion. This point is now under investigations: the error could be attributable to the boundary conditions.

10. Conclusions

A computation of a complete burner for a partially-premixed gas turbine combustor was performed using LES, for both non-reacting and reacting cases. The flame is described using a two-step chemical scheme, combined with the thickened-flame (TF) model which has been validated in this situation from DNS data. LES results are validated from velocity and temperature measurements obtained at the University of Karlsruhe. Results show that the inlet boundary conditions (especially the swirl level) are critical in determining the flow topology: the strength and size of the recirculation zone, and therefore the flame position, appear to be very sensitive to the profiles imposed at the diagonal swirler inlet. The overall agreement with experiment is very good, both for cold flow and for reacting conditions as long as the correct inlet conditions are imposed.

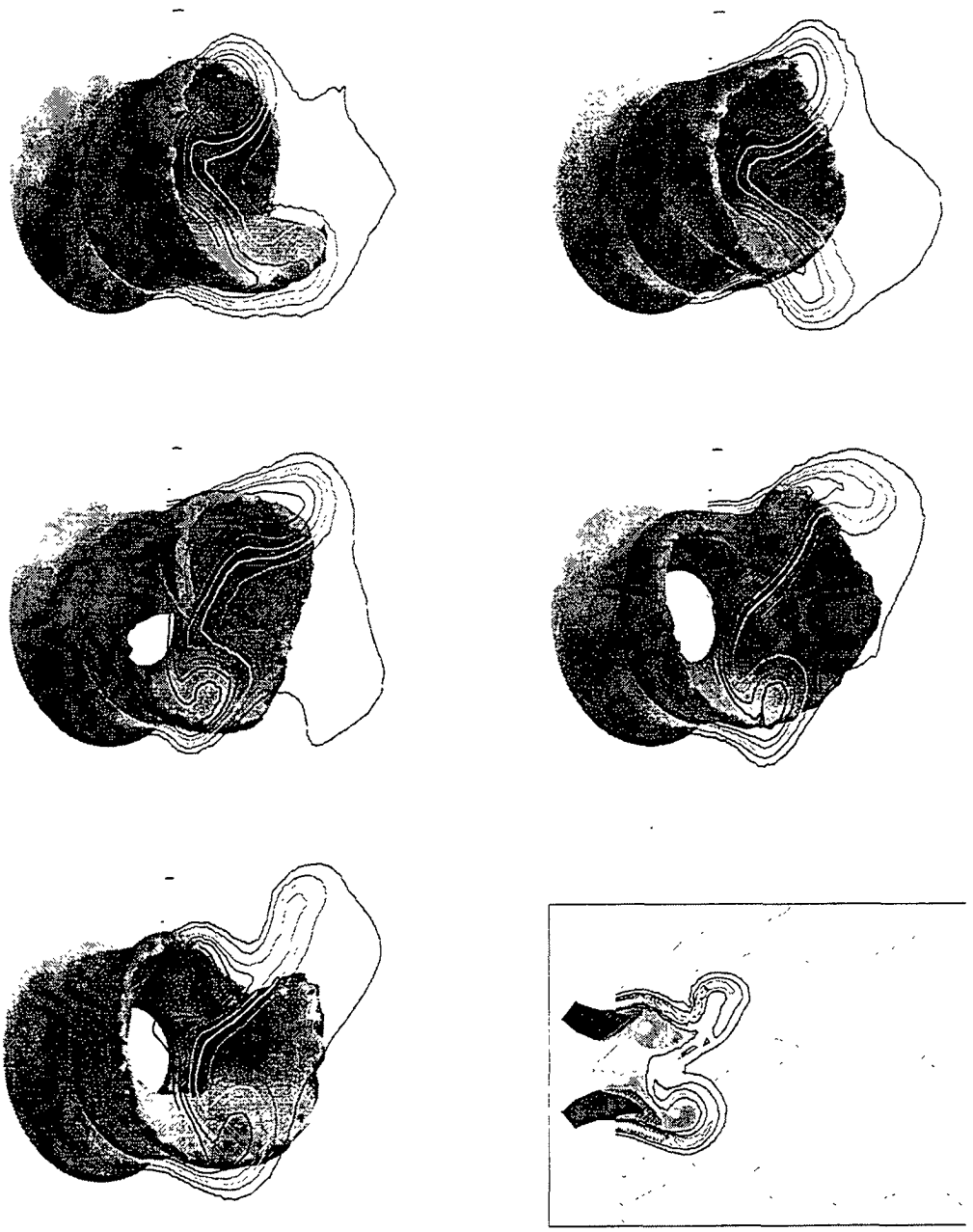

FIGURE 12. Reacting case. 3D visualizations of the reacting flow field for five consecutive times corresponding to a rotating period of the swirling flow (gray surface: fuel mass fraction; lines: temperature field in the vertical plane). A vertical 2D cut is also shown for the last time (gray scale: fuel mass fraction; bold line: reaction rate. Thin lines delineate the recirculation zones where the axial velocity is negative). Only a part of the combustion chamber is shown (zoom in the vicinity of the injector device).

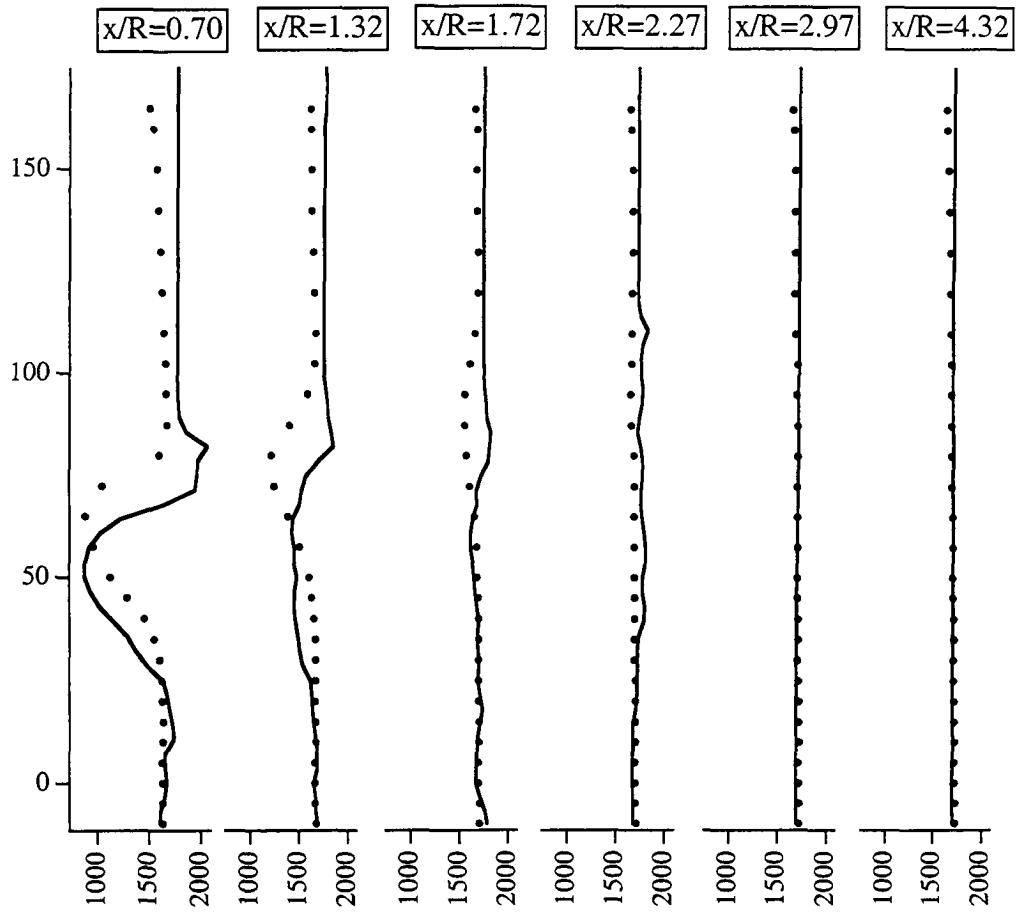

FIGURE 13. Reacting flow mean temperature: experiment (o) and LES (———) data. Measurements are conducted only in one half of the combustion chamber.

Acknowledgments

Numerical simulations have been conducted on the computers of IDRIS (Institut de Développement et de Recherche en Informatique Scientifique) and CINES French national computing centers.

REFERENCES

ANGELBERGER, C., VEYNANTE, D., EGOLFOPOULOS, F. & POINSOT, T. 1998 Large eddy simulations of combustion instabilities in premixed flames. *Proceedings of the 1998 Summer Program*, Center for Turbulence Research, NASA Ames/Stanford Univ., 61–82.

ANGELBERGER, C., EGOLFOPOULOS, F. & VEYNANTE, D. 2000 Large Eddy Simulations of chemical and acoustic effects on combustion instabilities. *Flow, Turb. and Comb.* **65**, 205-222.

BAUM, M., POINSOT, T. J. & THÉVENIN, D. 1994 Accurate boundary conditions for multispecies reacting flows *J. Comp. Phys* **116**, 247-261.

BAUM, M., THÉVENIN, D. AND POINSOT, T. Accurate boundary conditions for multicomponent reactive flows. *J. Comp. Phys.* **116**, 247–261.

CHARLETTE, F., VEYNANTE, D. & MENEVEAU, C. 2001 A power-law wrinkling model for LES of premixed turbulent combustion: Part I – non-dynamic formulation and initial tests. *Comb. and Flame*, in press.

CHARLETTE, F., VEYNANTE, D. & MENEVEAU, C. 2001 A power-law wrinkling model for LES of premixed turbulent combustion: Part II – dynamic formulation. *Comb. and Flame*, in press.

COLIN, O., DUCROS, F., VEYNANTE, D. & POINSOT, T. 2000 A thickened flame model for large eddy simulations of turbulent premixed combustion. *Phys. Fluids* **12**, 1843–1863.

COLIN, O. & RUDGYARD M. 2000 Development of high-order Taylor-Galerkin schemes for unsteady calculations, *J. Comp. Phys.*, **162**, 2, 338–371.

DESJARDINS, P. E. & FRANKEL, S. H. 1999 Two dimensional Large Eddy Simulation of soot formation in the near field of a strongly radiating nonpremixed acetylene-air jet flame. *Comb. and Flame* **119**, 121–133.

DOMINGO, P., VERVISCH, L., BRAY, K.N.C. 2002 Modeling partially premixed flamelets in Large Eddy Simulation. *Comb. Th. Mod.*, in press.

NICOUD, F. & DUCROS, F. 1999 Subgrid-scale stress modelling based on the square of the velocity gradient *Flow Turb. Comb.* **62**, 183–200.

JONES, W. P. & LINDSTEDT, R. P. 1988 Global reaction schemes for hydrocarbon combustion. *Comb. and Flame* **73**, 222–233.

LÉGIER, J. P., POINSOT, T. & VEYNANTE, D. 2000 Dynamically thickened flame Large Eddy Simulation model for premixed and non-premixed turbulent combustion.*Proceedings of the 2000 Summer Program*, Center for Turbulence Research, NASA Ames/Stanford Univ., 157–168.

LÉGIER, J.P. 2001 Simulations numériques des instabilités de combustion dans les foyers aéronautiques. *PhD Thesis*, CERFACS, INP Toulouse.

MENEVEAU, C. & POINSOT, T. 1991 Stretching and quenching flamelet in premixed turbulent combustion. *Comb. and Flame* **86**, 311–332.

PETERS, N. 2000 *Turbulent Combustion.* Cambridge University Press.

POINSOT, T. & LELE, S. 1992 Boundary conditions for direct simulations of compressible viscous flows. *J. Comp. Phys.* **101**, 104–129.

POINSOT, T. & VEYNANTE, D.2001 *Theoretical and Numerical Combustion.* R.T. Edwards, Flourtown, PA.

PIERCE C. & MOIN, P. 1998 Large Eddy Simulation of a confined coaxial jet with swirl and heat release. *AIAA Paper* 98-2892.

PITSCH, H. AND DUCHAMP DE LAGENESTE, L. 2002 Large-eddy simulation of premixed turbulent combustion using a level-set approach. *Proc. 29th Sympo. on Comb.* In press.

VEYNANTE, D. & POINSOT, T. 2000 Large Eddy Simulation of combustion instabilities in turbulent premixed burners. *Annual Research Briefs*, Center for Turbulence Research, NASA Ames/Stanford Univ., 253-274.

Non-reflecting boundary conditions for acoustic transfer matrix estimation with LES

By Wolfgang Polifke † AND Cliff Wall

The estimation of (thermo-)acoustic transfer matrices from numerically-generated time series of pressure and velocity fluctuations with correlation analysis appears to be an efficient and flexible way of employing CFD for the study of combustion instabilities. In the present investigation, the use of large-eddy simulation (LES) for this technique is explored for the first time. For this purpose, a novel formulation for boundary conditions, which is fully non-reflecting for plane acoustic waves, was derived, implemented and successfully tested. It was observed that large-scale turbulent fluctuations, which are explicitly resolved in LES, can generate spurious signal contributions inside the computational domain and additional acoustic waves at the outlet boundary of the domain. To allow accurate transfer matrix estimation with LES, these signal components must be suppressed or eliminated from the time-series data by suitable post-processing.

1. Introduction

Thermoacoustic instabilities are a cause for concern in combustion applications ranging from small household burners to rocket engines. The "brute-force" application of computational fluid mechanics (CFD) to the analysis of thermo-acoustic systems can be forbiddingly expensive due to the high computational demands of a time- and space-accurate simulation of a (low Mach number) compressible, turbulent, reacting flow. An efficient and often adequate description of the (thermo-)acoustic properties of a combustion system is provided by acoustic multi-port or "network" representations, see e.g. Bohn & Deuker (1993); Poinsot & Veynante (2001); Polifke *et al.* (2001*a*). Within this framework, both the response to an external or fluid-mechanic internal excitation as well as stability with respect to self-excited oscillations can be analyzed.

In order to represent a combustion system with these tools, the so-called *transfer matrices* of all multi-ports of the system must be known. The transfer matrices provide a mathematical description of the dynamical characteristics of a multi-port (within the limits of a linear analysis). For simple components, the transfer matrix can be derived from the (linearized) equations of conservation of mass and momentum and suitable additional assumptions. In general, however, the determination of the transfer matrix from first principles is not possible, and one has to resort to experiment (see e.g. Paschereit & Polifke (1998)) or numerical simulation.

Bohn and co-workers have suggested (see e.g. Bohn & Deuker (1993); Deuker (1995); Krüger *et al.* (1998)) determining the acoustic properties of an element - e.g. a burner or a flame - by numerically simulating and evaluating its response to a sudden disturbance. Specifically, the frequency response function $F(\omega)$ of a flame is obtained as the Laplace transform of the response (in the time domain) to a unit-step perturbation of the mass flux approaching the flame. It is thereby possible to determine the frequency

† Lehrstuhl für Thermodynamik, Technische Universität München, Germany

response function for a range of frequencies from one single time-dependent CFD simulation! Polifke *et al.* (1998, 2001*b*) have extended this idea, using modern tools of *system identification* (Ljung (1999); Bellanger (1984)) to determine the complete transfer *matrix* of an acoustic multi-port with time-lagged heat release and pressure loss ("n-τ-ζ model").

This advanced approach, known as *correlation analysis*, has since been applied by Gentemann *et al.* (2003) to turbulent pipe flow through a sudden change in cross section (an "area change") and successfully validated with experimental data. In that work, a RANS turbulence model was used. In the present paper – using the same simple geometry – the use of large eddy simulation for transfer matrix estimation with correlation analysis (TME) is explored for the first time. Emphasis is placed on the optimal choice of boundary conditions for successful transfer matrix estimation.

2. Correlation analysis basics

Consider the values of fluctuating variables up- and downstream of an acoustic element as *signals* s and *responses* r. A time-dependent numerical simulation will produce a time series $s_i = s(i\Delta t), i = 0, \ldots, N$ and similarly r_i. The coupling between signal and response is approximated as

$$r_i \approx \hat{r}_i = \sum_{k=0}^{L} h_k s_{i-k} \text{ for } i = L, \ldots, N. \tag{2.1}$$

In the terminology of digital signal processing or system identification, see e.g. Rabiner & Gold (1975); Bellanger (1984), (2.1) describes a *finite impulse response* (FIR) filter with *impulse response* $\underline{h}$.

The so-called *Wiener-Hopf equation* relates the *autocorrelation matrix* Γ of the signal $\underline{s}$ and the impulse-response vector $\underline{h}$ to the *cross-correlation* $\underline{c}$ between $\underline{s}$ and $\underline{r}$ (Ljung (1999); Bellanger (1984)):

$$\Gamma \underline{h} = \underline{c}, \tag{2.2}$$

For time-series data generated by time-dependent CFD, the auto- and cross-correlations are approximated as follows:

$$c_i \approx \frac{1}{N-L+1} \sum_{l=L}^{N} s_{l-i} r_l \text{ for } i = 0, \ldots, L, \tag{2.3}$$

$$\Gamma_{ij} \approx \frac{1}{N-L+1} \sum_{l=L}^{N} s_{l-i} s_{l-j} \text{ for } i, j = 0, \ldots, L. \tag{2.4}$$

The impulse response $\underline{h}$ is determined from time-series data by inversion of the Wiener-Hopf equation, (2.2). A frequency response $F(\omega)$ is then computed as the z-transform $H(z)$ of $\underline{h}$ with argument $z = \exp\{i\omega\Delta t\}$:

$$F(\omega) = H\left(e^{i\omega\Delta t}\right) = \sum_{k=0}^{L} h_k e^{-i\omega\Delta t k}. \tag{2.5}$$

3. Correlation analysis and acoustic multi-ports

The discussion in the previous section was limited to a scalar frequency response $F(\omega)$. However, an $m \times m$ transfer matrix describing an m-port filter can be estimated with correlation analysis if a signal vector $\underline{s}$, defined as a suitable combination of the m

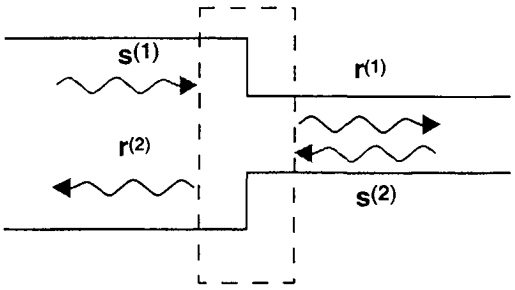

FIGURE 1. Incident acoustic waves as signals $s^{(1)}, s^{(2)}$ and reflected / transmitted waves as responses $r^{(1)}, r^{(2)}$ of an acoustic two-port.

signal variables $s^{(n)}, n = 1, \ldots, m$, and m impulse response functions $\underline{h}^{(n)}$ - one for each response port of the element - are introduced (Polifke *et al.* (2001*b*)). For acoustic systems, $m = 2$ typically and the variables s, r are the fluctuations of pressure $\tilde{p}$ and velocity $\tilde{u}$ or the in- and outgoing Riemann invariants f and g at the up- and downstream side of the acoustic multi-port, respectively (see figure 1 and section 4.2).

Estimation of a complete transfer matrix or scattering matrix from a single computation provides a significant advantage over alternative approaches (Deuker (1995), Poinsot & Veynante (2001)). Also note that the signal shape is quite arbitrary; superposed sine waves and in particular bandwidth-limited "white noise" have produced good results, while step functions – which are not easily represented accurately in a time-dependent fluid dynamics computation – can be avoided. The amount of data required to produce dependable estimates of auto- and crosscorrelation is not excessive. It is not required that initial transients die out completely, and simulation times of the order of just one period of the lowest frequencies involved have been found to be sufficient.

It is, however, required that the signals $s^{(n)}$ incident on the acoustic element be 1) broad-band, with fairly uniform amplitude throughout the frequency range of interest, to probe the system dynamics with adequate signal-to-noise ratio and 2) not degenerate, i.e. input signals $s^{(n)}$ at different ports must not be strongly correlated with each other. Otherwise, the Wiener-Hopf equation (2.2) is ill-conditioned and its inversion is very sensitive to numerical or statistical errors.

4. Boundary conditions

When estimating the acoustic transfer matrix with time-dpeendent CFD, the acoustic element of interest is usually only part of the computational domain; see figure 2. It follows from the discussion of required signal properties in the preceding section that particular attention must be paid to the definition of the boundary conditions. Wave processes at the boundary are shown in figure 2. Outgoing, reflected and external waves are expressed in terms of the Riemann invariants $f = f(x-(u+c)t)$ and $g = g(x-(u-c)t)$, traveling in the positive and negative x-direction, respectively.

The Riemann invariants are related to fluctuations (denoted by "~") of acoustic pressure and velocity as follows:

$$\frac{\tilde{p}}{\rho c} = f + g, \quad \tilde{u} = f - g, \tag{4.1}$$

$$f = \frac{1}{2}\left(\frac{\tilde{p}}{\rho c} + \tilde{u}\right), \quad g = \frac{1}{2}\left(\frac{\tilde{p}}{\rho c} - \tilde{u}\right). \tag{4.2}$$

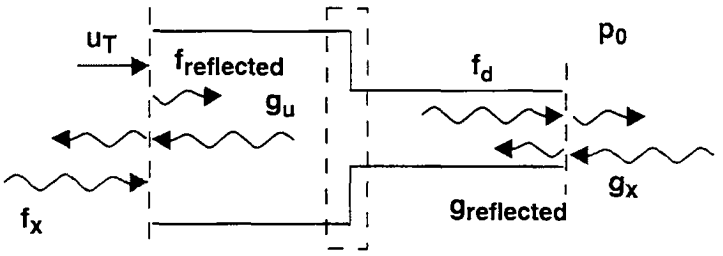

FIGURE 2. Boundaries of computational domain with outgoing waves g_u, f_d and forcing f_x, g_x at inlet and outlet, respectively. Reflected and transmitted wave components are also shown. The dashed line indicates the acoustic multi-port, i.e. the area change.

For harmonic waves with angular frequency ω,

$$f(x,t) = \hat{f}e^{i(\omega t - k_{x+}x)},\ g(x,t) = \hat{g}e^{i(\omega t - k_{x-}x)}. \tag{4.3}$$

Here $k_{x\pm} \equiv \pm\omega/c(1 \pm M)$ are the wave numbers of the invariants, and the "$\hat{}$" indicates a complex-valued wave amplitude.

As indicated in figure 2, the boundary conditions must first provide an excitation signal of suitable amplitude and frequency content. However, in general the signals $s^{(1)}$ and $s^{(2)}$ are related neither directly nor uniquely to external waves f_x and g_x imposed at the boundary. If there is reflection of outgoing waves at the boundary, then the signal $s^{(1)}$, say, will be influenced strongly by $f_{\text{reflected}}$, and similarly for the outlet. A closed feedback loop of acoustic waves traveling in the up- and downstream directions throughout the system is established, resulting in significant correlation between signals $s^{(1)}$ and $s^{(2)}$. Resonant amplification near acoustic eigenmodes of the acoustic system will lead to large signal amplitudes at the eigenfrequencies, which will dominate the autocorrelation matrix in an undesirable manner. These effects will make robust estimation of the transfer matrix difficult or impossible. It follows that the boundary conditions must be formulated in such a way that outgoing acoustic waves are not reflected back into the computational domain.

Finally, the boundary conditions must maintain certain values for the target velocity u_T – which in the case of large-eddy simulation includes a time-dependent turbulent component – at the inlet, as well as the far-field pressure p_∞ at the outlet.

4.1. *Characteristics-based boundary conditions*

A strategy for defining boundary conditions in compressible viscous flow is outlined in Thompson (1987) and Poinsot & Lele (1992). The boundary conditions are formulated in terms of characteristic wave relations. In the present context, acoustic waves with incidence normal to a boundary are of particular interest. If the boundary lies in the (y,z)-plane, say, the corresponding boundary conditions are formulated with the help of two quantities $\mathcal{L}_5$ and $\mathcal{L}_1$ defined as follows:

$$\mathcal{L}_i \equiv \lambda_i \left(\frac{\partial p}{\partial x} \pm \rho c \frac{\partial u}{\partial x} \right), \tag{4.4}$$

where the "+" sign corresponds to the index "5", and the $\lambda_i \equiv u \pm c$ are propagation speed of the waves. It has been shown by Poinsot & Lele (1992), that the $\mathcal{L}_i$'s can be interpreted as the time variations of wave amplitudes at the boundary.

4.2. *LODI relations and Riemann invariants*

Poinsot & Lele (1992) introduced local one-dimensional inviscid (LODI) relations to obtain approximate values for the wave-amplitude variations in terms of the primitive flow variables. For pressure and the velocity component normal to the boundary, the expressions

$$\frac{\partial p}{\partial t} + \frac{1}{2}(\mathcal{L}_5 + \mathcal{L}_1) = 0, \qquad \frac{\partial u}{\partial t} + \frac{1}{2\rho c}(\mathcal{L}_5 - \mathcal{L}_1) = 0 \tag{4.5}$$

are given. In the present context, plane harmonic waves are of particular interest, so – using the definitions (4.4) and (4.2) – we express the wave-amplitude variations $\mathcal{L}$ and the LODI relations in terms of the Riemann invariants. Subtracting the second part of (4.5) from the first, one obtains

$$\frac{\partial}{\partial t}\left(\frac{\tilde{p}}{\rho c} - \tilde{u}\right) + \frac{1}{\rho c}\mathcal{L}_1 = 0 \;\text{ or }\; \mathcal{L}_1 = -i\,2\omega\rho c\, g, \tag{4.6}$$

with (4.2) and $\partial g/\partial t = i\omega g$ for harmonic waves. Similarly,

$$\mathcal{L}_5 = -i\,2\omega\rho c\, f. \tag{4.7}$$

4.3. *(Partially) reflecting boundary conditions*

In this section, various types of boundary conditions, which can be implemented with the approach proposed in Poinsot & Lele (1992), are presented and their acoustic properties are briefly discussed.

4.3.1. *Subsonic reflecting outlet – "open end"*

A subsonic reflecting outlet should correspond to an "open-end" boundary condition in acoustics, where $\tilde{p} = f + g = 0$. Indeed we infer from (4.6) and (4.7) that $\mathcal{L}_1 + \mathcal{L}_5 = 0$ at an "open end", which is equivalent to equation (38) in Poinsot & Lele (1992). Note that an open-end boundary is strongly reflecting, with a reflection factor $r = -1$. (The reflection factor r is defined as the ratio of the reflected to the outgoing Riemann invariant, e.g. $r = g/f$ at an outlet, provided that there is no external incoming acoustic signal.)

4.3.2. *Subsonic partially-reflecting outlet*

If the temporal evolution of velocity and pressure at an outlet ($x = L$) would be determined solely from an outgoing wave $\mathcal{L}_5$ via the appropriate LODI relation, then – neglecting viscous and multidimensional effects – the outgoing wave would leave the domain without reflection.

However, the static pressure at the boundary must be "informed" somehow about the plenum or far-field pressure p_∞. Poinsot & Lele (1992) suggest prescribing, for this purpose, an ingoing wave at a flow outlet as

$$\mathcal{L}_1 = \frac{\sigma c}{L}(p - p_\infty), \tag{4.8}$$

where σ is a coupling parameter which is to be chosen appropriately. The speed of sound c and length L are introduced for dimensional consistency and represent characteristic scales of the problem. Then, if there is no outgoing wave $\mathcal{L}_5$, we see with (4.5) that an excess pressure $\Delta p = p - p_\infty$ will be reduced exponentially to zero according to

$$\frac{\partial \Delta p}{\partial t} = -\frac{\sigma c}{2L}\Delta p, \tag{4.9}$$

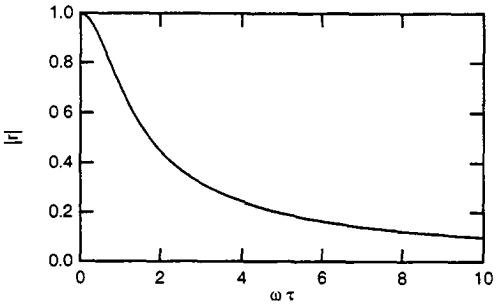

FIGURE 3. Absolute value of reflection coefficient $|r|$ vs. non-dimensional frequency $\omega\tau$ for partially reflecting in- or outflow boundary condition according to (4.8) and (4.13).

with a decay time

$$\tau \equiv \frac{2L}{\sigma c} \tag{4.10}$$

inversely proportional to the coupling coefficient σ.

Unfortunately, with such a prescription the boundary is no longer truly non-reflecting, because the pressure p which appears in (4.8) depends both on the in- as well as the outgoing waves. The reflection coefficient $r = g/f$ for plane waves at an outflow boundary, which is set up according to (4.8), can be estimated as follows: Assuming that pressure deviations from the prescribed value p_∞ at the outlet are dominated by acoustic waves f, g with angular frequency ω, (4.6) yields

$$r = \frac{g}{f} = \frac{\sigma c/L\,(p - p_\infty)}{-2i\,\rho c\,\omega\,f} \approx \frac{i\,\sigma c}{2\omega L}\frac{f+g}{f} = \frac{i}{\omega\tau}(1+r). \tag{4.11}$$

Solving for r, a complex-valued reflection coefficient is obtained:

$$r = \frac{-1}{1+i\omega\tau} = \begin{cases} i\,0 & \text{for } \omega\tau \to \infty \text{ (high-frequency limit),} \\ -1 & \text{for } \omega\tau \to 0 \text{ (low-frequency limit).} \end{cases} \tag{4.12}$$

For waves with relatively high frequency – with a period of oscillation much smaller than the decay constant τ – the restoration of the pressure at the outlet according to (4.8) is too slow to respond to the acoustic perturbations, such that the boundary is indeed effectively non-reflecting. Conversely, a low-frequency signal is reflected as if it had encountered an "open end" ($\tilde{p} = 0$), because the boundary condition (4.8) succeeds in keeping the pressure at the outlet close to the target value p_∞ due to the comparatively short decay time constant τ.

4.3.3. *Subsonic partially-reflecting inlet*

In order to have correct turbulence statistics at an inlet, the flow velocity u has to be imposed, which leads to difficulties in the definition of a fully-non-reflecting boundary condition very similar to those described in the previous subsection. From the LODI relations (4.5), one infers that with

$$\mathcal{L}_5 = \frac{\sigma c}{L}\rho c(u - u_T) \tag{4.13}$$

a deviation of the inflow velocity from the target value u_T should again decay exponentially with a time constant $2L/\sigma c$. For the reflection coefficient one obtains

$$r = \frac{f}{g} = \frac{1}{1 + i\omega\tau} = \begin{cases} -i\,0 & \text{for } \omega\tau \to \infty \text{ (high-frequency limit)}, \\ 1 & \text{for } \omega\tau \to 0 \text{ (low-frequency limit)}. \end{cases} \tag{4.14}$$

i.e. in the low-frequency limit the boundary condition (4.13) acts like a "closed end" without (acoustic) fluctuations of velocity.

In figure 3, the absolute value of the reflection coefficient $|r|$ is plotted as a function of the non-dimensional frequency $\omega\tau$. The absolute value $|r|$ of the reflection coefficient is the same for (4.12) and (4.14). If the magnitude of the reflection coefficient $|r|$ is not to exceed a certain value for a given frequency ω, then the corresponding minimum time constant τ can be deduced from this plot. Unfortunately, large values of τ correspond to low values of the coupling coefficient σ, which may result in divergence of the flow solver or drift of the values of velocity and pressure from the target values u_T and p_∞, respectively.

To summarize, although the boundary conditions (4.8) and (4.13) are often referred to as "non-reflecting" boundary conditions in the literature, they will lead to significant reflection of outgoing waves for sufficiently low frequencies. In thermo-acoustic problems unstable modes often correspond to low-order eigenmodes ("1/4-wave"-mode, etc.), and the corresponding low frequencies are of particular interest.

Note that Selle (2002) has independently obtained similar results concerning the frequency-dependence of the reflection coefficient by integrating a differential equation for pressure perturbations resulting from Eqns. (4.8) and (4.13).

4.3.4. *Boundaries with incoming waves*

With the help of (4.6) and (4.7), wave amplitudes $\tilde{\mathcal{L}}_1$ and $\tilde{\mathcal{L}}_5$ corresponding to external waves f_x and g_x can be specified as additional terms in the boundary conditions,

$$\mathcal{L}_i = \ldots + \tilde{\mathcal{L}}_i, \tag{4.15}$$

where "..." stands for the coupling terms discussed above, or terms which correspond to inflow turbulence.

For example, if a random number generator and a Butterworth filter are used to generate a time series $f_x(t)$ with uniform power spectral density over a certain range of frequencies, then the time derivative of this series provides the related wave amplitude variation $\tilde{\mathcal{L}}_5$,

$$\tilde{\mathcal{L}}_5 = -2\rho c \frac{\partial f_x(t)}{\partial t}, \tag{4.16}$$

see Eqn. (4.6). If the incoming signal is a superposition of sine-waves, then the corresponding wave amplitude variation equals

$$\tilde{\mathcal{L}}_5 = -2\rho c \sum A_n \omega_n \cos(\omega_n t + \phi_n). \tag{4.17}$$

4.4. *Plane wave non-reflecting boundary conditions*

It is possible to construct boundary conditions which – at least for plane waves with normal incidence – should be nearly non-reflecting even at low frequencies $\omega\tau \to 0$. The idea is to identify plane waves impinging on the boundary either from the outside (e.g. an excitation signal f_x or g_x) or from the inside, and then eliminate the plane wave contribution to the velocity coupling term (4.13) at an inflow boundary, and similarly for the pressure coupling (4.8) at an outflow. The use of an absorbing "sponge layer"

is often not possible in thermo-acoustic problems due to the very low frequencies and correspondingly large wave lengths typically involved. In the case of an inflow, these considerations suggest:

$$\mathcal{L}_5 = \frac{\sigma c}{L}\rho c\,(u - (f_x - g) - u_T) + \tilde{\mathcal{L}}_5. \tag{4.18}$$

Similarly, for an outflow,

$$\mathcal{L}_1 = \frac{\sigma c}{L}\,(p - \rho c\,(f + g_x) - p_\infty) + \tilde{\mathcal{L}}_1. \tag{4.19}$$

4.4.1. *Area-averaged reflection coefficient for plane waves*

In order to determine the reflection coefficient resulting from (4.18) or (4.19) for outgoing plane waves, we recall that plane waves which are incident normally to a boundary exhibit – with the exception of the acoustic boundary layer, which is usually very thin – no spatial variation over the boundary. Therefore, as far as plane waves are concerned, the reflection coefficient for an inflow boundary, say, may be written as follows:

$$r = \langle\frac{\mathcal{L}_5}{\mathcal{L}_1}\rangle \approx \frac{\langle\mathcal{L}_5\rangle}{\langle\mathcal{L}_1\rangle}\left(1 - \frac{\langle\mathcal{L}_5'\mathcal{L}_1'\rangle}{\langle\mathcal{L}_5\rangle\langle\mathcal{L}_1\rangle}\right) \approx \frac{\langle\mathcal{L}_5\rangle}{\langle\mathcal{L}_1\rangle} = \frac{i\sigma c}{2\omega L}\left(\frac{\langle u - u_T\rangle - (f - g)}{g}\right). \tag{4.20}$$

Here an (instantaneous) area average over the inflow boundary and local deviations from this average are denoted as $\langle\ldots\rangle$ and "$\ldots'$", respectively. For the application that we have in mind, it is reasonable to assume that the incoming and outgoing $\mathcal{L}$s are not strongly correlated, $\langle\mathcal{L}_5'\mathcal{L}_1'\rangle \approx 0$, while $\langle f\rangle = f$ and similarly for the outgoing Riemann invariant g. The boundary condition (4.18) has been employed, and of course the external forcing $\mathcal{L}_5$ is not considered in the determination of the reflection coefficient.

It follows that the reflection coefficient r indeed vanishes for plane harmonic waves of arbitrary frequency if one can assume that the area-averaged deviations of velocity from the target value are primarily due to plane acoustic waves at the boundary, because in this case $\langle u - u_T\rangle = f - g$.

Similar arguments suggest that an outflow boundary condition satisfying (4.19) should also be non-reflecting even at very low frequencies. Again, it must be assumed that area-averaged deviations of pressure from the target value p_∞ are primarily due to the plane acoustic waves – whether this assumption actually holds true in LES computations will be discussed below.

4.4.2. *Estimation of Riemann invariants at the boundary*

The Riemann invariants in (4.18) and (4.19) must be determined from the boundary conditions or the primitive variables at grid points at or near the boundary. By design, the area-averaged amplitude variation of the incoming waves f_x, g_x should be well approximated by the external excitation signal,

$$\langle\mathcal{L}_5\rangle \approx \tilde{\mathcal{L}}_5, \tag{4.21}$$

and it is has been shown in section 4.3.4 how the external Riemann invariants are related to the wave amplitude variations $\mathcal{L}_1$ and $\mathcal{L}_5$.

The outgoing waves must be constructed from interior grid points. At an inlet, say, we assume that area-averaged deviations δu and δp from the target values u_T and p_0 (the steady state average pressure at the inlet) are due to harmonic waves only, i.e.

$$g(t) = \frac{1}{2}\left(\frac{\delta p}{\rho c} - \delta u\right), \tag{4.22}$$

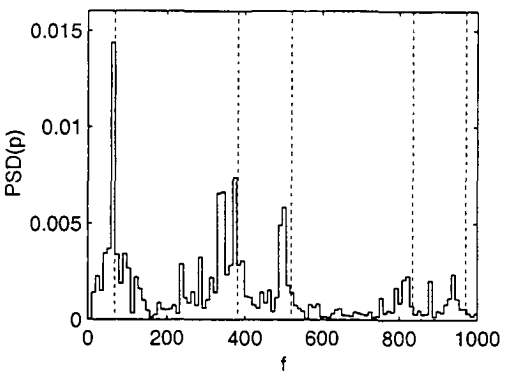

FIGURE 4. Power spectral distribution of pressure at the area change in LES simulation. The dotted lines indicate acoustic eigenfrequencies with "closed end" and "open end" boundary conditions up- and downstream, respectively.

where $\delta u \equiv \langle u - u_T \rangle$, $\delta p \equiv \langle p - p_0 \rangle$, and similarly for an outflow boundary.

5. Simulation results

An LES of the configuration shown in figure 2, with an area ratio of 4:1 and a total length of 0.8 m, has been performed using the method of Wall *et al.* (2002). This method is an extension of the low Mach number method of Pierce (2001) to compressible flow, and is efficient at low Mach number without introducing any artificial damping of acoustic waves. Turbulent inflow data for u_T as well as the v and w components of velocity at the inlet plane are obtained from a separate, incompressible, channel flow calculation using the method of Pierce (2001). Both quasi-two- and three-dimensional simulations have been performed, using a mean velocity of 7 m/s at the inlet, and a time step of 1.5×10^{-5} s. At each time step the code generates averaged values of both pressure and streamwise velocity at planes $0.5, 0.10, 0.20, 0.30$, and 0.38 m from the plane of the contraction in both the up- and downstream directions.

A simulation with the partially-reflecting boundary conditions according to (4.8) and (4.13) and broadband excitation both up- and downstream produced the power spectral distribution of pressure at the area change shown in figure 4. Strong resonance peaks are observed, suggesting that the boundaries are strongly reflecting (non-reflecting boundaries would yield a uniform PSD). Indeed, the location of the strongest peaks agrees reasonably well with the acoustic eigenfrequencies (indicated by the dotted lines in the figure) predicted by a simple acoustic network-model of this configuration with "closed end" and "open end" boundary conditions up- and downstream, respectively.

These observations prompted the investigation of the acoustic properties of partially reflecting boundary conditions described in Sections 4.3.2, 4.3.3 and the new formulation for boundary conditions described in Section 4.4. Reflection factors actually observed with the new and old formulations for the inflow boundary are shown in figure 5. In this run, the maximum possible time constant is $\tau = 8.4 \times 10^{-5}$ s. With larger values of τ, i.e. a smaller coupling constants σ for the inflow velocity, the solver diverges. According to Eqn. (4.13) this value should yield, even for the highest frequency $f = 1000$ Hz considered, a reflection factor close to unity. This is confirmed by LES results obtained with the old formulation for the inflow boundary (4.14), while the new formulation results in a very

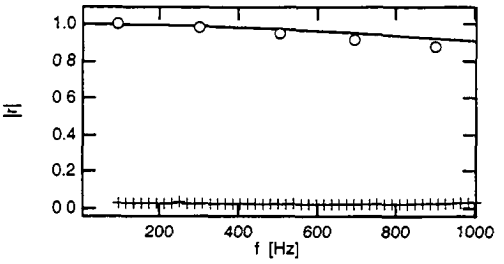

FIGURE 5. Inlet reflection factors observed in LES computations with boundary conditions (4.13) (∘) and (4.18) (+), respectively and according to Eqn. (4.14) (——).

small reflection factor even at the lowest frequencies $f = 100$ Hz considered in these runs; see figure 5. Note that the coherence – expressed as a normalized, oversampled cross-power spectral density – between signals $s^{(1)}$ and $s^{(2)}$ is significantly influenced by the boundary conditions: the coherence is very close to unity when the reflection factor is large, while it fluctuates between 0 and 1 with a mean value of approximately 0.4 with the new boundary conditions (not shown).

At the outflow, near-zero reflection factors cannot be observed, no matter which boundary condition is used. When using the standard formulation (4.8) at the outlet, it is possible to work with a rather low value of the coupling coefficient σ, corresponding to a time constant $\tau = 0.02$ s, without divergence or "drift" of the outlet pressure. Thus one should – according to (4.12) or figure 3 – expect a near-zero reflection coefficient $|r| < 0.01$ for $f = 1000$, while for frequencies around 100 Hz $|r| \approx 0.08$. Instead, reflection coefficients larger than unity are observed, i.e. the upstream-traveling Riemann invariant g is larger than its companion f traveling in the downstream direction – even for frequency bands where there is no forcing signal g_x imposed at the outlet. Similar results are obtained with the new formulation (4.19) for the outflow boundary.

The explanation proposed for these findings is that turbulent fluctuations originating from the contraction 1) generate spurious signals ("pseudo-sound") at the monitor planes downstream of the contraction 2) give rise to upstream-travelling acoustic waves g as they impinge on the downstream boundary. This hypothesis is supported by power spectrum distributions of the signals $s^{(1)}$ (the downstream-traveling wave f on the upstream side of the contraction) and $s^{(2)}$ (the upstream wave g downstream of the contraction) observed in an LES run, where both the upstream and downstream forcing functions, f_x and g_x, comprise a sum over 20 sinusoids of equal amplitude in the frequency range 50 – 1000 Hz. The PSD of $s^{(1)}$ shows as expected 20 equally spaced peaks of approximately equal amplitude, while the spectrum of $s^{(2)}$ displays amplitudes which vary significantly and are overall much larger than expected, see figure 6. Also, the location of the peaks does not correspond well to the spectrum of g_x.

These spurious contributions to the signals recorded at the monitor planes make it impossible to reconstruct the transfer matrix of the area change with acceptable accuracy from the LES data (not shown). Conversely, in unsteady RANS calculations, turbulent fluctuations are not explicitly resolved, and the agreement between computed and measured transfer matrices is very good and agrees well with theoretical expectations as well as experimental results, see Gentemann *et al.* (2003)

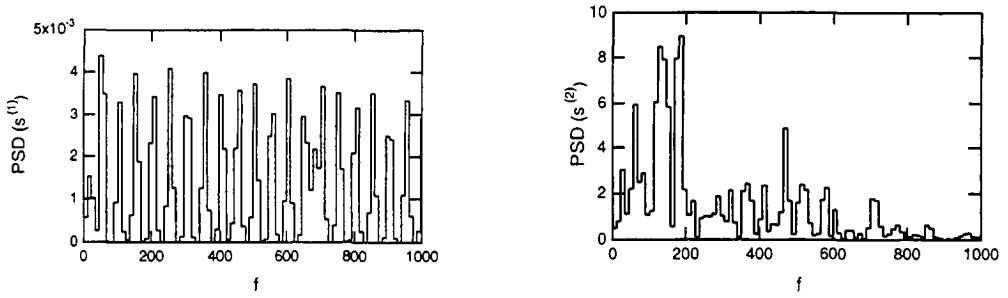

FIGURE 6. Power spectral distributions of signals $s^{(1)}$ (left) and $s^{(2)}$ (right) with plane-wave non-reflecting boundary conditions and broad-band sinusoidal external forcing at inflow and outflow boundaries

6. Conclusion

The estimation of (thermo-)acoustic transfer matrices from numerically-generated time series of pressure and velocity fluctuations through correlation analysis is arguably a flexible and efficient way of employing CFD for the study of combustion instabilities. First investigations based on unsteady laminar flow and Reynolds-averaged Navier-Stokes formulations for turbulent flow have shown promising results. In this study, the utilization of large eddy simulation for this technique is explored for the first time.

To this purpose, a novel formulation for boundary conditions was derived, implemented and successfully tested: it allows plane acoustic waves to leave the computational domain without reflection – even at very low frequencies, where the standard formulation for partially reflecting boundaries is strongly reflecting.

However, it was not possible to reconstruct the transfer matrix of the simple test configuration used in this study with acceptable accuracy from LES data. Turbulent fluctuations are held responsible, as they can generate spurious signal contributions at the monitor planes inside the computational domain, and also acoustic waves as they impinge on the outlet boundary of the domain.

Fortunately, it should be possible to eliminate the spurious contributions to the signals with the "Multi-Microphone Method" developed for the experimental determination of transfer matrices; see Paschereit & Polifke (1998). Acoustic waves generated at the outlet by turbulent fluctuations could actually be tolerated in transfer matrix estimation, unless they completely overwhelm in amplitude the upstream forcing signal. If this is the case, a thin "sponge layer" near the outlet could be used to dampen the amplitude of turbulent fluctuations impinging on the boundary (Lele (2002)). These modifications to the tranfer matrix estimation scheme and the boundary conditions shall be implemented in future work.

7. Acknowledgments

The Matlab-implementation of the Wiener-Hopf inverter used in this study was written by Alexander Genteman. Discussions with Summer Program participants and CTR staff, in particular Andre Kaufmann, Thierry Poinsot, Laurent Selle and Sanjiva Lele were exciting and enlightening. Thanks to Heinz Pitsch for reviewing this report. Financial support by the Center for Turbulence Research and the German Ministry for Education and Research (AG Turbo Project 4.4) is gratefully acknowledged.

REFERENCES

BELLANGER, M. 1984 *Digital Processing of Signals*. Wiley Interscience.

BOHN, D. & DEUKER, E. 1993 An acoustical model to predict combustion driven oscillations. In *20th Intl. Congr. on Combustion Engines*, **G20**. London, UK: CIMAC.

DEUKER, E. 1995 Ein Beitrag zur Vorausberechnung des akustischen Stabilitätsverhaltens von Gasturbinen-Brennkammern mittels theoretischer und experimenteller Analyse von Brennkammerschwingungen. *PhD thesis*, RWTH Aachen.

GENTEMANN, A. M., FISCHER, A. & POLIFKE, W. 2003 Acoustic transfer matrix reconstruction. In preparation.

KRÜGER, U., HOFFMANN, S., KREBS, W., JUDITH, H., BOHN, D. & MATOUSCHEK, G. Stockholm, Sweden, 1998 Influence of turbulence on the dynamic behaviour of premixed flames. *ASME paper* 98-GT-323.

LELE, S. 2002 Private communication.

LJUNG, L. 1999 *System Identification-Theory For the User*. Prentice Hall, 2nd Edition.

PASCHEREIT, C. O. & POLIFKE, W. 1998 Investigation of the thermo-acoustic characteristics of a lean premixed gas turbine burner. In *Int'l Gas Turbine and Aeroengine Congress & Exposition*. Stockholm, Sweden.

PIERCE, C. D. 2001 Progress-variable approach for large-eddy simulation of turbulent combustion. *PhD thesis*, Stanford University.

POINSOT, T. & LELE, S. K. 1992 Boundary conditions for direct simulation of compressible viscous flows. *J. Comp. Phys.* **101**, 104–129.

POINSOT, T. & VEYNANTE, D. 2001 *Theoretical and Numerical Combustion*. R. T. Edwards, Inc.

POLIFKE, W., PASCHEREIT, C. O. & DÖBBELING, K. 2001*a* Constructive and destructive interference of acoustic and entropy waves in a premixed combustor with a choked exit. *Int. J. of Acoustics and Vibration* **6**, 135–146.

POLIFKE, W., PONCET, A., PASCHEREIT, C. O. & DÖBBELING, K. 1998 Determination of (thermo-)acoustic transfer matrices by time-dependent numerical simulation. *7th Int. Conference on Numerical Combustion*. York, UK.

POLIFKE, W., PONCET, A., PASCHEREIT, C. O. & DÖBBELING, K. 2001*b* Reconstruction of acoustic transfer matrices by instationary computational fluid dynamics. *J. Sound Vib.* **245**, 483–510.

RABINER, L. R. & GOLD, B. 1975 *Theory and Application of Digital Signal Processing*. Prentice Hall.

SELLE, L. 2002 Private communication.

THOMPSON, K. W. 1987 Time dependent boundary conditions for hyperbolic systems. *J. Comp. Phys.* **68**, 1–24.

WALL, C., PIERCE, C. D. & MOIN, P. 2002 A semi-implicit method for resolution of acoustic waves in low mach number flows. *J. of Comp. Phys.* **181**, 545–563.

Large-eddy simulation of pool fires with detailed chemistry using an unsteady flamelet model

By R. Rawat †, H. Pitsch and J. F. Ripoll

An unsteady flamelet approach is implemented as a subgrid combustion model for large-eddy simulation (LES) of buoyancy-dominated large-scale pool fires. In fires, soot plays a major role in the overall heat transfer, and therefore in the dynamics of fires. In simulations of soot formation in laminar flames, it has been shown that an accurate description is crucial to achieving reasonable predictions. Chemical reaction mechanisms accounting for the formation and oxidation of soot and of polycyclic aromatic hydrocarbons are typically described by hundreds of species and therefore are computationally expensive to incorporate if there is no simplification of the LES computation. Unsteady flamelet models permit consideration of detailed chemical kinetic mechanisms and a state-of-the-art description of soot formation and oxidation processes. The Lagrangian Flamelet model is incorporated in an existing LES fire code and compared with data from an experiment on a methane fire in a pool of one meter diameter. Results for soot predictions compare well with qualitative observations from the experiment. To discuss the influence of the description of radiative transport, a three-dimensional post-processing radiation simulation, using an averaged form of the M_1 radiation model with mean absorption coefficients, is also performed. For this latter simulation, distributions of temperature and of species volume fraction have been taken from the LES results.

1. Introduction

Accidental fires in the United States result in billions of dollars of property damage, and over 2000 deaths, per year. In the majority of accidental fires, the thermo-physical characteristics of the fuel are not sufficiently known to asses the fuel's fire safety properties, such as heat-release rate or effectiveness of fire-suppression agents. Also, experimental studies of large fires are hindered by monetary expense, sensitivity to environmental conditions, and harshness to diagnostic equipment. Numerical simulations provide a promising tool to complement experimental studies to further our understanding of fire safety and fire physics. The wide range of length and time scales present in large fires prohibits the use of three-dimensional direct numerical simulations. Also, accidental fires often involve the highly unsteady processes of fluid-structure interaction, flame spread across fuels, and wind effects. These processes will be better captured by large eddy simulations (LES) as opposed to Reynolds averaging approaches. Furthermore, in large pool fires, soot plays a major role in the overall heat transfer through radiation and therefore, in the dynamics of the fire. The solution of a full set of species transport equations, required by a detailed kinetic mechanism describing soot formation, is computationally unfeasible. An unsteady flamelet model is a viable approach to model chemistry/transport interactions allowing for the use of complex chemistry. This model has been developed by Pitsch *et al.* (1998) and has been applied to a series of momentum-driven reacting jets with good predictions of temperature and species mass fractions, including pollutants such as NO_x and

† University of Utah

soot. More recently, the model has been formulated for LES by Pitsch & Steiner (2000). In the present work, this model is incorporated into the LES fire code by Rawat *et al.* (2001). The model is applied in an LES of the experiment on a gaseous methane fire in a pool of one meter diameter by Tieszen *et al.* (2002), and compared with qualitative experimental observations and quantitative velocity data.

2. Numerical Formulation

The LES approach applied here in the numerical modeling of a pool fire is based on the set of spatially density-weighted filtered, time-dependent conservation equations for mass, momentum, mixture fraction, and enthalpy in a Cartesian coordinate system, given as (Moin *et al.* (1991))

$$\frac{\partial \bar{\rho}}{\partial t} + \nabla \cdot (\bar{\rho}\tilde{\mathbf{u}}) = 0 \tag{2.1}$$

$$\frac{\partial \bar{\rho}\tilde{\mathbf{u}}}{\partial t} + \nabla \cdot (\bar{\rho}\tilde{\mathbf{u}}\tilde{\mathbf{u}}) = -\nabla \bar{p} + \nabla \cdot \tilde{\sigma} - \nabla \cdot (\bar{\rho}(\widetilde{\mathbf{u}\mathbf{u}} - \tilde{\mathbf{u}}\tilde{\mathbf{u}})) + (\rho - \rho_{\text{ref}})\mathbf{g} \tag{2.2}$$

$$\frac{\partial \bar{\rho}\tilde{Z}}{\partial t} + \nabla \cdot \left(\bar{\rho}\tilde{\mathbf{u}}\tilde{Z}\right) = \nabla \cdot (\bar{\rho}\widetilde{D_z}\nabla \tilde{Z}) - \nabla \cdot \left(\bar{\rho}(\widetilde{\mathbf{u}Z} - \tilde{\mathbf{u}}\tilde{Z})\right) \tag{2.3}$$

$$\frac{\partial \bar{\rho}\tilde{h}}{\partial t} + \nabla \cdot \left(\bar{\rho}\tilde{\mathbf{u}}\tilde{h}\right) = \nabla \cdot (\bar{\rho}\widetilde{\Gamma}\nabla \tilde{h}) - \nabla \cdot \left(\bar{\rho}(\widetilde{\mathbf{u}h} - \tilde{\mathbf{u}}\tilde{h})\right) - \nabla \cdot \tilde{\mathbf{q}}_{\text{rad}} \tag{2.4}$$

Here, ρ is the density, t is the time, $\mathbf{u}$ is the velocity vector, p is the pressure, σ is the viscous stress tensor, Z is the mixture fraction, D_z is the molecular diffusion coefficient of the mixture fraction, h is the enthalpy, Γ is the thermal diffusion coefficient, and $\nabla \cdot \mathbf{q}_{\text{rad}}$ is the net radiative heat flux. The hydrostatic pressure contribution from the pressure gradient is subtracted and combined with the buoyancy term to obtain $(\rho - \rho_{\text{ref}})\mathbf{g}$. Pool fires can be described as low-speed flows where acoustic waves do not play a significant role in describing the dynamics. Therefore, the low-Mach-number variable-density formulation, as described by Najm *et al.* (1998), is used for the present calculations. These filtered equations are discretized on a 3-D, structured, Cartesian staggered grid using a second-order differencing scheme. An explicit, Runge-Kutta second-order time integration scheme is used for advancing the variables in time. The pressure equation for imposing mass conservation is obtained using the projection described by Najm *et al.* (1998). In their approach, the intermediate velocity is computed from the pressure-free momentum equation and then projected to satisfy the divergence-free constraint. The Poisson pressure equation obtained from this step is solved using Krylov methods. The intermediate velocity is then corrected by projecting it onto the calculated pressure field.

One of the important characteristics of the present fire scenario is that it occurs in an open domain. Pressure-based boundary conditions for fires, where crosswind is not important, are employed. At the inlet boundary, the boundary condition is a specified mass flux with a top hat velocity profile. At the lateral boundary, a traction-free boundary condition with a fixed specified pressure is used, allowing for air entrainment (Boersma *et al.* (1998)). At the outlet boundary a convective boundary condition as described by Akselvoll & Moin (1996) is specified.

The unresolved subgrid-scale Reynolds stress and the subgrid scalar fluxes are modeled using eddy-viscosity and eddy-diffusivity approaches. Thus the subgrid fluxes in the

momentum and mixture fraction transport equations are given by

$$\bar{\rho}(\widetilde{\mathbf{u}\mathbf{u}} - \tilde{\mathbf{u}}\tilde{\mathbf{u}}) = -2\bar{\rho}\nu_t\tilde{\mathbf{S}} \tag{2.5}$$

and

$$\bar{\rho}(\widetilde{\mathbf{u}} - \tilde{\mathbf{u}}\tilde{Z}) = -\bar{\rho}D_t\tilde{Z} \tag{2.6}$$

with

$$\tilde{\mathbf{S}} = \frac{1}{2}((\nabla\tilde{\mathbf{u}}) + (\nabla\tilde{\mathbf{u}})^T), \tag{2.7}$$

where ν_t is the subgrid kinematic eddy viscosity and D_t is the subgrid eddy diffusivity. The eddy viscosity ν_t is given by the Smagorinsky model as

$$\nu_t = C\Delta^2 \mid \tilde{\mathbf{S}} \mid, \tag{2.8}$$

where C is the Smagorinsky coefficient and Δ is the filter width. The subgrid diffusivity D_t is determined from

$$D_t = \nu_t/\mathrm{Sc}_t, \tag{2.9}$$

where Sc_t is the turbulent Schmidt number, assumed to be a constant in the current calculation. Similarly, the turbulent diffusivity for the energy equation is computed assuming a constant turbulent Prandtl number. For the present calculations, the Smagorinsky coefficient is computed from the dynamic procedure and a value of 0.4 is used for both the turbulent Prandtl and Schmidt numbers as suggested by Pitsch & Steiner (2000). An assumed β-function PDF approach for the mixture fraction is used to compute the filtered density, temperature, and species mass fractions: this has been shown to be very accurate provided a good estimate of the subgrid mixture fraction variance (Cook & Riley (1994) and Wall *et al.* (2000)). The mixture fraction variance is modeled using the scale-similarity assumption.

3. Unsteady-flamelet model

An unsteady-flamelet approach is used to implement the complex chemistry mechanism described above. Formulation of the model follows the work of Pitsch & Steiner (2000) who applied this model in an LES of a momentum-dominated coflowing jet flame. This model has also been applied in RANS simulations of a sooting jet diffusion flame (Pitsch *et al.* (2000)). In these simulations it has been demonstrated that for predictions of NO_x and soot formation, the description of the slow underlying chemical and physical processes is important and therefore an unsteady flamelet model has to be used.

In the unsteady-flamelet approach, the state space variables are obtained by solving the one-dimensional unsteady laminar flamelet equations. As in steady-state flamelet equations parameters accounting for the influence of the turbulent flow field on the unsteady flame structure are required. In the current implementation, this coupling is based on the assumption that flamelets are introduced at the base of the pool fire inlet, and are convected downstream with the axial velocity at the stoichiometric mixture fraction. The flamelet time therefore corresponds to a Lagrangian-like lifetime of a portion of the flame within the flow field. While moving downstream, the flamelets experience different local scalar dissipation and radiative heat losses. Based on these assumptions, the flamelet time appearing in the unsteady term of the flamelet equations can be correlated to the distance from the nozzle. The scalar dissipation rate describing the effect of the turbulent flow field on the laminar flamelets is also required in the coupling of the flamelet

equations with the LES flow solver. All parameters are obtained by radially averaging the filtered quantities obtained from the flow solver, conditional on the mixture fraction.

The filtered scalar-dissipation rate is modeled using the assumption that on the subgrid scale, the scalar variance production and dissipation rates are in equilibrium, as proposed by Pierce & Moin (1998). The radiative heat loss is obtained by using the Rosseland model. Since this model becomes singular if the soot volume fraction tends to zero, an optically-thin gas model is used for $f_v < 5 \cdot 10^{-7}$. This assumption, however, is not expected to be very accurate for pool fires, where radiation is dominated by soot. The sensitivity of the results to this assumption will be discussed in the following section.

Current chemical-kinetic reaction mechanisms describing the formation and oxidation of polycyclic aromatic hydrocarbons (PAH) and soot are too large to be included directly in a fire simulation. Traditionally, soot chemistry has been incorporated into combustion simulations via an assumption of equilibrium gas-phase chemistry coupled with empirical correlations for soot volume fraction (Tien & Lee (1982)). In the past decade, researchers have devised various methods for including more detailed soot chemistry in combustion simulations. Fairweather *et al.* (1992) performed simulations of soot formation in turbulent jet flames by coupling flamelet libraries to a global reaction scheme for soot formation following the model of Leung *et al.* (1991) including soot nucleation, surface growth, particle coagulation, and oxidation steps. Belardini *et al.* (1996) modeled diesel engine combustion with a simplified six-step kinetic scheme which included both combustion and soot formation models. Brown & Fletcher (1996) described soot formation in 3-D coal combustion by solving gas phase transport equations for soot mass fraction and tar mass fraction. The rate of soot formation is based on the local tar mass fraction while soot and tar destruction are based on global one-step Arrhenius oxidation rates.

The chemistry model used in the present study to capture detailed soot kinetics is divided into three parts: a) The gas phase chemistry including 400 elementary reactions among 90 chemical species describing fuel oxidation, the formation of benzene, and the further growth to small PAHs consisting of up to four aromatic rings, b) a model for the growth of PAHs to possible infinite size, c) and a model describing the formation of particles from large PAHs, the further growth by heterogeneous surface reactions following an extended HACA mechanism, the oxidation of soot particles by O_2 and OH surface reactions, and particle-particle and particle-PAH coagulation processes. Flamelet equations are solved for the first two moments of the soot particle-size distribution, allowing for thermophoresis and differential diffusion effects. These models essentially follow the work of Frenklach & Harris (1987), Mauss et al. (1994) and Mauss (1998).

4. Radiation model

Because of the complexity of the simultaneous coupling of the turbulent combustion model, the soot model, and the radiation model, the large-eddy simulation results for the pool fire described in the next section have been obtained using a simplified radiation model. However, to assess the applicability of simplified models and to investigate radiative processes occurring in a turbulent fire, we have performed post-processing simulations using an instantaneous three-dimensional temperature distribution from the LES results, with a more sophisticated model for the radiative heat transfer, including emission and absorption by soot, gaseous water and carbon dioxide.

The macroscopic M_1 radiation model developed by Levermore (1984), Fort (1997), Dubroca & Feugeas (1999) and Brunner & Holloway (2001) is chosen here to describe

radiative heat transfer. The model is hyperbolic and the speed of propagation of disturbances is unlimited, which is different from the commonly-used diffusion models. The model also dissipates entropy locally. The M_1 model with mean absorption coefficients has been derived in Ripoll *et al.* (2001) to account for the frequency dependence of the opacity at a microscopic level. The mean absorption coefficients take the anisotropic form of the photon absorption into account, and lead to a better description of the photon flow away from radiative equilibrium. An averaged form of this model has been derived by Ripoll (2002) and Ripoll & Pitsch (2002). In this formulation, closure is achieved by assuming the anisotropy factor f and the radiative temperature T_R to be uncorrelated. Here, all radiative correlations, except for the contribution from soot emission, are neglected.

The M_1 radiation model describes the evolution of the radiative energy E_R and the radiative flux vector $\mathbf{F_R}$ of a non-scattering gray medium at temperature T.

$$\partial_t \overline{E}_R + \nabla \cdot \overline{\mathbf{F}}_\mathbf{R} = c C_s \overline{Y_s a T^5} - c C_s \overline{Y}_s \, \overline{G}_E \, \overline{T}_R \, \overline{E}_R + c \overline{C}_g^{\,e} \, a \overline{T}^4 - c \overline{C}_g^{\,a} \, \overline{E}_R, \quad (4.1)$$

$$\partial_t \overline{\mathbf{F}}_\mathbf{R} + c^2 \, \nabla \cdot (\overline{\mathbf{D}}_\mathbf{R} \, \overline{E}_R) = -c C_s \overline{Y}_s \, \overline{G}_F \, \overline{T}_R \, \overline{\mathbf{F}}_\mathbf{R} - c \, \overline{C}_g^{\,a} \, \overline{\mathbf{F}}_\mathbf{R}, \quad (4.2)$$

The Eddington tensor $\overline{\mathbf{D}}_\mathbf{R}$ is defined by

$$\overline{\mathbf{D}}_\mathbf{R}(\mathbf{f}) = \mathbf{D}_\mathbf{R}(\overline{\mathbf{f}}) = \frac{1-\chi(\overline{\mathbf{f}})}{2} \, \mathbf{Id} + \frac{3\chi(\overline{\mathbf{f}})-1}{2} \, \frac{\overline{\mathbf{f}} \otimes \overline{\mathbf{f}}}{\| \overline{\mathbf{f}} \|}, \text{ with } \chi(\overline{\mathbf{f}}) = \frac{3 + 4\| \overline{\mathbf{f}} \|^2}{5 + 2\sqrt{4 - 3\| \overline{\mathbf{f}} \|^2}} \quad (4.3)$$

where $\mathbf{Id}$ is the identity matrix, $\overline{\mathbf{f}} = \overline{\mathbf{F}}_\mathbf{R}/(c\overline{E}_R)$ is the anisotropy factor, $\| . \|$ denotes an Euclidian norm, and χ is the Eddington factor. The radiative temperature, which represents an absorption temperature, is directly deduced from the radiative energy by $\overline{T}_R = \overline{E_R^{1/4}} = \overline{E}_R^{1/4}$.

The opacity, coming from the presence of the soot, is described through $C_s = 360 \frac{k \zeta_5}{\pi^4 h} C_1$ with $C_1 = 8.33 \times 10^{-9}$ (Lee & Tien (1981)). The opacity from gas radiation is given as $\overline{C}_g^{\,e} = C_g(\overline{T}, \overline{Y}_{\mathrm{H_2O}}, \overline{Y}_{\mathrm{CO_2}}) = C_{\mathrm{H_2O}}(\overline{T})\overline{Y}_{\mathrm{H_2O}} + C_{\mathrm{CO_2}}(\overline{T})\overline{Y}_{\mathrm{CO_2}}$ for emission and $\overline{C}_g^{\,a} = C_g(\overline{T}_R, \overline{Y}_{\mathrm{H_2O}}, \overline{Y}_{\mathrm{CO_2}})$ for absorption. The functions $C_{\mathrm{H_2O}}$ and $C_{\mathrm{H_2O}}$ are given elsewhere†. The anisotropy dependence of the mean absorption coefficients introduces the functions G_E and G_F in the absorption terms. These are given by

$$\overline{G}_E(\mathbf{f}) = G_E(\overline{\mathbf{f}}) = 1 + \frac{3}{4}\| \overline{\mathbf{f}} \|^2, \quad (4.4)$$

$$\overline{G}_F(\mathbf{f}) = G_F(\overline{\mathbf{f}}) = \frac{5}{4}(1 + \frac{1}{2}\| \overline{\mathbf{f}} \|^2). \quad (4.5)$$

The positive terms on the right-hand side of the M_1 model are the emission term while the negative terms represents those of absorption. The radiative net heat flux is given by the right hand side of 4.2. If full radiative heat transfer is considered, then this term also appears in the energy equation.

5. Results

Only pool fires around one meter in diameter and larger develop a fully turbulent flow, and only a few experiments have been done in this regime (Gritzo *et al.* (1998)). Tieszen

† www.ca.sandia.gov/tdf/Workshop/Submodels.html#Rad

FIGURE 1. Instantaneous temperature contours of a one meter diameter methane fire at different times (increasing left to right), illustrating the puffing behavior of the pool fire.

et al. (2002) have studied a one-meter-diameter methane fire with boundary conditions and flow rate comparable to a large jet-fuel pool fire. The experimental data include averaged and instantaneous velocity fields close to the base of the fire. This experiment has been conducted to provide a database for validation of numerical simulations of pool fires. Soot volume fraction is validated qualitatively, based on general observations in this and other experiments.

The $3\,\mathrm{m}^3$ computational domain for the one-meter-diameter methane fire simulation was discretized into a uniform mesh of 100^3. The same computational mesh has been used for the radiation simulations. Figure 1 illustrates computed instantaneous temperature contours from longitudinal cross-sections at different times. The calculation demonstrates the capability of the fire simulation tool to capture the puffing nature of pool fires. The time sequence of one puff cycle illustrates the formation of a vortical structure at the toe of the fire that grows in size as it is convected downstream. These finger-like structures have been attributed to the baroclinic vorticity generation mechanism (Tieszen *et al.* (1996)). For buoyancy-dominated pool fires, this is the most important mechanism for the production of vortical structures. This time sequence also illustrates an initial vortex, formed at the toe, rolling up and breaking off from the main flame zone, which is consistent with the observation that an intermittent turbulent region follows a continuous flame region where most of the combustion takes place (Tieszen *et al.* (1996)). Figure 2 shows mean axial velocities at different axial locations compared with the experimental data. The simulation results capture the velocity trends well. However, the spreading rate is larger in the numerical simulation than was observed in the experiments. These differences might be attributed to several factors. First, mesh resolution is not fine enough to capture all the relevant large-scale, energy-containing eddies that control mixing, which leads to a wider spreading rate. Secondly, only a simple radiation model is used for the current calculations, which might not be accurate enough for pool fires As a result,

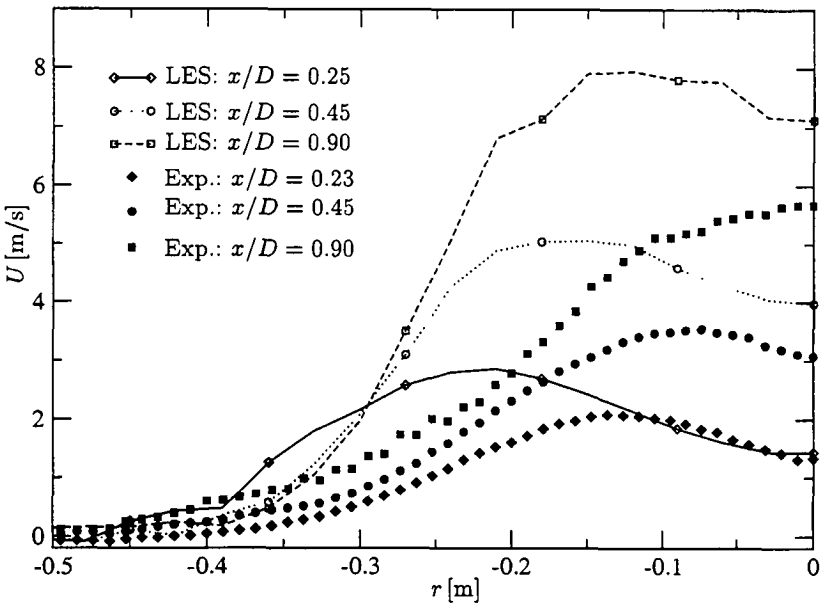

FIGURE 2. Comparison of radial time-averaged streamwise velocity profiles for a one-meter-diameter methane pool fire at different axial locations.

overall radiative emission from the simulated fire is lower than observed in real fires. Lower radiative emission produces higher fire temperatures, which leads to increased buoyancy and, consequently, higher velocities.

Figure 3 shows instantaneous soot volume fraction in a 2-D slice and a volume-rendered representation. The results indicate that soot is distributed throughout large regions of the flame, as is observed experimentally by Gritzo *et al.* (1998). The soot is completely oxidized before leaving the domain, which implies that there is no smoke formation in this fire. This is consistent with the experimental observation that smoke formation occurs only in pool fires larger than about 2 m in diameter. Radiative heat transfer for large-scale fires is dominated by emission and absorption, mainly from soot particles. To accurately predict radiative heat transfer from large scale fires, it is necessary to accurately predict local soot temperature and concentration. Time-averaged temperatures and soot volume fractions are shown in figure 4 at different axial locations. It is clearly seen that maximum soot concentration and maximum flame temperature do not occur at the same spatial location. Lower soot temperatures as seen in the figure have also been measured in experiments by Gritzo *et al.* (1998).

Figure 5 shows some results from a radiative calculation that has been done with a fixed instantaneous temperature field obtained from the LES. The radiative net heat flux shows that there is an absorption region in the center of the fire. A comparison with the soot volume-fraction distribution, shown in figure 3, indicates that because of the absence of soot in this region, the absorption here is caused by gaseous water and carbon dioxide. However, the regions of strong emission are governed mainly by

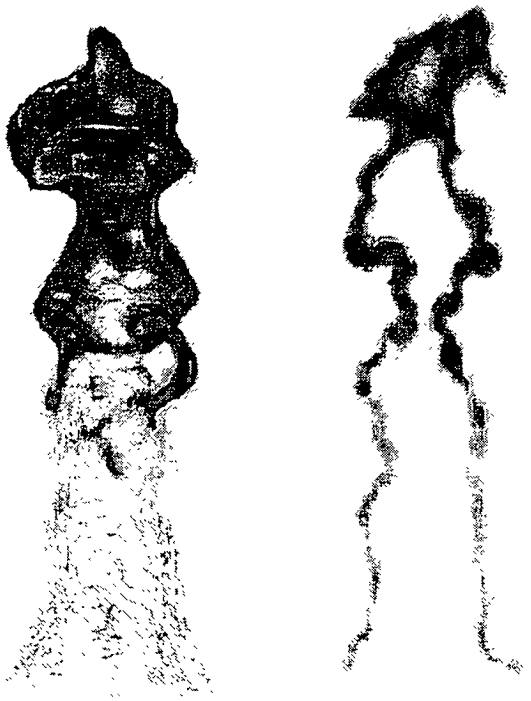

FIGURE 3. Instantaneous soot volume fraction at different times. The left figure shows a volume-rendered representation.

soot radiation. The M_1 model assures a transition of the anisotropy factor from $f = 0$, when radiation is isotropic, to its maximal value $f = 1$, when radiation is anisotropic. Isotropic regions are typically found in the central part of a fire, while the outside regions are usually anisotropic. This can also be observed in the present simulations, as shown in figure 5. Small values of the anisotropy factor usually indicate radiative equilibrium zones. Here, however, the small anisotropy in the center of the fire is due mainly to the symmetry about the centerline. Indeed, the radiative equilibrium, where emission balances absorption, $T \simeq T_R$, and hence $f = 0$, is almost never achieved for the present case. The thin radiative equilibrium zone can be identified T_R/T_m-field given in figure 5 as the region enclosed by the bold contour lines.

6. Conclusions

The Lagrangian Flamelet model has been successfully implemented for large-eddy simulation of buoyancy-dominated large-scale pool fires. The results from a one-meter-diameter methane pool fire simulation are compared with the experimental data for the time-averaged axial velocity field. The results capture the velocity trends well. The differences from the data have been attributed to the mesh resolution and the radiation model. Soot predictions from the simulations are in good agreement with the experimental observations for large-scale fires. Simulations also captured the negative spatial correlation between temperature and soot as seen in experiments. The importance of using a comprehensive three-dimensional radiative-transfer model for pool fires has been

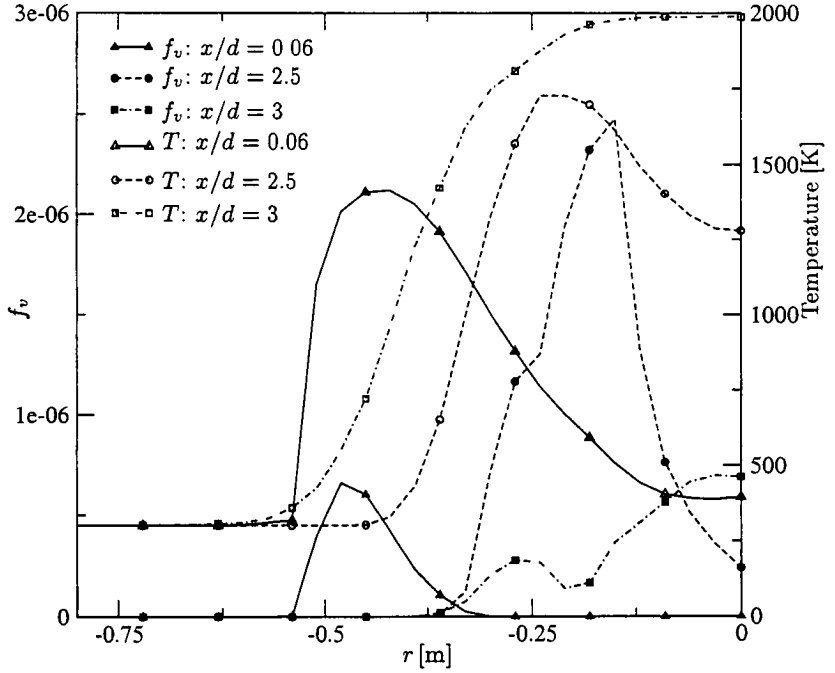

FIGURE 4. Radial time-averaged profiles of soot volume fraction and temperature for a one meter diameter methane pool fire at different axial locations

shown by comparing simulation results from the M_1 radiation model with the simplified radiation model.

REFERENCES

AKSELVOLL, K. & MOIN, P. 1996 Large-eddy simulation of turbulent confined annular jets. *J. Fluid Mech.* **315**, 387–411.

BILGER, R. 1980 Turbulent flows with nonpremixed reactants. *Topics in Applied Physics: Turbulent Reacting Flows* (P. A. Libby and F. A. Williams, eds.), Springer, Berlin, 65–113.

BOERSMA, B. J., BRETHOUWER, G. & NIEUWSTADT, F. T. M. 1998 A numerical investigation on the effect of the inflow conditions on the self-similar region of a round jet. *Phys. Fluids* **10**, 899–909.

BELARDINI, P., BERTOLI, C., BEATRICE, C., D'ANNA, A. & DEL GIACOMO, N. 1996 Application of a reduced kinetic model for soot formation and burnout in three-dimensional diesel combustion computations. *Proc. Combust. Inst.* **26**, 2517–2524.

BROWN, A. L. & FLETCHER, T. H. 1996 Modeling soot in coal combustion flames. *Western States Section of the Combust. Inst.*

BRUNNER, T. A. & HOLLOWAY, J. P. 2001 One-dimensional Riemann solvers and the maximum entropy closure. *J. Quant. Spectrosc. Radiat. Transfer* **69**, 543–566.

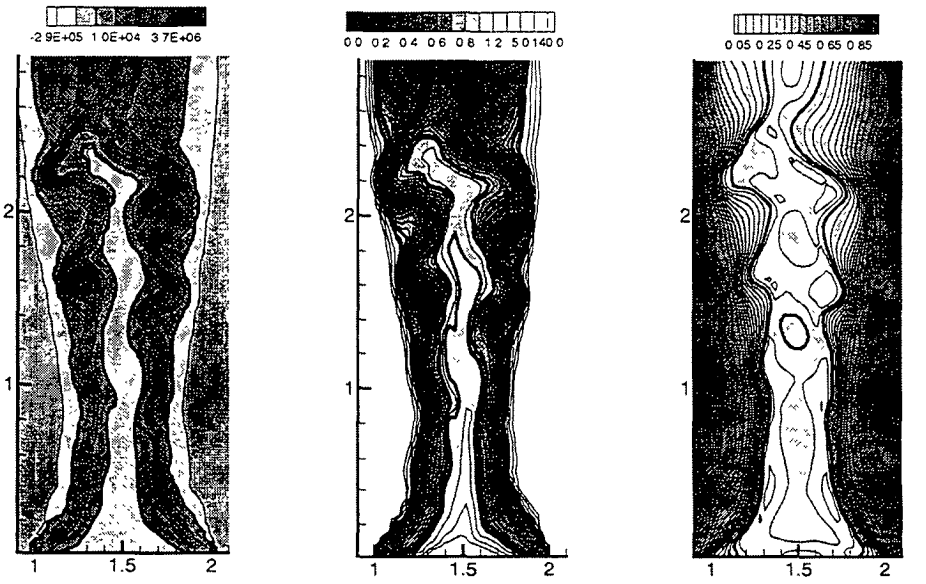

FIGURE 5. Net radiative heat flux, ratio of radiative to matter temperature T_R/T_m, and norm of the anisotropy factor $||f||$. Bold lines indicate zero net radiative heat flux in the left, $T_R/T_m = 0.8$ and $T_R/T_m = 1.2$ in the middle, and $||f|| = 0.2$ in the right figures.

COOK, A. W. & RILEY, J. J. 1994 A subgrid model for equilibrium chemistry in turbulent flows. *Phys. Fluids* **6**, 2868–2870.

DUBROCA, B. & FEUGEAS, J.-L. 1999 Etude théorique et numérique d'une hiérarchie de modèles aux moments pour le transfert radiatif. *C. R. Acad. Sci. Paris* **329**, 915–920.

FAIRWEATHER, M., JONES, W. P., LEDIN, H. S. & LINDSTEDT, R. P. 1992 Predictions of soot formation in turbulent, non-premixed propane flames. *Proc. Combust. Inst.* **24**, 1067–1074.

FORT, J. 1997 Information-theoretical approach to radiative transfer. *Phys. A.* **243**, 275–303.

FRENKLACH, M. & HARRIS, S. J. 1987 Aerosol dynamics modeling using the method of moments. *J. Coll. Interf. Sci.* **118**, 252–261.

GRITZO, L. A., SIVATHANU, Y. R. & GILL, W. 1998 Transient measurements of radiative properties, soot volume fraction and soot temperature in a large pool fire. *Combust. Sci. and Tech.* **139**, 113–136.

LEE, S. C. & TIEN, C. L. 1981 Optical constants of soot in hydrocarbon flames. *Proc. 18th International Symposium on Combustion.* The Combustion Institute, 1159–1166.

LEUNG, K. M., LINDSTEDT, R. P. & JONES, W. P. 1991 *Combust. Flame* **87**, 289–305.

LEVERMORE, D. 1984 Relating Eddington factors to flux limiters. *J. Quant. Spectrosc. Radiat. Transfer*, **31**, 149–160.

MAUSS, F., TRILKEN, B., BREITBACH, H. & PETERS, N. 1994 Soot formation in par-

tially premixed diffusion flames at atmospheric pressure. *Soot Formation in Combustion*, (H. Bockhorn, ed.), Springer, Berlin, 325–349.

MAUSS, F. 1998 Development of a kinetic soot model for soot formation with fast polymerization. *Ph.D Thesis*, RWTH Aachen.

NAJM, H. N., WYCKOFF, P. S. & KNIO, O. M. 1998 A semi-implicit numerical scheme for reaction flow: 1. Stiff chemistry. *J. Comput. Phys.* **143**, 389-406.

MOIN, P., SQUIRES, K., CABOT, W. & LEE, S. 1991 A dynamic subgrid-scale model for compressible turbulence and scalar transport. *Phys. Fluids* **3**, 2746–2757.

PIERCE, C. D. & MOIN, P. 1998 A dynamic model for subgrid-scale variance and dissipation rate of a conserved scalar. *Phys. Fluids* **10**, 3041–3044.

PITSCH, H., CHEN, M. & PETERS, N. 1998 Unsteady flamelet modeling of turbulent hydrogen/air diffusion flames. *Proc. Comb. Inst.* **27**, 1057–1064.

PITSCH, H. & STEINER, H. 2000 Large-eddy simulation of a turbulent piloted methane/air diffusion flame (Sandia flame D). *Phys. Fluids* **12**, 2541–2554.

PITSCH, H., RIESMEIER, E. & PETERS, N. 2000 Unsteady flamelet modeling of soot formation in turbulent diffusion flames. *Combust. Sci. and Tech.*, **158**, 389–406.

RAWAT, R., PARKER, S. G., SMITH, P. J. & JOHNSON, C. R. 2001 Parallelization and integration of fire simulations in the Uintah PSE. *Proc. 10th SIAM Conference on Parallel Processing for Scientific Computing, Portsmouth, VA.*

RIPOLL, J.-F., DUBROCA, B. & DUFFA, G. 2001 Modelling radiative mean absorption coefficients. *Comb. Theory and Mod.* **5**, 261–275.

RIPOLL, J.-F., DUBROCA, B. & AUDIT, E. 2002 A factored operator method for solving coupled radiation-hydrodynamics models. Preprint, to appear in Trans. Theor. and Stat. Phys.

RIPOLL, J.-F. 2002 An averaged formulation of the M_1 radiation model with presumed probability density functions for turbulent flows. Preprint, submitted for publication.

RIPOLL, J.-F. & PITSCH, H. 2002 Modelling turbulence-radiation interactions for large sooting turbulent flames. Preprint.

TIEN, C. L. & LEE, S. C. 1982 Flame radiation. *Prog. Energy Combust. Sci.* **8**, 41–59.

TIESZEN, S. R., NICOLETTE, V. F., GRITZO, L. A., HOLEN, J. K., MURRAY, D., & MOYA, J. L. 1996 Vortical structures in pool fires: observation, speculation, and simulation. *Sandia National Lab. Report No.* SAND96-2607.

TIESZEN, S. R., O'HERN, T. J., SCHEFER, R. W., WECKMAN, E. J. & BLANCHAT, T. K. 2002 Experimental study of the flow field in and around a one meter diameter methane fire. *Combust. and Flame,* **129**, 378–391.

WALL, C., BOERSMA, B. J. & MOIN, P. 2000 An evaluation of the assumed beta PDF subgrid-scale model for LES of non-premixed, turbulent combustion with heat release.*Phys. Fluids* **12**, 2522–2529.

Lagrangian PDF mixing models for reacting flows

By **Rodney O. Fox†, Chong M. Cha AND Philippe Trouillet**

The Lagrangian Fokker-Planck (LFP) model of Fox is further developed to describe multi-stream mixing and reaction. The problem of three-stream mixing is used to illustrate the extension to multi-stream mixing. Qualitative comparisons are made with the direct numerical simulations (DNS) of three-stream mixing of Juneja & Pope (1996). A simplified case with one-step chemistry is used to investigate modeling issues associated with the application of the LFP model to a reacting case. Predictions of the DNS results of Sripakagorn *et al.* (2000), which exhibit varying degrees of local extinction of the flame, are used to validate the LFP model for the reacting case. Future modeling challenges are discussed.

1. Introduction

Over the past decade, a novel Lagrangian PDF mixing model for use with transported PDF simulations has been developed and tested for scalar mixing (Fox 1994, 1995, 1996, 1997, 1999; Fox & Yeung 1999; Fox *et al.* 2001; Fox & Yeung 2002). This model differs substantially from other available mixing models (e.g., IEM, EMST, CD, Mapping Closure, etc.), and includes the following characteristics: (i) Accounts for the effect of the initial spectral distribution of the scalar on the scalar dissipation rates; (ii) Can treat multiple scalars with different molecular diffusivities; (iii) Effects of turbulence (Re), molecular diffusion (Sc_α), and chemistry (Da) on the scalar dissipation rates are handled explicitly; (iv) The characteristic "mixing time" is scalar-dependent, and fluctuates due to turbulent intermittency; and (v) Lagrangian time series for scalars and scalar dissipation rates are in good agreement with DNS. The complete mixing model involves two parts: the Lagrangian spectral-relaxation (LSR) model, which is used to predict the scalar dissipation rates; and the Lagrangian Fokker-Planck (LFP) model, which is used to predict the Lagrangian scalar time series. The work reported here focuses on validation of the LFP model.

Prior to this work, DNS validation studies of the LSR/LFP model had concentrated on inert scalar mixing (two-stream mixing of bounded inert scalars, and scalars with uniform mean gradients) using data sets generated by Yeung (2001) over a range of Reynolds numbers (R_λ = 38–240) and Schmidt numbers (1/8–1). Both *a priori* tests of the terms in the governing equations (Fox & Yeung 1999; Fox *et al.* 2001) and *a posteriori* tests of model predictions (Fox *et al.* 2001; Fox & Yeung 2002) have shown excellent agreement. Due to the simple shape of the scalar PDFs in these cases, the ability of the LFP model to predict the PDF shape could not be demonstrated. The next logical step in developing the LFP model is thus to test it against DNS results for more complex scalar-mixing problems. The results reported here focus on two such cases:

† Iowa State University

(*a*) Three-stream mixing of inert, bounded scalars (Juneja & Pope 1996).

(*b*) One-step second-order reaction (Sripakagorn *et al.* 2000).

Each of these DNS studies provides unique challenges to the mixing model.

The three-stream case involves two bounded scalars, and the initial tri-modal joint PDF evolves to a joint Gaussian PDF. For this case, the scalars can have different molecular diffusivities (differential diffusion) and/or different initial integral length scales. The time evolution of the joint PDF is clearly different for each case, and the mixing model must be able to account correctly for these differences. Before this work, no mixing model had demonstrated the ability to account for all of these effects. As shown below, we have now developed a form of the LFP model that satisfies most of these requirements.

The one-step reaction case also involves two independent scalars. However, for this case, the joint PDF is strongly affected by the chemical source term. In order to predict transitions between reacting and non-reacting states correctly, the mixing model must account for the dependence of the mixing time (i.e., the scalar dissipation rates) and the shape of the PDF on the reaction rate. The only quantities that are required to close the LSR/LFP model formulation are the scalar-conditioned scalar dissipation rates. In the present study, these rates are extracted directly from the DNS database of Sripakagorn *et al.* (2000) and utilized in the LFP model to predict the evolution of the joint scalar PDF. The results are compared with the DNS.

2. Model formulation

The vector of N scalars following a Lagrangian fluid particle will be denoted by $\boldsymbol{\phi}^*$. The scalar fluctuations are defined by $\boldsymbol{\phi}'^* \equiv \boldsymbol{\phi}^* - \langle\boldsymbol{\phi}\rangle$. In the two cases considered in this work, $\boldsymbol{\phi}^*$ has length two. In a Lagrangian PDF model, the scalars evolve (in the absence of mean scalar gradients) according to

$$\frac{\mathrm{d}\boldsymbol{\phi}'^*}{\mathrm{d}t} = \langle \mathbf{D}\nabla^2\boldsymbol{\phi}'|\boldsymbol{\phi}^*\rangle^* + \mathbf{S}(\boldsymbol{\phi}^*), \tag{2.1}$$

where the diagonal diffusion matrix is defined by $\mathbf{D} \equiv \mathbf{diag}(D_1, \ldots, D_N)$, $\mathbf{S}(\boldsymbol{\phi}^*)$ is the chemical source term, and $\langle\cdot|\boldsymbol{\phi}^*\rangle^*$ denotes the expected value conditioned both on the scalars $\boldsymbol{\phi} = \boldsymbol{\phi}^*$ and on the turbulence frequency $\{\epsilon = \epsilon^*(s), s \le t\}$ (Fox 1997).

The molecular mixing term $\langle \mathbf{D}\nabla^2\boldsymbol{\phi}'|\boldsymbol{\phi}^*\rangle^*$ in (2.1) is unclosed and must be modeled. On the other hand, the chemical source term is closed and requires no further modeling. The LSR model provides the mixing time scales conditioned on the turbulence frequency. In this work, we will concentrate on the LFP model, and thus simplify the description by using only the scalar-conditioned scalar diffusion $\langle \mathbf{D}\nabla^2\boldsymbol{\phi}'|\boldsymbol{\phi}^*\rangle$.

2.1. *LFP model*

The LFP model (Fox 1999) provides a closure for the conditional diffusion term:

$$\langle \mathbf{D}\nabla^2\boldsymbol{\phi}'|\boldsymbol{\phi}^*\rangle\mathrm{d}t = -\mathbf{A}\boldsymbol{\phi}'^*\mathrm{d}t + \mathbf{B}(\boldsymbol{\phi}^*)\mathrm{d}\mathbf{W}(t) \tag{2.2}$$

where $\mathrm{d}\mathbf{W}(t)$ is a multivariate Gaussian white-noise process. The diffusion matrix $\mathbf{B}(\boldsymbol{\phi}^*)$ is defined such that $\mathbf{B}(\boldsymbol{\phi}^*)\mathbf{B}(\boldsymbol{\phi}^*)^{\mathrm{T}} = C\langle\boldsymbol{\chi}|\boldsymbol{\phi}^*\rangle \Longrightarrow \mathbf{B}(\boldsymbol{\phi}^*) = \boldsymbol{\Psi}_\chi(C\boldsymbol{\Lambda}_\chi)^{1/2}$, where the matrix of the scalar-conditioned scalar dissipation rates is given by $\langle\boldsymbol{\chi}|\boldsymbol{\phi}\rangle \equiv [\langle\chi_{\alpha\beta}|\boldsymbol{\phi}^*\rangle]$, and the joint scalar dissipation rate is defined by $\chi_{\alpha\beta} \equiv 2D(\nabla\phi_\alpha)\cdot(\nabla\phi_\beta)$. Here, we will assume that all scalars have the same molecular diffusivity D. By definition, the matrix $\langle\boldsymbol{\chi}|\boldsymbol{\phi}^*\rangle$ is non-negative and symmetric. The decomposition into eigenvectors $\boldsymbol{\Psi}_\chi$ and eigenvalues $\boldsymbol{\Lambda}_\chi$ is a convenient (although non-unique) procedure for computing $\mathbf{B}$.

The parameter C controls the rate of relaxation of the joint PDF towards its equilibrium shape (for given values of the means and covariances). The nominal value is $C = 1$.

In order to use the LFP model, the user must supply appropriate forms for $\langle \chi | \phi^* \rangle$. In general, these functions control the characteristic time scales for the scalars, and the shape of the joint composition PDF. Moreover, these functions must be chosen such that particles do not escape the boundaries of the so-called "allowable region" in composition space. For bounded inert scalars, simple functional forms exist and, as shown below, yield good predictions for the joint PDF. For reacting scalars, the components of $\langle \chi | \phi^* \rangle$ will be functions of the chemical source term, and hence are more difficult to model *a priori*.

The form of the drift matrix $\mathbf{A}$ in (2.2):

$$\mathbf{A} \equiv \frac{(1+C)}{2} \chi \langle \phi' \phi'^{\mathrm{T}} \rangle^{-1} \tag{2.3}$$

is imposed by the constraint that (for decaying inert scalars) the scalar covar iances are governed by

$$\frac{\mathrm{d}\langle \phi' \phi'^{\mathrm{T}} \rangle}{\mathrm{d}t} = -\mathbf{A} \langle \phi' \phi'^{\mathrm{T}} \rangle - \langle \phi' \phi'^{\mathrm{T}} \rangle \mathbf{A}^{\mathrm{T}} + \langle \mathbf{B}(\phi) \mathbf{B}(\phi)^{\mathrm{T}} \rangle = -\chi. \tag{2.4}$$

However, (2.3) should be viewed as a linear approximation for the exact term: $\mathbf{A}\phi' = -(1+C)\langle D \nabla^2 \phi' | \phi \rangle$. The LFP model thus represents Lagrangian particle trajectories in phase space by a linear deterministic term for the conditional scalar diffusion (2.3) and a (correlated) stochastic "noise" term ($\mathbf{B}(\phi)\mathrm{d}\mathbf{W}(t)$). The presence of $\mathbf{B}(\phi)$ in the noise term ensures that particle compositions remain in the allowable region of phase space.

In general, $\langle \phi' \phi'^{\mathrm{T}} \rangle$ in (2.3) may not be full rank (e.g., if any variance is null or if two or more scalars are perfectly correlated), so that the inverse matrix appearing in (2.3) may not exist. However, these special cases can be treated by using an eigenvalue decomposition of the covariance matrix. Singularities in the covariance matrix will correspond to zero eigenvalues, which can simply be set to zero in the inverse matrix. The LSR model provides the unconditional scalar dissipation rate matrix χ. Thus, the functional forms used to describe $\langle \chi | \phi^* \rangle$ must be consistent with $\chi = \langle \langle \chi | \phi^* \rangle \rangle$, where the outermost angle brackets denote integration with respect to the joint composition PDF. In this work, we will assume that χ is known.

2.2. *Multi-stream mixing*

The formulation of the LFP model for the multi-stream mixing problem is here illustrated with three streams for simplicity in exposition. The extension to N-stream mixing follows with no additional complications.

The generic three-stream mixing problem involves three inlet streams or (for homogeneous flow) mixing between three regions with different initial concentrations. The initial joint scalar PDF is thus composed of at most three weighted delta functions:

$$\begin{aligned} f_{\boldsymbol{\phi}}(\psi_1, \psi_2; 0) = {} & p_1 \delta(\psi_1 - \phi_{11}) \delta(\psi_2 - \phi_{21}) \\ & + p_2 \delta(\psi_1 - \phi_{12}) \delta(\psi_2 - \phi_{22}) + p_3 \delta(\psi_1 - \phi_{13}) \delta(\psi_2 - \phi_{23}), \end{aligned} \tag{2.5}$$

where the means $\langle \phi_1 \rangle = p_1 \phi_{11} + p_2 \phi_{12} + p_3 \phi_{13}$ and $\langle \phi_2 \rangle = p_1 \phi_{21} + p_2 \phi_{22} + p_3 \phi_{23}$ are constant. (Singular cases, where one or more of the delta functions have zero weight, are treated using the eigenvalue decomposition of the covariance matrix described above.) For non-degenerate cases, the delta functions will not be collinear. This can be expressed

in terms of the rank of the matrix

$$\mathbf{\Phi}_0 \equiv \begin{bmatrix} (\phi_{11} - \langle\phi_1\rangle) & (\phi_{12} - \langle\phi_1\rangle) & (\phi_{13} - \langle\phi_1\rangle) \\ (\phi_{21} - \langle\phi_2\rangle) & (\phi_{22} - \langle\phi_2\rangle) & (\phi_{23} - \langle\phi_2\rangle) \end{bmatrix}. \tag{2.6}$$

If $\text{rank}(\mathbf{\Phi}_0) = 2$, then the three-stream mixing problem is non-degenerate.

For the non-degenerate case, any of the columns of (2.6) can be used as a reference vector. Choosing the third column, we can map the variables into mixture-fraction space $\boldsymbol{\xi} = [\xi_1\ \xi_2]^{\mathrm{T}}$ using $\boldsymbol{\phi} - \boldsymbol{\phi}_3 = \mathbf{M}\boldsymbol{\xi}$ where

$$\mathbf{M} \equiv \begin{bmatrix} (\phi_1 - \phi_3) & (\phi_2 - \phi_3) \end{bmatrix} = \begin{bmatrix} (\phi_{11} - \phi_{13}) & (\phi_{12} - \phi_{13}) \\ (\phi_{21} - \phi_{23}) & (\phi_{22} - \phi_{23}) \end{bmatrix} \tag{2.7}$$

and

$$\mathbf{M}^{-1} = \frac{1}{|\mathbf{M}|} \begin{bmatrix} (\phi_{22} - \phi_{23}) & -(\phi_{12} - \phi_{13}) \\ -(\phi_{21} - \phi_{23}) & (\phi_{11} - \phi_{13}) \end{bmatrix}. \tag{2.8}$$

(The inverse will exist if $\text{rank}(\mathbf{\Phi}_0) = 2$.) The initial conditions ($\mathbf{\Phi}_0$) are recovered from the initial mixture-fraction vectors:

$$\boldsymbol{\xi}_0 \equiv \begin{bmatrix} 1 & 0 & 0 \\ 0 & 1 & 0 \end{bmatrix} \tag{2.9}$$

using the linear mapping. We can thus derive the mixing closure in terms of $\boldsymbol{\xi}$, and use the mapping matrix $\mathbf{M}$ to move to and from composition ($\boldsymbol{\phi}$) space.

In order to use the LFP model, we must define the conditional scalar-dissipation matrix in $\boldsymbol{\xi}$-space: $\langle\boldsymbol{\chi}_\xi|\boldsymbol{\xi}\rangle$. It is related to $\langle\boldsymbol{\chi}|\boldsymbol{\phi}\rangle$ by $\langle\boldsymbol{\chi}|\boldsymbol{\phi}\rangle = \mathbf{M}\langle\boldsymbol{\chi}_\xi|\boldsymbol{\xi} = \mathbf{M}^{-1}(\boldsymbol{\phi} - \boldsymbol{\phi}_3)\rangle\mathbf{M}^{\mathrm{T}}$. Likewise, the covariance matrix for $\boldsymbol{\xi}$ is related to the composition covariance matrix by $\langle\boldsymbol{\phi}'\boldsymbol{\phi}'^{\mathrm{T}}\rangle = \mathbf{M}\langle\boldsymbol{\xi}'\boldsymbol{\xi}'^{\mathrm{T}}\rangle\mathbf{M}^{\mathrm{T}}$. For non-degenerate cases, $\text{rank}(\langle\boldsymbol{\phi}'\boldsymbol{\phi}'^{\mathrm{T}}\rangle) = 2$ and $\langle\boldsymbol{\xi}'\boldsymbol{\xi}'^{\mathrm{T}}\rangle = \mathbf{M}^{-1}\langle\boldsymbol{\phi}'\boldsymbol{\phi}'^{\mathrm{T}}\rangle(\mathbf{M}^{\mathrm{T}})^{-1}$.

As noted earlier, $\langle\boldsymbol{\chi}_\xi|\boldsymbol{\xi}\rangle$ provides time-scale information and must keep the mixture-fraction vector in the domain bounded by the two axes and the line $\xi_1 + \xi_2 = 1$. A generic method to enforce boundedness is to require that

$$\langle\boldsymbol{\chi}_\xi|\boldsymbol{\xi}_b\rangle\mathbf{n}_b(\boldsymbol{\xi}_b) = \mathbf{0}, \tag{2.10}$$

where $\boldsymbol{\xi}_b$ is a point on the boundary and $\mathbf{n}_b(\boldsymbol{\xi}_b)$ is a boundary-normal vector. For the three-stream mixing problem with equal molecular diffusivities, the three boundaries are straight lines so that $\mathbf{n}_b$ is constant on each boundary. (With differential diffusion, the boundaries can be time-dependent. Consider, for example, the case where $D_1 = 0$ and $D_2 > 0$. For this case, ϕ_1^* will be constant and ϕ_2^* will move towards its mean value.) Applying (2.10) then yields

$$\begin{aligned} &\langle\chi_{\xi 11}|0,\xi_2\rangle = 0, \quad \langle\chi_{\xi 12}|\xi_1,0\rangle = 0, \quad \langle\chi_{\xi 11}|\xi_1+\xi_2=1\rangle + \langle\chi_{\xi 12}|\xi_1+\xi_2=1\rangle = 0, \\ &\langle\chi_{\xi 12}|0,\xi_2\rangle = 0, \quad \langle\chi_{\xi 22}|\xi_1,0\rangle = 0, \quad \langle\chi_{\xi 12}|\xi_1+\xi_2=1\rangle + \langle\chi_{\xi 22}|\xi_1+\xi_2=1\rangle = 0. \end{aligned} \tag{2.11}$$

The simplest quadratic functions that satisfy these constraints are

$$\begin{aligned} \langle\chi_{\xi 11}|\xi_1,\xi_2\rangle &= C_1\xi_1(1-\xi_1-\xi_2) - C_2\xi_1\xi_2, \\ \langle\chi_{\xi 12}|\xi_1,\xi_2\rangle &= C_2\xi_1\xi_2, \\ \langle\chi_{\xi 22}|\xi_1,\xi_2\rangle &= C_3\xi_2(1-\xi_1-\xi_2) - C_2\xi_1\xi_2, \end{aligned} \tag{2.12}$$

where the constants C_1–C_3 are determined by the requirement that $\boldsymbol{\chi}_\xi = \langle\langle\boldsymbol{\chi}_\xi|\boldsymbol{\xi}\rangle\rangle$.

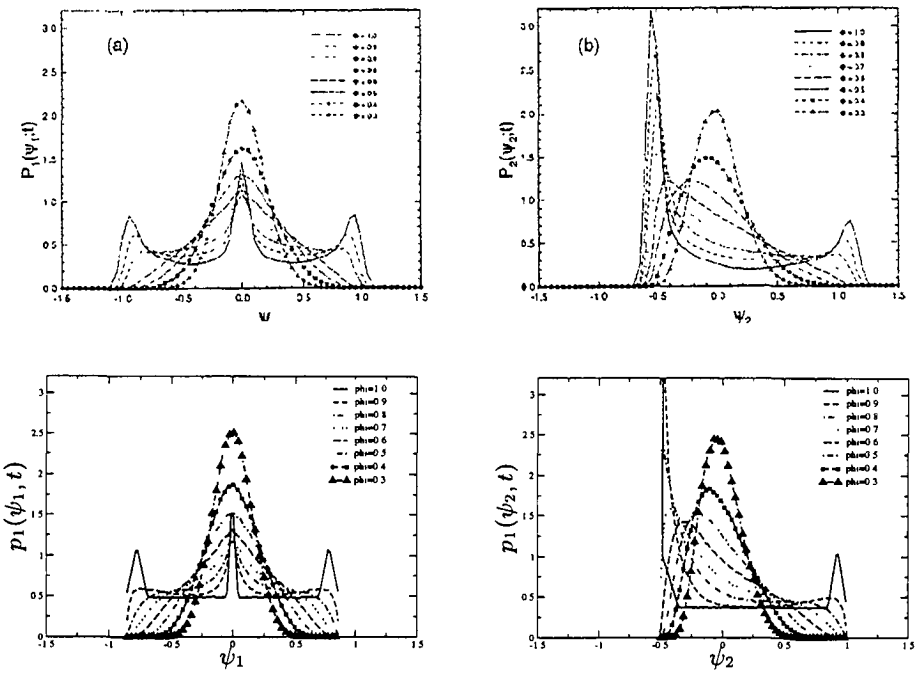

FIGURE 1. LFP modeling predictions of the marginal PDFs for the three-stream mixing problem at various times.

Note that higher-order functions could also be used. (Alternatively, one could extract these functions from DNS.) However, truncation at second order is consistent with a multivariate beta PDF whose coefficients depend only on the means and covariances. Indeed, it can be easily shown that (2.12) combined with the linear drift term (2.3) generates a steady-state beta PDF in the univariate case. Finally, note that the extension of (2.12) to N-stream mixing is straightforward using this procedure.

If $\mathbf{M}$ is invertible, one has the choice of solving the mixing problem in either ϕ or ξ-space. In most applications, the scalar dissipation rates χ and the covariances $\langle \phi' \phi'^{\mathrm{T}} \rangle$ will be available (e.g., from the LSR model), in which case it may be preferable to work in ϕ-space. However, for degenerate cases where $\mathbf{\Phi}_0$ is rank-deficient, the mixing model is best solved in ξ-space, and then "projected"into ϕ-space. A general method for treating degenerate cases has been developed, but is not included here due to space constraints.

3. Results

3.1. *Homogeneous three-stream mixing*

The DNS data of Juneja and Pope (1996) corresponds to three-stream mixing with

$$\mathbf{M} = \frac{1}{2}\begin{bmatrix} -\sqrt{3} & \sqrt{3} \\ -3 & -3 \end{bmatrix} \quad \text{and} \quad \phi_3 = \begin{bmatrix} 0 \\ 1 \end{bmatrix}. \tag{3.1}$$

The rank of $\mathbf{M}$ is two, and the correlation coefficient and the scalar means in ϕ-space are null. (The initial joint PDF is symmetric about the origin.) We model χ by $\chi = \frac{1}{\tau}\langle \phi' \phi'^{\mathrm{T}} \rangle$ with $\tau = 1$ and the variances computed from the particles. In ξ-space, the scalar dissipation rate is modeled by $\chi_\xi = \frac{1}{\tau}\langle \xi' \xi'^{\mathrm{T}} \rangle$.

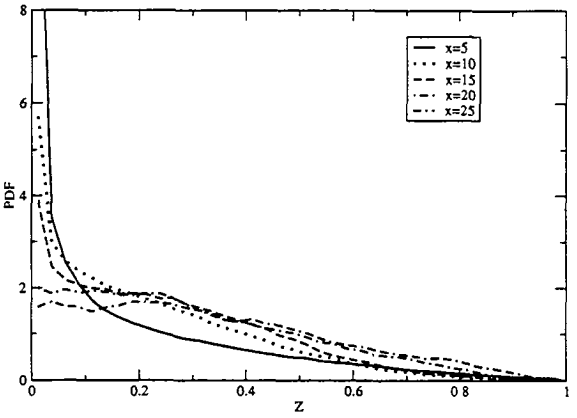

FIGURE 2. LFP modeling results of an inhomogeneous case.

LFP modeling results for the marginal PDFs of ϕ_1 and ϕ_2 are shown in subplots (c) and (d) of figure 1. These results correspond to figure 9 in Juneja & Pope (1996), here reproduced in subplots (a) and (b) for convenience. The Monte Carlo calculations are initialized with a triple-delta function for the joint PDF of the scalars, which estimates the actual, approximate triple-delta joint PDF of the Juneja & Pope (1996) DNS.

The relaxation of the joint (or marginal) PDFs from an initially-segregated scalar field towards a Gaussian distribution, due to turbulent mixing, is a critical issue for any mixing model used in transported PDF approaches. Currently, no existing model is able to reproduce the correct evolution of the joint/marginal PDFs for the three-stream mixing problem. The results of figure 1 show that the LFP model is able to accurately predict the evolution of both the joint and marginal PDFs of the DNS.

3.2. *Inhomogeneous three-stream mixing*

The LFP model has been implemented in a LES/Filtered Density Function code to demonstrate the applicability of the model to handle flows of practical interest. In this approach, the velocity-field calculation is handled by a structured, finite-volume LES code from CTR. This LES solver is coupled to a Lagrangian Monte-Carlo module to compute scalar fields using the filtered density function approach (Colucci *et al.* 1998). The implementation of the LFP model proved to be quite straightforward. Nevertheless, some extra care had to be taken to enforce strict conservation of the scalar means during the mixing step, to avoid any drift due to the statistical errors arising from the stochastic part of the model. To test the model behavior, a double planar mixing layer was computed. It is composed of three streams of water with respective velocities, from top to bottom, of 0.5, 1.0, and 0.5. This configuration corresponds to an experimental setup under investigation at Iowa State University. Both velocity and scalar fields will eventually be available for comparison with the results of the simulation. In the scope of this study, we present only the evolution of the shape of the marginal PDF of one of the two scalars, along a line propagating in the streamwise direction and starting from the tip of one of the two splitter plates. Figure 2 shows the PDFs corresponding to five successive downstream locations, at 5, 10, 15, 20 and 25 channel heights from the tip of the plate. We clearly see here the progressive relaxation from a highly segregated state at $x = 5$ towards a very wide distribution that peaks slightly around the mean value $\langle Z \rangle = 0.333$ at $x = 25$.

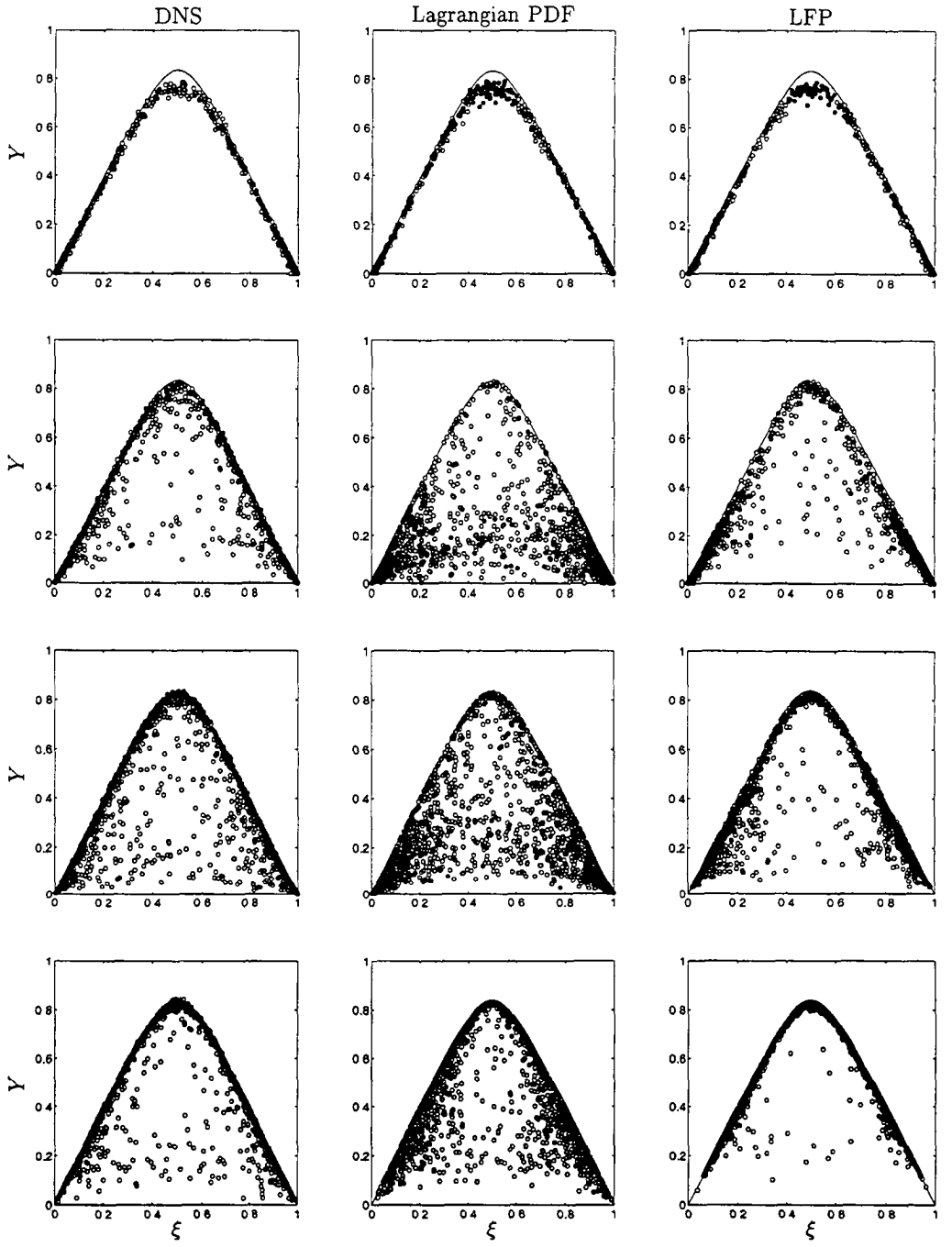

FIGURE 3. Qualitative comparisons of DNS and Lagrangian PDF modeling results. First column: 10^3 randomly-chosen particles from the DNS at times $t^* = 1/10$, $1/2$, 1, and 2; 10^3 randomly-chosen particles from the Lagrangian PDF simulations using the exact conditional diffusion term from the DNS (second column) and the linear, LFP approximation for the mixing term (last column).

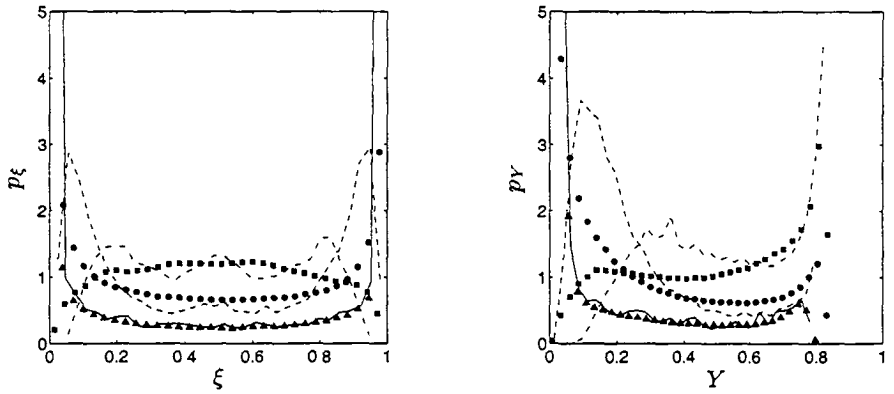

FIGURE 4. LFP modeling predictions of marginal PDFs at times $t^* = 1/10$, 1, and 2: symbols = DNS and lines = modeling results.

3.3. *Homogeneous one-step reaction*

The DNS results of Sripakagorn *et al.* (2000) involve fuel (F), oxidizer (O), and product (P) in a one-step, second-order, reversible reaction: $\mathrm{F} + \mathrm{O} \underset{k/K}{\overset{k}{\rightleftharpoons}} 2\mathrm{P}$, where k is the forward reaction rate and K the equilibrium constant. The species evolve in isotropic, homogeneous decaying turbulence, governed by the Navier-Stokes equations. F and O are initially segregated. The forward reaction rate has an Arrhenius temperature dependence with the equilibrium constant held fixed. The production rates for fuel, oxidizer, and product are $\dot{w}_\mathrm{F} = -\dot{w}$, $\dot{w}_\mathrm{O} = -\dot{w}$, and $\dot{w}_\mathrm{P} = 2\dot{w}$, respectively, where

$$\dot{w} = A \exp\left(-\frac{\mathrm{Ze}}{\alpha}\right) \exp\left[-\frac{\mathrm{Ze}(1-\theta)}{1-\alpha(1-\theta)}\right] \left(Y_\mathrm{F} Y_\mathrm{O} - \frac{1}{K} Y_\mathrm{P}^2\right) \tag{3.2}$$

is the reaction rate. Here, A is the frequency factor, $\alpha \equiv (T_f - T_\infty)/T_f$ is the heat release parameter, $\mathrm{Ze} \equiv \alpha T_a / T_f$ is the Zeldovich number, and T_a is the activation temperature. The turbulent flow is incompressible, and the molecular diffusivities and viscosity are independent of the temperature. The Schmidt number is 0.7 and the Lewis numbers are all unity. (See Sripakagorn *et al.* (2000) for details of the simulation).

For this binary mixing and reacting system, there are two independent variables, currently chosen to be the mixture fraction, ξ, a passive scalar, and the reaction-progress variable, $Y = Y_\mathrm{P} = \theta$. The first column of figure 3 shows the DNS data in ξ–Y phase space at various, increasing times. The solid line in each subplot is the equilibrium solution. The chemistry rate parameters in figure 3 are $A = 8 \times 10^4\ \mathrm{s}^{-1}$, $\alpha = 0.87$, $\mathrm{Ze} = 4$, and $K = 100$, corresponding to "Case B". Additional cases were computed in which the degree of extinction was changed by varying only the frequency factor A. For $A = 13 \times 10^4\ \mathrm{s}^{-1}$ ("Case A"), there is little to no extinction; for $A = 0.3 \times 10^4\ \mathrm{s}^{-1}$ ("Case C"), there are high levels of local extinction and reignition.

Assumed PDF modeling approaches to describe this DNS have included a doubly-conditional moclosure approach (Cha *et al.* 2001), a higher-order conditional-moment-closure approach (Cha & Pitsch 2002), and an extended flamelet modeling treatment (Pitsch *et al.* 2002). In the present Lagrangian PDF modeling study, the scalar-dissipation-

rate matrix is

$$\langle \chi | \phi^* \rangle \equiv \langle \chi | \xi, Y \rangle = \begin{bmatrix} \langle \chi_\xi | \xi, Y \rangle & \langle \chi_{\xi Y} | \xi, Y \rangle \\ \langle \chi_{\xi Y} | \xi, Y \rangle & \langle \chi_Y | \xi, Y \rangle \end{bmatrix} \tag{3.3}$$

for the one-step reaction. (For compactness of notation, no distinction is made between the conditioning variables themselves and their sample spaces.) Currently, the diffusion matrix in the LFP model, $\mathbf{B}$, is specified directly from the DNS results using linear interpolation in phase space and time. The conditional diffusion term is $\mathbf{A} = 2\left[\langle D\nabla^2\xi|\phi^*\rangle \;\; \langle D\nabla^2 Y|\phi^*\rangle\right]^{\mathrm{T}}$ for the simplified system.

Figure 3 shows a qualitative comparison between the DNS results (first column), the Lagrangian PDF modeling results using the exact conditional Laplacian (second column), and the LFP modeling results (third column). Recall that the molecular mixing term in the LFP model uses the linear approximation for $\mathbf{A}$ in the Lagrangian PDF equations. The exact conditional Laplacian is also taken directly from the DNS using linear interpolation. For the DNS results, 10^3 different particles are shown (out of 128^3), randomly chosen at each time. In the modeling results, the trajectories of the same 10^3 particles are shown (out of 10^4), randomly chosen at the time of initialization. Recall that, in the present implementation of the governing Lagrangian equations, only the scalar-conditioned scalar diffusion is used, and thus the particle "trajectories" shown from the Lagrangian PDF results in figure 3 are "notional".

The ensemble of notional particles (*e.g.* those shown in figure 3 at a given time) represents the joint PDF of ξ and Y. Figure 4 shows the marginal PDFs of ξ and Y at various times for Case B, using the total number of 10^4 particles binned into 50 equally-spaced increments in their phase space. Lines show the predictions, and symbols are the DNS results. From the ensemble of particles, statistics can readily be derived. Figure 5 shows the LFP modeling predictions for the first and second moments of ξ and Y for Cases A–C. The DNS results are represented by the symbols. As ξ is a passive scalar, independent of the chemistry, predictions of ξ are identical for each case and are in excellent agreement with the DNS experiment.

As an initial study of the LFP model, the deviations between the DNS results and modeling results focus on the linear approximation for the conditional Laplacian (the "LFP approximation"). All modeling results use the conditional dissipation calculated from the DNS. A discussion of the modeling challenges associated with the conditional dissipation closes the section.

Figure 6 shows the conditional diffusion term for Y calculated from the DNS (top row) and the corresponding linear approximation employed in LFP modeling (bottom row) for Case B. The agreement between the modeling predictions and DNS in figure 5 is remarkable, considering the simplicity of the approximation for the mixing term. Figure 7 shows the marginal PDFs predicted by the Lagrangian PDF model (with the exact conditional diffusion term specified by the DNS). A comparison with figure 4 illustrates the impact of the linear approximation on the marginal PDFs. The impact is weak, only increasing the probability of unburned particles due to the linear approximation at low values of Y, as shown in figure 6. The impact on the first and second moments is negligible (results not shown).

The modeling challenges for the conditional dissipation in the LFP model can be decomposed into a model for (i) the unconditional means, $\langle \chi_{ij} \rangle$, and (ii) the "shape functions", $h_{ij} \equiv \langle \chi_{ij} | \phi^* \rangle / \langle \chi_{ij} \rangle$. Here we focus on issue (ii). (Recall that issue (i) is addressed by the LSR model.) Figure 8 shows $\langle \chi_{ij} | \xi, Y \rangle$, where $i, j = \xi, Y$, for Cases

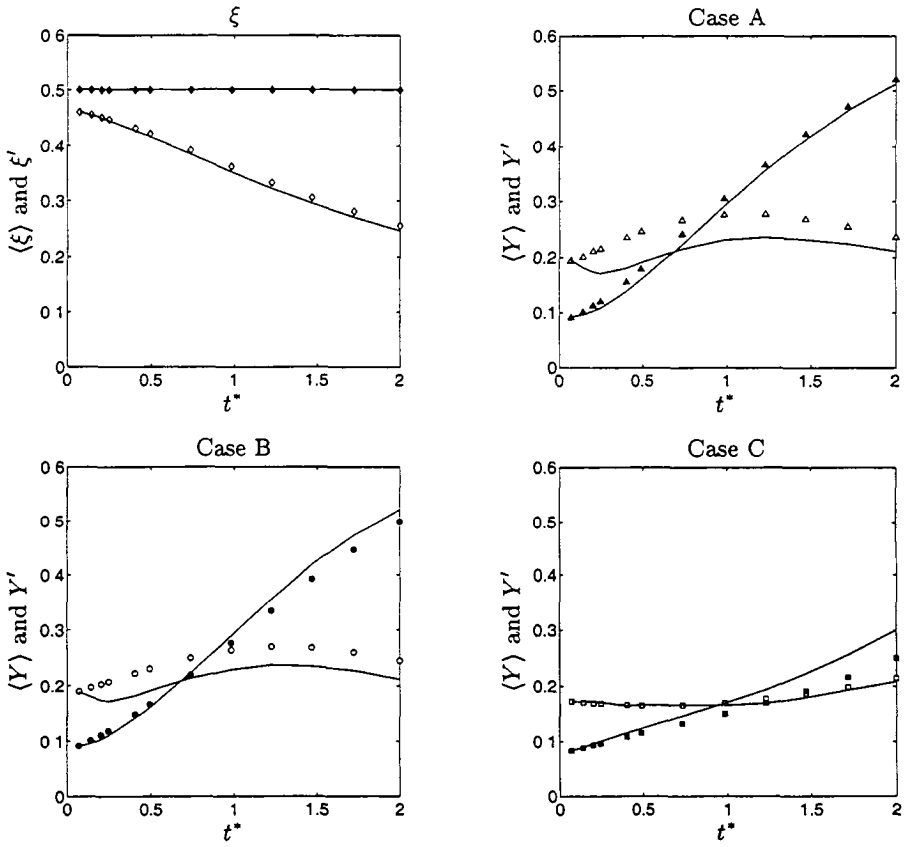

FIGURE 5. LFP modeling predictions of unconditional statistics: symbols = DNS (closed symbols = mean, open symbols = rms) and lines = modeling results.

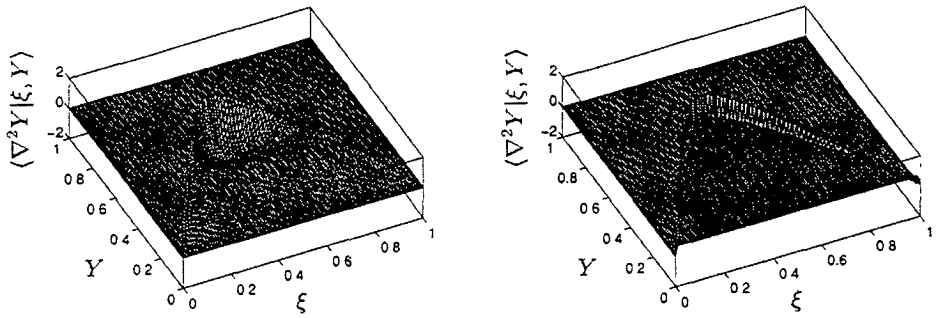

FIGURE 6. The "LFP approximation": Exact conditional diffusion term for Y calculated from the DNS (left) and corresponding linear approximation employed by LFP modeling (right).

A–C at $t^* = 1$. The figures illustrate the similarity of the shape functions irrespective of the levels of extinction and/or reignition (although the scaling of course differs between cases). In future work, studies of the sensitivity to slight differences in the shape functions are to be performed.

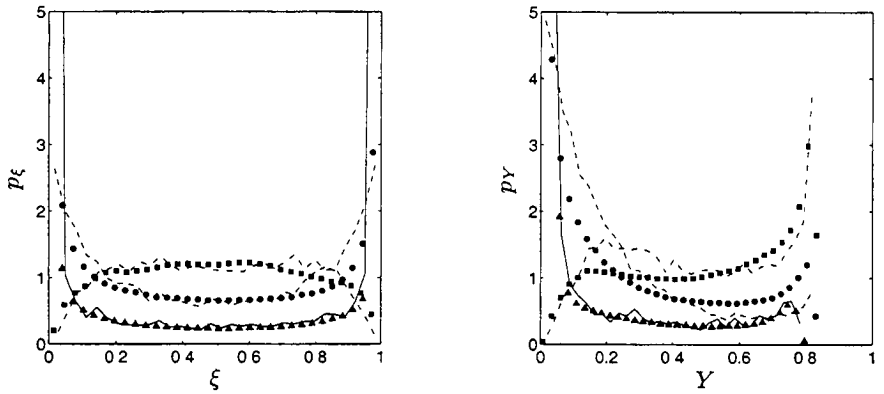

FIGURE 7. Lagrangian PDF modeling predictions of the marginal PDFs at times $t^* = 1/10$, 1, and 2: symbols = DNS and lines = modeling results. Modeling results are analogous to figure 4, but without making the LFP approximation.

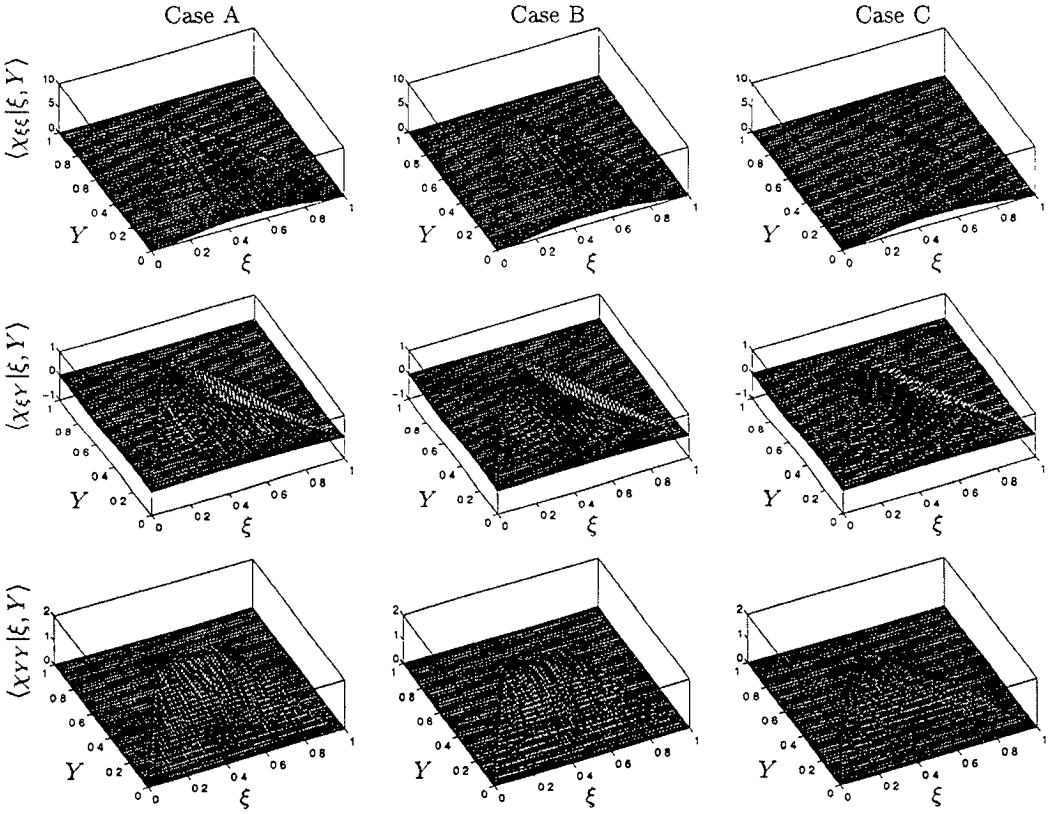

FIGURE 8. Conditional dissipation shape functions ($t^* = 1$).

4. Conclusions

The LFP model has been successfully extended to multi-stream, inert-scalar mixing and to a one-step, second-order reaction. For the former, a complete model for the conditional scalar-dissipation rates has been derived, and the model predictions are in good

agreement with DNS. For the latter, the LFP model was successfully validated by extracting the conditional scalar-dissipation rates from DNS.

The principal conclusion resulting from this study is that knowledge of the conditional scalar-dissipation rate matrix $\langle \chi | \phi^* \rangle$ is sufficient to accurately predict the joint scalar PDF. Thus, the remaining challenge is to find models for $\langle \chi | \phi^* \rangle$ that can be applied to turbulent reacting flows with complex chemistry. This will most likely be a difficult step, but one that would be greatly aided by results from DNS of turbulent reacting flows.

REFERENCES

CHA, C. M., KOSÁLY, G. & PITSCH, H. 2001 Modeling extinction and reignition in turbulent nonpremixed combustion using a doubly-conditional moment closure approach. *Phys. Fluids* **13**, 3824–3834.

CHA, C. M. & PITSCH, H. 2002 Higher-order conditional moment closure modeling of local extinction and reignition in turbulent combustion. *Combust. Theory Modelling* **6**, 425–437.

COLUCCI, P. J., JABERI, F. A., GIVI, P. & POPE, S. B. 1998 Filtered density function for large eddy simulation of turbulent flows. *Phys. Fluids* **10**, 499–515.

FOX, R., YEUNG, P. & VEDULA, P. 2001 Application of an improved lagrangian spectral relaxation model to differential diffusion. In *APS Fluid Dynamics Annual Meeting*.

FOX, R. O. 1994 Improved Fokker-Planck model for the joint scalar, scalar gradient PDF. *Phys. Fluids* **6**, 334–348.

FOX, R. O. 1995 The spectral relaxation model of the scalar dissipation rate in homogeneous turbulence. *Phys. Fluids* **7**, 1082–1094.

FOX, R. O. 1996 On velocity-conditioned scalar mixing in homogeneous turbulence. *Phys. Fluids* **8**, 2678–2691.

FOX, R. O. 1997 The Lagrangian spectral relaxation model of the scalar dissipation in homogeneous turbulence. *Phys. Fluids* **9**, 2364–2386.

FOX, R. O. 1999 The Lagrangian spectral relaxation model for differential diffusion in homogeneous turbulence. *Phys. Fluids* **11**, 1550–1571.

FOX, R. O. & YEUNG, P. K. 1999 Forward and backward spectral transfer in the modeling of scalar mixing in homogeneous turbulence. In *Proceedings of the 3rd ASME/JSME Joint Fluids Engineering Conference*. San Francisco, CA.

FOX, R. O. & YEUNG, P. K. 2002 Lagrangian mixing models for differential diffusion in homogeneous turbulence. *Phys. Fluids* Submitted.

JUNEJA, A. & POPE, S. B. 1996 A DNS study of turbulent mixing of two passive scalars. *Phys. Fluids* **8**, 2161–2184.

PITSCH, H., CHA, C. M. & FEDOTOV, S. 2002 Flamelet modeling of non-premixed turbulent combustion with local extinction and re-ignition. *Combust. Theory Modelling* Submitted.

SRIPAKAGORN, P., KOSÁLY, G. & PITSCH, H. 2000 Local extinction-reignition in turbulent nonpremixed combustion. In *CTR Annual Research Briefs*, Stanford University / NASA Ames, pp. 117–128.

YEUNG, P. K. 2001 Lagrangian characteristics of turbulence and scalar transport in direct numerical simulations. *J. Fluid Mech.* **427**, 241–274.

Center for Turbulence Research
Proceedings of the Summer Program 2002

Dynamics and dispersion in Eulerian-Eulerian DNS of two-phase flows

By A. Kaufmann †, O. Simonin ‡, T. Poinsot †, AND J. Helie ‡

A DNS approach for Eulerian-Eulerian dispersed two-phase flows is tested. The need for a subgrid stress term in the dispersed phase momentum equation is identified and a simple model for this stress term allows the calculation of an experimental test case with inertial particles in homogeneous turbulence. Results are compared to Eulerian-Lagrangian simulations.

1. Introduction and motivation

Particle-laden flows are of great interest since they occur in a variety of industrial applications. Knowledge of particle transport and concentration properties are crucial for the design of such applications. Numerical simulations coupling Lagrangian tracking of discrete particles with DNS of the carrier-phase turbulence provide a powerful tool to investigate such flows. When particle numbers become large, particle-particle and turbulence modification effects become important and such numerical simulations have the drawback of being numerically expensive. Numerical simulations based on separate Eulerian balance equations for both phases, coupled through inter-phase exchange terms, might be an alternative approach in such cases. Such Eulerian-Eulerian DNS approach has been validated for the case of particles with low inertia which follow the carrier fluid flow almost instantaneously due to their small response time compared to the integral time scales of the turbulence (Druzhini & Elghobashi (1999)).

In the case of inertial particles, with response times comparable to the integral time scales, additional effects have to be taken into account. Indeed, as pointed out by Février (2000) and Février *et al.* (2002), particle phase transport equations must account for dispersion effects due to a local random motion which is induced by particle-turbulence and particle-particle interactions. Following Février *et al.* (2002), a conditional average of the dispersed phase with respect to the carrier phase flow realization allows the derivation of instantaneous mesoscopic particle fields and instantaneous Eulerian balance equations accounting for the effect of random motion. From forced isotropic turbulence simulations, Février *et al.* (2002) showed that the uncorrelated, quasi-Brownian motion of the particles increases with inertia (high Stokes numbers). In cases such that the particle relaxation time is comparable to the Lagrangian integral time scale, the kinetic energy of quasi-Brownian motion is about 30% of the total kinetic energy of the dispersed phase.

The importance of quasi-Brownian motion (QBM) is illustrated in a preliminary test case of decaying homogeneous isotropic turbulence. The Eulerian model is then applied to the experimental case of Snyder & Lumley (1971) which has previously been simulated by Elghobashi & Truesdell (1992) using a Lagrangian approach. This allows the present Eulerian simulation to be compared to experiment and Lagrangian simulation.

† CERFACS, 42 Av. G. Coriolis, 31057 Toulouse, France
‡ IMFT, Av. C. Soula, 31400 Toulouse, France

by Elghobashi & Truesdell (1992) using a Lagrangian approach. This allows the present Eulerian simulation to be compared to experiment and Lagrangian simulation.

2. The Eulerian model

Eulerian equations for the dispersed phase may be derived by several means. A popular simple way consists of volume filtering of the the separate, local, instantaneous phase equations accounting for the interfacial jump conditions (Druzhini & Elghobashi (1999)). Such an averaging approach is very restrictive, because particle size and particle distance have to be smaller then the smallest length scale of the turbulence.

A different, not totally equivalent way is the statistical approach in the framework of kinetic theory. In analogy to the derivation of the Navier-Stokes equations by non-equilibrium statistics (Chapman & Cowling (1939)), a point probability density function (pdf) $f_p^{(1)}(\mathbf{c}_p; \mathbf{x}_p, t)$ which defines the local instantaneous probable number of particle centers with the given translation velocity $\mathbf{u}_p = \mathbf{c}_p$ may be defined. This function obeys a Boltzmann-type kinetic equation, which accounts for momentum exchange with the carrier fluid and for the influence of external force fields such as gravity and inter-particle collisions. Reynolds-averaged transport equations of the first moments (such as particle concentration, mean velocity and particle kinetic stress) may be derived directly by averaging from the pdf kinetic equation (Simonin (1996))

To derive local instantaneous Eulerian equations in dilute flows (without turbulence modification by the particles) Février *et al.* (2002) proposed to use an averaging over all dispersed-phase realizations conditioned by one carrier-phase realization. Such an averaging leads to a conditional pdf for the dispersed phase,

$$\tilde{f}_p^{(1)}(\mathbf{c}_p; \mathbf{x}, t, H_f) = \left\langle W_p^{(1)}(\mathbf{c}_p; \mathbf{x}, t) \,|H_f \right\rangle. \tag{2.1}$$

$W_p^{(1)}$ are the realizations of position and velocity in time of any given particle (Reeks (1991)). With this definition one may define a local instantaneous particulate velocity field, which is here named "mesoscopic Eulerian particle velocity field". This field is obtained by averaging the discrete particle velocities measured at a given position and time for all particle-flow realizations and one given carrier-phase realization,

$$\tilde{u}_p(\mathbf{u}, t, H_f) = \frac{1}{\tilde{n}_p^{(1)}} \int \mathbf{c}_p \tilde{f}_p^{(1)}(\mathbf{c}_p; \mathbf{x}, t, H_f)\, d\mathbf{c}_p. \tag{2.2}$$

Here

$$\tilde{n}_p^{(1)} = \int \tilde{f}_p^{(1)}(\mathbf{c}_p; \mathbf{x}, t, H_f)\, d\mathbf{c}_p \tag{2.3}$$

is the mesoscopic particle-number density. For simplicity, the dependence of the above variables on H_f is not shown explicitly. Application of the conditional-averaging procedure to the kinetic equation governing the particle pdf leads directly to the transport equations for the first moments of number density and mesoscopic Eulerian velocity,

$$\frac{\partial}{\partial t}\tilde{n}_p + \frac{\partial}{\partial x_i}\tilde{n}_p \tilde{u}_{p,i} = 0 \tag{2.4}$$

$$\tilde{n}_p \frac{\partial}{\partial t}\tilde{u}_{p,i} + \tilde{n}_p \tilde{u}_{p,j} \frac{\partial}{\partial x_j}\tilde{u}_{p,i} = -\frac{\tilde{n}_p}{\tilde{\tau}_p^F}\left[\tilde{u}_{p,i} - u_{f,i}\right] - \frac{\partial}{\partial x_j}\tilde{n}_p \delta\tilde{\sigma}_{p,ij} + \tilde{n}_p g_i. \tag{2.5}$$

Here $\delta\tilde{\sigma}_{p,ij}$ is the mesoscopic kinetic stress tensor of the particle Quasi-Brownian velocity distribution.

The current objective is to show that this term is non-negligible for inertial particles in turbulent flow.

2.1. *The stress tensor of quasi-Brownian motion (QBM)*

The stress term in (2.5) arises from an ensemble average of the nonlinear term in the transport equation for particle momentum,

$$\tilde{n}_p \delta\tilde{\sigma}_{p,ij} = \int (c_{p,i} - \tilde{u}_{p,i})(c_{p,j} - \tilde{u}_{p,j}) \tilde{f}_p^{(1)}(\mathbf{c}_p; \mathbf{x}, t, H_f)\, d\mathbf{c}_p \tag{2.6}$$

$$= \tilde{n}_p \delta u_{p,i} \widetilde{\delta u_{p,j}}. \tag{2.7}$$

When the Euler or Navier-Stokes equations are derived from kinetic gas theory the trace of $\delta u_{p,i} \widetilde{\delta u_{p,j}}$ is interpreted as temperature (ignoring the Boltzmann constant and molecular mass) and related to pressure by an equation of state. In the case of the Euler or Navier-Stokes equations temperature is defined as the uncorrelated part of the kinetic energy. Here the uncorrelated part of the particulate kinetic energy is defined as

$$\delta q_p^2 = \frac{1}{2} \widetilde{\delta u_{p,i} \delta u_{p,i}}. \tag{2.8}$$

In analogy to the Euler or Navier-Stokes equations a quasi-Brownian pressure (QBP) may be defined by the product of uncorrelated kinetic energy and particle number density, as

$$\tilde{P}_p = \tilde{n}_p \frac{2}{3} \delta q_p^2 \tag{2.9}$$

When the particle number distribution becomes nonuniform, as in the case of a compressible gas, this pressure term tends to homogenize particle number density.

The non-diagonal part of the stress tensor can be identified, in analogy to the Navier Stokes equations, as a viscous term ($\theta_{p,ij}$). The momentum-transport equation (2.5) becomes

$$\tilde{n}_p \frac{\partial}{\partial t} \tilde{u}_{p,i} + \tilde{n}_p \tilde{u}_{p,j} \frac{\partial}{\partial x_j} \tilde{u}_{p,i} = -\frac{\tilde{n}_p}{\tilde{\tau}_p^F} [\tilde{u}_{p,i} - \tilde{u}_{f,i}] - \frac{\partial}{\partial x_i} \tilde{P}_p + \frac{\partial}{\partial x_j} \theta_{p,ij} + \tilde{n}_p g_i. \tag{2.10}$$

Furthermore it can be shown mathematically (Le Veque (1996)) that (2.10) without a pressure-like term leads to non physical solutions characterised by "shock"-like fronts in number density.

2.2. *Simulations without and with QBM*

First, preliminary simulations were performed without any stress term related to QBM. Particles tend to accumulate rapidly in small regions, causing unphysically high number densities. This causes the numerical simulation to fail. In order to ensure that failure was not due to a numerical problem, different simulations with different turbulence Reynolds numbers and Stokes numbers were performed, leading to the same result.

Simulations with a quasi-Brownian pressure (QBP) and without quasi-Brownian viscous stress were performed on the same test cases. Février *et al.* (2002) measured, in forced homogeneous isotropic turbulence, a mean quasi-Brownian kinetic energy $\langle \delta q_p^2 \rangle$ proportional to the mean mesoscopic kinetic energy $\tilde{q}_p^2 = \frac{1}{2} \langle \tilde{u}_{p,i} \tilde{u}_{p,i} \rangle$ with a proportionality coefficient depending on the Stokes number. Here a simple relation between

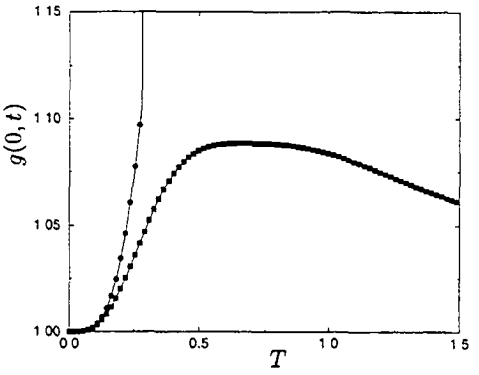

FIGURE 1. Segregation of the dispersed phase with QBP —■— , without QBP —●— .

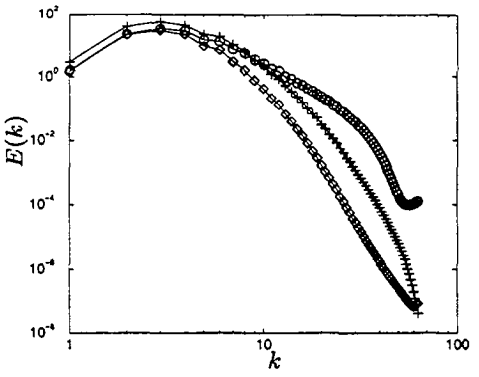

FIGURE 2. non-dimensional spectra of a test case ($128^3, Re = 42$) carrier phase + , dispersed phase without QBM ○ , dispersed phase with QBM ◇ .

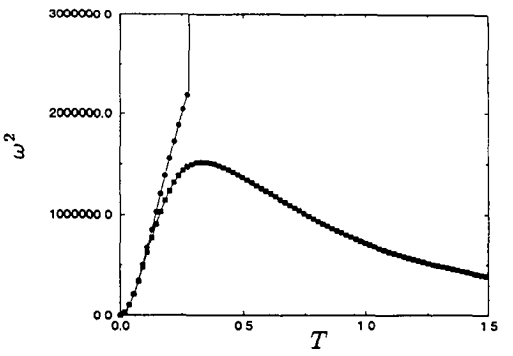

FIGURE 3. Enstrophy of the dispersed phase: with QBP —■— , without QBP —●— .

the quasi-Brownian kinetic energy δq_p^2 needed in the QBP equation (2.9) and the mean resolved kinetic energy $\tilde{q}_p^2$ was used:

$$\delta q_p^2 = 5 * \tilde{q}_p^2. \tag{2.11}$$

Such a QBP modeling allows all the test cases that failed without a quasi-Brownian stress term to be simulated. But, compared to the value found by Février *et al.* (2002), relation (2.11) strongly overestimates the quasi-Brownian kinetic energy and so the effect of QBP. The need for such a large pressure term to carry out the simulation is probably due to the fact that the viscous-stress term is neglected.

In order to quantify the effect of particle segregation, the normalized variance of particle number density is introduced:

$$g(r,t) = \frac{\langle n(x,t)n(x+r,t)\rangle}{\langle n(x,t)\rangle^2} \tag{2.12}$$

figure 1 compares the time evolution of $g(0,t)$ from simulations with and without QBP.

The quasi-Brownian pressure is found to limit the particle segregation effect to reasonable values.

figure 2 compares the kinetic energy spectra of the carrier phase and the dispersed phase with and without QBP. When simulations are performed without QBP, particle kinetic energy for small scales becomes larger then the carrier-phase kinetic energy in contrast with available results (Février *et al.* (2002)). This effect increases in time and can be characterized by the temporal increase of the particle enstrophy as shown by figure 3. This is probably due to the unphysically large accumulation of particles in specific regions of the carrier phase turbulent flow (regions of high strain and low vorticity). Indeed, when accounting for the QBP contribution limiting segregation, the particle enstrophy behavior looks much more reasonable. The quasi-Brownian viscous stress should also play an important role by inducing a strong dissipative effect to the small scales in addition to the one due to the drag force.

2.3. *Measurement of particle dispersion*

Particle dispersion is usually measured in Lagrangian simulations by tracking individual particle path and calculating the variance of the relative displacement

$$\left\langle X_p^2(t)\right\rangle = \frac{1}{N}\sum_{j=1}^{N}\left[x_{p,j}(t) - x_{p,j}(t_0)\right]^2 . \tag{2.13}$$

Particle dispersion can then be related to the time derivative of this quantity (see Monin & Yaglom (1987)),

$$D_p^L(t) = \frac{1}{2}\frac{d}{dt}\left\langle X_p^2(t)\right\rangle . \tag{2.14}$$

In Eulerian simulations one does not have access to individual particle paths. Particle dispersion can still be measured by a semi-empirical method (Monin & Yaglom (1987)): Suppose that the simulation is being carried out with colored particles and a transport equation is written for the ratio of colored particles to total particles ($\tilde{c} = \tilde{n}_c/\tilde{n}_p$). This transport equation is similar to the transport equation for particle number density (2.4):

$$\frac{\partial}{\partial t}\tilde{c}\tilde{n}_p + \frac{\partial}{\partial x_i}\tilde{c}\tilde{n}_p\tilde{u}_{p,i} = \frac{\partial}{\partial x_i}\tilde{c}\tilde{n}_p\left(\tilde{u}_{p,i} - \tilde{u}^c_{p,i}\right) \tag{2.15}$$

Here, $\tilde{u}^c_{p,i}$ is the mesoscopic velocity of colored particles. Since only the velocity of the total droplet number is resolved, a supplementary term arises on the right-hand side of (2.15). This term takes into account the slip velocity between colored particles and the mesoscopic velocity of the particle ensemble. Comparing the above equation to the Navier-Stokes equations, this term is the equivalent of molecular diffusion in a species equation. Since the slip velocity can arise only from uncorrelated movement of the particles, this term can be modeled as a diffusion related to the quasi-Brownian motion.

If the ensemble-averaged mean number-density fraction of colored particles $\langle\tilde{n}_p\rangle C = \langle\tilde{n}_p\tilde{c}\rangle$, ($\tilde{c} = C + c'$) is uniformly stratified, say in the k-direction, and fluctuations are assumed periodic with respect to the computational domain, the fluctuating number density of colored particles $c'\tilde{n}_p$ can be extracted from the total colored number density and one obtains a transport equation for the fluctuations of colored-particle concentration:

$$\frac{\partial}{\partial t}c'\tilde{n}_p + \frac{\partial}{\partial x_i}c'\tilde{n}_p\tilde{u}_{p,i} = -\tilde{n}_p\tilde{u}_{p,k}\frac{\partial}{\partial x_k}C + \frac{\partial}{\partial x_i}\tilde{c}\tilde{n}_p(\tilde{u}_{p,i} - \tilde{u}^c_{p,i}) \tag{2.16}$$

Averaging the colored number-density equation ((2.15)) one obtains a Reynolds-averaged

transport equation,

$$\frac{\partial}{\partial t}\left\langle \tilde{n}_p \right\rangle C + \frac{\partial}{\partial x_i}\left\langle \tilde{n}_p \right\rangle C \left\langle \tilde{u}_{p,i} \right\rangle_p = -\frac{\partial}{\partial x_i}\left\langle \tilde{n}_p c' u_{p,i} \right\rangle + \frac{\partial}{\partial x_i}\left\langle \tilde{c}\tilde{n}_p \left(\tilde{u}_{p,i} - \tilde{u}^c_{p,i} \right) \right\rangle . \quad (2.17)$$

Equation 2.16 has been solved neglecting the quasi Brownian motion term. Particle dispersion can be derived by making a gradient assumption: $(\langle c'\tilde{n}_p\tilde{u}_{p,k}\rangle = \langle \tilde{n}_p \rangle D^t_{p,k}\frac{\partial}{\partial x_k}C)$ A semi-empirical diffusion coefficient is defined by:

$$D^t_{p,k} = \frac{\langle \tilde{n}_p c' u_{p,k} \rangle}{\langle \tilde{n}_p \rangle \frac{\partial}{\partial x_k} C} \quad (2.18)$$

This dispersion coefficient is comparable to the Lagrangian dispersion coefficient (2.14) in the long-time limit of stationary turbulence. Nevertheless simulations neglecting the quasi-Brownian motion are likely to underestimate the Lagrangian dispersion.

3. Numerical implementation

The Eulerian equations for the dispersed phase have been implemented into the Navier-Stokes Solver AVBP (Schönfeld & Rudyard (1999)). It is based on a 2D/3D finite Volume/ finite Element method for unstructured, structured and hybrid meshes.

4. Description of the test case

Particle dynamics and particle dispersion have been studied by experiments and by Lagrangian computations. One appealing test case is that of Snyder & Lumley (1971) (hereafter referred to as SL). They inserted particles with different inertial properties into grid generated spatially decreasing turbulence and measured particle dynamics as well as particle dispersion. This test case has been computed with a Lagrangian approach by Elghobashi & Truesdell (1992) (from heron referred to as ET). The carrier phase was taken as a temporarily decreasing homogeneous isotropic turbulence corresponding to the grid generated turbulence of SL. After an initial calculation for two turnover times ($t = l_{ii}/u'_f$), particles were inserted. Analysis of particle dynamics as well as dispersion was carried out by ET on particles corresponding to those of SL, and a direct comparison was made. Here the procedure of ET is followed, but the calculation is performed by an Eulerian-Eulerian approach and a comparison with the experimental results of SL and the Lagrangian computation of ET is attempted. The present numerical simulation was performed on a periodic 128^3 grid.

4.1. *Initialization of the homogeneous isotropic turbulence*

The carrier-phase velocity field is initialized at dimensionless time $T = 0$ with a divergence-free velocity field such that the kinetic energy satisfies the spectrum (Elghobashi & Truesdell (1992)):

$$E(k,0) = \frac{3}{2}u'^2_{f,0}\frac{k}{k_p}\exp\left(-\frac{k}{k_p}\right) \quad (4.1)$$

where u'_f is the dimensionless rms velocity, k is the wavenumber and k_p is the wavenumber of peak energy. All wave numbers are normalized by the minimal wavenumber k_{min}. In the present simulation the values of ET were taken. Properties of the carrier-phase turbulence are validated against the properties of carrier-phase turbulence of SL and ET.

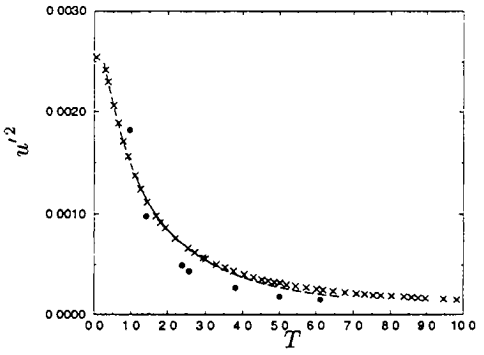

FIGURE 4. Evolution of dimensionless carrier phase u'^2_f for experiment (SL) • , Lagrangian simulation (ET) × , and present simulation ----

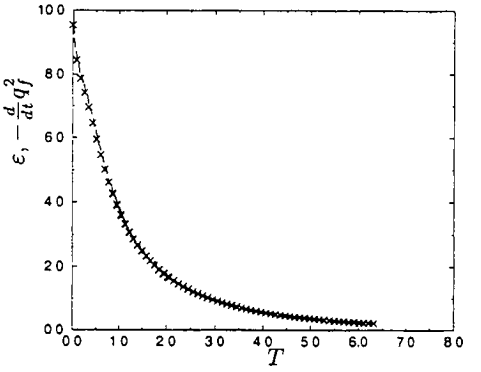

FIGURE 5. Comparison of dissipation ε ---- with change of kinetic energy $-\frac{d}{dt}q_f^2$ × of the carrier phase in the present simulation.

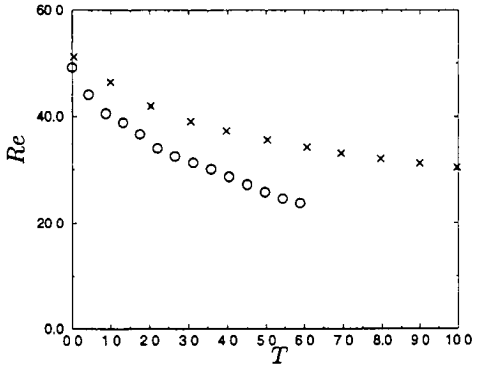

FIGURE 6. Evolution of carrier phase Reynolds number Lagrangian simulation (ET) Re_l × , and present simulation Re_l o .

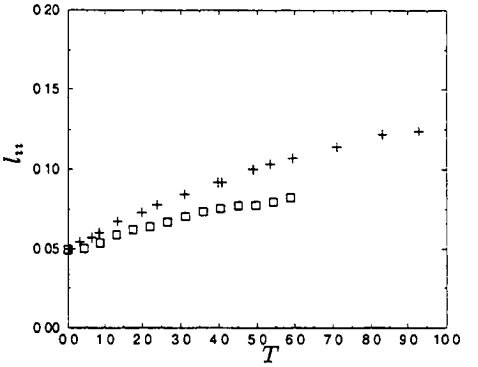

FIGURE 7 Evolution of integral length scale l for the Lagrangian simulation (ET) + , and present simulation □ .

The spatial evolution of the flow in the experiment of SL is converted to a temporal evolution of the flow by $t = x/\bar{U}$. Here $\bar{U}$ is the mean convection velocity in the experiment.

In figure 4 the dimensionless velocity square u'^2_f of the carrier phase is compared to experiment (SL) and Lagrangian simulation (ET). Since the temporally-decaying turbulence was chosen with the same initial parameters as that of ET, it has the same decay behavior.

To verify numerical resolution, dissipation ε is compared to temporal change of kinetic energy $\frac{d}{dt}q_f^2$ in figure 5. It shows excellent agreement between calculated dissipation and kinetic energy decrease. Therefore it can be assumed that numerical dissipation is negligible compared to viscous dissipation.

In figure 6 the Reynolds number of the present simulation is compared to the Lagrangian simulation (ET). In the present simulation the turbulent Reynolds number (based on integral length scale) decays more rapidly compared to the simulation of ET.

	hollow glass	corn pollen	solid glass	copper
d [m]	$4.65*10^{-5}$	$8.7*10^{-5}$	$8.7*10^{-5}$	$4.65*10^{-5}$
density ratio (ρ_p/ρ_f)	260	1000	2500	8900
Re_d	0.25	0.47	0.47	0.25
initial τ_p (SL) [s]	0.0055	0.020	0.045	0.049
initial τ_p (ET) [s]		0.027	0.061	0.067
initial τ_p (non dimensional)	0.053	0.193	0.432	0.473
terminal velocity $v_{t,0}/u_0'$		3.16	6.69	7.57
St ($\tau_p/\tau_{f,0}$)	0.024	0.09	0.203	0.221

TABLE 1. Particle properties in experiment (SL), Lagrangian simulation (ET) and present simulation.

This is due to the slower temporal increase of the integral length scale (figure 7) in the present simulation.

4.2. *Particle properties and initialization*

The Eulerian-Eulerian simulation was performed with one-way coupling. Therefore the carrier-phase turbulence had no feedback from the dispersed phase. The only interaction force taken into account in the momentum equation of the dispersed phase was drag. This is justified in the limit of large density ratios (ρ_p/ρ_g). The characteristic particle relaxation time is computed by the standard formulation.

$$\tau_p = \frac{\rho_p d^2}{18 f(Re_p)\mu} \tag{4.2}$$

$$f(Re_p) = 1 + 0.15 Re_p^{0.687 d0} \tag{4.3}$$

The particle Reynolds number for the drag force correction $f(Re_p)$ is based on the slip velocity $Re_p = (|\tilde{u}_p - u_f|\, d)/\nu_f$. For the present numerical simulation, particle properties are chosen such that they have the same particle Reynolds number $Re_d = (u'd)/\nu_f$ as in the experiment and the same Stokes number in terms of turnover time $St = \tau_p/\tau_{f,0}$ ($\tau_{f,0} = l_0'/u_0'$). † For the Eulerian-Eulerian simulation, particles corresponding to corn pollen or glass beads were retained. Particles were inserted as in the Lagrangian simulation (ET) at the dimensionless time $T = 2.0$. They were given the same velocity as the carrier phase in both simulations when inserted into the turbulent flow. In the Lagrangian simulation, particles had relaxed to the carrier-phase turbulence at $T = 2.67$ and evaluation of particle-dispersion statistics started at that time, corresponding to the equivalent particle-dispersion measurements of (SL). Particle properties were then analyzed in turbulence with and without gravity. When particles are subject to gravity they establish a mean terminal velocity in the direction of gravity, given by $v_t = g * \tau_p$. The gravity constant g was chosen such that the Eulerian-Eulerian simulation predicts the same ratio of $v_{t,0}/u_0'$ (see Tab. 1) as in the experiment and the Lagrangian simulations.

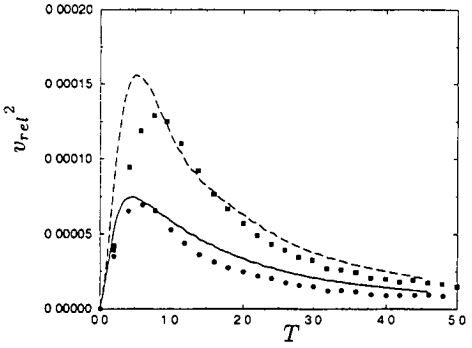

FIGURE 8. Evolution of dimensionless relative square velocity without gravity: Lagrangian simulation (ET) corn pollen • , Lagrangian simulation (ET) glass beads ▪ , present simulation corn pollen ——— , and present simulation glass beads - - - - .

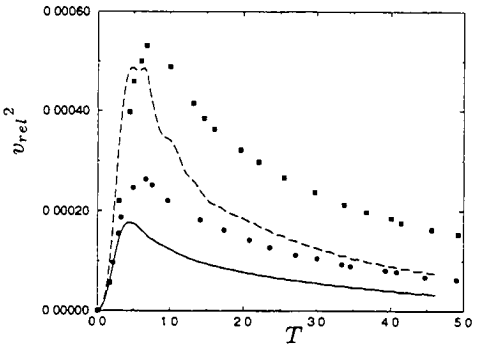

FIGURE 9. Evolution of dimensionless relative square velocity with gravity (perpendicular to gravity): Lagrangian simulation (ET) corn pollen • , Lagrangian simulation (ET) glass beads ▪ , present simulation corn pollen ——— , and present simulation glass beads - - - - .

5. Particle dynamics

Particle dynamics are analyzed in simulations with and without gravity. In the publication of ET only the square of the relative velocity, not the total kinetic energy is given. In the publication of SL, on the other hand, only the square of the particle velocity given. Therefore those quantities are compared separately.

5.1. *Particle dynamics without gravity*

For both types of particles, corn pollen and glass beads, the relative square velocity in the present simulation shows the same qualitative behavior as in the Lagrangian simulation. However the slip velocity is overestimated In both cases (figure 8). The Eulerian mean-square relative velocity $\tilde{v}_{rel}^2 = \langle (u_f - \tilde{u}_p)^2 \rangle$ differs from the Lagrangian mean-square relative velocity $v_{rel}^2 = \langle (u_f - u_p)^2 \rangle$ by the quantity δu_p^2, from QBM. Therefore the predicted Eulerian mean-square relative velocity should be lower than the Lagrangian mean-square relative velocity.

Fig. 10 shows the temporal development of the carrier phase $\langle u_f^2 \rangle$ and the square velocities of corn pollen and glass beads. Since both particles are in the same range of Stokes numbers, the square velocities differ only very little. This quantity was not given by ET and can therefore not be compared.

5.2. *Particle dynamics with gravity*

As expected, when gravity is taken into account, particle dynamics are modified. Indeed, the crossing-trajectory effect due to the mean settling velocity of the particles leads to a decrease of the integral time scale of the fluid turbulence viewed by the particles. Such an effect leads to an increase of the effective particle Stokes number and so to an increase of the relative squared velocity with respect to the non-settling case, as shown by figure 9.

After about one turnover time particle square velocity perpendicular to gravity shows qualitatively similar behavior as the experimental values of SL (figure 11). The predicted

† The index $_0$ is used for values at the dimensionless time $T = 2.67$ as in SL.

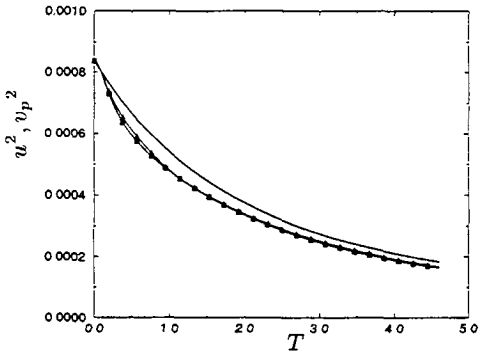

FIGURE 10. Evolution of dimensionless squared velocities without gravity in the present simulation: carrier phase ——— corn pollen —▲— , glass beads —■— .

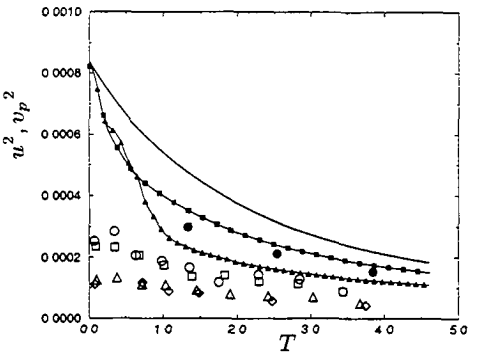

FIGURE 11. Evolution of dimensionless squared particle velocities (perpendicular to gravity) with gravity: experiment (SL) carrier phase • , experiment (SL) hollow glass ○ , experiment (SL) corn pollen □ , experiment (SL) glass beads △ , experiment (SL) copper △ , present simulation carrier phase ——— , present simulation corn pollen —■— , and present simulation glass beads —▲— .

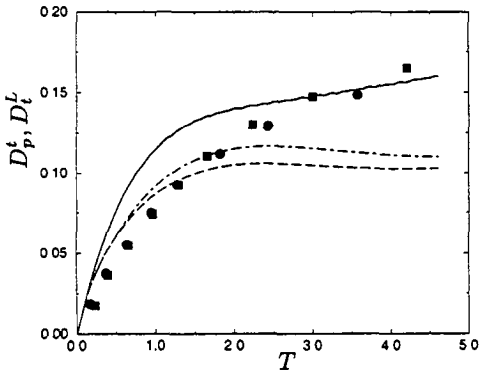

FIGURE 12. Evolution of the dispersion coefficient without gravity: Lagrangian simulation (ET) carrier phase • , Lagrangian simulation (ET) corn pollen ■ , present simulation fluid particle ——— , present simulation corn pollen - - - - , and present simulation glass beads —·—

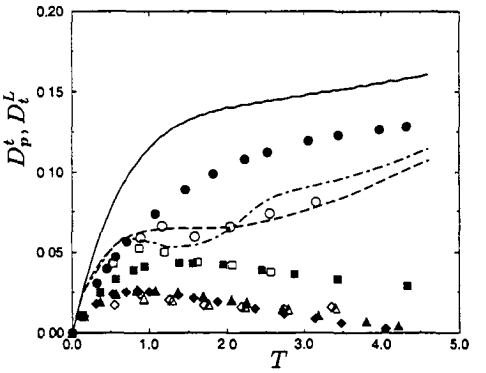

FIGURE 13. Evolution of the dispersion coefficient with gravity: experiment (SL) hollow glass ○ , experiment (SL) corn pollen □ , experiment (SL) glass beads △ , Lagrangian simulation (ET) carrier phase • , Lagrangian simulation (ET) corn pollen ■ , present simulation carrier phase ——— , present simulation corn pollen - - - - , and present simulation glass beads —·—

particle square velocity is larger than the measured one. This may be due to the fact that simulated carrier phase $< u_f^2 >$ is also higher than the experimental value.

6. Particle dispersion

Particle dispersion is measured as explained in section 2.3 for the dispersed phase. In order to compare with the carrier phase, the equivalent of (2.16) is solved for the carrier phase without molecular diffusion. As in the work of ET, dispersion coefficients are normalized by the integral length scale at $T = 2.67$.

6.1. *Particle dispersion without gravity*

Figure 12 shows the evolution of the Lagrangian and Eulerian dispersion coefficient in the simulations without gravity. ET calculated the Lagrangian dispersion without gravity only for the carrier phase and corn pollen. In the Eulerian simulation the carrier phase shows the same qualitative behavior as the Lagrangian simulation of ET, but the dispersion of corn pollen is lower then the dispersion of the carrier phase. As discussed previously (section. 2.3) this might be due to the missing QBM part of the dispersion.

6.2. *Particle dispersion with gravity*

In the Eulerian simulations with gravity, particle dispersion is significantly lower then in the simulations without gravity, consistent with the Csanady (1963) analysis. This observation matches the Lagrangian simulation. Quantitatively, however, dispersion measured in the Eulerian simulations is high compared to Lagrangian simulations.

7. Conclusion

In the first part of this paper it was shown that unsteady Eulerian-Eulerian simulations need to take into account the stress tensor related to the uncorrelated quasi-Brownian motion in the case of inert particles. It is not clear how this term needs to be handled in more complex LES computations, and further investigation of this term is necessary.

In the second part, a preliminary model for QBM was used by relating unresolved particle kinetic energy to the resolved particle kinetic energy by a fixed coefficient. This model allowed simulations to be performed for the experiment of Snyder & Lumley (1971) and to compare the results to the Lagrangian simulations of Elghobashi & Truesdell (1992). Even if the numerical results of the Eulerian simulation do not quantitatively match the Lagrangian simulations exactly, this test showed that Eulerian simulations could be an alternative tool for simulations of dispersed two-phase flows.

REFERENCES

CHAPMAN, S., & COWLING, T.G. 1939 *The Mathematical Theory of Non-Uniform Gases.* Cambridge University Press.

CSANADY, G.T. 1963 Turbulent diffusion of heavy particles in the atmosphere. *J. Atmos. Sci.* **20**, 201–208.

DREW, D.A. & PASSMAN, S.L. 1998 *Theory of Multicomponent Fluids.* Springer Series in Applied Mathematical Sciences vol. 135.

DRUZHINI, O.A. & ELGHOBASHI, S. 1999 On the decay rate of isotropic turbulence laden with micro-particles. *Phys. Fluids* **11**, 602–610.

ELGHOBASHI, S. & TRUESDELL, G.C. 1992 Direct simulation of particle dispersion in a decaying isotropic turbulence. *J. Fluid Mech.* **242**, 655–700.

FÉVRIER P. & SIMONIN, O. 2000 Statistical and continuum modeling of turbulent reactive particulate flows. *VKI Lecture Series* 2000-06.

FÉVRIER, P. 2000 Etude numerique des effets de concentration preferentielle et de correlation spatiale entre vitesses des particles solides en turbulence homogene isotrope stationaire. *PhD Thesis*, INP, Toulouse.

FÉVRIER, P., SIMONIN, O. & SQUIRES, K. D. 2002 On the continous field and quasi-Brownian distribution of particle velocities in turbulent flows: theoretical formalism and numerical study. Submitted to J. Fluid. Mech.

FUCHS, N. A. 1964 *The Mechanics of Aerosols.* Dover, Mineola, NY.

LE VEQUE, R. J. 1996 *Numerical Methods for Conservation Laws.* Birkhäuser, Boston.

MONIN, A. S. & YAGLOM, A. M. 1987 *Statistical Fluid Mechanics*, Vol. 1 MIT Press, Cambridge, MA.

REEKS M. W. 1991 On a kinetic equation for the transport of particles in turbulent flows *Phys. Fluids A* **3**, 446–456.

SNYDER, W. H. & LUMLEY, J. L. 1971 Some measurements of particle velocity autocorrelation functions in a turbulent flow. *J. Fluid Mech.* **48**, 41–71.

SCHÖNFELD, T. & RUDYARD, M. 1999 Steady and unsteady flow simulations using the hybrid flow solver AVBP. *AIAA J.* **37**, 1378–1385.

SIMONIN, O., FÉVRIER, P. & LAVIEVILLE, J. 2002 On the spatial distribution of heavy particle velocities in turbulent flow: From continuous field to particulate chaos. *Journal of Turbulence* **Vol 3**, 40.

SIMONIN, O. 1996 Combustion and turbulence in two-phase flows *VKI Lecture Series* 1996-02.

Center for Turbulence Research
Proceedings of the Summer Program 2002

Analysis and modeling of the dispersion of vaporizing polydispersed sprays in turbulent flows

By J. Réveillon †, M. Massot ‡ AND C. Pera ¶

Direct numerical simulations (DNS) of turbulent two-phase flows have been carried out to study the polydispersion of a vaporizing spray in statistically-stationary grid turbulence. The evolution of various classes of droplet size has been studied, exhibiting different dynamical behavior for droplets of different sizes. The results have been used to evaluate successfully a new Eulerian model, which proves its ability to capture the polydisperse spray dynamics and vaporization.

1. Introduction

In industrial combustion configurations, the fuel is most of the time injected as a dispersed phase of liquid droplets. In gas turbines, diesel engines, industrial furnaces and combustion chambers, the behavior of the gaseous fuel mixture fraction plays a crucial role in determining the combustion characteristics and efficiency of the process. Consequently, the description of the motion of the spray, its vaporization and its coupling with the gaseous turbulent flow field are important for the prediction of two-phase turbulent combustion. Even if the process has to be understood as a whole from injection up to combustion, one of the key issues will be the turbulent mixing and vaporization of the cloud of fuel droplets, a phenomenon strongly influenced by the polydisperse character of the spray. In this paper, we therefore focus our attention on the turbulent dispersion of a vaporizing liquid spray and on its polydispersion.

The purpose of the present study is two-fold: first, we investigate the physics of this phenomenon using a DNS Euler/Lagrange approach in the configuration of statistically-stationary spatially decaying turbulence, with a monodisperse injection. We analyze the DNS results for the dispersed phase from an Eulerian point of view, and demonstrate the strong coupling of the dynamics and vaporization which generates droplets of various sizes. Second, we provide a Eulerian model and description of this phenomenon, extending the recently-introduced Eulerian multi-fluid models which are well suited to the presence of a polydisperse spray. These approaches will then be compared, thus proving the ability of the Eulerian model to capture the physics and the complementarity of Lagrangian and Eulerian tools for the description of two-phase flows.

Two types of models may be actually considered for the description of the polydisperse liquid phase. The first one is of Lagrangian and particular type as described originally by Dukowicz (1980), O'Rourke (1981). The distribution of droplets is approximated using a finite number of computational parcels; each parcel represent a number of droplets of identical size, velocity and temperature. This kind of method is currently used in

† CNRS-UMR 6614 - CORIA - University of Rouen, INSA - Avenue de l'Université, 76801 St Etienne du Rouvray cdx, FRANCE, reveillon@coria.fr, corresponding author
‡ CNRS-UMR5585 - MAPLY, Université Claude Bernard, Lyon 1, 69622 Villeurbanne cdx, FRANCE, massot@maply.univ-lyon1.fr
¶ CNRS-UMR 6614 - CORIA, pera@coria.fr

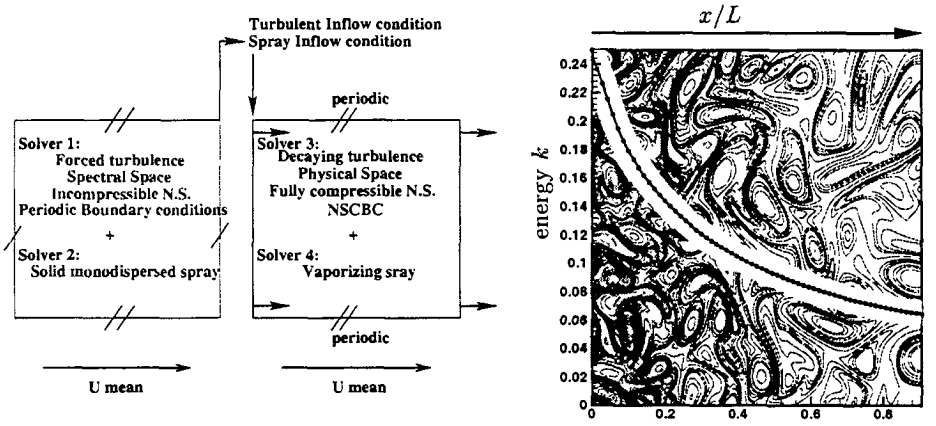

Light	τ_p/τ_v	τ_p/τ_t	evaporation	Heavy	τ_p/τ_v	τ_p/τ_t	evaporation
T0V0	195	0.06	$s = cte$	**T2V0**	3.5	3.3	$s = cte$
T0V1	195	0.06	$s/s_0 = 1 - t/\tau_v$	**T2V1**	3.5	3.3	$s/s_0 = 1 - t/\tau_v$

FIGURE 1. Left: sketch of the coupling between the four solvers, right: vorticity isocontours of the decaying turbulence, bottom: data concerning the injected droplets for each simulation.

many codes and is especially suited for DNS calculations since it does not introduce any numerical diffusion, the particle trajectories in the phase space being exactly resolved. It is then particularly accurate as long as the sampling of the phase space is rapid enough, a constraint that becomes expensive for unsteady flows.

In the context of RANS and LES numerical simulations, where some scales are not resolved but modeled, the perspective of a Eulerian model for polydisperse sprays becomes very attractive. Indeed, it is interesting to study the Eulerian form of the spray equations and to deduce the structure of physical phenomena such as waves, diffusion, etc. On another hand, modeling of coalescence and break-up phenomena, as well as the coupling with the combustion process, is more straightforward using an Eulerian formulation. Besides, a coherent way of treating the two phases yields a better ability for parallel computations and optimization.

The existing Eulerian models belong to the broad class of moment methods and can be subdivided into two general branches. On the one side, the population-balance methods usually consider very small particles without inertia. They are concerned with a precise description of the size distribution which evolves due to vaporization, aggregation or breakage – see e.g. Wright et al. (2001), Marchisio, Vigil & Fox (2002) – and usually rely on the method of quadrature of size moments. On the other side, the classical two-fluid models have been the subject of many publications, either in the mathematics community by Sainsaulieu (1991), Domelevo & Sainsaulieu (1997) or in the engineering one (see Kaufmann et al. (2002) and references therein). Their validity extends up to churning flows where the liquid phase is not dispersed any more such as near the injector (Vallet et al., 2001) or for interface phenomena such as in Chanteperdrix et al. (2002).

However, actual Eulerian models present two major drawbacks: the inability to capture the polydispersion in size of the spray (only through a couple of moments such as in Vallet

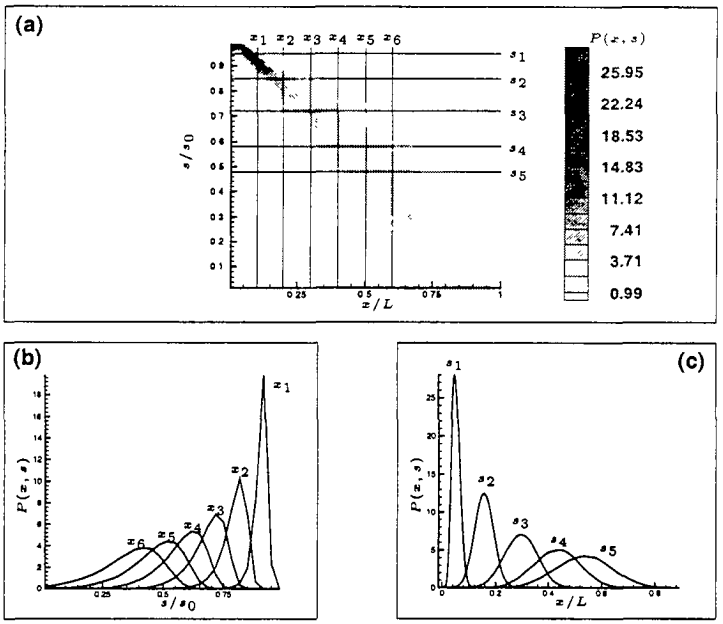

FIGURE 2. Isocontours (top) and profiles (bottom left and right) of the pdf $P(s,x)$. The profiles are made along both x (bottom right) and s (bottom left) directions for several different positions shown on the top figure. $x_1/L = 0.092$, $x_2/L = 0.198$, $x_3/L = 0.304$, $x_4/L = 0.41$, $x_5/L = 0.516$, $x_6/L = 0.622$, and $s_1/s_0 = 0.95$, $s_2/s_0 = 0.85$, $s_3/s_0 = 0.72$, $s_4/s_0 = 0.58$, $s_5/s_0 = 0.48$

et al., 2001) and the lack of direct link with the kinetic level of description for sprays. Thus, in the context of laminar flows, Laurent and Massot (2001) have introduced a multi-fluid approach, rigorously derived from the kinetic level of description, which has the capability to include coalescence and break-up as shown in Laurent et al. (2001) and to describe the vaporization, dynamics and heating of droplets of various sizes as studied in Laurent et al. (2002). In order to extend the work done in these papers to turbulent flows and derive a kinetic model "in the mean" where an ensemble averaging is performed on some scales, we make use of the results introduced by Reeks (1991) and proved by Clouet and Domelevo (1997), and connect with the work on Eulerian analysis of the turbulent dispersion of particles initiated by Taylor (1921) and Batchelor (1949). An Eulerian system of semi-fluid equations is obtained by preserving the size phase space but considering some velocity-moment closure. We then show the ability of such an approach to capture the physics of the turbulent dispersion of a vaporizing spray by comparing with success the results from the Eulerian model to DNS statistics. We show in particular that the use of surface-conditioned moments is really well-suited to characterize the phenomenon and to obtain a precise Eulerian description.

The paper is organized as follows: in a second section, the physical configuration and numerical methods are presented. We then focus on the analysis of the DNS results where we emphasize a surface-conditioned Eulerian analysis of the polydisperse spray. We then conduct, in a fourth section, the derivation of the Eulerian model and present the numerical method used in the particular configuration under consideration. The DNS results and the simulations obtained from the Eulerian solver are then compared in the last section.

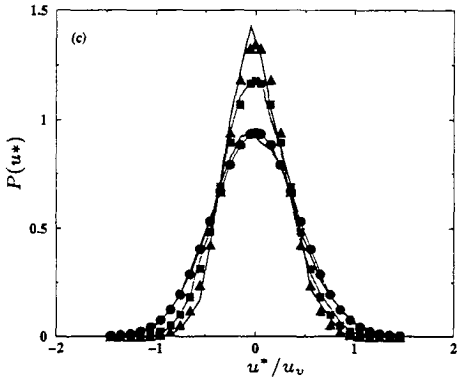

FIGURE 3. Profiles of $P(u)$, lines: DNS extracted, symbols: corresponding Gaussian reconstruction (circles: x_1, squares: x_3 and triangles: x_6).

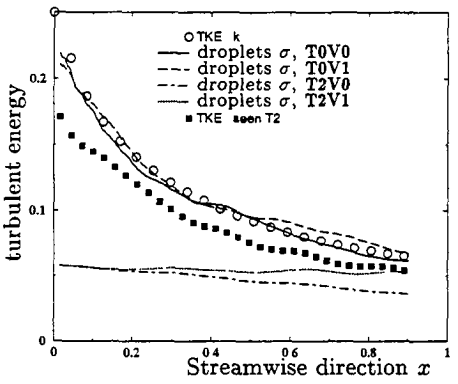

FIGURE 4. Comparison of the spatial evolution of the droplets energy σ with the gas turbulent kinetic energy k.

2. Geometry and numerical considerations

In this paper, a geometry with one inhomogeneous direction has been considered: 2D spatially-decaying turbulence (SDT) with statistically-stationary properties. It simulates grid turbulence with a high kinetic energy at the inlet that decays in the streamwise direction. A monodisperse spray is injected through the inlet boundary and follows the main flow while being locally dispersed by the turbulent fluctuations. It is particularly interesting to notice that the coupling of vaporization and turbulent mixing generates a polydisperse spray, even if the liquid phase is injected monodisperse. This configuration is also a good candidate since the number of dimensions of the phase space remains reasonable.

To ensure statistically-coherent behavior of the injected droplets with local turbulence, four solvers (figure 1) are running simultaneously. An independent spectral code is solving the incompressible Navier-Stokes (NS) equations, coupled with a one-way Lagrangian solver for the computation of the dispersion of solid particles. These two solvers are used to generate accurate turbulent boundary conditions for a physical-space DNS solver (sixth order in space and third order in time) running together with another one-way Lagrangian solver. The fully-compressible NS equations are then solved with periodic boundary conditions along the spanwise direction, and NS characteristic boundary conditions (Poinsot and Lele, 1992) for the inlet and the outlet along the streamwise direction.

Forced turbulence, such as in Overholt and Pope, 1998, is simulated in the spectral space so that the prescribed main properties of the turbulence (kinetic energy, dissipation, integral scale) are statistically stationary in time. The dispersion of particles in the phase space was checked to be in dynamical equilibrium before the coupling with the physical space solvers took place.

This coupling is done through the inlet boundary of the physical space solver where the turbulent fluctuations as well as the incoming particles are inserted. Because of the presence of the spectral solver, the vortices are really able to rotate at the boundary and therefore, local negative velocities may be considered. The technical details of the injection procedure may be found in Vervisch-Guichard et al. (2001). Once injected in the physical space DNS, the previously-solid particles are considered as droplets of liquid

and they vaporize, following a *d-square* law, and undergo the effects of drag forces. Again, a one-way interaction with the turbulent flow is used to describe the dispersion of the droplets. It allows us to keep identical turbulence parameters while the spray properties are modified.

Before presenting the various test cases and results of this work, normalization parameters should be introduced. They are based on the properties of the flow and the spray. The droplet geometry is expressed in term of a surface and it is normalized by their unique (monodisperse) injection value s_0. The motion of the droplets in the gaseous flow and their evaporation rate lead to the characteristic times τ_p and τ_v; τ_p is the velocity response time (or kinetic time) of the droplets, quantifying their ability to follow or not the fluctuations of the flow, and $\tau_v = -s_0/\mathcal{R}$ is the vaporization time based on the initial size. They have to be compared with τ_t, the turbulent eddy turnover time. It leads to the following normalized *d-square* law: $s/s_0 = 1 - t/\tau_v$. The other parameters are the career phase mean velocity $\overline{\mathbf{U}}$ and consequently, the characteristic distance $L = \overline{\mathbf{U}} * \tau_v$ covered by a droplet before its total vaporization.

3. Spray turbulent dispersion

3.1. *Statistical considerations*

The study of the dispersion of droplets in spatially-decaying turbulence implies to define some new parameters. An individual tracking has been introduced for every droplet in the flow whose Lagrangian time, position, velocity and surface are $(t_l,\ \mathbf{x_d},\ \mathbf{V}_d,\ s_d(t_l))$. As soon as a droplet is injected and begins to evaporate, it is associated to a 'reference particle' whose initial properties $(t_l,\ \mathbf{x_r},\ \overline{\mathbf{U}},\ s_r = s_d)$ are the same. The reference particle travels at the mean streamwise velocity, whereas its corresponding droplet is affected by turbulent fluctuations. By statistically studying the difference of position and velocity between the real droplet and its 'reference', we may characterize the turbulent dispersion. The dispersion statistics are then deduced from the following parameters: $\mathbf{x}^* = \mathbf{x_d} - \mathbf{x_r}$, $\mathbf{v}^* = \mathbf{V_d} - \overline{\mathbf{U}}$ and $\xi = s_d - s_0(1 - x_d/L)$. ξ is the relative surface between the tracked droplet and a droplet that would be at the same position if unaffected by turbulence.

Statistics are considered in time and along the spanwise direction. Therefore the mean value of any Eulerian variable $A(x, y, t)$ is defined by the following relation

$$\overline{A}(x) = \frac{1}{T}\int\left(\frac{1}{L_y}\int\int A(x,y,t)dy\right)dt. \tag{3.1}$$

3.2. *Spray polydispersion*

Figure 2-(a) shows an example of the evolution of the coupled PDF: $P(x, s)$ of the droplets streamwise position x and their surface s. It allows us to observe the **joint** effects of the evaporation and of the turbulence on the injected spray. Several positions of analysis along both x and s directions have been plotted. These positions, labeled respectively x_i ($i = 1$ to 6) and s_j ($j = 1$ to 5), have been extensively used in this work. The profiles of $P(x, s)$ along the x direction for the fixed surfaces s_j show (figure 2(c)) a symmetrical Gaussian dispersion around a reference position $x_j^r/L = (1 - s_j/s_0)$ corresponding to the position of a droplet with the same s_j surface but which was not affected by turbulence. Similarly, a spreading of the droplets surface may be observed (figure 2(b)) for a given x_i streamwise position. But, in contrast with the previous profiles, the dispersion is not symmetric around the reference surface $s_i^r/s_0 = (1 - x_i/L)$, corresponding to the surface of a vaporizing droplet moving with the reference velocity $\overline{\mathbf{U}}$.

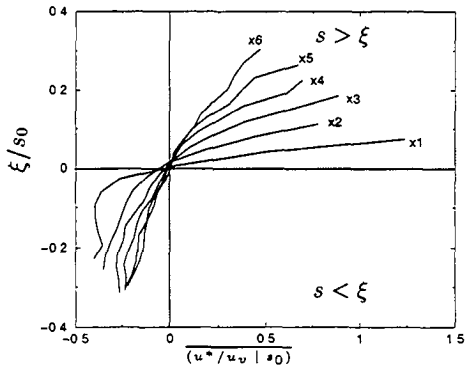

FIGURE 5. Mean droplet velocity conditioned by the droplet surface (**T0V1**, Eulerian positions: x_i, $i = 1, 6$).

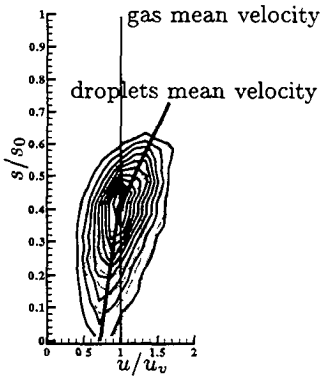

FIGURE 6. Comparisons of the spray velocity dispersion function $P(u, s)$ (black lines) with an assumed Gaussian shape dispersion function (dotted lines), case **T0V1**, Eulerian position: x_6.

It is possible to examine the PDF: $P(u^*)$ corresponding to the droplet velocity fluctuations with respect to the gas mean flow. Indeed, as will be shown later, a distinction has to be made between the gas-phase mean velocity and the particle mean velocity. The u^* statistics have been evaluated for all droplets without distinction of class, and a Gaussian shaped dispersion may be observed along the streamwise direction. Figure 3 shows that $P(u^*)$ develops a general Gaussian shape centered on $u^* = 0$. Three profiles of $P(u^*)$ extracted from the DNS are plotted in figure 3(a) along with the corresponding PDF deduced from the first two moments $(\overline{u}^*, \sigma)$ of the velocity dispersion. A Gaussian shape function (4.3) has been used, and σ has been determined from the values of $P(u^*)$ extracted from the DNS. The assumed Gaussian shape and the DNS data are similar. This confirms a Gaussian behavior of dispersion for the droplets considered as a whole, without reference to their size. Moreover, the fact that the Gaussian curves are centered on $u^* = 0$ shows that the mean droplet velocity is equal to the mean flow velocity (as long as the droplets are not considered by classes).

The droplet energy σ has been determined for every streamwise position and is compared to the decaying kinetic energy k of the gas flow in figure 4. For each droplet family, vaporizing and non-vaporizing cases have been plotted. As expected, it is possible to observe a mass-dependent behavior of the droplets. The light droplets (**T0Vx**, x= 0, 1), with a small Stokes number ($S_t = 0.06$), closely follows the turbulent fluctuations of the gas. As soon as the droplets' mass (and therefore Stokes number) increases (**T2Vx**), the inertia of the droplets is increasingly significant and they no longer exactly capture the fluctuations of the carrier phase. Thus, for a given spray, three energy levels can be differentiated according to the characteristic kinetic time of the droplets: k the real level of the gas kinetic energy, κ_p the level seen by the droplets and σ the level reached by the droplets. For light droplets with small τ_p, these levels coincide. As soon as τ_p increases, the three levels are differentiated with a fixed hierarchy: $k > \kappa_p > \sigma$.

3.3. *Surface-conditioned dispersion*

The spray is initially monodisperse but it undergoes the effects of both droplet vaporization and turbulent mixing. These two phenomena lead to a polydisperse spray in both x

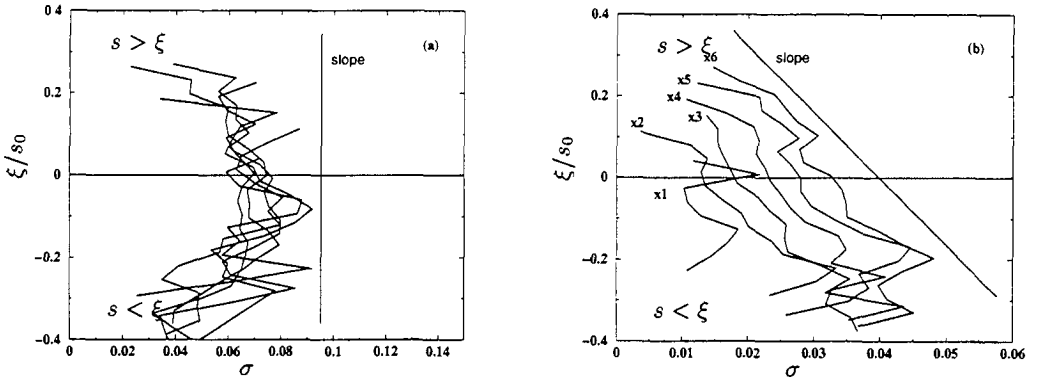

FIGURE 7. Droplet velocity dispersion parameter σ as a function of the droplet relative surface ξ. Left: **T0V1** case, the profiles are similar, right: **T1V1** case a significant effect of the droplet volume may be observed on the dispersion.

and s directions of the phase space. In the previous section it was shown that the spray position dispersion for a fixed droplet surface follows a Gaussian behavior. Now, it seems interesting to focus on the velocity behavior of the droplets considered class by class.

First, from an analytical point of view, it is possible to affirm that the mean velocities of the droplets depend on their surface for a given Eulerian position x. At any x position, by using the reference parameters ξ and u^*, we know that the droplets such as $\xi = 0$ and $u^* = 0$ have the same mean properties as the reference droplets which are supposed unaffected by the turbulence. If $\xi > 0$, then the droplet surface is larger than the reference one. Thus, these droplets traveled more quickly than the average flow. In the same way, the droplets such as $\xi < 0$ went more slowly. This is confirmed by figure 5 where the mean droplet velocity conditioned by droplet surface $\overline{(u^* \mid \xi)}$ has been plotted. The analysis has been done for several Eulerian positions previously defined (figure 2). Close to the injection (x_1), the surface range dispersion is limited but, because of the high turbulent energy of the flow, velocity levels of the droplets are the highest. As the droplets move away in the flow, their surface range increases but their mean velocity range decreases because of the weaker turbulent mixing.

The conditioned mean velocity being known, it is now particularly interesting to focus on the velocity dispersion of the droplets around this mean. Figure 6 shows, for a given streamwise position, the PDF $P(u, s)$ representing the velocity dispersion as a function of the droplet surface. Gaussian reconstructions around this mean value have been carried out. The deduced isocontours are shown figure 6 (dotted contours) and are very close to the dispersion levels extracted from the DNS (plain contours). It appears that even by considering the dispersion as a function of the droplets surface, it follows a Gaussian law. But this is true only around the mean velocity of the particles and not around the local mean velocity of the gas flow, the two of them being different. Moreover, an integration of the dispersion along the s direction gives a global Gaussian dispersion around the mean flow velocity (figure 3). But the corresponding energy σ is a global property for the whole spray and it does not allow a description of the dynamic of every class of droplets. This dynamic depends strongly on the mass of the droplets; thus, to have an accurate description of their dispersion, a surface dependence should be introduced in any model developed to describe the dispersion of evaporating or polydisperse droplets.

Examples of the surface-conditioned energy $\sigma(\xi)$ are shown figure 7 for both **T0V1**

and **T2V1** cases. The statistics have been extracted for the reference Eulerian positions and correspond to the agitation energy of the droplets around their mean velocity. For the whole Eulerian positions, the light droplets have a similar $\sigma(\xi)$ whatever the droplet surface is. In fact, even the 'heaviest' ($\xi > 0$) of the light droplets (**T0V1**) are small and follow the turbulent fluctuations of the carrier phase without noticeable damping due to their inertia. Therefore, $\sigma(\xi)$ is almost constant for every value of the surface. On another hand, the vaporizing heavy droplets case (**T2V1**) leads to another conclusion. Indeed, because of their large Stokes number, the droplets prove to have an inertial behavior, going through turbulent structures without fully undergoing every one of them. Two main conclusions can be drawn from the figure 7-(b). First of all, for every increasing analysis Eulerian position (x_1, x_2, ...) the general energy level $\sigma(\xi)$ increases as well, because the droplets' loss of mass implies a decrease of the effects of their inertia. In the same way, for a given analysis position, the dependence of $\sigma(\xi)$ on the surface of the droplets (ξ) is significant and has a quasi-linear behavior.

4. Multi-fluid modeling

The fact that the turbulent dispersion of a vaporizing spray is a surface-conditioned phenomenon is very coherent with the work done on the Eulerian multi-fluid modeling of polydisperse sprays conducted by Laurent and Massot (2001). The purpose of this section is to present the derivation of such an approach in the turbulent case and the associated numerical methods.

4.1. *Derivation of the model*

The spray is described at the kinetic level by a distribution function $f(t, x, s, \boldsymbol{V}_d)$ which satisfies a transport equation introduced by Williams (1958):

$$\frac{\partial f}{\partial t} + \boldsymbol{V}_d \cdot \nabla_x f + \frac{\partial \mathcal{R} f}{\partial s} + \nabla_{\boldsymbol{V}_d}(\mathcal{F} f) = 0, \tag{4.1}$$

where $\mathcal{F}$ is the Stokes-drag acceleration. The vaporization rate $\mathcal{R}$ is assumed to be independent of $\boldsymbol{U}$, thus neglecting the convective correction term (see Laurent and Massot (2001) for detailed modeling assumptions).

For turbulent flows, the gas velocity seen by the particles can be decomposed into $\boldsymbol{U} = \overline{\boldsymbol{U}} + \boldsymbol{U}'$, where $\overline{\boldsymbol{U}}$ is its average value and $\boldsymbol{U}'$ is a fluctuation which is assumed to be a Gaussian Wiener process characterized by a Lagrangian correlation time along the trajectories τ_d as well as a turbulent kinetic energy κ_p. It is at this level that we can choose the scales which will be resolved. In this paper, for the first investigation of the Eulerian multi-fluid model, we will consider that the fluctuation describes the whole of the gas turbulence and the average value will be taken as the mean gas velocity. The LES point of view will be investigated in a subsequent study.

Once the scales have been chosen we need to derive a kinetic equation "in the mean" where the effects of the gas turbulence appear only through its characteristic quantities τ_d and κ_p. We use the framework introduced by Reeks (1991) and justified rigorously by Clouet and Domelevo (1997). We obtain an averaged equation for $\bar{f}$, which is the statistical expectation of f; it reads

$$\frac{\partial \bar{f}}{\partial t} + \boldsymbol{V}_d \cdot \nabla_x \bar{f} + \frac{\partial \mathcal{R} \bar{f}}{\partial s} + \nabla_{\boldsymbol{V}_d}(\bar{\mathcal{F}} \bar{f}) - \nabla_{\boldsymbol{V}_d} \cdot \left(D_x \nabla_x \bar{f} + D_{\boldsymbol{V}_d} \nabla_{\boldsymbol{V}_d} \bar{f} \right) = 0, \tag{4.2}$$

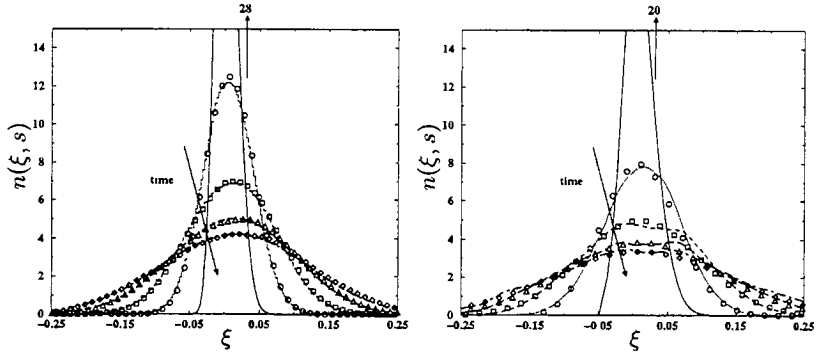

FIGURE 8. Droplet number density in a frame moving with the mean flow for various droplet sizes (or Lagrangian times). Symbols: DNS statistics (circles: s_2, squares: s_3, trianglesd: s_4, diamonds: s_5). Lines (**left**): Eulerian simulations of system (4.4-4.6), **T2V1** case and lines (**right**): Eulerian simulations of the diffusion equation (4.7), **T0V1** case.

where the averaged drag force is

$$\bar{\mathcal{F}} = \frac{1}{\tau_p\, s}(\overline{\boldsymbol{U}} - \boldsymbol{V}_d).$$

The random fluctuations in the gas velocity then generate, on average, a diffusion process in the phase space. This approach requires the use of a simple vaporization model, which decouples the vaporization process from the velocity fluctuations; in a more general case, some additional terms should be added in (4.2). An exact expression of the diffusion coefficients can be obtained as functions of τ_d and κ_p along the lines given in Clouet and Domelevo (1997), Reeks (1991). These coefficients appear in the averaging process where one has to evaluate the statistical expectation of $\boldsymbol{E}(f\boldsymbol{U}')$. This expectation can be proved, under the assumptions made on the alea $\boldsymbol{U}'$, to be a combination of two terms $D_x\, \nabla_x \bar{f} + D_{V_d}\, \nabla_{V_d} \bar{f}$ where the coefficients are deduced from a characteristics analysis.

Once the kinetic equation "in the mean" is derived, we can generalize the framework of the Eulerian multi-fluid model to the present case. As in Laurent and Massot (2001), we make an assumption on $\bar{f}$ which appears as a closure at the kinetic level. We assume that, for a given size, there is only one characteristic velocity, with a Gaussian dispersion around it:

$$\bar{f}(t, x, s, \boldsymbol{V}_d) = n(t, x, s)\, \varphi_{\sigma(t,x,s)}(\boldsymbol{V}_d - \tilde{\boldsymbol{V}}_d(t, x, s)),$$

where φ_σ is a Gaussian of dispersion σ in the d-dimensional space:

$$\varphi_\sigma(v) = \frac{1}{\left(\frac{4}{d}\pi\sigma\right)^{d/2}} \exp\left(-\frac{v^2}{\frac{4}{d}\sigma}\right). \tag{4.3}$$

We will then obtain the semi-fluid equations on the three moments n, $\tilde{\boldsymbol{V}}_d$ and σ, which can be interpreted as an internal energy of a monoatomic gas. It is worth noting that this is a very natural introduction of the "quasi-Brownian" motion in Kaufmann et al. (2002).

We introduce the non-dimensional quantities $\overline{V} = (\overline{\mathbf{V}}_d - \overline{\mathbf{U}})/\overline{\mathbf{U}}$ and $\bar{\sigma} = \sigma/\overline{\mathbf{U}}^2$. From the equation (4.2), we obtain a non-dimensional Eulerian semi-fluid model:

$$\frac{\partial n}{\partial \tau} + \nabla_\xi \cdot (n\overline{V}) - \frac{\partial n}{\partial \bar{s}} = 0 \tag{4.4}$$

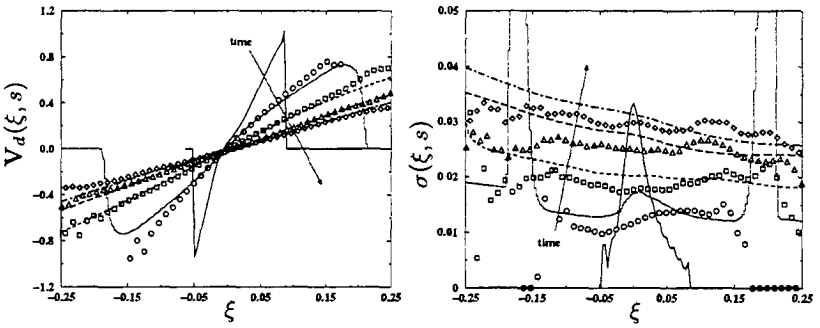

FIGURE 9. Evolution of droplets mean velocity **left** and droplets internal energy **right** in the frame moving with the mean for various droplet sizes in the **T2V1** case. Symbols: DNS statistics (circles: s_2, squares: s_3, triangles: s_4, losanges: s_5). Lines: Eulerian simulations of system (4.4-4.6).

$$\frac{\partial n\overline{V}}{\partial \tau} + \nabla_\xi \cdot \left(n\overline{V} \otimes \overline{V} + n\frac{2}{3}\bar{\sigma}\mathbf{I} \right) - \frac{\partial n\overline{V}}{\partial \bar{s}} = -\frac{\tau_v}{\tau_p} n\overline{V} - \bar{D}_x \nabla_\xi n \tag{4.5}$$

$$\frac{\partial}{\partial \tau}\left[n\left(\frac{\overline{V}^2}{2} + \bar{\sigma} \right) \right] + \nabla_\xi \cdot \left(n\left(\frac{\overline{V}^2}{2} + \bar{\sigma} \right) + n\frac{2}{3}\bar{\sigma}\overline{V} \right) - \frac{\partial}{\partial \bar{s}}\left[n\left(\frac{\overline{V}^2}{2} + \bar{\sigma} \right) \right]$$

$$= -2n\frac{\tau_v}{\tau_p}\left(\frac{\overline{V}^2}{2} + \bar{\sigma} \right) - \bar{D}_x \nabla_\xi \cdot (n\overline{V}) + d\, n\, \bar{D}_{\mathbf{V}_d} \tag{4.6}$$

where $\bar{D}_x = D_x/\overline{\mathbf{U}}^2$ and $\bar{D}_{\mathbf{V}_d} = \tau_v D_{\mathbf{V}_d}/\overline{\mathbf{U}}^2$. In the case $\sigma = 0$, $D_x = 0$ and $D_{\mathbf{V}_d} = 0$, we recover the equations used in the laminar case derived in Laurent and Massot (2001). So far the term "multi-fluid" was used for the upwind discretization in the size variable of the semi-fluid model. However, since the semi-fluid model is also composed of a continuous superposition of "fluids" which correspond to the surface conditioned velocity moments, we will indifferently call it semi-fluid or multi-fluid in this paper.

In the case of very small droplets, D_x takes the following asymptotic expression:

$$D_x \approx \frac{2}{d}\kappa_p \frac{\tau_d}{\tau_p}.$$

The source term in the momentum conservation equation (4.4) then reads

$$-\frac{\tau_v}{\tau_p}\left(n\overline{V} + \frac{2}{d}\frac{\tau_d \kappa_p}{\tau_v \overline{\mathbf{U}}^2}\nabla_\xi n \right).$$

and can be considered, in the formal singular limit of small s, to be zero. This provides an expression for the mass flux in equation (4.4) which can be rewritten

$$\frac{\partial n}{\partial t} - \nabla_\xi \cdot (\mu \nabla_\xi n) - \frac{\partial n}{\partial \bar{s}} = 0, \tag{4.7}$$

with $\mu = 2\tau_d \kappa_p/(d\,\tau_v\,\overline{\mathbf{U}}^2)$. Consequently, if we consider the gas turbulence in the white noise limit, i.e. when τ_d approaches zero and turbulence induces a diffusion process in the velocity phase space only (Chandrasekhar (1943), Lightstone and Raithby (1998)), we cannot retrieve the diffusion process in the limit of small particles. Let us also notice that the singular perturbation analysis allows us to relate $\mathbf{V}_d$ and σ to the number density

field n once it is evaluated by solving (4.7). We then not only recover the usual spatial diffusion equation in the limit of small droplets, where the diffusion coefficient is related to a Lagrangian correlation time and a diffusion process coupled to the vaporization one. It is possible to recover as well the relation between the number density field, the associated velocity and the internal energy through the diffusion coefficients $\bar{D}_x$ and $\bar{D}_{V_d}$.

4.2. *Resolution and results*

It is interesting to notice that the system (4.4-4.6), in the stationary configuration considered, is exactly related to the classical one-dimensional Euler equations where the time has become $1-s$ and where the turbulent dispersion comes into play through source terms involving the defined diffusion coefficients. An initial surface $s_1 = 0.95$ is selected close to the injection point. Initial fields of density, velocity and internal energy as a function of ξ are extracted from the s_1 DNS profiles. The resulting initial value problem for the system of equation is then resolved using a MUSCL second-order extension of a finite-volume method with a minmod slope limiter and explicit second-order time discretization on a fine discretization, which is practicable in this one-dimensional problem.

Comparisons between DNS statistics issued from the Lagrangian dispersion of the droplets and the Eulerian resolution of the multi-fluid model are shown in figures 8 and 9. For both heavy (**T2V1**) and light (**T0V1**) droplets, the evolution of the density of droplets is accurately captured by the multi-fluid formulation (figure 8). Moreover, in the case **T2V1** where the droplets are not strictly following the gas evolution, the Eulerian resolution of the evolution of the droplets' conditioned velocity and internal energy has been captured by the model (figure 9).

5. Conclusions

For the first time, comparisons between a DNS (coupled with a Lagrangian solver) of a statistically stationary turbulent two-phase flow and an Eulerian model dedicated to spray dispersion have been carried out. DNS showed its ability to capture the evolution of some complex interactions between the flow and the vaporizing droplets. Then, the Eulerian multi-fluid model has been resolved and compared with the DNS results. The multi-fluid model proved able to capture the evolution of a polydisperse vaporizing spray in a turbulent environment. This is a very encouraging result for the modeling of complex configurations such as combustion chambers. Indeed, even if more tests and development are needed, the multi-fluid formulation may be an alternative to the actual Lagrangian model, which may have difficulties in representing some phenomena such as coalescence or breakup of the droplets.

Acknowledgments

The authors wish to thank the members of the CTR Summer Program. In particular, the help of their CTR hosts Dr. S. Apte and Dr. H. Pitsch is gratefully acknowledged.

REFERENCES

BATCHELOR G. K. 1949 Diffusion in a field of homogeneous turbulence. I. Eulerian analysis. *Australian J. Sci. Research. Ser. A.***2**, 437–450.

CHANDRASEKHAR S. 1943 Stochastic problems in physics and astronomy. *Rev. Mod. Phys.* **15**, (1).

CHANTEPERDRIX G., VILLEDIEU P. AND VILA J.P. 2002 A compressible model for separated two-phase flows computations *ASME/ FEDSM'02 Paper* 31141.

CLOUET J. F.AND DOMELEVO K. 1997 Solution of a kinetic stochastic equation modeling a spray in a turbulent gas flow. *Math. Models Methods Appl. Sci.* **7**, 239–263.

DOMELEVO K. & SAINSAULIEU L. 1997 A numerical method for the computation of the dispersion of a cloud of particles by a turbulent gas flow field. *J. Comput. Phys.* **133**, 256–278.

DUKOWICZ, J.K. 1980 A particle-fluid numerical model for liquid sprays. *J. Comput. Phys.* **35**, 229–253.

KAUFMANN A., POINSOT T., AND SIMONIN O. 2002 Les of turbulent two-phase flows using an eulerian-eulerian approach. In *Proceedings of the Summer Program 2002*, Center for Turbulence Research, NASA Ames/Stanford Univ.

LAURENT L. AND MASSOT M. 2001 Multi-fluid modeling of laminar poly-dispersed spray flames, origin, assumptions and comparison of the sectional and sampling methods. *Combust. Theory and Modelling* **5**, 537–572.

LAURENT F., MASSOT M., AND VILLEDIEU P. 2001 Eulerian multi-fluid modeling for the numerical simulation of polydisperse dense liquid spray. Preprint, MAPLY, UMR 5585 Lyon. (http, //maply.univ-lyon1.fr/publis/publiv/2001/335/publi.ps.gz). g

LAURENT F., SANTORO V., NOSKOV N., GOMEZ A., SMOOKE M.D., AND MASSOT M. 2002 Accurate treatment of size distribution effects in polydispersed spray diffusion flames, multi-fluid modeling, computations and experiments. Preprint, MAPLY, UMR 5585 Lyon. (http, //maply.univ-lyon1.fr/publis/publiv/2002/publis.html).

LIGHTSTONE M.F. AND RAITHBY G.D. 1998 A stochastic model of particle dispersion in a turbulent gaseous environment. *Combustion and Flame* **113**, 424–441.

MARCHISIO D.L., VIGIL R.D. & FOX, R.O. 2002 Quadrature method of moments for aggregation-breakage processes. *J. of Colloid and Interface Science*, to appear.

O'ROURKE, P.J. 1981 *Collective drop effects on vaporizing liquid sprays. PhD thesis*, University of California/Los Alamos National Laboratory.

OVERHOLT AND POPE, S. B. 1998 A deterministic forcing scheme for direct numerical simulation of turbulence. *Computer and Fluid*, **27**,11-28.

POINSOT, T. AND LELE, S. K. 1992. Boundary conditions for direct simulations of compressible viscous flows. *J. Comput. Phys.*, **1(101)**,104-129.

REEKS M. W. 1991 On a kinetic equation for the transport of particles in turbulent flows. *Phys. Fluids*, 3, 446–456.

SAINSAULIEU L. 1991 *Modélisation, Analyse Mathématique et Numérique d'écoulements diphasiques constitués d'un brouillard de gouttes.* PhD thesis, Ecole Polytechnique.

TAYLOR G. I. 1921 Diffusion by continuous movements. *Proc. R. Soc. London*, 20, 421–478.

VALLET A., BURLUKA A.A., AND BORGHI R. 2001 Development of an Eulerian model for the "atomization" of a liquid jet. *Atomization and Sprays*, 11(5), 521–544.

VERVISCH-GUICHARD, L., RÉVEILLON, J., AND HAUGUEL, R. 2001 Stabilization of a turbulent premixed flame. *Proceedings of the second Symposium on turbulent shear flows phenomena, Stockholm, June 2001.*

WILLIAMS F.A. 1958 Spray combustion and atomization. *Phys. Fluids*, 1, 541–545.

WRIGHT, D. L., MCGRAW, R. & ROSNER D. E. 2001 Bivariate extension of the quadrature method of moments for modeling simultaneous coagulation and sintering of particle populations. *J. of Colloid and Interface Sci.*, 236, 242–251.

Participants' Countries/Institutions

Country	Institution
Australia	University of Melbourne
Belgium	Universite Libre de Bruxelles Universite Catholique de Louvain
China	Institute of Mechanics, Chinese Academy
France	C.N.R.S. at Ecole Centrale Paris CERFACS Electricite de France (EDF) University Claude Bernard-Lyon University de Rouen University of Montpellier
Germany	Technische Universitat Munchen
Italy	Italian Ship Model Basin (INSEAN) Italian Aerospace Research Center (CIRA) University of Rome
Japan	Kyoto University
Netherlands	Delft University of Technology
Norway	Norwegian Defense Research Establishment
Spain	Universite Politecnica de Madrid
Switzerland	Swiss Federal Institute of Technology Zurich
USA	City College of New York Colorado Research Associates Cornell University Iowa State University Rice University, Texas Sandia National Laboratories, New Mexico Stanford University University of Califonia at Riverside University of Illinois at Urbana University of Utah University of California at San Diego